EQUATORIAL PALEOMAGNETIC DIRECTION AND PALEOINTENSITY STUDIES ON LAVA FLOWS FROM GALAPAGOS FOR THE PLIOCENE-PLEISTOCENE

by

HUAPEI WANG

A Dissertation submitted to the

Graduate School-New Brunswick

Rutgers, The State University of New Jersey

in partial fulfillment of the requirements

for the degree of

Doctor of Philosophy

Graduate Program in Geological Sciences

written under the direction of

Dr. Dennis V. Kent

and approved by

_____

_____

_____

_____

New Brunswick, New Jersey

JANUARY, 2014

ABSTRACT OF THE DISSERTATION

Equatorial Paleomagnetic Direction and Paleointensity Studies on Lava Flows from Galapagos for the Pliocene-Pleistocene

By Mr. Huapei Wang

Dissertation Director:

Dr. Dennis V. Kent

The current geomagnetic field (GMF) of the Earth is mostly geocentric dipolar with directions on the equatorial regions being horizontal and on the polar regions being vertical, while the field intensities in polar regions (~60 μT) are about twice as much as in equatorial regions (~30 μT). Previous time average field initiative (TAFI) studies suggested that the average directions of the geomagnetic field for the Pliocene-Pleistocene time period (0-5 Ma) coincide with the geocentric axial dipole (GAD) model predictions very well. However, both of the average paleointensities from the equatorial and the polar regions were about 30 μT, which did not agree with the GAD model. In this dissertation, I study the paleomagnetic directions and paleointensities recorded in the lava flows from Galapagos Islands, which are around 1° South of the Equator. The paleomagnetic directions from Galapagos coincide with the GAD model very well. In order to acquire reliable paleointensities, I develop a comprehensive BZF (back-zero-forth) experiment protocol along with a multidomain correction technique. The resultant equatorial paleointensities from Galapagos are much lower than previous estimates, which suggest a major dipolar component for the GMF in the Pliocene-Pleistocene.

ACKNOWLEDGEMENTS

To my parents, Sijiao and Lingli Wang, I owe everything for being brought to this world, eating, seeing, hearing, feeling, loving and getting a Ph.D. I thank them from the bottom of my heart for providing the best they can to me, leaving the most bitter for themselves without letting me notice. I also thank my lovely wife, Hui, for always being supportive to my study and research, for taking care of my life, for bringing joys to me when I need them the most, and for consistently providing her entire love to me.

I thank my fellow classmates and graduate students for many fruitful discussions and all the good times that we spend together. I particularly thank Morgan Schaller, David Bord, Christopher Lepre, Samuel Henderson, Ashley Harris and Andrew Kulpecz, for helping me in every way they can for my past six years in the United States. I also thank my Ph.D. committee members, Drs. Carl Swisher, Mike Carr and Jeff Gee for helpful discussions, comments and suggestions during the years of my graduate study, especially when I am writing this dissertation.

I am forever in debt to Dr. Rixiang Zhu, who brought me into the field of paleomagnetics, which I find myself good at and love. I also thank many colleagues in the Beijing PGL, especially Drs. Yongxin Pan, Qingsong Liu, Chenglong Deng, Huafeng Qin, Chunxia Zhang and Jinhua Li, for help to my life and supports for my research.

Last and the most important, I really like to express my absolute appreciation to my Ph.D. advisor, Dr. Dennis Kent, who changes my entire course of life by deciding to take me on the journey to the frontiers of paleomagnetics with him. I will never forget his kind manner, vast knowledge, generous help, patient guidance and amazing efficiency, which have influenced me so much that I will try hard to pass on to my future students.

TABLE OF CONTENTS

LIST OF TABLES

LIST OF FIGURES

Introduction

William Gilbert (1540-1603) was the first to suggest the Earth itself was like a giant magnet. He constructed a *terrella* (little Earth) with a magnetized sphere of lodestone and studied the field directions by placing small compasses around it, and found it closely resemble the geomagnetic field, which was mainly dipolar [*Gilbert*, 1600].

In 1838, Carl F. Gauss firstly used a set of spherical harmonics to quantitatively describe the geomagnetic field of the Earth [*Turner*, 2011]. Recent modern satellite missions (e.g. Orsted, CHAMP and SAC-C) allowed the geomagnetic field to be described by a set of spherical harmonic coefficients up to degree 13 (195 coefficients), among which, the dipole components (g_1^0, g_1^1 and h_1^1) constitute over 95% of the power spectrum [*Finlay et al.*, 2010].

If the geomagnetic field has only the g_1^0 component, then it is a geocentric axial dipole (GAD). It predicts that the geomagnetic field directions on the Equator are horizontal, while on the Poles are vertical. The field intensities on the Poles should be twice as much as on the Equator.

Previous time average field initiative (TAFI) studies [*Opdyke et al.*, 2010] suggested that the average directions of the geomagnetic field for the past 5 million years

coincide with the GAD model very well. However, the average paleointensity from polar regions (30 μT) is almost equal to that from equatorial regions (30 μT), not fulfilling the predictions of the GAD [*Lawrence et al*., 2009].

In chapter 1 of this dissertation, I study the thermal demagnetized paleomagnetic directions recorded by 58 lava flows for the Pliocene-Pleistocene time period from Galapagos, which is about 1º South from the Equator. I find the average paleomagnetic field direction (overall mean inclination = 1.9º) from 51 qualified lava flow sites is almost horizontal, which agrees with the predictions of the GAD, and other previous studies. This study was carried out by my advisor Dr. Dennis V. Kent (initiated the study, generated and analyzed paleomagnetic direction data and wrote the paper for publication), myself (participated the study, generated and analyzed preliminary paleointensity data and wrote the paper for publication) and Dr. Pierre Rochette (provided Galapagos lava samples), which was published in 2010 on the Journal of *Physics of the Earth and Planetary Interiors* [*Kent et al*., 2010].

In chapter 2 of this dissertation, I develop a comprehensive experiment procedure (Back-Zero-Forth protocol and multidomain correction technique), which solves the problem of acquiring reliable paleointensity estimates from igneous rocks that mainly contain multidomain magnetite grains as major natural remanent magnetization carriers. I successfully apply the new technique on basalt samples from a trial lava flow site from Galapagos, which yields satisfying results. This study was carried out by myself (developed paleointensity technique, generated and analyzed data and wrote paper for

publication) and my advisor Dr. Dennis V. Kent (supervised the study, analyzed data and wrote paper for publication), which was published in 2013 on the Journal of *Geochemistry Geophysics Geosystems* [*Wang and Kent*, 2013].

In chapter 3 of this dissertation, I use the multidomain correction technique developed in chapter 2 to conduct paleointensity experiments on 47 lava flow sites from Galapagos for the Pliocene-Pleistocene. Finally 27 qualified lava flows give the mean paleointensity of 21.6 μT, which is about 65% of those from Antarctica (mean = 33.4 μT [*Lawrence et al*., 2009]). These results suggest a major GAD component for the geomagnetic field paleointensity for the past a few million years. This study was carried out by myself (generated and analyzed data and wrote paper for publication) and my advisor Dr. Dennis V. Kent (conceptualized and supervised the study, analyzed data and wrote paper for publication), which would be submitted for publication soon.

Chapter 4 is a brief conclusion of this dissertation, in which I conclude that both paleomagnetic direction and paleointensity of the geomagnetic field for the past a few million years in the Pliocene-Pleistocene time period agree with the GAD prediction.

Chapter A1 in Appendices is the supplementary material for chapter 2, in which I conduct rock magnetic measurements to study thermal alterations for magnetization carrying minerals in Galapagos lavas during paleointensity experiments in detail. First-order reversal curves (FORC), thermal fluctuation tomography (TFT) measurements, field cooled and zero-field cooled (FC–ZFC) remanence warming curves, low

temperature demagnetization (LTD) cooling and warming curves of room temperature saturation isothermal remanence ($SIRM_{RT}$), and stepwise high-resolution FORC diagrams for selected specimens from Galapagos lavas are presented. This study was carried out by myself (initiated the study, generated and analyzed data) and my advisor Dr. Dennis V. Kent (supervised the study, analyzed data), which would be written to a scientific paper to be submitted for publication soon.

Chapter A2 in Appendices is the supplementary material for chapter A1, which introduces the rock magnetic experiment procedures that used in chapter A1. This chapter contains detailed technical information on how the rock magnetic experiments (high resolution first-order reversal curves and thermal fluctuation tomography) are conducted. This study was carried out by myself (initiated the study, generated and analyzed data and wrote paper for publication), my advisor Dr. Dennis V. Kent (supervised the study, analyzed data and wrote paper for publication) and Dr. Michael J. Jackson (developed experimental technique and software, analyzed data and wrote paper for publication), which was published on the Journal of *Proceedings of National Academy of Sciences, USA* [*Wang et al.*, 2013].

Future studies of this scientific problem are to acquire more high quality multidomain corrected paleointensity results from around the globe for the same time period (~ 0-5 Ma), especially equatorial and polar regions to confirm the findings presented here in this dissertation.

Reference

Finlay, C. C., S. Maus, C. D. Beggan, T. N. Bondar, A. Chambodut, T. A., et al., (2010) International Geomagnetic Reference Field: the eleventh generation, *Geophys. J. Int.*, 183, 1216-1230

Gilbert, W. (1600), *De Magnete*, Peter Short, London.

Kent, D. V., H. Wang, and P. Rochette (2010), Equatorial paleosecular variation of the geomagnetic field from 0-3 Ma lavas from the Galapagos Islands, *Physics of the Earth and Planetary Interiors*, *183*, 404-412.

Lawrence, K. P., L. Tauxe, H. Staudigel, C. Constable, A. Koppers, W. McIntosh, and C. L. Johnson (2009), Paleomagnetic field properties at high southern latitude, *Geochemistry Geophysics Geosystems*, *10*, Q01005, doi:01010.01029/02008GC002072.

Opdyke, N. D., D. V. Kent, K. Huang, D. A. Foster, and J. P. Patel (2010), Equatorial paleomagnetic time averaged field results from 0-5 Ma lavas from Kenya and the latitudinal variation of angular dispersion, *Geochemistry Geophysics Geosystems*, *11*, Q05005, doi:05010.01029/02009GC002863.

Turner, G. (2011), *North Pole, South Pole: The Epic Quest to Solve the Great Mystery of Earth's Magnetism*, The Experiment, New York

Wang, H. and D. V. Kent, (2013), A Paleointensity Technique for Multidomain Igneous Rocks, *Geochemistry Geophysics Geosystems, 14*, 4195-4213, doi: 10.1002/ggge.20248

Wang, H., D. V. Kent, and M. J. Jackson (2013), Evidence for abundant isolated magnetic nanoparticles at the Paleocene-Eocene boundary, *Proceedings of the National Academy of Sciences, USA*, *110*, 425-430.

Chapter 1

Equatorial paleosecular variation of the geomagnetic field from 0 to 3 Ma lavas from the Galapagos Islands

1.1. Abstract

Complete progressive thermal demagnetization of nearly 400 oriented samples from 58 sites (lava flows) from the Galapagos Islands of Santa Cruz, San Cristobal and Floreana provide data for the statistical characterization of the time-averaged geomagnetic field near the Equator for the past few million years. Estimates of VGP dispersion due to paleosecular variation range from 9.2° to 11.8° depending on site selection criteria; our preferred estimate based on 64 site VGPs (51 accepted from this study and 13 from the 1971 study by Cox) is 11.4° (95% confidence interval 10.2-13.0°), consistent with previous estimates from the Galapagos Islands as well as paleosecular variation Model G, and confirming that angular dispersion of VGPs near the Equator is relatively low. The mean direction is not significantly different from a geocentric axial dipole field when account is taken of southward plate motion over the Galapagos hotspot. Preliminary paleointensity results from a comparison of the natural remanence with a total thermal remanence produced in a lab field of 15μT on a subset of 321 samples from 48 sites that had relatively small changes in magnetic susceptibility after laboratory

heating suggest that the time averaged field was about 21μT, or only two-thirds the present strength, in agreement with some other recent estimates.

1.2. Introduction

Secular variation is a quintessential feature of the geomagnetic field (GMF) and indicative of a geodynamo generating mechanism. Direct measurements of the GMF extend back ~400 years (Jackson et al., 2000), starting in the late 16th century at about the time of the age of exploration and widespread use of the magnetic compass, the discovery of magnetic inclination and, soon thereafter, the model of Earth as a magnet by William Gilbert in 1600 (Short, 2000). However, the quadracentennial span of the historic data is insufficiently long to capture the full scope of secular variation, which consequently requires analysis of paleomagnetic data.

Lava flows, which provide accurate readings of the GMF upon emplacement and rapid cooling, are an important source of information on secular variation over million year time scales. A key finding of paleosecular variation of recent lava (PSVRL) studies was a latitudinal variation in the dispersion of directions or their transformation into virtual geomagnetic poles (VGPs) (Cox, 1962, 1970; Creer, 1962; Creer et al., 1959; Doell and Cox, 1971; Irving and Ward, 1964; McElhinny and Merrill, 1975). PSVRL data from the equator are thus of particular importance as an end-member in the geographical dispersion spectrum. However, global analyses (e.g., McElhinny and

McFadden, 1997; McFadden et al., 1988) have had to rely on very limited PSVRL data from the equatorial belt, such as the venerable study by Cox (1971) of lavas from the Galapagos Islands. New PSVRL data that meet modern reliability criteria are becoming available, for example, from Equador and Kenya (Opdyke et al., 2006, 2010); these studies tend to support relatively low VGP dispersion at the equator but questions have nevertheless been raised about the validity of any latitudinal dependence in secular variation (Johnson et al., 2008). The recommendation by McElhinny and McFadden (1997), that the PSVRL database needs to be updated, continues to be pertinent and indeed, one of the studies listed by them as worth repeating - the Galapagos lavas by Cox (1971) - is the subject of the present report.

Rochette et al. (1997) reported preliminary results from 79 sites in lavas from the Galapagos; only overall statistics were presented and the results were largely based on blanket alternating field (AF) demagnetization treatment of the samples. Given the historic importance of the Galapagos to PSVRL studies and motivated by the good possibility of obtaining high-quality data from the lavas, which were collected near sea-level and thus less likely to be affected by lightning strikes (the bane of PSVRL studies), we undertook a thermal demagnetization study of 400+ specimens remaining from more than 60 sites from 3 islands in the Galapagos (San Cristobal, Santa Cruz and Floreana); these results are presented here.

1.3. Geology and sampling

The Galapagos Archipelago consists of volcanic islands on the Nazca plate that formed over several million years above the Galapagos hotspot, whose present eruptive center is Fernandina Island (0.37°S 91.55°W) (Fig. 1.1). The geology, petrology and geochemistry of the islands were described by McBirney (1994) and McBirney and Williams (1969), amongst others, and summarized by White et al. (1993) who also presented new radioisotopic age data that confirm that of the basaltic foundations of the islands extend back only a few million years (Bailey, 1976; Cox and Dalrymple, 1966; Swanson et al., 1974; see also Sinton et al., 1996).

Paleomagnetic data from Galapagos lavas were initially reported in terms of only polarities (Cox and Dalrymple, 1966) and subsequently as site-mean directions in an influential study (Cox, 1971) that constituted for many years virtually the only discrete estimate of dispersion due to PSV at the equator, even though it was based on only 17 sites from one island (San Cristobal) with hardly any demagnetization treatments. More recently, a reconnaissance study of samples collected from more than 79 sites from four of the Galapagos Islands was reported by Rochette et al. (1997); their results based on an independent set of lava sites basically agreed with Cox's estimate for dispersion due to PSV.

We report results for a subset of samples collected by Rochette et al. (1997) from sites on three Galapagos Islands: 19 sites from Santa Cruz (~0.6°S), 31 sites from San Cristobal (~0.8°S), and 24 sites from Floreana (~1.3°S) (Fig. 1.1). Typically eight

oriented drill core samples oriented by magnetic compass were collected at each site on shore exposures. Available geochronological data (White et al., 1993) indicate that the Galapagos Islands are younger than ~3 Ma, which would constrain the reverse and normal polarity lavas reported from these islands (Cox, 1971; Cox and Dalrymple, 1966) mainly to the Matuyama reverse chron (2.6-0.78 Ma) and Brunhes normal chron (0.78 Ma to Present).

Using the preliminary results from AF treatments to 20 mT (Rochette et al., 1997) and excluding six sites sampled on Pinzon that targeted a polarity transition, we focused on those sites which met minimum acceptance criteria (dispersion factor, $k > 50$); this excluded three sites from Santa Cruz (net 16 sites), seven sites from San Cristobal (net 24 sites), and four sites from Floreana (net 20 sites). Samples were no longer available for two additional sites (GA46 from Santa Cruz and GA61 from Floreana) that would have been otherwise acceptable, leaving a total of 58 sites (393 samples) for further analyses.

1.4. Paleomagnetic data

After measurement of natural remanent magnetization (NRM), a specimen from every sample was thermally demagnetized (TD) in 10-12 steps: 100 °C, (150 °C), 200 °C, (250 °C), 300 °C, 350 °C, 400 °C, 450 °C, 500 °C, 525 °C, 550 °C and 575 °C. Examples of vectors end-point demagnetization degrees are shown in Fig. 1.2, which show straightforward behavior characterized in most samples by linear trajectories converging

to the origin after removal of minor spurious components by 300–350 °C. The unblocking temperature spectra are typically block-shaped with only a few percent of the initial NRM remaining by 575 °C, consistent with fine-grained magnetite as the main carrier of remanence. Room-temperature magnetic susceptibility measured after each demagnetization step typically showed only minor changes (Fig. 1.2).

The characteristic magnetization (ChRM) was estimated from each sample's demagnetization data with principal component analysis (Kirschvink, 1980) using seven steps between 350 and 575 °C. The ChRM are well defined: the average maximum angular deviation (MAD) is <1.5° and more than 95% of the sample MAD values are <5°. Grouped by site, only two sites (GA47 and GA76) had pathologically scattered directions with precision parameters <50 and were excluded. A total of 14 other samples diverged markedly (two angular standard deviations) from their site means and were regarded as outliers (e.g., misoriented or mislabeled) and excluded. The resulting 368 sample ChRM directions provide 54 site means with k > 50 (except GA28 that we chose not to exclude with k = 47) and a95s averaging 6° (Table 1.1).

The site-mean ChRM directions have a bimodal distribution: 26 sites with shallow northerly (normal polarity) directions and 28 sites with shallow southerly (reverse polarity) directions (Fig. 1.3a). Sites from Santa Cruz had only normal polarities whereas those from San Cristobal and Floreana had normal and reverse polarities. Four sites from Floreana (GA78, 79, 84 and 85; Table 1.1) give a very similar but somewhat unusual direction (D = 212.2°, I = -29.8°, a95 = 5.0°) and probably represent sampling of

the same lava or closely synchronous lava flows; we combine these four site means for further analyses. The resulting 51 site data have normal and reverse polarity means with virtually identical dispersions: D = 354.4°, I = 3.6°, a95 = 5.9°, k = 24.3, N = 26 versus D = 179.8°, I = -0.1°, a95 = 5.6°, k = 27.3, N = 25. These directions are within 6.4° of antipodal and pass the reversal test at 95% confidence (classification B; McFadden and McElhinny, 1990). The overall mean direction after inverting the reverse site means is D = 357.1°, I = 1.9°, a95 = 4.1°, k = 25.2.

The blanket AF demagnetized data from Rochette et al. (1997) for the same sites as the TD results give very comparable results (Table 1.2): overall mean for the AF data (D = 0.3°, I = 2.3°, a95 = 4.1°, k = 25.0, N = 51) is within a few degrees of the TD results and the dispersions are essentially the same. Clearly these basalts have very stable magnetizations with little overprinting and respond favorably to TD or even nominal AF treatments.

The limited but independent results (5-10 mT AF for only 13 sites) from San Cristobal from Cox (1971) are shown in Fig. 1.3b. Only one of the 24 sites tabulated by Cox (1971) had reverse polarity but all of the 13 sites with some AF treatment had normal polarity directions. Nevertheless, the statistical measures of this dataset (D = 358.5°, I = 5.2°, a95 = 6.9°, k = 36.7,N = 13; Table 1.2) are not significantly different from either the AF results (Rochette et al., 1997) or the TD results reported here for 51 sites from Santa Cruz, Floreana, as well as San Cristobal. Each of these datasets

apparently captured a sufficient time span in rocks with stable magnetizations to yield comparable estimates of the time-averaged GMF.

1.5. Paleosecular variation estimate

VGPs calculated from theChRMsite means and site locations are well grouped around a mean paleopole located at 86.5°N 217.3°E A95 = 3.0°, K = 44.8, N =51 (Fig. 1.3c). The paleopole is slightly (but significantly) near-sided with respect to the geographic axis; we will return to this point in Section 7. Three site VGPs depart from the mean paleopole somewhat more than a cutoff angle of 25.5° obtained by the method of Vandamme (1994); we chose to retain these sites but include statistics for the filtered dataset in Table 1.2 for reference.

The independent dataset of VGPs from the AF sites from Cox (1971) (Fig. 1.3d) can be combined with the TD dataset to improve the overall basis for statistical inference. The combined dataset of 64 site VGPs gives an overall mean paleopole at 86.5°N 222.9°E A95 = 2.6°, K = 48, which is also slightly but significantly near-sided.

We use standard procedures to estimate angular dispersion of the GMF from the distribution of site VGPs (e.g., McElhinny and Merrill, 1975). The angular standard deviation, S, is estimated as:

$S = 81/\mathrm{sqrt}(K)$

where K is Fisher's concentration factor:

$K = (N-1)/(N-R)$.

where R is the resultant vector length of N unit (site VGP) vectors.

The total dispersion (St) is a combination of the scatter caused by GMF variations from site to site (Sb) and the within-site scatter (Sw) due to measurement and recording errors:

$S_t^2 = S_b^2 + S_w^2/n$

where n is the average number of samples used per site.

Estimates of Sb are summarized in Table 1.2 for various combinations of datasets and selection criteria. A relatively conservative estimate is 11.8° (95% confidence interval 10.4-13.7°) for the 51 TD sites, which is practically the same as 11.7° for the same 51 sites using AF demagnetization and 11.2° for 66 AF demagnetized sites after filtering with an optimal cutoff angle of 26.2° (Rochette et al., 1997). If the same filtering method of Vandamme (1994) is used on the 51 TD sites, the optimal cutoff angle of 25.5° reduces the number of sites to 48 and results in a corrected between-site dispersion

of 9.2° (confidence interval 8.1-10.7°). The choice of cutoff angle is clearly important (McElhinny and Merrill, 1975). The 48 filtered TD and 13 Cox AF sites are independent and can be combined to yield an estimate of 9.5° (confidence interval 8.5-10.8°) for angular dispersion. Without a cutoff, the combined 64 sites (51 TD plus 13 Cox AF) would yield an angular dispersion of 11.4° (confidence interval 10.2-13.0°).

1.6. Comparison to other dispersion estimates

The between-site VGP dispersion for the Galapagos lavas most probably (95% confidence) lies somewhere between 8.1 and 13.8 °C, depending on which subset of acceptable data is selected from the 51 TD sites from Santa Cruz, San Cristobal and Floreana and 13 AF sites from San Cristobal from Cox (1971). This range is consistent with previous estimates for VGP dispersion from Galapagos lavas (Cox, 1971; Rochette et al., 1997) but it is now based on fully demagnetized and tabulated data. The chances of redundancy are reduced since the TD dataset comes from three different islands (i.e., volcanic centers) and independent laboratory studies. The correct value of dispersion may very well be at the lower end of the estimated range but a representative estimate is 11.4° (confidence interval 10.2–13.0°) based on 51 TD sites reported here and 13 AF sites from Cox (1971) without a cutoff.

The VGP angular dispersion from Galapagos lavas compares well with some recent estimates from other near-equatorial PSVRL studies (Fig. 1.4 and Table 1.3),

notably Mt. Kenya at 0° latitude (Sb = 11.0°, confidence interval 9.2-12.7°) and Loiyangalani at 2.6°N (Sb = 9.3°, confidence interval 7.9-11.1°) (Opdyke et al., 2010). However, the angular dispersion for Equador at 0.6°S (Sb = 14.0°, confidence interval 12.3-16.2°; Opdyke et al., 2006) is several degrees higher than these estimates; we suspect this is because of jitter from undetected tilting of lavas in that active Andean tectonic setting. According to a compilation by Opdyke et al. (2010), the only other datasets within 15° of the equator that meet modern reliability standards are from Java at 7.4°S (Sb = 12.9°, confidence interval 11.0–15.4°; Elmaleh et al., 2004), Costa Rica at 10°N (Sb = 17.2°, confidence interval 14.9–21.0°; Johnson et al., 2008), and the Afar region of Ethiopia at 12°N (Sb = 12.6°, confidence interval 11.5-13.9°; Kidane et al., 2003). The Costa Rica dispersion estimate seems anomalously high, which as suspected for Equador might also reflect a contribution from undetected tectonic tilts of the lava flows. In contrast, the more quiescent tectonic setting of the Galapagos may have reduced this potential source of recorder noise.

To compensate for the small size of individual datasets and improve temporal sampling, lava data have also been binned into latitude bands (McElhinny and Merrill, 1975). In an important and widely used compilation of 0-5 Ma lava data, McElhinny and McFadden (1997) estimated a VGP dispersion of 11.1° (95% confidence interval 10.2–12.1°) for 138 sampling sites within 5° of the equator (average latitude 2.1°) that passed reasonably stringent selection criteria (all samples demagnetized, site a95 <10°, more than 2 samples per site). The new dispersion estimates from Kenya (Opdyke et al., 2010) and the Galapagos (this paper) are in good agreement with this binned estimate, which

together reinforce the notion that VGP dispersion at the equator over the past few million years was in fact low compared to higher latitudes.

1.7. Preliminary time-averaged paleointensity

The excellent directional results from thermal demagnetization of NRM suggested that the Galapagos lavas may also be good recorders of geomagnetic field intensity. Reconnaissance rock magnetic studies on about two dozen samples also indicated favorable properties: susceptibility versus temperature curves are often nearly reversible with Curie points predominantly around 575 °C consistent with magnetite whereas hysteresis parameters (Day et al., 1977) indicate that the remanence carriers tend to be fine grained (Mr/Ms ~0.1–0.4, mean ~0.20) (Fig. 1.5). These magnetic characteristics are similar to those reported for other subaerial basalts such as from Hawaii (e.g., Herrero-Bervera and Valet, 2009) and Kenya (Opdyke et al., 2010). In anticipation of mounting a full-fledged Thellier paleointensity campaign with more detailed rock magnetic investigations, we compared the NRM vector that was unblocked between 350◦C (sufficient to exclude viscous components) and 575 °C (close to the maximum unblocking temperature) to a corresponding laboratory thermoremanence (TRM) produced by heating the sample to 575 °C, cooling it to room temperature in a field of 15 μT, and thermally demagnetizing the resultant TRM at 350 °C. Measurements of room-temperature magnetic susceptibility were made after each heating to monitor laboratory-induced thermomagnetic alteration; after 575 °C, most of the samples had susceptibility

changes of less that 50% compared to initial values, which we used as a criteria for rejecting about 10% of the samples with greater changes.

Ideally, the ratio of NRM to TRM multiplied by the laboratory field (15 μT), which we refer to as Pint, should be a measure of the ancient GMF intensity in which the sample acquired the stable fraction of its NRM during initial cooling. Although our data were produced using the underlying principles of the classic Thellier-Thellier paleointensity experiment (Thellier and Thellier, 1959) and its variants (e.g., Coe, 1967; Aitken et al., 1988; Tauxe and Staudigel, 2004), which include numerous and elaborate internal checks for reliability, our procedure is intended to provide only a rough estimate of the paleointensity distribution, relying on a modest criteria for laboratory-induced alteration (susceptibility changes) and statistical coherence in both directions and paleointensities at the within-site level. The main virtue of our experimental strategy is that a large population of samples that had been thermally demagnetized can be quickly processed for paleointensity and the prospects of success for full Thellier experiments assessed at a site-by-site level. Another mitigating benefit of using a total TRM method is that it minimizes nonlinear effects from multidomain contributions (e.g., see Fig. 49 in Dunlop and Ozdemir (2007)).

In the case of the Galapagos lavas, the mean Pint value for 321 accepted samples is 20.8 μT; grouped and averaged by site (after excluding as within-site outliers a handful of samples with values more than twice the standard deviation away from the initial site mean), the overall mean Pint value for 48 sites, which best represents the time-averaged

field intensity, was practically the same (21.0 μT) since the number of samples per site is similar (Fig. 1.6). The sample or site-mean Pint values have a tail toward higher values and may be better represented by a log-normal distribution; the corresponding geometric mean value for the 48 sites is 17 μT. In comparison, the field intensity in the Galapagos today is ~30 μT.

1.8. Discussion

In their compilation of 0–5 Ma lava data, McElhinny and McFadden (1997) found an overall latitudinal variation of VGP dispersion that was fit to Model G (McFadden et al., 1988) with a zero-latitude (equatorial) value of 11.9°±0.7° (Fig. 1.4), which was used, for example, to constrain GMF statistical model TK03 (Tauxe and Kent, 2004). In contrast, Johnson et al. (2008) suggested that the available PSVRL data made it difficult to discriminate between PSV models that predict virtually no VGP dispersion with latitude (e.g., Constable and Parker, 1988) from those with a latitudinal increase in Sb (e.g., McElhinny and McFadden, 1997; Tauxe and Kent, 2004). However, the new equatorial results from lavas in Kenya (Opdyke et al., 2010) and the Galapagos (this paper) and recent results from ~78°S in Antarctica (Lawrence et al., 2009) are consistent with a significant increase in VGP dispersion by around a factor of two from equatorial (Sb ~11°) to polar (Sb ~24°) latitudes, as suggested by Model G of McElhinny and McFadden (1997).

The time-averaged mean direction or pole position in the Galapagos dataset departs by a few degrees from that of a geocentric axial dipole, which for the mean site latitude of 0.95°S would predict a mean normal polarity inclination of −1.9°. Instead, the mean inclination (TD +AF Cox dataset with reverse sites inverted) is 2.6°±3.5°, which is just significantly different as is the mean VGP (86.5°±2.6° latitude) from the geographic axis (Table 1.2). One interpretation is that the departure is evidence of a few percent contribution from an axial quadrupole field; however, since the mean VGP is near-sided and the inclination anomaly is positive, this would imply the time-averaged quadrupole contribution would have to be of opposite sign to most previous estimates (e.g., Johnson et al., 2008; Wilson, 1971). Alternatively, once formed over the hotspot the Galapagos Islands on the Nazca plate have been moving south and this needs to be taken into account. Assuming that the hotspot has remained relatively fixed at the present locus of hotspot activity at 0.37°S (Fernandina Island), the sampling sites have moved nearly 0.6° in latitude; in other words, the predicted inclination would be -0.7°. This would be sufficient to account for much of the apparent departure and make the mean directions indistinguishable (95% confidence level) from that of a geocentric axial dipole field.

Lastly, a rudimentary total TRM paleointensity procedure that takes advantage of the thermal demagnetization of NRM data provides coherent results from 321 samples from 48 sites. The mean value of the distribution suggests that the intensity of the time averaged GMF at the equator was only about 21 μT, or roughly the two-thirds the present-day value at the Galapagos locality (~30 μT). It is entirely possible that the lavas have increased their ability to acquire TRM when they alter during laboratory heating,

which would result in underestimates of paleointensity, although using a somewhat more stringent acceptance criteria does not seem to markedly change the mean paleointensity value (e.g., 21.3 μT for 286 accepted samples for <20% susceptibility change compared to 20.8 μT for 321 accepted samples for <50% susceptibility change). Compilations of paleointensity data for the past few million years have tended to produce average values that are close to the present-day field although there is some suspicion the data distribution may not adequately reflect paleointensity variations at the million-year time scale (Selkin and Tauxe, 2000). The Galapagos total TRM results obviously need to be confirmed by full Thellier experiments with thorough checks for lab-induced irreversible magnetic behavior that can skew paleointensity estimates. In the meantime, it is intriguing that some other analyses have already suggested that the intensity of the time-averaged GMF was considerably lower than the present-day value (Selkin and Tauxe, 2000; Yamamoto and Tsunakawa, 2005; Lawrence et al., 2009).

1.9. Acknowledgements

The 1993 field sampling was funded by INSU and organized by Hélène Collombat, with authorization of the National Park of the Galapagos Islands. We are grateful to Hélène Collombat and Pablo Samaniego for their essential contribution in the field work. This phase of laboratory work on the Galapagos samples was supported by NSF grant EAR0609339 (DVK). We thank the journal reviewers for helpful comments and Lisa Tauxe for ongoing discussions about paleosecular variation.

References

Aitken, M.J., Allsop, A.L., Bussell, G.D., and Winter, M.B., 1988, Determination of the intensity of the earth's magnetic field during archealogical times - reliability of the Thellier technique. Reviews of Geophysics, v. 26, p. 3-12.

Bailey, K., 1976. Potassium-argon ages from the Galapagos Islands. Science, 192: 465–467.

Coe, R.S., 1967. The determination of paleo-intensities of the earth's magnetic field with emphasis on mechanisms which could cause non-ideal behavior in Thellier's method. Journal of Geomagnetism and Geoelectricity, 19 (3): 157-179.

Constable, C.G. and Parker, R.L., 1988. Statistics of the geomagnetic secular variation for the past 5 m.y. Journal of Geophysical Research, 93: 11,569-11,581.

Cox, A., 1962. Analysis of present geomagnetic field for comparison with paleomagnetic results. Journal of Geomagnetism and Geoelectricity, 13: 101-112.

Cox, A., 1969. Confidence limits for the precision parameter k. Geophysical Journal of the Royal Astronomical Society, 18: 545-549.

Cox, A., 1970. Latitude dependence of the angular dispersion of the geomagnetic field. Geophysical Journal of the Royal Astronomical Society, 20: 253-269.

Cox, A., 1971. Paleomagnetism of San Cristobal Island, Galapagos. Earth and Planetary Science Letters, 11: 152-160.

Cox, A. and Dalrymple, G.B., 1966. Paleomagnetism and potassium-argon ages of some volcanic rocks from the Galapagos Islands. Nature, 209: 776-777.

Creer, K.M., 1962. The dispersion of the geomagnetic field due to secular variation and its determination for remote times from paleomagnetic data. Journal of Geophysical Research, 67(J. Geophys. Res.): 3461-3476.

Creer, K.M., Irving, E. and Nairn, A.E.M., 1959. Palaeomagnetism of the Great Whin Sill. Geophysical Journal of the Royal Astronomical Society, 2: 306–323.

Day, R., Fuller, M. and Schmidt, V.A., 1977. Hysteresis properties of titanomagnetites: Grain-size and compositional dependence. Physics of the Earth and Planetary Interiors, 13: 260-267.

Doell, R.R. and Cox, A., 1971. Pacific Geomagnetic Secular Variation. Science, 171(3968): 248-254.

Dunlop, D.J. and Ozdemir, O., 2007. Magnetizations of Rocks and Minerals. In: M. Kono (Editor), Treatise on Geophysics. Elsevier, Amsterdam, pp. 277–336.

Elmaleh, A., Valet, J.P., Quidelleur, X., Solihin, A., Bouquerel, H., Tesson, T., Mulyadi, E., Khokhlov, A., and Wirakusumah, A.D., 2004. Palaeosecular variation in Java and Bawean Islands (Indonesia) during the Brunhes chron. Geophysical Journal International, 157: 441-454.

Herrero-Bervera, E. and Valet, J.-P., 2009. Testing determinations of absolute paleointensity from the 1955 and 1960 Hawaiian flows. Earth and Planetary Science Letters, 287(3-4): 420-433.

Irving, E. and Ward, M.A., 1964. A statistical model of the geomagnetic field. Geofisica pura e applicata (Pure and Applied Geophysics), 57: 47–52.

Jackson, A., Jonkers, A.R.T. and Walker, M.R., 2000. Four centuries of geomagnetic secular variation from historical records. Philosophical Transactions of the Royal Society London, A358: 957–990.

Johnson, C.L., Constable, C.G., Tauxe, L., Barendregt, R., Brown, L.L., Coe, R.S., Layer, P., Mejia, V., Opdyke, N.D., Singer, B.S., Staudigel, H., and Stone, D.B.,, 2008. Recent investigations of the 0–5 Ma geomagnetic field recorded by lava flows. Geochemistry Geophysics Geosystems, 9: Q04032, doi:10.1029/2007GC001696

Kidane, T., Courtillot, V., Manighetti, I., Audin, L., Lahitte, P., Quidelleur, X., Gillot, P.-Y., Gallet, Y., Carlut, J., and Haile, T., 2003. New paleomagnetic and geochronologic results from Ethiopian Afar: Block rotations linked to rift overlap ad propagation and determination of a ~2 Ma reference pole for stable Africa. Journal of Geophysical Research, 108: 2102, doi:10.1029/2001JB000645.

Kirschvink, J.L., 1980. The least-squares line and plane and the analysis of palaeomagnetic data. Geophysical Journal of the Royal Astronomical Society, 62: 699-718.

Lawrence, K.P., Tauxe, L., Staudigel, H., Constable, C., Koppers, A., McIntosh, W., and Johnson, C.L., 2009. Paleomagnetic field properties at high southern latitude. Geochemistry Geophysics Geosystems, 10: Q01005, doi:10.1029/2008GC002072.

McBirney, A.R., 1994. Differentiated rocks of the Galapagos hotspot. Journal Geological Society of London.

McBirney, A.R. and Williams, H., 1969. Geology and Petrology of teh Galapagos Islands. Geological Society of America Memoir 118: 197.

McElhinny, M.W. and McFadden, P.L., 1997. Paleosecular variation over the past 5 Myr based on a new generalized database. Geophysical Journal International, 131: 240-252.

McElhinny, M.W. and Merrill, R.T., 1975. Geomagnetic secular variation over the past 5 m.y. Reviews of Geophysics and Space Physics, 13: 687-708.

McFadden, P.L. and McElhinny, M.W., 1990. Classification of the reversal test in palaeomagnetism. Geophysical Journal International, 103: 725-729.

McFadden, P.L., Merrill, R.T. and McElhinny, M.W., 1988. Dipole/quadrupole family modeling of paleosecular variation. Journal of Geophysical Research, 93: 11,583-11,588.

Opdyke, N.D., Hall, M., Mejia, V., Huang, K. and Foster, D.A., 2006. The time averaged field at the equator: Results from Ecuador. Geochemistry, Geophysics, Geosystems, 7: Q11005, doi:10.1029/2005GC001221

Opdyke, N.D., Kent, D.V., Huang, K., Foster, D.A. and Patel, J.P., 2010. Equatorial paleomagnetic time averaged field results from 0-5 Ma lavas from Kenya and the latitudinal variation of angular dispersion. Geochemistry Geophysics Geosystems, 11: Q05005, doi:10.1029/2009GC002863.

Rochette, P., Ben Atig, F., Collombat, H., Vandamme, D. and Vlag, P., 1997. Low paleosecular variation at the equator: a paleomagnetic pilgrimage from Galapagos to Esterel with Allan Cox and Hans Zijderveld. Geologie en Mijnbouw, 76: 9-19.

Selkin, P.A. and Tauxe, L., 2000. Long-term variations in paleointensity. Philosophical Transactions of the Royal Society of London, A358: 1065-1088.

Short, P., 2000. Gilbert's De Magnete: An Early Study of Magnetism and Electricity. EOS, 81: 233-234.

Sinton, C.W., Christie, D.M. and Duncan, R.A., 1996. Geochronology of Galapagos seamounts. Journal of Geophysical Research, 101: 13,659-13,700.

Swanson, F.J., Baitis, H.W., Lexa, J. and Dymond, J., 1974. Geology of Santiago, Rabida and Pinzon Islands, Galapagos. Geological Society of America Bulletin, 85: 1803–1810.

Tauxe, L. and Kent, D.V., 2004. A simplified statistical model for the geomagnetic field and the detection of shallow bias in paleomagnetic inclinations: Was the ancient magnetic field dipolar? In: J.E.T. Channell, D.V. Kent, W. Lowrie and J. Meert (Editors),

Timescales of the Paleomagnetic Field, Geophysical Monograph 145. American Geophysical Union, Washington, D.C., pp. 101–116.

Tauxe, L., and Staudigel, H., 2004, Strength of the geomagnetic field in the Cretaceous Normal Superchron: New data from submarine basaltic glass of the Troodos Ophiolite: Geochemistry, Geophysics, Geosystems, v. 5, Q02H06, doi:10.1029/2003GC000635.

Thellier, E. and Thellier, O., 1959. Sur l'intensité du champ magnétique terrestre dans le passé historique et géologique. Annales de Geophysique, 15: 285-376.

Vandamme, D., 1994. A new method to determine paleosecular variation. Physics of the Earth and Planetary Interiors, 85: 131-142.

White, W.M., McBirney, A.R. and Duncan, R.A., 1993. Petrology and geochemistry of the Galapagos Islands: portrait of a pathological mantle plume. Journal of Geophysical Research, 98: 19533–19563.

Wilson, R.L., 1971. Dipole offset - the time-averaged palaeomagnetic field over the past 25 million years. Geophysical Journal of the Royal Astronomical Society, 22: 491-504.

Yamamoto, Y. and Tsunakawa, H., 2005. Geomagnetic field intensity during the last 5 Myr: LTD-DHT Shaw palaeointensities from volcanic rocks of the Society Islands, French Polynesia. Geophysical Journal International, 162: 79-114.

Figure Captions

Figure 1.1. Location map of sites from Galapagos Islands. The topographic maps are generated by Lamount-Doherty Earth Observatory contributed software GeoMapApp version 2.4.0 using the NASA ASTER Global Digital Elevation Model (GDEM). White circles are the sampling site locations in this study; filled circles are site locations in the study by Cox (1971).

Figure 1.2. Vector end-point diagrams of thermal demagnetization of NRM of representative samples of lavas from Santa Cruz (a, b), San Cristobal (c, d), and Floreana (e, f). Open (closed) symbols are projections on vertical (horizontal) planes. Thermal demagnetization steps typically were at 100, 200, 300, 350, 400, 450, 500, 525, 550, and 575°C. Insets show relative changes of sample magnetization intensity (J) and magnetic susceptibility (k) after each step.

Figure 1.3. Site-mean directions for Galapagos lavas based on a) most stable component isolated with thermal demagnetization (TD) or b) alternating field demagnetization (AF; data from Cox (1971)). Open (closed) symbols plotted on lower (upper) hemispheres of equal-area projections. Larger open circle with cross is the mean of four sites (GA78, 79, 84, 85) with nearly the same direction (see Table 1). Corresponding site VGPs for Galapagos lavas are plotted in common (normal) polarity for c) thermal demagnetization (TD) data and d) alternating field (AF) data from Cox (1971); statistics for 64 site VGPs are mean pole: 222.9°E 86.5°N (A95 = 2.6°); dispersion, S_b = 11.4° (confidence interval = 10.2-13.0°): elongation, E = 2.08 (confidence interval = 1.27-3.95), which is consistent with model TK03 (L. Tauxe, 2010 personal communication).

Figure 1.4. VGP angular dispersion (S_b, with lower and upper 95% confidence limits) for Galapagos lavas compared to other estimates within 15° of the Equator (see Table 3 for references). Curve is latitudinal variation of S_b (with 95% confidence envelope) of latitudinally-binned PSVRL data fitted to Model G (McElhinny and McFadden, 1997).

Figure 1.5. a, b) Magnetic susceptibility versus temperature for two basalt samples from the Galapagos Islands; heating and cooling curves are indicated by arrows. Sample Ga09.7t (a) is from site with *Pint* estimate of 57.4 μT; sample Ga60.5t (b) is from site with *Pint* estimate of 7.2 μT. c) Histogram of Mr/Ms values from 18 basalt samples from the Galapagos Islands. Hysteresis measurements were made in up to a 1 T direct field on a Princeton Measurements VSM Model 2900.

Figure 1.6. Estimates of paleointensity for 321 samples (bottom histogram) based on ratio of stable component of NRM (350° to 575°C) to TRM produced by cooling from 575°C in laboratory field of 15 μT and thermally demagnetized to 350°C. Histogram in

top panel shows distribution of site mean paleointensity estimates compared to strength of present Earth's field (PEF); GM is geometric mean and AM is arithmetic mean for the 48 site values.

Table 1.1. Site mean locations, stable magnetic directions and VGPs for sampling sites from San Cristobal, Santa Cruz and Floreana in Galapagos Archipelago.

Site	sLat (°)	sLon (°)	n	R	k	a95 (°)	Dec (°)	Inc (°)	vgpLO (°)	vgpLA (°)
San Cristobal (TD data)										
GA01	-0.92667	-89.42633	7	6.9476	114.6	5.7	181.9	17.9	257.7	-81.5
GA02	-0.92667	-89.42633	5	4.9934	604.9	3.1	177.1	22.2	285.6	-79.0
GA03	-0.92533	-89.42350	7	6.9437	106.7	5.9	354.0	-7.4	155.5	83.4
GA05	-0.92533	-89.42350	5	4.9264	54.3	10.5	340.3	-.9	181.8	70.3
GA06	-0.92383	-89.42000	8	7.9092	77.1	6.3	352.0	3.4	198.7	81.6
GA09	-0.92483	-89.41600	7	6.9726	219.1	4.1	343.6	-3.2	178.1	73.6
GA10	-0.92983	-89.43017	4	3.9408	50.7	13.0	175.7	3.2	351.6	-85.6
GA11	-0.93267	-89.43250	6	5.9582	119.7	6.1	354.4	-4.4	167.7	84.3
GA12	-0.93333	-89.43600	6	5.9717	176.8	5.1	344.0	2.4	188.1	73.9
GA15	-0.94183	-89.49300	6	5.9771	218.0	4.5	182.9	5.6	213.3	-86.6
GA18	-0.94950	-89.55417	7	6.9172	72.5	7.1	181.2	.7	153	-88.7
GA19	-0.95100	-89.55250	7	6.9594	147.6	5.0	178.3	5.1	317.1	-87.7
GA20	-0.95167	-89.55133	6	5.9843	317.7	3.8	185.0	10.4	221.2	-83.4
GA21	-0.94100	-89.58283	5	4.9845	257.4	4.8	185.0	-3.9	150.4	-84.2
GA22	-0.94033	-89.58466	6	5.9402	83.6	7.4	179.0	9.5	285.0	-86.0
GA23	-0.88267	-89.59950	7	6.9064	64.1	7.6	162.5	3.2	357.9	-72.5
GA24	-0.88267	-89.59950	7	6.9753	242.8	3.9	167.1	1.3	1.3	-77.1
GA25	-0.88033	-89.59700	8	7.9555	157.3	4.4	179.3	-1.9	69.5	-88.0
GA26	-0.88033	-89.59500	8	7.9562	159.8	4.4	166.3	13.1	337.2	-75.2
GA27	-0.87800	-89.59400	8	7.9689	224.8	3.7	186.2	-3.0	159.4	-83.4
GA28	-0.87667	-89.59200	5	4.9146	46.8	11.3	179.7	-2.9	83.1	-87.7
GA29	-0.87583	-89.58850	5	4.9734	150.1	6.3	184.2	-40.7	99.8	-65.5
GA30	-0.86550	-89.57300	8	7.9408	118.2	5.1	356.3	-4.9	157.1	86.0
GA31	-0.86717	-89.57550	8	7.9044	73.3	6.5	358.8	-9.5	107.4	85.9
Santa Cruz (TD data)										
GA33	-0.60117	-90.53934	8	7.9279	97.1	5.7	345.7	-.5	180.8	75.7
GA34	-0.59950	-90.53967	7	6.9710	207.2	4.2	346.1	2.8	187.7	76.0
GA35	-0.59683	-90.53983	8	7.9728	257.1	3.5	346.2	3.6	189.3	76.0
xGA38	-0.60683	-90.53833	8	7.8916	64.6	6.9	333.6	22.3	205.2	61.1
xGA39	-0.60800	-90.54134	8	7.9352	108.0	5.4	18.5	45.1	301.3	57.4
GA40	-0.60967	-90.54200	7	6.9678	186.6	4.4	351.2	-13.0	145.0	79.4
GA44	-0.59150	-90.53767	9	8.9442	143.5	4.3	352.4	-1.1	179.7	82.4
GA45	-0.59033	-90.53584	7	6.9568	139.0	5.1	350.1	-.4	181.7	80.1
GA47	*-0.57083*	*-90.53484*	*5*	*4.4360*	*7.1*	*30.9*	*346.4*	*9.3*		
GA48	-0.57083	-90.53484	5	4.9974	1512.9	2.0	354.4	23.5	246.2	76.0
GA49	-0.55117	-90.51534	7	6.9821	335.5	3.3	359.0	-4.4	120.7	88.1

GA50	-0.53667	-90.51317	8	7.9688	224.2	3.7	358.7	-9.3	106.9	85.7
GA58	-0.67983	-90.54050	6	5.9662	148.0	5.5	6.7	3.2	340.7	82.9
GA59	-0.67333	-90.53550	7	6.9633	163.7	4.7	1.8	1.5	321.1	87.7
Floreana (TD data)										
GA60	-1.26083	-90.36383	6	5.9263	67.8	8.2	351.7	12.9	223.0	78.6
GA63	-1.25833	-90.35516	8	7.9322	103.3	5.5	187.2	4.4	187.2	-82.7
GA64	-1.25517	-90.37200	7	6.9692	194.8	4.3	180.5	1.3	129.2	-89.2
GA65	-1.25450	-90.37217	8	7.8664	52.4	7.7	172.3	2.0	1.4	-82.3
GA66	-1.24867	-90.37984	7	6.9829	351.4	3.2	185.0	-.6	162.4	-84.8
GA67	-1.24817	-90.38200	5	4.9603	100.8	7.7	180.2	-.3	97.8	-88.6
GA69	-1.24600	-90.39267	5	4.9280	55.5	10.4	1.7	4.6	295.2	86.1
GA70	-1.23867	-90.38633	6	5.9827	289.2	3.9	177.9	-13.3	74.9	-81.7
GA71	-1.23867	-90.38633	7	6.9645	169.1	4.7	176.0	-9.8	56.7	-82.6
GA72	-1.24600	-90.39400	6	5.9441	89.5	7.1	4.9	5.1	321.8	83.8
GA74	-1.23417	-90.44833	7	6.9771	262.0	3.7	8.9	-7.2	14.7	80.8
GA76	*-1.23817*	*-90.45333*	*4*	*3.9257*	*40.4*	*14.6*	*351.5*	*39.5*		
*GA78	-1.24650	-90.48383	8	7.9693	228.4	3.7	212.2	-29.8	149.8	-53.8
*GA79	-1.25117	-90.48717	7	6.9189	74.0	7.1	210.0	-28.6	149.3	-56.1
GA82	-1.27433	-90.49050	7	6.9084	65.5	7.5	177.6	-3.4	50.6	-86.2
GA83	-1.27433	-90.49050	8	7.9486	136.1	4.8	7.9	32.8	291.3	69.3
*GA84	-1.27433	-90.49050	8	7.9349	107.6	5.4	217.1	-25.0	156.9	-50.5
*GA85	-1.25733	-90.48850	7	6.9773	264.3	3.7	211.5	-22.4	156.2	-56.1
xGA78-85	-1.25730	-90.48800	4	3.9913	344.6	5.0	212.7	-26.5	153.1	-54.2
San Cristobal (AF data from Table 1 in Cox (1971))										
G104	-0.778	270.537	8	10.9194	655	2.2	349.0	21.2	227.8	74.0
G102	-0.810	270.522	8	3.9898	792	2.0	359.7	-17.2	92.6	82.0
G112	-0.686	270.665	8	8.9775	1260	1.6	014.1	7.4	343.2	75.2
G100	-0.822	270.478	8	2.9835	416	2.7	003.3	11.4	296.8	82.7
G107	-0.717	270.610	8	2.9941	1379	1.5	354.8	9.0	225.7	82.6
G113	-0.690	270.697	8	3.9731	387	2.8	358.4	8.8	253.6	84.6
G110	-0.700	270.639	8	2.9974	703	2.1	005.0	4.5	329.9	84.2
G111	-0.696	270.639	8	3.9919	871	1.9	005.0	6.8	321.1	83.6
G116	-0.712	270.753	8	2.9930	996	1.8	338.1	13.4	200.0	66.9
G118	-0.759	270.543	8	3.9871	993	1.8	352.7	-11.2	146.3	81.2
G098	-0.841	270.458	8	2.9941	1295	1.5	358.0	6.6	224.8	85.4
G096	-0.867	270.433	8	3.9922	617	2.2	359.2	-3.7	129.6	88.8
G122	-0.903	270.377	8	3.9816	744	2.0	001.9	9.6	288.7	84.0

sLat and sLon are the latitudes and longitudes for the sampling sites. n is the number of samples that provided acceptable data from a site, R is the resultant of their unit vector length, k is the best estimate of Fisher's precision parameter, a95 is the radius of the 95%

confidence circle around the site mean direction in terms of declination, Dec, and inclination, Inc. The corresponding virtual geomagnetic pole is located at vgpLO, the longitude, and vgpLA, the latitude. The sites marked by * were averaged to a single mean labeled GA78-85; the sites marked with x would be excluded from overall averages on basis of VGP exceeding a cutoff angle according to method of Vandamme (1994); sites GA47 and GA76 were rejected due to poor within-site grouping.

Table 1.2. Estimates of VGP dispersion for Galapagos lavas datasets.

ID	DMG	N	k	a95 (°)	DEC (°)	INC (°)	VGP K	VGP A95 (°)	VGP LON (°E)	VGP LAT (°N)	VGP S_b (°)	VGP lS_b (°)	VGP uS_b (°)
A	TD	51	25.2	4.1	357.1	1.9	44.8	3.0	217.3	86.5	11.8	10.4	13.7
B	AF	51	25.0	4.1	0.3	2.3	46.0	3.0	280.9	87.6	11.7	10.3	13.6
C	TD	48	37.9	3.4	356.6	0.1	72.6	2.4	198.2	86.4	9.2	8.1	10.7
D	AF	66									11.2	9.9	12.9
E	AF	13	36.7	6.9	358.5	5.2	63.9	5.2	253.9	86.3	10.1	8.0	13.8
F	NRM	17	33.0	6.4	358.8	2.5	54.0	4.9	239.3	87.6	10.9	9.1	14.8
A+E	**TD+AF**	**64**	**27.0**	**3.5**	**357.4**	**2.6**	**48.2**	**2.6**	**222.9**	**86.5**	**11.4**	**10.2**	**13.0**
C+E	TD+AF	61	37.2	3.0	357.0	1.2	70.8	2.2	207.8	86.6	9.5	8.5	10.8

Various dispersion estimates for datasets are identified in column ID (see below); DMG is treatment (TD, thermally demagnetized; AF: alternating field; NRM is natural remanent magnetization with no TD or AF treatment); N is number of sites, k is Fisher's precision parameter and a95 is radius of circle of confidence around mean declination, DEC, and inclination, INC, whereas K and A95 are corresponding precision parameter and circle of confidence for mean longitude, LON, and latitude, LAT, of site VGPs. S_b is between-site dispersion of VGPs with respect to mean pole position and corrected for within-site dispersion, with lower (lS_b) and upper (uS_b) bounds of 95% confidence interval using method of Cox (1969). In column ID, A: TD sites with k>50 and combining GA78, 79, 84 and 85 (this paper). B: same sites as A using blanket AF, k>50 (Rochette et al., 1997). C: same as A with cutoff angle of 25.5°. D: blanket AF, k>20, and cutoff angle of 26.3° (Rochette et al., 1997). E: AF sites from Cox (1971). F: mainly NRM sites filtered to remove redundancies, providing the dispersion value often quoted for the Galapagos (Cox, 1971). A+E: combined TD and Cox AF sites as our preferred estimate (in bold). C+E: combined TD and Cox AF sites with cutoff angle of 25.5°.

Table 1.3. Estimates of VGP angular dispersion within 15° of the equator.

Locality	sLat (°)	sLon (°)	N	S_b (°)	lS_b (°)	uS_b (°)	Reference
Java	-7.4	112.0	35	12.9	11.1	15.4	Elmaleh *et al*. (2004)
Equador	-0.6	51.0	51	14.0	12.3	16.2	Opdyke *et al*. (2006)
Galapagos	-0.4	268.4	64	11.4	10.2	13.0	This paper
Mt Kenya	0.0	36.5	69	11.0	9.2	12.7	Opdyke *et al*. (2010)
Loiyangalani	2.6	36.5	32	9.3	7.9	11.1	"
Costa Rica	10.0	276.0	28	17.2	14.9	21.0	Constable *et al*. in Johnson *et al*. (2008)
Ethiopia	12.0	41.5	103	12.6	11.5	13.9	Kidane *et al*. (2003)
Binned 0-4.9°	2.1		138	11.1	10.2	12.1	McElhinny and McFadden (1997)
Binned 5-14.9°	11.5		113	12.3	11.2	13.6	"

sLat is the nominal latitude and sLon the longitude of the sampling localities, N is the number of lava sites, S_b is between-site dispersion of VGPs with respect to mean pole position and corrected for within-site dispersion, with lower (lS_b) and upper (uS_b) bounds of 95% confidence interval using method of Cox (1969). Binned entries were averaged in latitudinal bands from both hemispheres and are from Table 4b in McElhinny and McFadden (1997).

Figure 1.1

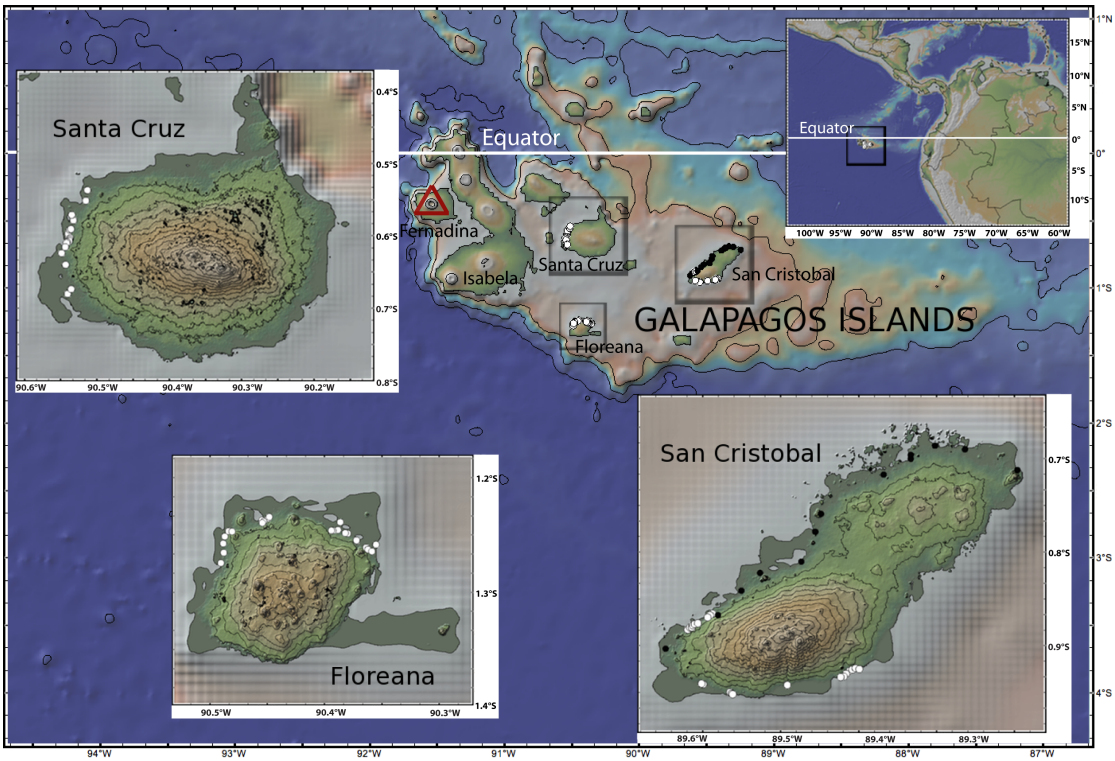
Santa Cruz
Equator
Fernadina
Isabela
Santa Cruz
San Cristobal
GALAPAGOS ISLANDS
Floreana
Equator
San Cristobal
Floreana

Figure 1.2

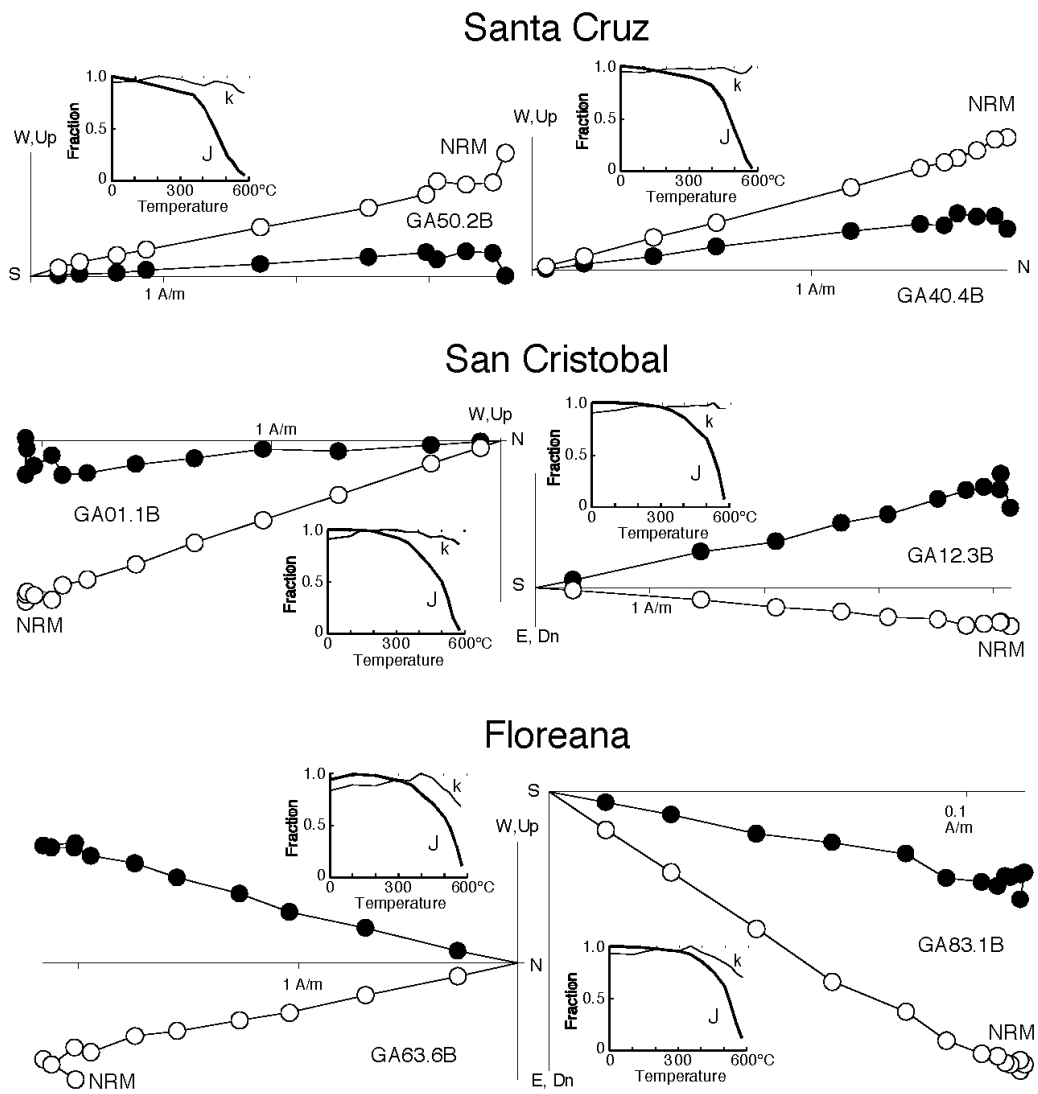
Santa Cruz
W,Up
S
1 A/m
NRM
GA50.2B
Fraction
1.0
0.5
0
k
J
0
300
600°C
Temperature
W,Up
N
1 A/m
NRM
GA40.4B
San Cristobal
1 A/m
W,Up
N
GA01.1B
NRM
GA12.3B
S
E, Dn
1 A/m
NRM
Floreana
S
W,Up
0.1
A/m
GA83.1B
NRM
N
1 A/m
GA63.6B
NRM
E, Dn

Figure 1.3

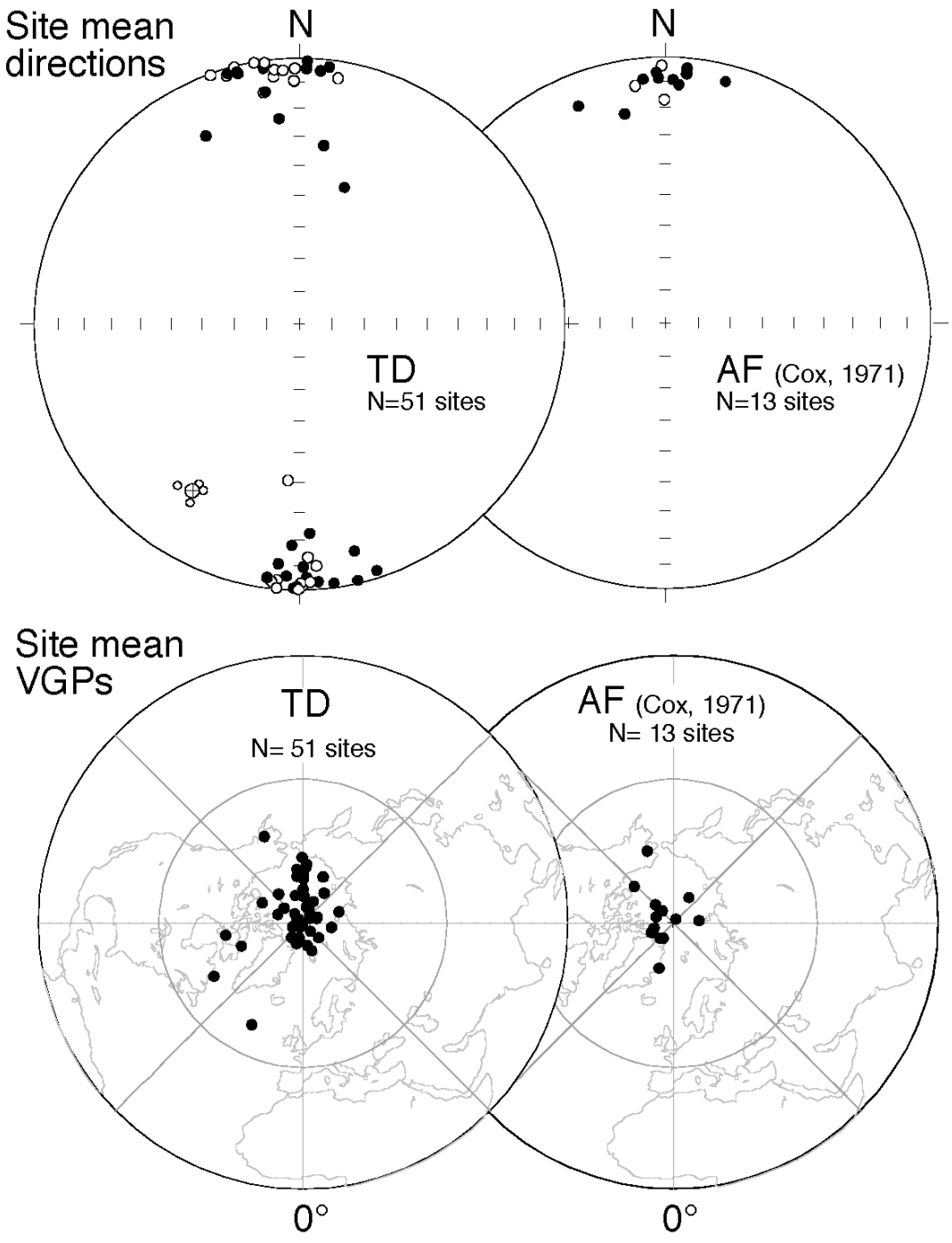
Site mean directions
N
N
TD
N=51 sites
AF (Cox, 1971)
N=13 sites
Site mean VGPs
TD
N= 51 sites
AF (Cox, 1971)
N= 13 sites
0°
0°

Figure 1.4

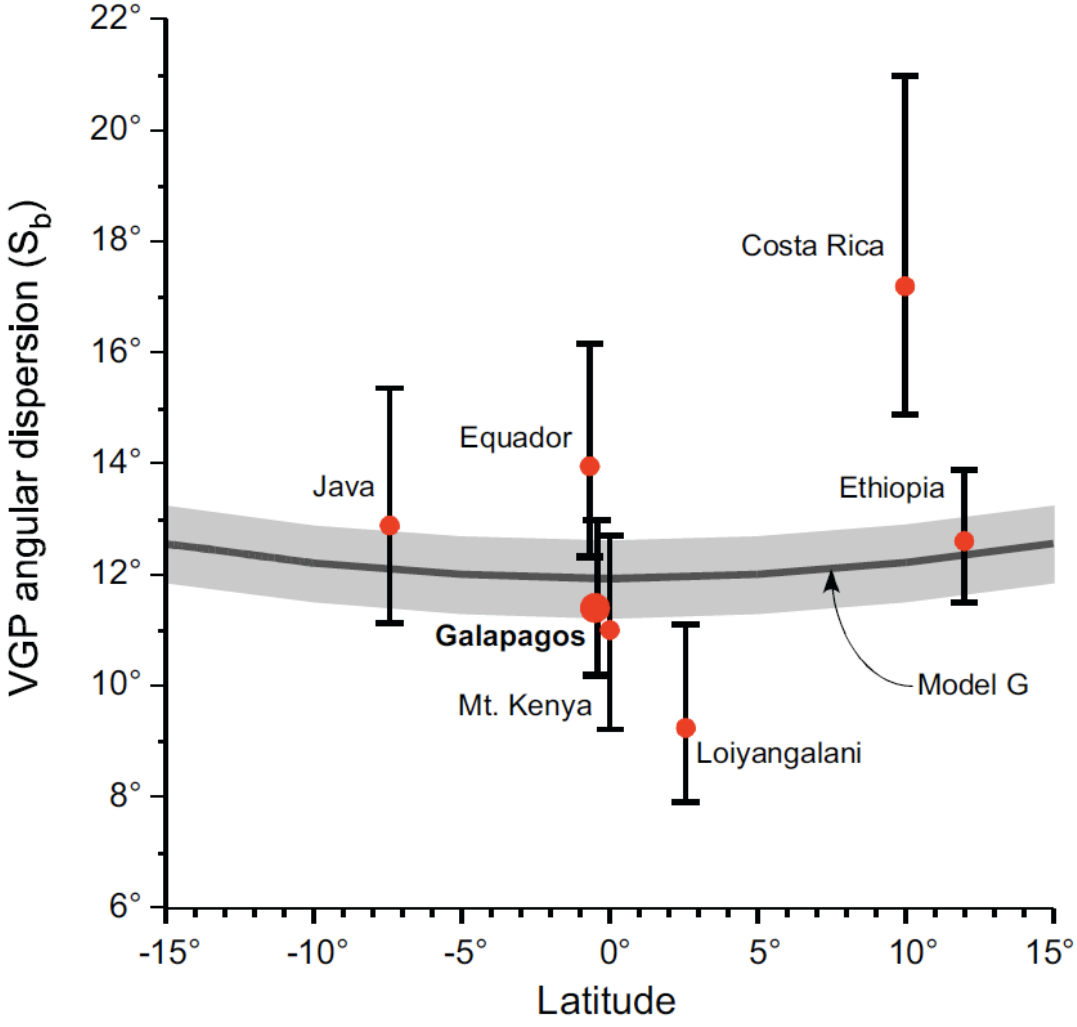
22°
20°
18°
16°
14°
12°
10°
8°
6°
VGP angular dispersion (S_b)
-15°
-10°
-5°
0°
5°
10°
15°
Latitude
Costa Rica
Equador
Java
Ethiopia
Galapagos
Mt. Kenya
Loiyangalani
Model G

Figure 1.5

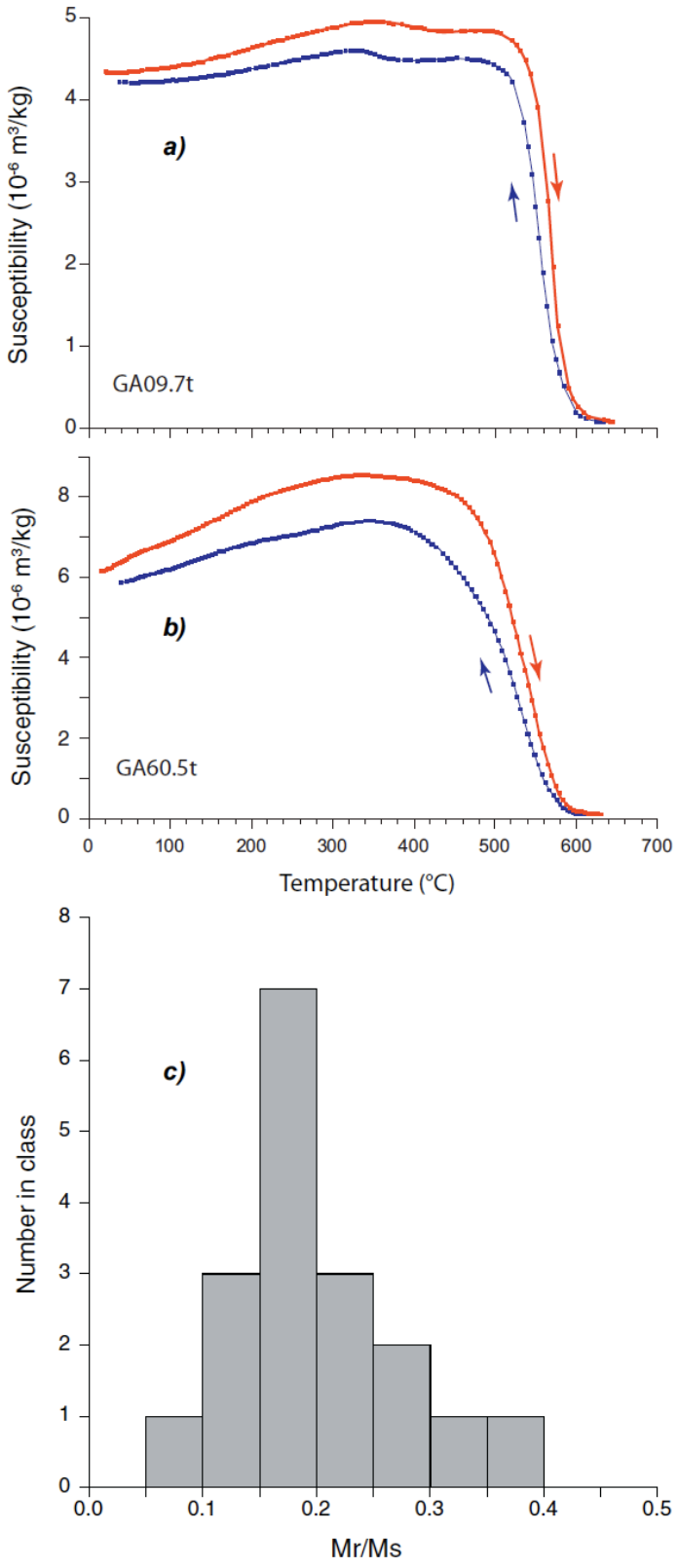
a)
GA09.7t
Susceptibility (10⁻⁶ m³/kg)
b)
GA60.5t
Susceptibility (10⁻⁶ m³/kg)
Temperature (°C)
c)
Number in class
Mr/Ms

Figure 1.6

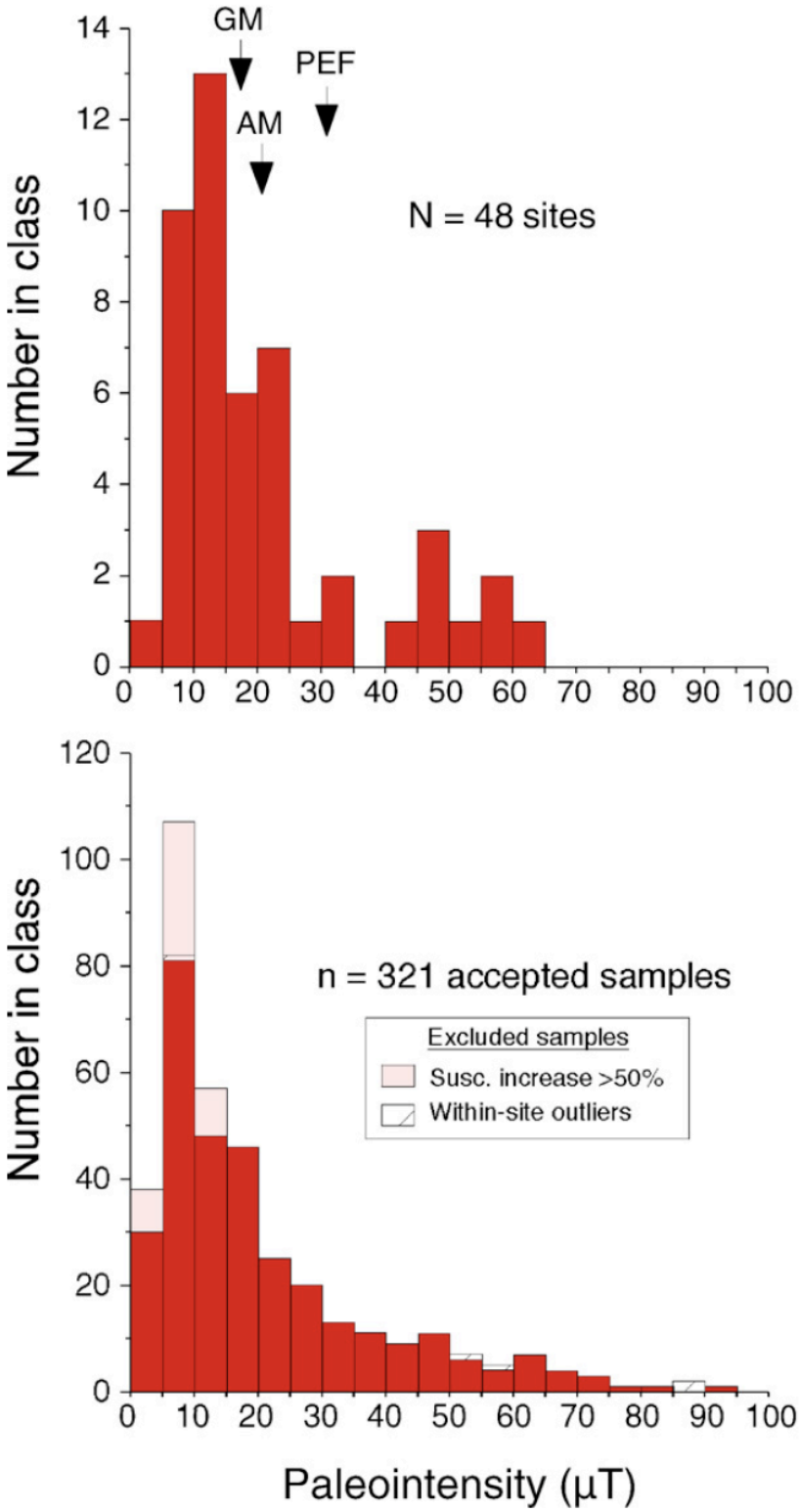
GM
PEF
AM
N = 48 sites
Number in class
n = 321 accepted samples
Excluded samples
Susc. increase >50%
Within-site outliers
Paleointensity (μT)

Chapter 2

A Paleointensity Technique for Multidomain Igneous Rocks

2.1. Abstract

We developed a paleointensity technique to account for concave-up Arai diagrams due to multidomain (MD) contributions to determine unbiased paleointensities for 24 trial samples from site GA-X in Pleistocene lavas from Floreana Island, Galapagos Archipelago. The main magnetization carrier is fine-grained low-titanium magnetite of variable grain size. We used a comprehensive back-zero-forth (BZF) heating technique by adding an additional zero-field heating between the Thellier two opposite infield heating steps in order to estimate paleointensities in various standard protocols and provide internal self-consistency checks. After the first BZF experiment, we gave each sample a total thermal remanent magnetization (tTRM) by cooling from the Curie point in the presence of a low (15 μT) laboratory-applied field. Then we repeated the BZF protocol, with the laboratory-applied tTRM as a synthetic natural remanent magnetization (NRM), using the same laboratory-applied field and temperature steps to obtain the synthetic Arai signatures, which should only represent the domain-state dependent properties of the samples. We corrected the original Arai diagrams from the first BZF experiment by using the Arai signatures from the repeated BZF experiment, which neutralizes the typical MD concave-up effect. Eleven samples meet the Arai diagram

post-selection criteria and provide qualified paleointensity estimates with a mean value for site GA-X of 4.23 ± 1.29 μT, consistent with an excursional geomagnetic field direction reported for this site.

2.2. Introduction

Various techniques have been developed to determine the intensity of Earth's ancient magnetic field (paleointensity). The earliest double heating methods, which compare the incremental demagnetization of the natural remanent magnetization (NRM) and laboratory-acquired thermal remanent magnetization (TRM) to simulate the original remanence acquisition processes, developed by Thellier and Thellier [1959] and later modified by Coe [1967] and Aitken et al. [1988], still provide the most reliable paleointensity estimations. However, TRM theory [Neel, 1951] is only strictly applicable to stable single-domain (SSD) particles, which are expected to meet the requirements of the three Thellier laws (additivity, reciprocity, and independence of partial TRM (pTRM) [Thellier, 1938]). The grain size range for SSD magnetite, an ideal remanence carrier, is very narrow, usually only between about 30 and 200 nm at room temperature depending on grain shape [Butler and Banerjee, 1975]. Therefore, magnetite grains in even rapidly cooled volcanic rocks tend to have grain size distributions that extend into the multidomain (MD) range, where a single ferrimagnetic crystal is naturally divided into multiple magnetic domains separated by domain walls. Even for those materials that are thought to contain mainly SSD magnetite, such as submarine basaltic glass [Tauxe and

Love, 2003] and copper slag [Ben-Yosef et al., 2008], it is often difficult to exclude the presence of some larger yet volumetrically significant MD grains. MD (titano)- magnetite is expected to be an important contributor to the magnetization of most igneous rocks. Therefore, developing techniques to acquire reliable paleointensities from such material is critical for further analyses of the paleomagnetic field.

The problem of trying to obtain reliable paleointensity estimates from samples that contain MD magnetite grains has been described by Levi [1977]. He concluded that paleointensities might be over-estimated due to the concave-up Arai diagram [Nagata et al., 1963] and the tendency to use the lower temperature segment of the NRM-pTRM curve to calculate paleointensity to avoid complications due to thermochemical alterations. Xu and Dunlop [2004] theoretically and experimentally studied the shapes of Arai diagrams for sized SSD and MD magnetite assemblages and found that the larger the MD particles are, the greater the curvature of the Arai diagram is, which eventually approaches the curve predicted by MD field blocking theory. Nevertheless, both studies found that the beginning and end points of the Arai diagram are not affected by the concave shape of the curve, which indicates that the total TRM (tTRM) is reproducible.

Shcherbakov et al. [1993] and Shcherbakova et al. [2000] studied the properties of pTRM of MD magnetite grains within natural and synthetic samples. They found that the Thellier laws of additivity and independence are violated in MD grains in the process of Thellier series paleointensity experiments. Dunlop and Ozdemir [2000] and Fabian [2000, 2001] studied the blocking temperatures (T_b) and the unblocking temperatures

(T_{ub}) of magnetite particles of various grain size ranges. They found that the concave-up Arai diagram for MD magnetite samples are exclusively due to the fact that their $T_{ub}<T_b$.

Previous work has attempted to detect nonlinear MD behavior in paleointensity experiments by inserting additional heating steps into the Coe [1967] protocol [Riisager and Riisager, 2001] or by analyzing Arai diagram curvatures [Paterson, 2011]. The objective is to provide sufficient criteria to exclude non-ideal MD paleointensities, leaving only the contribution from specimens with well-behaved SSD grains. Other attempts to improve the Thellier series experiment protocols, for instance the IZZI (alternating between Infield + Zero-field and Zero-field + In-field heating steps) method [Tauxe and Staudigel, 2004; Yu et al., 2004], are mainly designed to detect non-reciprocity in the paleointensity data. Biggin and Thomas [2003], Fabian [2001], and Leonhardt et al. [2004] discussed the use of pTRM checks in MD samples within the paleointensity experiments. Biggin and Boehnel [2003] and Fabian and Shcherbakov [2004] discussed possible effects of repeated heating during lab procedure. Leonhardt et al. [2004] and Paterson [2013] discussed the effects of anisotropy of remanent magnetization carriers on absolute paleointensity results. However, due to the threshold nature of these criteria, the final average paleointentisy results may still be biased even after the typical exclusion of most specimens in a study.

Wilson [1961, 1962] developed a paleointensity method that compares the continuous thermal demagnetization curve of NRM to that of a laboratory-applied tTRM. The Wilson method is domain-status independent because it is comparing the

magnetization unblocking spectra of the NRM and laboratory-applied tTRM. However, due to the fact that it measures a sample's magnetization at elevated temperature and provides no means to monitor thermal alteration, the Wilson method is not widely used.

A previous theoretical model [Fabian, 2001] suggested an extended treatment for Thellier series paleointensity experiments, in which the tTRM produced after completion of the original Thellier experiment is stepwise thermally demagnetized. Fabian [2001] also suggested that if a specimen did not experience alteration during heating, accurate paleointensity could be estimated by plotting its stepwise NRM losses versus tTRM losses (ideal pTRM) from a higher temperature range that avoided viscous remanent magnetization (VRM).

In this study, we develop a Thellier series paleointensity technique that can not only detect the presence of MD remanence carriers but also provide a method to correct concave-up Arai diagrams to obtain unbiased paleointensity determinations. We selected 24 basaltic lava specimens from four sites (GA78, 79, 84, 85) from Floreana Island, Galapagos Archipelago, for detailed study. These sites were part of an extensive study of paleosecular variation for 0-3 Ma based on more than 50 sites from various Galapagos islands [Kent et al., 2010; Rochette et al., 1997]. The four sites, which we refer to collectively as locality GA-X, had virtually the same mean paleomagnetic direction that was moreover widely divergent from the overall mean bipolar directional axis. Thus, the four sites from the GA-X sampling locality are thought to represent the same short time interval. We expect to process the rest of the Galapagos collection of more than 300

samples to derive a time-averaged paleointensity value. Site GA-X simply provided a large number of individually oriented samples to develop and test a paleointensity technique that can be applied to the rest of the Galapagos sample collection. The GA-X samples had some of the lowest preliminary paleointensity values from the studied Galapagos lavas, and only a small fraction of today's field strength [Kent et al., 2010] and should, thus, provide a severe test of the efficacy of a paleointensity technique in the face of relatively larger effects of magnetic overprinting (VRM) and other secondary processes including laboratory-induced artifacts. Moreover, the divergent mean characteristic paleomagnetic direction allowed any VRM acquisition in the present-day field to be readily detected and discounted.

2.3. Samples

The Galapagos Archipelago consists of volcanic islands on the Nazca plate just south of the Equator (Figure 2.1). The islands formed over a period of several million years, during which the Nazca plate moved east-southeast relative to the presumed Galapagos hotspot. Floreana Island (yellow square in Figure 2.1 inset), from which our samples were collected, is about 160 km to the southeast of the current eruptive center on Fernandina Island (red triangle in Figure 2.1 inset, 0.37ºS, 91.55ºW). The samples studied in this paper were taken with a hand-held gasoline-powered drill from four sites (GA78, GA79, GA84, and GA85) along the northwest coast of Floreana Island (Figure 2.1) on a 1993 expedition [Rochette et al., 1997]. Alternating field (AF) and thermal

demagnetization (TD) analyses [Kent et al., 2010; Rochette et al., 1997] revealed that these four sites had virtually the same paleomagnetic directions (mean Decl = 212.7º; mean Incl = -26.5º; A95 = 5.0º), which deviated by about 40_ from the average direction for all of the studied reverse polarity sites (N = 25; Decl = 179.8º; Incl = -0.1º; A95 = 5.6º) (Figure 2.2). Paleointensities from these four sites (31 specimens) by a brute-force two-point total TRM technique [Kent et al., 2010] yielded low values (mean.5.7 μT, median.4.4 μT; Table 2.1), less than 20% of today's equatorial dipole field. Judging from the coincidence of the paleomagnetic directions and paleointensities (Figure 2.2 and Table 2.1), as well as the close spatial proximity of these sites (Figure 2.1), we conclude that they are from essentially contemporaneous lava flows, if not from a single one. The samples can thus be combined to one site, GA-X, with not only the same paleomagnetic direction, but also the same expected paleointensity. The 25 mm diameter paleomagnetic core samples were sliced into several 12 mm height specimens, which were used in previous paleomagnetic directional studies (a and b specimens) [Rochette et al., 1997; Kent et al., 2010] and in this paleointensity study (c specimens). We also cut small (~20 mg) chips directly from c specimens for rock magnetic studies in the hope of minimizing any mineralogical differences between paleointensity bulk specimens and the chips used for rock magnetic characterization. In total, data from 24 available c specimens from site GA-X were generated and analyzed in this study (Table 2.1).

2.4. Rock Magnetic Experiments and Results

2.4.1. High-Temperature Magnetic Properties

We heated each of the 24 chip specimens to 600ºC and cooled them back to room temperature at a rate of 50ºC/min on a Alpha Precision Instruments translation Curie balance at the Rutgers paleomagnetic laboratory in a 0.15 T field to measure their thermomagnetic properties as induced magnetization versus temperature (Js-T) curves. We repeated the thermomagnetic experiments to check if the chips had been thermochemically altered, by comparing the Js-T curves for the first and second heatings (Figures 2.3a–d). Chips that experienced little alteration should provide reversible first Js-T curves and similar second Js-T curves.

First and second Js-T curves for all 24 rock chips give Curie temperatures typically around between 550ºC and 580ºC, which indicates that the major magnetization carrier is low-titanium magnetite. For almost all chips, heating and cooling curves for both the first and second Js-T experiments are similar, which indicates minimal thermochemical alteration in the course of the laboratory experiment (Figures 2.3a–d). According to the shape of the curves, we categorize the samples into two groups: Type I, in which the induced magnetization decreases slowly at low temperatures (<400ºC) and then decreases rapidly to the Curie point (see Figures 2.3c and d); and Type II, in which the induced magnetization decreases gradually over the entire temperature range to the Curie point (see Figures 2.3a and b). Results for different Js-T types are listed in Table 2.1. Most samples from sites GA78 and GA84 have Type I Js-T curves, whereas most samples from sites GA79 and GA85 have Type II Js-T curves.

3.4.2. Magnetic Hysteresis Loops

To check if the chips had been thermophysicochemically altered (‘‘physico’’ referring to domain state or structure), we measured hysteresis loops, isothermal remanent magnetization (IRM) acquisition curves and back field direct current demagnetization (DCD) curves for each of the 24 chips before and after the first thermomagnetic (Js-T) experiments, using a Princeton Measurement Corporation alternating gradient magnetometer (AGM) MicroMag2900 in a maximum field up to 1 T at the Rutgers paleomagnetic laboratory. Each of our rock magnetic chip specimens was visually aligned in the same direction for hysteresis measurements before and after heating to factor out any contribution to the hysteresis signal due to anisotropy, whose effects are not expected to be important in these basalts. Representative hysteresis loops, IRM, and DCD curves are shown in Figures 2.3e–h. Hysteresis properties (magnetic coercivity, Bc; remanent coercivity, Bcr; and the ratio of the remanent to the saturation magnetization, Mr/Ms) of the samples are also listed in Table 2.1.

Samples with Type I Js-T curves tend to have higher remanent coercivities and Mr/Ms ratios than samples with Type II Js-T curves (Figure 2.3 and Table 2.1). Generally, samples from sites GA78 and GA84 have higher coercivities and remanent coercivities (Bcr ~ 10–20 μT; Bcr ~ 30–45 μT) and Mr/Ms ratios (~ 0.15–0.30) than samples from sites GA79 and GA85 (Bcr ~ 5–10 μT; Bcr ~ 15– 25 μT and Mr/Ms ~ 0.10–0.20).

Hysteresis properties of the 24 GA-X chips are summarized in Figure 2.4 in a Day

plot [Day et al., 1977], on which data tend to be distributed along a theoretical SSD and MD mixing curve (#3 from Dunlop and Xu [1994] and Xu and Dunlop [1994]). Samples from site GA79 have the highest concentration of MD grains of around 80% (by volume), followed by site GA85 and GA78 with around 70%. Site GA84 has the lowest MD percentage of around 50%.

After heating to 600ºC, samples tend to move to the SSD corner of the Day plot, which indicates a reduction in the average effective grain size (increase of SSD domain state). The lower the MD percentage (the smaller overall grain size) the sample initially had, the more severe the change it experienced due to heating. Samples from sites GA78, GA79, and GA85 experienced relatively less domain state changes, while the domain state of samples from site GA84 experienced greater changes (Figure 2.4).

To summarize, rock magnetic properties of the 24 GA-X samples indicate that the dominant magnetic mineral is fine-grained, low-titanium magnetite with subequal SSD and MD-like contributions for sites GA78 and GA84 and with a more MD character for sites GA79 and GA85. Almost all of the samples are thermochemically stable even when heated to just above the Curie temperature of 580ºC. However, small but detectable thermophysical effective grain size (domain state) changes occurred during heating for the more SSD samples (i.e., those with the higher Mr/Ms ratios), which are mainly from sites GA78 and GA84. The GA-X samples should thus be ideal candidates for Thellier paleointensity experiments in terms of their thermochemical stability, but less obviously so in terms of magnetic grain size, which tends to be dominated by MD carriers.

2.5. Paleointensity Experiments and Results

2.5.1. Back-Zero-Forth (BZF) Protocol for Thellier Experiments and Results

There are three main double-heating paleointensity protocols: the classic Thellier method [Thellier and Thellier, 1959], and the Coe [1967] and Aitken et al. [1988] variants. Only the classical Thellier method is thought to be free from dependence on initial state [Yu and Tauxe, 2005]. In order to compare these paleointensity protocols for individual samples, we developed a hybrid triple-heating method, the BZF protocol, that consists of successive back-field heating, zero-field heating and forward-field heating. Samples were heated to target temperatures in zero-field and cooled to room temperature for the three BZF heating cycles per temperature step: the first cooling was performed in a 15 μT laboratory-applied field (used throughout) along the sample +Z axis; the second cooling was performed in a zero-field environment; the third cooling was performed in the same 15 μT laboratory-applied field but in the opposite direction (sample -Z axis) used for the first cooling. Partial TRM (pTRM) back checks were performed every other temperature step by reheating samples to lower temperatures in the same 15 μT laboratory-applied field along the sample -Z axis after the second zero-field heating cycle (Figure 2.5). From room temperature, we used 100ºC, 200ºC, 300ºC, 350ºC, 375ºC, 400ºC (350ºC), 425ºC, 450ºC (400ºC), 475ºC, 500ºC (450ºC), 525ºC, 550ºC (500ºC), and 575ºC as the heating target temperatures (with pTRM back check heating temperatures in parentheses) for all 24 specimens. Combination of the first and third heating cycles

corresponds to the original Thellier (two infield heating) protocol, combination of the second and third cycles corresponds to the Coe (zero-field and in-field) protocol, and combination of the first and second cycles corresponds to the Aitken (infield and zero-field) protocol. However, due to the MD high blocking temperature tails from the first heating of each temperature steps, which are conducted in a laboratory-applied back-field, the calculation of the Coe protocol in the BZF method is slightly different from the original Coe method. Hence, we note this calculation as the Coe* protocol.

Besides testing the internal consistency of these three standard Thellier series protocols, the BZF protocol also allows paleointensities to be calculated from three extra NRM and pTRM combinations, due to the capability of the BZF protocol to calculate the NRM residual in two ways and the pTRM gain in three ways. However, we only used the outcomes calculated using the Thellier, Coe* and Aitken protocols from the BZF experiments to estimate and compare paleointensity results. If the experimental conditions are ideal, the outcomes from the three classic methods (Thellier, Coe*, and Aitken) using the BZF protocol are expected to be identical for samples that contain only SSD particles, as predicted by Neel theory [Neel, 1951]. However, for samples dominated by MD particles, the outcome may be different due to the low- and high-temperature pTRM tails associated with MD behavior.

After plotting the vector end-point [Zijderveld, 1967] and Arai diagrams [Nagata et al., 1963] (Figure 2.6) for the two possible NRM outcomes and the three classic paleointensity methods from the BZF protocol, we used a relatively generous set of

criteria to automatically calculate the paleointensities using the program ThellierTool v.4.22 [Leonhardt et al., 2004]: number of points (N) ≥ 4; standard deviation (Std) ≤ 0.2; fraction of NRM (f) ≥ 0.3; quality factor (q) > 0; maximum angular deviation (MAD) ≤ 20º; alpha ≤ 20; relative check error (dCK) ≤ 10; cumulative check diff (dPAL) ≤ 15; normalized tail of pTRM (dt^*) ≤ 8; relative intensity diff ≤ 25; relative AC error (dAC) ≤ 15. We set the program to use as many data points as possible to estimate the paleointensity value. The paleointensity results and automated criteria temperature segments are listed in Table 2.2.

As illustrated in Figure 2.6 for a typical specimen (GA79.1c), using the above set of criteria to automatically calculate paleointensity resulted in a variety of selected temperature segments and paleointensity outcomes for the three standard methods. The NRM thermal demagnetization vector end-point diagram in Figure 2.6d is calculated from B and F steps in the BZF experiment, corresponding to the Arai diagram in Figure 2.6a. Figure 2.6e is based on Z steps, corresponding to Arai diagrams in both Figures 2.6b and c. Figure 2.6f is the actual NRM thermal demagnetization vector endpoint diagram for specimen GA79.1b [Kent et al., 2010]. Although strong VRM components can be identified up to 250ºC, sample GA79.1 shows a dominant primary TRM component going toward the origin as temperature increased to the Curie temperature. Use of a fixed middle temperature segment (350º–500ºC), which may be a relatively small fraction of the NRM yet avoids low-temperature VRM and high-temperature alteration, yielded much more consistent values so all three standard methods yield almost the same value for site GA-X, with median paleointensity estimates of 5.63, 5.67,

and 5.55 μT, for the Thellier, Coe*, and Aitken protocols, respectively (Figure 2.7 and Table 2.2). By comparison, the 350º–575ºC two-point paleointensity estimates for 24 b specimens from site GA-X [Kent et al., 2010] yielded a median value of 4.14 μT (Table 2.2). The relatively more scattered outcomes of the automated-selection compared to the fixed temperature segment paleointensity calculation is clearly seen in the histograms for the 24 results (Figure 2.7). However, the risk of using a fixed temperature segment for all the samples is that the overall site-mean value could be biased due to concave-up Arai diagrams for MD grain contribution.

2.5.2. Correction for MD Concave-Up Arai Diagrams by Repeating BZF experiments

In order to perform a correction for the MD concave-up pattern on the Arai diagram, we gave each specimen a total TRM (tTRM) by cooling from 575ºC in the presence of a laboratory-applied field (15 μT) along the X-axis, i.e., perpendicular to the applied-field direction for the initial BZF experiments. The BZF protocol described above was then repeated with the laboratory-applied tTRM as a synthetic NRM, using the same laboratory-applied field (both the same direction and intensity) and target temperatures as before. We name the Arai diagrams for this repeated BZF experiment ‘‘Arai signatures’’ that represent only the TRM recording properties of the specimens, if no severe thermal alteration occurs in the laboratory heating process. Due to the range of effective magnetic grain sizes in the specimens, which cause differences in the resulting Thellier series protocols, each specimen is expected to have a unique Arai signature associated with a particular experiment protocol (Thellier, Coe*, and Aitken).

We performed MD corrections by plotting the NRM unblocking remaining from the first BZF against the laboratory-applied tTRM unblocking from the repeated BZF to generate the corrected Arai diagrams. The corrected Arai diagrams, therefore, use the Arai signatures to neutralize MD concave-up contributions in the original Arai diagrams by plotting original NRM unblocking versus synthetic NRM unblocking, and should thus provide unbiased paleointensity estimates.

All specimens from site GA-X produce concave-up Arai diagrams in both the first and second BZF experiments, which confirms that all specimens contain portions of MD magnetization carriers as anticipated by the hysteresis results. Representative results produced from the first and second BZF experiments for a specimen are shown in Figure 2.8a (also see Figures 2.9 and 2.10 for more concave-up Arai diagrams). The MD contribution (δMD) can be parameterized from the ratio of the area enclosed between the Arai signature and the line joining the beginning and end points (green dashed line in Figure 2.8a) divided by the triangular area enclosed by this line and the axes. For example, δMD for the specimen GA79.8c in Figure 2.8a is 0.183. However, because the line connecting the beginning and end points in the Arai diagram is not affected by the δMD content, the total TRM (tTRM) should be reproducible as shown in previous work [Levi, 1977; Xu and Dunlop, 2004]. A plot of the first against repeated pTRM acquisitions can be used as an indicator of thermophysicochemical alterations (red line in Figure 2.8a), whose linearity decreases and slope diverts from 1 if the recording capability of pTRM changes from the first to the second BZF experiment. We quantify this expected agreement by using its least-squares fit slope (tTRM K) and linear

regression correlation coefficient (tTRM-R). We call it ‘‘tTRM check’’ for alteration, as opposed to ‘‘pTRM checks’’ as shown in yellow lines for both the original Arai diagram and Arai signature. The pTRM that is carried by a tTRM check is equivalent to type pTRM* defined by Shcherbakov et al. [1993]. The tTRM check offers a quantitative measurement of specimen alteration before and after it has been thoroughly heated to its Curie temperature, as opposed to the stepwise pTRM checks.

The NRMs in both the first and second BZF experiments obviously have contributions from secondary VRMs, as evidenced by the component structure in vector end-point demagnetization diagrams (Figure 2.6), which affect the first BZF experiments and cause curvatures of the corrected Arai diagrams in the low temperature ranges up to 350º–400ºC. Accordingly, we used the corrected Arai diagram from 400ºC to 575ºC to estimate the unbiased paleointensity for a specimen and the associated absolute value of linear regression correlation coefficient (P-Int-R) as a representative measure of the qualities of that estimate.

Specimen GA79.8c gives tTRM-K.0.9663, tTRM-R.0.9969 (Figure 2.8a), and P-Int-R.0.9985 (Figure 2.8b). With the support of good linearities of both the tTRM check and the corrected Arai diagram, specimen GA79.8c provides a reliable paleointensity estimation of 4.08 μT (Figure 2.8b). In order to systematically assess the quality of paleointensity estimates, we arbitrarily set a simple quality parameter threshold as follows: the absolute values of tTRM-R and the P-Int- R need to be greater than 0.9900. We used the calculation method (Thellier, Coe*, and Aitken) that provided the best P-Int-

R and then tTRM-R to estimate the paleointensity (e.g., we used the Coe* method for specimen GA79.8c).

Typical results calculated by the best methods for four representative specimens that meet the aforestated quality criteria (GA79.4c-Coe*, GA7 9.5c-Thellier, GA85.2c-Aitken, and GA85.3c- Thellier) are shown in Figure 2.9. Together, they provide well-clustered paleointensity estimates that range from 4.21 to 4.64 μT. Beside the five specimens shown in Figures 2.8 and 2.9, six other specimens from site GA-X also pass the 0.9900 qualification criteria, making the total success rate 11 out of 24 (Table 2.3).

Typical results calculated by the best method for each of four representative specimens that fail the earlier described quality criteria are presented in Figure 2.10. Specimen GA78.2c failed both tTRM-R and P-Int-R; GA79.3c failed tTRM-R but passed P-Int-R; GA78.8c and GA84.6 both passed tTRM-R but failed P-Int-R. For specimens GA78.2 and GA79.3, the tTRM checks reveal large non-linear features, which indicate thermophysicochemical alterations between the same temperature steps of the first and second BZF experiments. It is therefore reasonable to conclude that they are disqualified to provide reliable paleointensity estimates. Paleointensity values from these specimens (1.35 μT and 2.22 μT) are also consistently lower than the values estimated from the qualified specimens. For specimens GA78.8c and GA84.6c, tTRM checks pass, which indicates no alteration. However, their corrected Arai diagrams fail to present linear features as expected. Paleointensity values from these specimens (8.28 and 5.57 μT) are consistently high compared to the values estimated from the qualified specimens. The

reason why they fail to yield linear corrected Arai diagrams is complicated, which we attempt to explain below. All 24 of the results from the new MD paleointensity technique for site GA-X are listed in Table 2.3.

Vector end-point diagrams for thermal demagnetization of NRM of selected ‘‘b’’ specimens from Kent et al. [2010] are shown in Figure 2.11. Despite clearly identified low-temperature VRM components up to 300º–400ºC, most of the samples from site GA-X yield trajectories going toward the origin up to the Curie temperature, consistent with primary TRMs. The ‘‘c’’ counterparts of specimens GA79.8b, GA79.5b, and GA85.3b (Figures 2.11a–c) provide acceptable corrected paleointensity results (Figures 2.8 and 2.9), whereas the ‘‘c’’ specimens of GA78.8, GA79.3, and GA84.6 (Figures 2.11d–f) provide failed paleointensity results (Figure 2.10).

2.6. pTRM Checks

The pTRM check is usually taken for granted as a valid indicator of thermophysicochemical alterations. However, for GA79.5c (Figures 2.9e and f), and GA79.8c (Figures 2.8a and b), the pTRM checks are not consistent with the original pTRM acquisition for both original Arai diagrams and Arai signatures, yet data for these samples yield two of the best P-Int-Rs, and provide very satisfactory paleointensity estimates. This suggests that the pTRM checks are false alarms in these cases and more generally suggests that it may be inappropriate to automatically disqualify paleointensity

results on the basis of pTRM checks. Nevertheless, the tTRM checks (tTRM-K and tTRM-R) that we developed in this study, which compare the stepwise pTRM acquisitions of the first BZF against the second BZF experiments, behaved well. The difference between the pTRM check and tTRM check is that the tTRM check compares exactly the same processes (pTRM stepwise blocking for the exact same temperature step), whereas the pTRM check compares somewhat different processes (the original pTRM blocking and the back-check pTRM blocking after a zero-field step partial thermal demagnetization). For SSD specimens, the pTRM checks may work as intended. But for MD specimens, the partial demagnetization step between the original pTRM acquisition and pTRM check acquisition is not completely clean due to the non-linear (concave-up) Arai diagram. Thus, the signals in pTRM checks reflect not only the thermophysicochemical alteration but also the non-ideal behavior of MD contributions. We therefore suggest that the tTRM check is a more powerful and appropriate technique to identify alterations instead of the pTRM check for samples with significant MD contributions.

Based on many previous works that have experimentally and theoretically studied effects of thermochemical alteration over the blocking spectra of SSD particles [McClelland, 1996; Draeger et al., 2006; Yamamoto, 2006; Fabian, 2009], we also suggest that the pTRM check should not be automatically relied on for SSD samples. Specimens GA78.8c (Figure 2.10c) and GA84.6c (Figure 2.10g) have satisfactory pTRM checks for the original Arai diagrams as well as acceptable tTRM checks, which indicate little alteration from room temperature to the Curie temperature. However, their corrected

Arai diagrams are still curved at high temperatures (475º–500ºC), which is not likely to be caused by sudden demagnetization of VRM. This is because both the pTRM check and the tTRM check are only capable of detecting alteration of ferrimagnetic grains with blocking unblocking temperatures lower than the current checking temperature. If a specimen is heated from step T_i to step T_{i+1}, particles with blocking/unblocking temperatures between T_i and T_{i+1}may have altered but are not able to be detected by pTRM check back to T_i. In the BZF experiments, it happens during the first back-field heating steps. But the pTRM or tTRM checks back to T_i are not capable of detecting such alteration because they occur outside of the blocking/unblocking temperature ranges for those grains. Figure 2.12 illustrates the actual data from GA84.6 by using the Coe paleointensity protocol. For the temperature step at 550ºC, the sample is heated in zero-field for step 1; and then in-field for step 2; followed by another in-field heating to 500ºC for step 3 to perform pTRM check (Figure 2.12). But the sudden TRM recording capability increase for the grains that have blocking/unblocking temperatures between 500ºC and 550ºC (gray bar in Figure 2.12) cannot be detected by a pTRM check back to 500ºC, which only applies to those grains that have blocking/unblocking temperatures between room temperature and 500ºC. The alternative way to check this type of hidden (T_i to T_{i+1}) alteration is to see if the corrected Arai diagram is linear. If the corrected Arai diagram is linear from a certain high temperature that avoids VRM (400ºC selected here) to the maximum blocking temperature near the Curie point (575ºC in the BZF experiments), this would likely indicate not only that the corrected Arai diagram provides a reliable paleointensity estimate but also that the specimen has not experienced serious thermophysicochemical alteration. Fortunately for site GA-X, 11 of 24 specimens

behaved in this way (Figures 2.8, 9, and 13 and Table 2.3).

We find that pTRM checks from repeated BZF experiments work well for detecting thermophysicochemical alterations that occurred during the first back-field heating steps of the original BZF experiment (Figures 2.10c, e, and g), with the hidden increased pTRM carrying capabilities coinciding with the pTRM check failures over 500ºC. This is because when the hidden pTRM recording capability increases due to alteration, its high and low temperature tails also increase, allowing them to be detectable during repeated BZF experiments with the pTRM checks.

De Groot et al. [2011] reported that small magnetite grains (< ~3 μm) in a lava flow sample appeared to undergo greater change in magnetic domain configurations during heating than larger grains (> ~10–15 μm). This is consistent with our results. Hysteresis loops (Figure 2.3) and Day plots (Figure 2.4) provide evidence that samples with larger MD contributions (GA79.5) tend to undergo less thermophysicochemical alteration, whereas samples more dominated by a SSD contribution (GA84.6) tend to undergo greater thermophysicochemical alteration. Moreover, the before and after heating rock magnetic results (stable Js-T curves but varying hysteresis properties) also reveal that the thermophysicochemical alteration path is from more MD toward more SSD properties. The finer-grain size the original grains are (i.e., greater the Mr/Ms for the assemblage), the more likely they tend to undergo this kind of thermophysicochemical alteration in domain status, so SSD-like samples undergo greater alteration than MD-behaved samples. Thermophysicochemical alteration in the SSD-like samples are often of

the hidden (T_i to T_{i+1}) type (Figure 2.10: GA78.8c and GA84.6c), which is not detected by pTRM or even tTRM checks. The benefit of using samples containing MD grains is that, even if some thermophysicochemical alteration occurs, the MD grains remain MD grains. Arai diagrams predicted by MD field blocking theory [Xu and Dunlop, 2004] for MD grains tend to vary little even with large MD grain size changes. The Arai signature of a sample containing MD grains will therefore remain similar to its original Arai diagram, which still closely represents the original TRM recording properties of the sample.

2.7. Discussion

Certain sets of data qualifying criteria similar to those used in this study for automatic estimations have usually been used to include or exclude specimens in most previous paleointensity studies. The main judging factors are usually the linearity of the Arai diagram and the pTRM checks. This often results in variable temperature segments chosen by the criteria to estimate paleointensities. Automatic criteria-based paleointensity selection for the GA-X samples (Table 2.2) yields temperature segments as low as room temperature and as high as the Curie temperature for paleointensity estimates. This is obviously inappropriate because the low and high temperature ranges of Arai diagram are likely to be affected by VRM and thermophysicochemical alteration, respectively. Moreover, for non-SSD specimens with concave-up Arai diagrams, selection of inconsistent temperature segments introduces large random errors, which usually

overwhelm and disguise the potential biases. We therefore used a fixed temperature segment of 400º–575ºC for the corrected paleointensity estimations, in order to avoid low temperature VRM and to minimize uncertainties from using automatically selected temperatures.

Based on the rock magnetic data and results of our repeated BZF experiments, we developed a simple set of sample pre-selection criteria in an attempt to increase the success rate of future paleointensity estimations. If we only used samples with Mr/Ms less than 0.19 (to avoid SSD thermal alteration) and Bcr larger than 20 µT (to avoid unstable remanences) (see Tables 2.1 and 2.3), our success rate would have increased from 46% (11/24) to 64% (7/ 11). However, this would also reduce the qualified paleointensity estimates from 11 to 7.

The Arai signature correction technique developed in this study offers an unbiased approach to estimate reliable paleointensities from MD specimens. The traditional three Thellier laws (additivity, reciprocity, and independence of pTRM [Thellier, 1938]) do not have to be completely met to provide accurate paleointensity estimations. However, this MD technique still requires the samples to be relatively thermophysicochemically stable, which happens to be largely true for samples from site GA-X.

Sbarbori et al. [2009] used the IZZI method to estimate paleointensities from volcanic rocks from Isla Socorro, Mexico. They repeated their original IZZI method after

giving their samples laboratory-applied tTRM cooling from 610ºC at an orthogonal direction to the laboratory field used in the IZZI experiments, in an attempt to effectively perform the ‘‘Arai signature correction’’ that we propose in this study. However, for the repeated IZZI experiment, their non-ideal Type-II specimens, which yielded typical concave-up original Arai diagrams [Sbarbori et al., 2009, Figure 8b], produced almost linear Arai signatures [Sbarbori et al., 2009, Figure 10b]. Thus they did not manage to perform the MD correction and gave up the idea of repeating the original paleointensity experiments. In this study, by studying igneous rock samples of various overall grain size (domain status), we conclude that the Type-II specimen in Sbarbori et al. [2009] that was used for the repeated IZZI experiment was more SSD dominant, and hence provided Arai diagrams and Arai signatures like the specimen GA84.6c in this study (Figure 2.10g). The concave-up original Arai diagram is due to thermal alteration, which causes the TRM recording capability to increase over the 500º–600ºC temperature range (Figures 2.10g and 2.12 in this study and Figures 8a and 8b in [Sbarbori et al., 2009]), rather than the MD effect. This thermal alteration belongs to the hidden type that we discussed in section 2.6, which cannot be detected by pTRM checks.

In this study, we do not consider possible anisotropy of the studied specimens from site GA-X. Anisotropy of samples can introduce slight uncertainties in the paleointensity estimations because the NRM and the laboratory-applied pTRM directions are not necessarily the same. However, any anisotropy effect can be readily compensated by applying the laboratory-applied tTRM in the same direction as the NRM before conducting the repeated BZF experiments. We will take this into account in future

studies.

2.8. Conclusions

The main magnetization carriers for the 24 studied samples from site GA-X are fine-grained low-titanium magnetite with various range of grain sizes (GA78 and GA 84 have more SSD grains; GA79 and GA 85 have more MD grains). The BZF protocol applied to the studied specimens is able to estimate paleointensities according to various methods, which provide self-consistency checks. This protocol can also be used in microwave and AF-based paleointensity techniques. For specimens dominated by MD magnetite grains, the standard pTRM checks can be affected by both thermophysicochemical alterations and non-linear (concave-up) Arai diagrams. Thus, pTRM checks are not always reliable indicators of alteration. The tTRM check, which detects the effects of alteration but not MD effects, is a more powerful and appropriate check than the pTRM check, although neither check is capable of detecting the hidden (T_i to T_{i+1} type) thermophysicochemical alterations for both SSD or MD samples.

Specimen pre-selection criteria based on rock magnetic properties developed in this study could be used to improve both paleointensity experiment success rate and quality of the results. Specimens that contain MD remanence carriers (low Mr/Ms ratios) and that undergo minimal laboratory thermophysicochemical alteration during heating (reversible Js-T curves and similar rock magnetic properties before and after heating)

yield the most satisfactory Arai signature MD corrected paleointensity estimates. Rock magnetic criteria and results from our repeated BZF experiments suggest that MD-dominated samples provide more reliable and unbiased paleointensity estimates than more SSD-like samples, as long as the Arai signature MD correction is performed. Due to the fact that MD samples are much more common than SSD samples in nature, we suggest that our MD correction technique can be more generally used for paleointensity determinations.

The final paleointensity estimate for site GAX, which is based on 11 out of 24 specimens analyzed, is 4.23 ± 1.29 μT (mean6standard deviation; 4.16 μT for median, Table 2.3), which happens to be almost identical to the median of the two-point paleointensity estimates (4.14 μT, Table 2.2) from Kent et al. [2010].

2.9Acknowledgments

We thank Pierre Rochette for generously providing the Galapagos lava samples, Helene Collombat for organizing the sample collection with authorization of the National Park of the Galapagos Island, funded by INSU, and Lisa Tauxe for discussions on the properties of MD particles during paleointensity experiments. We thank the Associate Editor of our previous submission, Andrew Roberts, for his careful editing of the manuscript and two reviewers (Lisa Tauxe and Yongjae Yu) for their constructive comments. We also thank G-cubed Editor James Tyburczy, Associate Editor Joshua

Feinberg, and two anonymous reviewers of our current submission for their constructive comments, all of which have helped to improve this version of our paper. Finally, we thank the Wiley G-Cubed Production Editor and many others who have helped us to produce this article successfully. Research was supported by NSF grant EAR-1113569. LDEO contribution 7722.

References

Aitken, M. J., A. L. Allsop, G. D. Bussell, and M. B. Winter (1988), Determination of the intensity of the Earth's magnetic-field during archaeological times—Reliability of the Thellier technique, Rev. Geophys., 26, 3–12.

Ben-Yosef, E., H. Ron, L. Tauxe, A. Agnon, A. Genevey, T. E. Levy, U. Avner, and M. Najjar (2008), Application of copper slag in geomagnetic archaeointensity research, J. Geophys. Res., 113, B08101, doi:10.1029/2007JB005235.

Biggin, A. J., and H. N. Bohnel (2003), A method to reduce the curvature of Arai plots produced during Thellier palaeointensity experiments performed on multidomain grains, Geophys. J. Int., 155, F13–F19.

Biggin, A. J., and D. N. Thomas (2003), The application of acceptance criteria to results of Thellier palaeointensity experiments performed on samples with pseudo-single-domain-like characteristics, Phys. Earth Planet. Inter., 138, 279–287.

Butler, R. F., and S. K. Banerjee (1975), Theoretical singledomain grain size range in magnetite and titanomagnetite, J. Geophys. Res., 80, 4049–4058. Coe, R. S. (1967), Paleo-intensities of the Earth's magnetic field determined from Tertiary and Quaternary rocks, J. Geophys. Res., 72, 3247–3262.

Day, R., M. Fuller, and V. A. Schmidt (1977), Hysteresis properties of titanomagnetites: Grain-size and compositional dependence, Phys. Earth Planet. Inter., 13, 260–267.

De Groot, L. V., E. A. Bakelaar, and M. J. Dekkers (2011), Detecting changes in magnetic domain configuration after heating using MFM imaging, Abstract GP23A-1023 presented at 2011 Fall Meeting, AGU, San Francisco, Calif., 5–9 Dec.

Draeger, U., M. Prevot, T. Poidras, and J. Riisager (2006), Single- domain chemical, thermochemical and thermal remanences in a basaltic rock, Geophys. J. Int., 166, 12–32.

Dunlop, D. J., and O. Ozdemir (2000), Effect of grain size and domain state on thermal demagnetization tails, Geophys. Res. Lett., 27, 1311–1314.

Dunlop, D. J., and S. Xu (1994), Theory of partial thermoremanent magnetization in multidomain grains: 1. Repeated identical barriers to wall-motion (single microcoercivity), J. Geophys. Res., 99, 9005–9023. Fabian, K. (2000), Acquisition of thermoremanent magnetization in weak magnetic fields, Geophys. J. Int., 142, 478–486.

Fabian, K. (2001), A theoretical treatment of paleointensity determination experiments on rocks containing pseudosingle or multi domain magnetic particles, Earth Planet. Sci. Lett., 188, 45–58.

Fabian, K. (2009), Thermochemical remanence acquisition in single-domain particle

ensembles: A case for possible overestimation of the geomagnetic paleointensity, Geochem. Geophys. Geosyst., 10, Q06Z03, doi:10.1029/2009GC 002420.

Fabian, K., and V. P. Shcherbakov (2004), Domain state stabilization by iterated thermal magnetization processes, Geophys. J. Int., 159, 486–494.

Kent, D. V., H. Wang, and P. Rochette (2010), Equatorial paleosecular variation of the geomagnetic field from 0 to 3 Ma lavas from the Galapagos Islands, Phys. Earth Planet. Inter., 183, 404–412.

Kirschvink, J. L. (1980), The Least-squares line and plane and the analysis of palaeomagnetic data, Geophys. J. R. astr. SOC, 62, 699–718.

Leonhardt, R., C. Heunemann, and D. Krasa (2004), Analyzing absolute paleointensity determinations: Acceptance criteria and the software ThellierTool4.0, Geochem. Geophys. Geosyst., 5, Q12016, doi:10.1029/2004GC000807.

Levi, S. (1977), The effect of magnetite particle size on paleointensity determinations of the geomagnetic field, Phys. Earth Planet. Inter., 13, 245–259.

McClelland, E. (1996), Theory of CRM acquired by grain growth, and its implications for TRM discrimination and
palaeointensity determination in igneous rocks, Geophys. J. Int., 126, 271–280.

Nagata, T., Y. Arai, and K. Momose (1963), Secular variation of the geomagnetic total force during the last 5000 years, J. Geophys. Res., 68, 5277–5281.

Neel, L. (1951), Le trainage magnetique, J. Phys. Radium, 12, 339–351.

Paterson, G. A. (2011), A simple test for the presence of multidomain behavior during paleointensity experiments, J. Geophys. Res., 116, B10104, doi:10.1029/2011JB008369.

Paterson, G. A. (2013), The effects of anisotropic and nonlinear thermoremanent magnetizations on Thellier-type paleointensity data, Geophys. J. Int., 193, 694–710.

Riisager, P., and J. Riisager (2001), Detecting multidomain magnetic grains in Thellier palaeointensity experiments, Phys. Earth Planet. Inter., 125, 111–117.

Rochette, P., F. Ben Atig, H. Collombat, D. Vandamme, and P. Vlag (1997), Low paleosecular variation at the equator: A paleomagnetic pilgrimage from Galapagos to Esterel with Allan Cox and Hans Zijderveld, Geol. Mijnbouw., 76, 9–19.

Sbarbori, E., L. Tauxe, A. Goguitchaichvili, J. Urrutia-Fucugauchi, and W. A. Bohrson (2009), Paleomagnetic behaviorof volcanic rocks from Isla Socorro, Mexico, Earth Planets Space, 61, 191–204.

Shcherbakov, V. P., E. McClelland, and V. V. Shcherbakova (1993), A model of multidomain thermoremanent magnetization incorporating temperature-variable domain-structure, J. Geophys. Res., 98, 6201–6216.

Shcherbakova, V. V., V. P. Shcherbakov, and F. Heider (2000), Properties of partial thermoremanent magnetization
in pseudosingle domain and multidomain magnetite grains, J. Geophys. Res., 105, 767–781.

Tauxe, L., and J. J. Love (2003), Paleointensity in Hawaiian Scientific Drilling Project Hole (HSDP2): Results from submarine basaltic glass, Geochem. Geophys. Geosyst., 4, 8702, doi:10.1029/2001GC000276.

Tauxe, L., and H. Staudigel (2004), Strength of the geomagnetic field in the Cretaceous Normal Superchron: New data from submarine basaltic glass of the Troodos Ophiolite, Geochem. Geophys. Geosyst., 5, Q02H06, doi:10.1029/ 2003GC000635.

Thellier, E. (1938), Sur l'aimantation des terres cuites et ses applications geophysiques, Ann. I. P. G. Paris, 16, 157–302.

Thellier, E., and O. Thellier (1959), Sur l'intensite du champ magnetique terrestre dans le passe historique et geologique, Ann. Geophys., 15, 285–378.

Wilson, R. L. (1961), Palaeomagnetism in Northern Ireland, Part 1, The thermal demagnetization of natural magnetic moments in rocks, Geophys. J. Int., 5, 45–58.

Wilson, R. L. (1962), An instrument for measuring vector magnetization at high temperatures, Geophys. J. Int., 7, 125– 130.

Xu, S., and D. J. Dunlop (1994), Theory of partial thermoremanent magnetization in multidomain grains: 2. Effect of microcoercivity distribution and comparison with experiment, J. Geophys. Res., 99, 9025–9033.

Xu, S., and D. J. Dunlop (2004), Thellier paleointensity theory and experiments for multidomain grains, J. Geophys. Res., 109, B07103, doi:10.1029/2004JB003024.

Yamamoto, Y. (2006), Possible TCRM acquisition of the Kilauea 1960 lava, Hawaii: Failure of the Thellier paleointensity determination inferred from equilibrium temperature of the Fe-Ti oxide, Earth Planets Space, 58, 1033–1044.

Yu, Y. J., L. Tauxe, and A. Genevey (2004), Toward an optimal geomagnetic field intensity determination technique, Geochem. Geophys. Geosyst., 5, Q02H07, doi:10.1029/ 2003GC000630.

Yu, Y., and L. Tauxe (2005), Testing the IZZI protocol of geomagnetic field intensity

determination, Geochem. Geophys. Geosyst., 6, Q05H17, doi:10.1029/2004GC 000840.

Zijderveld, J. D. A. (1967), A.C. demagnetization of rocks: Analysis of results, Methods in paleomagnetism, edited by D. W. Colllnson, K. M. Creer, and S. K. Runcorn, New York, Amsterdam, pp. 254–286.

Figure Captions:

Figure 2.1. Location map of sites GA78 (blue), GA79 (orange), GA84 (green) and GA85 (red) from Floreana, Galapagos Islands. White dots are sampling sites from Rochette et al. [1997] that are not discussed in this paper. The map was generated by GeoMapApp using the Global Multi-Resolution Topography data (GMRT version 2.4)

Figure 2.2. Filled and open circles are characteristic site mean paleomagnetic directions plotted on an equal-area stereographic projection for all Galapagos sample sites (after Kent et al. [2010]). Colored symbols in the inset are paleomagnetic directions for samples from site GA-X (colored empty circles indicate samples used in previous paleo-directions studies; colored crosses indicate samples used in this paleointensity study).

Figure 2.3. Js–T curves for (a, c) the first and (b, d) second heating; hysteresis, IRM and back field DCD curves (e, g) before and (f, h) after heating for specimens GA79.5s and GA84.6s.

Figure 2.4. Day plot [Day et al., 1977] for GA-X samples. Dashed line is SSD-MD mixing curve 3 [Dunlop and Xu, 1994; Xu and Dunlop, 1994], with crosses indicating the volume percentage of MD grains in the mixture. Filled circles are data before heating, and open circles are data after heating to 600ºC. Arrows indicate the alteration path for specimens GA79.5s and GA84.6s.

Figure 2.5. Schematic diagram with heating steps (H1-Backward field, H2-Zero field, H3-forward field to a previous lower temperature to perform pTRM check, H4-Forward field) for target temperatures (T1, T2, T3, . . .) in the proposed hybrid BZF protocol.

Figure 2.6. Arai diagrams for GA79.1c from the hybrid BZF protocol for (a) Thellier, (b) Coe^*, and (c) Aitken methods (solid lines are linear regressions for fixed temperature segments of 350º–500ºC; dashed lines are for auto-selected temperature segments), with (d and e) corresponding calculated NRM thermal demagnetization vector end-point diagrams [Zijderveld, 1967] (d corresponds to a; e corresponds to both b and c) and actual NRM thermal demagnetization vector end-point diagram for specimen GA79.1b [Kent et al., 2010].

Figure 2.7. Histograms of BZF paleointensity results for different calculation methods for (top) automated temperature selection and (bottom) fixed 350º–500ºC temperature range.

Figure 2.8. Paleointensity results for GA79.8c from the first and repeated BZF experiments, calculated using the Coe^* method according to the highest quality control factors. (a) Arai diagram of the first (thick black line) and repeated (thin black line) BZF experiments, with circles indicating temperatures 20º–375ºC and squares indicating 400º–575ºC. The orange line connects the pTRM checks. The red line represents the first BZF pTRM gains versus the pTRM gains in the repeated BZF experiment (tTRM check). The light blue dashed line is the 1:1 ratio of the first and the repeated pTRM gains. The green

dashed line is the theoretical linear prediction of Arai diagrams for SSD grains for repeated BZF experiment. (b) Arai diagrams of the first (thick black line) BZF experiments with pTRM checks (orange line). The pink line is the original NRM unblocking remaining from the first BZF experiment versus the laboratory-applied tTRM unblocking from the repeated BZF experiment with the blue dashed line representing the linear regression for the 400º–575ºC temperature segment.

Figure 2.9. Paleointensity results for four of the nominally qualified specimens (GA79.4c, GA79.5c, GA85.2c, and GA85.3c).

Figure 2.10. Paleointensity results for four of the disqualified specimens (GA78.2c, GA78.8c, GA79.3c, and GA84.6c).

Figure 2.11. NRM thermal demagnetization vector end-point diagrams [Zijderveld, 1967] for ‘‘b’’ specimens (qualified paleointensity results: (a) GA79.8b, (b) GA79.5b, and (c) GA85.3b; disqualified paleointensity results: (d) GA78.8b, (e) GA79.3b, and (f) GA84.6b) from site GA-X from Kent et al. [2010].

Figure 2.12. pTRM model from actual GA84.6 data, which indicates the hidden pTRM increase that cannot be detected by pTRM checks. White boxes are NRM spectra calculated from GA84.6b thermal demagnetization experiment from Kent et al. [2010]. Red bars are pTRM acquisitions for each temperature segment calculated using Coe^* method from GA84.6c. Green bars are pTRM checks for each temperature segment method from GA84.6c up to 500ºC. Gray bar is the hidden alteration from 500º-550ºC (happened during (a) Step 1; becames visible after (b) Step 2) that cannot be detected by pTRM check in (c) Step 3.

Figure 2.13. Paleointensity probability distributions for 11 qualified results from site GA-X.

Table 2.1. Samples Used in This Study and Their Rock Magnetic Properties

Sample	Used for P-Int	MAD^K (°)	Core PCA Decl^K (°)	Core PCA Incl^K (°)	In Situ PCA Decl^K (°)	In Situ PCA Incl^K (°)	$J_{350–575}{}^K$ E-7 (Am^2)	Kent10 P-Int^K (μT)	J_s-T Type	B_c (mT)	B_{cr} (mT)	M_r/M_s Ratio
GA78.1	Yes	2.1	51.8	−10.5	214.2	−26.5	14.49	3.18	I	15.66	38.58	0.170
GA78.2	Yes	3.5	283.1	−28.1	222.1	−30.0	10.38	1.70	II	5.71	16.76	0.153
GA78.3	No	1.6	282.0	−25.3	213.9	−27.8	37.06	7.05	N/A	N/A	N/A	N/A
GA78.4	No	1.0	291.1	−22.9	212.4	−30.5	56.29	18.33	N/A	N/A	N/A	N/A
GA78.5	Yes	2.5	266.2	−29.5	210.1	−27.1	17.14	3.58	I	15.94	39.01	0.219
GA78.6	Yes	2.1	11.2	−8.6	206.2	−32.1	20.16	4.74	I	13.04	32.92	0.189
GA78.7	No	1.2	317.7	−3.9	203.8	−31.7	67.98	26.09	N/A	N/A	N/A	N/A
GA78.8	Yes	0.6	294.6	−21.9	214.3	−32.2	35.15	8.14	I	14.57	36.70	0.161
GA79.1	Yes	2.7	21.9	−4.3	228.4	−30.0	26.52	4.10	II	5.20	18.43	0.111
GA79.2	Yes	2.9	298.4	−18.6	205.2	−28.0	26.52	3.14	II	6.19	18.96	0.121
GA79.3	Yes	2.2	50.9	−11.4	214.8	−23.9	23.80	2.97	I	6.18	18.01	0.168
GA79.4	Yes	1.4	97.2	−31.1	213.1	−27.6	30.33	4.98	I	12.75	38.45	0.204
GA79.5	Yes	1.5	8.7	−3.6	207.9	−28.3	42.41	5.90	II	6.62	23.34	0.122
GA79.7	Yes	2.1	288.4	−24.0	206.1	−29.7	66.38	8.15	I	11.55	30.90	0.163
GA79.8	Yes	2.8	294.6	−24.3	194.2	−30.6	30.30	4.07	II	6.46	21.97	0.121
GA84.1	Yes	1.6	57.8	−18.1	211.5	−26.0	34.46	4.12	I	20.00	48.21	0.285
GA84.2	Yes	1.9	155.9	−35.6	205.9	−25.4	27.71	2.80	I	9.59	25.27	0.199
GA84.3	Yes	1.4	107.0	−26.9	220.9	−21.7	33.90	3.67	I	18.13	44.51	0.265
GA84.4	No	2.0	22.5	−1.4	222.4	−22.5	19.66	4.69	N/A	N/A	N/A	N/A
GA84.5	No	3.6	70.4	−20.5	230.8	−25.9	34.66	4.18	N/A	N/A	N/A	N/A
GA84.6	Yes	1.3	323.0	−20.0	208.6	−30.1	50.37	6.73	I	19.21	45.46	0.255
GA84.7	No	1.3	89.2	−23.6	219.1	−22.9	27.11	3.08	N/A	N/A	N/A	N/A
GA84.8	Yes	1.6	63.8	−18.0	216.7	−23.6	32.10	3.95	II	7.10	18.56	0.196
GA85.1	Yes	0.7	68.7	−13.0	213.3	−18.5	35.21	5.70	II	4.99	15.57	0.143
GA85.2	Yes	1.2	18.7	−10.4	218.9	−21.8	32.96	4.88	II	7.02	19.79	0.180
GA85.3	Yes	0.7	202.3	−41.9	208.9	−23.1	35.78	5.30	II	8.50	26.16	0.173
GA85.4	Yes	1.1	204.3	−43.6	205.6	−21.2	34.46	4.17	II	8.78	22.93	0.210
GA85.5	Yes	1.6	354.8	−7.6	210.2	−25.6	34.86	4.70	II	8.51	24.88	0.178
GA85.7	Yes	2.6	114.7	−38.6	216.3	−23.4	19.54	2.63	II	7.36	25.69	0.135
GA85.8	Yes	0.9	176.1	−33.8	207.5	−22.9	31.16	4.69	I	12.74	37.76	0.205

MAD is the maximum angular deviation, Core (In Situ) PCA Decl and Incl are the declination and inclination in sample core (in-situ geographic) coordinate frame from principal component analysis [Kirschvink, 1980], $J_{350–575}$ is the magnetization vector length from principal component analysis between 350º and 575ºC, Js-T is the high field magnetization versus temperature curve, Kent10 P-Int is the two-point preliminary paleointensity estimation, Bc is the coercivity, Bcr is the remanent coercivity, Mr/Ms is the saturation remanent magnetization to saturation magnetization ratio. Columns superscripted by ‘‘K’’ are data from Kent et al. [2010]. Those used in previous paleomagnetic direction studies but not in this paleointensity study are due to unavailability of ‘‘c’’ specimens. For Js-T curves, Type-I for more SSD dominating specimens; type-II for more MD dominating specimens.

Table 2.2. Paleointensity Results of the Original BZF Paleointensity Experiments

Sample	$\Delta susc^K$ %	$Kent10_{350–575}$ P-Int^K (μT)	Auto Thellier P-Int (μT)	Temp Low (°C)	Temp High (°C)	Auto Coe* P-Int (μT)	Temp Low (°C)	Temp High (°C)	Auto Aitken P-Int (μT)	Temp Low (°C)	Temp High (°C)
GA78.1	−7.7%	3.18	7.21	0	300	5.73	400	500	N/A	N/A	N/A
GA78.2	−16.3%	1.70	N/A	N/A	N/A	1.50	350	550	N/A	N/A	N/A
GA78.5	−13.2%	3.58	3.20	400	575	2.99	400	575	N/A	N/A	N/A
GA78.6	−5.6%	4.74	4.45	350	500	3.44	400	500	N/A	N/A	N/A
GA78.8	−11.8%	8.14	13.41	400	500	14.10	400	500	8.85	425	525
GA79.1	−26.3%	4.10	3.96	100	575	4.78	100	500	N/A	N/A	N/A
GA79.2	−26.3%	3.14	3.80	0	575	3.44	475	575	N/A	N/A	N/A
GA79.3	−36.2%	2.97	3.10	400	550	2.46	400	575	2.33	475	575
GA79.4	−30.5%	4.98	7.84	400	500	12.23	100	500	4.13	425	550
GA79.5	−32.3%	5.90	4.38	350	575	3.79	425	575	3.69	425	575
GA79.7	−27.9%	8.15	22.65	0	500	6.44	450	575	N/A	N/A	N/A
GA79.8	−24.1%	4.07	5.72	400	500	7.61	200	500	2.73	500	575
GA84.1	−33.3%	4.12	3.14	450	550	2.04	475	575	5.34	100	550
GA84.2	−33.3%	2.80	1.98	450	550	1.73	450	550	2.38	375	550
GA84.3	−29.1%	3.67	3.22	100	575	1.87	475	575	3.95	100	550
GA84.6	−33.1%	6.73	4.03	475	575	3.97	475	575	8.81	300	550
GA84.8	−24.0%	3.95	N/A	N/A	N/A	N/A	N/A	N/A	N/A	N/A	N/A
GA85.1	−24.7%	5.70	N/A	N/A	N/A	5.64	200	575	N/A	N/A	N/A
GA85.2	−27.5%	4.88	4.47	100	550	3.53	375	525	N/A	N/A	N/A
GA85.3	−22.2%	5.30	3.96	350	575	3.92	350	575	N/A	N/A	N/A
GA85.4	−30.6%	4.17	2.83	400	575	3.31	400	550	N/A	N/A	N/A
GA85.5	−31.4%	4.70	4.28	100	550	3.78	100	575	N/A	N/A	N/A
GA85.7	−40.2%	2.63	1.55	475	575	1.98	375	575	2.02	375	575
GA85.8	−33.8%	4.69	5.41	425	575	4.81	450	575	4.59	450	575
Sample number		24	21			23			11		
Mean		4.50	5.46			4.57			4.44		
Median		4.14	4.03			3.78			3.95		
Std. dev.		1.60	4.67			3.14			2.40		

Δsusc is the change of magnetic susceptibility from before to after heating, $Kent10_{350–575}$ P-Int is the paleointensity estimated using only two points at 350ºC and 575ºC, Auto (Thellier, Coe* and Aitken) P-Int are paleointensities estimated using automatic temperature range selection for these three protocols, Temp Low and Temp High mark the automatic selected temperature ranges for each protocol. Columns superscripted by ‘‘K’’ are data from Kent et al. [2010].

Table 2.3. Paleointensity Results After Using Arai Signatures to Conduct MD Corrections

Specimen	Rock Magnetic Pre-selection	Quality Control	Best Method	Original P-Int (μT)	95% Confident Range (μT)	Corrected P-Int (μT)	95% Confident Range (μT)	δMD	tTRM-K Regression Slope	tTRM-R Correlation Coefficient	Corrected P-Int-R Correlation Coefficient
GA78.1c	Yes	Failed	Coe*	3.52	0.46	3.55	0.38	0.22	0.9910	0.9980	-0.9883
GA78.2c	No	Failed	Coe*	1.34	0.26	1.35	0.25	0.19	0.8646	0.9890	-0.9661
GA78.5c	**No**	**Passed**	**Coe***	**2.93**	**0.43**	**3.08**	**0.30**	**0.16**	**0.9289**	**0.9970**	**-0.9907**
GA78.6c	**Yes**	**Passed**	**Thellier**	**2.99**	**0.49**	**3.38**	**0.24**	**0.11**	**0.9047**	**0.9963**	**-0.9948**
GA78.8c	Yes	Failed	Thellier	7.50	0.83	8.28	0.86	0.11	1.0024	0.9995	-0.9893
GA79.1c	No	Failed	Thellier	2.88	0.40	3.69	0.77	0.28	0.9094	0.9881	-0.9588
GA79.2c	**Yes**	**Passed**	**Coe***	**3.43**	**0.24**	**3.78**	**0.19**	**0.20**	**0.9992**	**0.9975**	**-0.9975**
GA79.3c	No	Failed	Aitken	2.42	0.19	2.22	0.14	0.14	0.9022	0.9896	-0.9959
GA79.4c	**No**	**Passed**	**Thellier**	**4.08**	**0.50**	**4.47**	**0.37**	**0.15**	**0.9894**	**0.9981**	**-0.9932**
GA79.5c	**Yes**	**Passed**	**Thellier**	**4.08**	**0.25**	**4.48**	**0.12**	**0.18**	**0.9941**	**0.9989**	**-0.9993**
GA79.7c	**Yes**	**Passed**	**Coe***	**7.05**	**0.96**	**7.64**	**0.63**	**0.20**	**1.0324**	**0.9988**	**-0.9932**
GA79.8c	**Yes**	**Passed**	**Coe***	**3.53**	**0.44**	**4.08**	**0.16**	**0.18**	**0.9663**	**0.9969**	**-0.9985**
GA84.1c	No	Failed	Thellier	2.79	0.79	2.85	0.59	0.15	0.9916	0.9944	-0.9587
GA84.2c	No	Failed	Aitken	1.57	0.44	1.52	0.32	0.15	0.9539	0.9918	-0.9574
GA84.3c	No	Failed	Aitken	2.34	0.64	2.45	0.53	0.17	1.0331	0.9950	-0.9556
GA84.6c	No	Failed	Thellier	5.24	1.29	5.57	1.28	0.10	1.0190	0.9979	-0.9503
GA84.8c	No	Failed	Aitken	2.74	0.59	2.40	0.51	0.17	0.9315	0.9847	-0.9570
GA85.1c	No	Failed	Aitken	5.46	0.81	5.73	0.90	0.16	0.9361	0.9937	-0.9760
GA85.2c	**Yes**	**Passed**	**Aitken**	**3.64**	**0.31**	**4.21**	**0.29**	**0.13**	**0.9925**	**0.9975**	**-0.9952**
GA85.3c	**Yes**	**Passed**	**Thellier**	**3.87**	**0.30**	**4.64**	**0.36**	**0.16**	**0.9736**	**0.9985**	**-0.9939**
GA85.4c	**No**	**Passed**	**Aitken**	**2.66**	**0.36**	**2.65**	**0.26**	**0.11**	**0.9349**	**0.9900**	**-0.9906**
GA85.5c	**Yes**	**Passed**	**Coe***	**3.77**	**0.34**	**4.16**	**0.30**	**0.13**	**0.9864**	**0.9983**	**-0.9947**
GA85.7c	Yes	Failed	Thellier	1.98	0.39	1.81	0.35	0.12	0.8640	0.9878	-0.9635
GA85.8c	No	Failed	Aitken	5.98	1.65	7.26	1.57	0.06	0.9585	0.9966	-0.9556
Qualified Specimen Number		**11**		**11**	**11**	**11**	**11**	**11**	**11**	**11**	**11**
Mean				**3.82**	**0.42**	**4.23**	**0.29**	**0.16**	**0.9729**	**0.9971**	**-0.9947**
Median				**3.64**	**0.36**	**4.16**	**0.29**	**0.16**	**0.9864**	**0.9975**	**-0.9947**
Std. dev.				**1.17**	**0.20**	**1.29**	**0.14**	**0.03**	**0.0369**	**0.0025**	**0.0029**

Original P-Int is the paleointensity estimated from the original BZF experiment, Corrected P-Int is the MD Arai signature corrected paleointensity estimated using both original and repeated BZF experiments, δMD is the MD contribution parameter, tTRM-K and tTRM-R are the linear regression slope and correlation coefficient of tTRM check, Corrected P-Int-R correlation coefficient is the linear regression correlation coefficient of corrected Arai diagram. Bold raws are qualified paleointensity results and their statistics.

Figure 2.1

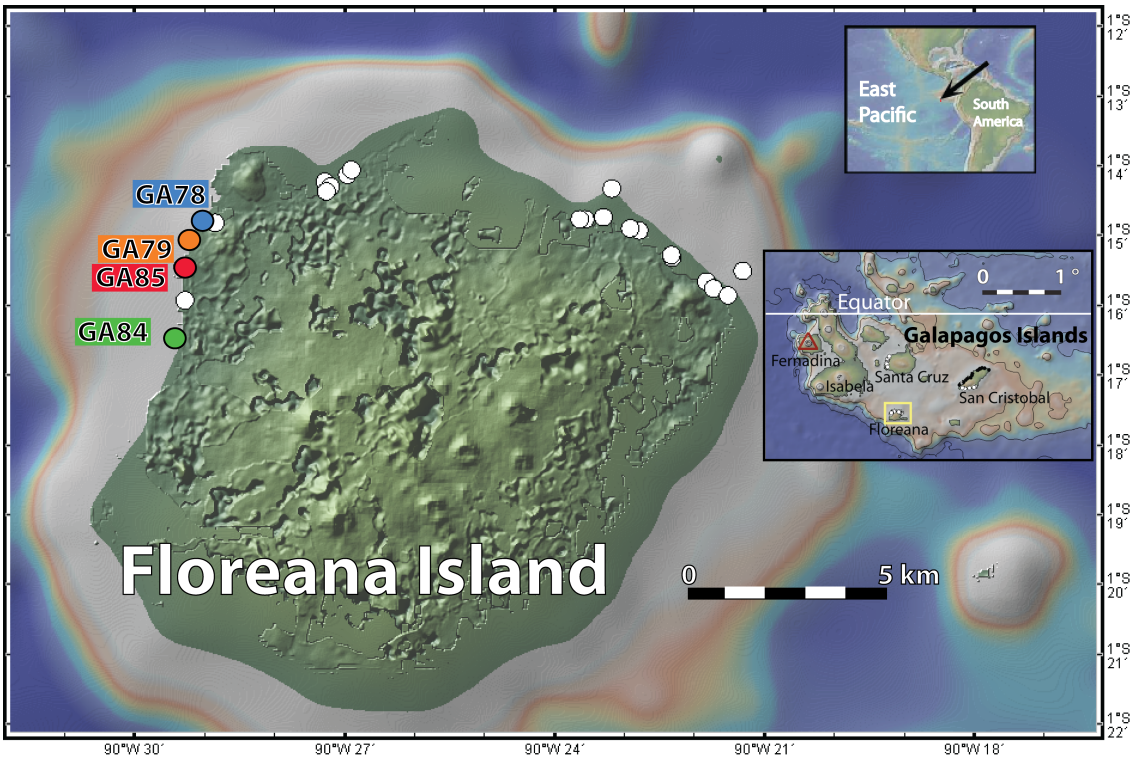
GA78
GA79
GA85
GA84
Floreana Island
0
5 km
East Pacific
South America
0
1 °
Equator
Galapagos Islands
Fernadina
Isabela
Santa Cruz
San Cristobal
Floreana
1°S 12´
1°S 13´
1°S 14´
1°S 15´
1°S 16´
1°S 17´
1°S 18´
1°S 19´
1°S 20´
1°S 21´
1°S 22´
90°W 30´
90°W 27´
90°W 24´
90°W 21´
90°W 18´

Figure 2.2

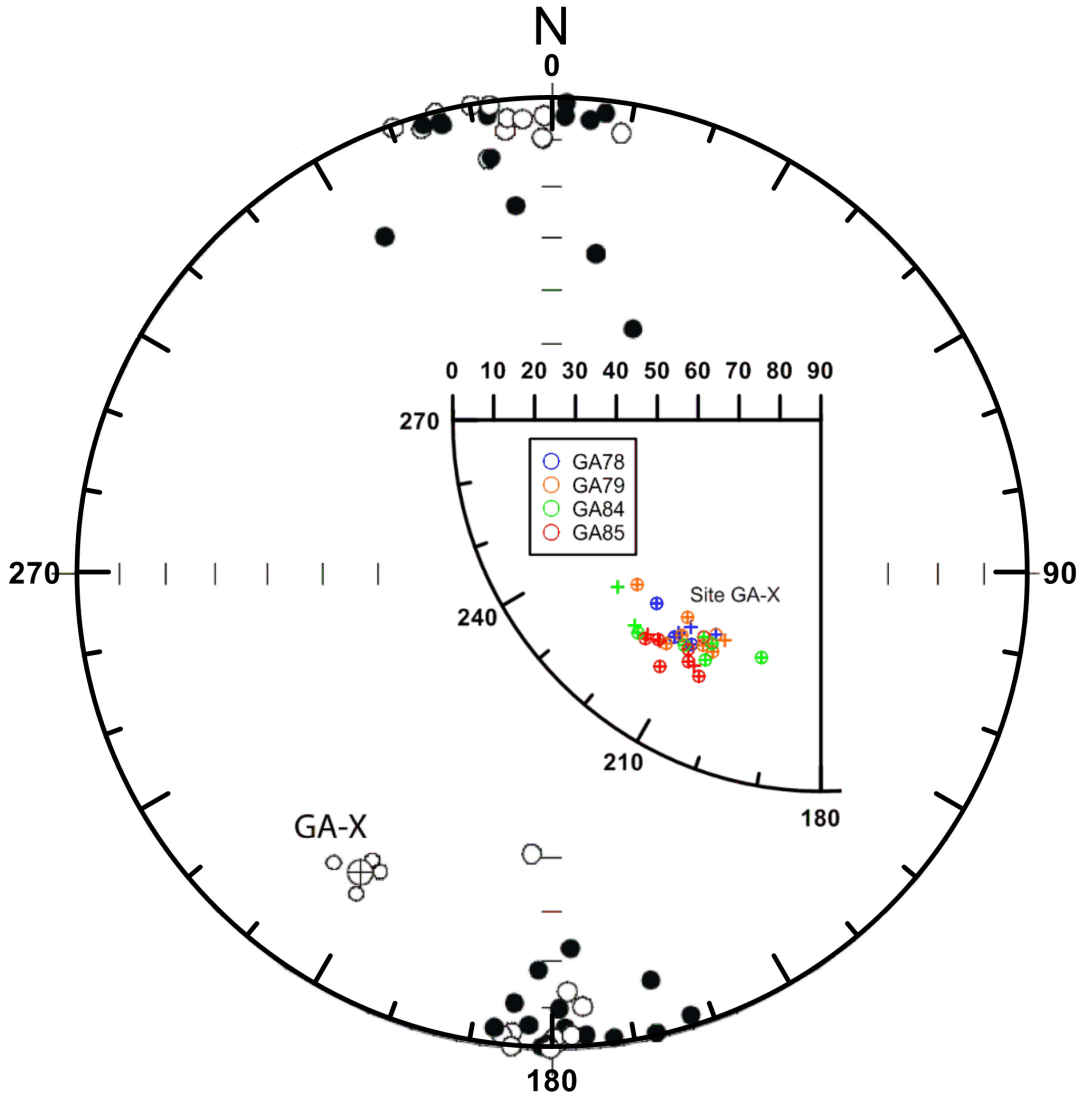
N
0
270
90
180
GA-X
0 10 20 30 40 50 60 70 80 90
270
240
210
180
GA78
GA79
GA84
GA85
Site GA-X

Figure 2.3

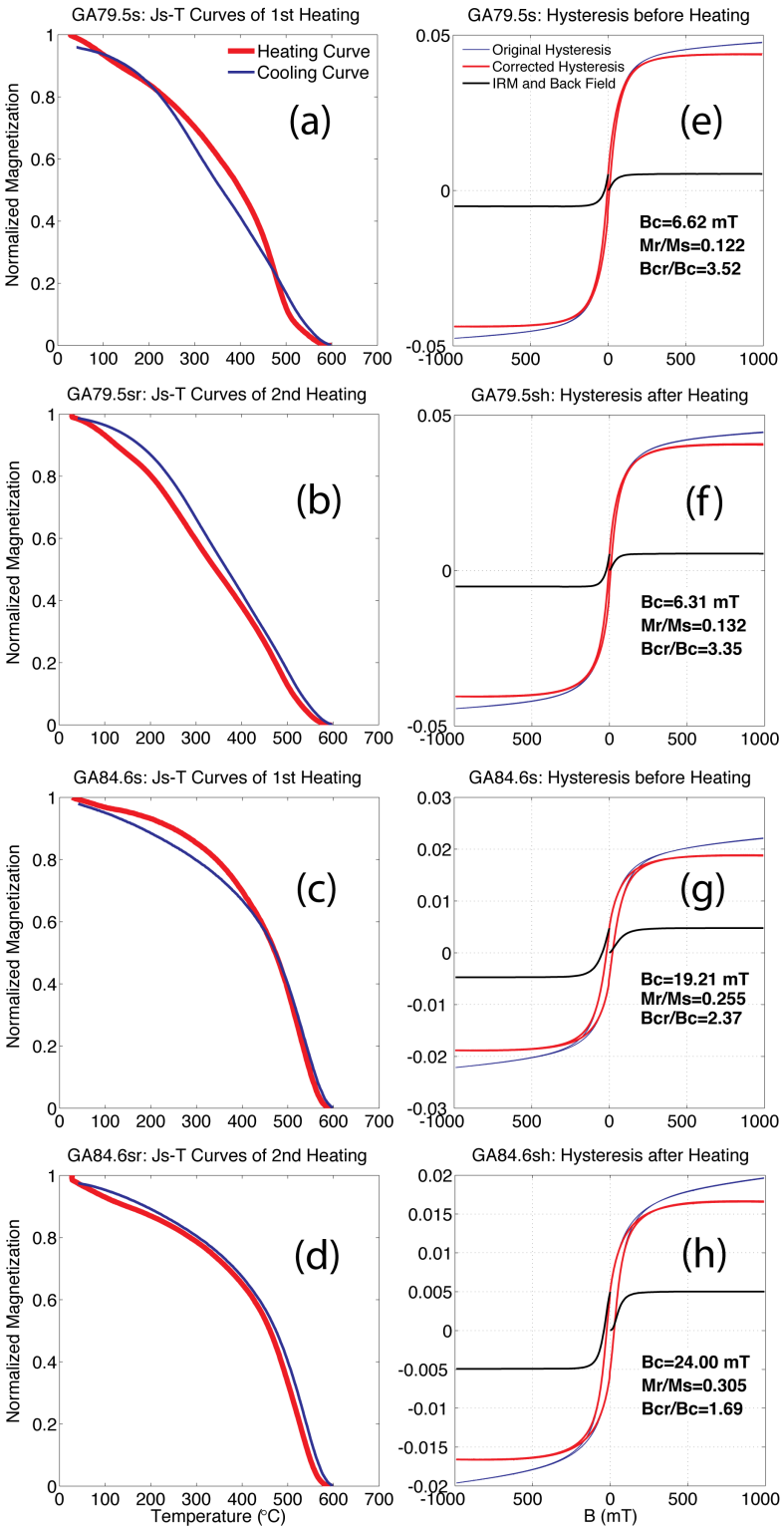
GA79.5s: Js-T Curves of 1st Heating
Heating Curve
Cooling Curve
(a)
GA79.5s: Hysteresis before Heating
Original Hysteresis
Corrected Hysteresis
IRM and Back Field
(e)
Bc=6.62 mT
Mr/Ms=0.122
Bcr/Bc=3.52
GA79.5sr: Js-T Curves of 2nd Heating
(b)
GA79.5sh: Hysteresis after Heating
(f)
Bc=6.31 mT
Mr/Ms=0.132
Bcr/Bc=3.35
GA84.6s: Js-T Curves of 1st Heating
(c)
GA84.6s: Hysteresis before Heating
(g)
Bc=19.21 mT
Mr/Ms=0.255
Bcr/Bc=2.37
GA84.6sr: Js-T Curves of 2nd Heating
(d)
GA84.6sh: Hysteresis after Heating
(h)
Bc=24.00 mT
Mr/Ms=0.305
Bcr/Bc=1.69
Normalized Magnetization
Temperature (°C)
B (mT)

Figure 2.4

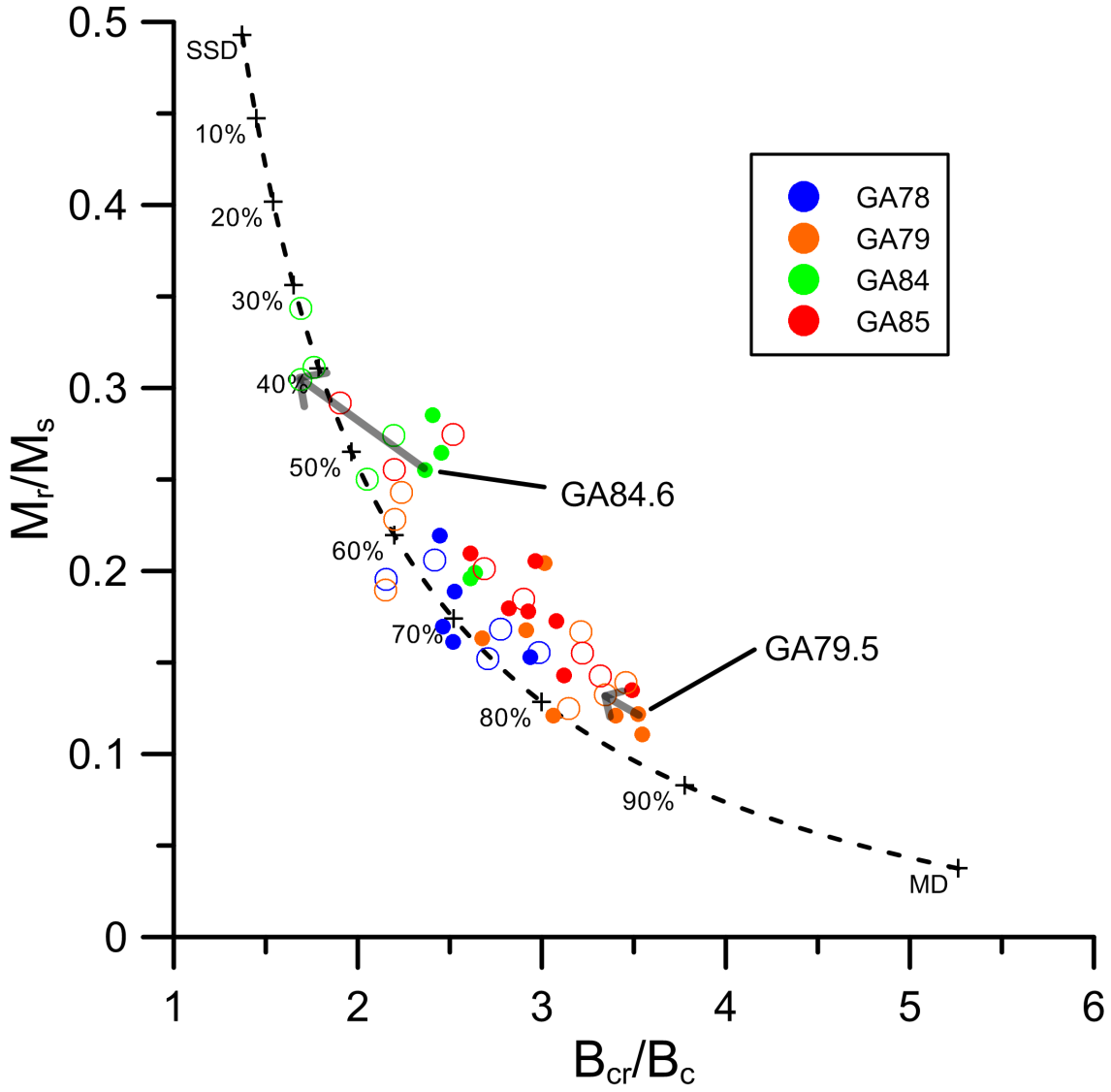
0.5
0.4
0.3
0.2
0.1
0
1
2
3
4
5
6
M_r/M_s
B_{cr}/B_c
SSD
10%
20%
30%
40%
50%
60%
70%
80%
90%
MD
GA84.6
GA79.5
GA78
GA79
GA84
GA85

Figure 2.5

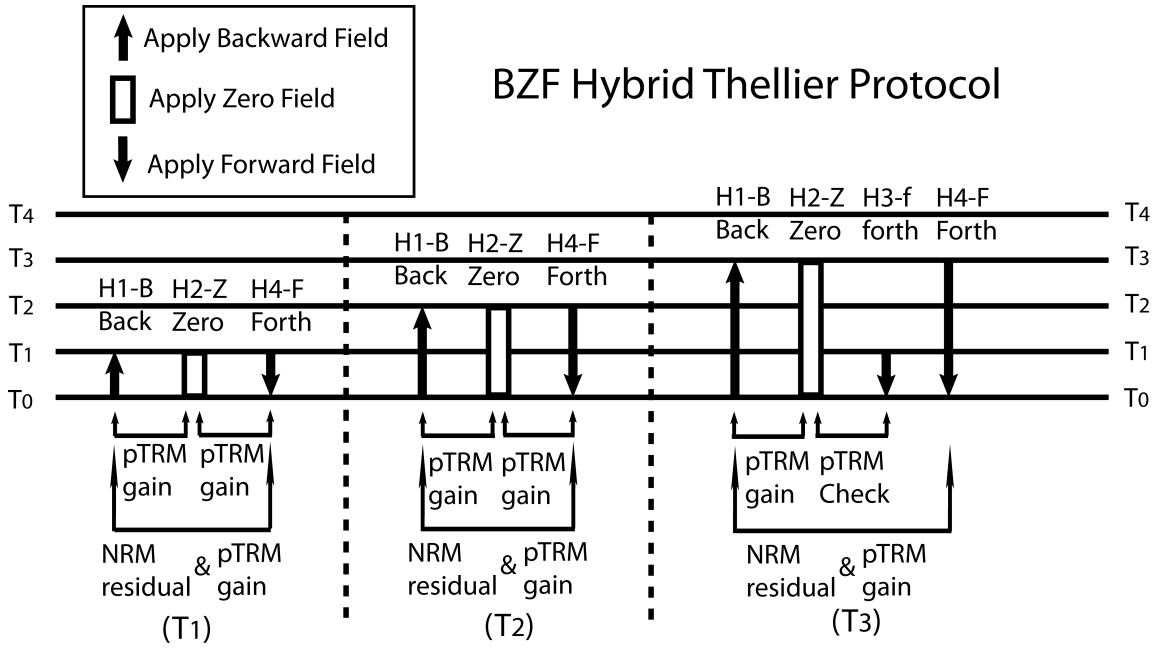
Apply Backward Field
Apply Zero Field
Apply Forward Field
BZF Hybrid Thellier Protocol
T4
T3
T2
T1
T0
H1-B Back
H2-Z Zero
H4-F Forth
H3-f forth
pTRM gain
pTRM Check
NRM residual & pTRM gain
(T1)
(T2)
(T3)

Figure 2.6

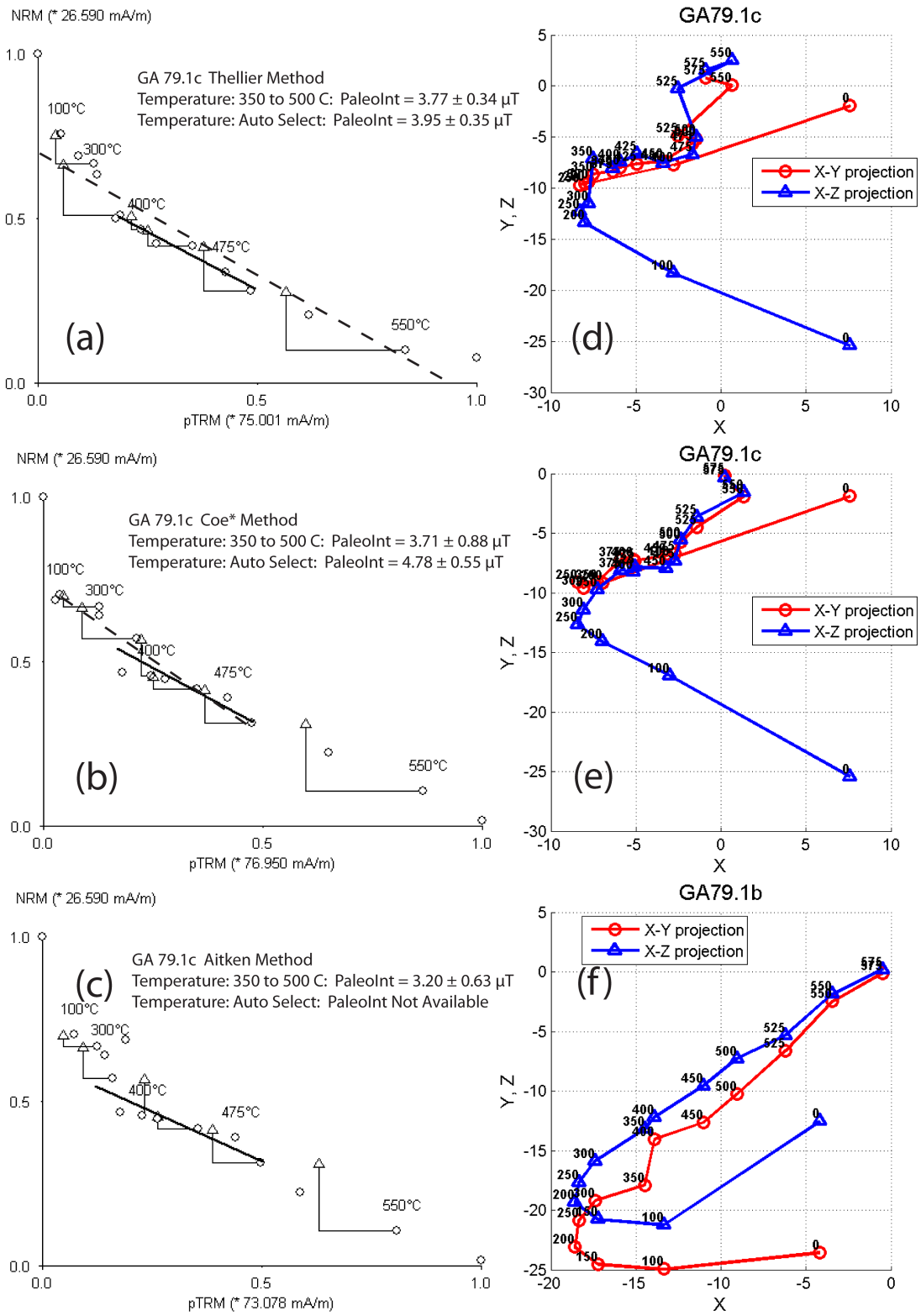
NRM (* 26.590 mA/m)
GA 79.1c Thellier Method
Temperature: 350 to 500 C: PaleoInt = 3.77 ± 0.34 µT
Temperature: Auto Select: PaleoInt = 3.95 ± 0.35 µT
100°C
300°C
400°C
475°C
550°C
(a)
pTRM (* 75.001 mA/m)
GA79.1c
X-Y projection
X-Z projection
(d)
Y, Z
X
NRM (* 26.590 mA/m)
GA 79.1c Coe* Method
Temperature: 350 to 500 C: PaleoInt = 3.71 ± 0.88 µT
Temperature: Auto Select: PaleoInt = 4.78 ± 0.55 µT
(b)
pTRM (* 76.950 mA/m)
(e)
NRM (* 26.590 mA/m)
GA 79.1c Aitken Method
Temperature: 350 to 500 C: PaleoInt = 3.20 ± 0.63 µT
Temperature: Auto Select: PaleoInt Not Available
(c)
pTRM (* 73.078 mA/m)
GA79.1b
(f)

Figure 2.7

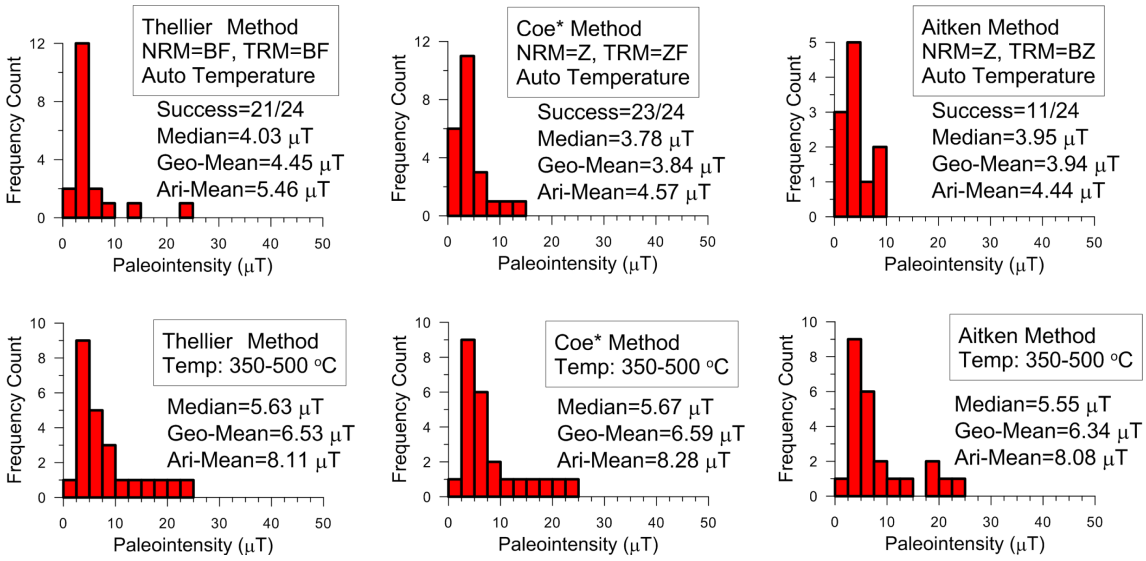
Thellier Method
NRM=BF, TRM=BF
Auto Temperature
Success=21/24
Median=4.03 μT
Geo-Mean=4.45 μT
Ari-Mean=5.46 μT
Coe* Method
NRM=Z, TRM=ZF
Auto Temperature
Success=23/24
Median=3.78 μT
Geo-Mean=3.84 μT
Ari-Mean=4.57 μT
Aitken Method
NRM=Z, TRM=BZ
Auto Temperature
Success=11/24
Median=3.95 μT
Geo-Mean=3.94 μT
Ari-Mean=4.44 μT
Thellier Method
Temp: 350-500 °C
Median=5.63 μT
Geo-Mean=6.53 μT
Ari-Mean=8.11 μT
Coe* Method
Temp: 350-500 °C
Median=5.67 μT
Geo-Mean=6.59 μT
Ari-Mean=8.28 μT
Aitken Method
Temp: 350-500 °C
Median=5.55 μT
Geo-Mean=6.34 μT
Ari-Mean=8.08 μT
Frequency Count
Paleointensity (μT)

Figure 2.8

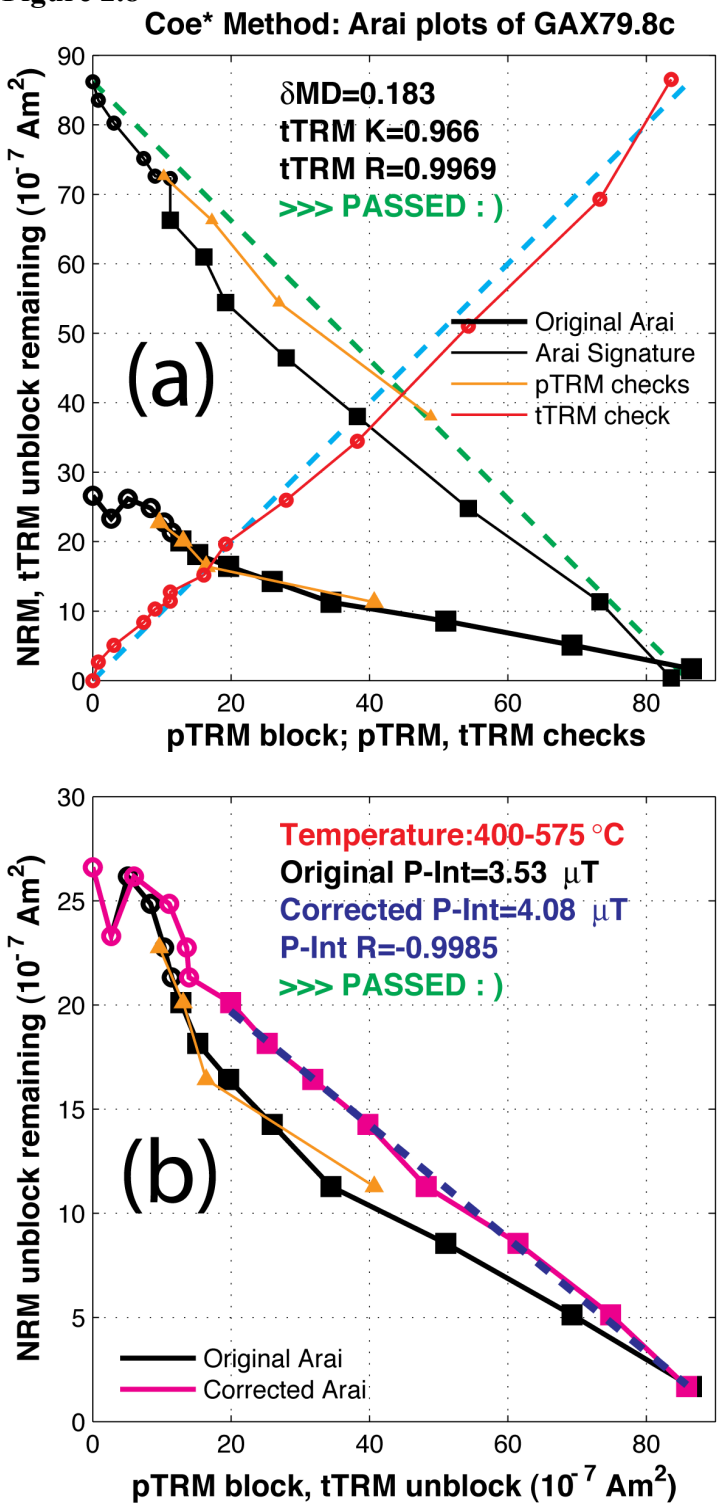
Coe* Method: Arai plots of GAX79.8c
δMD=0.183
tTRM K=0.966
tTRM R=0.9969
>>> PASSED :)
(a)
Original Arai
Arai Signature
pTRM checks
tTRM check
NRM, tTRM unblock remaining (10^-7 Am^2)
pTRM block; pTRM, tTRM checks
Temperature:400-575 °C
Original P-Int=3.53 μT
Corrected P-Int=4.08 μT
P-Int R=-0.9985
>>> PASSED :)
(b)
Original Arai
Corrected Arai
NRM unblock remaining (10^-7 Am^2)
pTRM block, tTRM unblock (10^-7 Am^2)

Figure 2.9

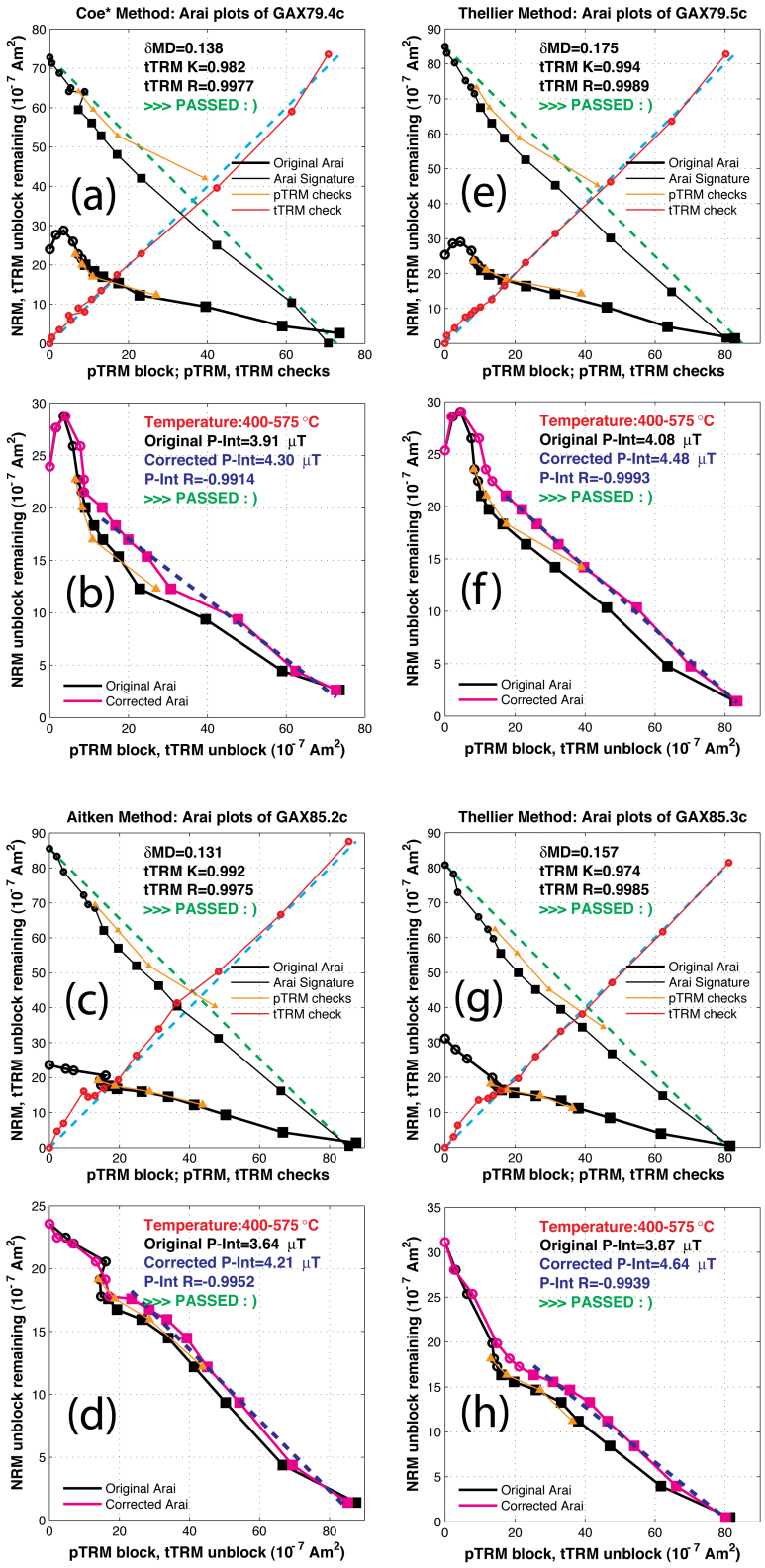
Coe* Method: Arai plots of GAX79.4c
δMD=0.138
tTRM K=0.982
tTRM R=0.9977
>>> PASSED :)
(a)
Original Arai
Arai Signature
pTRM checks
tTRM check
NRM, tTRM unblock remaining (10^-7 Am^2)
pTRM block; pTRM, tTRM checks
Thellier Method: Arai plots of GAX79.5c
δMD=0.175
tTRM K=0.994
tTRM R=0.9989
>>> PASSED :)
(e)
Temperature:400-575 °C
Original P-Int=3.91 μT
Corrected P-Int=4.30 μT
P-Int R=-0.9914
>>> PASSED :)
(b)
Original Arai
Corrected Arai
NRM unblock remaining (10^-7 Am^2)
pTRM block, tTRM unblock (10^-7 Am^2)
Temperature:400-575 °C
Original P-Int=4.08 μT
Corrected P-Int=4.48 μT
P-Int R=-0.9993
>>> PASSED :)
(f)
Aitken Method: Arai plots of GAX85.2c
δMD=0.131
tTRM K=0.992
tTRM R=0.9975
>>> PASSED :)
(c)
Thellier Method: Arai plots of GAX85.3c
δMD=0.157
tTRM K=0.974
tTRM R=0.9985
>>> PASSED :)
(g)
Temperature:400-575 °C
Original P-Int=3.64 μT
Corrected P-Int=4.21 μT
P-Int R=-0.9952
>>> PASSED :)
(d)
Temperature:400-575 °C
Original P-Int=3.87 μT
Corrected P-Int=4.64 μT
P-Int R=-0.9939
>>> PASSED :)
(h)

Figure 2.10

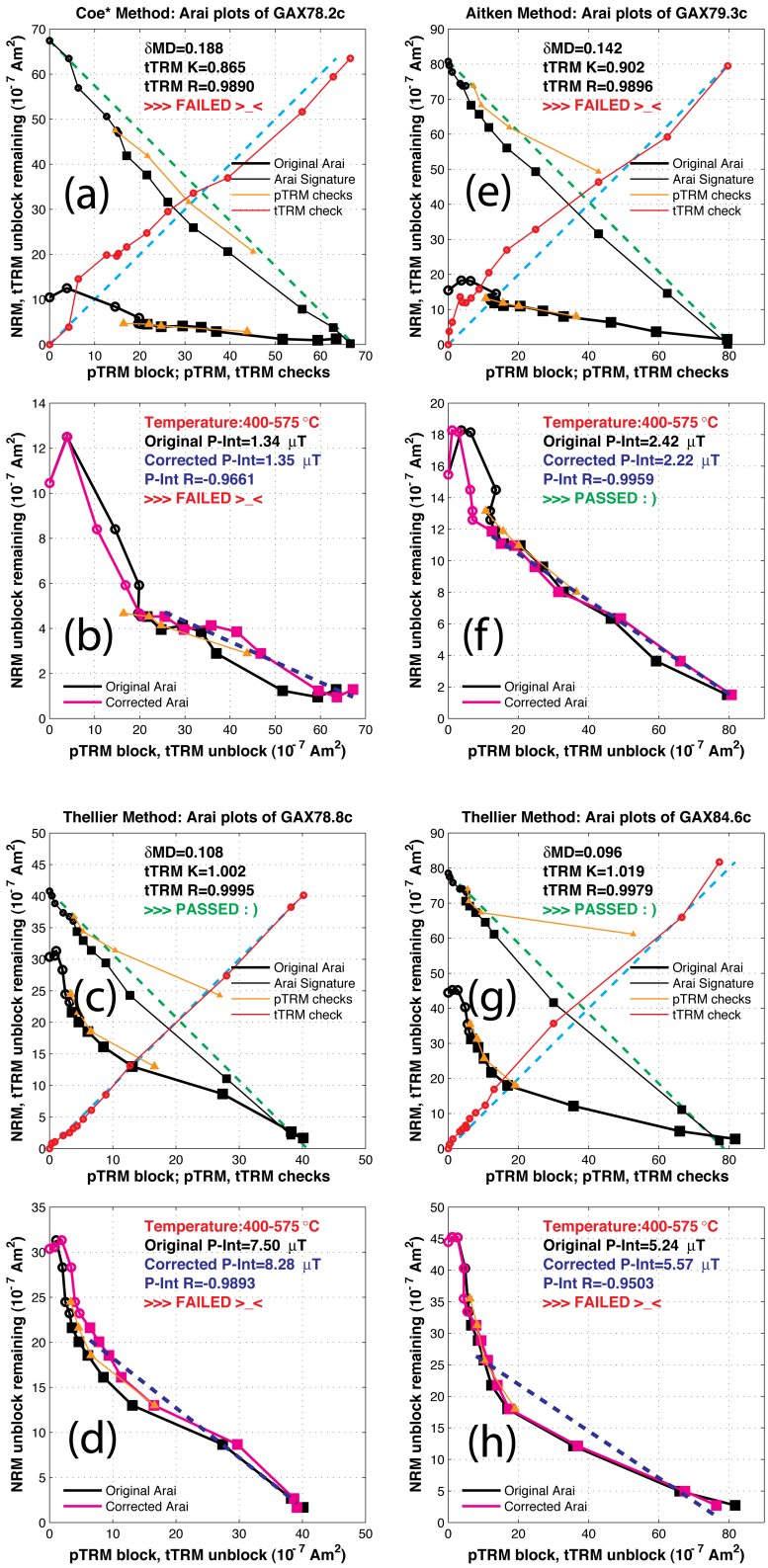
Coe* Method: Arai plots of GAX78.2c
δMD=0.188
tTRM K=0.865
tTRM R=0.9890
>>> FAILED >_<
(a)
Original Arai
Arai Signature
pTRM checks
tTRM check
NRM, tTRM unblock remaining (10^-7 Am^2)
pTRM block; pTRM, tTRM checks
Aitken Method: Arai plots of GAX79.3c
δMD=0.142
tTRM K=0.902
tTRM R=0.9896
>>> FAILED >_<
(e)
Temperature:400-575 °C
Original P-Int=1.34 μT
Corrected P-Int=1.35 μT
P-Int R=-0.9661
>>> FAILED >_<
(b)
Original Arai
Corrected Arai
NRM unblock remaining (10^-7 Am^2)
pTRM block, tTRM unblock (10^-7 Am^2)
Temperature:400-575 °C
Original P-Int=2.42 μT
Corrected P-Int=2.22 μT
P-Int R=-0.9959
>>> PASSED :)
(f)
Thellier Method: Arai plots of GAX78.8c
δMD=0.108
tTRM K=1.002
tTRM R=0.9995
>>> PASSED :)
(c)
Thellier Method: Arai plots of GAX84.6c
δMD=0.096
tTRM K=1.019
tTRM R=0.9979
>>> PASSED :)
(g)
Temperature:400-575 °C
Original P-Int=7.50 μT
Corrected P-Int=8.28 μT
P-Int R=-0.9893
>>> FAILED >_<
(d)
Temperature:400-575 °C
Original P-Int=5.24 μT
Corrected P-Int=5.57 μT
P-Int R=-0.9503
>>> FAILED >_<
(h)

Figure 2.11

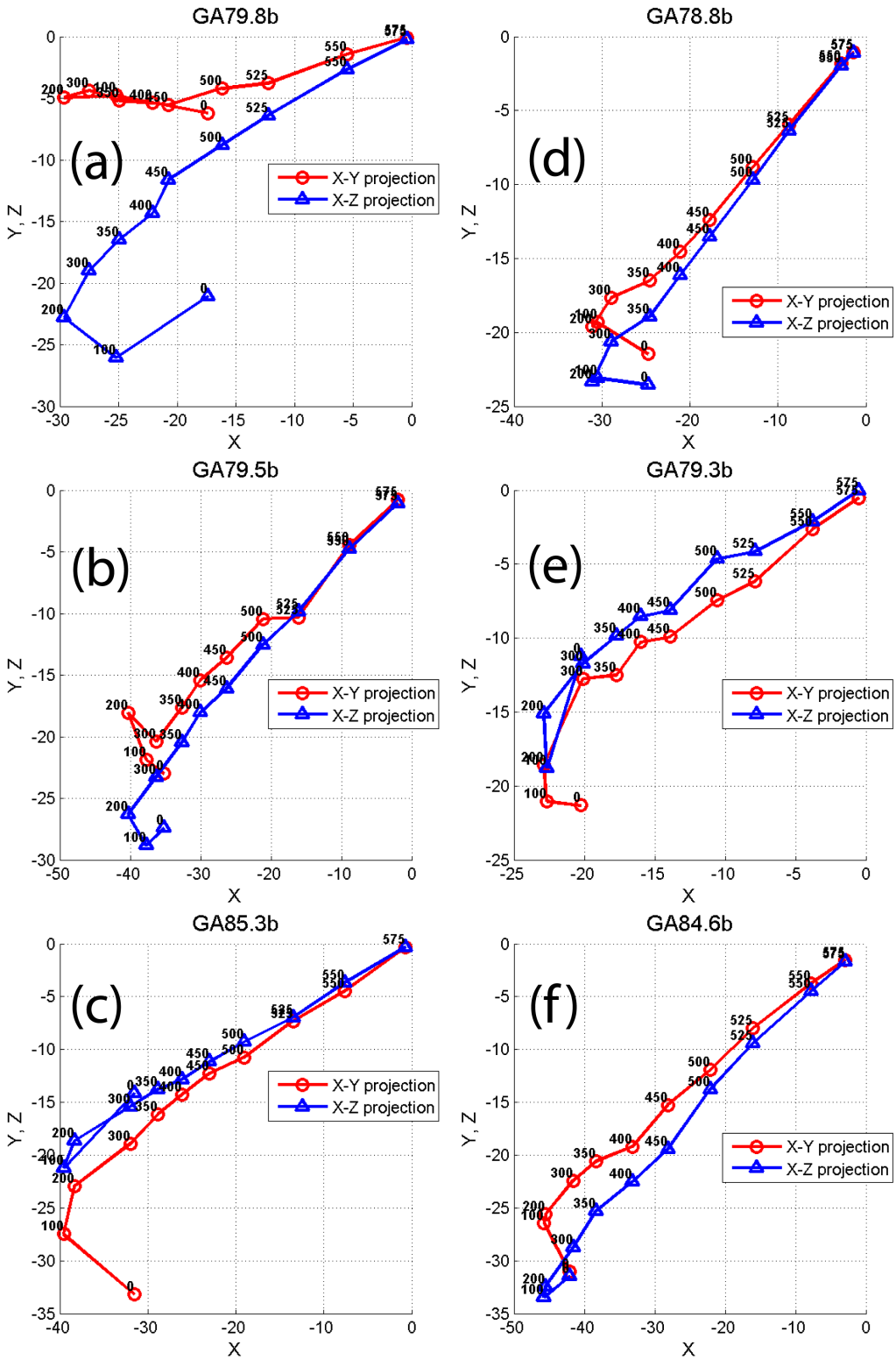
GA79.8b
(a)
X-Y projection
X-Z projection
Y, Z
X
GA78.8b
(d)
X-Y projection
X-Z projection
Y, Z
X
GA79.5b
(b)
X-Y projection
X-Z projection
Y, Z
X
GA79.3b
(e)
X-Y projection
X-Z projection
Y, Z
X
GA85.3b
(c)
X-Y projection
X-Z projection
Y, Z
X
GA84.6b
(f)
X-Y projection
X-Z projection
Y, Z
X

Figure 2.12

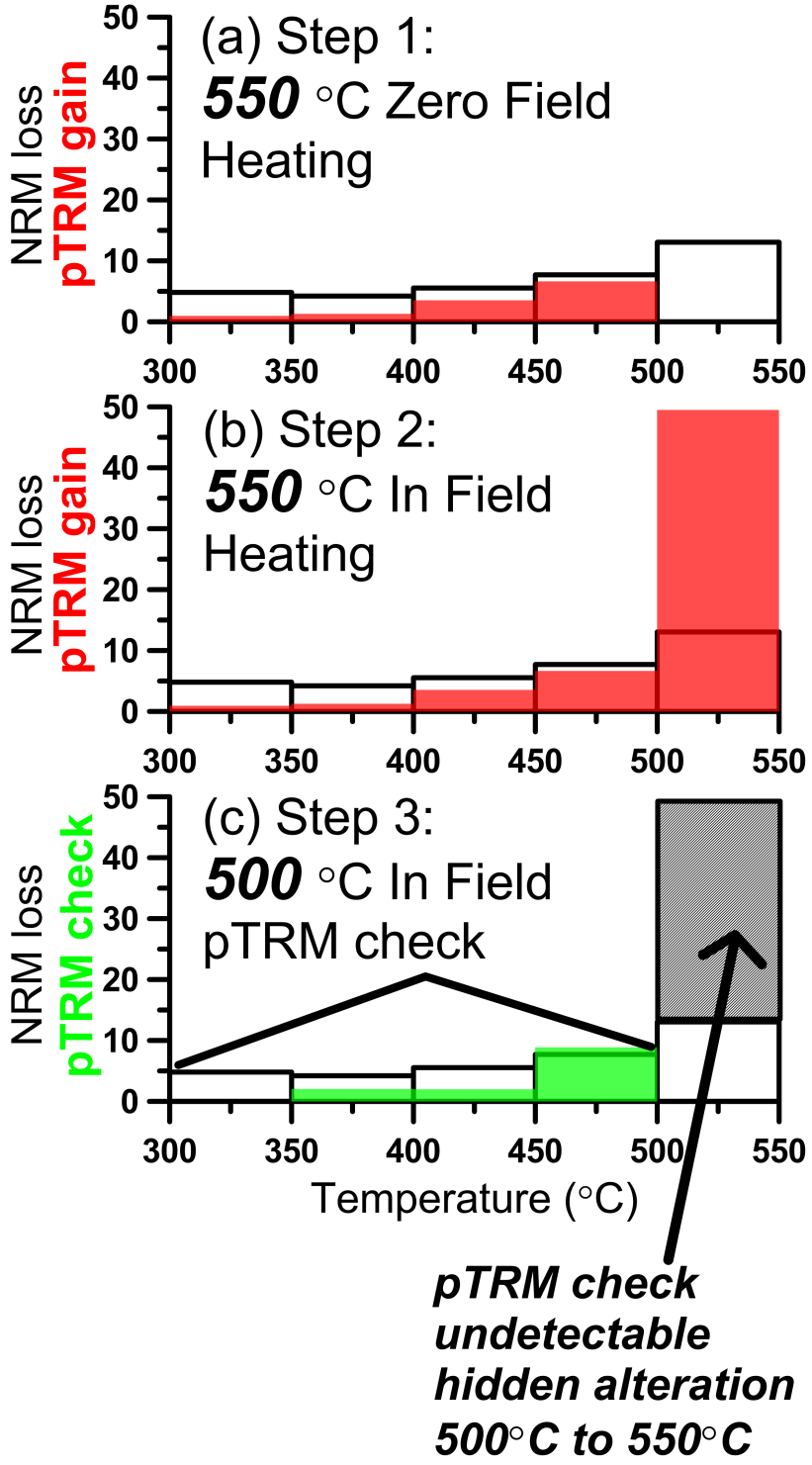
(a) Step 1:
550 °C Zero Field
Heating
NRM loss
pTRM gain
(b) Step 2:
550 °C In Field
Heating
NRM loss
pTRM gain
(c) Step 3:
500 °C In Field
pTRM check
NRM loss
pTRM check
0
10
20
30
40
50
300
350
400
450
500
550
Temperature (°C)
pTRM check
undetectable
hidden alteration
500°C to 550°C

Figure 2.13

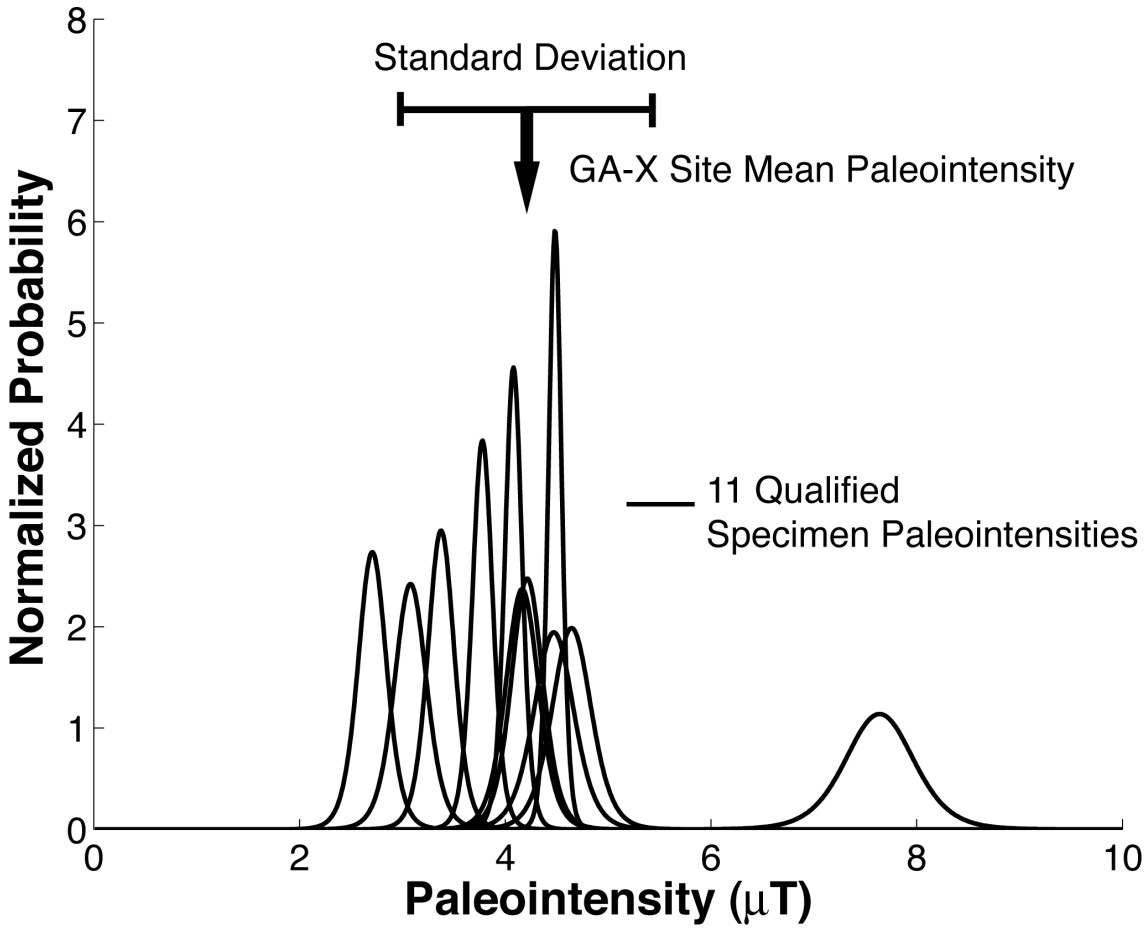
Standard Deviation
GA-X Site Mean Paleointensity
11 Qualified
Specimen Paleointensities
Normalized Probability
Paleointensity (μT)
0
1
2
3
4
5
6
7
8
0
2
4
6
8
10

Chapter 3

Equatorial paleointensities from Galapagos for the Pliocene-Pleistocene

3.1 Abstract

The current geomagnetic field (GMF) of the Earth is mostly geocentric dipolar with intensities at polar regions (~60 μT) about twice as high as at equatorial regions (~30 μT). However, data from *Lawrence et al*. [2009] suggested that the 0-5 Ma average paleointensity for non-transitional periods from 38 selected lava flow sites in Antarctica (~78°S) was only 33.4 μT. We present absolute paleointensity results from lava flows of similar age (0-3 Ma) from the Galapagos Islands located about 1°S of the Equator using a recently developed multidomain (MD) correction technique [*Wang and Kent*, 2013] on fresh subsets of the same samples that were recently analyzed for paleosecular variation PSV [*Kent et al.*, 2010]. After standard Thellier series paleointensity experiments, we gave the samples total thermal remanent magnetizations (tTRM) by cooling from their Curie point in presence of a laboratory-applied field (15 μT). We then repeated the paleointensity experiment on each sample, with the laboratory-applied tTRM as a synthetic natural remanent magnetization (NRM), using the same laboratory-applied field and temperature steps to obtain a synthetic Arai signature, which should only represent the domain-state dependent properties of the sample. We corrected the Arai diagrams from the original paleointensity experiment by using the Arai signatures from the

repeated experiment, which neutralizes the typical MD concave-up Arai effect. We experimented on 209 specimens from 47 lava sites, 27 of which gave acceptable paleointensity results from one or more specimen(s). The average paleointensity of the 27 successful lava flow sites is 21.6 μT. In these 27 sites, 8 of them are of normal polarity, yielding an average paleointensity of 19.6 μT, and 19 of them are of reverse polarity, yielding an average paleointensity of 22.4 μT. Mean paleomagnetic directions of the normal and reverse polarity sites are statistically antipodal and within a few degrees expected from the geocentric axial dipole (GAD) field, which together indicate that these data should be representative of the time-averaged geomagnetic field with no resolvable contributions from persistent non-dipole fields. Together with results from Antarctica, the paleointensities from Galapagos suggest that the average GMF intensity for the last a few million years is very close to the GAD prediction, but is only about 2/3 of the present day field intensity.

3.2 Introduction

Lavas are thought to provide accurate readings of ancient geomagnetic field directions and are widely used for statistical studies of paleosecular variation (PSV) [*Harrison*, 2009; *Johnson et al.*, 2008; *McElhinny and McFadden*, 1997]. In studies of paleosecular variation of recent lavas (PSVRL), angular dispersion of virtual geomagnetic poles (VGPs) is usually determined from multiple lavas emplaced over a few million years (over which plate motions should be negligibly small) at specific site

localities (or averaged within latitudinal bands) to examine the latitudinal dependence of dispersion as a long-sought signature of PSV [*Cox*, 1970; *Creer et al.*, 1959; *Irving and Ward*, 1964].

Paleointensity estimates are more sporadic in both their geographic and temporal distributions compared to directional results from lavas mainly because the success rate of traditional Thellier (or other) techniques for absolute values is typically low due to prevalence of non-ideal behavior. Emphasis has been placed on obtaining time-averaged global mean values that can be used to calibrate continuous relative paleointensity records (e.g., [*Valet et al.*, 2005]) or to document possible long-term trends [*Selkin and Tauxe*, 2000]. A standard procedure is to calculate virtual axial dipole moments (VADMs) from the local paleointensity estimates to account for the latitude-dependent variation expected for a geocentric axial dipole field and then average the VADMs by time interval and/or dipole polarity. Conversion to VADMs assumes that the localized paleointensity results are representative of a geocentric axial dipole field, which has yet to be demonstrated by a prescribed latitudinal-dependence of paleointensities.

Lawrence et al. [2009] published a high quality data set of paleomagnetic directions (N=133 sites) that met exacting quality control criteria on lavas from the Erebus Volcanic Province near the McMurdo station in Antarctica. At a latitude of 78°S, this is the most pole-ward volcanic data set available for PSV studies of the time-averaged field over the past few million years. The results indicate high VGP dispersion but low paleointensities. Depending on the VGP cutoff, the angular standard deviation

(ASD) of VGPs (taking antipodes of reverse polarity sites) is 34.4° for all data, 26.6° using the *Vandamme* [1994] colatitudinal cutoff of 37.1°, or 23.9±2.1° using a straight cutoff of 45°; there is no significant difference in ASD between normal (Brunhes) and reverse (Matuyama) polarity subsets for any given site selection criteria. Compared to global data, Lawrence et al. [2009] concluded that their McMurdo results support latitudinal variation in VGP dispersion (at least in the southern hemisphere), contrary to some nagging doubts that high dispersion with higher latitude might be due to poor data quality [*Johnson et al.*, 2008] or else agree with statistical field models that predict essentially the same dispersion with latitude [*Constable and Parker*, 1988]. Instead, the new EVP results are more compatible with paleosecular variation Model G [*McFadden et al.*, 1988] and to lesser extent model TK03 [*Tauxe and Kent*, 2004], which was effectively tuned to it. Recent PSVRL results from the equatorial belt [*Gromme et al.*, 2010; *Kent et al.*, 2010; *Opdyke et al.*, 2010] confirm that VGP dispersion at low latitude is about half that at the high southern latitude EVP site, i.e., ~12° versus ~24°, which is also compatible with Model G [*McElhinny and McFadden*, 1997].

PSVRL directional data from equatorial localities in Kenya [*Opdyke et al.*, 2010] and the Galapagos [*Gromme et al.*, 2010; *Kent et al.*, 2010] may be converging on a low value for VGP dispersion of about half that observed at EVP and broadly consistent with paleosecular variation Model G but there are very few reliable paleointensity data in global compilations within about 15° of the Equator, the region that should provide the best reference value for a geocentric axial dipole moment, to assess whether the low

dispersion is accompanied by paleointensities that are anomalous with respect to the McMurdo results.

Lawrence et al., [2009] also reported the mean paleointensity from 41 selected lava flow sites at McMurdo (78°S) was 31.5 μT, which was only about half of the local field intensity today. They also calculated the average paleointensities for different latitudinal bins from the paleointensity database [*Biggin et al.*, 2009] and found that the paleointensities for the past a few million years did not conform to a latitudinal distribution expected for a geocentric axial dipole field. Instead, both equatorial and polar paleointensities were about 30 μT (Fig 3.1), which was explained by the decreased convection within the tangent cylinder of the outer core of the geodynamo although an artifact of faulty paleointensity data could not be excluded.

Very preliminary paleointensity results from a TRM experiment on Galapagos lavas provide some tantalizing data from a low latitude location [*Kent et al.*, 2010]. Specimens that had been progressively demagnetized thermally to 575°C to isolate a characteristic component for the PSVRL directional study were subsequently given a total TRM from 575°C in a 15 μT field; after thermal demagnetization at 350°C to remove viscous magnetizations, the NRM from 350° to 575°C was compared to the TRM over the same temperature range to estimate the paleofield strength. An arithmetic mean paleointensity of 21 μT (geometric mean of 17 μT) was obtained for 48 sites (321 specimens) providing the most consistent within-site data after excluding the most egregiously altered samples that showed more than 50% change in magnetic

susceptibility after lab heating. This is only 1/2 to 2/3 of the present-day field strength of 30 μT at the equatorial site locality and would make the reported paleointensity of 31.5 μT from 41 selected lava flow sites at McMurdo (78°S) [*Lawrence et al.,* 2009] more consistent with the same geocentric axial dipole moment rather than be strongly influenced by tangent cylinder dynamics at high latitudes. The Galapagos preliminary paleointensity results obviously need to be verified by robust multistep heating techniques with internal checks for alteration and supporting rock magnetic data, which is a principal objective of this study. Some other analyses have also suggested that the intensity of the time-averaged geomagnetic field was considerably lower than the present-day value [*Selkin and Tauxe*, 2000; *Yamamoto and Tsunakawa*, 2005], but it remains to be determined how these estimates, in addition to the McMurdo results of *Lawrence et al.* [2009], can be reconciled with the apparent preponderance of paleointensity estimates that are typically closer to the modern value (e.g., [*Bogue*, 2001; *Laj and Kissel*, 1999; *Valet*, 2003]).

3.3 Sample preparation

The Galapagos Archipelago consists of volcanic islands on the Nazca plate just south of the Equator. The islands formed over a period of several million years [*Bailey*, 1976; *Cox and Dalrymple*, 1966; *Sinton et al.*, 1996; *Swanson et al.*, 1974; *White et al.*, 1993], during which the Nazca plate moved east-southeast relative to the presumed Galapagos hotspot. Santa Cruz, Floreana, and San Cristobal Islands, from which our

samples were collected, are to the Southeast of the current eruptive center on Fernandina Island at 0.37°S, 91.55°W (see Fig 1 in *Kent et al.*, [2010]) . The samples studied in this paper were taken with a hand-held gasoline-powered drill along the coasts of those islands on a 1993 expedition [*Rochette et al.*, 1997]. Back in the lab, the 25mm-diameter core samples were sliced into several ~12mm-high specimens (named "a", "b", "c", etc.). The "a" and "b" specimens were alternating field demagnetized and thermally demagnetized for PSV studies by *Rochette et al.*, [1997] and *Kent et al.*, [2010], respectively.

Prior to any thermal or magnetic treatments for paleointensity, we drilled 10mm-diameter sub-cylinders from the center of the "c" specimens using a countertop drill press with diamond tipped drill bits. We attached the suffix 'x' to the sub-cylinder specimens. We also drilled a 10mm-diameter half-cylinder from the edge of each "c" specimen. The half-cylinders were crushed into small ~30-50 mg rock chips, which we named specimen "s", "t", "u", etc., and used for rock magnetic studies. For stage one paleointensity experiments in this study, we used 138 "c" specimens from 51 select lava flow sites from the Galapagos collection that gave reliable normal or reverse polarity paleomagnetic directions in previous directional studies [*Kent et al.*, 2010]. As illustrated in Figure 3.2, the remaining portions of the "c" specimens were used for paleointensity experiments, by using BZF (Back-field, Zero-field and Forward-field heating steps [*Wang and Kent*, 2013]) and IZZI (alternating between In-field + Zero-field and Zero-field + In-field heating steps [*Tauxe and Staudigel*, 2004; *Yu et al.*, 2004]) protocols with the correction technique developed by *Wang and Kent*, [2013]. The rock magnetic chips came as

directly as possible from the paleointensity specimens and thus should closely represent the rock magnetic properties of the paleointensity specimens. For stage two paleointensity experiments in this study, we selected 71 "x" specimens from 23 lava sites based on the Arai diagram behavior of the "c" specimens to yield accurate paleointensity and specimen availability.

3.4 Rock magnetic characterization

We performed series of rock magnetic measurement before and after heating the same specimens to 650°C in order to characterize the major magnetization carrying minerals for the Galapagos lavas, as well as to detect their thermal alterations. We measured hysteresis loops and back-field demagnetization curves for each of the selected rock magnetic chip specimens on a Princeton Measurements Corporation AGFM (alternating gradient force magnetometer, 1T saturation field) in the Rutgers paleomagnetic lab. We calculated the saturation remanent magnetization (M_r), saturation magnetization (M_s), coercivity (B_c) and remanent coercivity (B_{cr}) for all measured specimens by using 0.7 to 1 T paramagnetic slope correction (Table 3.S1). Figure 3.3a shows a Day plot [*Day et al.*, 1977] of the hysteresis parameters from the 156 specimens. Most of the data are distributed along the stable single domain (SSD)-multidoman (MD) mixing curve #3 [*Dunlop and Xu*, 1994; *Xu and Dunlop*, 1994] and range from Mr/Ms of 0.09 to 0.48, which indicate a broad range of magnetic grain size variations, from ~20% SSD to ~100% SSD (or more pertinently for fulfilling Thellier conditions, up to 80%

MD). A few outliers are due to wasp-waist type of hyteresis loops, which indicates the contribution of SP particles [*Tauxe et al.*, 1996]. *Kent et al.* [2010] previously presented 18 hysteresis results (analyzed with a Princeton Measurements Vibration Sample Magnetometer 2900) from Galapagos in the PSV studies, which showed a similar range of hysteresis properties.

We also measured high-field thermomagnetic properties from saturation magnetization versus temperature (J_s-T) heating and cooling curves in air on 59 representative samples from a subset of samples that we conducted hysteresis measurements from different lava-flow sites (Fig. 3.S1-01 to 59), by using a Alpha Precision Instruments Curie balance in an applied DC field of 0.15 T and target temperature of 650°C at the rate of 50°C/min at the Rutgers paleomagnetic lab. We used the same rock magnetic chip specimens that we did the hysteresis measurements. Figure 3.4 shows some examples of typical reversible single-phase J_s-T curves (a, b, c, d), and some examples of typical problematic (irreversible, multiple phases) J_s-T curves (e, f, g, h). Most of the Js-T curves show the major phase Tc (Curie point) around 550-600°C (Fig. 3.5), which indicates the magnetic carrier are predominantly low-Titanium magnetite. However, a few samples have second phases around 300-400°C, which indicate the presents of high-titanium magnetite grains. For most of the samples, J_s-T heating and cooling curves are reversible, which augurs well for stability in paleointensity experiments. However, for a few samples the J_s-T cooling curve has a larger magnetization than the heating curve, which indicates detectable thermochemical alterations of mineralogy have happened during the heating process.

After measuring the J_s-T curves, we repeated hysteresis properties measurements on 51 rock magnetic chips with the aim of detecting possible thermophysicochemical alterations due to rapid heating and cooling to and from 650°C in air (Table 3.S2). Day plots of the 51 specimens before and after the J_s-T experiments are shown in Figure 3.3b. Figure 3.6 (a, b, c) shows histograms of the M_r/M_s ratios of these 51 specimens before and after heating processes. We found that the M_r/M_s ratios increased for most of the specimens after heating. However, more than half of the specimens experienced less than 20% increase in the M_r/M_s ratio, which we hope may be stable enough for paleointensity experiments. Figure 3.6 (d, e, f) shows the B_c changes of these 51 specimens. We found that more than half of the specimens experienced less than 50% B_c increasing.

Figure 3.7 (a, b, c) and (d, e, f) show the M_r and M_s changes of these 51 specimens before and after heating processes, respectively. We found that both M_r and Ms increased for most of the specimens after heating. However, more than half of the specimens experienced less than 50% M_r increasing, and for most of the specimens, the Ms experienced less than 20% change, which we hope stable enough for paleointensity experiments. Remeasuring the rock magnetic properties after J_s-T heating to 650°C in air provide severe tests for the thermal stabilities of specimens that to be used for paleointensity experiments, since the Curie temperatures of magnetite (~580°C) are usually used as the final maximum temperature.

In conclusion, rock magnetic properties of the selected samples indicate that the dominant magnetic mineral is fine-grained, low-titanium magnetite with various range of grain size. Most of the samples are thermochemically stable even when heated to above the Curie temperature. However, some detectable thermophysical effective grain size changes occurred during heating for the more SSD samples (i.e., those with the higher M_r/M_s ratios). Most of the Galapagos samples should thus be ideal candidates for Thellier paleointensity experiments in terms of their thermophysicochemical stability, but less obviously so in terms of magnetic grain size, which tends to be dominated by MD carriers.

3.5 Paleointensity experiments

For 34 of the 138 specimens from stage one of this study, we initially used the BZF paleointensity protocol (Back-field, Zero-field and Forward-field heating steps for each temperature) that was recently developed by *Wang and Kent* [2013]. We calculated the paleointensities using the Aitken method [*Aitken et al.*, 1988] by using the data from the Back-field and Zero-field step measurements. For 104 out of the 138 specimens, we initially used the IZZI paleointensity protocol (alternating between In-field + Zero-field and Zero-field + In-field heating steps; [*Tauxe and Staudigel*, 2004; *Yu et al.*, 2004]), which was designed to detect MD effects in the initial Thellier-series paleointensity experiments. From room temperature, we used 200°C, 350°C, 400°C (350°C), 425°C, 450°C (400°C), 475°C, 500°C (450°C), 525°C, 550°C (500°C) and 575°C as the heating

target temperatures (with pTRM back-checks in parentheses) for both experiment protocols. The paleointensity experiments for stage one are performed using ASC TD-48 demagnetizer and Mulspin Spinner Magnetometer at the Rutgers paleomagnetics laboratory.

After either the BZF or IZZI protocol, we repeated the paleointensity experiment after giving specimens total TRM for MD correction [*Wang and Kent*, 2013]. Specifically, after standard Thellier series paleointensity experiments, we gave each sample a total thermal remanent magnetization (tTRM) by cooling from 575°C, near the dominant Curie point, in the presence of a laboratory-applied field (15 μT). We then repeated the paleointensity experiment on each sample, with the laboratory-applied tTRM as a synthetic natural remanent magnetization (NRM), using the same laboratory-applied field and temperature steps. For the repeated paleointensity experiments, we omitted a few unnecessary pTRM acquisition steps (e.g. 425°C, 475°C, 525°C, and 575°C) to save lab work load. This provided a synthetic Arai signature, which should only represent the domain-state dependent properties of the sample. We corrected the Arai diagrams from the original paleointensity experiment by using the Arai signatures from the repeated experiment, which neutralizes the typical MD concave-up Arai effect. For the BZF protocol, we calculated the magnetizations using the Aitken method [*Aitken et al.*, 1988; *Wang and Kent*, 2013].

For each specimen, we plotted the original, repeated and corrected Arai diagrams [*Nagata et al.*, 1963] and tTRM checks (A plot of the original against repeated pTRM

acquisitions that used as an indicator of thermophysicochemical alterations) [*Wang and Kent*, 2013]. We calculated the paleointensity estimates from the 400°C to 575°C segments of the corrected Arai diagrams to avoid low temperature viscous remanent magnetization (VRM) as suggested by *Wang and Kent* [2013]. We also calculated the following quality control parameters as described by *Wang and Kent* [2013]: Pint-R (linear regression correlation coefficient for the used segment of corrected Arai diagram); tTRM-R (linear regression correlation coefficient for tTRM check); and tTRM-k (least-square fit slope for tTRM check). In order to ensure data quality, we set the following basic paleointensity qualification criteria: Pint-R $\geq$ 0.980; tTRM-R $\geq$ 0.980; 0.85 $\leq$ tTRM-k $\leq$ 1.15. We labeled the sample "Pass" for each quality criteria if its parameter was within the above threshold; otherwise, we labeled it "Fail" for that particular set of criteria. In order to be an overall qualified paleointensity result, the sample has to satisfy all three of the above criteria. We used pTRM checks simply as references but not for gauging thermal alteration following *Wang and Kent* [2013].

Among the 138 specimens that we conducted paleointensity experiments in stage one, 48 from 29 individual lava flow sites met our data qualification criteria. Within these qualified specimens, 17 were done by repeat-BZF protocol (calculated by the Aitken method) and 31 were done by repeat-IZZI protocol (Table 3.S3). There are no apparent differences between the paleointensity results from using these two different experiment protocols.

For stage two experiments, in the hope of acquiring more qualified paleointensity results, after analyzing the paleointensity results from stage one experiments, we selected 71 additional "x" specimens from 23 lava flows (Table 3.S3), that showed the least evidence of laboratory thermal alteration in the previous experiments. The selected "x" specimens are all from different samples than the "c" specimens that were used in stage one experiments.

For the 71 "x" specimens, we initially used the IZZI paleointensity protocol (alternating between In-field + Zero-field and Zero-field + In-field heating steps; [*Tauxe and Staudigel*, 2004; *Yu et al.*, 2004]). From room temperature, we used 200°C (NRM demagnetization only), 300°C (NRM demagnetization only), 350°C, 400°C, 425°C, 450°C (400°C), 475°C, 500°C (450°C), 525°C, 550°C (500°C) and 575°C as the heating target temperatures (with pTRM back-checks in parentheses) for both experiment protocols. After the IZZI protocol, we also repeated the paleointensity experiment after giving specimens total TRM for MD correction [*Wang and Kent*, 2013]. We also omitted a few unnecessary pTRM acquisition steps (e.g. 425°C, 475°C, 525°C, and 575°C) to save lab work load. The paleointensity experiments for stage one are performed using ASC TD-48 demagnetizer and 2G cryogenic superconductor magnetometer at the paleomagnetics laboratory at Lamont-Doherty Earth Observatory.

We used the same set of basic paleointensity qualification criteria (Pint-R $\geq$ 0.980; tTRM-R $\geq$ 0.980; 0.85 $\leq$ tTRM-k $\leq$ 1.15) for the "x" specimens. Finally 32 of 71

"x" specimens meet the criteria and provide valid paleointensity estimates. Arai diagrams and tTRM checks for all 209 specimens are shown in Fig. 3.S2.

3.6 MD corrected Paleointensity Results

Finally 80 specimens from 80 independently oriented lava samples from 31 sites provided good paleointensity estimates (see Table 3.S3). Sites GA03, GA05, GA06, GA09 and GA12 are very closely located and gave similar paleomagnetic directions (N = 5, mean Decl = 346.8, mean Incl = -1.1, K = 122.0, A95 = 7.0) and paleointensities (54.7 μT, 54.8 μT, 45.8 μT, 50.2 μT, 62.1 μT, respectively). It is very likely that these 5 sites are sampling the same lava flow unit or very closely erupted flows that sampling the same paleomagnetic field and intensity. Thus, we combined these 5 sites into a new site named GA-0 (yielding a site paleointensity estimation of 51.9 μT), which makes the total lava site number to be 47. After the combination, there are totally 27 Galapagos lava flow sites (8 normal and 19 reverse polarity) providing valid paleointensity results (Table 3.1). The average paleointensity of the 27 successful lava flow sites is 21.6 μT (11.0 μT for standard deviation). Of these 27 sites, 8 of them are of normal polarity, yielding an average paleointensity of 19.6 μT (standard deviation: 15.6 μT), and 19 of them are of reverse polarity, yielding an average paleointensity of 22.4 μT (standard deviation: 8.9 μT). Specimen level MD corrected paleointensities from each site are also shown in Figure 3.8.

Four typical Arai diagrams of qualified paleointensity results (GA06.1c, IZZI; GA21.6c, BZF; GA29.4c, IZZI; and GA33.1c, BZF) are shown in Figure 3.9. We found that the MD correction technique of *Wang and Kent* [2013] provided linear corrected Arai diagrams for paleointensity experiments that conducted by both IZZ and BZF protocols.

Four typical Arai diagrams of disqualified paleointensity results (GA03.7c, BZF; GA18.7c, IZZI; GA34.4c, IZZI; and GA82.4c, IZZI) are shown in Figure 3.10. GA03.7c did not meet the qualification criteria for all 3 parameters. tTRM check indicated that the specimen have thermally altered at low to middle temperature. Although GA18.7c met the qualification criteria for all 3 parameters, it's very likely to experience hidden type alterations, according to the possible huge increase of TRM recording capabilities at high temperature indicated by Arai diagrams and tTRM checks [*Wang and Kent*, 2013]. Thus, it was manually excluded those samples from qualified paleointensity results. Both GA34.4c and GA82.4c satisfied the Pint-R, but failed tTRM-R and tTRM-k. According to their tTRM checks, they are very likely to experience thermophysicochemical alterations during the heating processes of the paleointensity experiments.

Histograms of 27 Galapagos lava flow MD corrected site paleointensity results are shown in Figure 3.11. The peak of the distribution is around 15 μT, with the range from around 0 - 60 μT. Lognormal fits are also performed on the 27 sites, 8 normal polarity sites and 19 reverse polarity sites, respectively. Some distribution differences can be detected between the normal and reverse polarity sites, with reverse polarity sites

yielding slightly higher paleointensity mean than the normal sites. This could be due to the uneven number of sites that yield valid paleointensity results.

Mean paleomagnetic directions of the normal and reverse polarity sites (normal polarity sites: N = 8, mean Decl = 354.7°, mean Incl = 2.6°, K = 25.0, A95 = 11.3°; reverse polarity sites: N = 19, mean Decl = 178.6°, mean Incl = 2.4°, K = 32.4, A95 = 6.0°) are statistically antipodal and within a few degrees expected from the geocentric axial dipole (GAD) field (expected normal vs reverse polarity site mean Decl = 0° vs 180°, mean Incl = -2° vs 2°), and mean VGPs (normal polarity sites: N = 8, mean VGP Long = 205.5°, mean VGP Lat = 84.4°, K = 54.6, A95 = 7.6°; reverse polarity sites: N = 19, mean VGP Long = 357.9°, mean VGP Lat = -88.6°, K = 67.7, A95 = 4.1°) are statistically antipodal and within a few degrees expected from the geocentric axial dipole (GAD) field (expected normal vs reverse polarity site mean Decl = 0° vs 180°, mean Incl = -2° vs 2°; mean VGP Lat = 90° vs -90°), which together indicate that these data should be representative of the time-averaged geomagnetic field with no resolvable contributions from persistent non-dipole fields (Table 3.3).

3.7 Traditional Thellier-series paleointensity results

In order to compare our MD corrected paleointensity results with those traditional Thellier series methods, we also calculated paleointensity estimations only from the original BZF or IZZI Arai diagrams using ThellierTool v.4.22 [*Leonhardt et al.*, 2004].

We used both a relatively loose set of qualificaiton criteria (number of points (N) ≥ 4; standard deviation (Std) ≤ 0.2; fraction of NRM (f) ≥ 0.3; quality factor (q) > 0; maximum angular deviation (MAD) ≤ 20°; alpha ≤ 20; relative check error (dCK) ≤ 10; cumulative check diff (dPAL) ≤ 15; normalized tail of pTRM (dt*) ≤ 8; relative intensity diff ≤ 25; relative AC error (dAC) ≤ 15; exactly the same to the set used in [*Wang and Kent*, 2013]) and a relatively strict set of criteria (number of points (N) ≥ 5; standard deviation (Std) ≤ 0.15; fraction of NRM (f) ≥ 0.3; quality factor (q) > 0; maximum angular deviation (MAD) ≤ 10°; alpha ≤ 15; relative check error (dCK) ≤ 7; cumulative check diff (dPAL) ≤ 10; normalized tail of pTRM (dt*) ≤ 5; relative intensity diff ≤ 15; relative AC error (dAC) ≤ 10; extremely similar to the default criteria set Class B in ThellierTool v.4.22 [*Leonhardt et al.*, 2004]. The only difference is that in default Class B, "relative intensity diff" is set no more than 20 instead of 15 as used here.) that lets the program automatically determine the temperature interval used to calculate paleointensity. We set the program to use as many data points as possible to estimate the paleointensity value. Totally, 88 specimens meet the relatively loose set of criteria, within which, 51 specimens meet the more strict set of criteria. The specimen paleointensity results are concluded in Table 3.S4 and Figure 3.12. We found that the site level overall average paleointensities from 51 specimens from 21 sites (26.0 ± 15.3 μT; 1σ) and 88 specimens from 26 sites (26.0 ± 19.1 μT; 1σ) are the same when using different data qualification criteria respectively. Site level paleointensity results from 26 lava flow sites by using the relatively loose set of criteria is concluded in Table 3.2.

Due to the fact that the traditional automatic paleointensity estimations do not account for the MD effects, we think the difference between the traditional paleointensity results and the MD corrected paleointensity results is due to systematically overestimation of paleointensities. In this study, we think the MD corrected paleointensities are more accurate, since the design of experimental technique accounts for the concave-up Arai diagrams caused by the MD effects.

3.8 Discussion

Paleointensity estimates from McMurdo [*Lawrence et al.*, 2009] were based on the IZZI protocol for the Thellier-Thellier method on SD-behaved lava samples and using an array of stringent selection criteria, providing a mean paleointensity of 31.5 ± 15.2 μT (1σ) from 41 sites with $d\sigma_B \leq 15\%$ and $N_B \geq 2$. With in these 41 sites, sites MC132 and MC145 were during magnetic polarity transitions (VGP Lat = -9.8° and 9.0°, respectively) and site MC113 was estimated to be 6.73 Ma old, which are excluded from the calculation of the average paleointensity for the normal and reverse polarities for the last 5 Myr. The remaining 38 McMurdo lava flow sites (19 normal and 19 reverse polarity) provide valid paleointensity results with an overall mean value of 33.4 ± 13.9 μT (1σ). This is only about 1/2 the present field intensity at the sampling locality at the polar regions, which is about 63 μT.

We also performed the same histogram analysis on the 38 lava flow site paleointensity results (Figure 3.14). The peak of the distribution is around 30 μT, with the range from around 0 - 60 μT for 37 sites (with one site yielding ~80 μT). Lognormal fits are also performed on the 38 sites, 19 normal polarity sites and 19 reverse polarity sites, respectively. Slight distribution differences can be detected between the normal (32.3 ± 11.0 μT; 1σ) and reverse (34.6 ± 16.5 μT; 1σ) polarity sites, with normal polarity sites yielding slightly higher paleointensity mean than the reversed sites.

The results of *Lawrence et al*. [2009] from Antarctica also have mean paleomagnetic directions of normal and reverse polarity sites that are antipodal (normal polarity sites: N = 19, mean Decl = 28.0°, mean Incl = -83.6°, K = 39.3, A95 = 5.4°; mean VGP Long = 272.3°, mean VGP Lat = 84.6°, K = 12.6, A95 = 9.9°; reverse polarity sites: N = 19, mean Decl = 184.0°, mean Incl = 80.5°, K = 25.8, A95 = 6.7°; mean VGP Long = 1.8°, mean VGP Lat = -84.2°, K = 9.3, A95 = 11.6°) and conform to expectations from a GAD field, yet the mean GMF intensity (VADM = ~4.4×10^{22} Am^2) is only about 1/2 of the present day field intensity (VADM = ~8.3×10^{22} Am^2) calculated at the same locality (Table 3.3).

After scrutinizing alternative explanations such as data bias from poor selection criteria and inadequate spatiotemporal sampling, *Lawrence et al.* [2009] suggested that the association of high VGP dispersion and low intensity was consistent with an anticorrelation between directional variability and field strength observed by some in global data [*Bogue and Coe*, 1984; *Love*, 2000]. In the case of the McMurdo, *Lawrence*

et al. [2009] speculated that the high dispersion-low intensity relationship may result from differences in geodynamo activity in the outer core, specifically, with respect to the inner core tangent cylinder that projected to a latitudinal band at about the McMurdo locality. In a compilation of the best available global paleointensity data for the past few million years, *Lawrence et al.* [2009] showed that the expected latitudinal variation for a geocentric axial dipole field was not apparent (Figure 12 of *Lawrence et al.* [2009]): indeed, the mean McMurdo paleointensity of 33.4 μT was essentially the same as mean values at 10-20° latitude from the paleointensity database [*Biggin et al.*, 2009]. However, the Galapagos data in this study suggest that the average equatorial paleointensity is only 21.6 ± 11.0 μT, about 2/3 of the present day value. The VADM is ~5.6×10^{22} Am^2, which is more in accord with McMurdo for a GAD field.

In this study, we summarize the paleointensity statistical results for both McMurdo (McMurdo, Antarctica) and Galapagos in Table 3.3. We found that the overall average paleointensity for the 38 sites from McMurdo (mean paleointensity= 33.4 μT) was just significantly greater than the average for the 27 sites from Galapagos (mean paleointensity= 21.6 μT), a latitudinal difference that approaches the GAD prediction.

The site paleointensity results and histograms are concluded in Figure 3.17. The GAD fit of the average VADM of the McMurdo paleointensities from *Lawrence et al.* [2009] and the Galapagos paleointensities from this study (VADM is ~5.0×10^{22} Am^2) yields equatorial paleointensity of 19.3 μT and polar paleointensity of 38.6 μT (red dashed line in Figure 3.14). The Galapagos average paleointensity in this study

overestimates the GAD fit by only about 10%, while the McMurdo average paleointensity from *Lawrence et al.* [2009] underestimates the GAD fit by about 10%. As a reference, the present day dipole intensity is plotted by dashed green line in Figure 3.14. We found that the present day GMF intensity is about 50% greater than for the past a few million year average.

In order to test the stability of our Galapagos data set, we also calculated the average paleointensities by using lava sites that have at least two valid specimen paleointensities, which have standard deviation no more than 31% of their site mean paleointensity. Totally 18 sites (4 normal, 14 reversed) gave average paleointensity of 22.4 ± 11.8 μT (1σ), which is not essentially different from what we get from the 27 sites average (21.6 ± 11.0 μT; 1σ).

3.9 Conclusion

Rock magnetic properties indicate that the dominant magnetic mineral is fine-grained, low-titanium magnetite with various range of grain size for most of the lava flow samples from the Galapagos. Most of the samples are thermochemically stable even when heated to above the Curie temperature.

The paleointensity correction technique for MD igneous rock samples developed by *Wang and Kent* [2013] worked on both of the BZF and IZZI protocols for both "c"

specimens at Rutgers and "x" specimens at Lamont. The specimen paleointensity success rate is 38.3% (80/209) for this Galapagos lava flow collection. The site paleointensity success rate is more than 57.4% (27/47) for this Galapagos lava flow collection.

The average paleointensity for the past a few million years of the 27 successful lava flow sites is 21.6 μT (VADM = ~5.6×10^{22} Am^2). Average paleointensity for the 38 sites from McMurdo of 33.4 μT (VADM = ~4.4×10^{22} Am^2) is significantly greater than the average for the 27 sites from Galapagos, which is very close to a factor of two difference predicted by a GAD field.

Present day GMF intensity (VADM = ~8×10^{22} Am^2) is about 60% more than for the past few million year average (VADM = ~5×10^{22} Am^2), according to our Galapagos paleointensity results along with the McMurdo data from *Lawrence et al.* [2009].

3.10 Acknowledgements

We thank Pierre Rochette for generously providing the Galapagos samples. We thank Hui Wang and Christopher Lepre for providing laboratory assists on some of the sample preparation and measurements. Research was supported by NSF grant EAR-1113569.

References

Aitken, M. J., A. L. Allsop, G. D. Bussell, and M. B. Winter (1988), Determination of the intensity of the Earth's magnetic-field during archaeological times - reliability of the Thellier technique, *Rev. Geophys.*, *26*, 3-12.

Biggin, A. J., G. Strik, and C. G. Langereis (2009), The intensity of the geomagnetic field in the late-Archaean: new measurements and an analysis of the updated IAGA palaeointensity database, *Earth Planets and Space*, *61*, 9-22.

Bailey, K., 1976. Potassium-argon ages from the Galapagos Islands. *Science*, 192: 465–467.

Bogue, S. W. (2001), Geomagnetic field behavior before and after the Kauai reverse-normal polarity transition, *Journal of Geophysical Research*, *106*, 447-461.

Bogue, S. W., and R. S. Coe (1984), Transitional paleointensities from Kauai, Hawaii, and geomagnetic reversal models, *Journal of Geophysical Research*, *89*, 10,341-310,354.

Constable, C. G., and R. L. Parker (1988), Statistics of the geomagnetic secular variation for the past 5 m.y., *Journal of Geophysical Research*, *93*, 11,569-511,581.

Cox, A. (1970), Latitude dependence of the angular dispersion of the geomagnetic field, *Geophysical Journal of the Royal Astronomical Society*, *20*, 253-269.

Cox, A. and Dalrymple, G.B., 1966. Paleomagnetism and potassium-argon ages of some volcanic rocks from the Galapagos Islands. *Nature*, 209: 776-777.

Creer, K. M., E. Irving, and A. E. M. Nairn (1959), Palaeomagnetism of the Great Whin Sill, *Geophysical Journal of the Royal Astronomical Society*, *2*, 306–323.

Day, R., M. Fuller, and V. A. Schmidt (1977), Hysteresis properties of titanomagnetites: Grain-size and compositional dependence, *Phys. Earth Planet. Inter.*, *13*, 260-267.

Dunlop, D. J., and S. Xu (1994), Theory of partial thermoremanent magnetization in multidomain grains. 1. Repeated identical barriers to wall-motion (single microcoercivity), *J. Geophys. Res*, *99*, 9005-9023.

Gromme, S., E. A. Mankinen, and M. Prevot (2010), Time-averaged paleomagnetic field at the equator: Complete data and results from the Galapagos Islands, Ecuador, *Geochemistry Geophysics Geosystems*, *11*, Q11009, doi:11010.11029/12010GC003090

Harrison, C. G. A. (2009), Latitudinal signature of Earth's magnetic field variation over the last 5 million years, *Geochemistry Geophysics Geosystems*, *10*, Q02012, doi:02010.01029/02008GC002298.

Irving, E., and M. A. Ward (1964), A statistical model of the geomagnetic field, *Geofisica pura e applicata (Pure and Applied Geophysics)*, *57*, 47–52.

Johnson, C. L., et al. (2008), Recent investigations of the 0–5 Ma geomagnetic field recorded by lava flows, *Geochemistry Geophysics Geosystems*, *9*, Q04032, doi:04010.01029/02007GC001696

Kent, D. V., H. Wang, and P. Rochette (2010), Equatorial paleosecular variation of the geomagnetic field from 0-3 Ma lavas from the Galapagos Islands, *Physics of the Earth and Planetary Interiors*, *183*, 404-412.

Laj, C., and C. Kissel (1999), Geomagnetic field intensity at Hawaii for the last 420 kyr from the Hawaii Scientific Drilling Project core, Big Island, Hawaii, *Journal of Geophysical Research*, *104*, 15,317-315,338.

Lawrence, K. P., L. Tauxe, H. Staudigel, C. Constable, A. Koppers, W. McIntosh, and C. L. Johnson (2009), Paleomagnetic field properties at high southern latitude, *Geochemistry Geophysics Geosystems*, *10*, Q01005, doi:01010.01029/02008GC002072.

Leonhardt, R., C. Heunemann, and D. Krasa (2004), Analyzing absolute paleointensity determinations: Acceptance criteria and the software ThellierTool4.0, *Geochem. Geophys. Geosyst.*, *5*, Q12016, doi:10.1029/2004GC000807.

Love, J. J. (2000), On the anisotropy of secular variation deduced from paleomagnetic volcanic data, *Journal of Geophysical Research*, *105*, 5799-5806.

McElhinny, M. W., and P. L. McFadden (1997), Paleosecular variation over the past 5 Myr based on a new generalized database, *Geophysical Journal International*, *131*, 240-252.

McFadden, P. L., R. T. Merrill, and M. W. McElhinny (1988), Dipole/quadrupole family modeling of paleosecular variation, *Journal of Geophysical Research*, *93*, 11,583-511,588.

Nagata, T., Y. Arai, and K. Momose (1963), Secular variation of the geomagnetic total force during the last 5000 years, *J. Geophys. Res.*, *68*, 5277-5281.

Opdyke, N. D., D. V. Kent, K. Huang, D. A. Foster, and J. P. Patel (2010), Equatorial paleomagnetic time averaged field results from 0-5 Ma lavas from Kenya and the latitudinal variation of angular dispersion, *Geochemistry Geophysics Geosystems*, *11*, Q05005, doi:05010.01029/02009GC002863.

Opdyke, N. D., D. V. Kent, K. N. Huang, D. A. Foster, and J. P. Patel (2010), Equatorial paleomagnetic time-averaged field results from 0-5 Ma lavas from Kenya and the latitudinal variation of angular dispersion, *Geochemistry Geophysics Geosystems*, *11*, 20.

Rochette, P., F. Ben Atig, H. Collombat, D. Vandamme, and P. Vlag (1997), Low paleosecular variation at the equator: A paleomagnetic pilgrimage from Galapagos to Esterel with Allan Cox and Hans Zijderveld, *Geol. Mijnb.*, *76*, 9-19.

Selkin, P. A., and L. Tauxe (2000), Long-term variations in paleointensity, *Philosophical Transactions of the Royal Society of London*, *A358*, 1065-1088.

Sinton, C.W., Christie, D.M. and Duncan, R.A., 1996. Geochronology of Galapagos seamounts. *Journal of Geophysical Research*, 101: 13,659-13,700.

Swanson, F.J., Baitis, H.W., Lexa, J. and Dymond, J., 1974. Geology of Santiago, Rabida and Pinzon Islands, Galapagos. *Geological Society of America Bulletin*, 85: 1803–1810.

Tauxe, L., and D. V. Kent (2004), A simplified statistical model for the geomagnetic field and the detection of shallow bias in paleomagnetic inclinations: Was the ancient magnetic field dipolar?, in *Timescales of the Paleomagnetic Field, Geophysical Monograph 145*, edited by J. E. T. Channell, D. V. Kent, W. Lowrie and J. Meert, pp. 101–116, American Geophysical Union, Washington, D.C.

Tauxe, L., T. A. T. Mullender, and T. Pick (1996), Potbellies, wasp-waists, and superparamagnetism in magnetic hysteresis, *J. Geophys. Res.-Solid Earth*, *101*(B1), 571-583.

Thellier, E., and O. Thellier (1959), Sur l' intensite du champ magnetique terrestre dans le passe historique et geologique, *Ann. Geophys.*, *15*, 285-378.

Valet, J.-P., L. Meynadier, and Y. Guyodo (2005), Geomagnetic dipole strength and reversal rate over the past two million years, *Nature*, *435*, 802-805.

Valet, J. P. (2003), Time variations in geomagnetic intensity, *Reviews of Geophysics*, *41*, 4-1/4-44.

Vandamme, D. (1994), A new method to determine paleosecular variation, *Physics of the Earth and Planetary Interiors*, *85*, 131-142.

Wang, H., and D. V. Kent (2013), A Paleointensity Technique for Multidomain Igneous Rocks, *Geochemistry Geophysics Geosystems*, *14*, 4195-4213, doi:10.1002/ggge.20248

White, W.M., McBirney, A.R. and Duncan, R.A., 1993. Petrology and geochemistry of the Galapagos Islands: portrait of a pathological mantle plume. *Journal of Geophysical Research*, 98: 19533–19563.

Xu, S., and D. J. Dunlop (1994), Theory of partial thermoremanent magnetization in multidomain grains. 2. Effect of microcoercivity distribution and comparison with experiment, *J. Geophys. Res.*, *99*, 9025-9033.

Yamamoto, Y., and H. Tsunakawa (2005), Geomagnetic field intensity during the last 5 Myr: LTD-DHT Shaw palaeointensities from volcanic rocks of the Society Islands, French Polynesia, *Geophysical Journal International*, *162*, 79-114.

Yu, Y. J., L. Tauxe, and A. Genevey (2004), Toward an optimal geomagnetic field intensity determination technique, *Geochemistry Geophysics Geosystems*, *5*, 18.

Figure Captions

Figure 3.1. Paleointensity versus latitude of the Pint08 database (gray crosses) [*Biggin et al.*, 2009] and paleointensity estimates from 41 McMurdo lava sites of Antarctica study (red diamond for arithmetic mean) for data with $d\sigma_B \leq 15\%$, and $N_B \geq 2$. Southern Hemisphere data have been flipped to the Northern Hemisphere. Solid blue curve represents the intensity associated with a geocentric axial dipole with a dipole term (30 μT for Equator; 60 μT for Poles); dashed blue line represents field intensity of 30 μT. (Figure modified from *Lawrence et al.* [2009])

Figure 3.2. Example cutting schematics for specimen GA23.6c.

Figure 3.3. Rock magnetic hysteresis data from some Galapagos lava samples. (a) Hysteresis parameters from 156 samples from different sites (see Table 1); percentages on curve are modeled volume of MD contribution to SD-PSD-MD assemblage (SSD-MD mixing curve #3 [*Dunlop and Xu*, 1994; *Xu and Dunlop*, 1994]); (b) Hysteresis parameters before heating (black) and after heating to 650°C (red) from 51 selected samples from different sites (see Table 2).

Figure 3.4. Js-T thermal magnetic property curves of typical good samples (reversable heating and cooling curves and single phase): GA05.7 (a), GA30.1 (b), GA63.5 (c), GA66.3 (d); and typical bad samples (irreversable curves or multiple phases): GA28.3 (e), GA47.1 (f), GA50.7 (g), GA74.3 (h). Samples are heated in air with presence of 0.15T field. Tc is estimated by the intercept of the pre-Tc drop linear extrapolation and temperature axis from heating curves.

Figure 3.5. Histogram of Tc from 59 selected Galapagos specimens.

Figure 3.6. Rock magnetic hysteresis parameters: Mr/Ms ratio before (a) and after heaing (b) up to 650°C, and the value of after heating devided by before heating (c), which indicates the change of Mr/Ms ratio; Bc before (d) and after heaing (e) up to 650°C, and the value of after heating devided by before heating (f), which indicates the change of Bc.

Figure 3.7. Rock magnetic hysteresis parameters: Mr before (a) and after heaing (b) up to 650°C, and the value of after heating devided by before heating (c), which indicates the change of Mr; Ms before (d) and after heaing (e) up to 650°C, and the value of after heating devided by before heating (f), which indicates the change of Ms.

Figure 3.8. Corrected paleointensities for each site. Blue represent specimens that are experimented by IZZI protocol for "c" specimen; red represent specimens that are experimented by BZF protocol for "c" specimen; Green represent specimens that are experimented by IZZI protocol for "x" specimen. Error bars represent 95% confidence level. Paleointensities above 80 μT are not shown. Data with black center dots and crosses are qualified.

Figure 3.9. Typical qualified paleointensity Arai diagrams of GA06.1c (a, b, IZZI), GA21.6c (c, d, BZF), GA29.4c (e, f, IZZI), GA33.1c (g, h, BZF). (a, c, e, g): black lines are original Arai diagrams; red lines are corrected Arai diagrams. (b, d, f, h): blue lines are repeated Arai diagrams; red line are tTRM checks; blue and green dash lines are 1:1 reference lines.

Figure 3.10. Typical disqualified paleointensity Arai diagrams of GA03.7c (a, b, BZF), GA18.7c (c, d, IZZI), GA34.4c (e, f, IZZI), GA82.4c (g, h, IZZI). (a, c, e, f): black lines are original Arai diagrams; red lines are corrected Arai diagrams. (b, d, f, h): blue lines are repeated Arai diagrams; red line are tTRM checks; blue and green dash lines are 1:1 reference lines.

Figure 3.11. Histograms (upper) and lognormal fits (lower) of the site paleointensity results from Galapagos.

Figure 3.12. Traditional paleointensities for each site. Blue represent specimens that are experimented by IZZI protocol for "c" specimen; red represent specimens that are experimented by BZF protocol for "c" specimen; Green represent specimens that are experimented by IZZI protocol for "x" specimen. Error bars represent 95% confidence level. Paleointensities above 80 μT are not shown. Data with black center dots and crosses are qualified paleointensities that meet the strict set of selection criteria, while the rest meet the loose set of criteria.

Figure 3.13. Histograms (upper) and lognormal fits (lower) of the site paleointensity results from McMurdo, Antarctica (38 sites that satisfy $d\sigma_B \leq 15\%$, $N_B \geq 2$, Age ≤ 5 Ma and from non-transitional periods).

Figure 3.14. Paleointensity results for Galapagos and McMurdo plotted by their latitudes. Blue (white) crosses are paleointensities from normal and reverse polarities. Red dots are mean paleointensity with error bars as standard deviations. Histograms of both Galapagos and McMurdo are also plotted with blue (white) bars representing paleointensities from normal and reverse polarities. Red dashed line is the best GAD fit for the average paleointensity for the past a few million years, while green dashed line is the dipolar paleointensity for the present day. Inset map shows the sampling location of Galapagos (circle) and McMurdo (square).

Table 3.1. Qualified MD corrected paleointensity results of 27 lava flow sites from Galapagos collection.

Site	Polarity	Pint (μT)	Specimen Num	SD (μT)	SD/Pint
GA0*	N	51.9	10	5.9	11.3%
GA 1	R	35.7	5	10.8	30.2%
GA 2	R	12.5	2	0.2	1.8%
GA 10	R	16.3	1	N/A	N/A
GA 18	R	34.4	2	17.6	51.2%
GA 19	R	19.9	3	1.3	6.5%
GA 20	R	26.7	1	N/A	N/A
GA 21	R	11.1	2	2.3	20.6%
GA 22	R	12.2	2	3.0	25.1%
GA 23	R	32.4	2	6.4	19.9%
GA 24	R	26.3	2	6.7	25.5%
GA 26	R	40.7	4	3.8	9.4%
GA 27	R	25.8	1	N/A	N/A
GA 28	R	20.9	2	1.1	5.1%
GA 29	R	14.0	5	4.1	29.1%
GA 30	N	23.3	6	4.7	20.4%
GA 33	N	9.7	1	N/A	N/A
GA 40	N	18.0	1	N/A	N/A
GA 50	N	29.3	1	N/A	N/A
GA 60	N	5.4	2	1.6	30.7%
GA 63	R	16.5	2	4.9	29.8%
GA 64	R	20.5	5	3.6	17.6%
GA 65	R	13.5	1	N/A	N/A
GA 66	R	16.9	6	2.5	14.7%
GA 67	R	28.8	4	4.2	14.5%
GA 69	N	4.9	1	N/A	N/A
GA 83	N	14.5	6	2.9	19.9%
Mean		**21.6**			
Median		**19.9**			
GeoMean		**18.8**			
Std.Dev.		**11.0**			

* Combined from Sites 3, 5, 6, 9 and 12.

Table 3.2. 88 traditional paleointensity results of 26 qualified lava flow sites from Galapagos collection.

Site	Polarity	Pint (μT)	Specimen Num	SD (μT)	SD/Pint
GA 0	N	52.4	12	20.8	39.7%
GA 1	R	35.5	5	6.7	19.0%
GA 10	R	15.8	2	1.3	7.9%
GA 21	R	52.1	1	N/A	N/A
GA 22	R	15.2	1	N/A	N/A
GA 23	R	38.6	3	11.6	30.1%
GA 24	R	55.4	2	6.5	11.7%
GA 26	R	37.4	4	9.2	24.5%
GA 27	R	21.6	5	11.5	53.4%
GA 28	R	15.9	3	9.9	62.7%
GA 29	R	11.9	5	3.0	24.8%
GA 30	N	22.0	3	1.1	4.8%
GA 31	N	14.0	2	4.8	34.5%
GA 33	N	26.4	2	5.9	22.5%
GA 40	N	14.2	3	8.5	59.7%
GA 50	N	30.3	2	2.5	8.4%
GA 60	N	11.3	5	13.3	117.8%
GA 63	R	10.8	5	4.9	45.6%
GA 64	R	23.1	6	7.3	31.4%
GA 65	R	14.8	2	4.1	27.6%
GA 66	R	13.1	5	0.7	5.1%
GA 67	R	21.4	4	6.9	32.1%
GA 71	R	13.8	1	N/A	N/A
GA 74	N	3.7	1	N/A	N/A
GA 82	R	89.9	1	N/A	N/A
GA 83	N	14.8	3	0.3	2.3%
Mean		**26.0**			
Median		**18.6**			
GeoMean		**20.9**			
Std.Dev.		**19.1**			

* Combined from Sites 3, 5, 6, 9 and 12.

Table 3.3. MD corrected paleointensity result statistics of 27 Galapagos sites vs. 38 standard Thellier results from McMurdo, Antarctica.

Galapagos				McMurdo		
Normal	Reverse	**Total**	Paleo-Direction Statistics	Normal	Reverse	**Total**
8	19	**27**	Site Number	19	19	**38**
354.7°	178.6°	357.5°	Mean Paleo-Direction Decl	28.0°	184.0°	13.7°
2.6°	2.4°	-1°	Mean Paleo-Direction Incl	-83.6°	80.5°	-82.2°
25	32.4	29.9	Paleo-Direction K	39.3	25.8	31.2
11.3	6.0°	5.2°	Paleo-Direction A95	5.4°	6.7°	4.2°
205.5°	357.9°	195.5°	Mean VGP Long	272.3°	1.8°	225.8°
84.4°	-88.6°	87.4°	Mean VGP Lat	84.6°	-84.2°	86°
54.6	67.7	63.3	VGP K	12.6	9.3	10.7
7.6°	4.1°	3.5°	VGP A95	9.9°	11.6°	7.4°
Galapagos				McMurdo		
Normal	Reverse	**Total**	Paleointensity Statistics	Normal	Reverse	**Total**
8	19	**27**	Site Number	19	19	**38**
19.6	22.4	**21.6**	Mean Paleointensity (μT)	32.3	34.6	**33.4**
14.9	20.7	**18.8**	GeoMean Paleointensity (μT)	30.5	31.1	**30.8**
16.2	20.5	**19.9**	Median Paleointensity (μT)	30.0	30.3	**30.1**
15.6	8.9	**11.0**	Paleointensity Stdev (μT)	11.0	16.5	**13.9**

Galapagos paleomagnetic direction results are calculated from data by *Kent et al.*, [2010]; McMurdo paleomagnetic direction results are calculated from data by *Lawrence et al.*, [2009]. Field directions from reverse polarity periods are reverted in the calculation of the total site direction and VGP statistics.

Fig 3.1

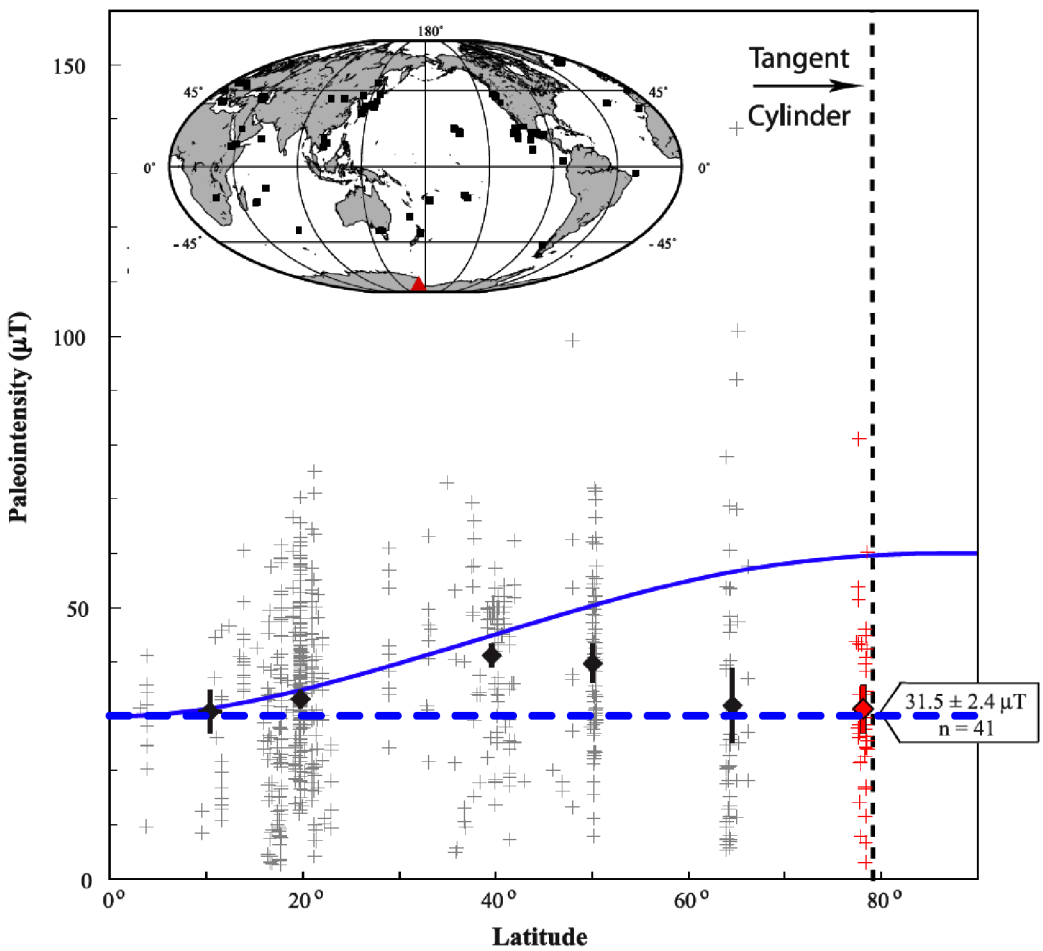
Tangent
Cylinder
180°
45°
0°
-45°
Paleointensity (μT)
150
100
50
0
0°
20°
40°
60°
80°
Latitude
31.5 ± 2.4 μT
n = 41

Fig 3.2

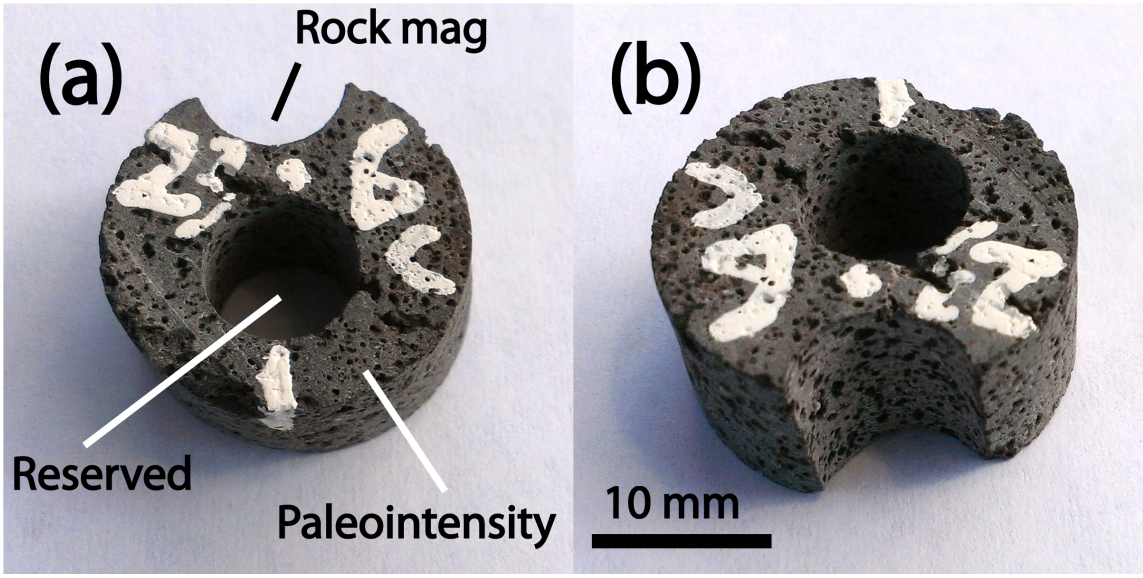

Fig 3.3

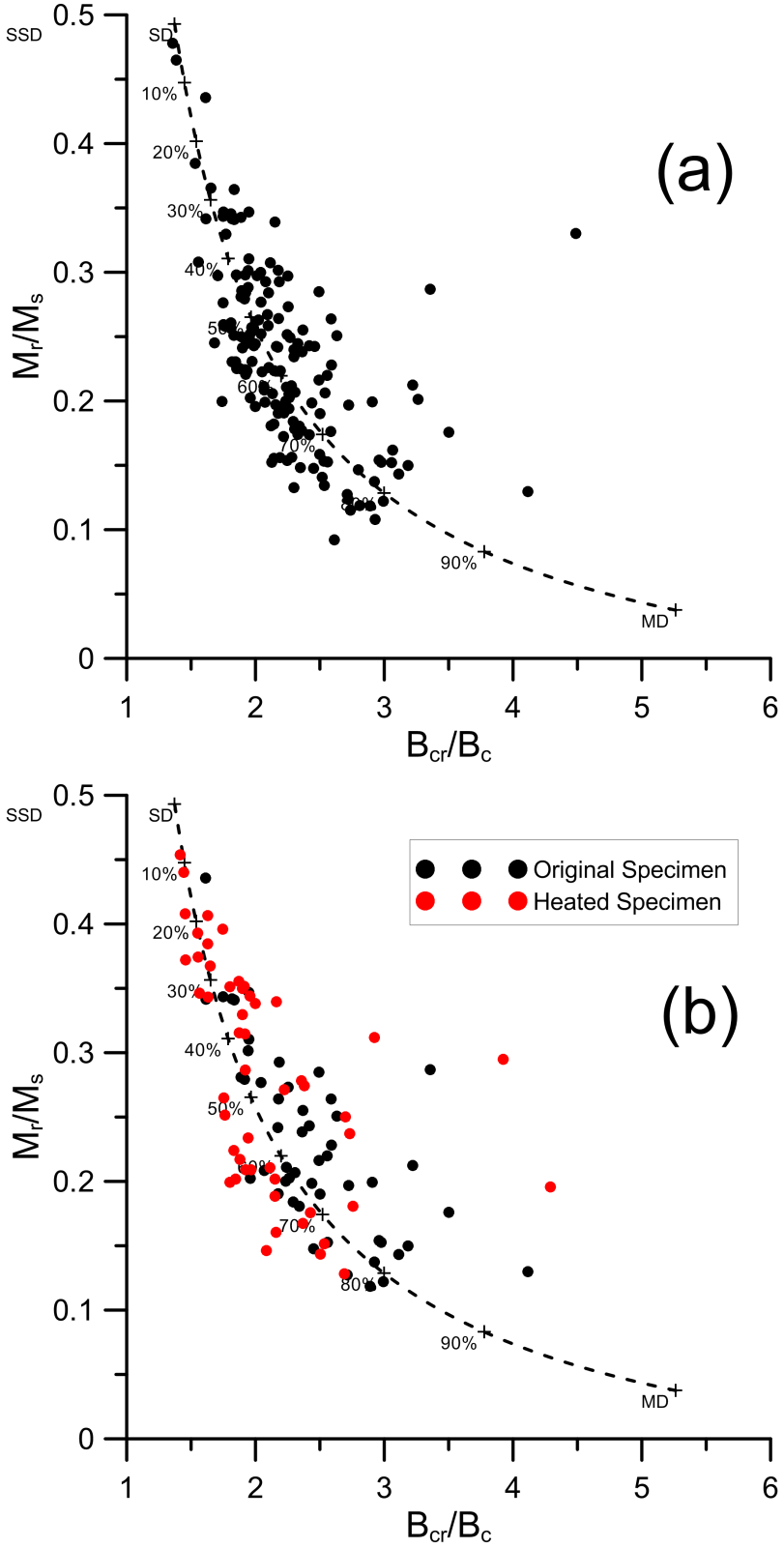
(a)
SSD
SD
10%
20%
30%
40%
50%
60%
70%
80%
90%
MD
M_r/M_s
B_{cr}/B_c
(b)
Original Specimen
Heated Specimen

Fig3.4

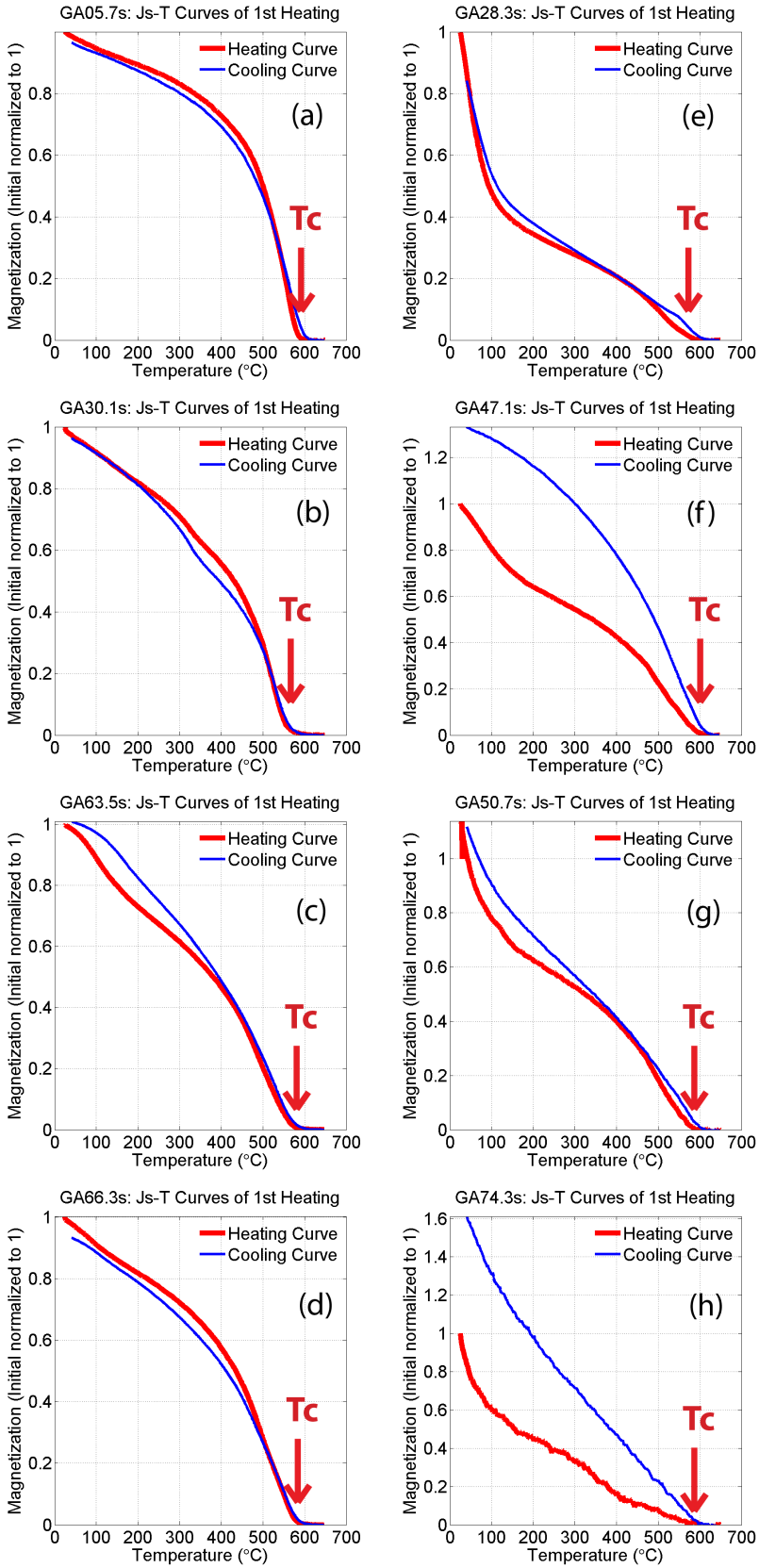
GA05.7s: Js-T Curves of 1st Heating
Heating Curve
Cooling Curve
(a)
Tc
Magnetization (Initial normalized to 1)
Temperature (°C)
GA28.3s: Js-T Curves of 1st Heating
(e)
GA30.1s: Js-T Curves of 1st Heating
(b)
GA47.1s: Js-T Curves of 1st Heating
(f)
GA63.5s: Js-T Curves of 1st Heating
(c)
GA50.7s: Js-T Curves of 1st Heating
(g)
GA66.3s: Js-T Curves of 1st Heating
(d)
GA74.3s: Js-T Curves of 1st Heating
(h)

Fig 3.5

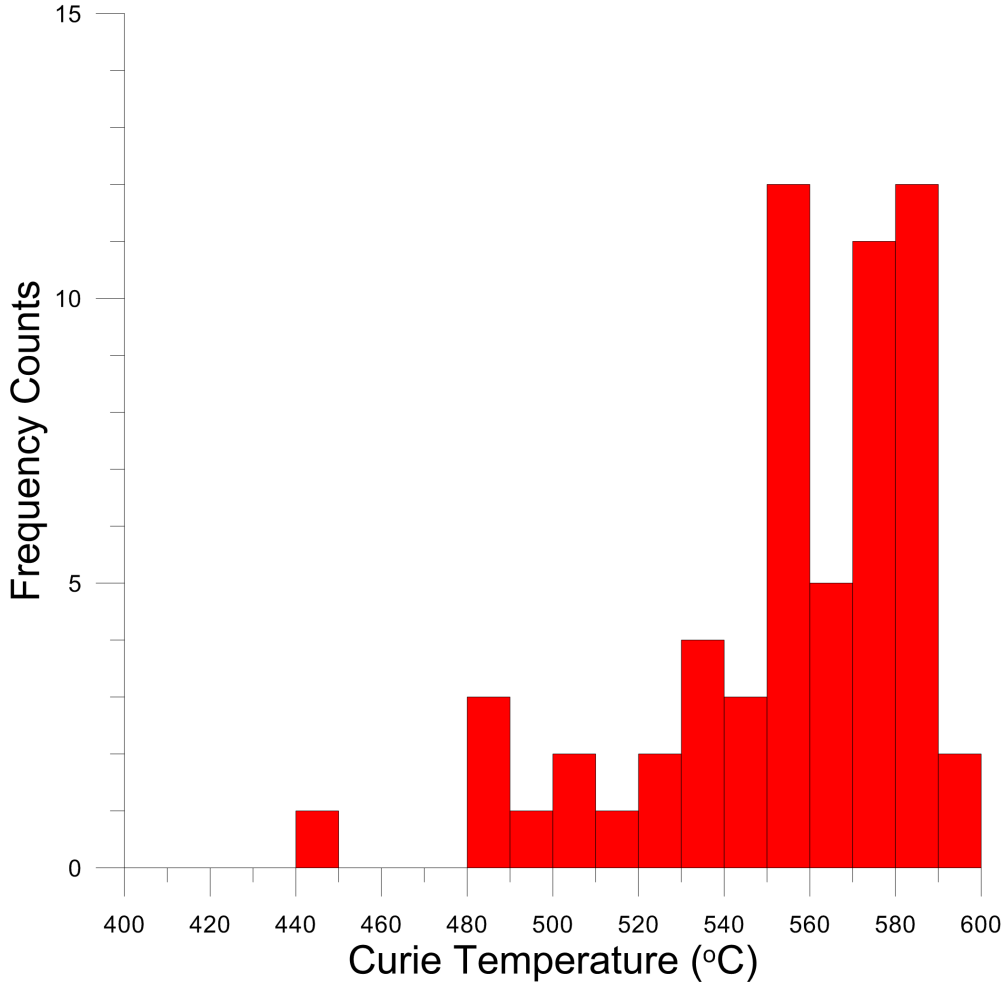
15
10
5
0
Frequency Counts
400
420
440
460
480
500
520
540
560
580
600
Curie Temperature (°C)

Fig 3.6

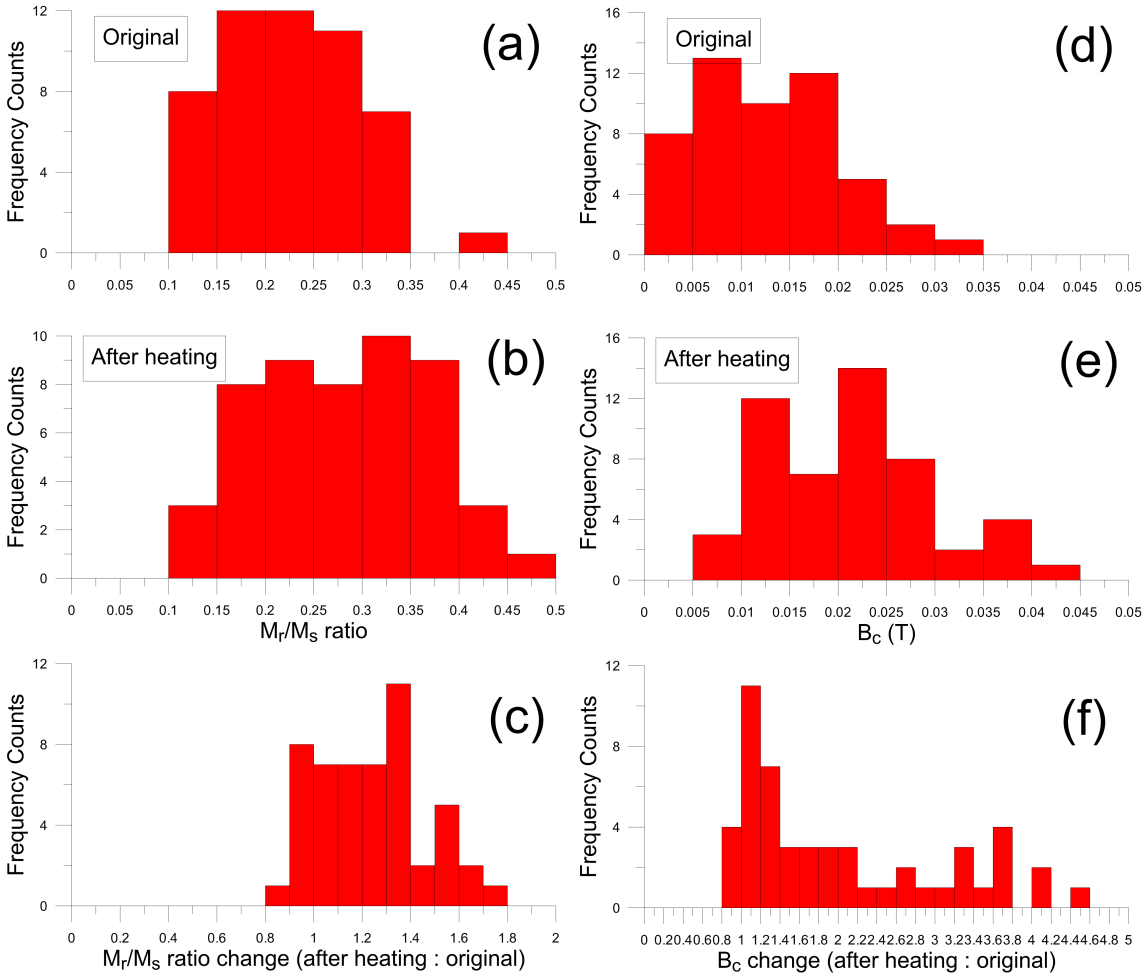
Original
(a)
Frequency Counts
After heating
(b)
M_r/M_s ratio
(c)
M_r/M_s ratio change (after heating : original)
Original
(d)
After heating
(e)
B_c (T)
(f)
B_c change (after heating : original)

Fig 3.7

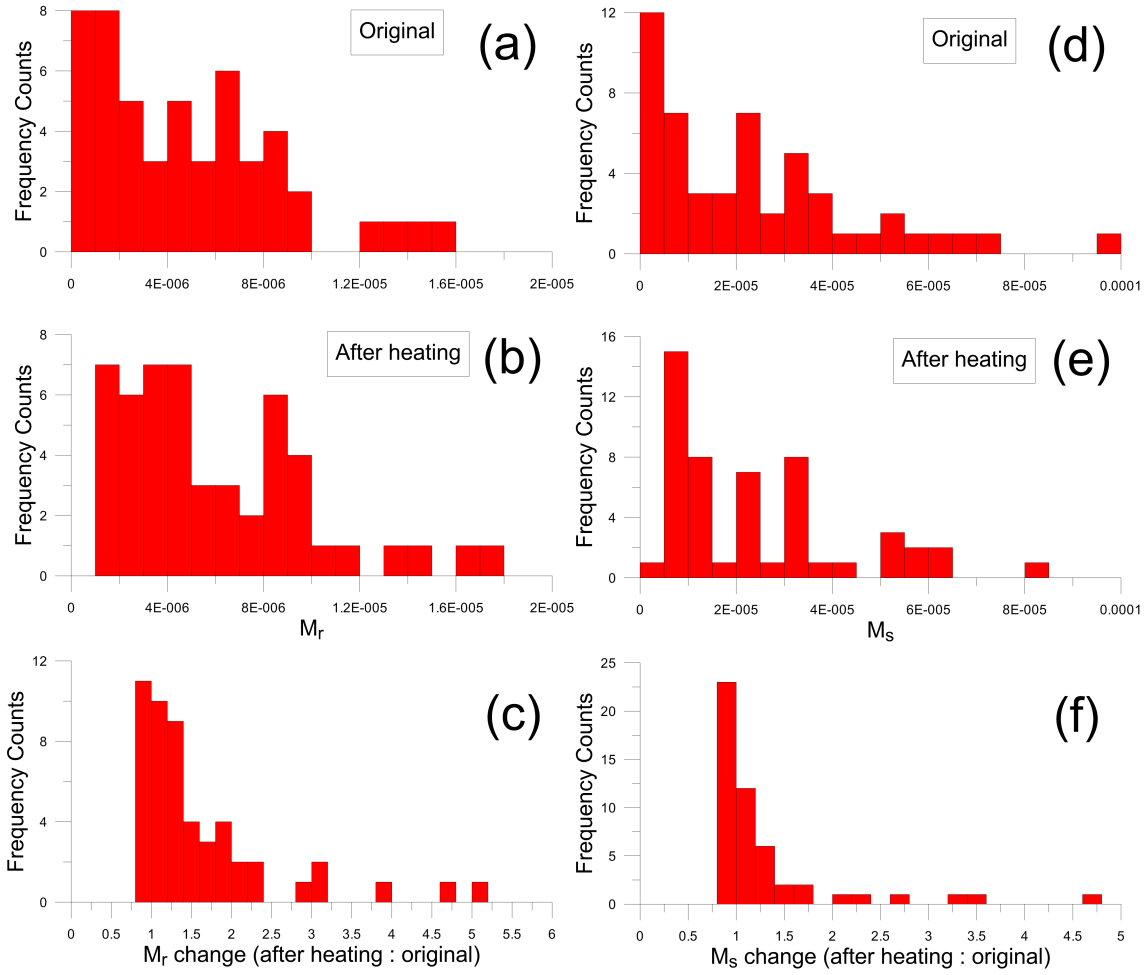
Original
(a)
Frequency Counts
0
2
4
6
8
0
4E-006
8E-006
1.2E-005
1.6E-005
2E-005
Original
(d)
Frequency Counts
0
4
8
12
0
2E-005
4E-005
6E-005
8E-005
0.0001
After heating
(b)
Frequency Counts
0
2
4
6
8
0
4E-006
8E-006
1.2E-005
1.6E-005
2E-005
Mr
After heating
(e)
Frequency Counts
0
4
8
12
16
0
2E-005
4E-005
6E-005
8E-005
0.0001
Ms
(c)
Frequency Counts
0
4
8
12
0
0.5
1
1.5
2
2.5
3
3.5
4
4.5
5
5.5
6
Mr change (after heating : original)
(f)
Frequency Counts
0
5
10
15
20
25
0
0.5
1
1.5
2
2.5
3
3.5
4
4.5
5
Ms change (after heating : original)

Fig 3.8

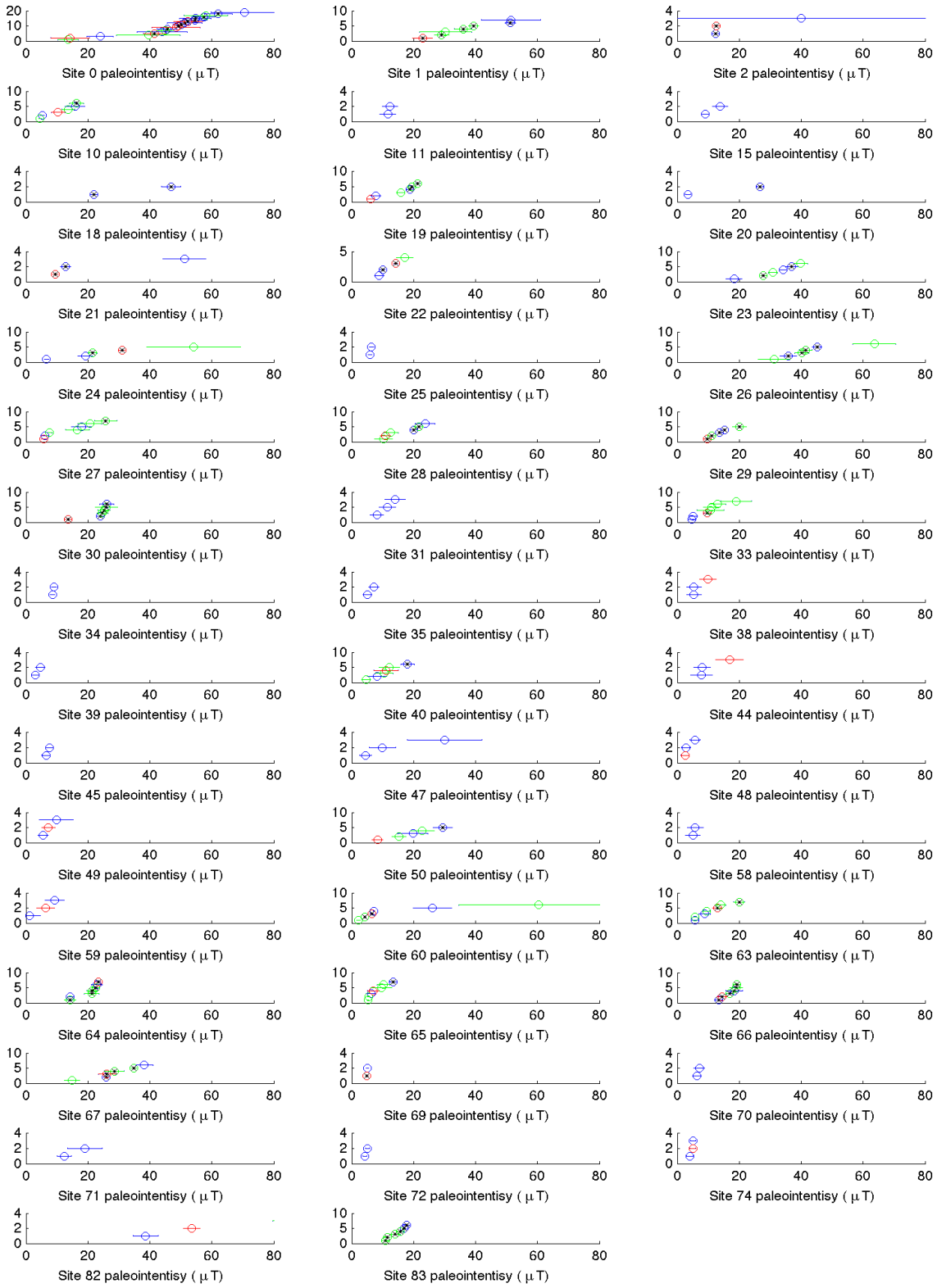
Site 0 paleointentisy (μ T)
Site 1 paleointentisy (μ T)
Site 2 paleointentisy (μ T)
Site 10 paleointentisy (μ T)
Site 11 paleointentisy (μ T)
Site 15 paleointentisy (μ T)
Site 18 paleointentisy (μ T)
Site 19 paleointentisy (μ T)
Site 20 paleointentisy (μ T)
Site 21 paleointentisy (μ T)
Site 22 paleointentisy (μ T)
Site 23 paleointentisy (μ T)
Site 24 paleointentisy (μ T)
Site 25 paleointentisy (μ T)
Site 26 paleointentisy (μ T)
Site 27 paleointentisy (μ T)
Site 28 paleointentisy (μ T)
Site 29 paleointentisy (μ T)
Site 30 paleointentisy (μ T)
Site 31 paleointentisy (μ T)
Site 33 paleointentisy (μ T)
Site 34 paleointentisy (μ T)
Site 35 paleointentisy (μ T)
Site 38 paleointentisy (μ T)
Site 39 paleointentisy (μ T)
Site 40 paleointentisy (μ T)
Site 44 paleointentisy (μ T)
Site 45 paleointentisy (μ T)
Site 47 paleointentisy (μ T)
Site 48 paleointentisy (μ T)
Site 49 paleointentisy (μ T)
Site 50 paleointentisy (μ T)
Site 58 paleointentisy (μ T)
Site 59 paleointentisy (μ T)
Site 60 paleointentisy (μ T)
Site 63 paleointentisy (μ T)
Site 64 paleointentisy (μ T)
Site 65 paleointentisy (μ T)
Site 66 paleointentisy (μ T)
Site 67 paleointentisy (μ T)
Site 69 paleointentisy (μ T)
Site 70 paleointentisy (μ T)
Site 71 paleointentisy (μ T)
Site 72 paleointentisy (μ T)
Site 74 paleointentisy (μ T)
Site 82 paleointentisy (μ T)
Site 83 paleointentisy (μ T)

Fig 3.9

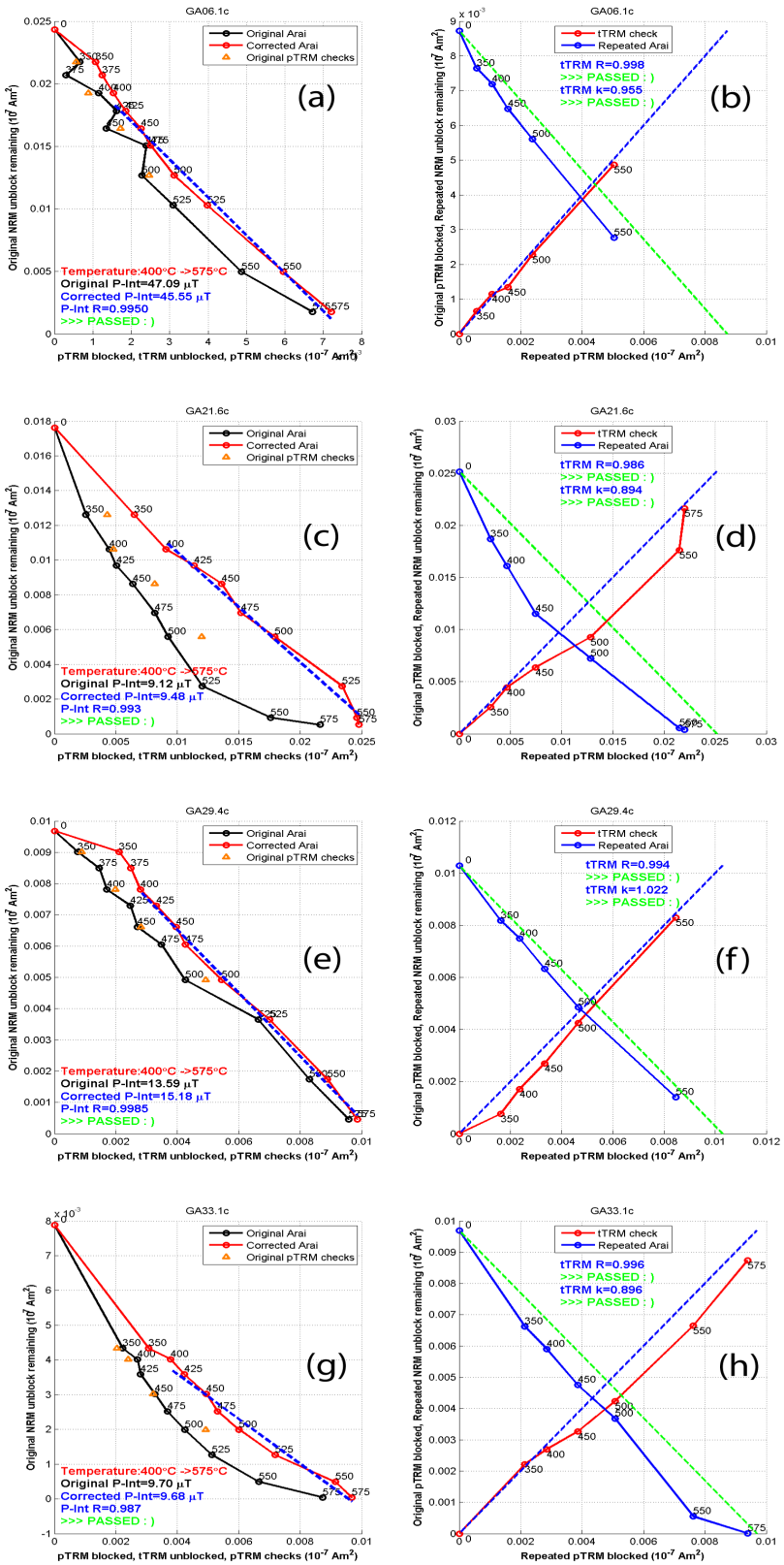
GA06.1c
Original Arai
Corrected Arai
Original pTRM checks
(a)
Temperature:400°C ->575°C
Original P-Int=47.09 μT
Corrected P-Int=45.55 μT
P-Int R=0.9950
>>> PASSED :)
Original NRM unblock remaining (10^-7 Am^2)
pTRM blocked, tTRM unblocked, pTRM checks (10^-7 Am^2)
GA06.1c
tTRM check
Repeated Arai
tTRM R=0.998
>>> PASSED :)
tTRM k=0.955
>>> PASSED :)
(b)
Original pTRM blocked, Repeated NRM unblock remaining (10^-7 Am^2)
Repeated pTRM blocked (10^-7 Am^2)
GA21.6c
Original Arai
Corrected Arai
Original pTRM checks
(c)
Temperature:400°C ->575°C
Original P-Int=9.12 μT
Corrected P-Int=9.48 μT
P-Int R=0.993
>>> PASSED :)
Original NRM unblock remaining (10^-7 Am^2)
pTRM blocked, tTRM unblocked, pTRM checks (10^-7 Am^2)
GA21.6c
tTRM check
Repeated Arai
tTRM R=0.986
>>> PASSED :)
tTRM k=0.894
>>> PASSED :)
(d)
Original pTRM blocked, Repeated NRM unblock remaining (10^-7 Am^2)
Repeated pTRM blocked (10^-7 Am^2)
GA29.4c
Original Arai
Corrected Arai
Original pTRM checks
(e)
Temperature:400°C ->575°C
Original P-Int=13.59 μT
Corrected P-Int=15.18 μT
P-Int R=0.9985
>>> PASSED :)
Original NRM unblock remaining (10^-7 Am^2)
pTRM blocked, tTRM unblocked, pTRM checks (10^-7 Am^2)
GA29.4c
tTRM check
Repeated Arai
tTRM R=0.994
>>> PASSED :)
tTRM k=1.022
>>> PASSED :)
(f)
Original pTRM blocked, Repeated NRM unblock remaining (10^-7 Am^2)
Repeated pTRM blocked (10^-7 Am^2)
GA33.1c
Original Arai
Corrected Arai
Original pTRM checks
(g)
Temperature:400°C ->575°C
Original P-Int=9.70 μT
Corrected P-Int=9.68 μT
P-Int R=0.987
>>> PASSED :)
Original NRM unblock remaining (10^-7 Am^2)
pTRM blocked, tTRM unblocked, pTRM checks (10^-7 Am^2)
GA33.1c
tTRM check
Repeated Arai
tTRM R=0.996
>>> PASSED :)
tTRM k=0.896
>>> PASSED :)
(h)
Original pTRM blocked, Repeated NRM unblock remaining (10^-7 Am^2)
Repeated pTRM blocked (10^-7 Am^2)

Fig 3.10

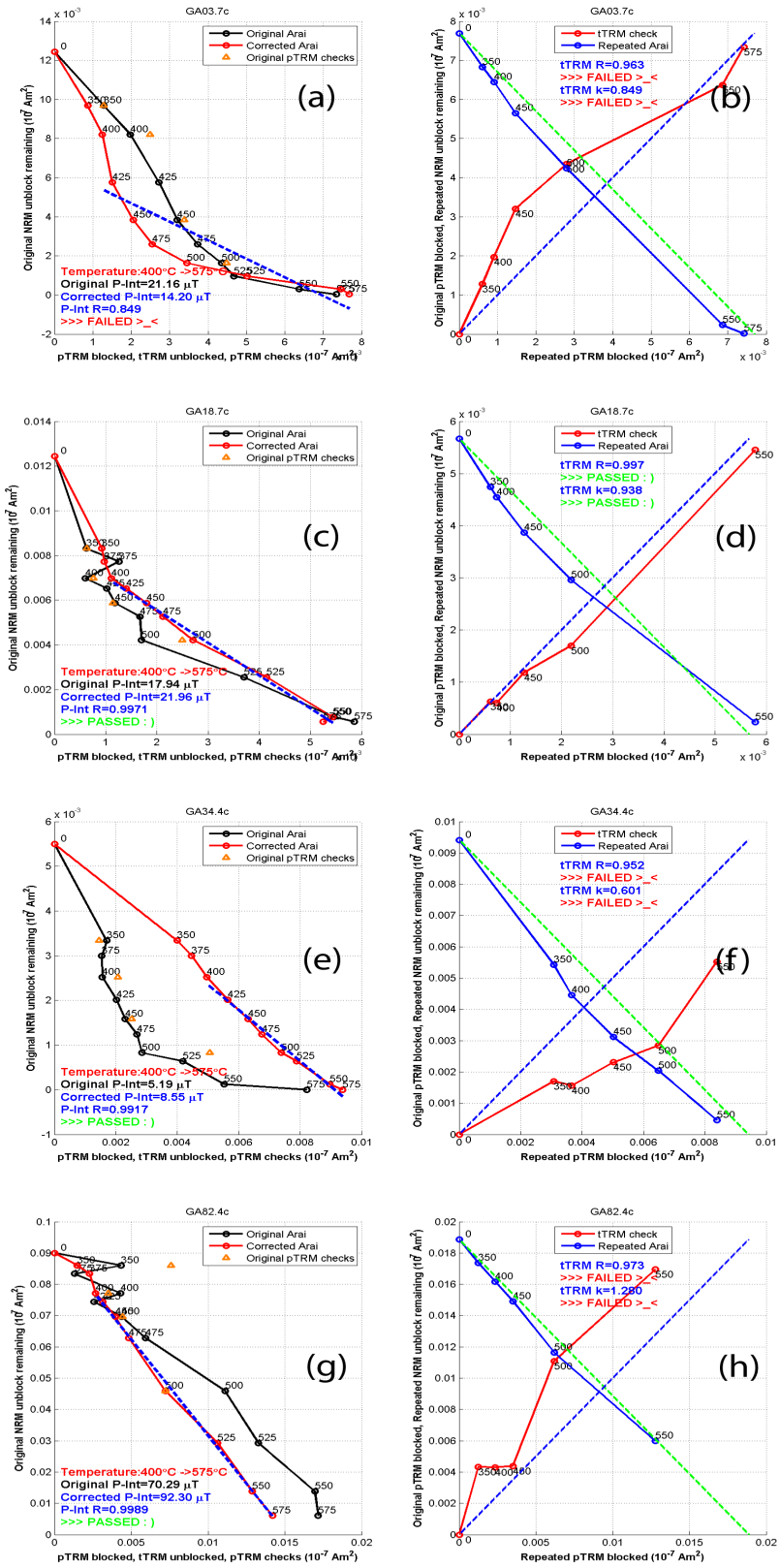
GA03.7c
Original Arai
Corrected Arai
Original pTRM checks
(a)
Temperature:400°C ->575°C
Original P-Int=21.16 μT
Corrected P-Int=14.20 μT
P-Int R=0.849
>>> FAILED >_<
Original NRM unblock remaining (10^-7 Am^2)
pTRM blocked, tTRM unblocked, pTRM checks (10^-7 Am^2)
GA03.7c
tTRM check
Repeated Arai
tTRM R=0.963
>>> FAILED >_<
tTRM k=0.849
>>> FAILED >_<
(b)
Original pTRM blocked, Repeated NRM unblock remaining (10^-7 Am^2)
Repeated pTRM blocked (10^-7 Am^2)
GA18.7c
Original Arai
Corrected Arai
Original pTRM checks
(c)
Temperature:400°C ->575°C
Original P-Int=17.94 μT
Corrected P-Int=21.96 μT
P-Int R=0.9971
>>> PASSED :)
Original NRM unblock remaining (10^-7 Am^2)
pTRM blocked, tTRM unblocked, pTRM checks (10^-7 Am^2)
GA18.7c
tTRM check
Repeated Arai
tTRM R=0.997
>>> PASSED :)
tTRM k=0.938
>>> PASSED :)
(d)
Original pTRM blocked, Repeated NRM unblock remaining (10^-7 Am^2)
Repeated pTRM blocked (10^-7 Am^2)
GA34.4c
Original Arai
Corrected Arai
Original pTRM checks
(e)
Temperature:400°C ->575°C
Original P-Int=5.19 μT
Corrected P-Int=8.55 μT
P-Int R=0.9917
>>> PASSED :)
Original NRM unblock remaining (10^-7 Am^2)
pTRM blocked, tTRM unblocked, pTRM checks (10^-7 Am^2)
GA34.4c
tTRM check
Repeated Arai
tTRM R=0.952
>>> FAILED >_<
tTRM k=0.601
>>> FAILED >_<
(f)
Original pTRM blocked, Repeated NRM unblock remaining (10^-7 Am^2)
Repeated pTRM blocked (10^-7 Am^2)
GA82.4c
Original Arai
Corrected Arai
Original pTRM checks
(g)
Temperature:400°C ->575°C
Original P-Int=70.29 μT
Corrected P-Int=92.30 μT
P-Int R=0.9989
>>> PASSED :)
Original NRM unblock remaining (10^-7 Am^2)
pTRM blocked, tTRM unblocked, pTRM checks (10^-7 Am^2)
GA82.4c
tTRM check
Repeated Arai
tTRM R=0.973
>>> FAILED >_<
tTRM k=1.280
>>> FAILED >_<
(h)
Original pTRM blocked, Repeated NRM unblock remaining (10^-7 Am^2)
Repeated pTRM blocked (10^-7 Am^2)

Fig 3.11

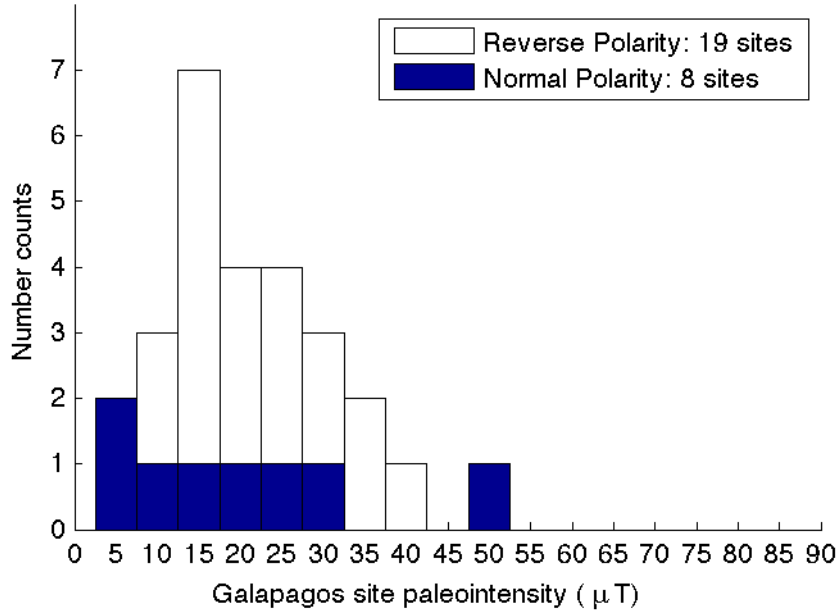
Reverse Polarity: 19 sites
Normal Polarity: 8 sites
Number counts
0
1
2
3
4
5
6
7
0 5 10 15 20 25 30 35 40 45 50 55 60 65 70 75 80 85 90
Galapagos site paleointensity (μT)

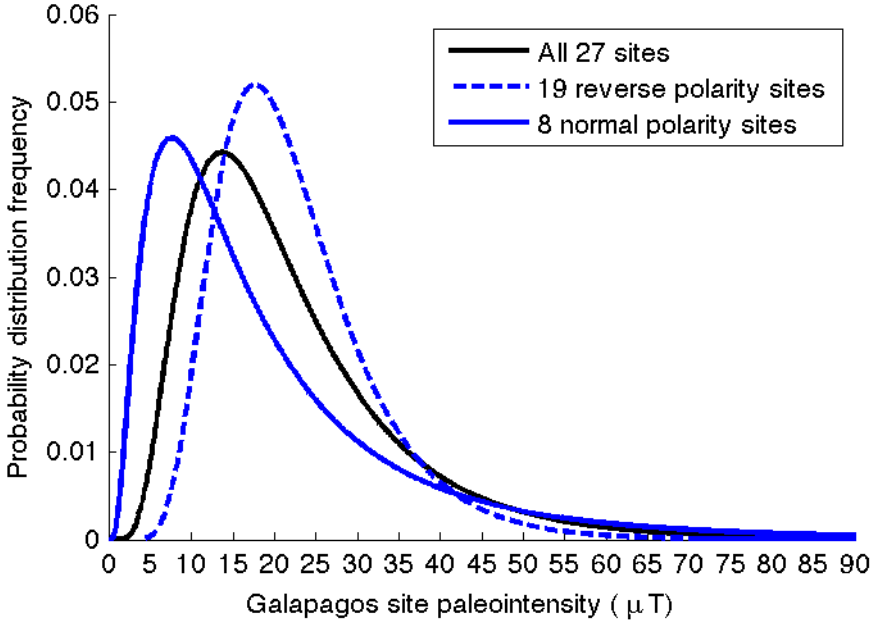
All 27 sites
19 reverse polarity sites
8 normal polarity sites
Probability distribution frequency
0
0.01
0.02
0.03
0.04
0.05
0.06
0 5 10 15 20 25 30 35 40 45 50 55 60 65 70 75 80 85 90
Galapagos site paleointensity (μT)

Fig 3.12

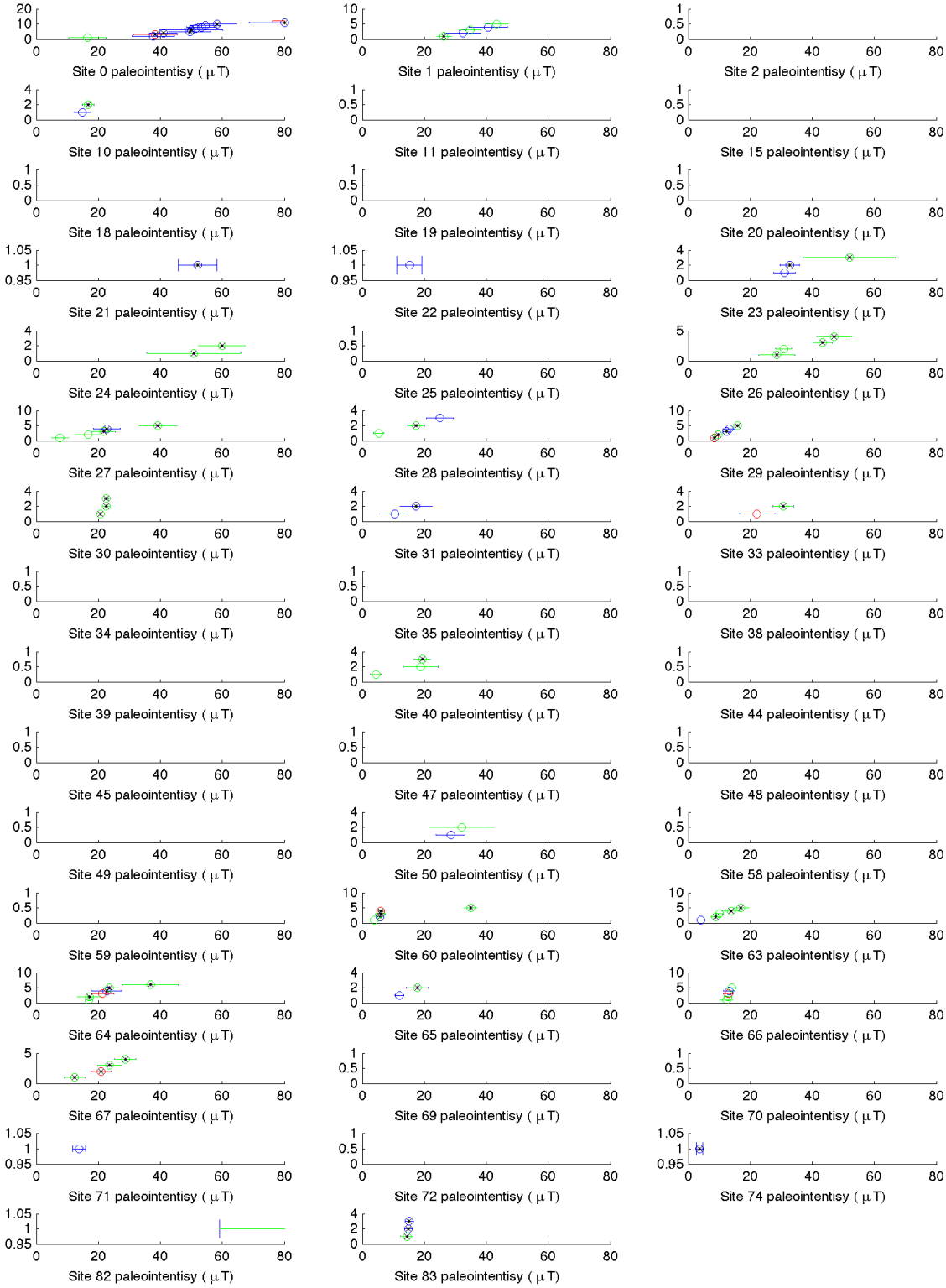
Site 0 paleointentisy (μ T)
Site 1 paleointentisy (μ T)
Site 2 paleointentisy (μ T)
Site 10 paleointentisy (μ T)
Site 11 paleointentisy (μ T)
Site 15 paleointentisy (μ T)
Site 18 paleointentisy (μ T)
Site 19 paleointentisy (μ T)
Site 20 paleointentisy (μ T)
Site 21 paleointentisy (μ T)
Site 22 paleointentisy (μ T)
Site 23 paleointentisy (μ T)
Site 24 paleointentisy (μ T)
Site 25 paleointentisy (μ T)
Site 26 paleointentisy (μ T)
Site 27 paleointentisy (μ T)
Site 28 paleointentisy (μ T)
Site 29 paleointentisy (μ T)
Site 30 paleointentisy (μ T)
Site 31 paleointentisy (μ T)
Site 33 paleointentisy (μ T)
Site 34 paleointentisy (μ T)
Site 35 paleointentisy (μ T)
Site 38 paleointentisy (μ T)
Site 39 paleointentisy (μ T)
Site 40 paleointentisy (μ T)
Site 44 paleointentisy (μ T)
Site 45 paleointentisy (μ T)
Site 47 paleointentisy (μ T)
Site 48 paleointentisy (μ T)
Site 49 paleointentisy (μ T)
Site 50 paleointentisy (μ T)
Site 58 paleointentisy (μ T)
Site 59 paleointentisy (μ T)
Site 60 paleointentisy (μ T)
Site 63 paleointentisy (μ T)
Site 64 paleointentisy (μ T)
Site 65 paleointentisy (μ T)
Site 66 paleointentisy (μ T)
Site 67 paleointentisy (μ T)
Site 69 paleointentisy (μ T)
Site 70 paleointentisy (μ T)
Site 71 paleointentisy (μ T)
Site 72 paleointentisy (μ T)
Site 74 paleointentisy (μ T)
Site 82 paleointentisy (μ T)
Site 83 paleointentisy (μ T)

Fig 3.13

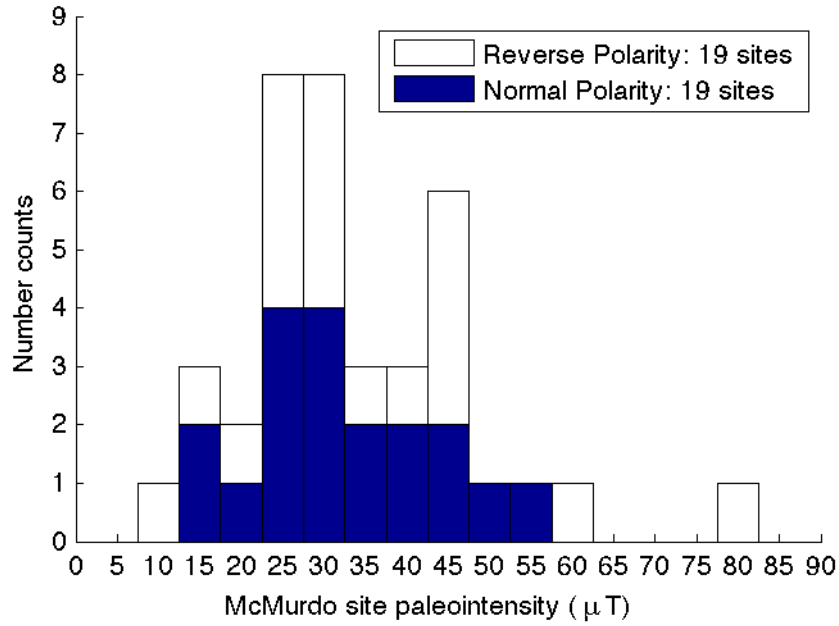
Reverse Polarity: 19 sites
Normal Polarity: 19 sites
Number counts
McMurdo site paleointensity (μ T)

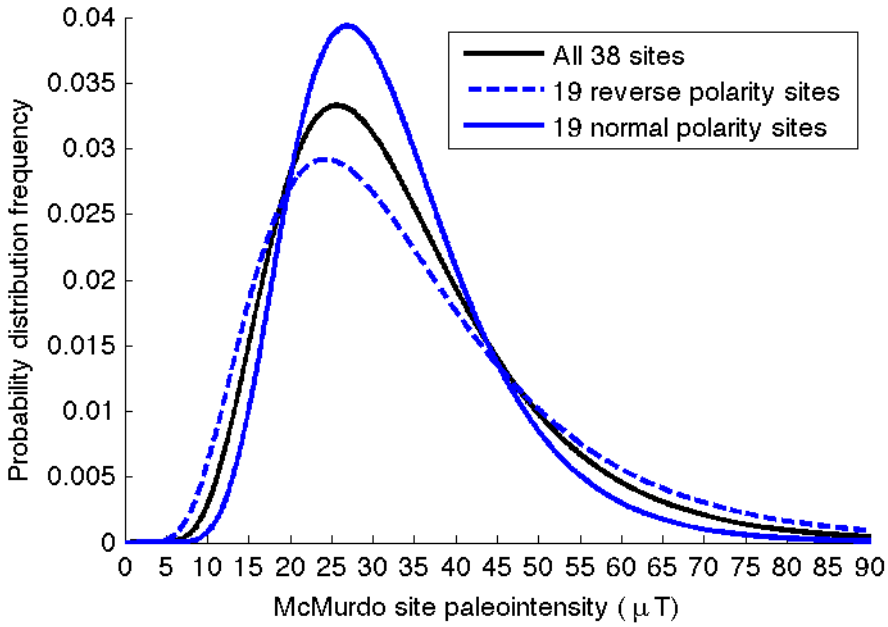
All 38 sites
19 reverse polarity sites
19 normal polarity sites
Probability distribution frequency
McMurdo site paleointensity (μ T)

Fig 3.14

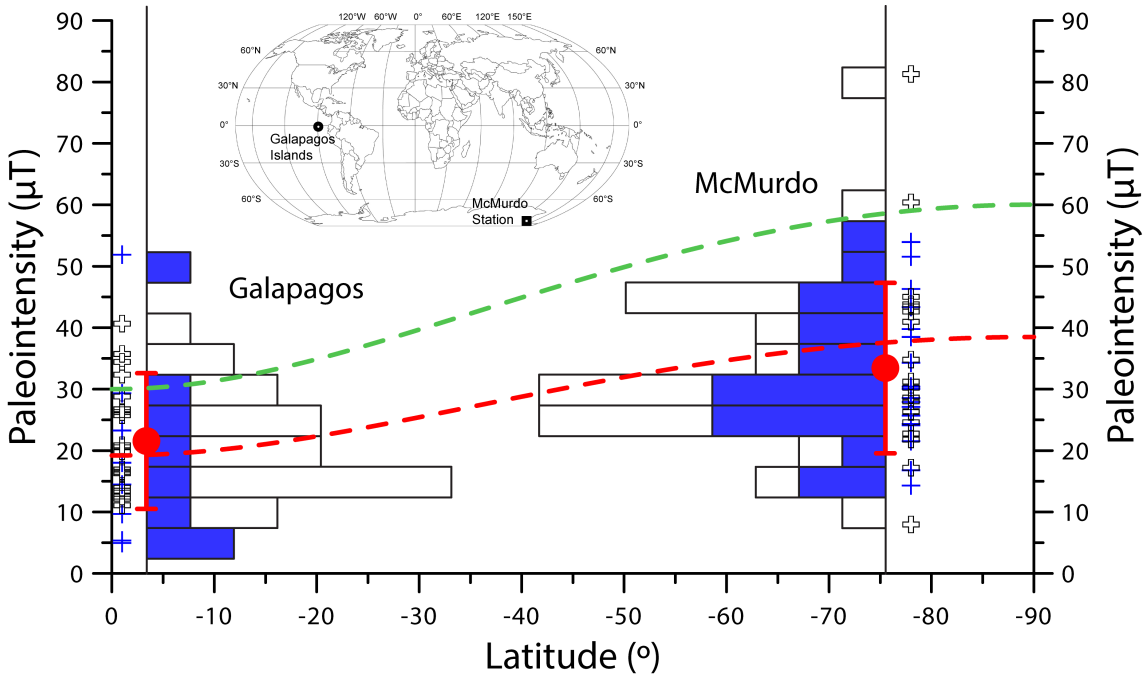
Paleointensity (µT)
Latitude (°)
Galapagos
McMurdo
Galapagos Islands
McMurdo Station
120°W 60°W 0° 60°E 120°E 150°E
60°N
30°N
0°
30°S
60°S

Table 3.S1. Rock magnetic hysteresis parameters of 156 selected samples from Galapagos collection.

Sample	Mr	Ms	Mr/Ms	Bc (T)	Bcr (T)	Bcr/Bc	Slope	Squareness
GA1.1	2.212E-06	1.070E-05	2.067E-01	1.559E-02	3.597E-02	2.308E+00	-2.372E-06	-1.130E-01
GA1.2	9.541E-06	3.207E-05	2.975E-01	2.214E-02	4.457E-02	2.013E+00	-4.832E-06	6.494E-02
GA1.3	2.271E-06	9.159E-06	2.480E-01	2.123E-02	4.150E-02	1.955E+00	-2.241E-06	8.250E-02
GA2.3	1.422E-05	7.109E-05	2.000E-01	1.804E-02	4.033E-02	2.236E+00	-7.033E-06	-6.620E-02
GA2.4	7.336E-06	3.555E-05	2.064E-01	1.881E-02	4.778E-02	2.540E+00	-4.949E-06	4.480E-02
GA2.7	1.833E-05	7.487E-05	2.448E-01	2.081E-02	4.033E-02	1.938E+00	-7.891E-06	6.659E-02
GA3.2	4.679E-06	1.694E-05	2.762E-01	1.874E-02	3.276E-02	1.748E+00	-5.597E-06	-2.546E-02
GA3.3	1.517E-05	5.902E-05	2.570E-01	1.660E-02	3.273E-02	1.971E+00	-5.886E-06	4.291E-02
GA3.7	5.225E-06	1.521E-05	3.434E-01	2.548E-02	4.451E-02	1.747E+00	-7.329E-06	-5.253E-02
GA5.1	9.488E-06	3.184E-05	2.980E-01	2.779E-02	5.336E-02	1.920E+00	-5.034E-06	6.340E-02
GA5.3	9.046E-06	3.442E-05	2.628E-01	2.590E-02	5.237E-02	2.022E+00	-7.954E-06	4.249E-02
GA5.7	4.420E-06	2.185E-05	2.023E-01	1.972E-02	3.868E-02	1.961E+00	-4.934E-06	-2.618E-02
GA6.1	9.004E-06	4.029E-05	2.235E-01	2.508E-02	5.503E-02	2.194E+00	-8.693E-06	4.476E-02
GA6.2	1.124E-05	5.035E-05	2.232E-01	1.951E-02	3.774E-02	1.934E+00	-6.670E-06	8.836E-02
GA6.5	4.756E-06	2.396E-05	1.985E-01	2.175E-02	5.300E-02	2.437E+00	-4.460E-06	-6.302E-02
GA9.1	9.672E-06	3.116E-05	3.104E-01	1.984E-02	3.865E-02	1.948E+00	-4.208E-06	-1.197E-02
GA9.2	1.065E-05	3.070E-05	3.469E-01	1.925E-02	3.372E-02	1.751E+00	-3.896E-06	9.578E-02
GA9.3	1.510E-05	5.068E-05	2.979E-01	2.195E-02	4.061E-02	1.850E+00	-7.108E-06	9.578E-02
GA10.1	2.872E-06	9.530E-06	3.013E-01	2.191E-02	4.260E-02	1.944E+00	-4.484E-06	-1.582E-01
GA10.4	3.466E-06	1.550E-05	2.236E-01	9.410E-03	2.019E-02	2.146E+00	-1.047E-05	-8.977E-02
GA10.6	7.272E-06	2.445E-05	2.975E-01	2.478E-02	4.231E-02	1.707E+00	-8.988E-06	3.132E-02
GA11.1	1.944E-06	1.118E-05	1.739E-01	6.778E-03	1.638E-02	2.417E+00	-6.678E-06	-3.683E-02
GA11.2	2.118E-06	1.196E-05	1.771E-01	6.402E-03	1.511E-02	2.361E+00	-1.061E-05	6.934E-03
GA11.8	3.380E-06	9.894E-06	3.416E-01	3.230E-02	5.214E-02	1.614E+00	-5.248E-06	4.134E-02
GA12.2	6.878E-06	3.298E-05	2.085E-01	2.148E-02	4.442E-02	2.068E+00	-7.220E-06	-1.990E-02
GA12.3	6.775E-06	2.773E-05	2.443E-01	2.480E-02	4.956E-02	1.999E+00	-4.522E-06	7.483E-02
GA12.4	6.322E-06	2.053E-05	3.079E-01	3.182E-02	4.951E-02	1.556E+00	-5.010E-06	1.526E-01
GA15.1	6.987E-06	3.314E-05	2.108E-01	1.887E-02	4.227E-02	2.240E+00	-6.678E-06	-1.035E-01
GA15.4	2.623E-06	1.688E-05	1.554E-01	4.348E-03	9.322E-03	2.144E+00	-5.951E-06	1.157E-02
GA15.6	2.232E-06	1.429E-05	1.561E-01	4.975E-03	1.135E-02	2.281E+00	-3.876E-06	-6.014E-02
GA18.5	8.680E-06	5.884E-05	1.475E-01	1.003E-02	2.459E-02	2.452E+00	-5.085E-06	-1.766E-01
GA18.7	5.121E-06	4.445E-05	1.152E-01	9.470E-03	2.593E-02	2.738E+00	-4.002E-06	3.497E-02
GA19.1	3.848E-06	4.177E-05	9.213E-02	4.047E-03	1.057E-02	2.611E+00	-4.289E-06	1.968E-02
GA19.4	8.663E-06	5.554E-05	1.560E-01	1.356E-02	2.971E-02	2.191E+00	-5.479E-06	4.510E-02
GA19.9	6.495E-06	5.321E-05	1.221E-01	3.577E-03	1.071E-02	2.993E+00	-6.607E-06	-1.258E-01
GA20.2	3.110E-06	2.076E-05	1.498E-01	4.448E-03	1.416E-02	3.184E+00	-3.592E-06	-1.347E-01
GA20.7	1.006E-05	8.482E-05	1.186E-01	9.766E-03	2.745E-02	2.811E+00	-7.525E-06	3.314E-02
GA21.3	1.207E-05	1.117E-04	1.081E-01	1.185E-02	3.472E-02	2.929E+00	-8.487E-06	4.677E-02
GA21.4	7.002E-07	2.917E-06	2.400E-01	5.258E-03	6.215E-02	1.182E+01	-1.439E-06	-1.264E-01
GA21.6	1.514E-05	9.928E-05	1.525E-01	9.328E-03	2.777E-02	2.977E+00	-7.329E-06	-2.630E-01
GA22.1	7.709E-06	2.761E-05	2.793E-01	2.102E-02	4.024E-02	1.915E+00	-3.940E-06	-1.110E-01
GA22.3	6.297E-06	4.947E-05	1.273E-01	9.339E-03	2.534E-02	2.714E+00	-4.649E-06	-1.552E-01
GA22.5	3.570E-05	1.976E-04	1.807E-01	1.530E-02	3.244E-02	2.120E+00	-7.888E-06	6.104E-02
GA23.1	4.845E-06	3.147E-05	1.540E-01	8.554E-03	2.531E-02	2.959E+00	-3.182E-06	-2.314E-01
GA23.2	1.282E-05	6.506E-05	1.970E-01	1.240E-02	2.676E-02	2.158E+00	-9.194E-06	-2.378E-02
GA23.3	8.361E-06	4.693E-05	1.782E-01	1.025E-02	2.361E-02	2.303E+00	-6.370E-06	2.711E-02
GA24.4	9.431E-06	3.651E-05	2.583E-01	1.734E-02	3.053E-02	1.760E+00	-7.913E-06	-1.420E-02
GA24.7	4.000E-06	2.173E-05	1.841E-01	1.015E-02	2.329E-02	2.294E+00	-2.997E-06	-2.215E-01
GA25.1	9.023E-07	4.585E-06	1.968E-01	6.783E-03	1.847E-02	2.723E+00	-5.201E-06	-4.220E-01
GA25.2	1.568E-06	7.631E-06	2.055E-01	9.268E-03	2.095E-02	2.261E+00	-6.032E-06	-8.069E-02
GA25.3	1.034E-06	5.345E-06	1.934E-01	6.684E-03	1.479E-02	2.212E+00	-6.953E-06	-5.276E-02
GA26.1	1.438E-05	5.706E-05	2.521E-01	1.568E-02	3.202E-02	2.042E+00	-6.948E-06	4.443E-02
GA26.2	7.818E-06	5.086E-05	1.537E-01	1.086E-02	2.440E-02	2.247E+00	-6.824E-06	3.428E-02

GA26.5	8.783E-06	3.633E-05	2.417E-01	1.872E-02	4.066E-02	2.172E+00	-4.900E-06	-5.400E-02
GA27.1	1.457E-06	5.958E-06	2.445E-01	1.325E-02	3.084E-02	2.328E+00	-2.758E-06	-2.578E-01
GA27.3	6.655E-06	2.956E-05	2.251E-01	2.710E-02	5.023E-02	1.854E+00	-6.999E-06	1.067E-01
GA27.4	2.765E-06	1.141E-05	2.423E-01	1.386E-02	2.998E-02	2.163E+00	-4.916E-06	-1.195E-01
GA28.1	1.021E-05	5.116E-05	1.996E-01	1.731E-02	3.012E-02	1.740E+00	-5.727E-06	9.239E-02
GA28.2	6.117E-06	3.041E-05	2.012E-01	1.019E-02	3.327E-02	3.264E+00	-6.414E-06	-1.829E-01
GA28.3	1.842E-06	1.420E-05	1.297E-01	2.665E-03	1.097E-02	4.116E+00	-5.275E-06	3.697E-01
GA29.2	9.723E-06	4.884E-05	1.991E-01	1.377E-02	2.854E-02	2.073E+00	-6.256E-06	6.145E-02
GA29.3	3.117E-06	2.268E-05	1.374E-01	1.033E-02	3.020E-02	2.925E+00	-3.305E-06	-2.099E-01
GA29.4	5.753E-06	3.755E-05	1.532E-01	1.191E-02	3.016E-02	2.531E+00	-4.447E-06	3.968E-02
GA30.2	1.321E-05	6.252E-05	2.113E-01	1.485E-02	3.066E-02	2.065E+00	-5.943E-06	2.956E-02
GA30.6	7.510E-06	6.337E-05	1.185E-01	9.741E-03	2.817E-02	2.891E+00	-6.206E-06	-1.905E-01
GA31.1	1.243E-05	6.884E-05	1.805E-01	1.646E-02	3.854E-02	2.341E+00	-8.735E-06	-1.142E-01
GA31.2	1.080E-05	4.685E-05	2.305E-01	2.457E-02	4.533E-02	1.845E+00	-8.751E-06	1.077E-01
GA31.3	1.218E-05	5.467E-05	2.227E-01	2.348E-02	4.816E-02	2.051E+00	-6.136E-06	6.942E-02
GA33.1	1.451E-06	6.366E-06	2.280E-01	7.723E-03	2.000E-02	2.589E+00	-3.922E-06	-3.436E-01
GA33.2	2.118E-06	1.163E-05	1.821E-01	6.216E-03	1.333E-02	2.144E+00	-6.629E-06	3.736E-02
GA33.3	3.220E-06	2.287E-05	1.408E-01	5.468E-03	1.376E-02	2.517E+00	-9.718E-06	-2.801E-02
GA34.1	1.752E-06	1.305E-05	1.342E-01	4.671E-03	1.184E-02	2.534E+00	-9.419E-06	-2.546E-02
GA34.2	6.935E-07	4.847E-06	1.431E-01	3.340E-03	1.040E-02	3.113E+00	-4.174E-06	-1.472E-01
GA34.4	2.068E-06	1.677E-05	1.233E-01	4.724E-03	1.286E-02	2.721E+00	-1.082E-05	4.129E-03
GA35.1	1.687E-06	6.586E-06	2.562E-01	5.121E-03	9.274E-03	1.811E+00	-1.075E-05	-7.479E-02
GA35.2	2.197E-06	9.793E-06	2.243E-01	5.605E-03	1.076E-02	1.919E+00	-1.139E-05	-7.005E-02
GA35.5	9.579E-07	6.301E-06	1.520E-01	3.459E-03	1.058E-02	3.058E+00	-5.098E-06	-1.607E-01
GA38.2	4.114E-06	1.942E-05	2.119E-01	9.345E-03	2.130E-02	2.280E+00	-8.889E-06	-1.291E-01
GA38.3	6.402E-07	3.953E-06	1.619E-01	3.679E-03	1.128E-02	3.065E+00	-5.291E-06	-4.383E-02
GA38.6	7.775E-07	4.422E-06	1.758E-01	3.528E-03	1.235E-02	3.501E+00	-5.365E-06	-6.442E-03
GA39.1	2.545E-06	1.012E-05	2.515E-01	1.390E-02	3.123E-02	2.246E+00	-6.459E-06	-1.155E-01
GA39.2	1.456E-06	9.182E-06	1.585E-01	6.477E-03	1.618E-02	2.498E+00	-5.307E-06	-4.311E-02
GA39.5	1.770E-06	6.710E-06	2.639E-01	1.398E-02	3.617E-02	2.587E+00	-3.235E-06	-3.925E-01
GA40.1	8.159E-06	2.388E-05	3.416E-01	2.922E-02	5.314E-02	1.819E+00	-7.007E-06	-1.435E-01
GA40.2	8.509E-06	2.582E-05	3.295E-01	2.812E-02	4.980E-02	1.771E+00	-1.077E-05	2.237E-02
GA40.4	6.587E-06	2.688E-05	2.451E-01	2.508E-02	4.221E-02	1.683E+00	-6.693E-06	1.039E-01
GA41.4	1.633E-06	5.732E-06	2.849E-01	1.013E-02	2.525E-02	2.492E+00	-3.934E-06	-4.631E-01
GA44.1	2.217E-06	1.671E-05	1.326E-01	3.632E-03	8.352E-03	2.300E+00	-9.435E-06	-1.076E-02
GA44.3	2.218E-06	1.259E-05	1.762E-01	7.310E-03	1.889E-02	2.585E+00	-4.792E-06	-9.049E-02
GA44.4	4.388E-06	1.607E-05	2.731E-01	1.766E-02	3.982E-02	2.255E+00	-4.931E-06	-2.550E-01
GA45.1	1.244E-06	8.396E-06	1.481E-01	5.450E-03	1.280E-02	2.349E+00	-4.807E-06	-1.333E-02
GA45.2	1.023E-06	4.651E-06	2.199E-01	3.620E-03	9.258E-03	2.558E+00	-7.668E-06	-1.563E-01
GA45.3	1.321E-06	5.730E-06	2.305E-01	4.754E-03	8.642E-03	1.818E+00	-8.085E-06	-3.549E-02
GA47.1	2.394E-06	8.651E-06	2.767E-01	9.806E-03	2.003E-02	2.042E+00	-3.276E-06	-2.303E-01
GA47.4	4.220E-06	1.245E-05	3.391E-01	2.215E-02	4.764E-02	2.151E+00	-4.116E-06	-2.094E-01
GA47.5	1.181E-06	4.860E-06	2.430E-01	8.313E-03	1.653E-02	1.988E+00	-4.989E-06	-1.599E-02
GA48.2	9.069E-07	4.407E-06	2.058E-01	6.912E-03	1.473E-02	2.131E+00	-2.937E-06	-1.457E-03
GA48.3	1.802E-06	6.010E-06	2.999E-01	1.299E-02	2.649E-02	2.040E+00	-4.352E-06	-1.437E-01
GA48.7	1.109E-06	4.652E-06	2.383E-01	7.895E-03	1.866E-02	2.363E+00	-3.683E-06	-3.140E-01
GA48.8	2.320E-06	7.696E-06	3.015E-01	1.178E-02	2.565E-02	2.178E+00	-4.287E-06	-3.321E-01
GA49.1	6.261E-07	2.173E-06	2.881E-01	4.770E-03	9.265E-03	1.942E+00	-6.589E-06	-1.268E-01
GA49.2	3.975E-07	1.696E-06	2.343E-01	4.277E-03	9.831E-03	2.299E+00	-4.414E-06	-1.804E-02
GA49.8	8.521E-07	3.506E-06	2.430E-01	6.315E-03	1.528E-02	2.419E+00	-4.570E-06	-3.012E-01
GA50.1	6.472E-06	2.211E-05	2.928E-01	1.855E-02	3.856E-02	2.079E+00	-6.698E-06	-1.523E-01
GA50.2	9.011E-06	3.476E-05	2.592E-01	1.967E-02	3.443E-02	1.750E+00	-6.895E-06	2.634E-02
GA50.7	2.972E-06	1.400E-05	2.123E-01	7.196E-03	2.317E-02	3.220E+00	-7.679E-06	-5.240E-01
GA51.5	5.199E-06	3.547E-05	1.466E-01	8.530E-03	2.387E-02	2.799E+00	-5.936E-06	-1.885E-01
GA53.2	7.847E-06	3.237E-05	2.424E-01	1.401E-02	3.445E-02	2.460E+00	-6.446E-06	-1.926E-01
GA55.2	1.466E-05	3.810E-05	3.847E-01	2.185E-02	3.350E-02	1.533E+00	-1.013E-05	-5.949E-02
GA56.3	2.078E-05	6.764E-05	3.072E-01	2.353E-02	4.977E-02	2.115E+00	-1.746E-05	-7.783E-02
GA58.1	2.498E-06	1.309E-05	1.907E-01	7.609E-03	1.691E-02	2.222E+00	-9.196E-06	-4.063E-02

GA58.2	5.412E-06	2.093E-05	2.586E-01	1.414E-02	2.966E-02	2.098E+00	-9.082E-06	-2.322E-01
GA58.8	5.182E-07	2.600E-06	1.993E-01	3.604E-03	1.048E-02	2.908E+00	-3.830E-06	-1.446E-01
GA59.3	2.827E-06	1.101E-05	2.569E-01	1.534E-02	3.044E-02	1.985E+00	-6.312E-06	-1.173E-01
GA59.5	5.002E-06	1.873E-05	2.671E-01	1.421E-02	2.974E-02	2.092E+00	-4.910E-06	-8.330E-02
GA59.6	7.049E-06	2.033E-05	3.467E-01	2.434E-02	4.745E-02	1.949E+00	-6.566E-06	-1.829E-01
GA60.2	6.167E-06	3.176E-05	1.942E-01	1.471E-02	3.324E-02	2.260E+00	-4.326E-06	7.372E-03
GA60.3	7.263E-06	2.541E-05	2.858E-01	2.245E-02	4.248E-02	1.892E+00	-3.604E-06	1.213E-01
GA60.4	6.592E-06	3.469E-05	1.900E-01	1.301E-02	3.255E-02	2.502E+00	-4.836E-06	-1.276E-01
GA63.2	1.108E-05	6.369E-05	1.739E-01	9.609E-03	2.238E-02	2.329E+00	-7.552E-06	1.927E-02
GA63.3	1.175E-05	4.897E-05	2.399E-01	1.029E-02	2.366E-02	2.298E+00	-8.747E-06	-1.067E-01
GA63.5	1.392E-05	5.458E-05	2.550E-01	1.283E-02	3.038E-02	2.368E+00	-9.275E-06	-2.442E-01
GA64.1	5.660E-06	2.973E-05	1.903E-01	1.645E-02	3.583E-02	2.178E+00	-4.118E-06	-1.082E-01
GA64.2	2.923E-06	1.919E-05	1.523E-01	1.084E-02	2.305E-02	2.125E+00	-2.573E-06	6.129E-02
GA64.3	1.277E-05	6.529E-05	1.956E-01	1.507E-02	3.013E-02	1.999E+00	-9.081E-06	3.526E-02
GA65.1	2.425E-06	1.073E-05	2.260E-01	1.089E-02	2.289E-02	2.103E+00	-6.794E-06	-1.080E-01
GA65.2	1.075E-06	4.970E-06	2.162E-01	7.182E-03	1.790E-02	2.492E+00	-5.357E-06	-3.378E-01
GA65.3	7.590E-06	3.038E-05	2.498E-01	1.457E-02	2.754E-02	1.891E+00	-8.940E-06	-1.202E-02
GA66.1	7.752E-06	3.109E-05	2.493E-01	1.477E-02	3.349E-02	2.267E+00	-7.433E-06	-1.180E-01
GA66.2	4.037E-06	1.751E-05	2.306E-01	2.092E-02	4.130E-02	1.974E+00	-3.441E-06	4.095E-02
GA66.3	9.859E-06	3.734E-05	2.641E-01	1.661E-02	3.621E-02	2.180E+00	-8.448E-06	-2.130E-01
GA67.1	8.123E-06	4.010E-05	2.026E-01	1.524E-02	3.448E-02	2.263E+00	-7.650E-06	-1.154E-01
GA67.2	6.513E-06	1.901E-05	3.426E-01	1.845E-02	3.484E-02	1.889E+00	-2.360E-06	1.790E-02
GA67.3	1.007E-05	2.763E-05	3.644E-01	2.724E-02	4.995E-02	1.834E+00	-4.813E-06	5.638E-02
GA69.1	2.426E-06	8.463E-06	2.867E-01	1.163E-02	3.901E-02	3.356E+00	-2.449E-06	-7.137E-01
GA69.2	4.876E-06	1.717E-05	2.840E-01	1.502E-02	3.156E-02	2.102E+00	-5.837E-06	-1.504E-01
GA70.1	3.623E-06	7.582E-06	4.779E-01	1.676E-02	2.275E-02	1.357E+00	-4.467E-06	7.836E-02
GA70.2	3.319E-06	7.142E-06	4.648E-01	1.559E-02	2.161E-02	1.386E+00	-4.142E-06	1.208E-01
GA70.6	1.893E-06	4.344E-06	4.357E-01	1.534E-02	2.474E-02	1.612E+00	-2.860E-06	8.554E-03
GA71.1	4.245E-06	1.228E-05	3.456E-01	1.965E-02	3.554E-02	1.809E+00	-3.716E-06	2.083E-02
GA71.3	5.038E-06	1.793E-05	2.810E-01	9.866E-03	1.863E-02	1.888E+00	-5.547E-06	-7.557E-02
GA71.5	9.613E-06	2.630E-05	3.655E-01	2.224E-02	3.681E-02	1.655E+00	-6.042E-06	2.247E-02
GA72.1	1.855E-06	7.113E-06	2.607E-01	8.507E-03	1.539E-02	1.809E+00	-3.718E-06	7.808E-03
GA72.3	2.455E-06	1.112E-05	2.208E-01	6.433E-03	1.237E-02	1.923E+00	-7.170E-06	3.303E-02
GA72.5	7.898E-07	2.317E-06	3.409E-01	6.634E-03	1.218E-02	1.836E+00	-7.174E-06	-3.530E-01
GA72.7	7.315E-07	2.462E-06	2.971E-01	5.255E-03	1.183E-02	2.251E+00	-3.804E-06	-2.697E-01
GA74.1	1.352E-06	5.605E-06	2.412E-01	8.264E-03	1.569E-02	1.899E+00	-5.174E-06	4.777E-02
GA74.2	7.032E-07	3.124E-06	2.251E-01	6.851E-03	1.288E-02	1.879E+00	-3.291E-06	2.146E-02
GA74.3	6.322E-07	2.523E-06	2.506E-01	4.900E-03	1.290E-02	2.633E+00	-4.877E-06	-2.114E-01
GA75.6	7.811E-07	2.670E-06	2.926E-01	1.065E-02	2.326E-02	2.185E+00	-2.389E-06	-3.224E-01
GA76.3	3.356E-06	1.016E-05	3.302E-01	1.370E-02	6.145E-02	4.486E+00	-4.368E-06	-1.157E+00
GA82.1	7.896E-06	3.145E-05	2.511E-01	1.830E-02	3.355E-02	1.833E+00	-5.230E-06	8.197E-03
GA82.4	2.269E-05	9.008E-05	2.518E-01	1.750E-02	3.424E-02	1.957E+00	-1.089E-05	8.023E-02
GA83.1	5.934E-06	3.443E-05	1.723E-01	1.509E-02	3.348E-02	2.218E+00	-5.860E-06	3.885E-02
GA83.2	7.720E-06	2.718E-05	2.840E-01	1.859E-02	3.578E-02	1.925E+00	-4.386E-06	5.643E-02
GA83.3	6.002E-06	3.935E-05	1.525E-01	1.134E-02	2.902E-02	2.559E+00	-5.366E-06	-1.603E-01

Table 3.S2. Rock magnetic hysteresis parameters before and after heating up to 650°C of 51 selected samples from Galapagos collection.

Sample	Mr/Ms	Bcr/Bc	Mr/Ms-Heated	Bcr/Bc-Heated	MrMs-heated/MrMs	Mr-heated/Mr	Ms-heated/Ms	Bc-heated/Bc	Bcr-heated/Bcr
GA1.1	0.207	2.308	0.188	2.150	0.911	0.807	0.886	0.987	0.920
GA2.3	0.200	2.236	0.265	1.755	1.325	1.156	0.873	1.371	1.076
GA3.7	0.343	1.747	0.440	1.443	1.281	1.260	0.983	1.719	1.419
GA5.7	0.202	1.961	0.199	1.802	0.985	1.000	1.016	1.047	0.962
GA6.5	0.199	2.437	0.202	2.150	1.017	1.025	1.008	0.985	0.869
GA9.1	0.310	1.948	0.286	1.921	0.923	0.950	1.030	0.930	0.917
GA10.1	0.301	1.944	0.374	1.556	1.242	1.253	1.009	1.653	1.322
GA11.8	0.342	1.614	0.372	1.458	1.089	0.994	0.913	1.148	1.037
GA12.2	0.209	2.068	0.217	1.881	1.041	0.981	0.942	1.118	1.016
GA15.1	0.211	2.240	0.209	1.967	0.991	0.967	0.976	1.162	1.020
GA18.5	0.148	2.452	0.146	2.085	0.991	0.862	0.870	1.126	0.958
GA19.9	0.122	2.993	0.176	2.426	1.439	1.433	0.996	1.894	1.535
GA20.2	0.150	3.184	0.237	2.733	1.582	1.457	0.921	2.068	1.776
GA21.6	0.152	2.977	0.181	2.758	1.184	0.962	0.812	1.119	1.037
GA22.1	0.279	1.915	0.346	1.565	1.240	1.093	0.881	1.406	1.150
GA22.3	0.127	2.714	0.143	2.503	1.126	1.355	1.203	1.082	0.998
GA23.1	0.154	2.959	0.167	2.369	1.086	0.966	0.890	1.255	1.005
GA24.7	0.184	2.294	0.252	1.762	1.367	1.479	1.082	2.070	1.589
GA25.1	0.197	2.723	0.330	1.898	1.675	1.678	1.002	3.785	2.638
GA26.5	0.242	2.172	0.211	2.114	0.871	0.833	0.956	0.879	0.856
GA28.3	0.130	4.116	0.196	4.292	1.509	1.219	0.808	2.525	2.632
GA29.3	0.137	2.925	0.128	2.691	0.932	0.852	0.914	1.030	0.948
GA30.6	0.119	2.891	0.152	2.534	1.279	1.147	0.897	1.251	1.096
GA31.1	0.181	2.341	0.209	1.923	1.158	1.054	0.910	1.263	1.037
GA33.1	0.228	2.589	0.344	1.958	1.509	1.769	1.172	3.220	2.435
GA34.2	0.143	3.113	0.250	2.698	1.748	1.988	1.137	4.163	3.608
GA38.6	0.176	3.501	0.274	2.378	1.560	2.006	1.286	4.193	2.849
GA39.5	0.264	2.587	0.351	1.913	1.332	1.228	0.922	2.073	1.533
GA40.1	0.342	1.819	0.408	1.454	1.194	1.153	0.965	1.239	0.990
GA41.4	0.285	2.492	0.396	1.747	1.389	1.863	1.341	2.926	2.051
GA44.4	0.273	2.255	0.315	1.873	1.155	1.006	0.872	1.414	1.174
GA45.2	0.220	2.558	0.295	3.923	1.341	1.754	1.308	3.269	5.014
GA47.1	0.277	2.042	0.384	1.629	1.389	1.837	1.322	3.235	2.580
GA48.7	0.238	2.363	0.355	1.871	1.492	2.180	1.461	3.101	2.455
GA49.8	0.243	2.419	0.338	2.000	1.392	3.838	2.758	3.643	3.011
GA50.7	0.212	3.220	0.278	2.356	1.311	1.339	1.021	2.331	1.706
GA58.8	0.199	2.908	0.271	2.223	1.361	3.103	2.280	3.739	2.858
GA59.6	0.347	1.949	0.406	1.630	1.172	1.273	1.086	1.440	1.204
GA60.4	0.190	2.502	0.234	1.942	1.230	1.236	1.005	1.338	1.039
GA63.5	0.255	2.368	0.315	1.918	1.233	1.224	0.992	1.612	1.306
GA64.1	0.190	2.178	0.202	1.847	1.060	1.426	1.345	1.151	0.976
GA65.2	0.216	2.492	0.351	1.803	1.625	2.316	1.426	3.790	2.742
GA66.3	0.264	2.180	0.343	1.632	1.300	1.099	0.846	1.885	1.411
GA67.1	0.203	2.263	0.224	1.832	1.105	1.115	1.008	1.284	1.040
GA69.1	0.287	3.356	0.312	2.923	1.088	1.820	1.673	1.106	0.963
GA70.6	0.436	1.612	0.393	1.550	0.901	3.076	3.412	1.895	1.822
GA71.3	0.281	1.888	0.367	1.648	1.307	2.344	1.793	2.712	2.367
GA72.5	0.341	1.836	0.340	2.163	0.996	4.718	4.734	3.489	4.112
GA74.3	0.251	2.633	0.350	1.898	1.396	2.879	2.062	4.539	3.272
GA75.6	0.293	2.185	0.454	1.416	1.550	5.022	3.239	2.648	1.715
GA83.3	0.153	2.559	0.160	2.158	1.052	0.903	0.859	1.156	0.975

Table 3.S3. MD corrected paleointensity results of 209 selected specimens from Galapagos collection. Bold fonts represent qualified data.

Specimen	OriPint	OriPintLow	OriPintHi	Method	CorPint	CorPintLow	CorPintHi	Pint-R	tTRM-R	tTRMk	Qualified
GA01.1c	**18.8**	**17.6**	**19.9**	**ReAitken**	**22.9**	**19.6**	**26.1**	**0.980**	**0.992**	**1.042**	**Yes**
GA01.2c	**41.0**	**35.2**	**46.8**	**ReIZZI**	**51.3**	**49.7**	**53.0**	**0.999**	**0.980**	**1.027**	**Yes**
GA01.3c	40.2	36.3	44.1	ReIZZI	51.4	41.9	60.9	0.967	0.990	1.036	No
GA01.4x	**33.7**	**30.4**	**37.0**	**Lamont**	**36.0**	**33.2**	**38.8**	**0.994**	**0.987**	**1.007**	**Yes**
GA01.6x	47.8	33.1	62.5	Lamont	30.3	21.8	38.8	0.929	0.810	0.918	No
GA01.7x	**42.6**	**39.0**	**46.1**	**Lamont**	**39.4**	**37.7**	**41.0**	**0.998**	**0.994**	**0.885**	**Yes**
GA01.8x	**25.8**	**24.6**	**27.1**	**Lamont**	**29.1**	**26.7**	**31.5**	**0.993**	**0.980**	**1.105**	**Yes**
GA02.3c	**12.3**	**10.2**	**14.4**	**ReAitken**	**12.7**	**11.7**	**13.7**	**0.994**	**0.999**	**1.023**	**Yes**
GA02.4c	32.4	30.0	34.7	ReIZZI	39.9	-19.1	98.9	0.430	0.986	0.976	No
GA02.7c	**11.3**	**9.7**	**12.8**	**ReIZZI**	**12.4**	**11.2**	**13.5**	**0.991**	**0.995**	**0.990**	**Yes**
GA03.2c	27.2	25.2	29.3	ReIZZI	23.9	19.6	28.2	0.969	0.969	0.952	No
GA03.3c	**57.7**	**52.2**	**63.3**	**ReIZZI**	**54.7**	**49.7**	**59.7**	**0.992**	**0.998**	**1.095**	**Yes**
GA03.7c	21.2	13.7	28.7	ReAitken	14.2	8.0	20.4	0.849	0.963	0.849	No
GA05.1c	**59.4**	**52.4**	**66.4**	**ReIZZI**	**54.6**	**50.7**	**58.5**	**0.995**	**0.994**	**1.006**	**Yes**
GA05.3c	**61.6**	**54.7**	**68.6**	**ReIZZI**	**57.5**	**54.0**	**61.0**	**0.996**	**0.983**	**0.979**	**Yes**
GA05.7c	**53.7**	**48.8**	**58.7**	**ReAitken**	**52.3**	**47.6**	**57.0**	**0.992**	**0.995**	**1.074**	**Yes**
GA06.1c	**47.1**	**39.3**	**54.8**	**ReIZZI**	**45.5**	**42.3**	**48.8**	**0.995**	**0.998**	**0.955**	**Yes**
GA06.2c	**52.9**	**47.4**	**58.4**	**ReIZZI**	**50.2**	**47.4**	**53.1**	**0.997**	**0.995**	**1.020**	**Yes**
GA06.5c	**41.4**	**35.1**	**47.8**	**ReAitken**	**41.6**	**37.9**	**45.2**	**0.992**	**1.000**	**1.062**	**Yes**
GA09.1c	**50.3**	**47.8**	**52.7**	**ReAitken**	**49.1**	**48.3**	**50.0**	**1.000**	**0.993**	**1.105**	**Yes**
GA09.2c	**46.9**	**44.2**	**49.6**	**ReIZZI**	**51.2**	**45.6**	**56.8**	**0.988**	**0.998**	**1.023**	**Yes**
GA09.3c	47.2	43.4	51.0	ReIZZI	70.5	59.7	81.3	0.977	0.982	1.111	No
GA10.1c	12.9	10.4	15.3	ReAitken	10.4	8.2	12.5	0.959	0.987	0.927	No
GA10.2x	14.2	11.9	16.5	Lamont	13.7	11.6	15.7	0.978	0.987	0.904	No
GA10.4c	5.5	3.8	7.2	ReIZZI	5.3	4.7	6.0	0.987	0.977	0.651	No
GA10.5x	3.2	1.5	4.9	Lamont	4.5	4.0	5.1	0.985	0.947	0.545	No
GA10.6c	17.1	14.3	19.9	ReIZZI	15.9	12.6	19.1	0.960	0.987	0.909	No
GA10.7x	**15.6**	**13.5**	**17.7**	**Lamont**	**16.3**	**14.1**	**18.5**	**0.982**	**0.994**	**0.973**	**Yes**
GA11.1c	10.9	6.6	15.1	ReIZZI	12.4	9.9	14.8	0.962	0.995	0.641	No
GA11.2c	11.3	7.0	15.7	ReIZZI	11.7	9.1	14.2	0.955	0.982	0.654	No
GA12.1x	37.8	25.3	50.2	Lamont	45.0	42.2	47.8	0.996	0.914	0.916	No
GA12.2c	40.3	32.9	47.8	ReAitken	48.5	40.7	56.2	0.975	0.999	1.076	No
GA12.3c	**43.3**	**36.5**	**50.1**	**ReIZZI**	**62.1**	**57.7**	**66.5**	**0.995**	**0.999**	**0.995**	**Yes**
GA12.4c	45.1	40.2	49.9	ReIZZI	44.0	35.9	52.1	0.967	0.984	1.105	No
GA12.5x	50.6	39.1	62.1	Lamont	58.2	51.1	65.2	0.985	0.950	1.065	No
GA12.6x	14.8	9.7	19.8	Lamont	13.6	10.3	16.9	0.945	0.962	0.742	No
GA12.7x	38.5	30.6	46.4	Lamont	39.5	29.3	49.7	0.938	0.990	1.072	No
GA15.4c	5.9	4.1	7.7	ReIZZI	9.0	7.9	10.2	0.984	0.989	0.739	No
GA15.6c	7.6	5.5	9.6	ReIZZI	13.9	11.4	16.4	0.969	0.975	0.746	No
GA18.5c	**37.1**	**30.1**	**44.2**	**ReIZZI**	**46.9**	**43.8**	**50.0**	**0.996**	**0.992**	**1.101**	**Yes**
GA18.7c	**17.9**	**15.5**	**20.4**	**ReIZZI**	**22.0**	**20.8**	**23.1**	**0.997**	**0.997**	**0.938**	**Yes**
GA19.1c	6.1	3.9	8.3	ReIZZI	7.8	6.1	9.5	0.955	0.992	0.676	No
GA19.4c	**14.2**	**12.6**	**15.8**	**ReIZZI**	**18.9**	**17.8**	**20.0**	**0.997**	**0.998**	**0.969**	**Yes**
GA19.5x	12.9	10.5	15.3	Lamont	15.8	14.5	17.2	0.993	0.955	0.837	No
GA19.6x	**15.4**	**13.3**	**17.5**	**Lamont**	**19.4**	**18.4**	**20.4**	**0.997**	**0.984**	**0.931**	**Yes**
GA19.7x	**16.4**	**14.1**	**18.7**	**Lamont**	**21.3**	**20.6**	**22.0**	**0.999**	**0.991**	**0.963**	**Yes**
GA19.9c	5.0	3.0	6.9	ReAitken	6.1	4.9	7.3	0.963	0.979	0.790	No
GA20.2c	3.7	2.6	4.9	ReIZZI	3.5	2.7	4.3	0.950	0.984	0.710	No
GA20.7c	**22.7**	**20.3**	**25.1**	**ReIZZI**	**26.7**	**25.7**	**27.8**	**0.998**	**0.991**	**1.070**	**Yes**

GA21.3c	**12.9**	**10.7**	**15.0**	**ReIZZI**	**12.7**	**11.1**	**14.4**	**0.983**	**0.998**	**0.981**	**Yes**
GA21.4c	54.7	46.9	62.5	ReIZZI	51.1	44.2	58.1	0.982	0.947	1.829	No
GA21.6c	**9.1**	**7.1**	**11.1**	**ReAitken**	**9.5**	**8.7**	**10.3**	**0.993**	**0.986**	**0.894**	**Yes**
GA22.1c	9.3	7.6	10.9	ReIZZI	8.9	7.3	10.4	0.970	0.997	0.988	No
GA22.3c	**13.2**	**11.4**	**15.1**	**ReAitken**	**14.3**	**13.7**	**14.9**	**0.998**	**0.999**	**0.975**	**Yes**
GA22.5c	**10.0**	**8.3**	**11.6**	**ReIZZI**	**10.0**	**9.2**	**10.8**	**0.994**	**0.997**	**0.885**	**Yes**
GA22.6x	13.7	10.9	16.5	Lamont	17.1	14.3	19.8	0.975	0.987	0.827	No
GA23.1c	**33.6**	**30.6**	**36.5**	**ReIZZI**	**36.9**	**34.9**	**38.9**	**0.997**	**0.999**	**1.080**	**Yes**
GA23.2c	21.2	19.4	22.9	ReIZZI	18.3	15.8	20.8	0.981	0.975	0.972	No
GA23.3c	33.1	30.4	35.7	ReIZZI	34.2	33.0	35.3	0.999	0.832	0.694	No
GA23.5x	29.1	25.2	33.0	Lamont	30.9	29.5	32.2	0.998	0.969	0.986	No
GA23.6x	**26.4**	**24.3**	**28.6**	**Lamont**	**27.8**	**26.9**	**28.8**	**0.999**	**0.993**	**1.109**	**Yes**
GA23.8x	36.2	30.0	42.4	Lamont	39.9	37.7	42.1	0.997	0.978	0.953	No
GA24.3c	7.6	5.6	9.6	ReIZZI	6.6	5.8	7.4	0.986	0.968	0.739	No
GA24.4c	22.2	20.1	24.3	ReIZZI	19.1	16.8	21.5	0.985	0.974	0.906	No
GA24.5x	**21.2**	**17.7**	**24.8**	**Lamont**	**21.5**	**20.1**	**23.0**	**0.995**	**0.993**	**0.877**	**Yes**
GA24.6x	37.6	34.1	41.1	Lamont	54.2	39.1	69.3	0.929	0.988	0.956	No
GA24.7c	**27.7**	**25.3**	**30.2**	**ReAitken**	**31.0**	**30.1**	**31.9**	**0.999**	**0.999**	**1.078**	**Yes**
GA25.2c	4.7	3.0	6.5	ReIZZI	6.4	5.6	7.1	0.987	0.949	0.550	No
GA25.3c	4.6	2.5	6.6	ReIZZI	5.9	5.3	6.5	0.990	0.950	0.505	No
GA26.1c	**47.0**	**42.1**	**52.0**	**ReIZZI**	**45.1**	**43.5**	**46.7**	**0.999**	**0.981**	**1.038**	**Yes**
GA26.2c	**32.5**	**29.1**	**36.0**	**ReIZZI**	**35.8**	**33.1**	**38.6**	**0.994**	**0.996**	**1.032**	**Yes**
GA26.3x	**36.9**	**32.3**	**41.5**	**Lamont**	**40.2**	**38.0**	**42.5**	**0.997**	**0.980**	**0.885**	**Yes**
GA26.4x	**43.2**	**40.6**	**45.9**	**Lamont**	**41.5**	**39.4**	**43.5**	**0.998**	**0.983**	**0.939**	**Yes**
GA26.5c	62.7	52.8	72.7	ReAitken	100.4	83.1	117.6	0.971	0.995	1.094	No
GA26.7x	46.6	41.7	51.4	Lamont	63.6	56.7	70.6	0.988	0.966	0.917	No
GA26.8x	33.4	27.3	39.5	Lamont	31.2	26.0	36.4	0.973	0.982	0.903	No
GA27.1c	6.1	4.6	7.6	ReAitken	5.7	4.8	6.5	0.979	0.984	0.818	No
GA27.3c	20.3	16.0	24.5	ReIZZI	17.9	14.7	21.2	0.968	0.991	0.836	No
GA27.4c	6.6	4.7	8.4	ReIZZI	6.0	4.6	7.5	0.948	0.983	0.731	No
GA27.5x	**22.5**	**16.4**	**28.7**	**Lamont**	**25.8**	**22.1**	**29.4**	**0.980**	**0.994**	**0.857**	**Yes**
GA27.6x	15.8	12.1	19.4	Lamont	16.6	12.8	20.5	0.950	0.991	0.916	No
GA27.7x	6.9	4.5	9.2	Lamont	7.7	6.9	8.5	0.990	0.944	0.606	No
GA27.8x	18.8	15.8	21.9	Lamont	20.6	16.6	24.5	0.965	0.990	0.949	No
GA28.1c	**19.5**	**16.7**	**22.4**	**ReIZZI**	**20.1**	**18.8**	**21.4**	**0.996**	**0.996**	**0.983**	**Yes**
GA28.2c	14.6	11.9	17.4	ReIZZI	23.7	20.5	26.9	0.982	0.972	0.856	No
GA28.3c	9.5	6.1	12.9	ReAitken	10.8	9.2	12.5	0.977	0.956	0.716	No
GA28.4x	6.8	4.8	8.9	Lamont	12.7	10.2	15.1	0.964	0.959	0.707	No
GA28.5x	5.7	4.7	6.6	Lamont	10.3	7.3	13.2	0.937	0.965	0.716	No
GA28.7x	**19.5**	**17.0**	**22.1**	**Lamont**	**21.6**	**20.1**	**23.1**	**0.995**	**0.999**	**0.890**	**Yes**
GA29.2c	**12.5**	**11.7**	**13.3**	**ReIZZI**	**13.7**	**13.1**	**14.3**	**0.998**	**0.997**	**1.059**	**Yes**
GA29.3c	**8.8**	**8.1**	**9.5**	**ReAitken**	**9.6**	**8.5**	**10.7**	**0.987**	**0.995**	**1.070**	**Yes**
GA29.4c	**13.6**	**12.6**	**14.6**	**ReIZZI**	**15.2**	**14.6**	**15.8**	**0.998**	**0.994**	**1.022**	**Yes**
GA29.5x	**16.0**	**15.6**	**16.5**	**Lamont**	**20.1**	**17.9**	**22.3**	**0.988**	**0.997**	**1.064**	**Yes**
GA29.6x	**9.9**	**8.7**	**11.1**	**Lamont**	**11.2**	**10.1**	**12.3**	**0.990**	**0.999**	**1.037**	**Yes**
GA30.1c	**24.3**	**22.5**	**26.0**	**ReIZZI**	**24.1**	**22.9**	**25.3**	**0.997**	**0.999**	**1.038**	**Yes**
GA30.2c	**24.5**	**21.4**	**27.5**	**ReIZZI**	**26.0**	**23.7**	**28.3**	**0.992**	**0.988**	**0.996**	**Yes**
GA30.3x	**22.9**	**22.2**	**23.7**	**Lamont**	**25.2**	**23.2**	**27.1**	**0.994**	**0.995**	**1.021**	**Yes**
GA30.5x	**22.9**	**20.9**	**24.9**	**Lamont**	**25.9**	**22.3**	**29.6**	**0.980**	**0.996**	**1.000**	**Yes**
GA30.6c	**12.5**	**10.7**	**14.3**	**ReAitken**	**13.7**	**12.5**	**14.9**	**0.993**	**0.996**	**1.035**	**Yes**
GA30.8x	**22.5**	**21.3**	**23.6**	**Lamont**	**24.7**	**23.0**	**26.4**	**0.995**	**0.999**	**1.004**	**Yes**
GA31.1c	11.1	8.5	13.7	ReIZZI	11.5	8.7	14.3	0.946	0.999	1.001	No
GA31.2c	13.4	9.8	17.1	ReIZZI	14.0	10.7	17.3	0.947	0.999	1.027	No
GA31.3c	7.8	5.5	10.2	ReIZZI	8.1	5.9	10.3	0.933	1.000	1.015	No
GA33.1c	**9.7**	**7.5**	**12.0**	**ReAitken**	**9.7**	**8.6**	**10.8**	**0.987**	**0.996**	**0.896**	**Yes**

GA33.2c	5.8	3.5	8.1	ReIZZI	4.7	3.4	6.1	0.929	0.803	0.688	No
GA33.3c	4.2	2.5	5.8	ReIZZI	5.1	3.6	6.5	0.927	0.982	0.793	No
GA33.4x	19.4	14.4	24.5	Lamont	19.0	14.1	24.0	0.938	0.972	0.861	No
GA33.6x	6.9	3.5	10.3	Lamont	11.1	8.5	13.7	0.948	0.986	0.555	No
GA33.7x	9.2	6.2	12.1	Lamont	13.0	10.3	15.7	0.959	0.994	0.714	No
GA33.8x	8.7	0.8	16.5	Lamont	10.7	6.3	15.0	0.864	0.807	0.768	No
GA34.1c	4.9	2.8	6.9	ReIZZI	9.1	8.3	9.8	0.993	0.948	0.572	No
GA34.4c	5.2	3.1	7.3	ReIZZI	8.6	7.8	9.3	0.992	0.952	0.601	No
GA35.1c	3.3	1.1	5.4	ReIZZI	5.1	3.6	6.6	0.926	0.945	0.638	No
GA35.2c	6.2	3.8	8.6	ReIZZI	7.2	5.5	8.8	0.950	0.971	0.760	No
GA38.2c	6.2	3.5	8.9	ReIZZI	5.3	3.0	7.7	0.846	0.996	0.962	No
GA38.3c	4.8	2.3	7.3	ReIZZI	5.3	2.9	7.7	0.842	0.995	0.842	No
GA38.6c	8.5	2.7	14.3	ReAitken	10.0	7.3	12.6	0.933	0.954	0.693	No
GA39.1c	5.1	3.5	6.7	ReIZZI	4.6	3.0	6.2	0.893	0.993	0.905	No
GA39.2c	2.4	1.2	3.7	ReIZZI	3.0	2.1	4.0	0.910	0.946	0.693	No
GA40.1c	9.2	6.8	11.6	ReAitken	11.1	7.2	15.0	0.894	0.989	0.997	No
GA40.2c	7.1	4.4	9.9	ReIZZI	8.3	5.1	11.4	0.881	0.990	0.883	No
GA40.4c	**16.8**	**14.5**	**19.1**	**ReIZZI**	**18.0**	**15.8**	**20.2**	**0.985**	**0.996**	**1.118**	**Yes**
GA40.6x	9.3	6.5	12.1	Lamont	10.5	7.7	13.4	0.933	0.996	0.826	No
GA40.7x	4.6	2.4	6.7	Lamont	4.7	3.1	6.2	0.908	0.988	0.651	No
GA40.8x	12.2	9.4	15.0	Lamont	12.2	8.9	15.4	0.933	0.994	1.088	No
GA44.1c	7.1	3.8	10.4	ReIZZI	7.8	4.3	11.2	0.844	0.959	0.752	No
GA44.3c	7.8	5.3	10.3	ReIZZI	8.1	5.3	10.8	0.902	0.989	0.815	No
GA44.4c	16.6	14.1	19.1	ReAitken	16.9	12.3	21.4	0.934	0.988	0.985	No
GA45.1c	5.6	3.2	8.1	ReIZZI	7.6	6.3	8.8	0.972	0.977	0.595	No
GA45.3c	4.1	1.8	6.5	ReIZZI	6.5	5.2	7.8	0.962	0.988	0.574	No
GA47.1c	35.9	18.3	53.4	ReIZZI	30.1	18.1	42.1	0.869	0.847	0.726	No
GA47.4c	13.4	8.7	18.1	ReIZZI	9.9	5.6	14.1	0.853	0.906	0.893	No
GA47.5c	7.0	4.6	9.5	ReIZZI	4.4	2.5	6.4	0.849	0.822	0.802	No
GA48.2c	4.3	2.4	6.2	ReIZZI	2.7	1.3	4.2	0.791	0.761	0.746	No
GA48.3c	8.2	6.2	10.2	ReIZZI	5.7	4.0	7.3	0.921	0.876	0.901	No
GA48.7c	4.3	2.6	6.1	ReAitken	2.5	1.2	3.8	0.803	0.934	0.741	No
GA49.1c	3.8	-15.9	23.4	ReIZZI	9.8	4.3	15.2	0.784	0.459	0.603	No
GA49.2c	5.5	3.1	8.0	ReIZZI	5.5	3.8	7.2	0.915	0.958	0.786	No
GA49.8c	12.6	8.8	16.4	ReAitken	7.3	5.1	9.5	0.918	0.920	0.777	No
GA50.1c	16.9	12.7	21.1	ReIZZI	19.8	14.9	24.7	0.944	0.995	0.987	No
GA50.2c	**32.2**	**28.0**	**36.4**	**ReIZZI**	**29.3**	**26.2**	**32.4**	**0.989**	**0.998**	**1.090**	**Yes**
GA50.3x	10.6	5.8	15.5	Lamont	15.2	12.9	17.5	0.978	0.997	0.597	No
GA50.4x	15.9	10.5	21.3	Lamont	22.8	19.0	26.7	0.973	0.994	0.651	No
GA50.7c	6.3	3.1	9.5	ReAitken	8.3	6.6	10.1	0.958	0.968	0.871	No
GA58.1c	5.9	2.9	8.8	ReIZZI	5.0	2.6	7.5	0.824	0.964	0.801	No
GA58.2c	7.6	3.9	11.3	ReIZZI	5.8	3.1	8.4	0.840	0.888	0.717	No
GA59.3c	5.3	2.8	7.8	ReIZZI	1.1	-2.5	4.7	0.205	0.680	0.477	No
GA59.5c	9.9	7.1	12.7	ReIZZI	9.3	6.1	12.4	0.900	0.997	1.104	No
GA59.6c	8.6	5.5	11.8	ReAitken	6.3	3.5	9.1	0.844	0.972	0.871	No
GA60.2c	6.0	5.4	6.6	ReIZZI	7.2	6.9	7.4	0.999	0.995	1.224	No
GA60.3c	26.0	23.8	28.3	ReIZZI	26.1	19.9	32.4	0.947	0.992	1.444	No
GA60.4c	**5.8**	**5.1**	**6.6**	**ReAitken**	**6.5**	**5.8**	**7.2**	**0.989**	**0.999**	**1.007**	**Yes**
GA60.5x	35.3	33.3	37.3	Lamont	60.4	34.5	86.3	0.854	0.997	1.081	No

GA60.6x	2.4	1.5	3.2	Lamont	2.2	1.5	2.8	0.919	0.992	0.730	No
GA60.7x	**3.8**	**3.4**	**4.3**	**Lamont**	**4.2**	**3.8**	**4.6**	**0.992**	**0.994**	**0.930**	**Yes**
GA63.2c	6.6	5.2	8.1	ReIZZI	5.7	4.4	7.0	0.951	0.985	0.851	No
GA63.3c	11.2	9.4	13.1	ReIZZI	8.9	7.0	10.8	0.957	0.953	0.930	No
GA63.4x	8.6	7.8	9.5	Lamont	5.7	5.1	6.3	0.989	0.869	0.784	No
GA63.5c	**15.1**	**13.5**	**16.6**	**ReAitken**	**13.1**	**11.4**	**14.7**	**0.984**	**0.985**	**0.918**	**Yes**
GA63.6x	15.4	13.2	17.6	Lamont	13.9	12.2	15.7	0.984	0.914	0.723	No
GA63.7x	**19.0**	**15.9**	**22.0**	**Lamont**	**20.0**	**18.3**	**21.8**	**0.992**	**0.997**	**1.072**	**Yes**
GA63.8x	10.5	9.5	11.5	Lamont	9.5	8.5	10.6	0.988	0.958	0.866	No
GA64.1c	**20.8**	**18.6**	**22.9**	**ReAitken**	**23.3**	**22.5**	**24.1**	**0.999**	**0.998**	**1.114**	**Yes**
GA64.2c	21.4	18.6	24.3	ReIZZI	22.9	21.2	24.7	0.994	0.996	1.238	No
GA64.3c	12.2	11.0	13.4	ReIZZI	14.3	13.4	15.2	0.996	0.997	1.163	No
GA64.4x	**20.2**	**17.1**	**23.4**	**Lamont**	**22.5**	**21.5**	**23.6**	**0.998**	**0.987**	**1.035**	**Yes**
GA64.5x	**14.9**	**11.6**	**18.2**	**Lamont**	**14.2**	**12.3**	**16.2**	**0.982**	**0.992**	**0.919**	**Yes**
GA64.6x	**18.2**	**16.2**	**20.3**	**Lamont**	**21.3**	**19.7**	**23.0**	**0.994**	**0.981**	**1.072**	**Yes**
GA64.7x	**22.5**	**19.7**	**25.3**	**Lamont**	**21.3**	**18.9**	**23.6**	**0.988**	**0.999**	**0.952**	**Yes**
GA65.1c	6.5	4.3	8.6	ReIZZI	6.3	4.8	7.8	0.945	0.990	0.850	No
GA65.2c	6.0	1.6	10.5	ReAitken	7.0	5.2	8.9	0.936	0.912	0.697	No
GA65.3c	**13.5**	**11.5**	**15.4**	**ReIZZI**	**13.5**	**12.3**	**14.6**	**0.992**	**0.998**	**1.041**	**Yes**
GA65.4x	6.0	4.0	8.1	Lamont	5.2	4.9	5.6	0.996	0.850	0.593	No
GA65.5x	11.0	6.0	16.0	Lamont	9.6	6.2	13.0	0.894	0.862	0.623	No
GA65.7x	8.0	4.5	11.5	Lamont	10.3	8.3	12.4	0.963	0.967	0.638	No
GA65.8x	6.8	4.1	9.6	Lamont	5.5	5.0	6.0	0.992	0.778	0.565	No
GA66.1c	**14.7**	**13.3**	**16.1**	**ReIZZI**	**13.3**	**12.0**	**14.6**	**0.990**	**0.994**	**1.008**	**Yes**
GA66.2c	**18.6**	**15.3**	**21.9**	**ReIZZI**	**18.4**	**15.8**	**21.1**	**0.980**	**0.999**	**1.107**	**Yes**
GA66.3c	**14.7**	**13.3**	**16.2**	**ReAitken**	**14.5**	**12.8**	**16.3**	**0.986**	**0.989**	**1.032**	**Yes**
GA66.4x	**17.3**	**14.3**	**20.4**	**Lamont**	**19.0**	**16.9**	**21.0**	**0.988**	**0.996**	**1.036**	**Yes**
GA66.7x	**15.6**	**14.0**	**17.1**	**Lamont**	**19.3**	**18.2**	**20.4**	**0.997**	**0.984**	**0.953**	**Yes**
GA66.8x	**13.1**	**11.8**	**14.4**	**Lamont**	**17.0**	**15.9**	**18.0**	**0.996**	**0.985**	**0.968**	**Yes**
GA67.1c	**22.3**	**20.4**	**24.2**	**ReAitken**	**26.1**	**23.3**	**29.0**	**0.988**	**0.999**	**1.072**	**Yes**
GA67.2c	**25.9**	**25.0**	**26.9**	**ReIZZI**	**25.8**	**25.1**	**26.5**	**0.999**	**0.997**	**1.051**	**Yes**
GA67.3c	31.5	23.5	39.4	ReIZZI	38.2	35.3	41.1	0.994	0.976	1.103	No
GA67.4x	**30.0**	**27.6**	**32.4**	**Lamont**	**34.8**	**34.0**	**35.6**	**0.999**	**0.997**	**0.976**	**Yes**
GA67.6x	**25.8**	**22.1**	**29.6**	**Lamont**	**28.5**	**25.2**	**31.8**	**0.987**	**0.998**	**1.020**	**Yes**
GA67.7x	12.8	9.7	15.9	Lamont	14.8	12.3	17.4	0.972	0.999	0.933	No
GA69.1c	**4.9**	**3.7**	**6.0**	**ReAitken**	**4.9**	**4.4**	**5.5**	**0.987**	**0.991**	**0.861**	**Yes**
GA69.2c	4.6	3.6	5.5	ReIZZI	5.1	4.7	5.6	0.992	0.984	0.804	No
GA70.1c	9.1	6.1	12.0	ReIZZI	7.1	5.3	8.9	0.941	0.622	0.701	No
GA70.2c	8.7	6.7	10.8	ReIZZI	6.4	4.9	7.9	0.949	0.742	0.684	No
GA71.1c	16.8	9.4	24.3	ReIZZI	19.0	13.4	24.5	0.923	0.963	1.040	No
GA71.5c	13.6	11.8	15.4	ReIZZI	12.4	10.0	14.7	0.965	0.978	1.427	No

GA72.1c	6.3	5.5	7.0	ReIZZI	5.1	4.4	5.8	0.981	0.930	1.105	No
GA72.3c	6.0	5.2	6.7	ReIZZI	4.3	3.7	5.0	0.979	0.912	0.859	No
GA74.1c	6.1	5.3	7.0	ReIZZI	5.1	4.3	5.9	0.974	0.925	0.996	No
GA74.2c	4.6	3.8	5.4	ReIZZI	4.0	2.9	5.0	0.938	0.967	1.062	No
GA74.3c	7.4	6.1	8.7	ReAitken	5.0	4.1	6.0	0.965	0.963	0.840	No
GA82.1c	34.9	28.4	41.4	ReIZZI	38.6	34.6	42.7	0.989	0.976	1.060	No
GA82.3c	52.4	46.0	58.8	ReAitken	53.5	50.8	56.2	0.997	0.999	1.210	No
GA82.4c	70.3	62.6	78.0	ReIZZI	92.3	89.3	95.3	0.999	0.973	1.280	No
GA82.6x	55.5	49.1	62.0	Lamont	89.9	79.6	100.1	0.987	0.993	1.169	No
GA83.1c	**15.4**	**14.2**	**16.6**	**ReIZZI**	**17.8**	**17.0**	**18.7**	**0.998**	**0.998**	**1.146**	**Yes**
GA83.2c	**18.4**	**17.5**	**19.3**	**ReIZZI**	**17.0**	**16.5**	**17.4**	**0.999**	**0.994**	**1.127**	**Yes**
GA83.3x	**14.2**	**12.5**	**15.9**	**Lamont**	**15.7**	**14.6**	**16.8**	**0.995**	**0.996**	**1.104**	**Yes**
GA83.4x	**9.9**	**8.2**	**11.6**	**Lamont**	**11.4**	**10.6**	**12.3**	**0.994**	**0.984**	**0.924**	**Yes**
GA83.5x	**10.0**	**8.2**	**11.9**	**Lamont**	**10.9**	**9.9**	**11.9**	**0.992**	**0.991**	**0.892**	**Yes**
GA83.6x	**13.3**	**10.8**	**15.8**	**Lamont**	**14.0**	**12.4**	**15.7**	**0.986**	**0.993**	**0.985**	**Yes**

Table 3.S4. 88 original paleointensities before MD correction by using a set of loose qualification criteria (as used by Wang and Kent, [2013]) and automatic temperature range selection, within which, 51 paleointensities meet a more strict set of qualification criteria (similar to default criteria Class B in ThellierTool).

Specimen	Method	Pint (μT)	Std.Dev. (μT)	Tmin (ºC)	Tmax (ºC)	N	f	g	q	w	Criteria
GA01.2c	ReIZZI	32.44	2.85	500	575	4	0.54	0.66	4.1	2.9	Loose
GA01.3c	ReIZZI	40.68	3.13	475	575	5	0.55	0.73	5.2	3	Loose
GA01.4x	Lamont	34.84	1.76	350	575	9	0.9	0.83	14.9	5.6	Loose
GA01.7x	Lamont	43.35	1.84	350	575	9	0.86	0.78	15.8	6	Loose
GA01.8x	Lamont	26.35	1.17	475	575	5	0.75	0.64	10.9	6.3	Strict
GA03.3c	ReIZZI	58.28	3.23	400	575	8	0.85	0.78	12	4.9	Strict
GA05.1c	ReIZZI	80.04	5.7	375	525	7	0.51	0.79	5.6	2.5	Strict
GA05.3c	ReIZZI	51.38	1.83	500	575	4	0.56	0.64	10.2	7.2	Loose
GA05.7c	ReAitken	98.25	11.03	0	500	12	0.59	0.81	4.2	1.3	Strict
GA06.1c	ReIZZI	37.71	3.43	500	575	4	0.61	0.64	4.3	3	Loose
GA06.2c	ReIZZI	54.48	2.49	350	575	10	0.94	0.79	16.3	5.8	Loose
GA06.5c	ReAitken	38.31	3.57	450	575	6	0.75	0.73	5.8	2.9	Strict
GA09.2c	ReIZZI	40.98	2.21	0	500	9	0.49	0.83	7.6	2.9	Strict
GA09.3c	ReIZZI	49.46	3.37	475	575	5	0.61	0.7	6.3	3.6	Strict
GA10.2x	Lamont	16.64	0.94	425	550	6	0.63	0.78	8.7	4.3	Strict
GA10.6c	ReIZZI	14.87	1.38	450	575	6	0.78	0.79	6.6	3.3	Loose
GA12.3c	ReIZZI	49.97	5.1	450	550	5	0.53	0.66	3.4	2	Strict
GA12.4c	ReIZZI	53.3	2.41	375	550	8	0.85	0.8	15	6.1	Loose
GA12.6x	Lamont	16.44	3.01	400	575	8	0.69	0.84	3.2	1.3	Loose
GA21.4c	ReIZZI	52.09	3.11	450	575	6	0.78	0.45	5.9	3	Strict
GA22.1c	ReIZZI	15.2	2.02	375	525	7	0.72	0.73	4	1.8	Loose
GA23.1c	ReIZZI	32.78	1.58	425	575	7	0.78	0.76	12.2	5.5	Strict
GA23.3c	ReIZZI	30.99	1.77	425	550	6	0.56	0.75	7.4	3.7	Loose
GA23.6x	Lamont	51.95	7.4	350	500	6	0.37	0.75	2	1	Strict
GA24.5x	Lamont	50.78	7.59	350	500	6	0.38	0.76	1.9	1	Strict
GA24.6x	Lamont	59.92	3.8	350	500	6	0.32	0.78	3.9	2	Strict
GA26.3x	Lamont	30.78	1.31	500	575	4	0.63	0.63	9.3	6.6	Loose
GA26.4x	Lamont	43.37	1.54	400	575	8	0.73	0.81	16.6	6.8	Strict
GA26.7x	Lamont	47.08	2.83	400	575	8	0.75	0.82	10.2	4.2	Strict
GA26.8x	Lamont	28.53	2.94	450	575	6	0.74	0.78	5.6	2.8	Strict
GA27.3c	ReIZZI	22.84	2.19	450	550	5	0.64	0.68	4.6	2.6	Strict
GA27.5x	Lamont	39.26	3.06	350	550	8	0.65	0.82	6.9	2.8	Strict
GA27.6x	Lamont	16.63	2.15	400	575	8	0.89	0.84	5.8	2.4	Loose
GA27.7x	Lamont	7.66	1.41	400	575	8	0.69	0.81	3.1	1.2	Loose
GA27.8x	Lamont	21.68	1.9	400	550	7	0.81	0.82	7.6	3.4	Strict
GA28.1c	ReIZZI	25	2.2	0	550	11	0.91	0.77	7.9	2.6	Loose
GA28.4x	Lamont	5.27	0.84	450	575	6	0.5	0.7	2.2	1.1	Loose
GA28.7x	Lamont	17.33	1.32	475	575	5	0.83	0.67	7.2	4.2	Strict
GA29.2c	ReIZZI	12.34	0.53	425	575	7	0.78	0.78	14.3	6.4	Strict
GA29.3c	ReAitken	8.38	0.38	450	575	6	0.75	0.72	11.9	5.9	Strict
GA29.4c	ReIZZI	13.19	1.02	475	575	5	0.61	0.74	5.8	3.3	Loose
GA29.5x	Lamont	15.84	0.15	425	575	7	0.68	0.75	55	24.6	Strict
GA29.6x	Lamont	9.65	0.67	425	575	7	0.79	0.73	8.3	3.7	Strict
GA30.3x	Lamont	22.64	0.37	425	575	7	0.76	0.77	36.5	16.3	Strict
GA30.5x	Lamont	20.75	0.59	475	575	5	0.62	0.74	16	9.3	Strict
GA30.8x	Lamont	22.54	0.67	400	575	8	0.82	0.77	21.4	8.7	Strict
GA31.1c	ReIZZI	17.4	2.6	0	575	12	1	0.81	5.4	1.7	Strict
GA31.3c	ReIZZI	10.58	2.09	375	550	8	0.95	0.78	3.8	1.5	Loose

GA33.1c	ReAitken	22.23	2.89	0	350	6	0.43	0.74	2.5	1.2	Loose
GA33.4x	Lamont	30.62	1.66	400	525	6	0.37	0.76	5.1	2.6	Strict
GA40.6x	Lamont	4.42	0.86	500	575	4	0.53	0.66	1.8	1.3	Loose
GA40.7x	Lamont	18.83	2.77	350	500	6	0.36	0.69	1.7	0.9	Loose
GA40.8x	Lamont	19.35	1.29	425	525	5	0.5	0.73	5.6	3.2	Strict
GA50.2c	ReIZZI	28.48	2.34	475	575	5	0.48	0.74	4.4	2.5	Loose
GA50.3x	Lamont	32.06	5.17	350	500	6	0.42	0.66	1.7	0.9	Loose
GA60.2c	ReIZZI	5.66	0.41	400	550	7	0.75	0.78	8	3.6	Strict
GA60.4c	ReAitken	5.93	0.45	400	575	8	0.89	0.82	9.6	3.9	Strict
GA60.5x	Lamont	34.94	0.98	350	575	9	0.79	0.85	23.9	9	Strict
GA60.6x	Lamont	5.87	0.79	300	575	10	0.93	0.63	4.3	1.5	Strict
GA60.7x	Lamont	3.89	0.27	400	575	8	0.89	0.8	10.3	4.2	Loose
GA63.2c	ReIZZI	4.09	0.5	500	575	4	0.5	0.63	2.6	1.8	Loose
GA63.4x	Lamont	8.86	0.89	475	575	5	0.45	0.71	3.2	1.9	Strict
GA63.6x	Lamont	13.73	1.38	475	575	5	0.58	0.69	3.9	2.3	Strict
GA63.7x	Lamont	17.01	1.3	450	575	6	0.72	0.75	7	3.5	Strict
GA63.8x	Lamont	10.15	0.52	425	575	7	0.73	0.82	11.7	5.3	Loose
GA64.1c	ReAitken	21.39	1.8	400	550	7	0.78	0.71	6.5	2.9	Loose
GA64.2c	ReIZZI	22.72	2.42	375	550	8	0.81	0.74	5.6	2.3	Strict
GA64.4x	Lamont	17.01	0.25	500	575	4	0.68	0.62	28.6	20.2	Loose
GA64.5x	Lamont	17.21	1.97	350	575	9	0.87	0.82	6.3	2.4	Strict
GA64.6x	Lamont	36.83	4.51	350	500	6	0.38	0.73	2.3	1.1	Strict
GA64.7x	Lamont	23.66	1.57	350	575	9	0.81	0.81	9.8	3.7	Strict
GA65.3c	ReIZZI	11.9	0.7	450	575	6	0.75	0.77	9.7	4.9	Loose
GA65.7x	Lamont	17.67	1.77	400	550	7	0.41	0.81	3.3	1.5	Strict
GA66.1c	ReIZZI	13.2	0.91	475	575	5	0.64	0.71	6.5	3.8	Loose
GA66.3c	ReAitken	12.93	0.8	475	575	5	0.68	0.73	8	4.6	Loose
GA66.4x	Lamont	12.82	0.45	500	575	4	0.64	0.63	11.6	8.2	Loose
GA66.7x	Lamont	14.09	0.76	475	575	5	0.67	0.73	9.1	5.2	Loose
GA66.8x	Lamont	12.29	1.09	475	575	5	0.63	0.73	5.2	3	Loose
GA67.1c	ReAitken	20.93	1.65	450	550	5	0.64	0.68	5.5	3.2	Strict
GA67.4x	Lamont	28.71	1.68	450	575	6	0.6	0.77	7.9	4	Strict
GA67.6x	Lamont	23.54	1.85	450	575	6	0.79	0.75	7.5	3.7	Strict
GA67.7x	Lamont	12.29	1.66	425	575	7	0.88	0.8	5.2	2.3	Strict
GA71.5c	ReIZZI	13.83	1.05	400	575	8	0.81	0.76	8.2	3.3	Loose
GA74.2c	ReIZZI	3.69	0.52	475	575	5	0.64	0.73	3.4	1.9	Strict
GA82.6x	Lamont	89.91	15.37	350	500	6	0.36	0.75	1.6	0.8	Loose
GA83.1c	ReIZZI	15.09	0.67	425	575	7	0.74	0.8	13.4	6	Strict
GA83.2c	ReIZZI	14.87	0.66	0	450	7	0.35	0.82	6.5	2.9	Strict
GA83.3x	Lamont	14.41	0.98	400	575	8	0.85	0.82	10.3	4.2	Strict

Supplementary Figures: Figure 3.S1-(01 to 59)

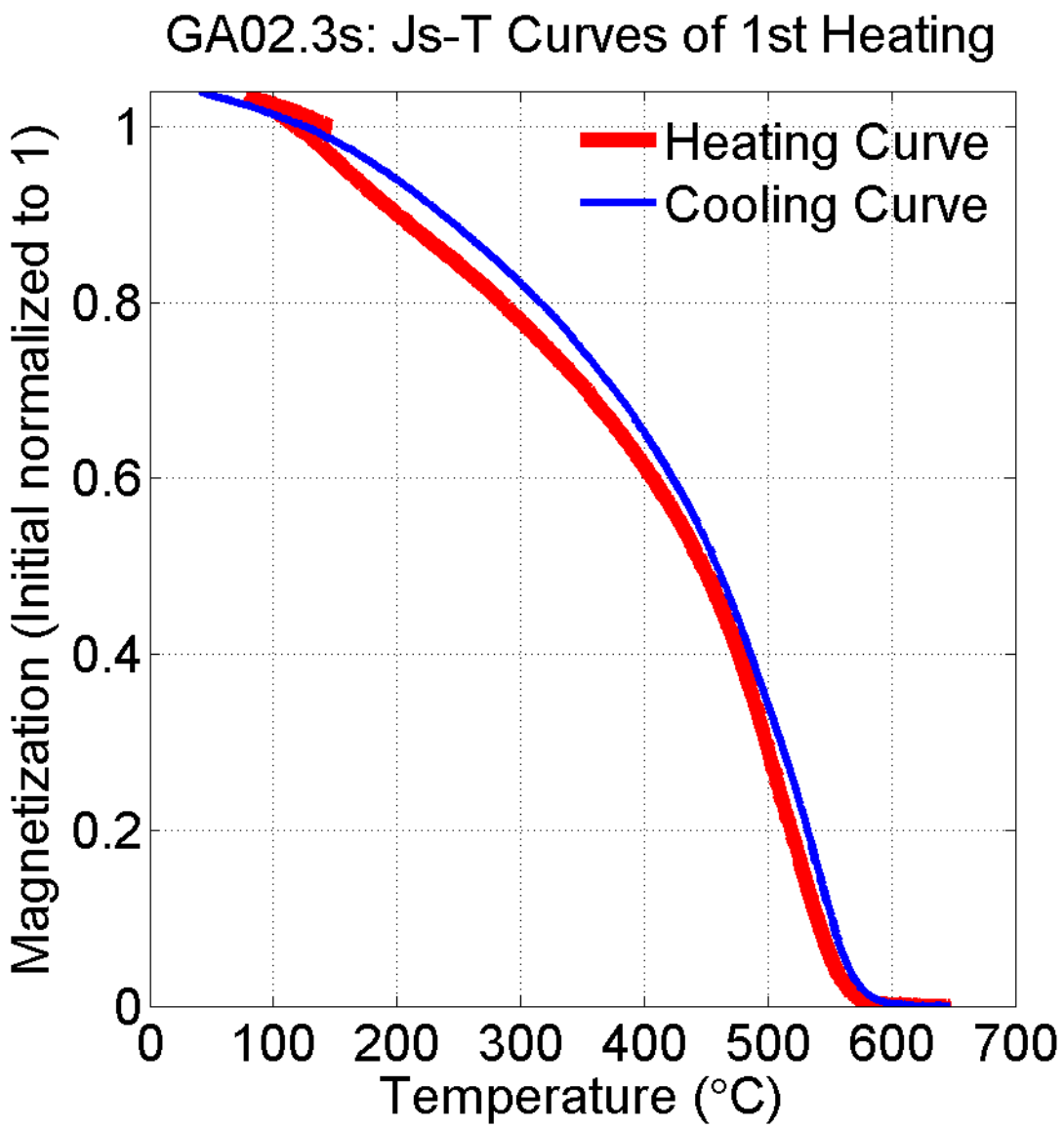

Figure 3.S1-01: Js-T curves of specimen GA02.3s.

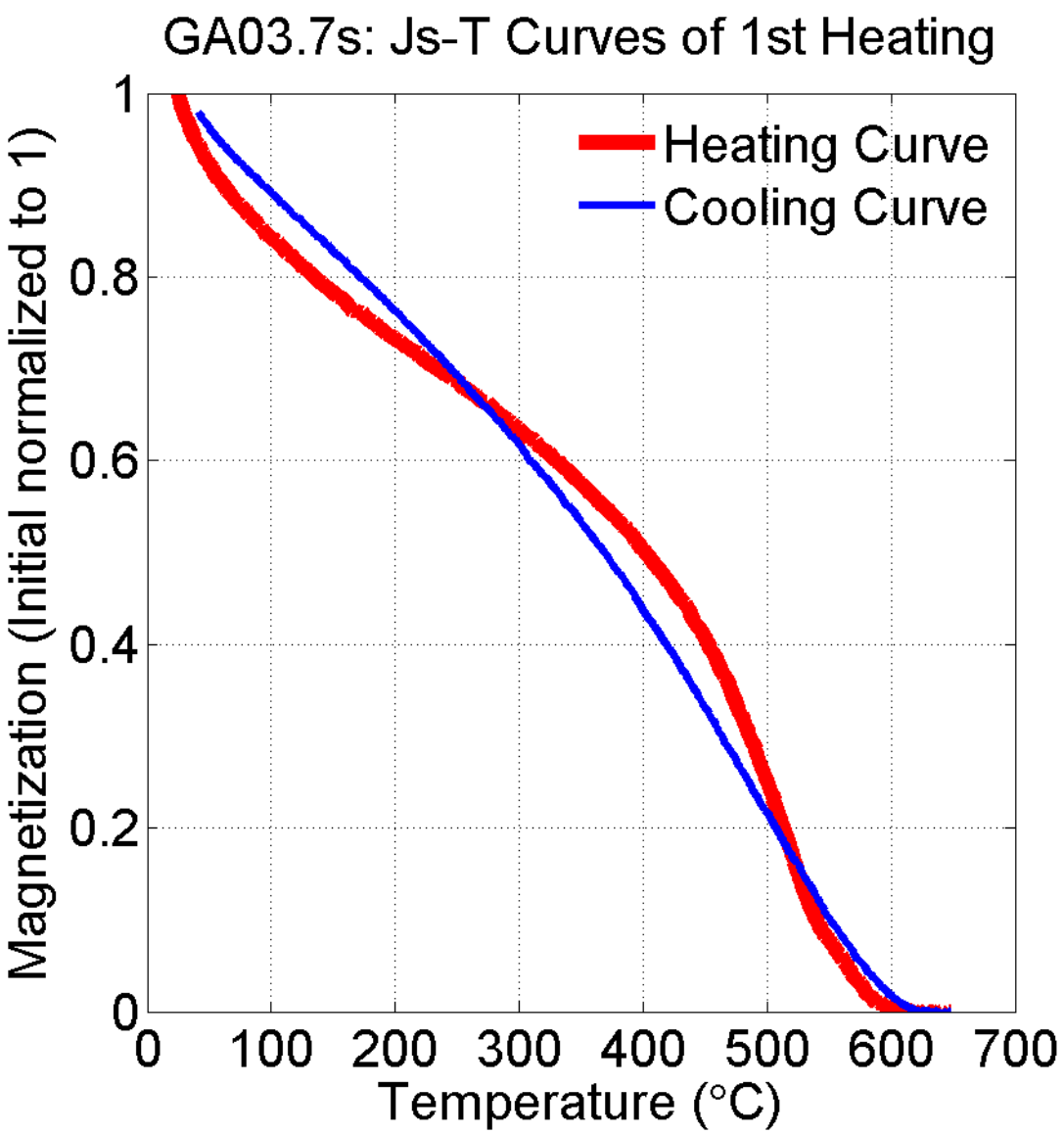

Figure 3.S1-02: Js-T curves of specimen GA03.7s.

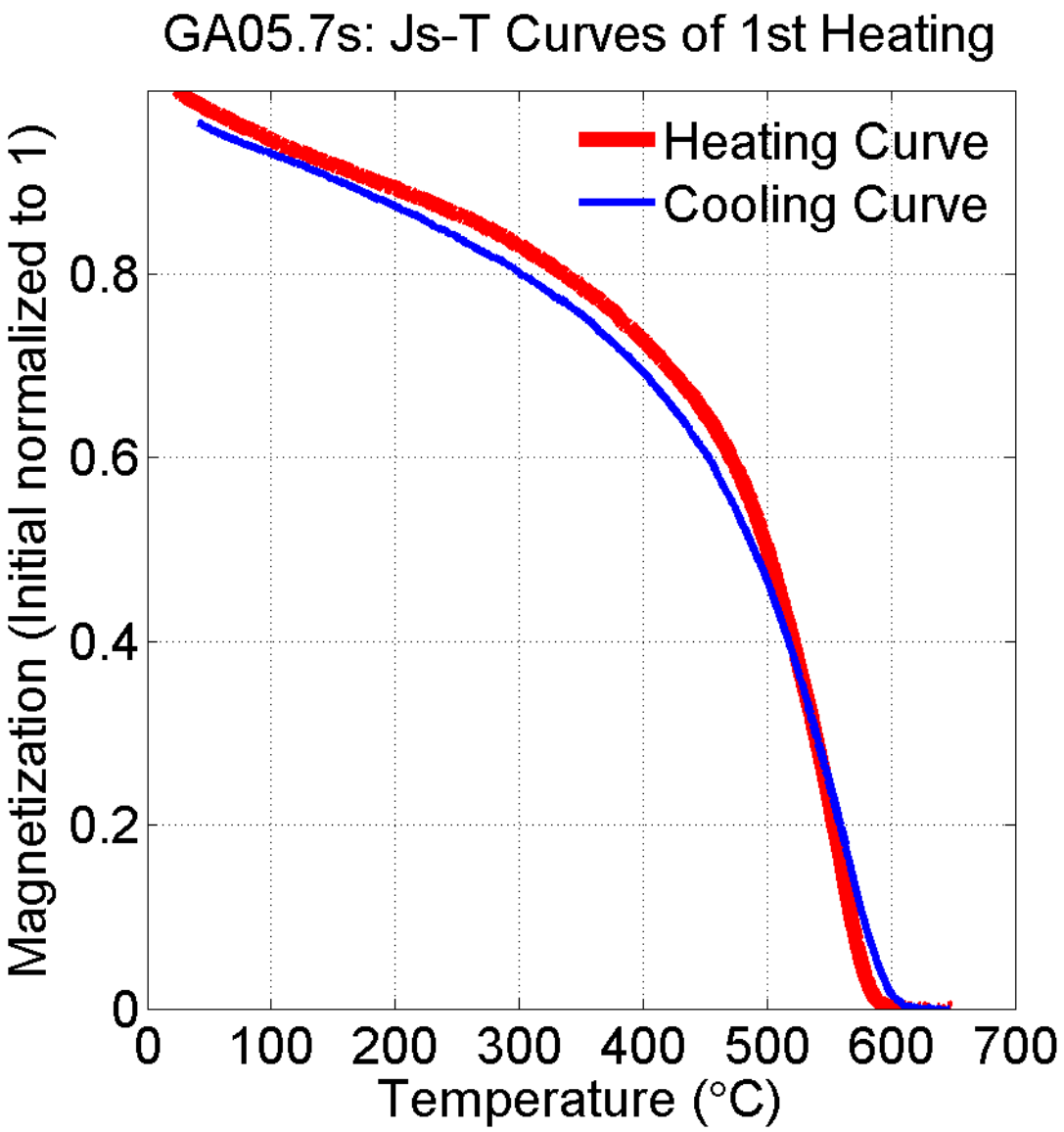

Figure 3.S1-03: Js-T curves of specimen GA05.7s.

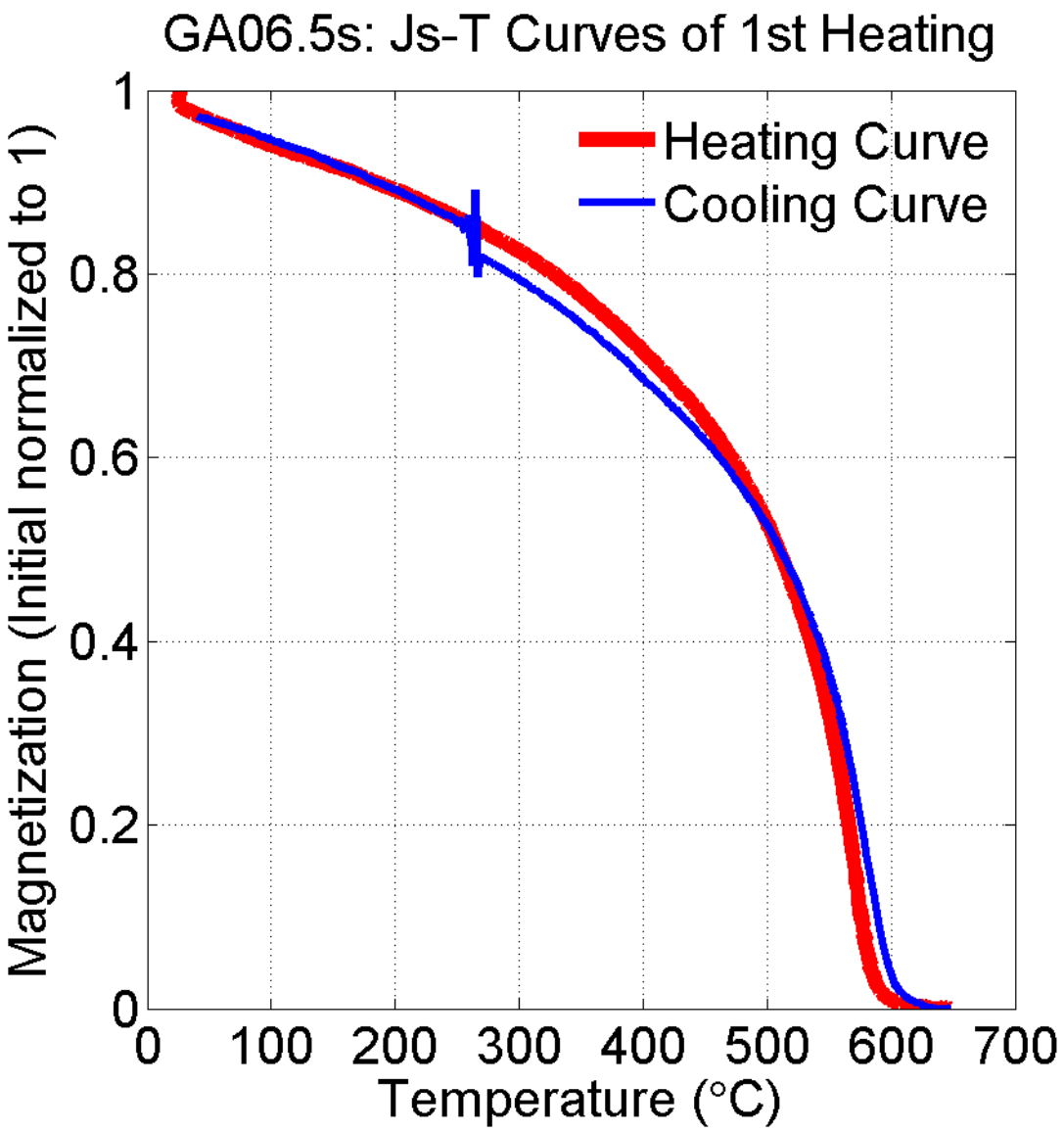

Figure 3.S1-04: Js-T curves of specimen GA06.5s.

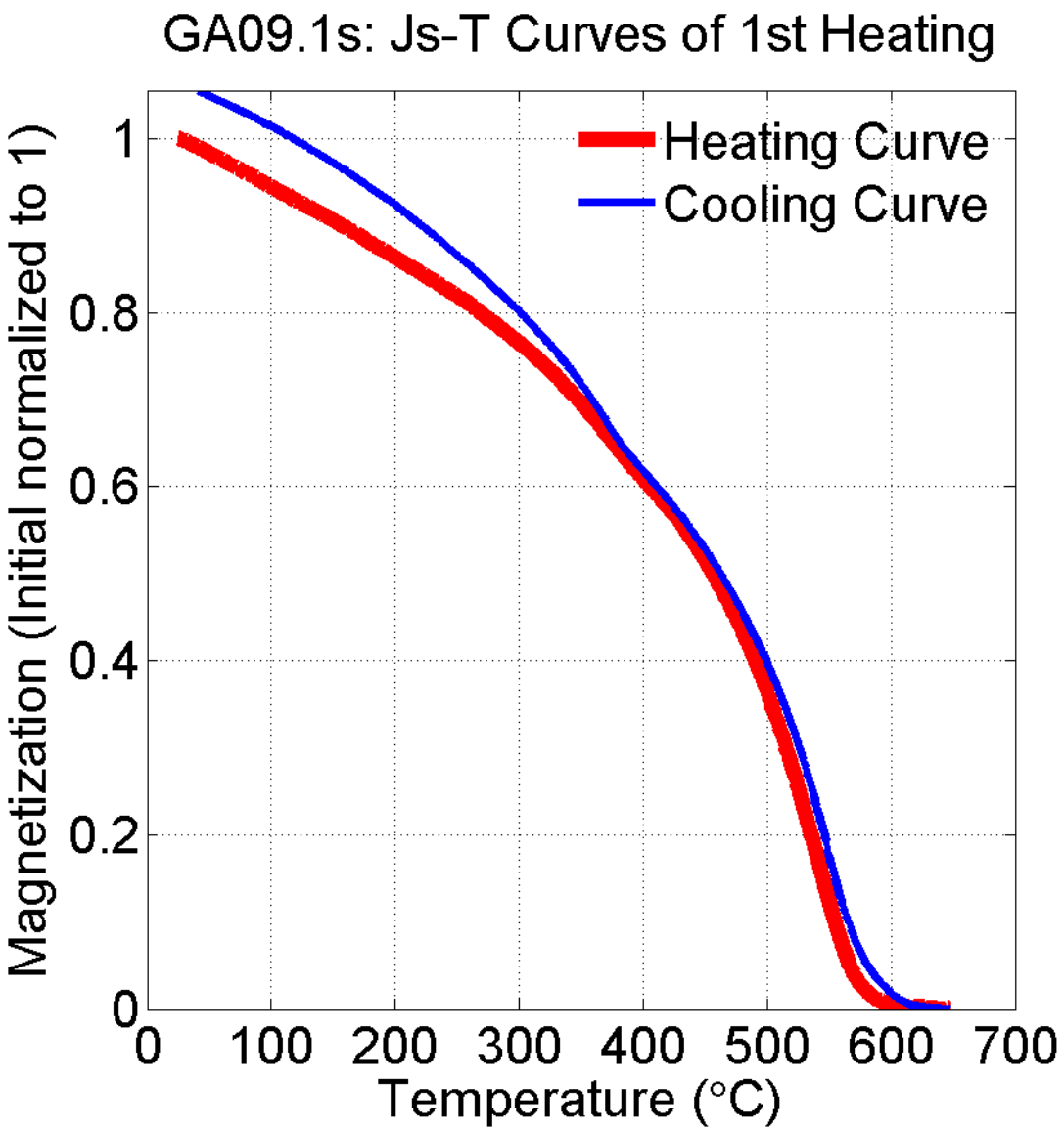

Figure 3.S1-05: Js-T curves of specimen GA09.1s.

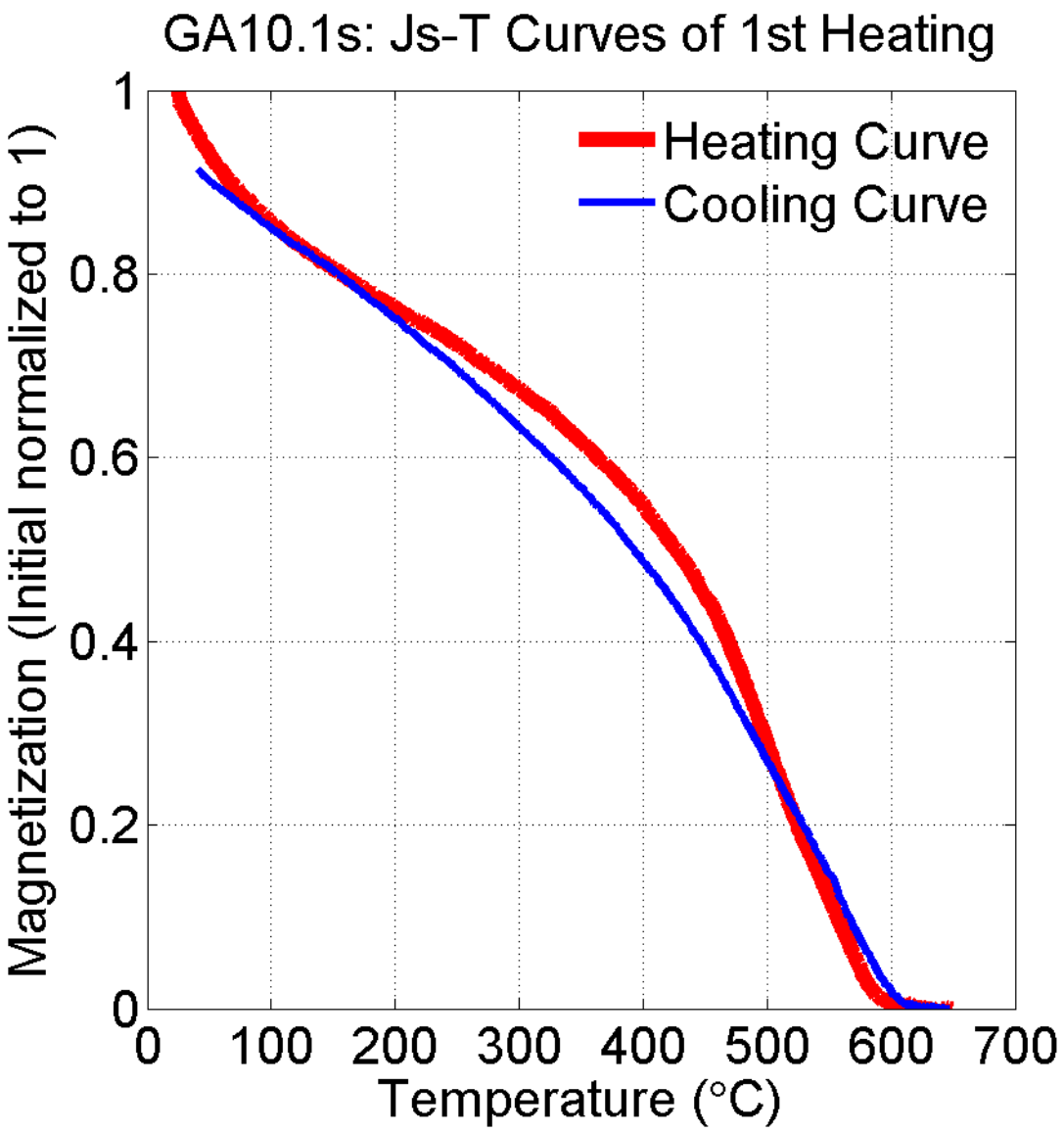

Figure 3.S1-06: Js-T curves of specimen GA10.1s.

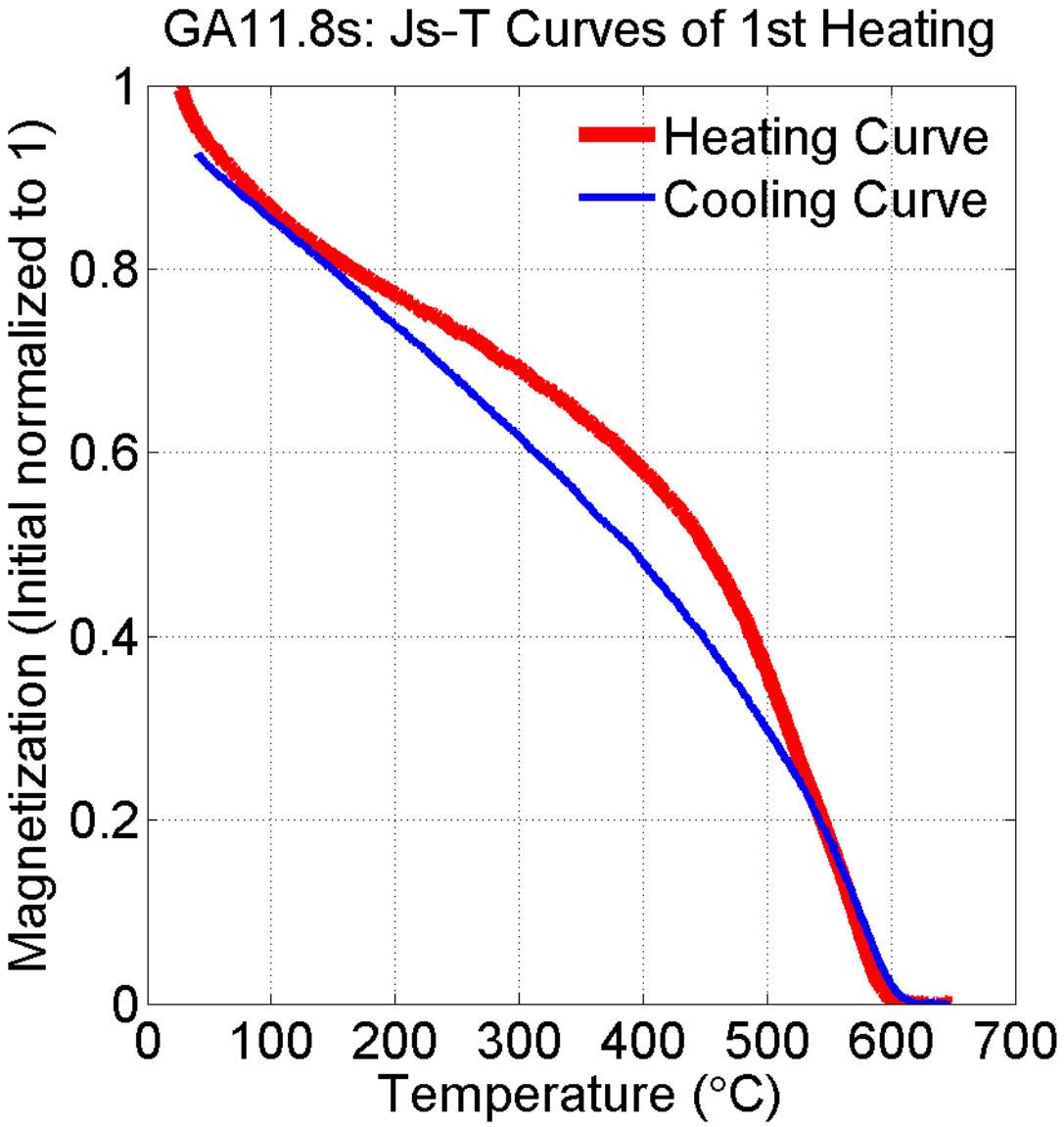

Figure 3.S1-07: Js-T curves of specimen GA11.8s.

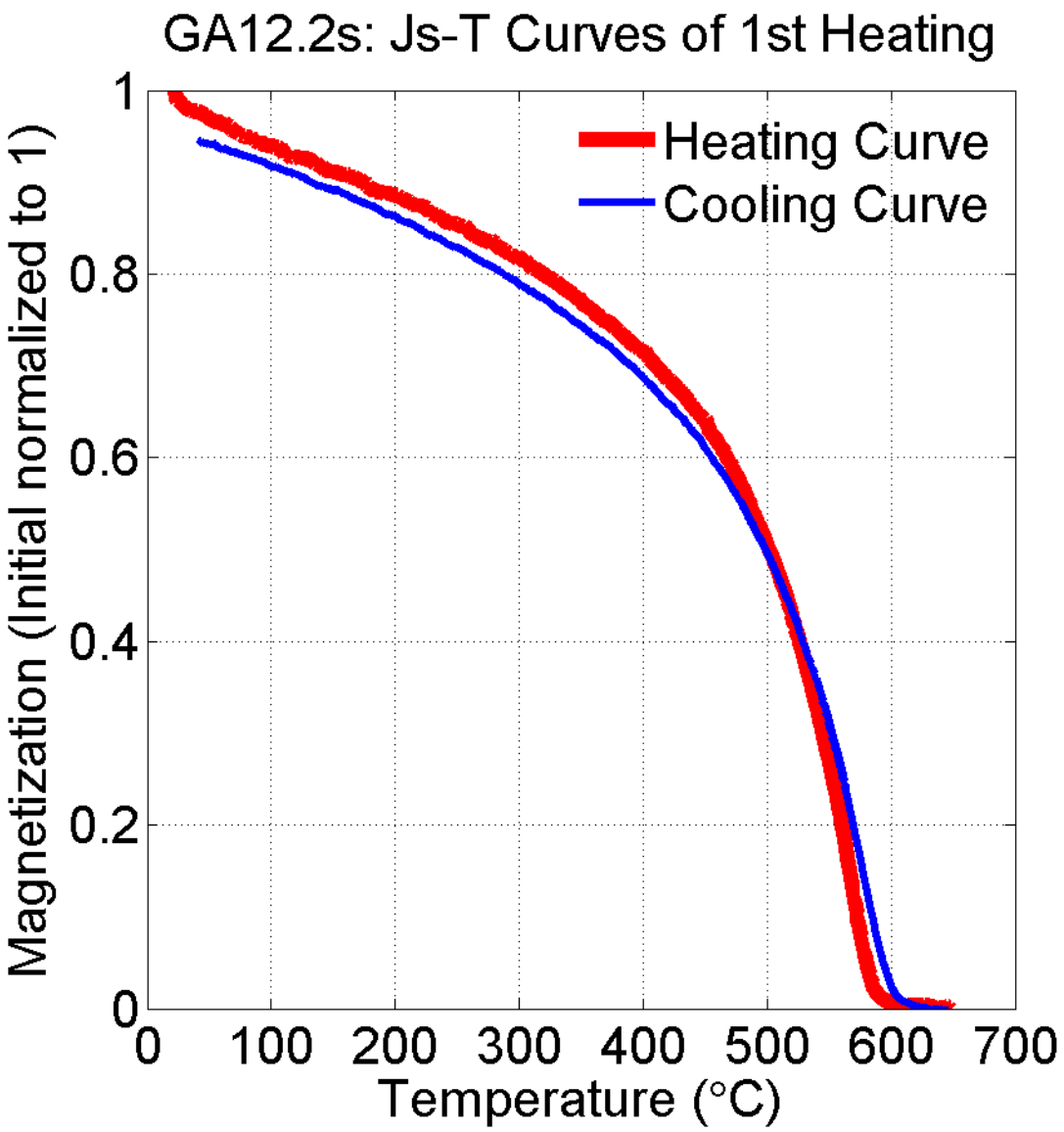

Figure 3.S1-08: Js-T curves of specimen GA12.2s.

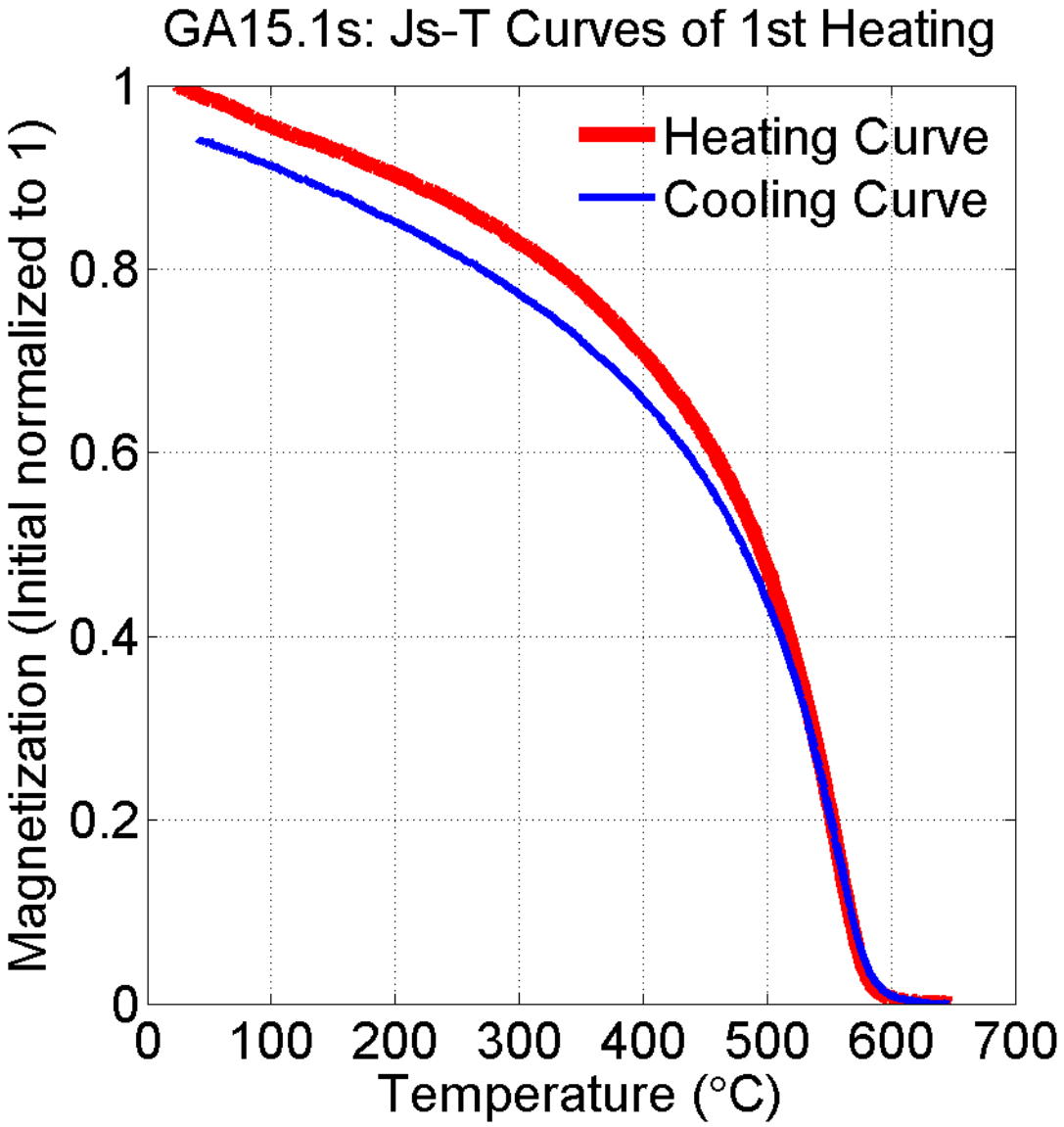

Figure 3.S1-09: Js-T curves of specimen GA15.1s.

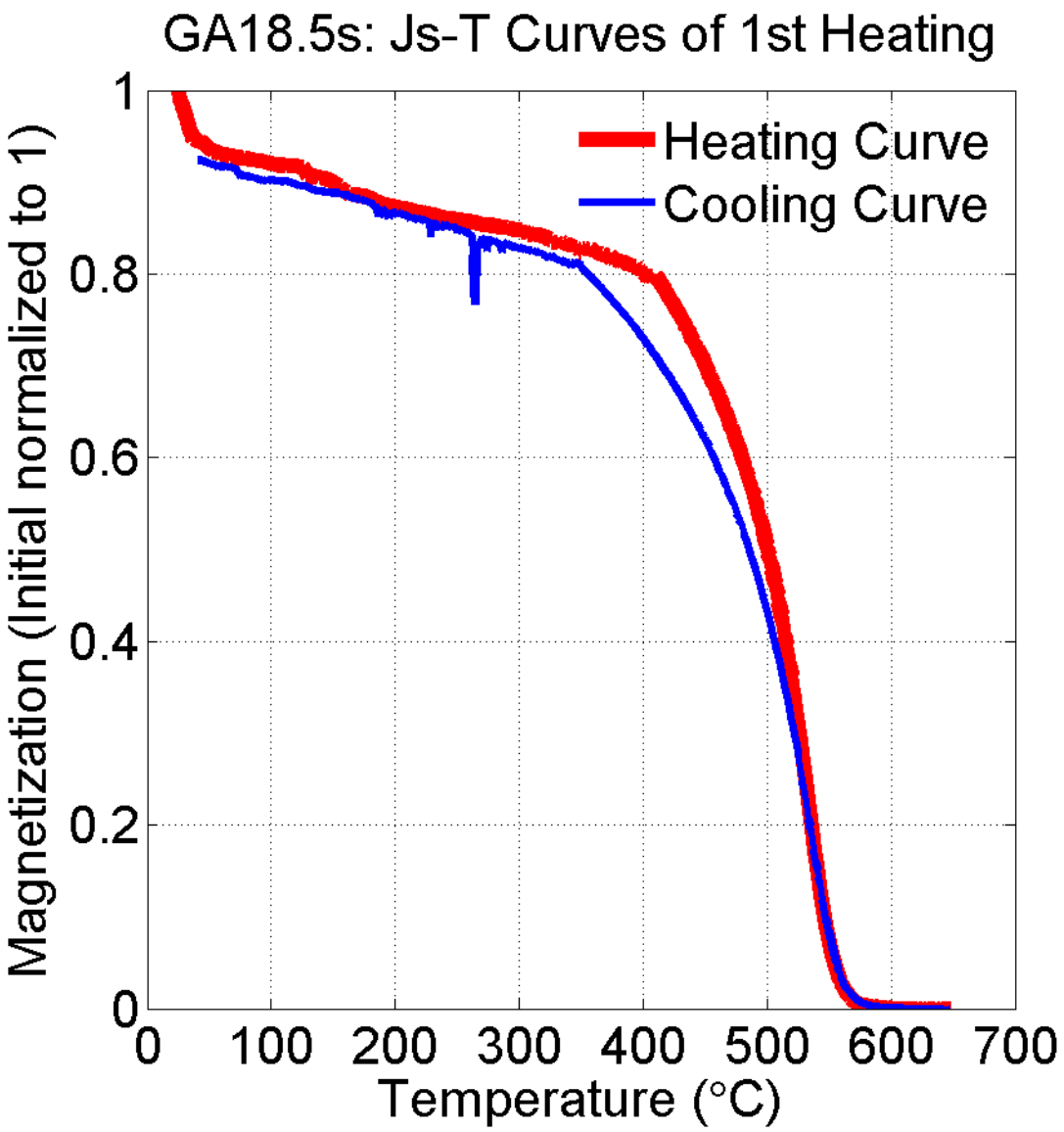

Figure 3.S1-10: Js-T curves of specimen GA18.5s.

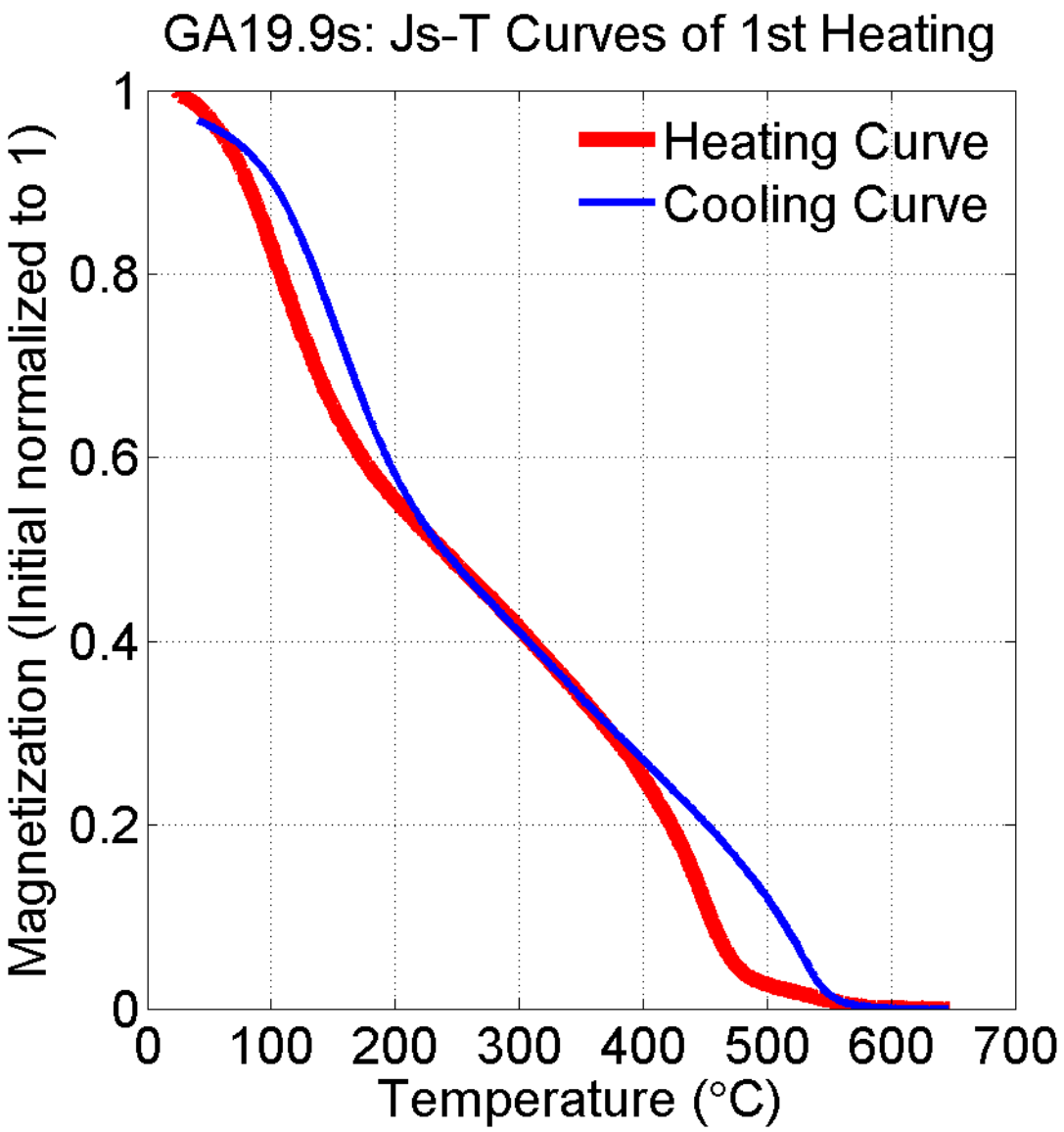

Figure 3.S1-11: Js-T curves of specimen GA19.9s.

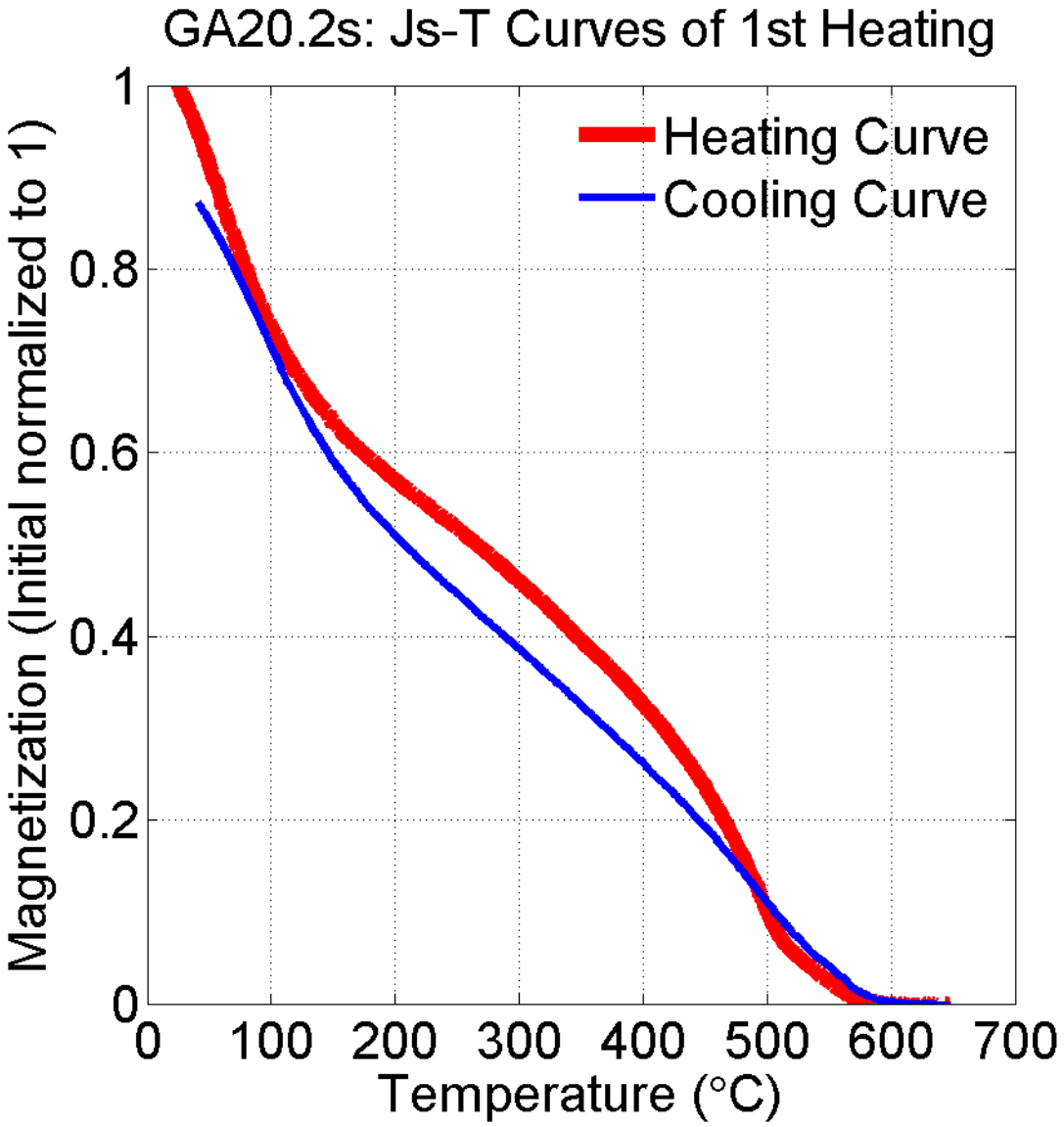

Figure 3.S1-12: Js-T curves of specimen GA20.2s.

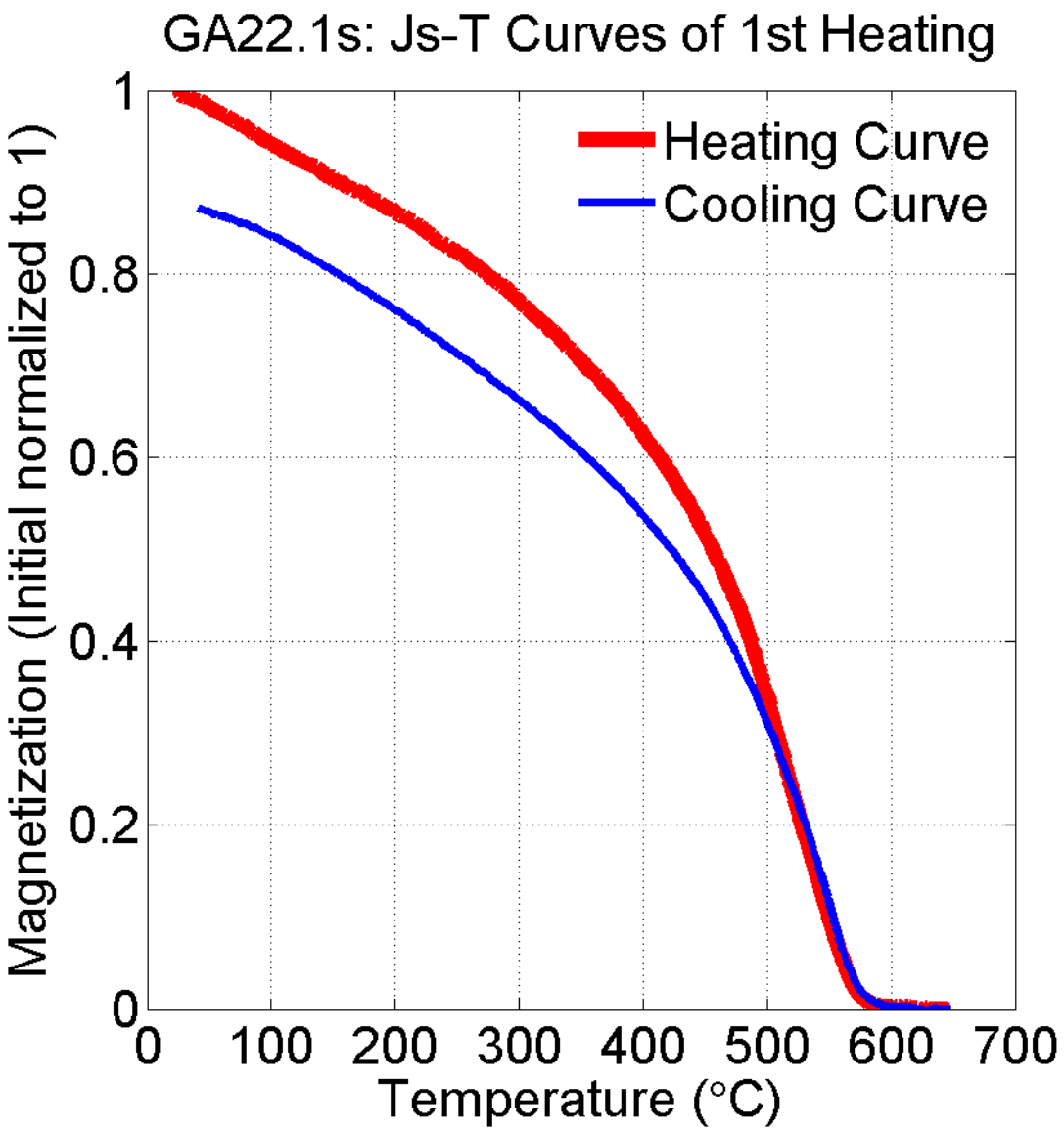

Figure 3.S1-13: Js-T curves of specimen GA22.1s.

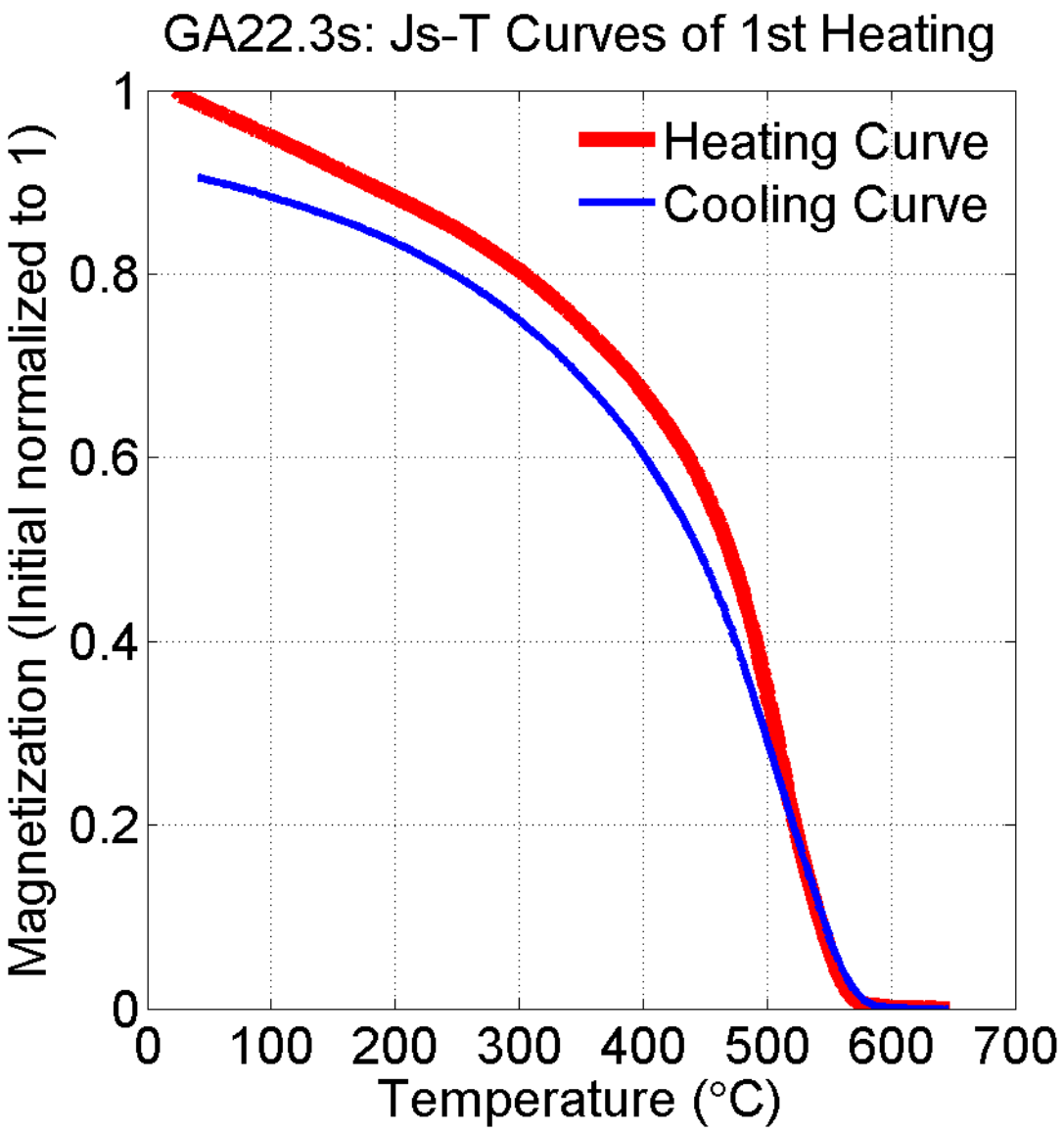

Figure 3.S1-14: Js-T curves of specimen GA22.3s.

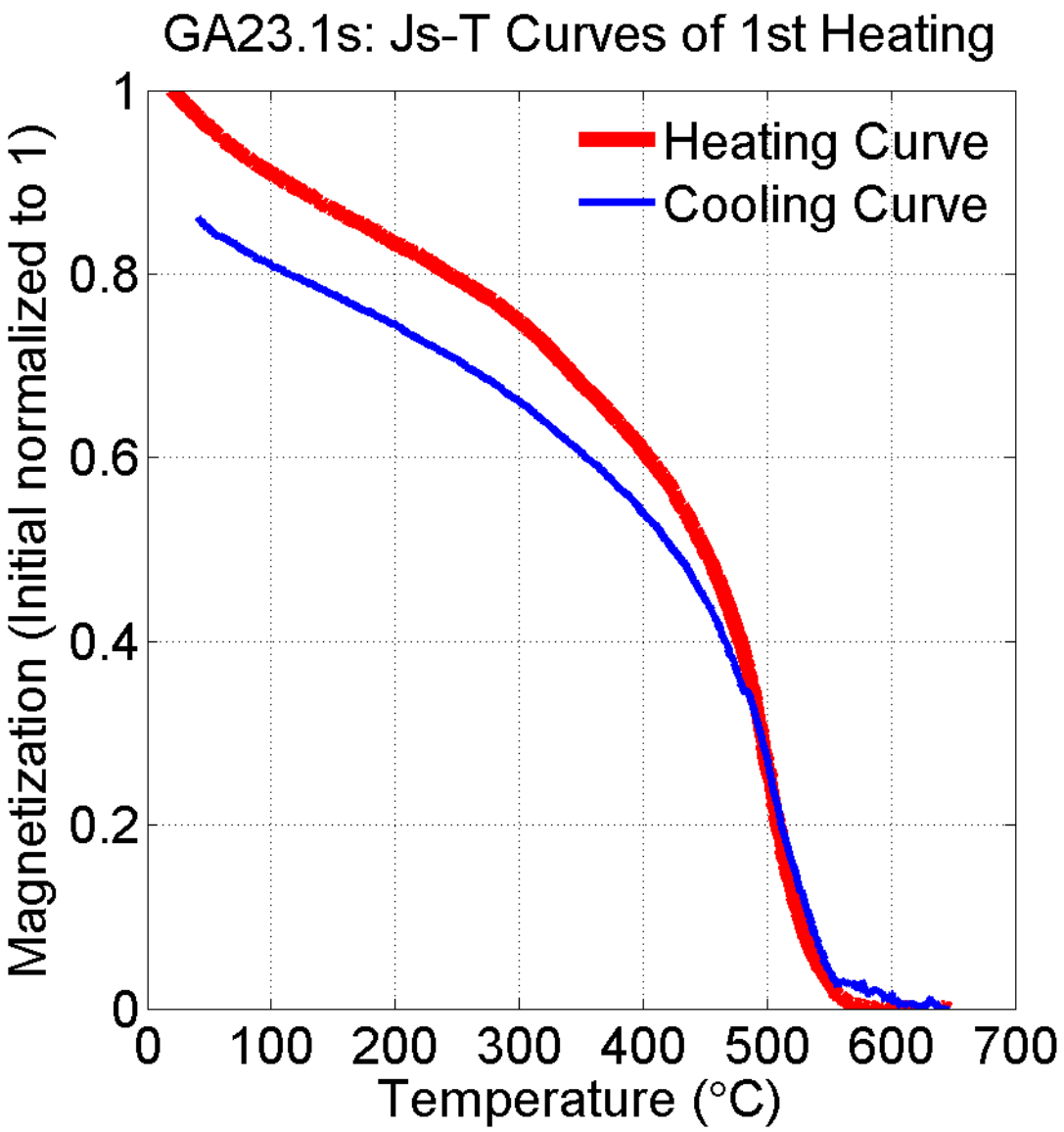

Figure 3.S1-15: Js-T curves of specimen GA23.1s.

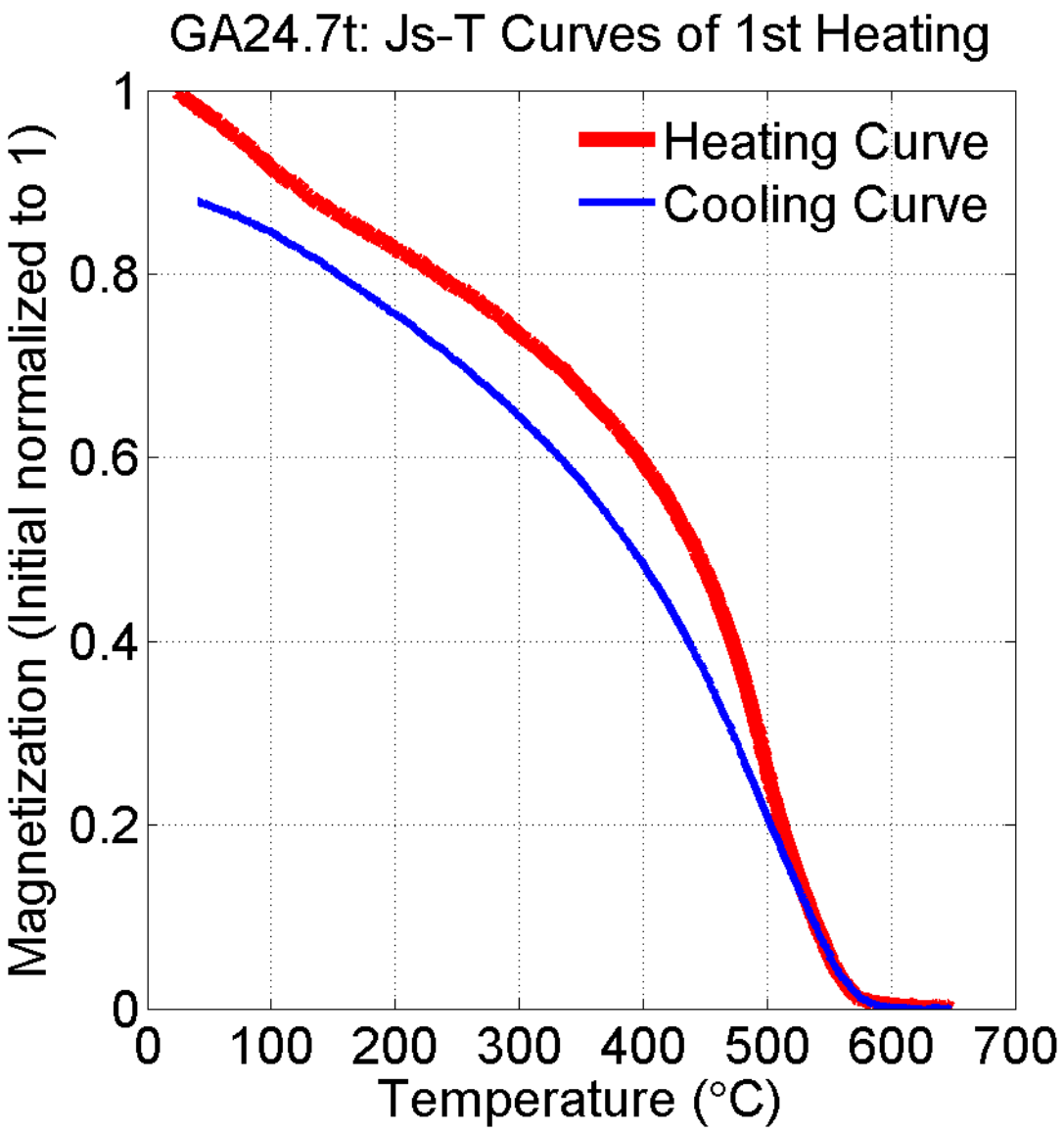

Figure 3.S1-16: Js-T curves of specimen GA24.7t.

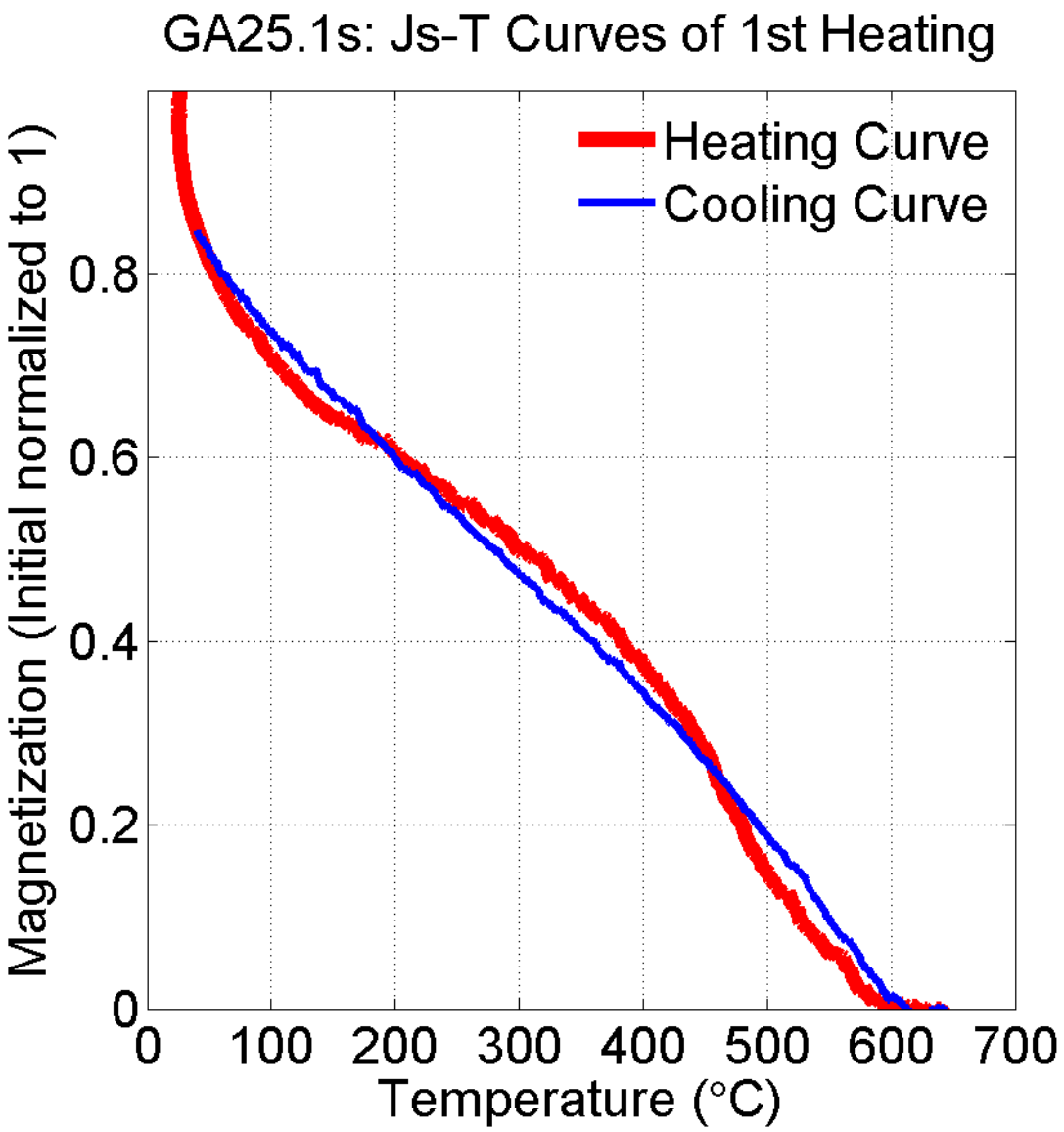

Figure 3.S1-17: Js-T curves of specimen GA25.1s.

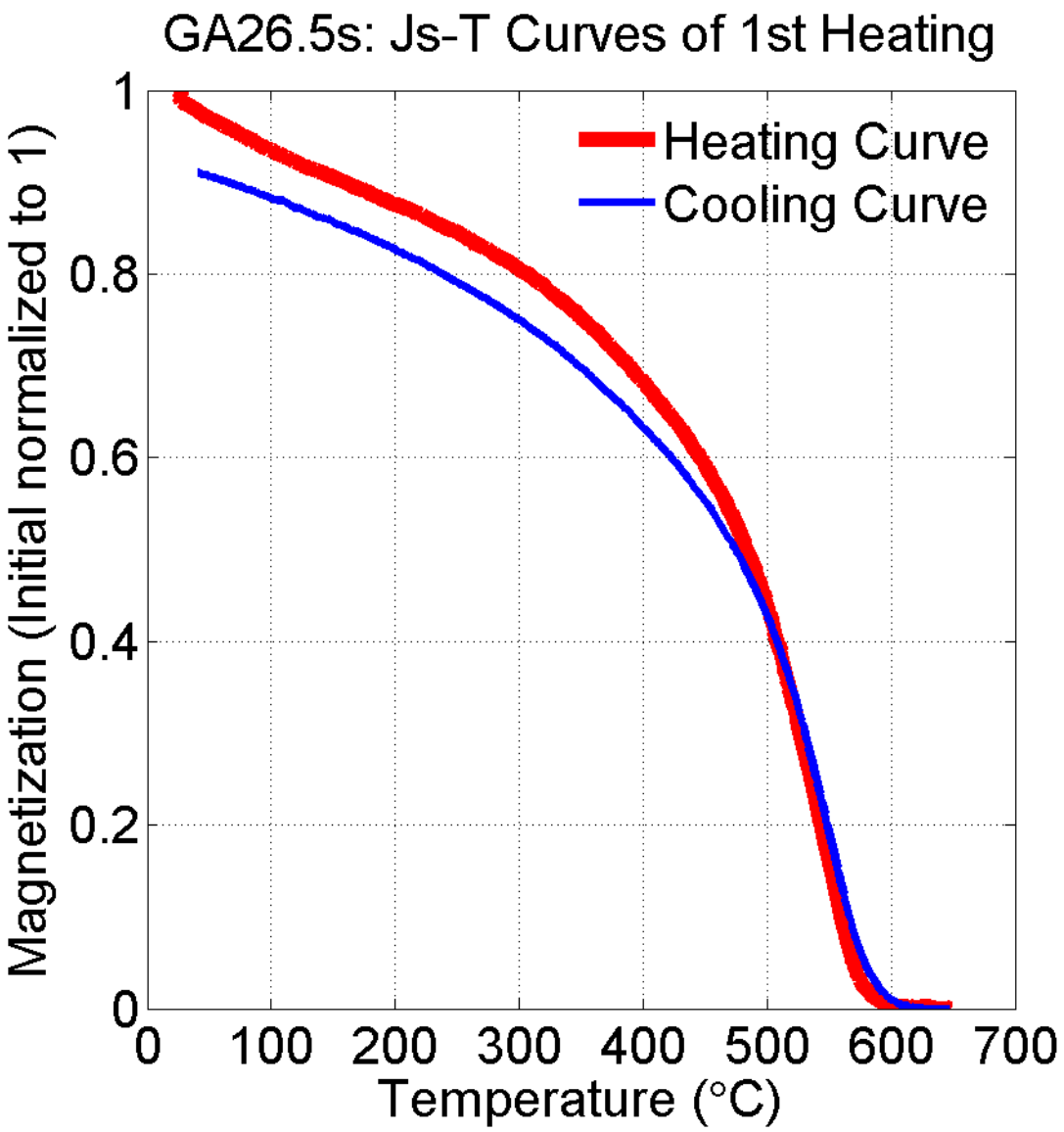

Figure 3.S1-18: Js-T curves of specimen GA26.5s.

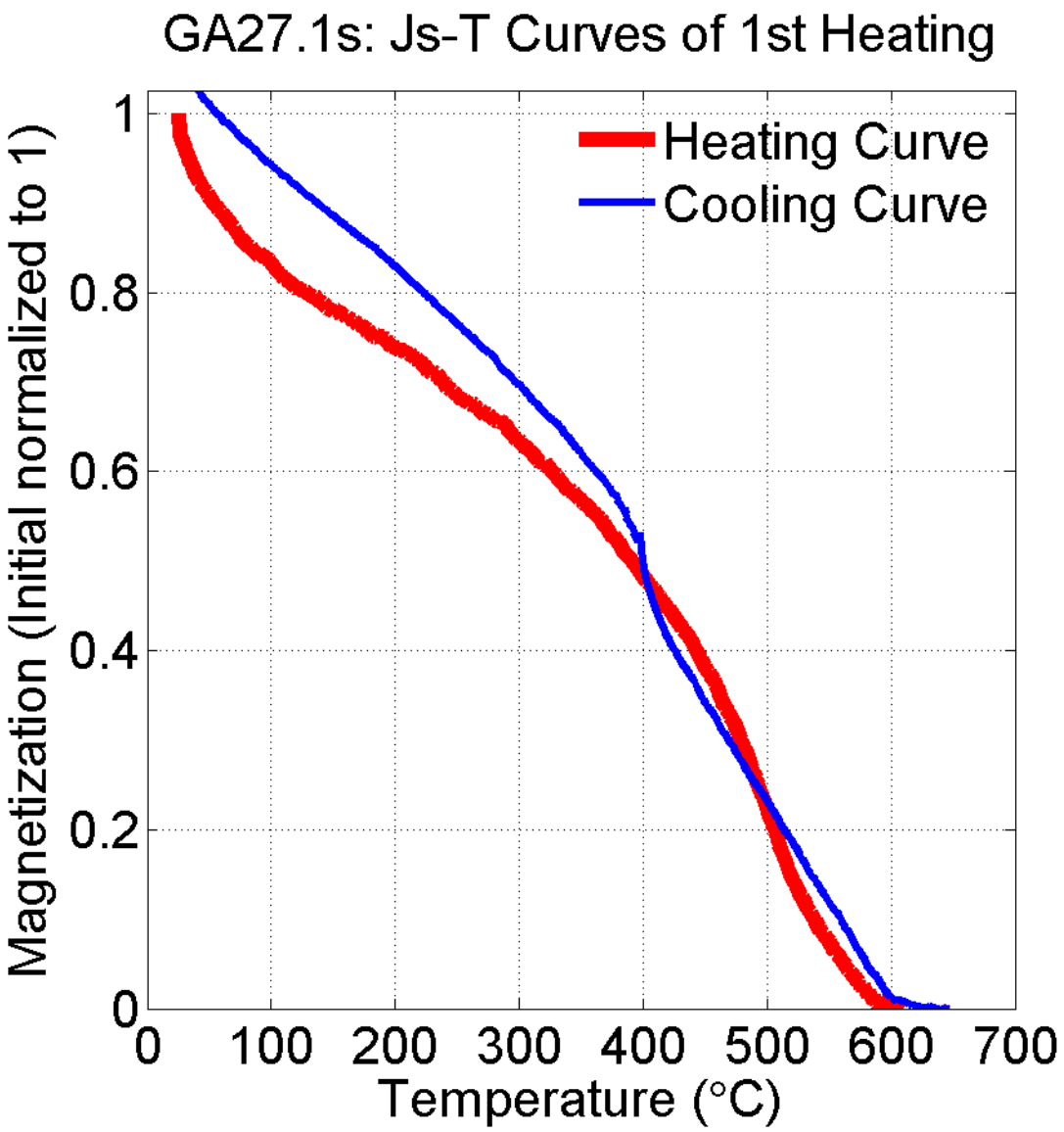

Figure 3.S1-19: Js-T curves of specimen GA27.1s.

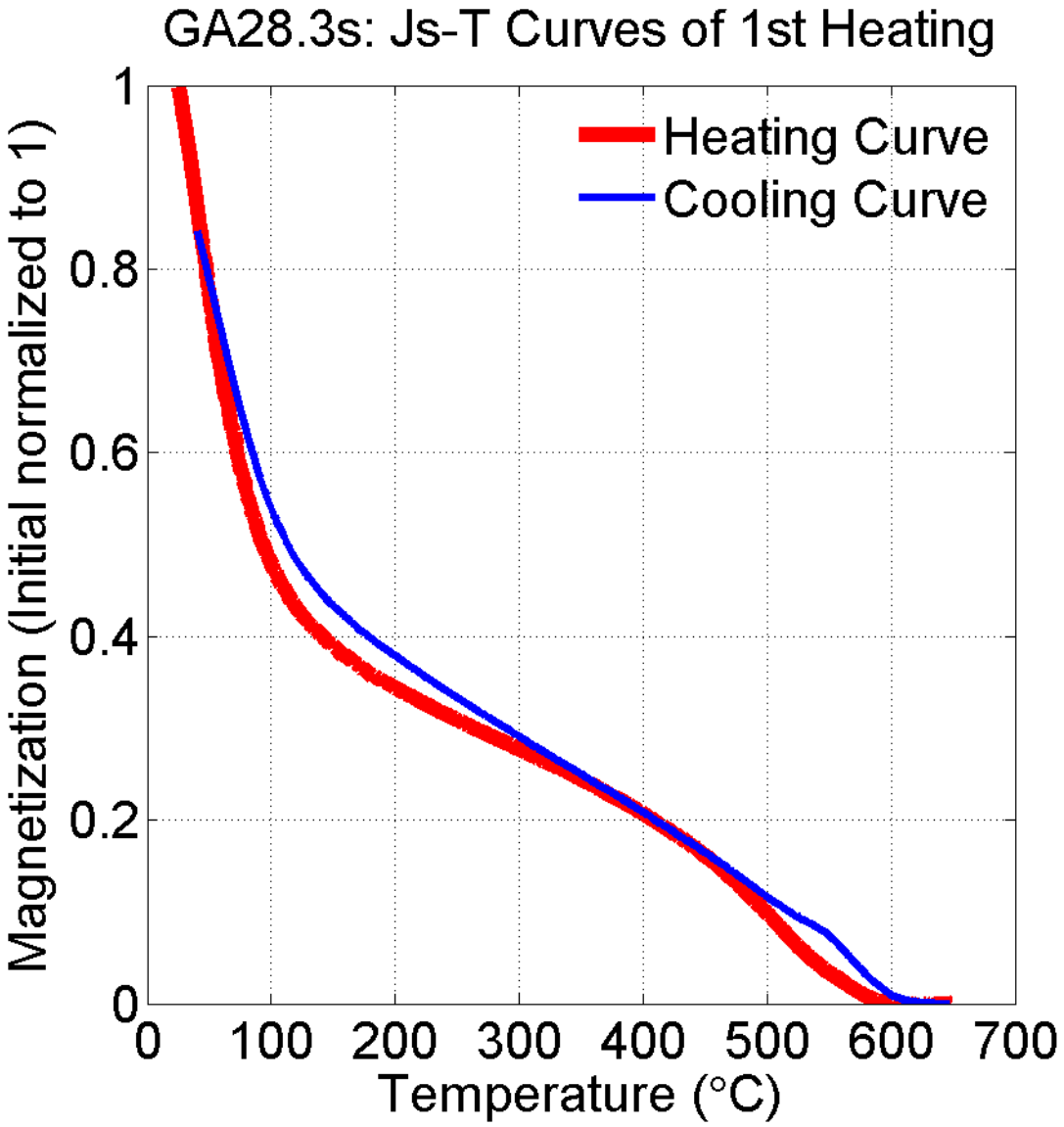

Figure 3.S1-20: Js-T curves of specimen GA28.3s.

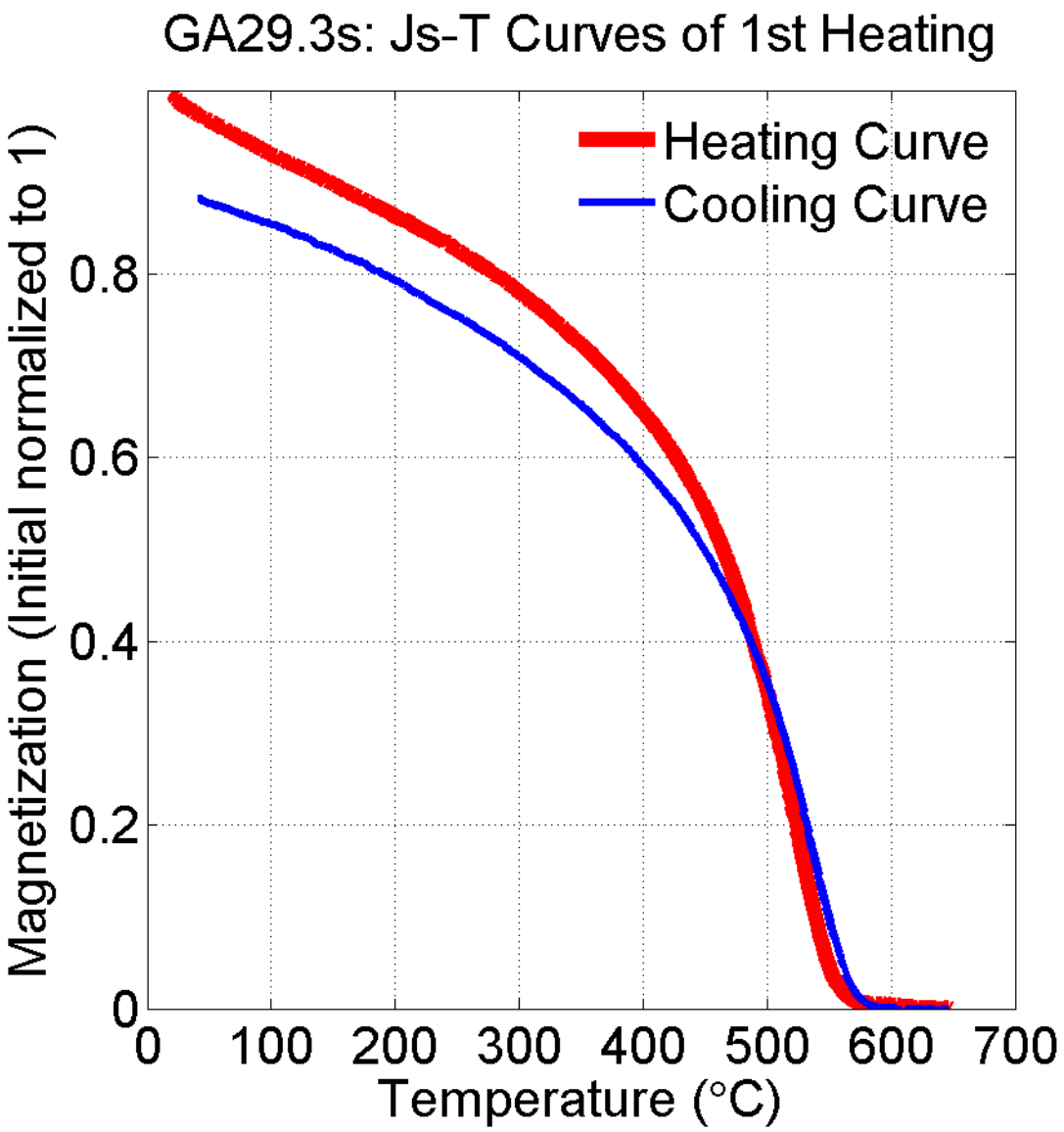

Figure 3.S1-21: Js-T curves of specimen GA29.3s.

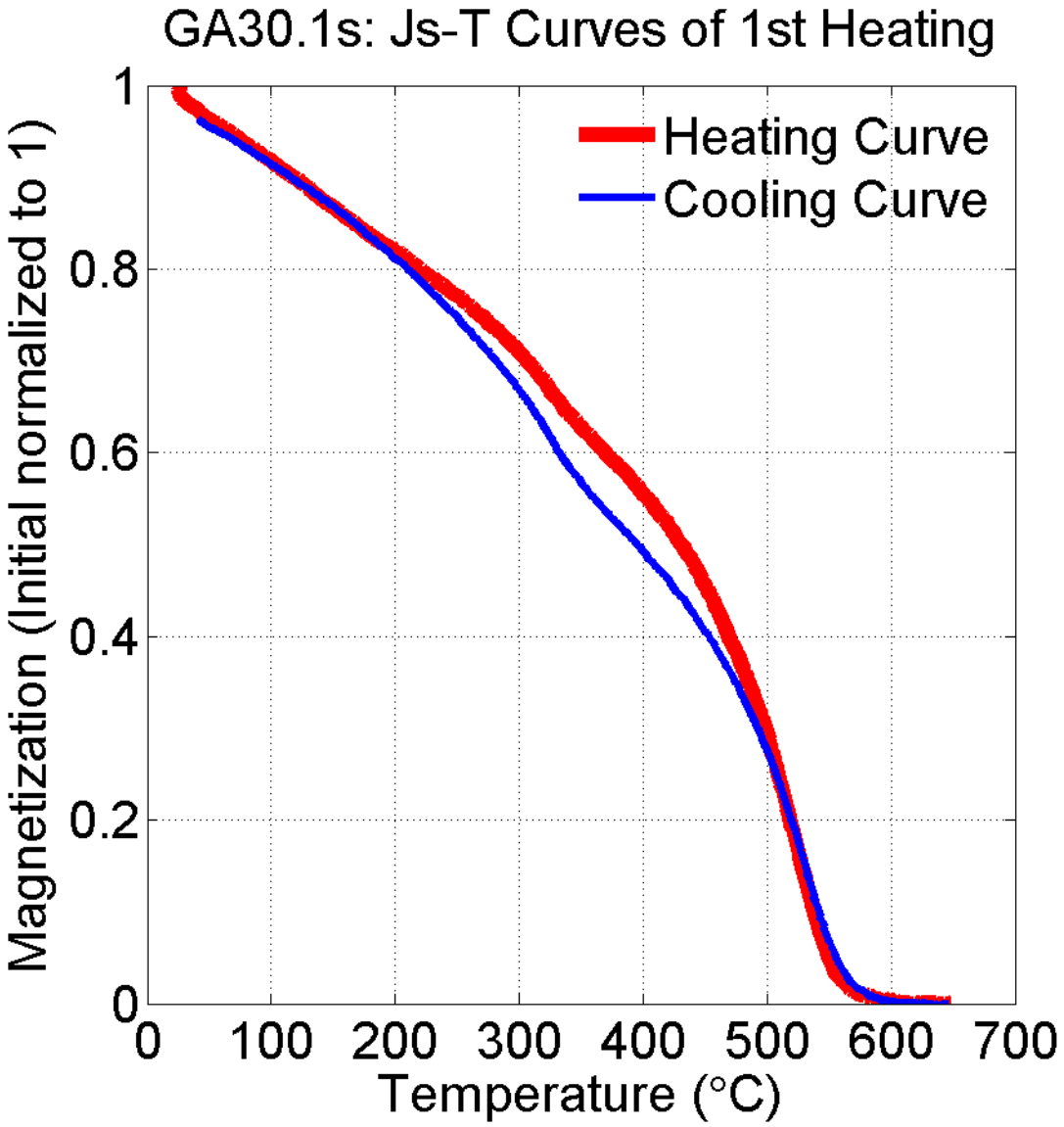

Figure 3.S1-22: Js-T curves of specimen GA30.1s.

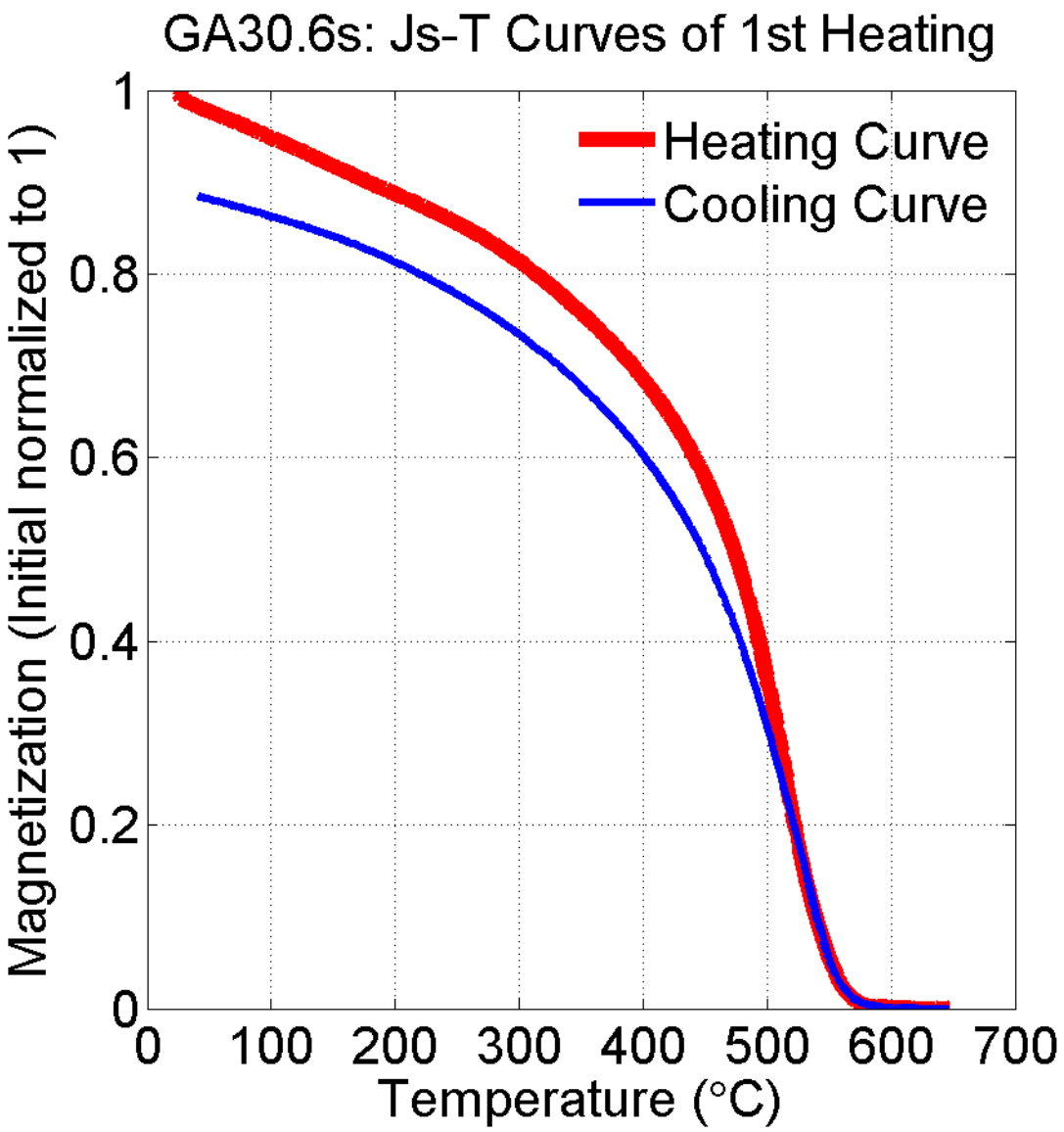

Figure 3.S1-23: Js-T curves of specimen GA30.6s.

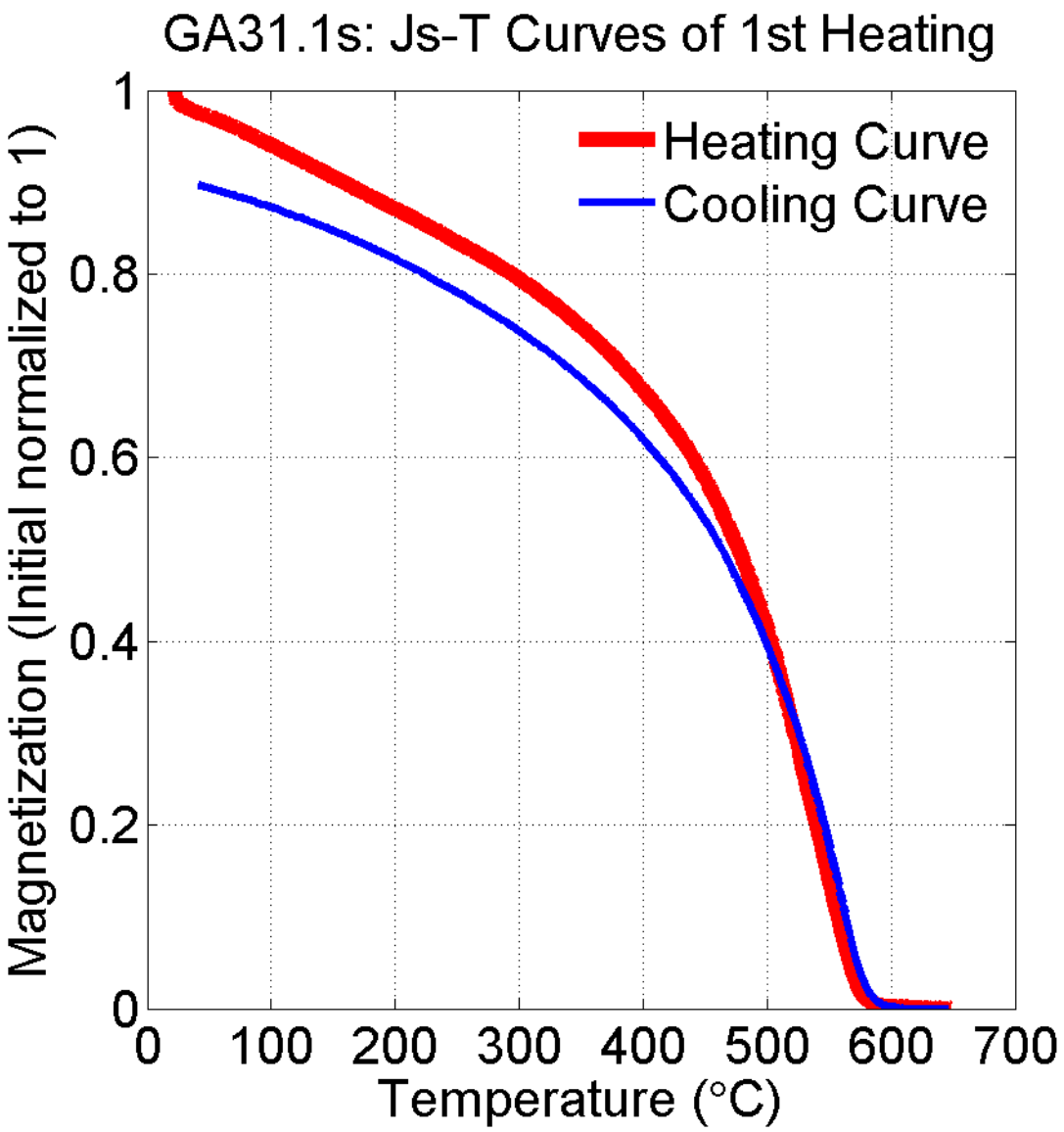

Figure 3.S1-24: Js-T curves of specimen GA31.1s.

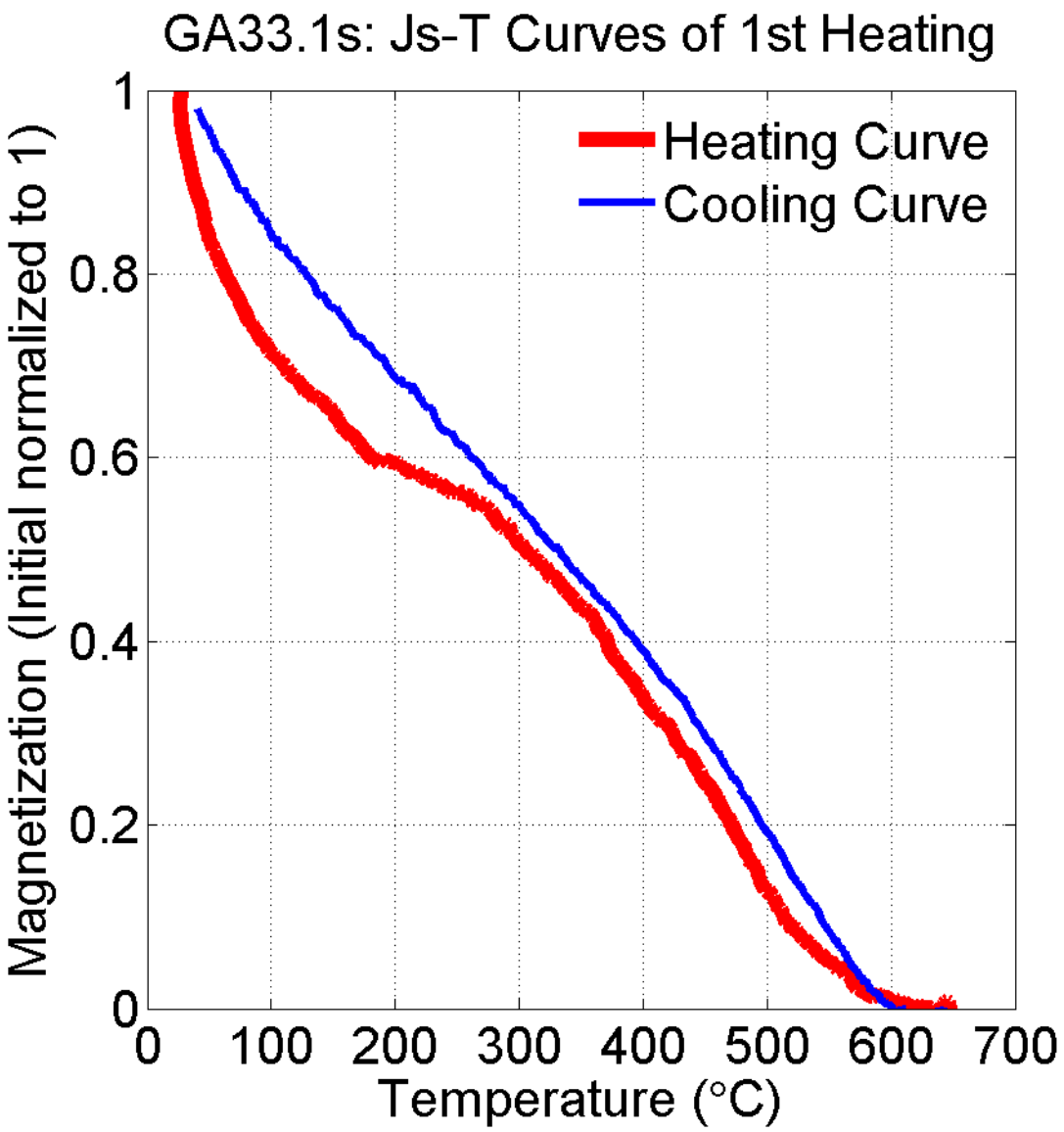

Figure 3.S1-25: Js-T curves of specimen GA33.1s.

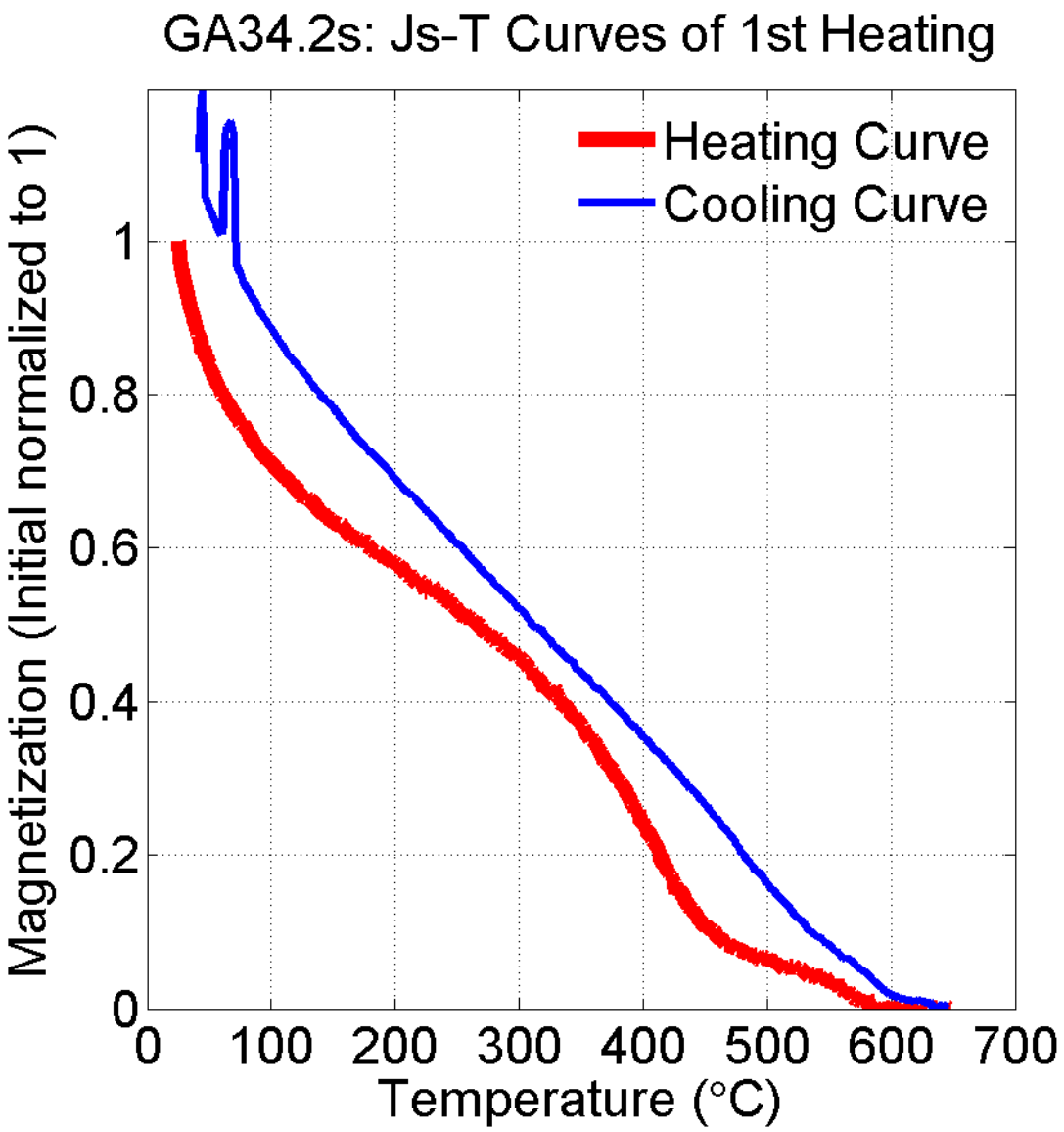

Figure 3.S1-26: Js-T curves of specimen GA34.2s.

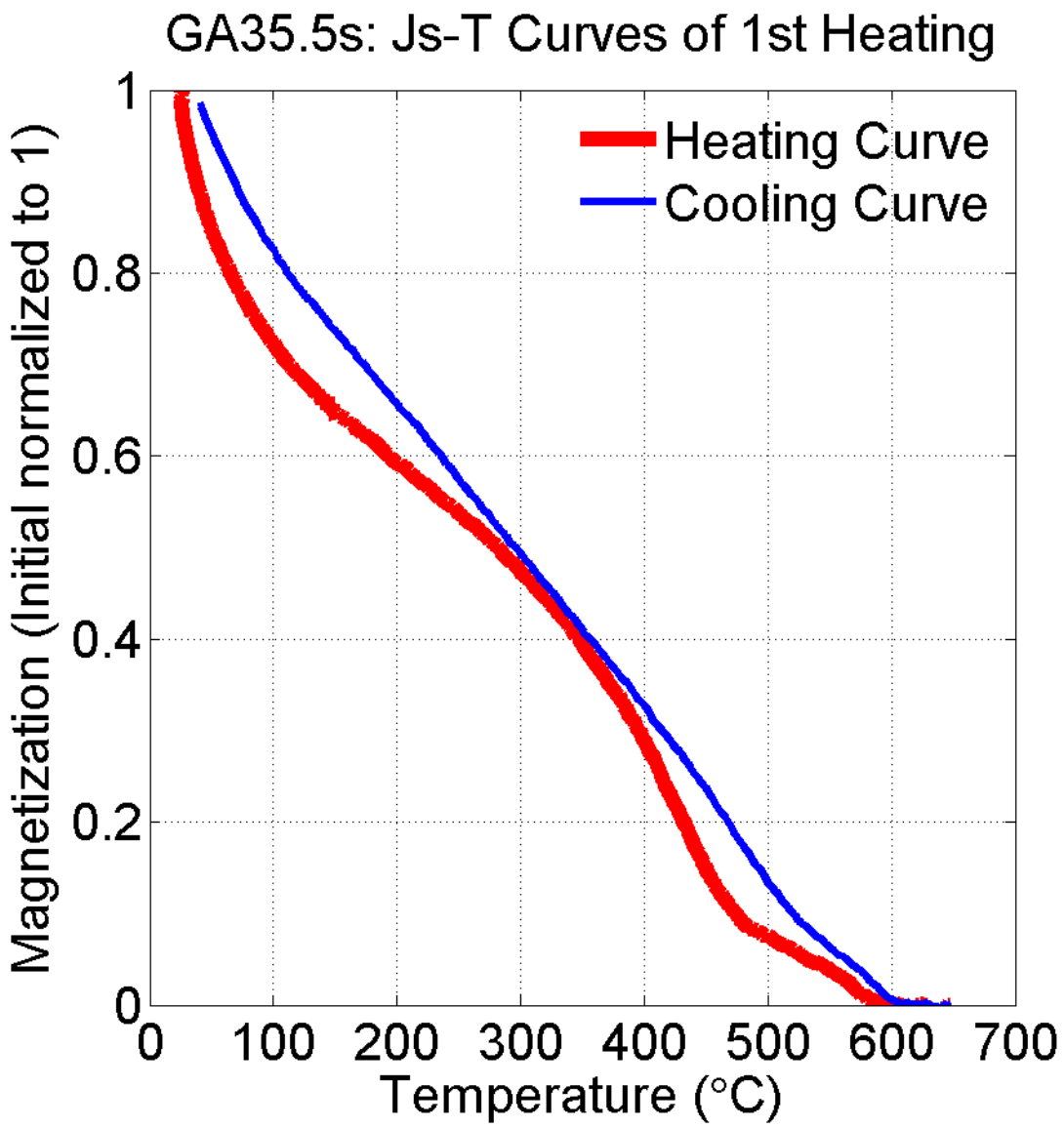

Figure 3.S1-27: Js-T curves of specimen GA35.5s.

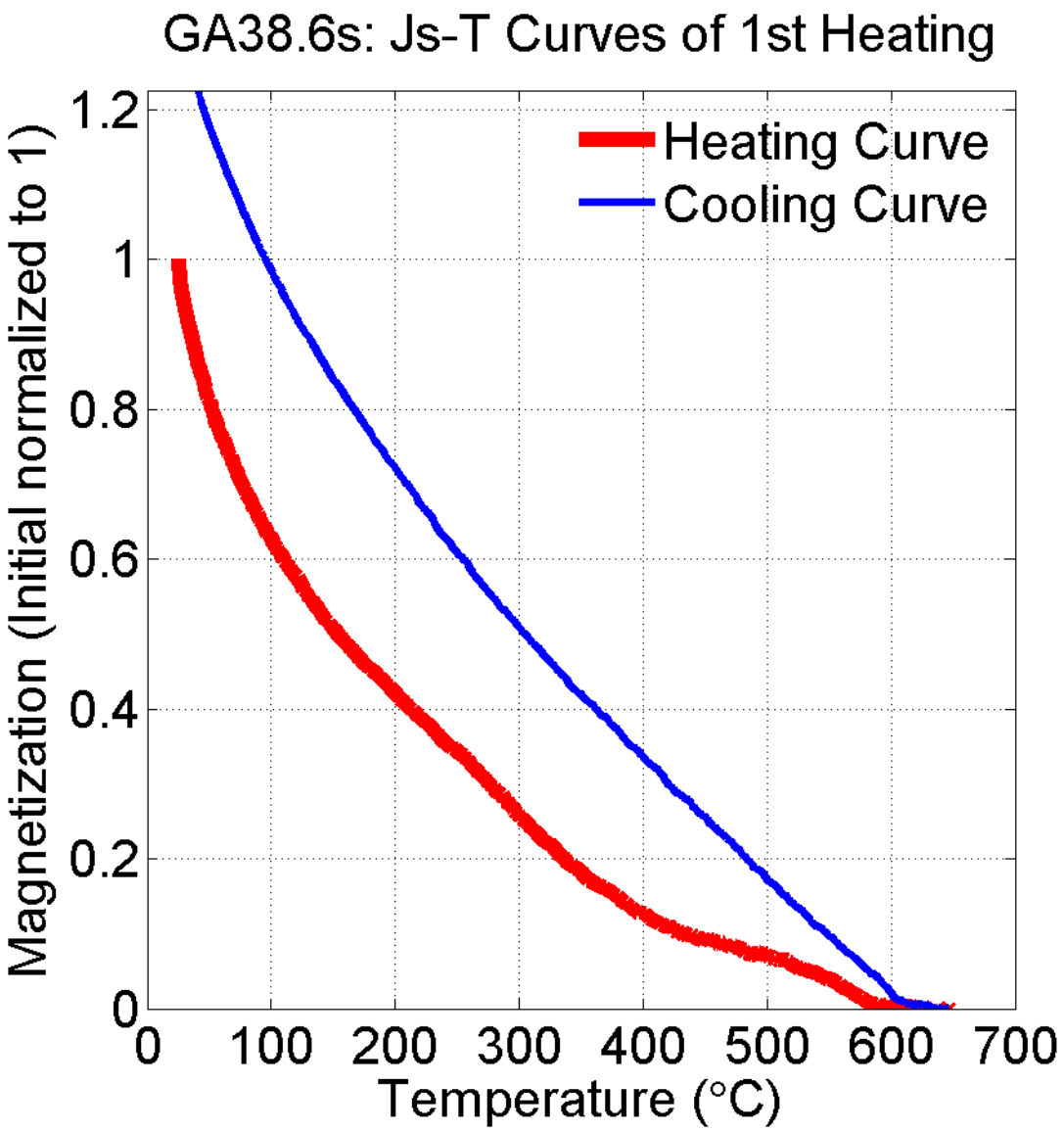

Figure 3.S1-28: Js-T curves of specimen GA38.6s.

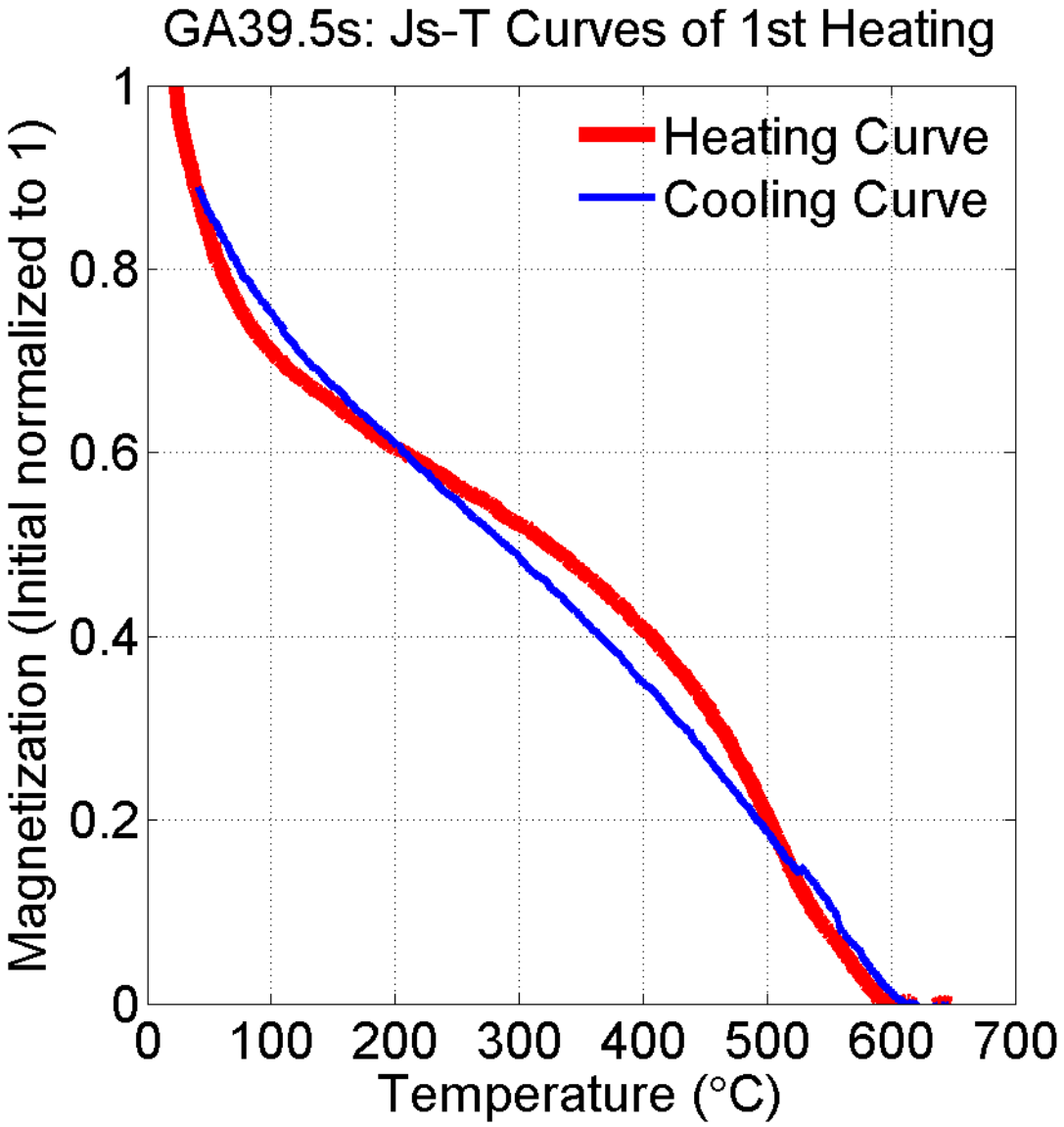

Figure 3.S1-29: Js-T curves of specimen GA39.5s.

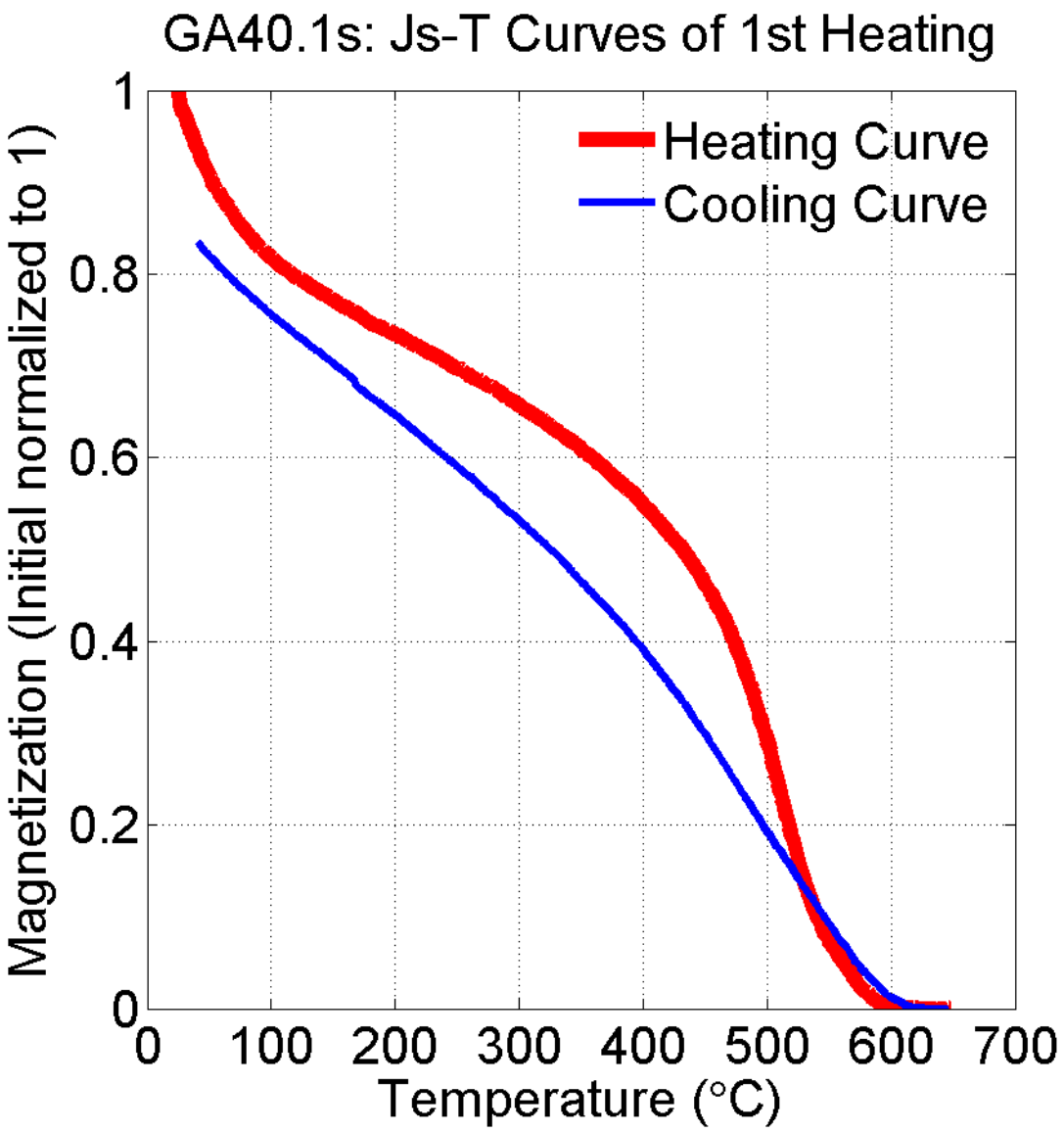

Figure 3.S1-30: Js-T curves of specimen GA40.1s.

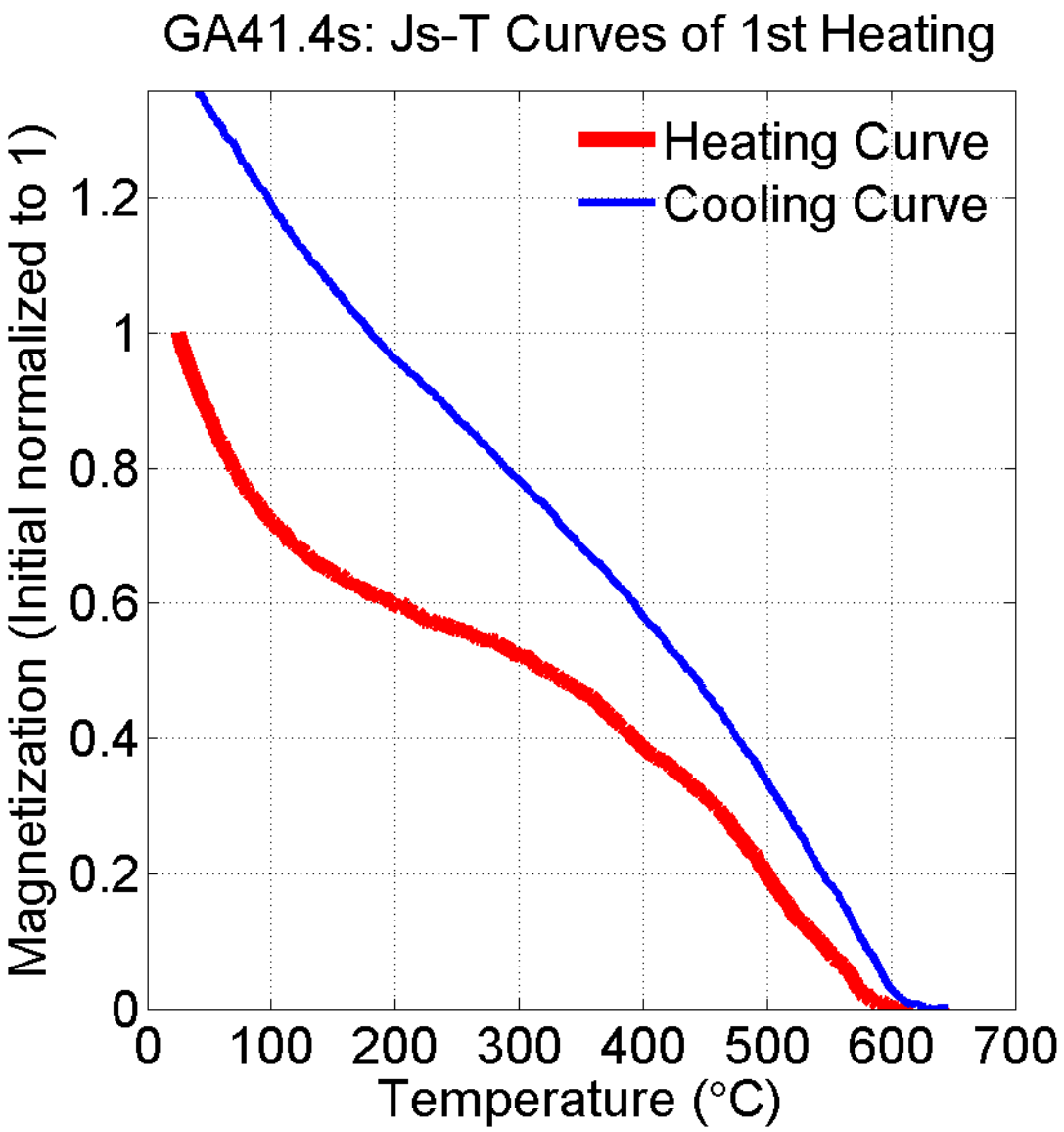

Figure 3.S1-31: Js-T curves of specimen GA41.4s.

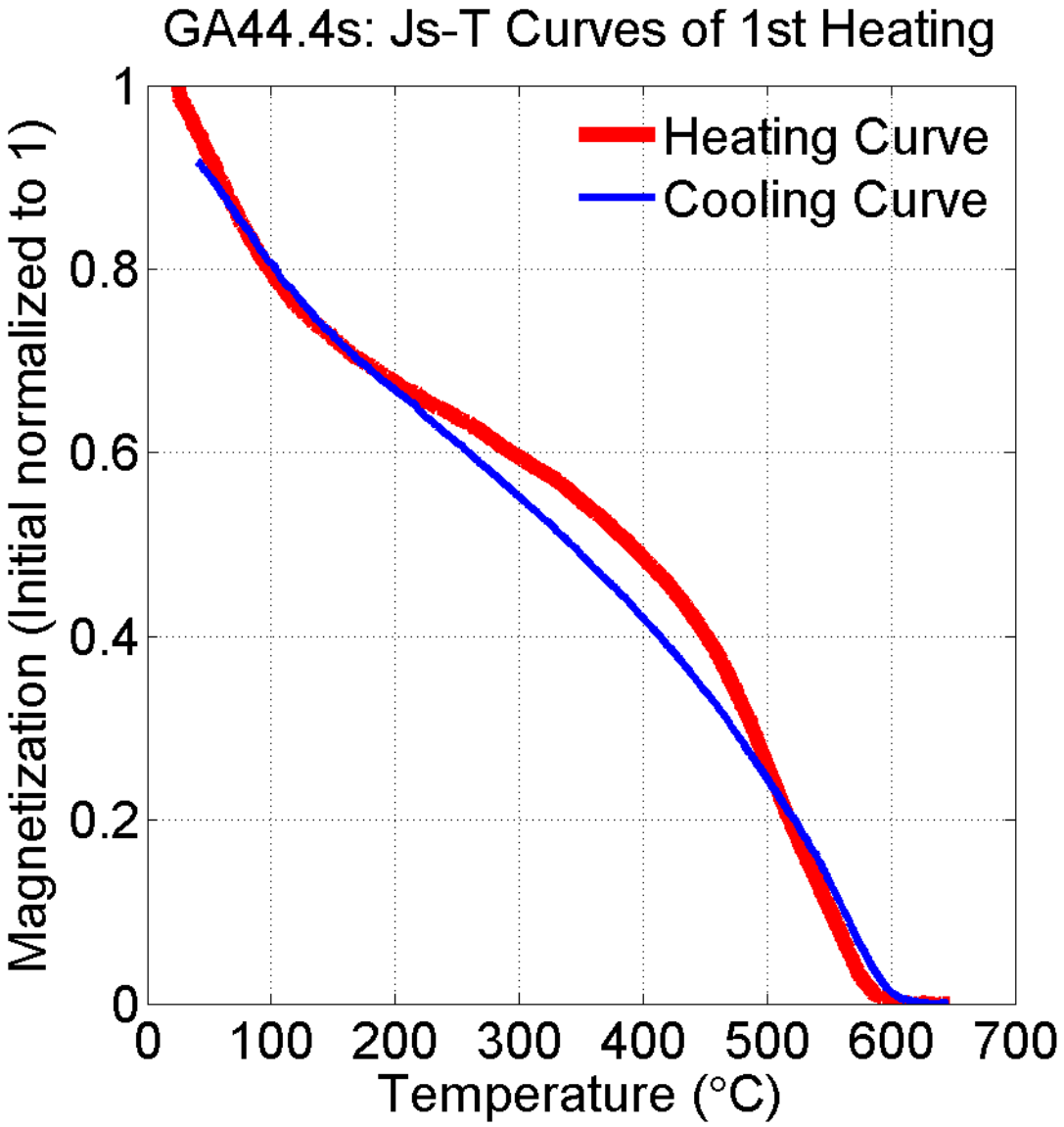

Figure 3.S1-32: Js-T curves of specimen GA44.4s.

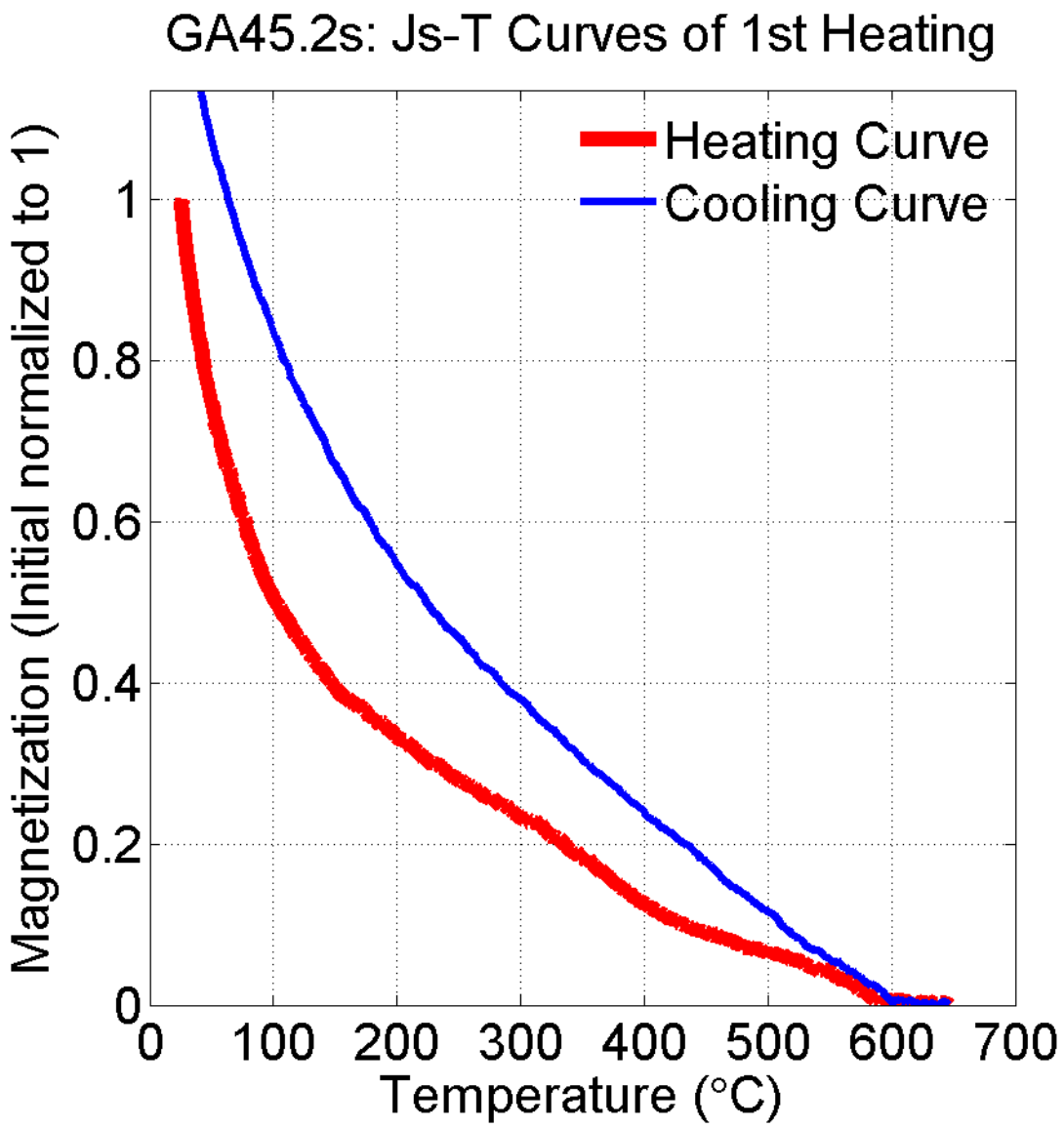

Figure 3.S1-33: Js-T curves of specimen GA45.2s.

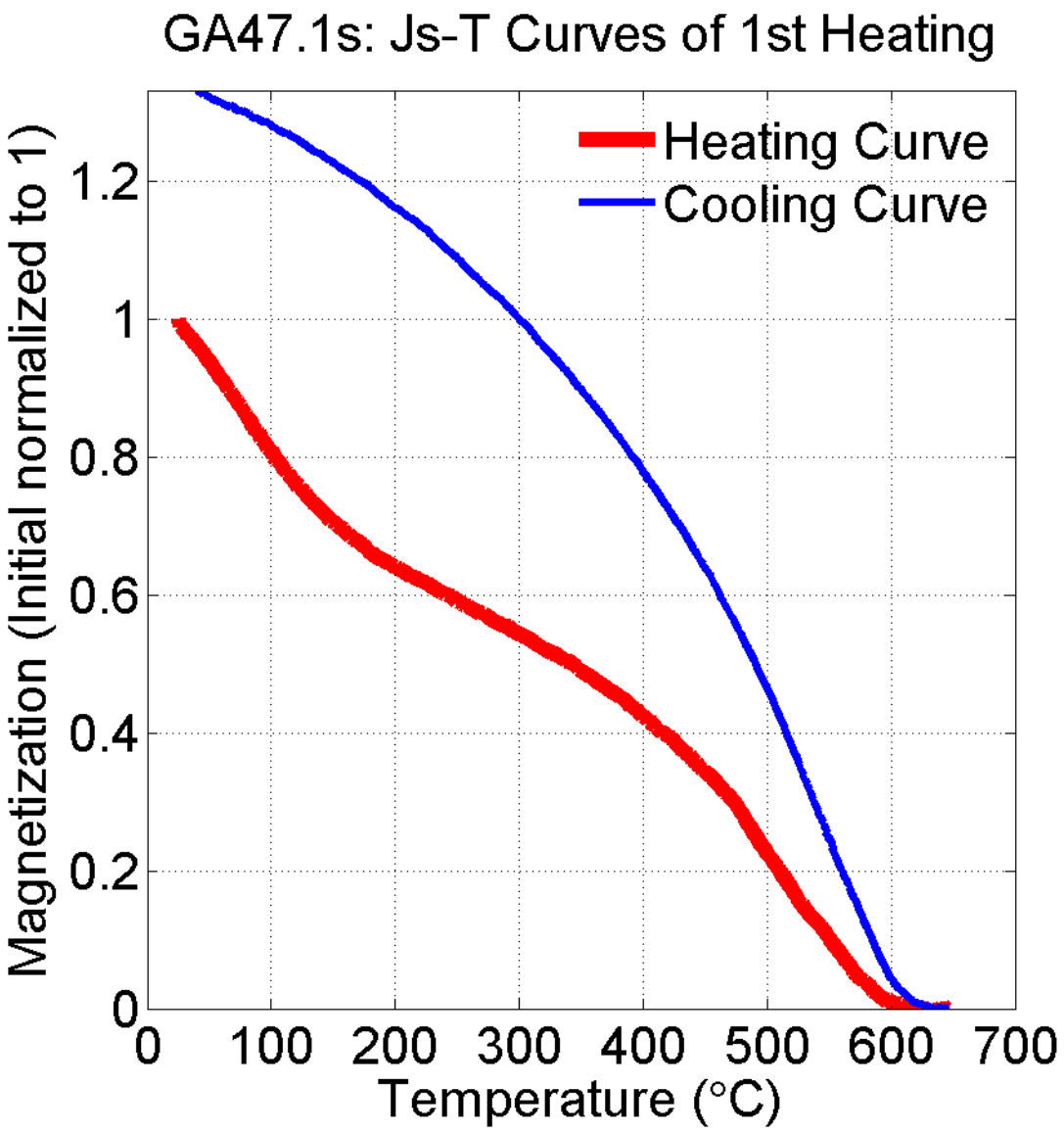

Figure 3.S1-34: Js-T curves of specimen GA47.1s.

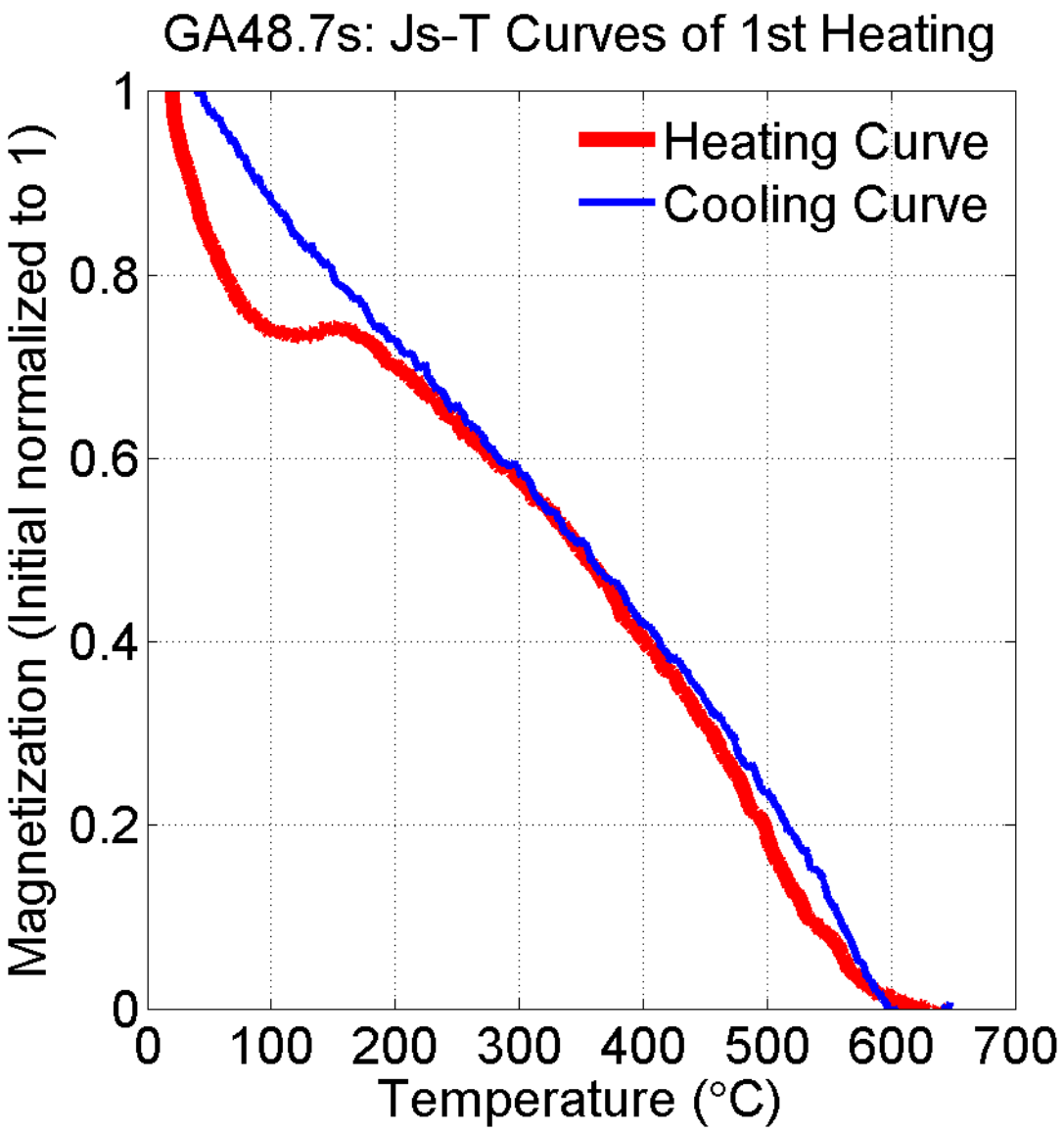

Figure 3.S1-35: Js-T curves of specimen GA48.7s.

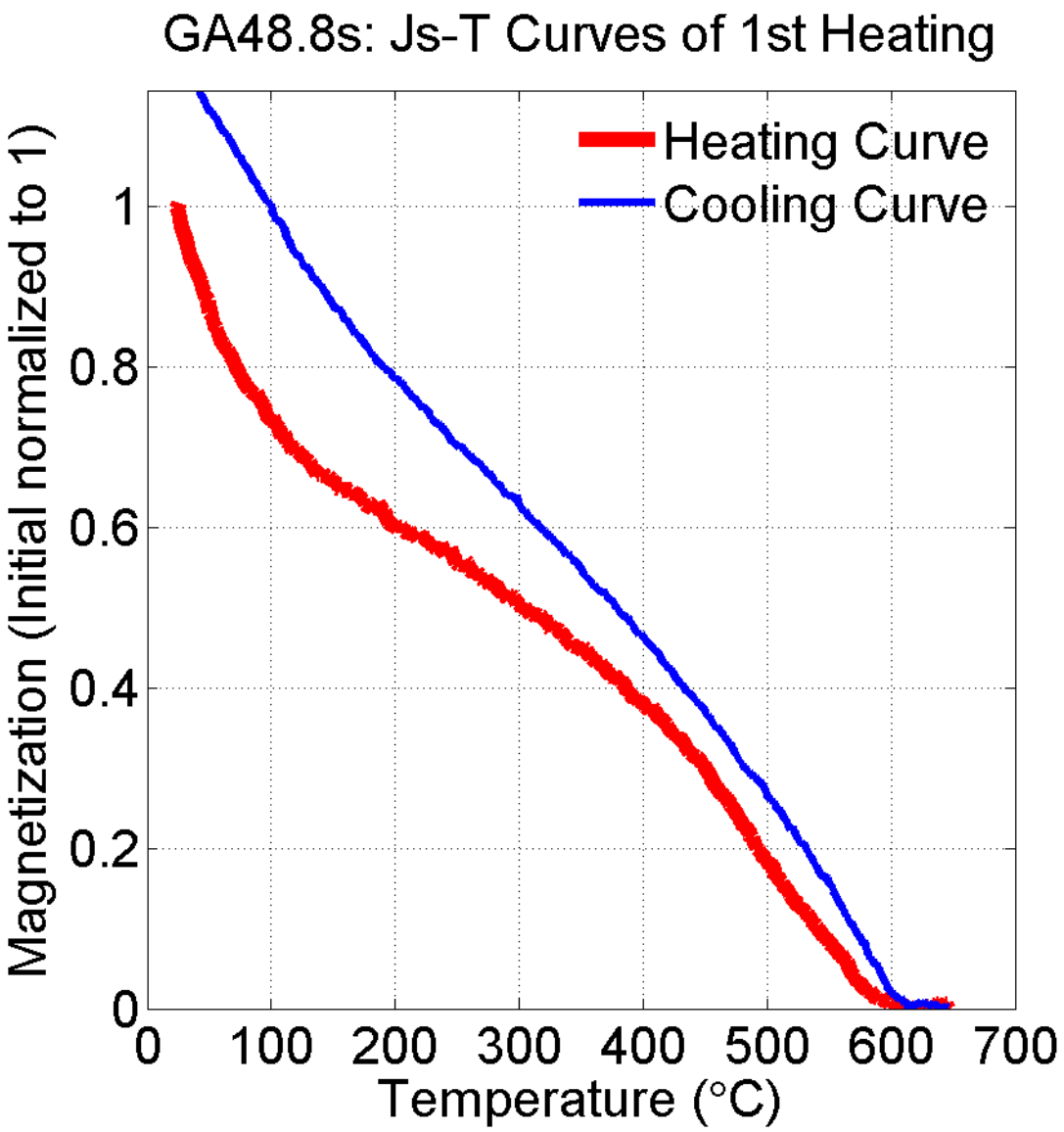

Figure 3.S1-36: Js-T curves of specimen GA48.8s.

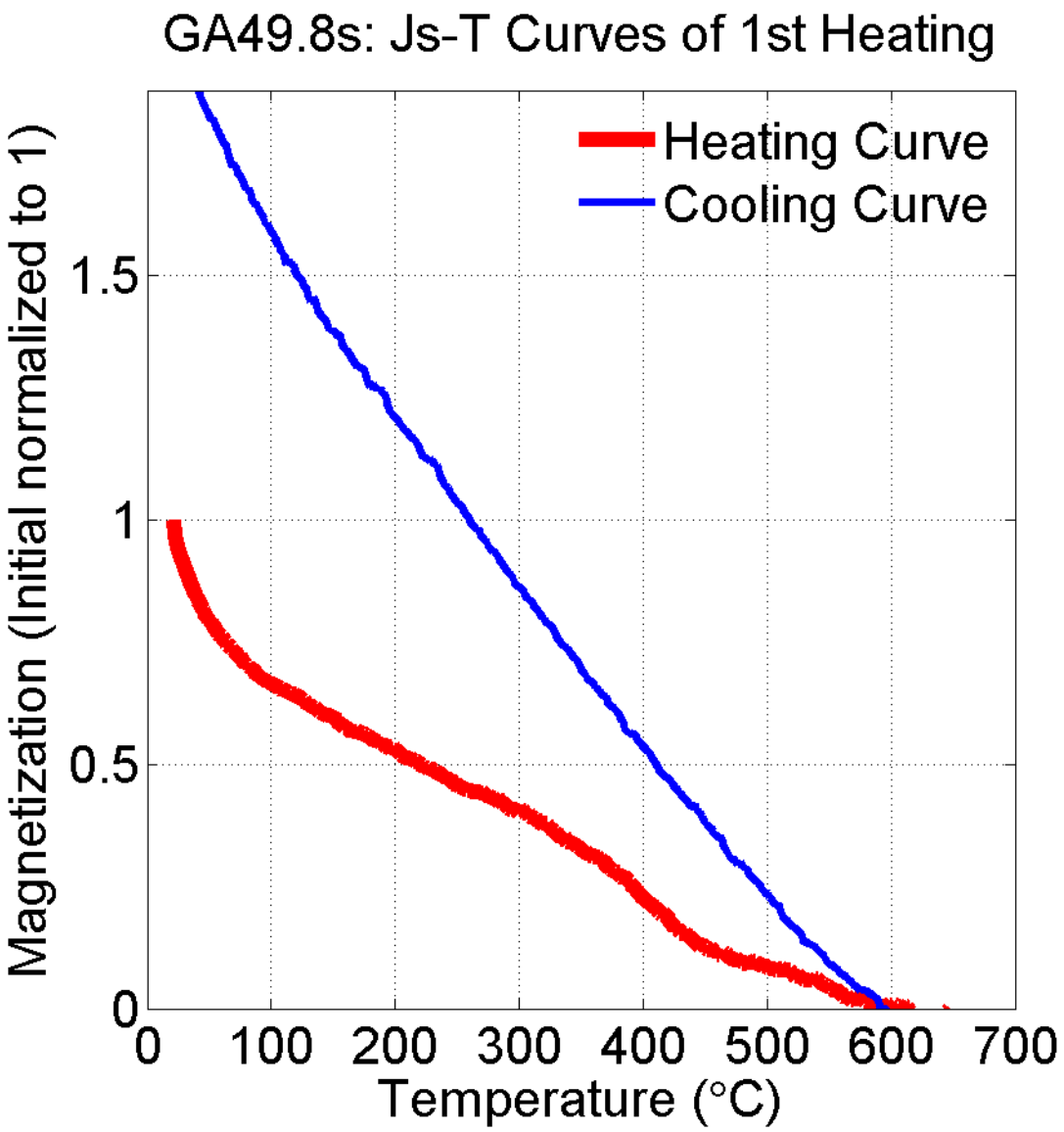

Figure 3.S1-37: Js-T curves of specimen GA49.8s.

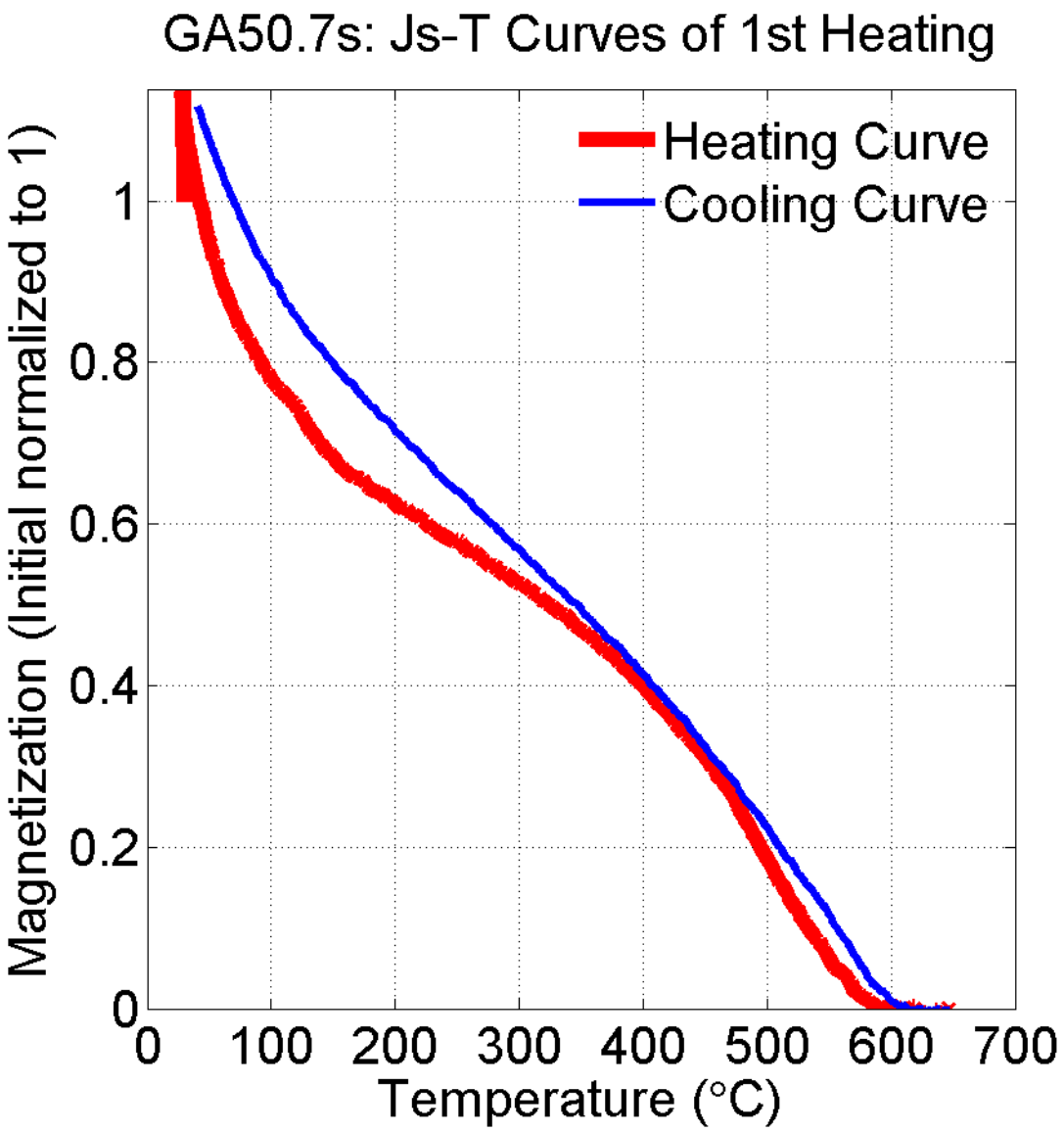

Figure 3.S1-38: Js-T curves of specimen GA50.7s.

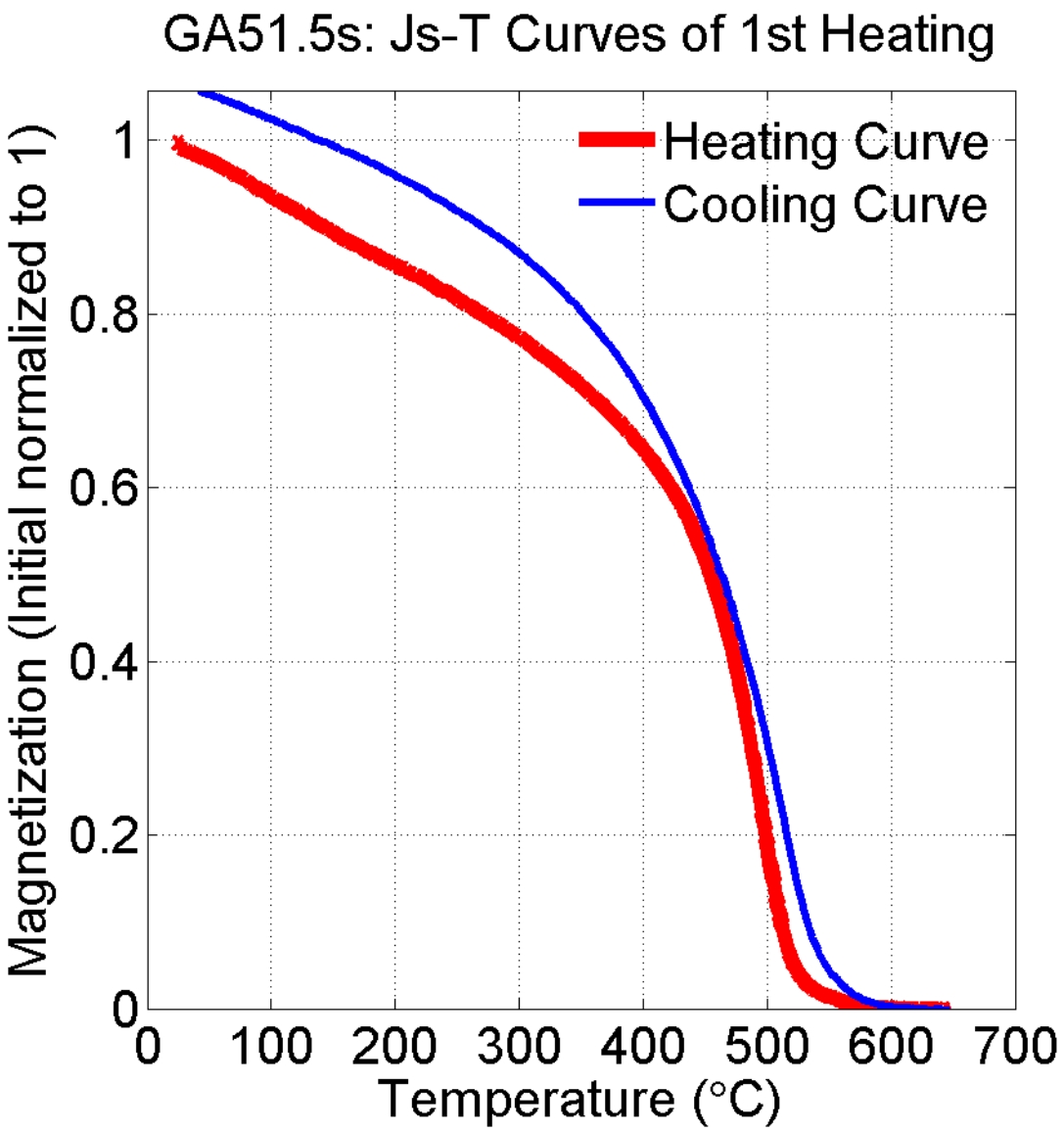

Figure 3.S1-39: Js-T curves of specimen GA51.5s.

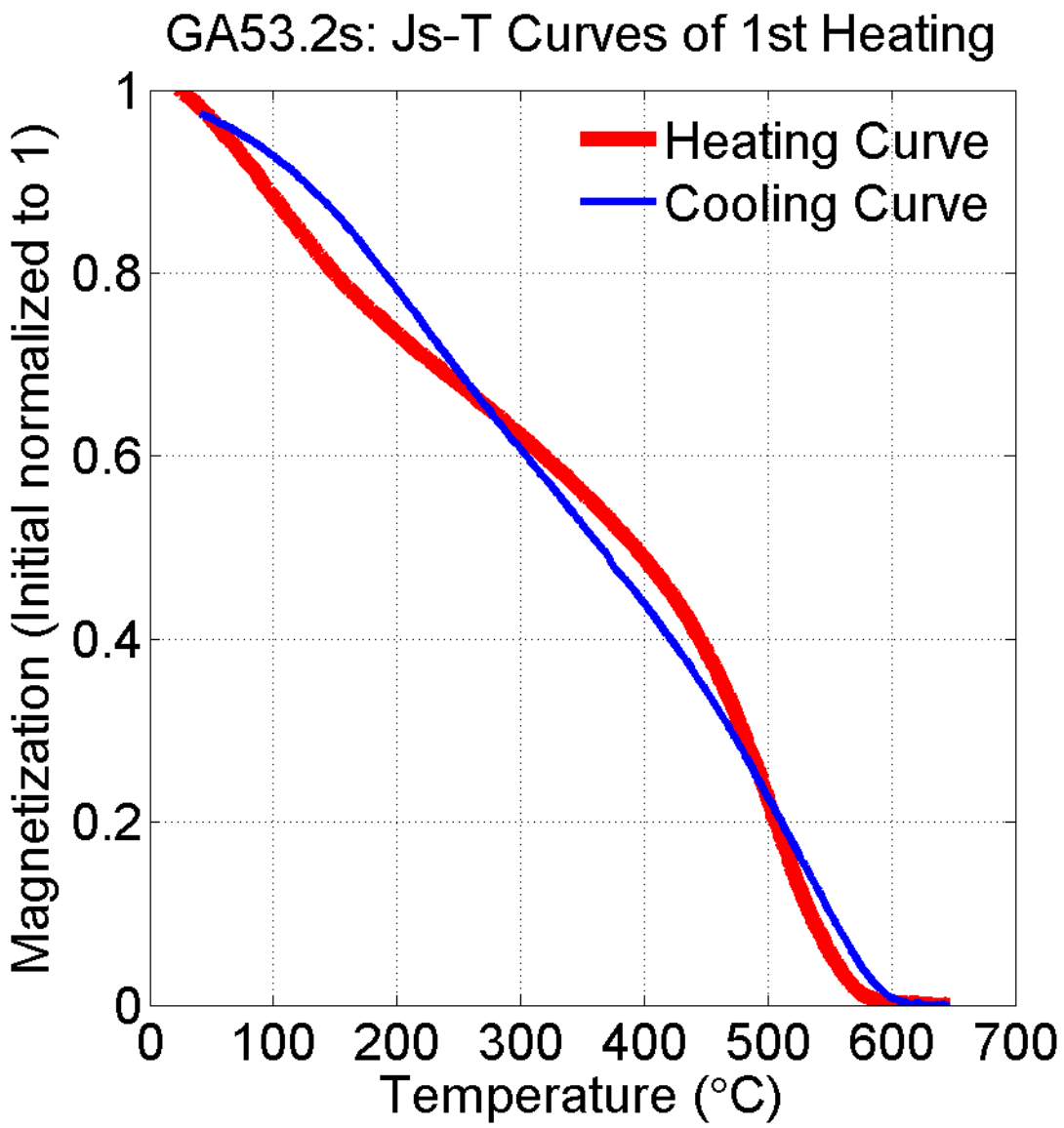

Figure 3.S1-40: Js-T curves of specimen GA53.2s.

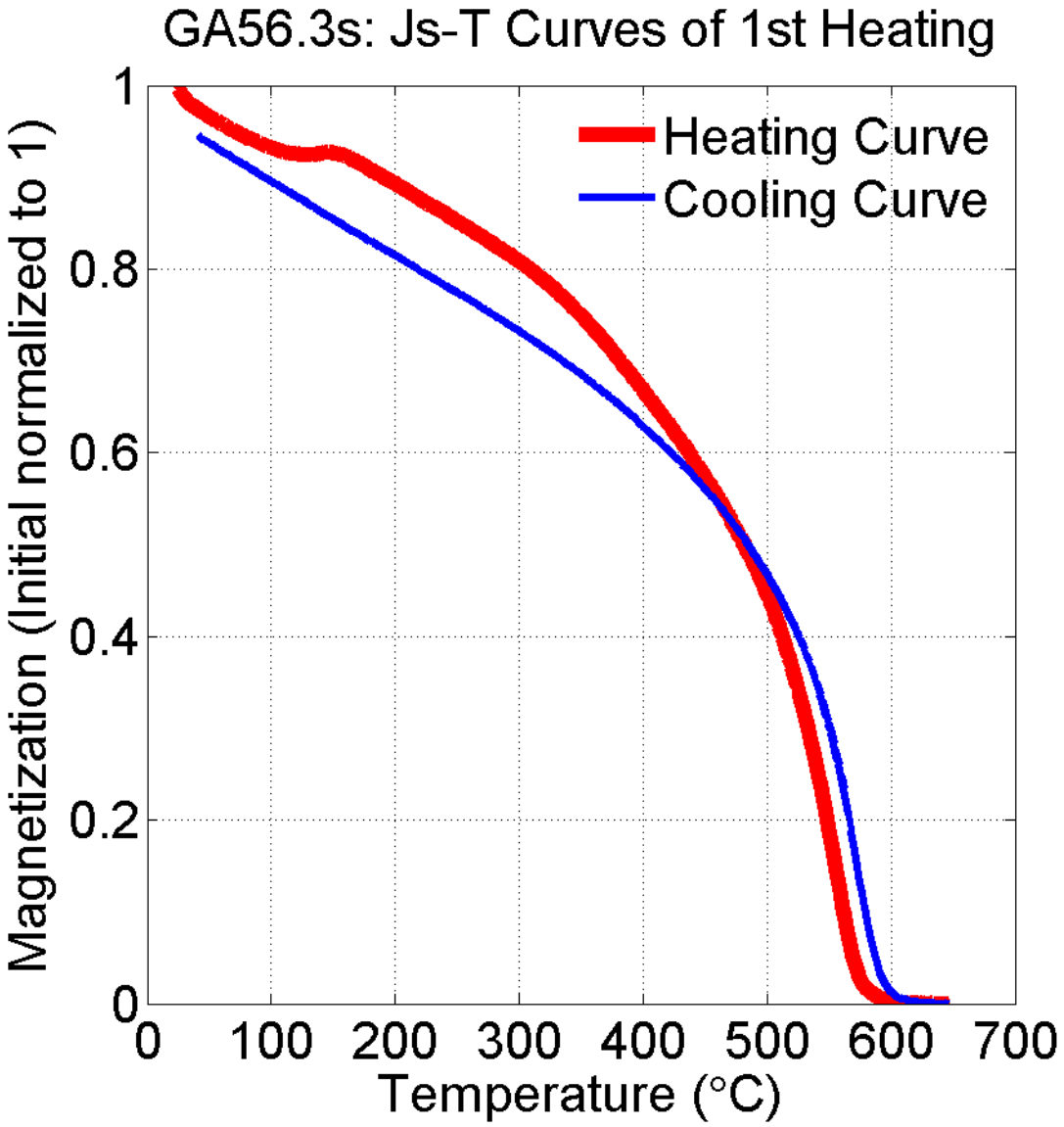

Figure 3.S1-41: Js-T curves of specimen GA56.3s.

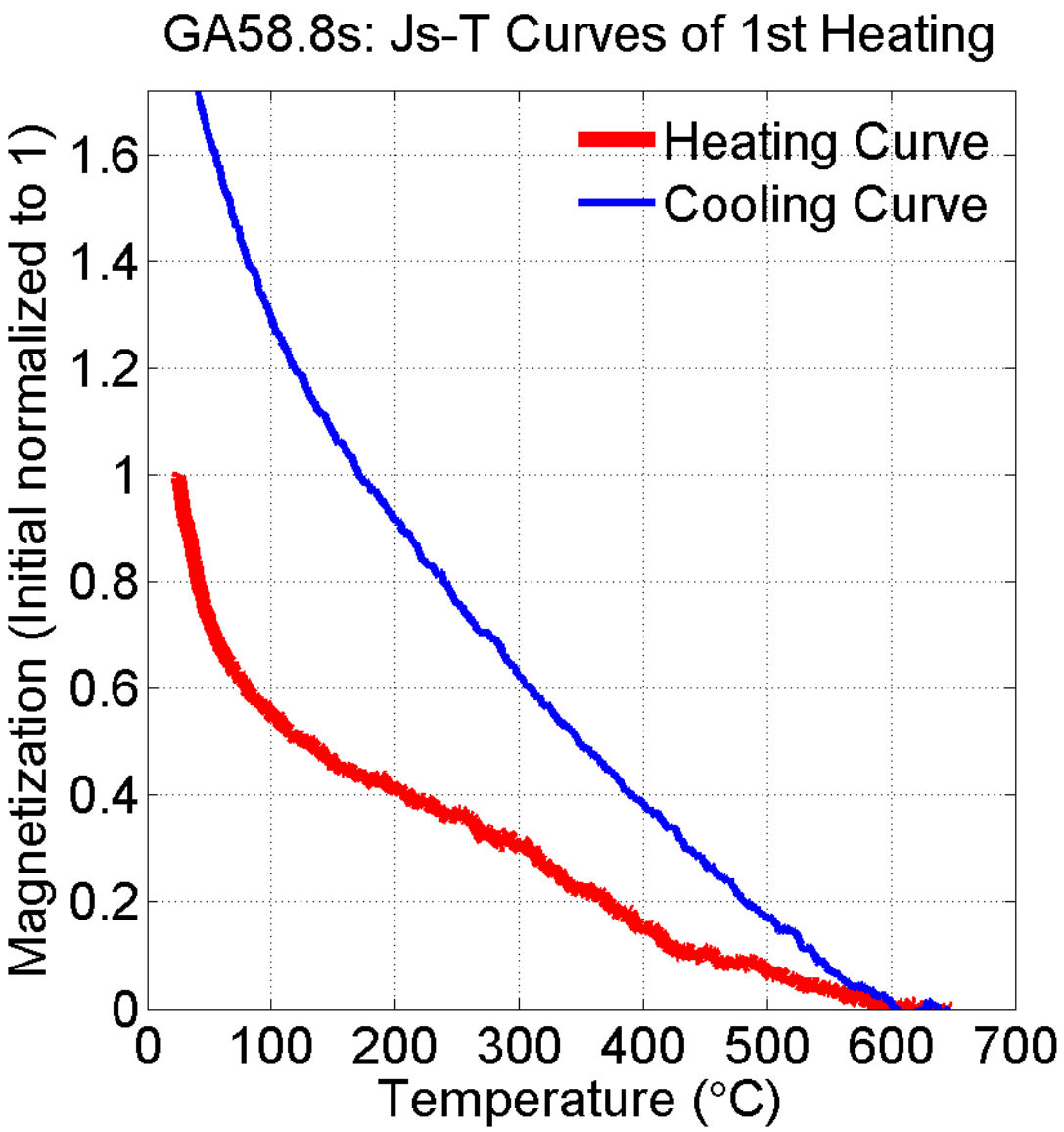

Figure 3.S1-42: Js-T curves of specimen GA58.8s.

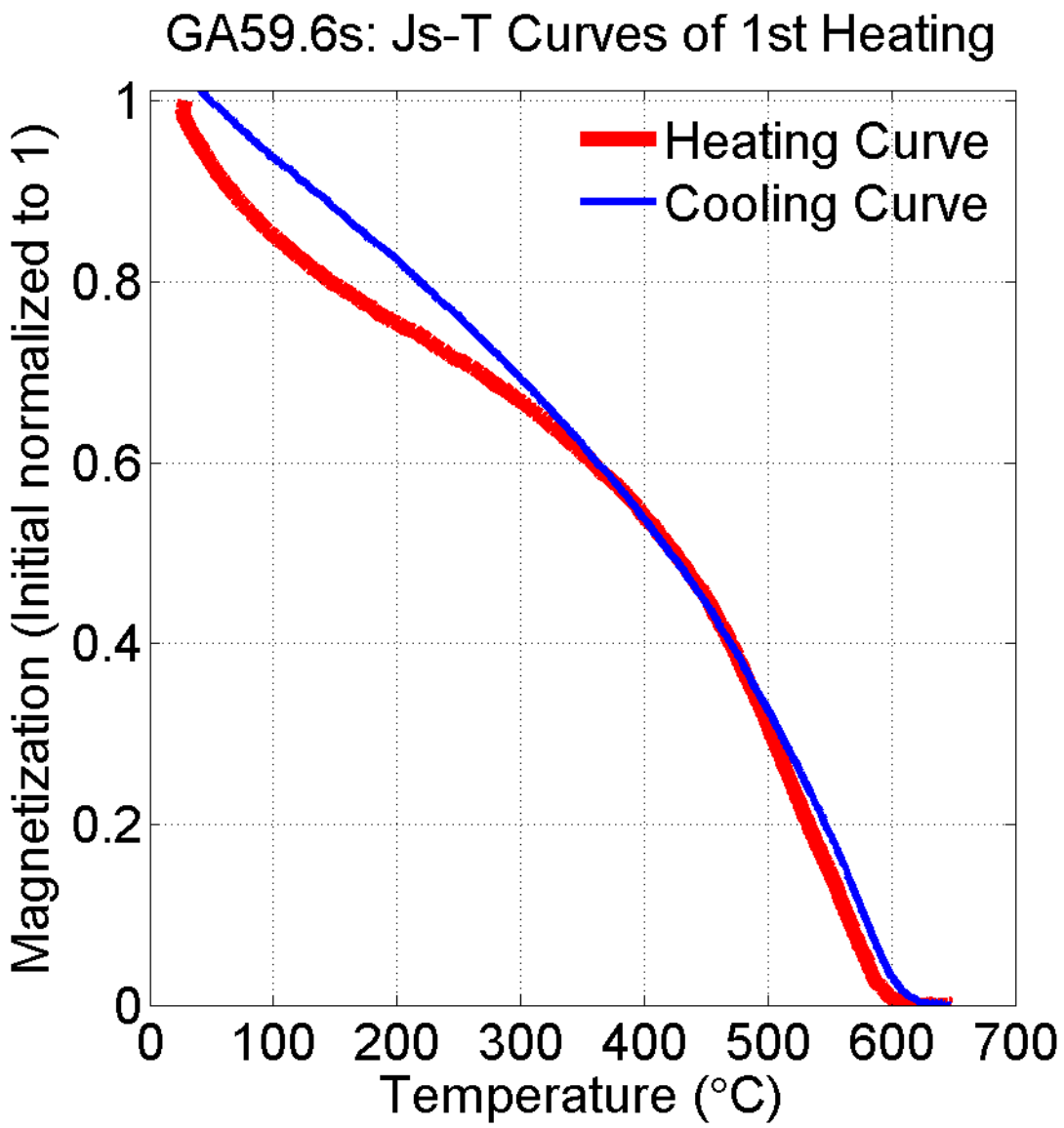

Figure 3.S1-43: Js-T curves of specimen GA59.6s.

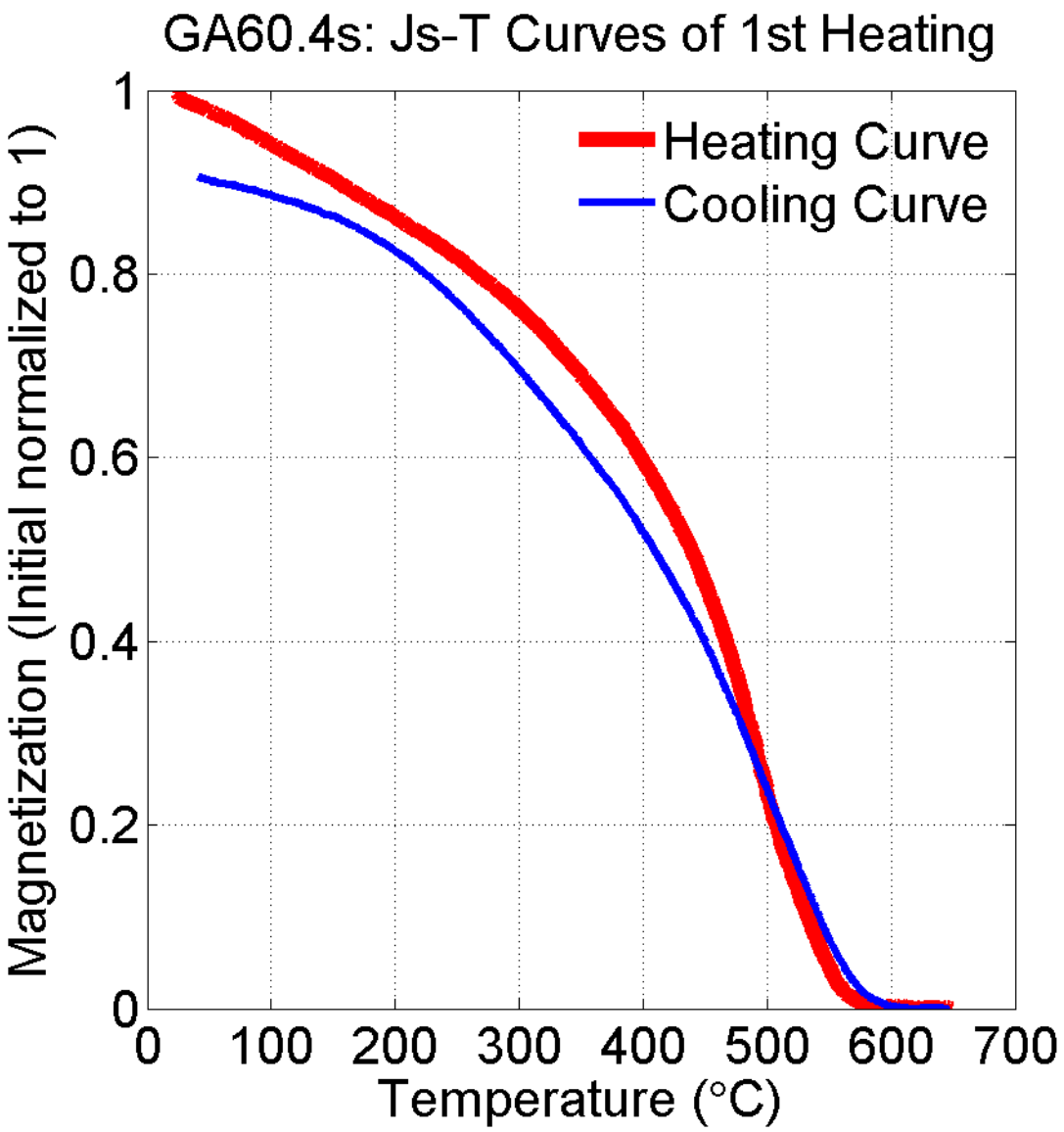

Figure 3.S1-44: Js-T curves of specimen GA60.4s.

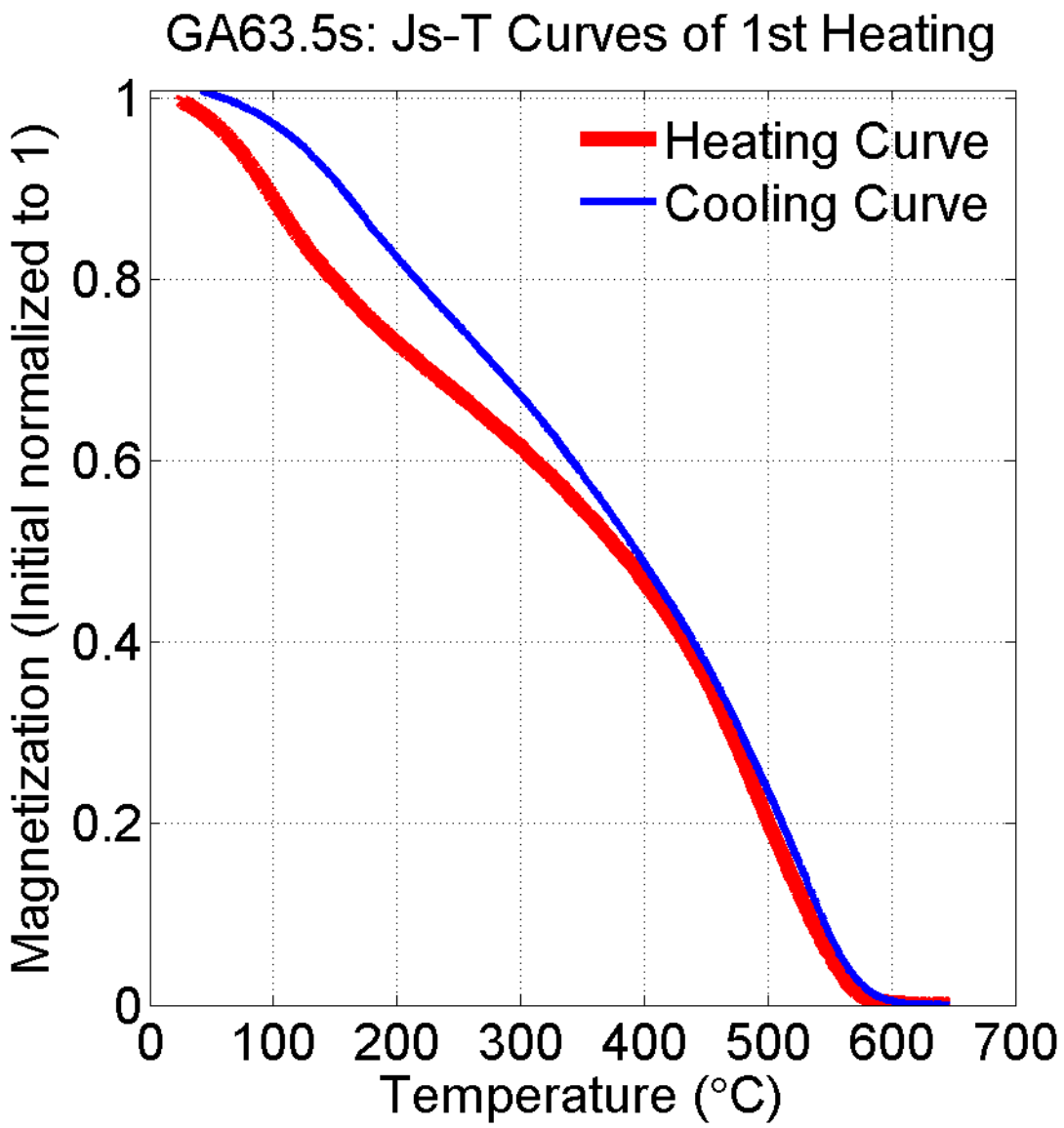

Figure 3.S1-45: Js-T curves of specimen GA63.5s.

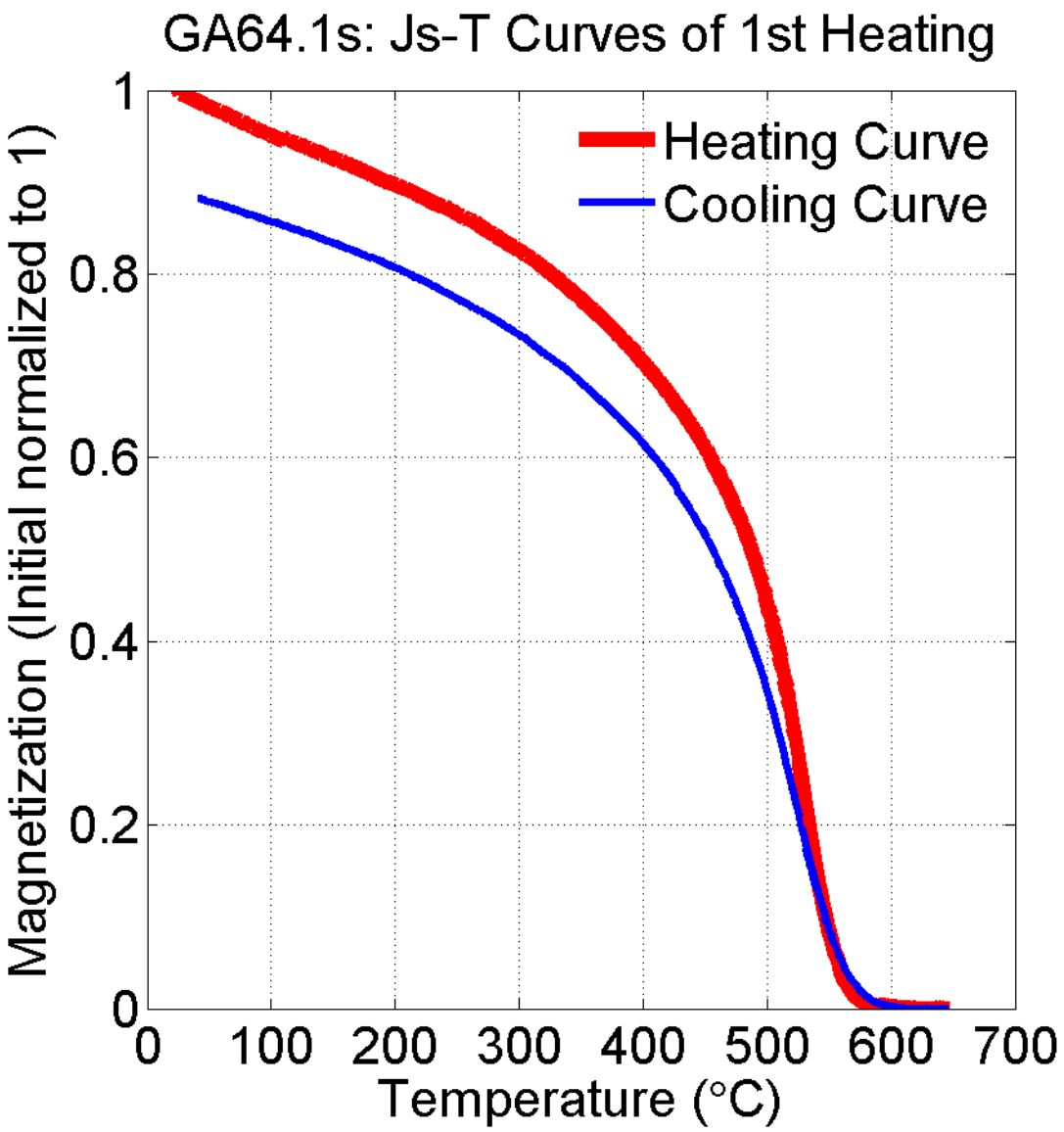

Figure 3.S1-46: Js-T curves of specimen GA64.1s.

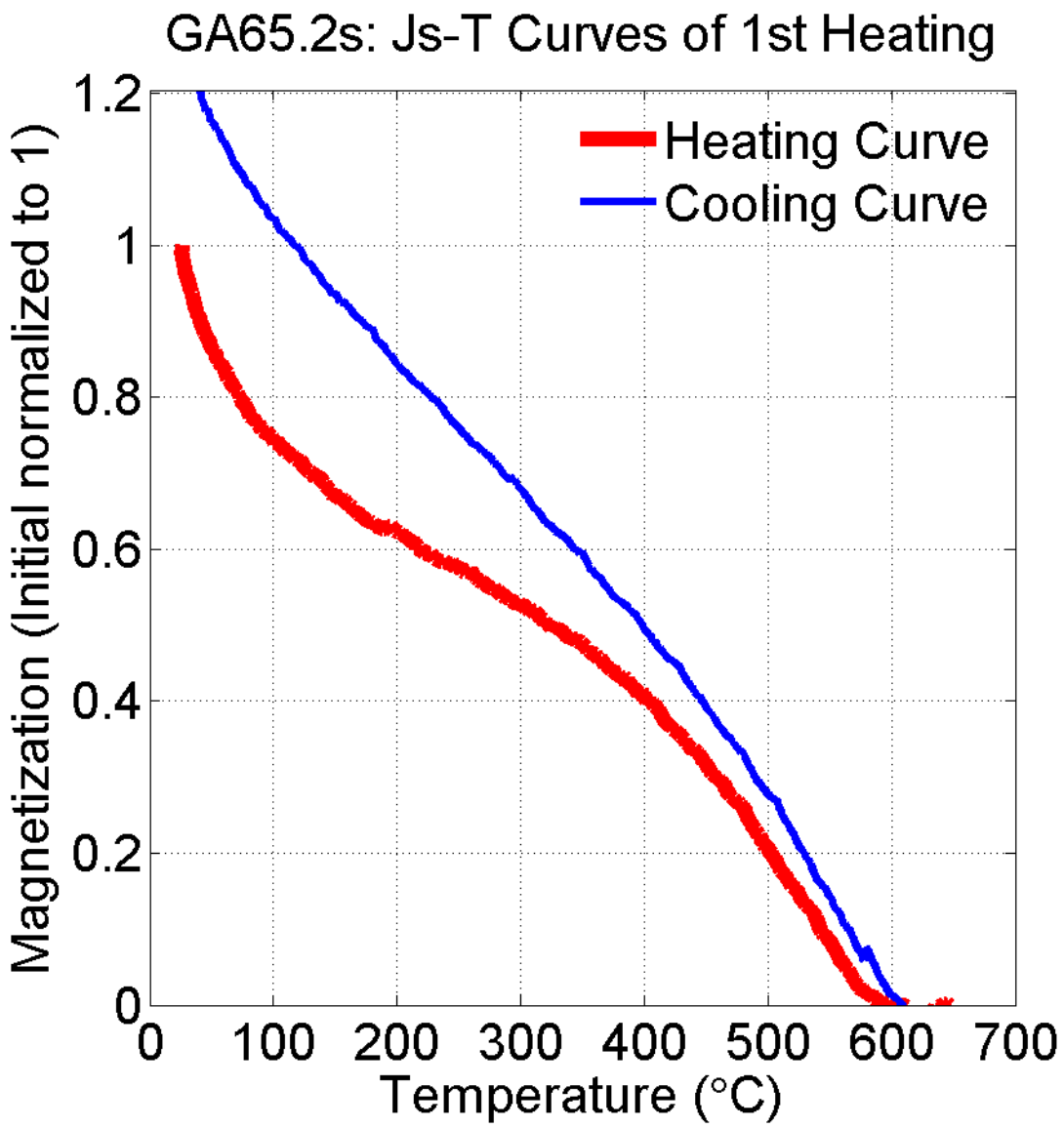

Figure 3.S1-47: Js-T curves of specimen GA65.2s.

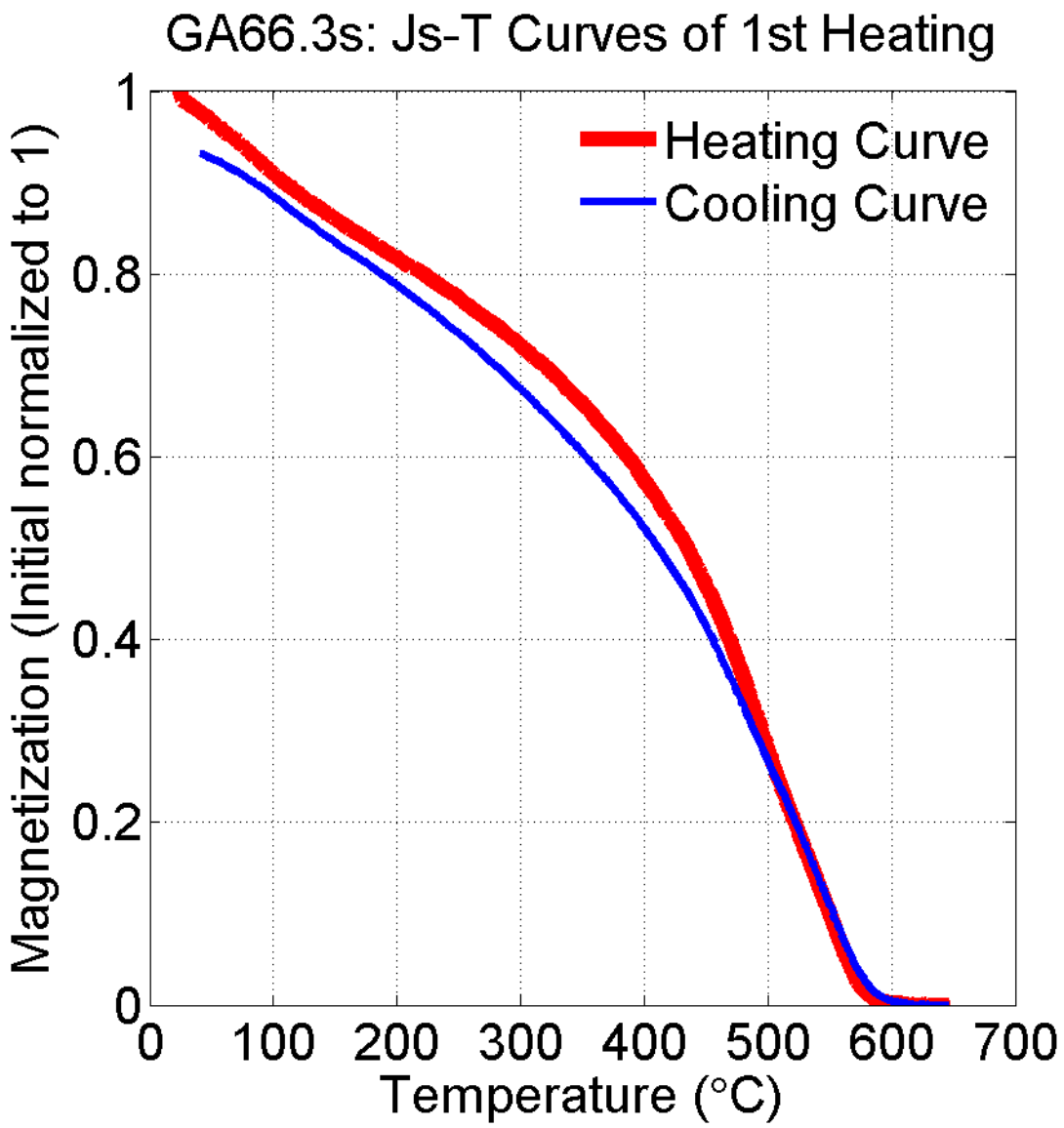

Figure 3.S1-48: Js-T curves of specimen GA66.3s.

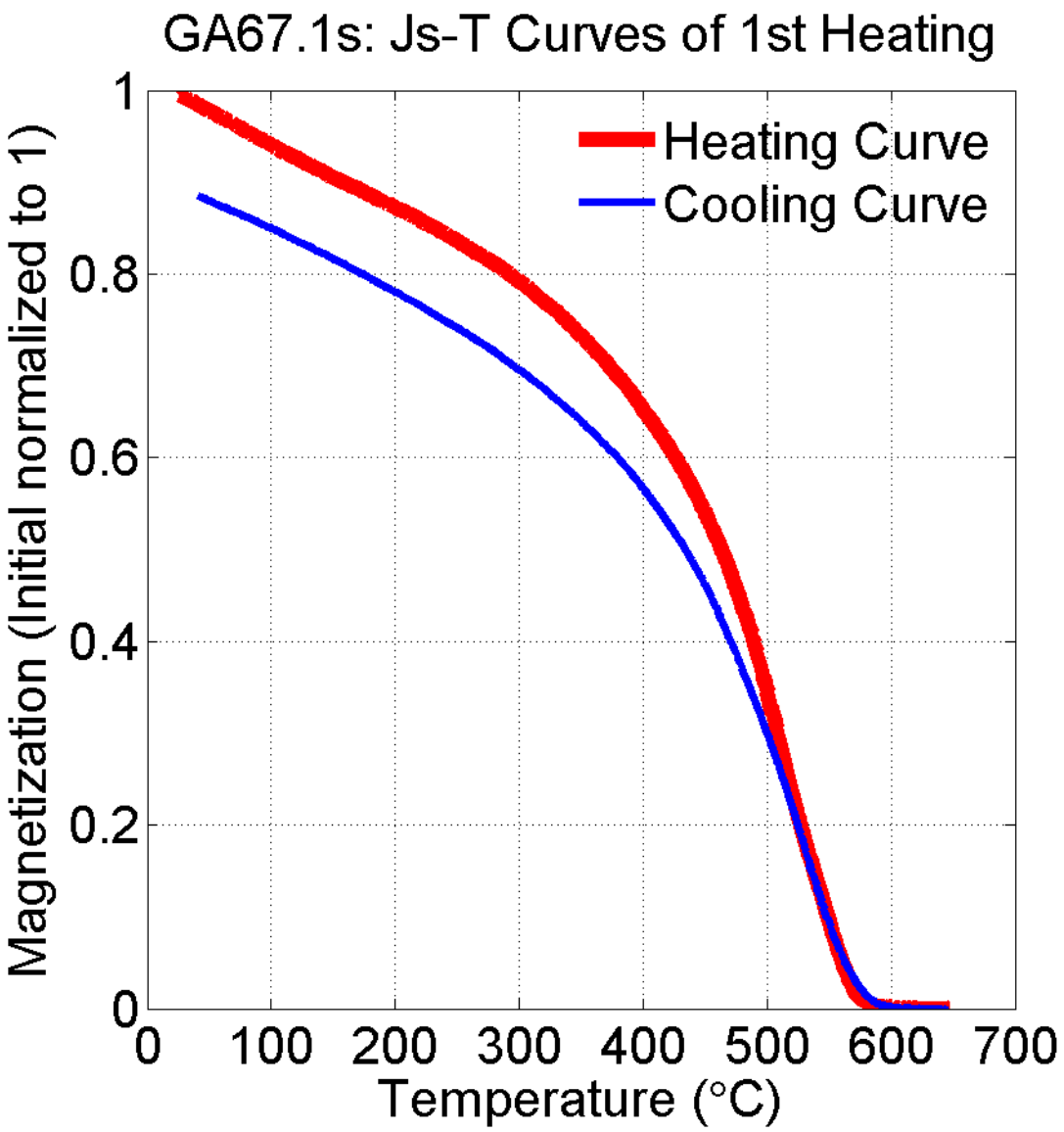

Figure 3.S1-49: Js-T curves of specimen GA67.1s.

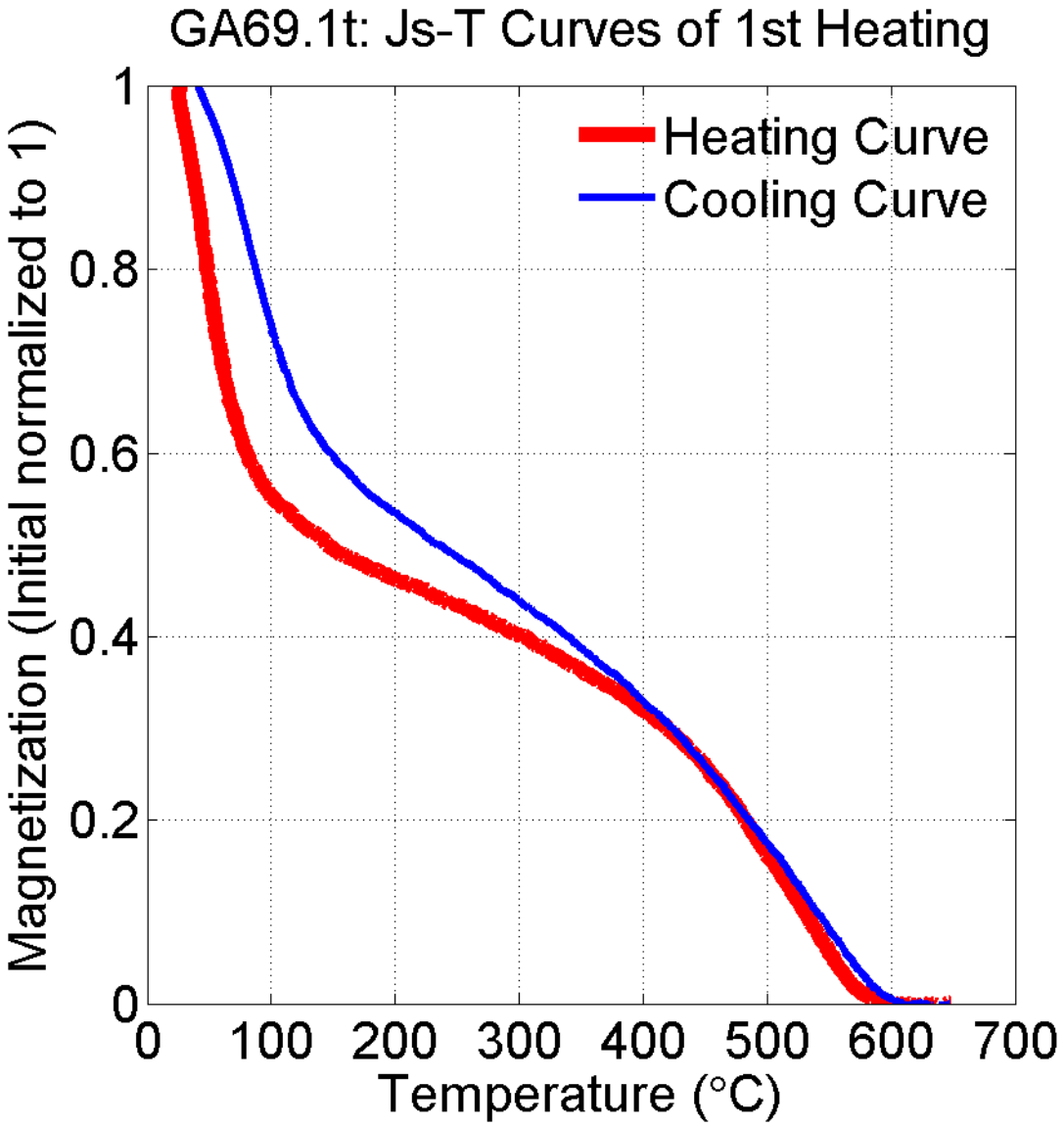

Figure 3.S1-50: Js-T curves of specimen GA69.1t.

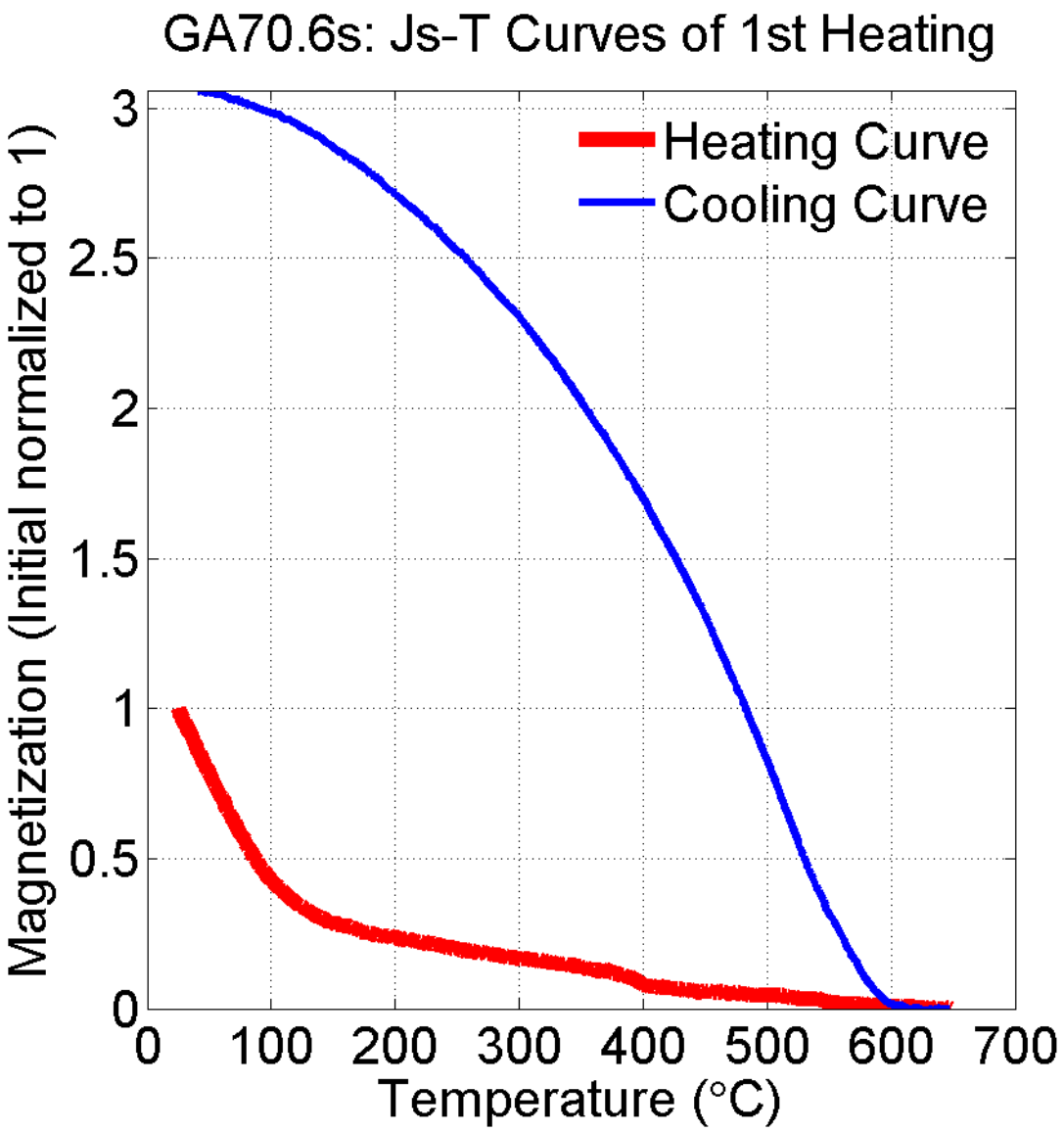

Figure 3.S1-51: Js-T curves of specimen GA70.6s.

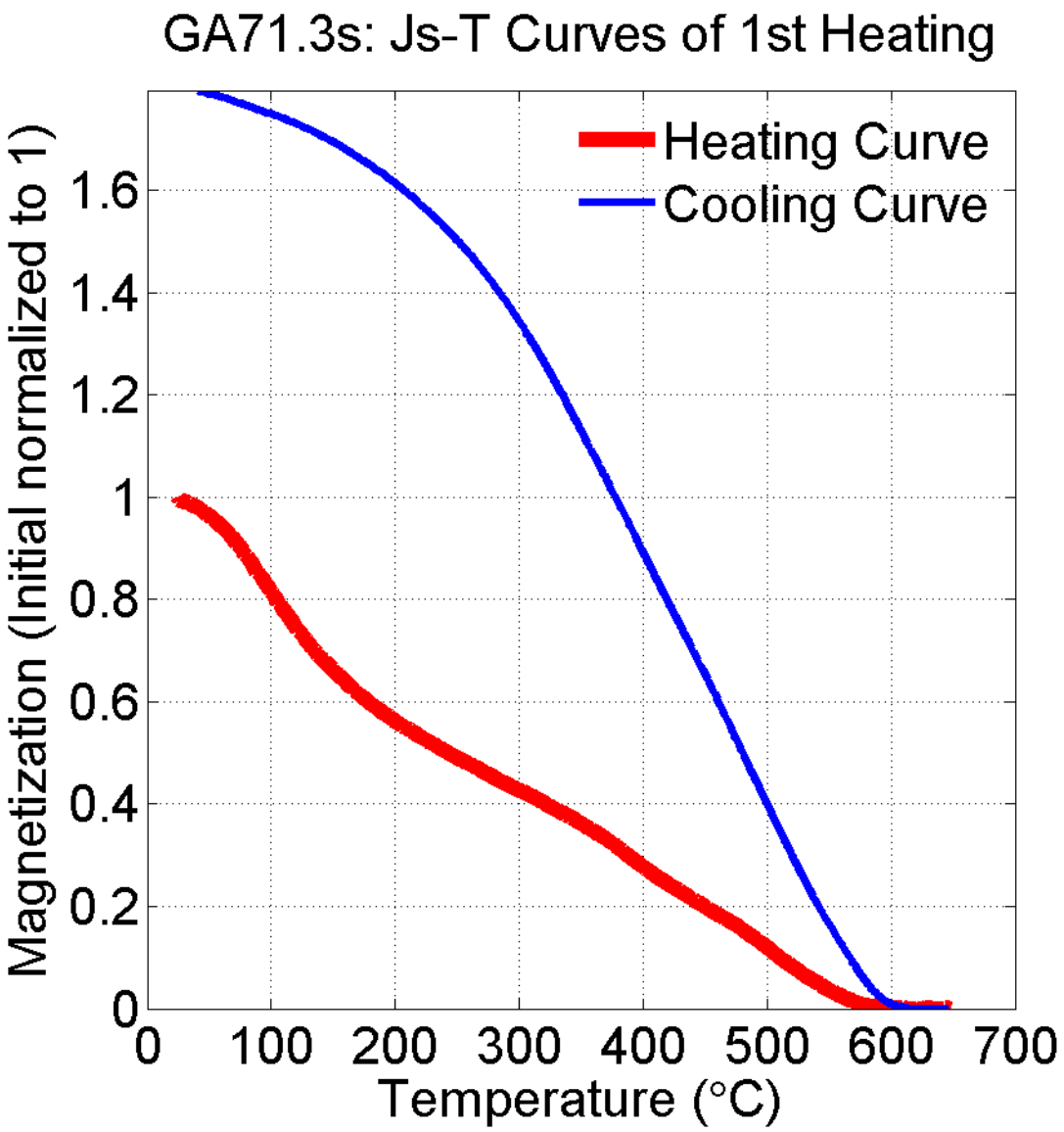

Figure 3.S1-52: Js-T curves of specimen GA71.3s.

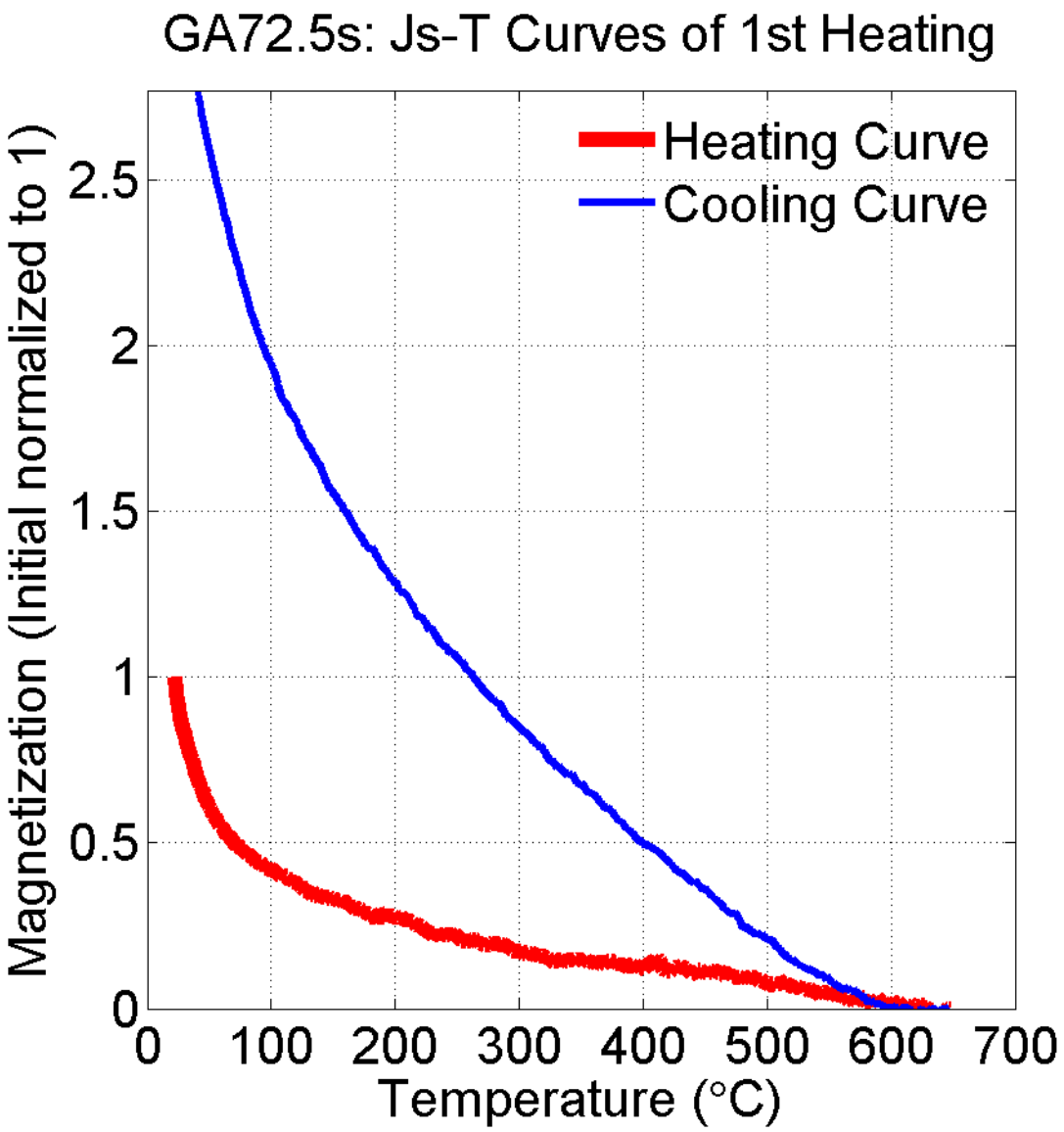

Figure 3.S1-53: Js-T curves of specimen GA72.5s.

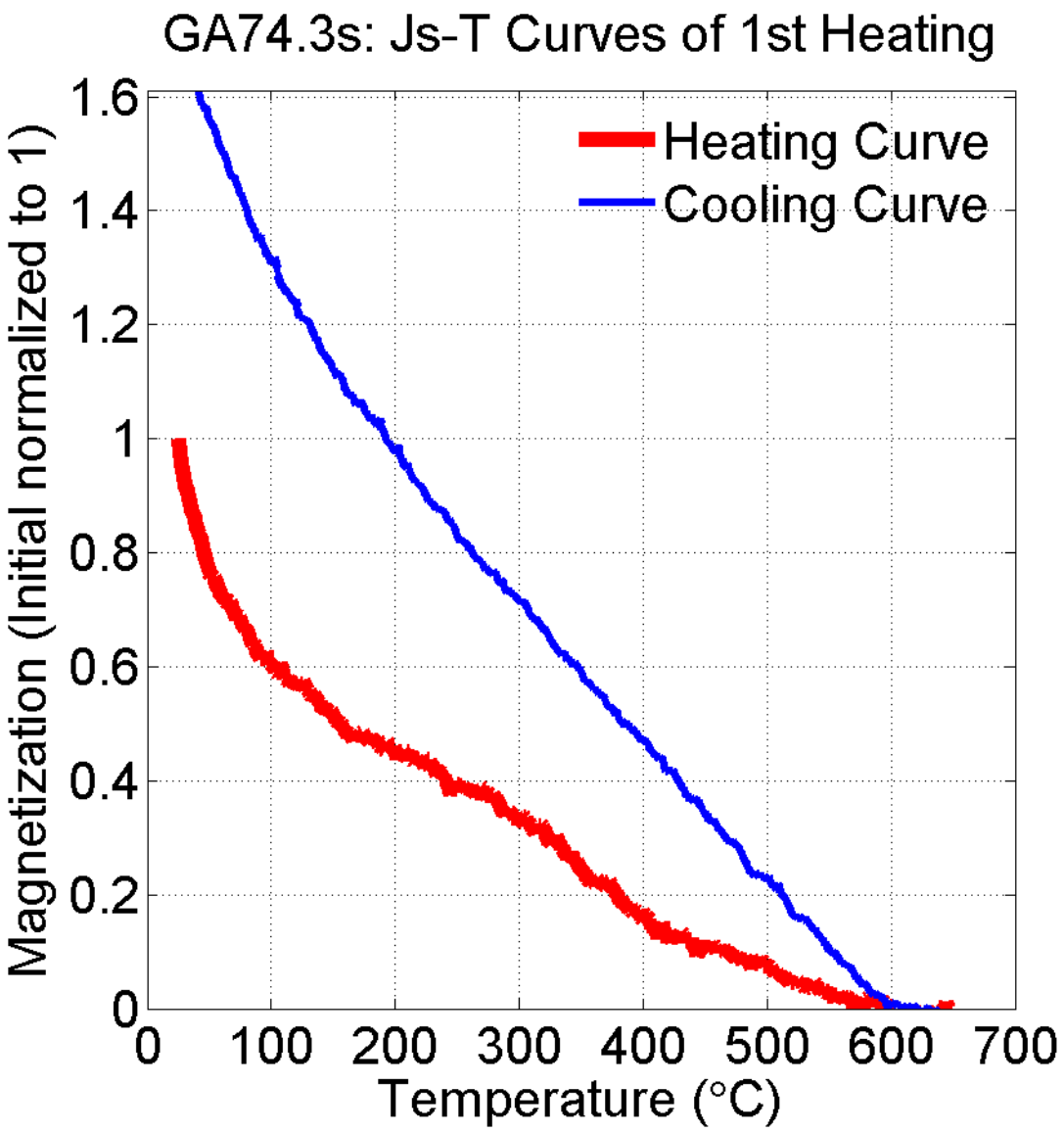

Figure 3.S1-54: Js-T curves of specimen GA74.3s.

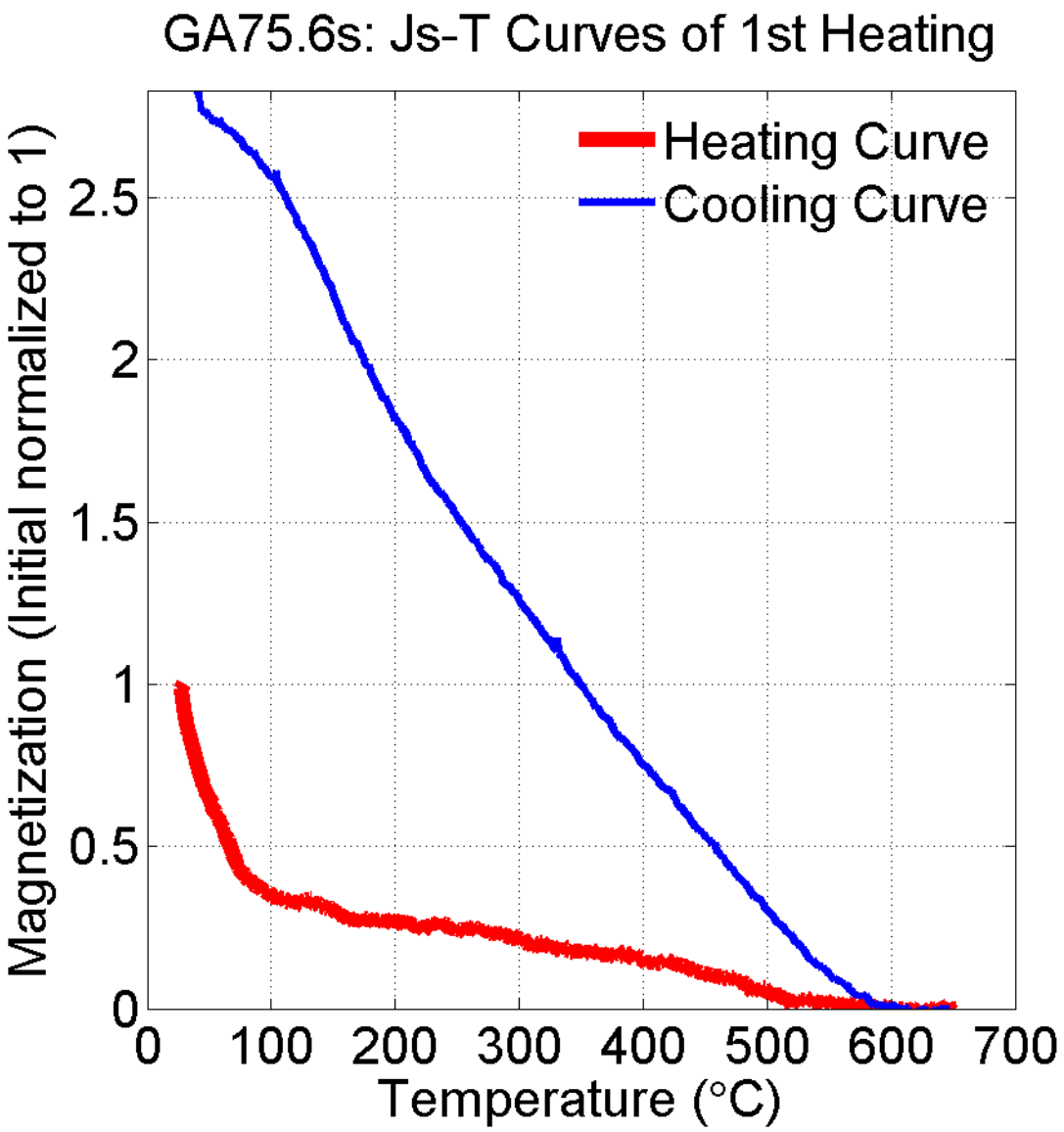

Figure 3.S1-55: Js-T curves of specimen GA75.6s.

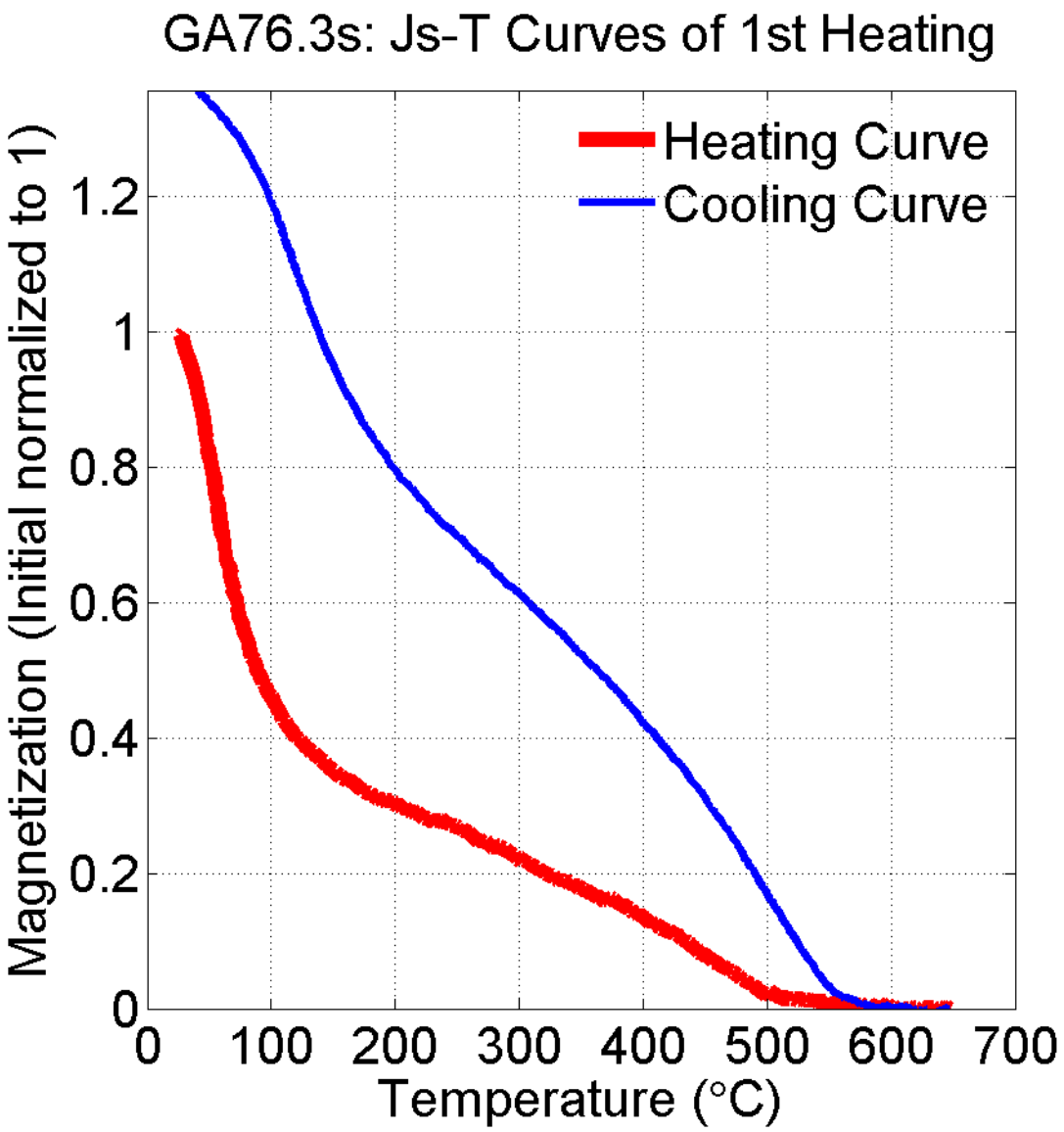

Figure 3.S1-56: Js-T curves of specimen GA76.3s.

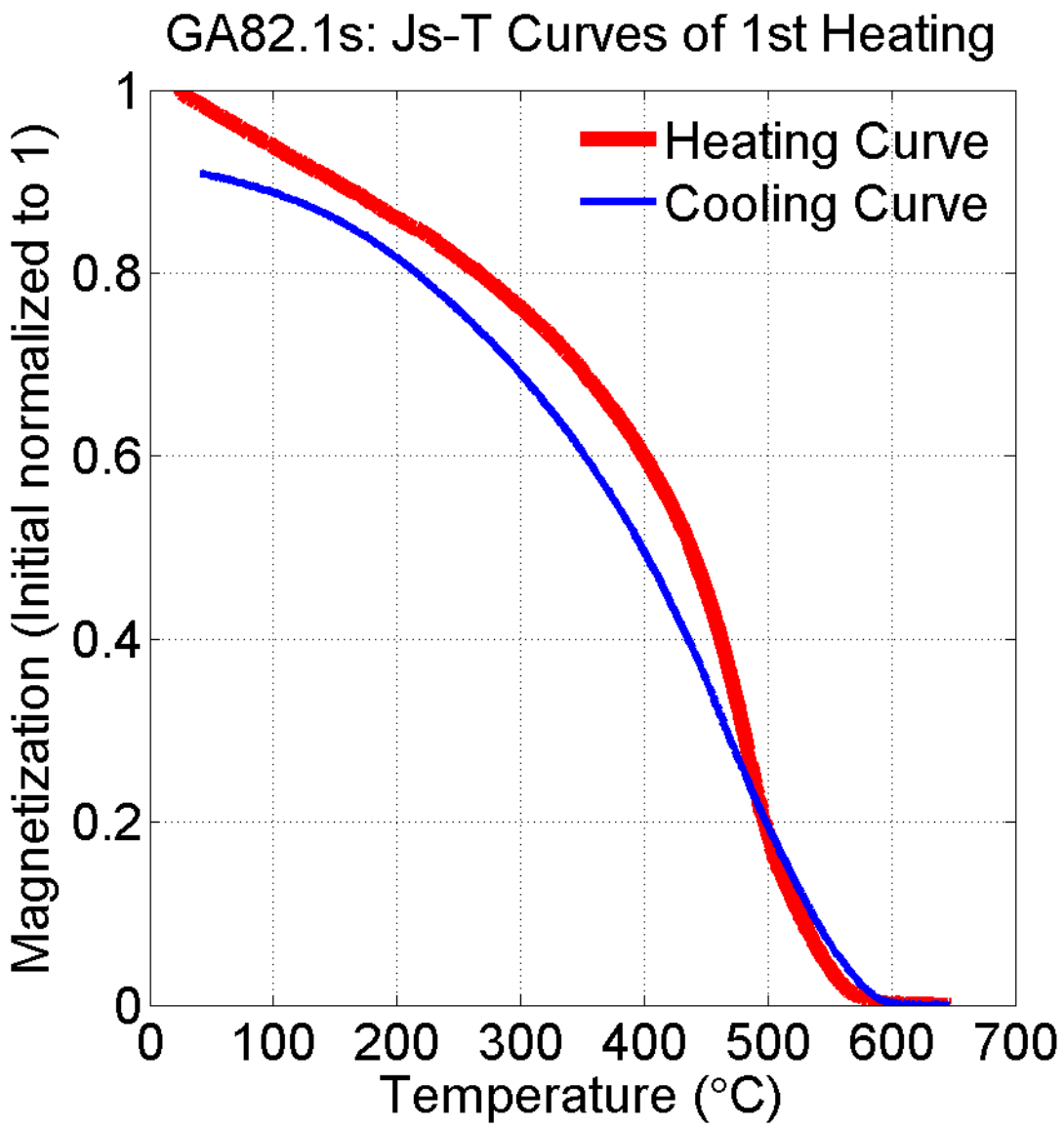

Figure 3.S1-57: Js-T curves of specimen GA82.1s.

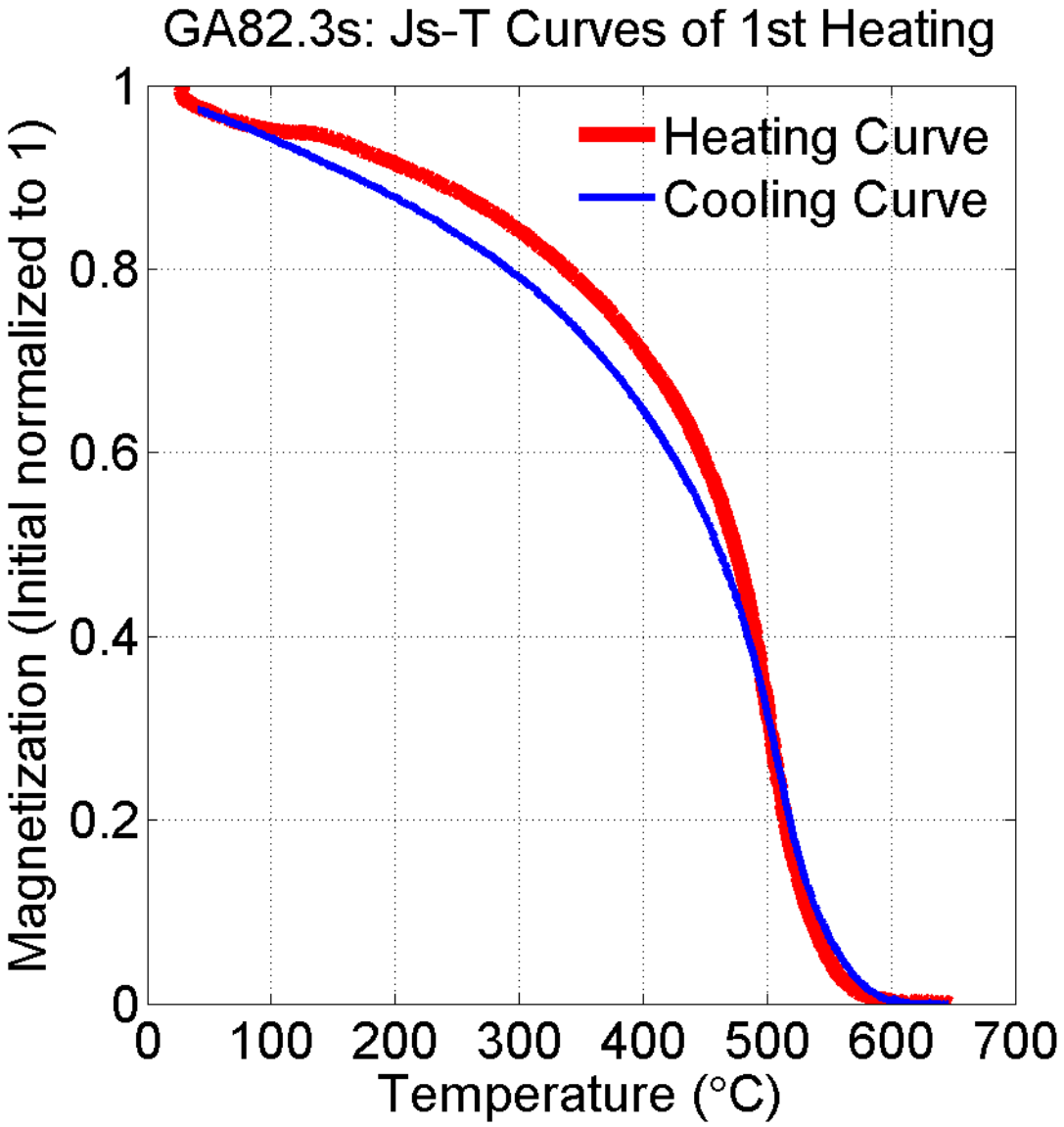

Figure 3.S1-58: Js-T curves of specimen GA82.3s.

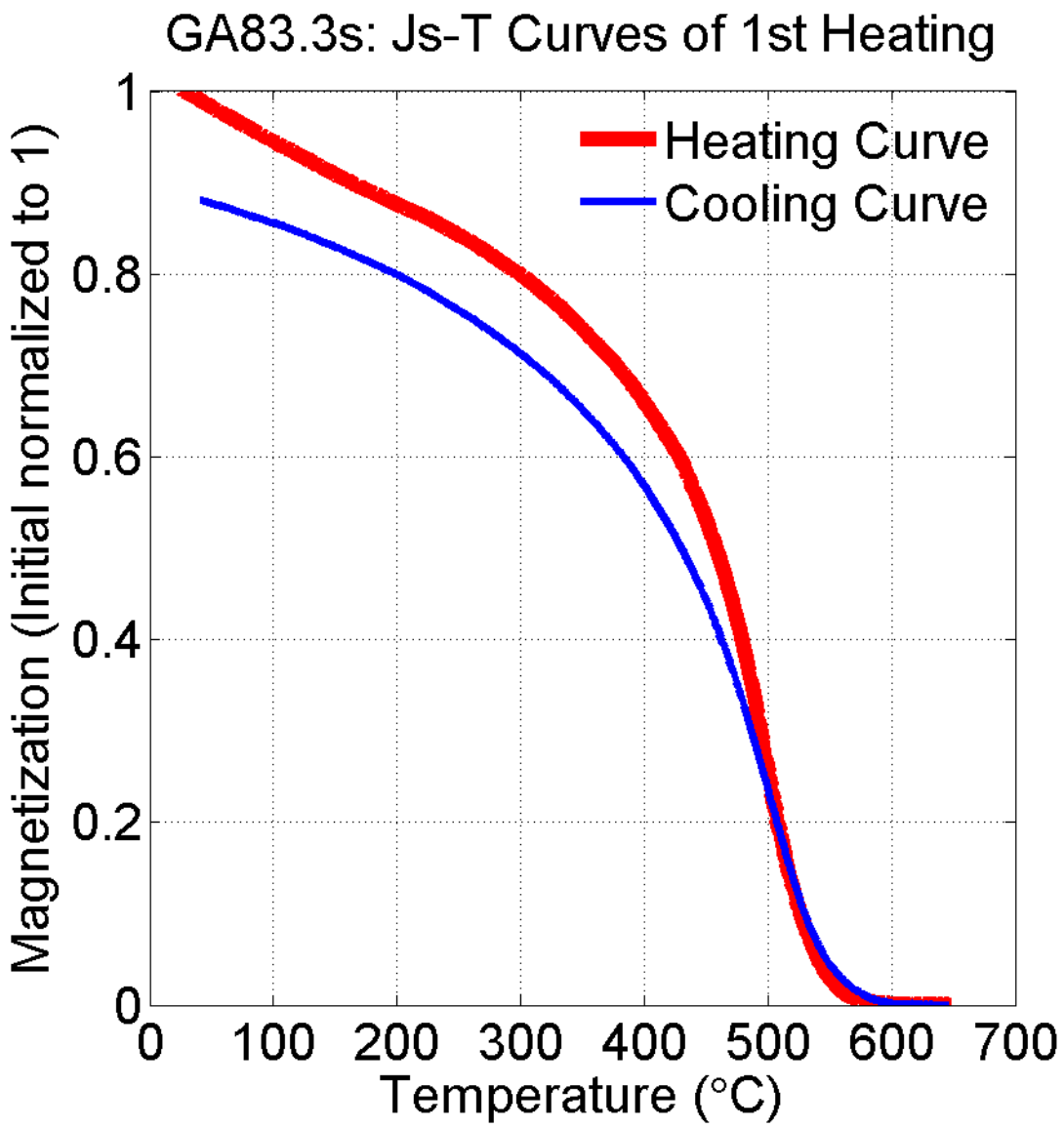

Figure 3.S1-59: Js-T curves of specimen GA83.3s.

Supplementary Figures: Figure 3.S2-(001 to 209)

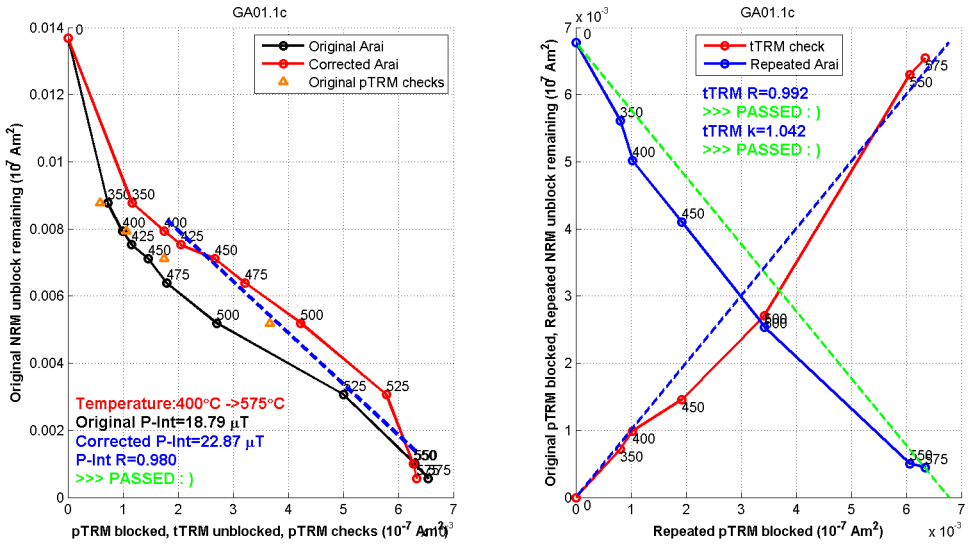

Figure 3.S2-001: Arai diagrams (left) and tTRM check (right) of specimen GA01.1c.

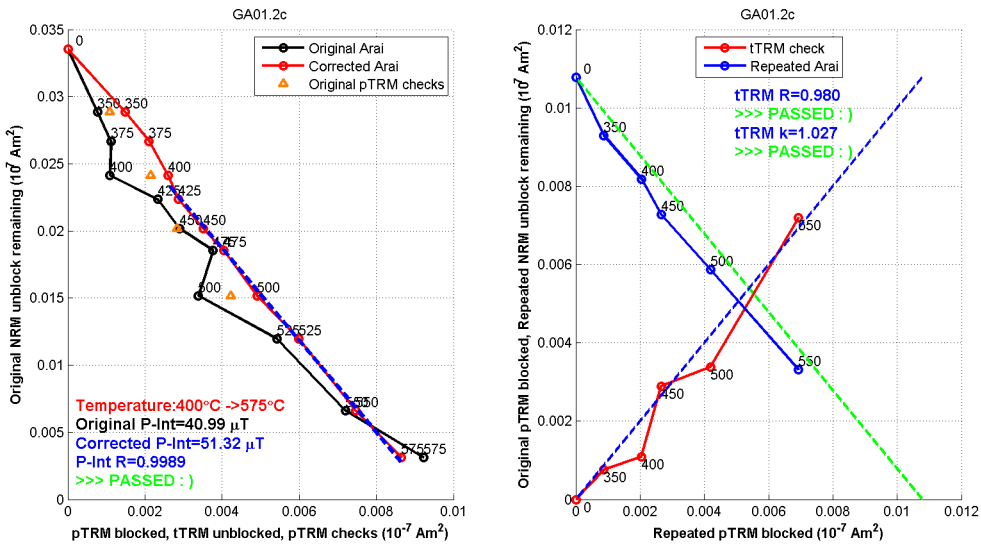

Figure 3.S2-002: Arai diagrams (left) and tTRM check (right) of specimen GA01.2c.

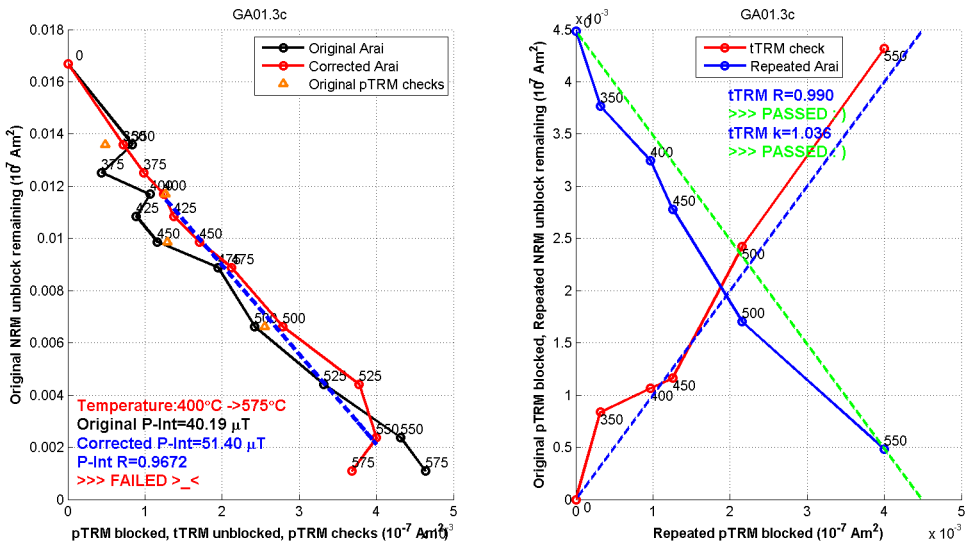

Figure 3.S2-003: Arai diagrams (left) and tTRM check (right) of specimen GA01.3c.

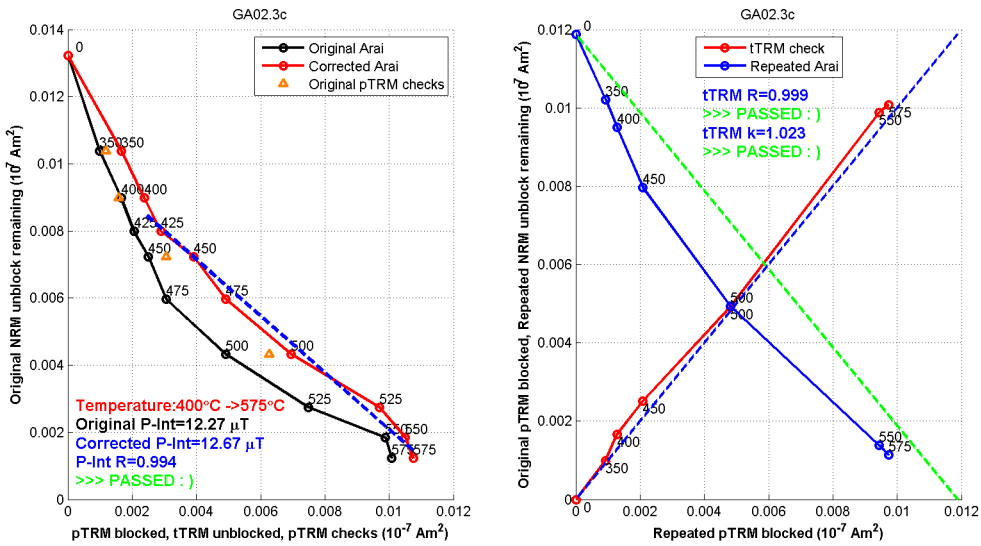

Figure 3.S2-004: Arai diagrams (left) and tTRM check (right) of specimen GA02.3c.

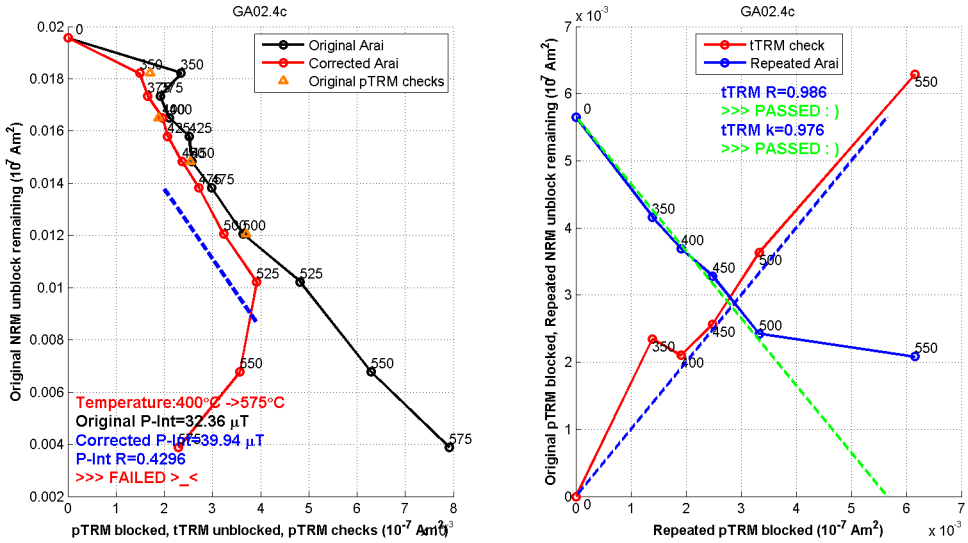

Figure 3.S2-005: Arai diagrams (left) and tTRM check (right) of specimen GA02.4c.

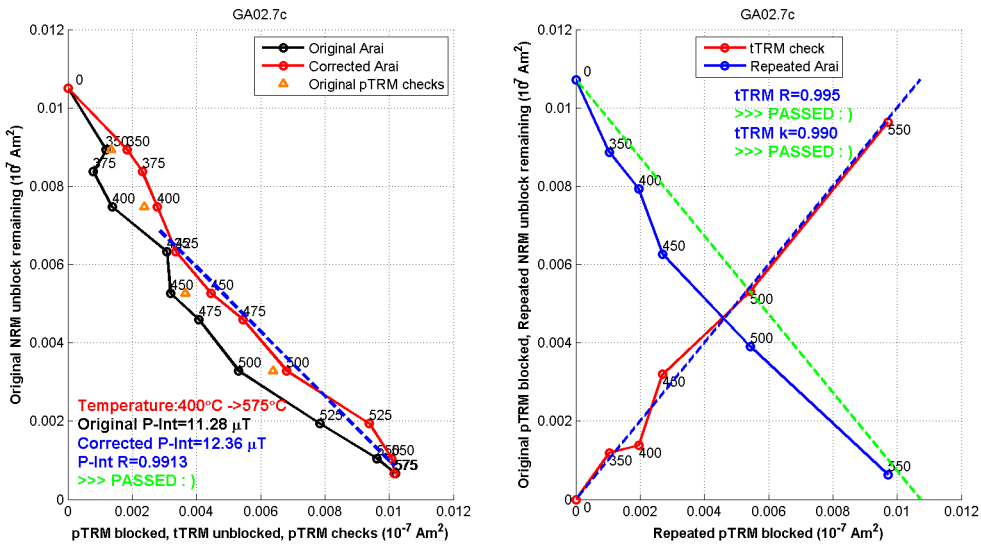

Figure 3.S2-006: Arai diagrams (left) and tTRM check (right) of specimen GA02.7c.

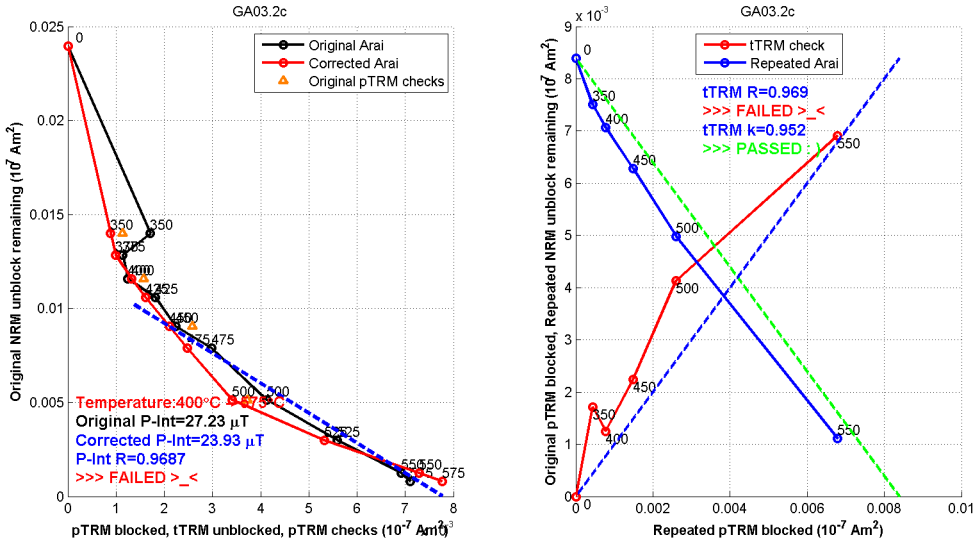

Figure 3.S2-007: Arai diagrams (left) and tTRM check (right) of specimen GA03.2c.

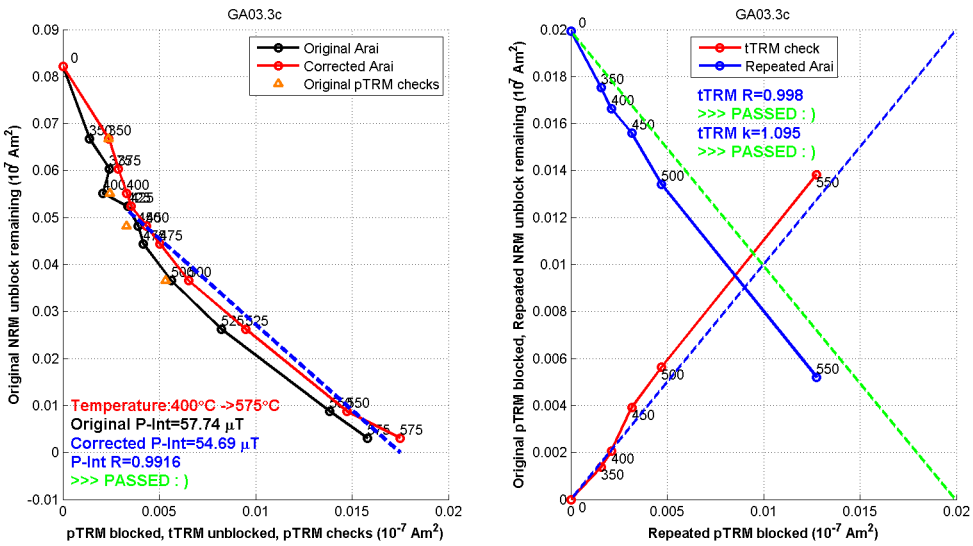

Figure 3.S2-008: Arai diagrams (left) and tTRM check (right) of specimen GA03.3c.

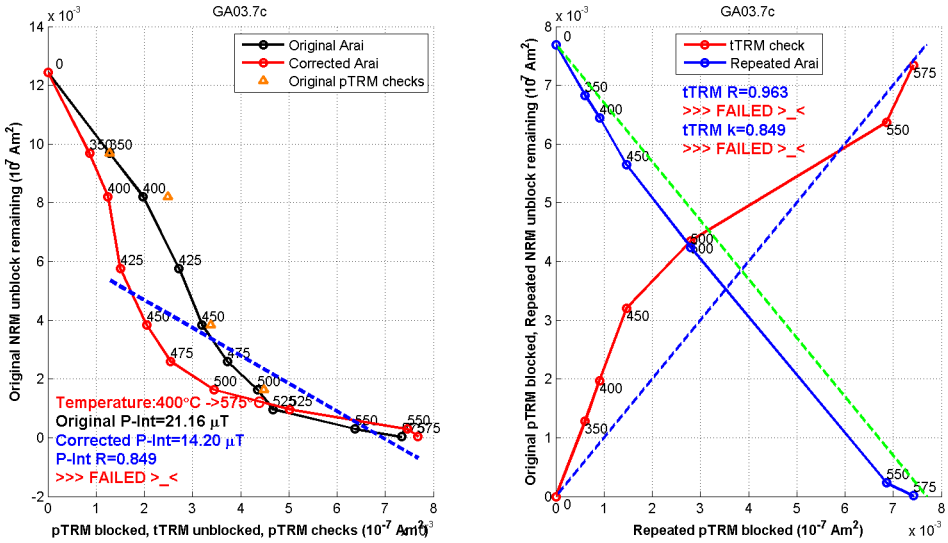

Figure 3.S2-009: Arai diagrams (left) and tTRM check (right) of specimen GA03.7c.

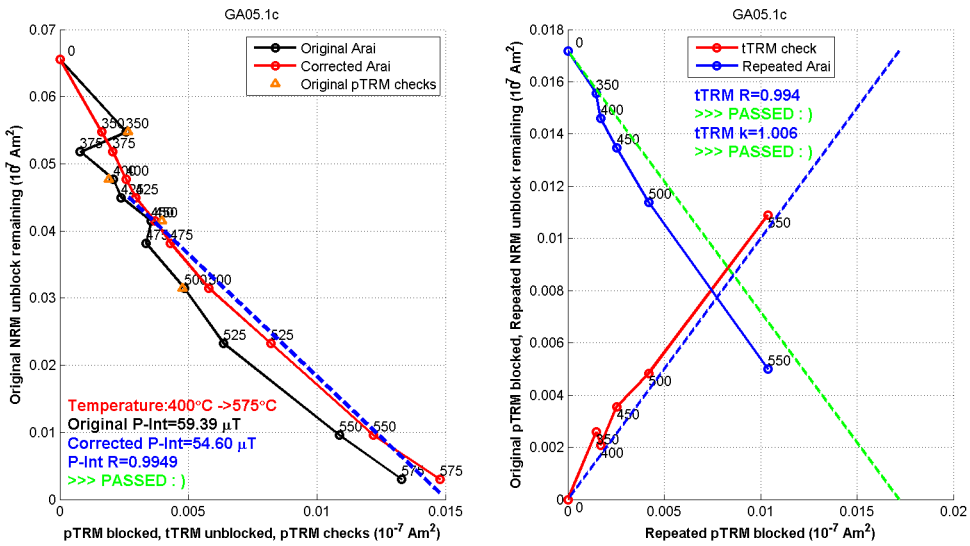

Figure 3.S2-010: Arai diagrams (left) and tTRM check (right) of specimen GA05.1c.

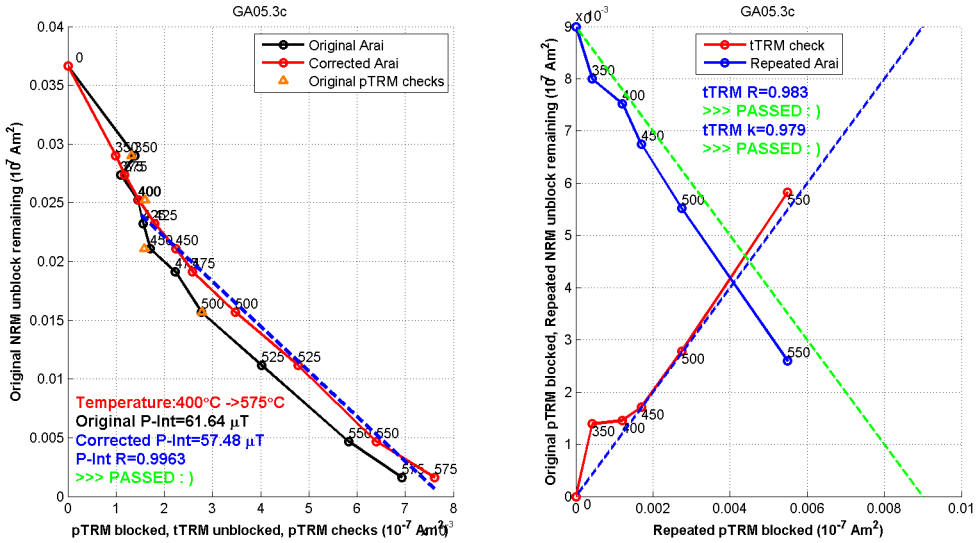

Figure 3.S2-011: Arai diagrams (left) and tTRM check (right) of specimen GA05.3c.

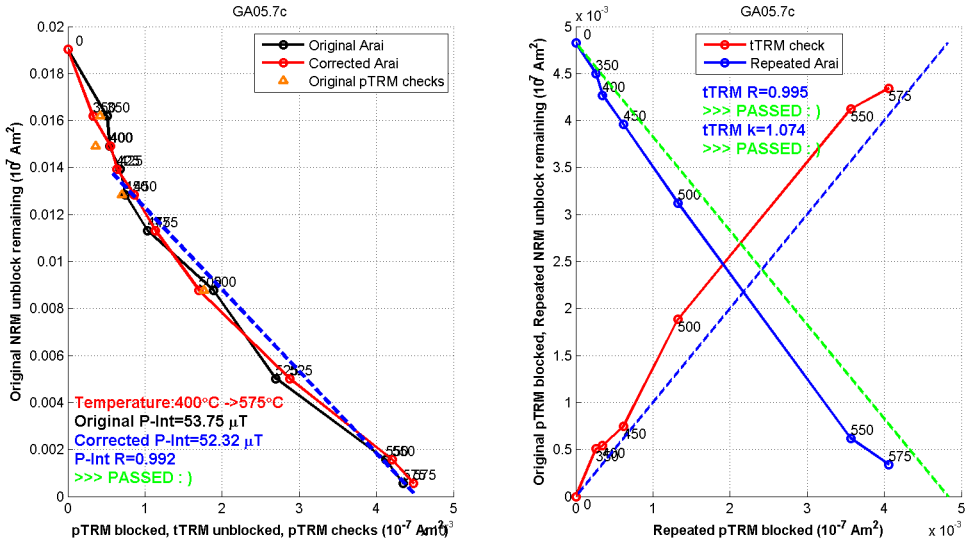

Figure 3.S2-012: Arai diagrams (left) and tTRM check (right) of specimen GA05.7c.

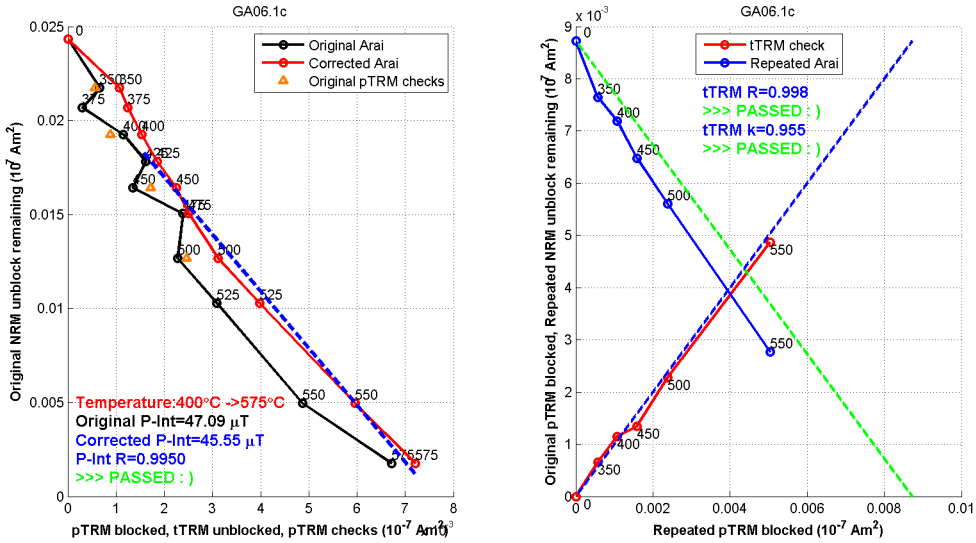

Figure 3.S2-013: Arai diagrams (left) and tTRM check (right) of specimen GA06.1c.

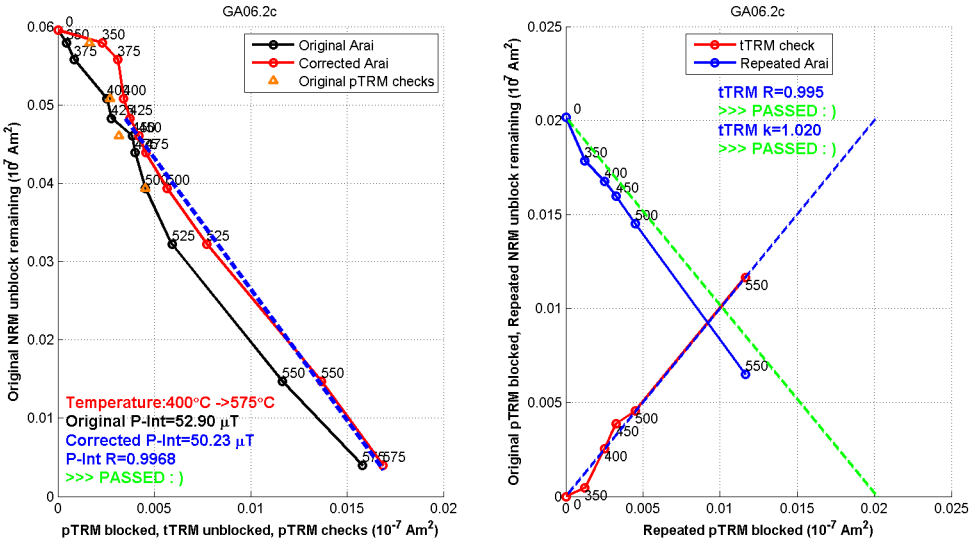

Figure 3.S2-014: Arai diagrams (left) and tTRM check (right) of specimen GA06.2c.

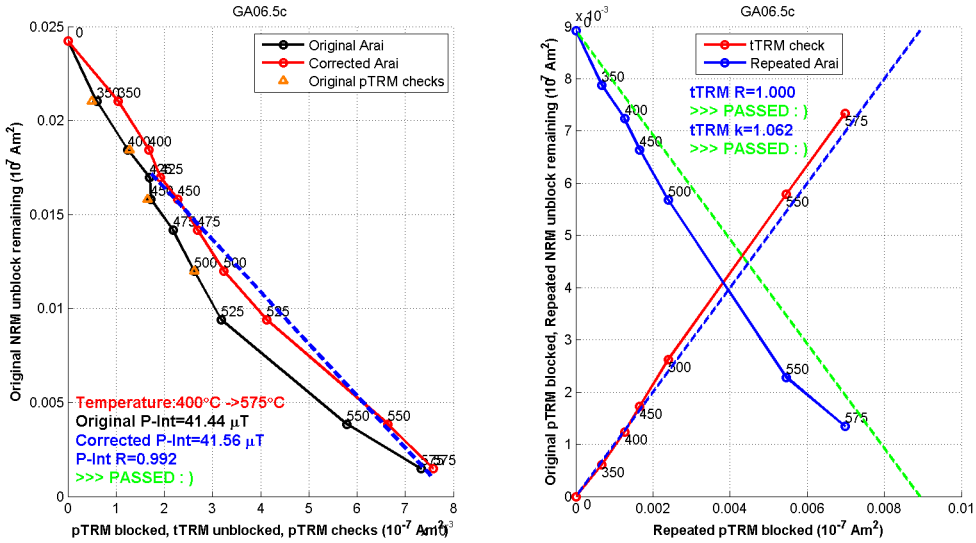

Figure 3.S2-015: Arai diagrams (left) and tTRM check (right) of specimen GA06.5c.

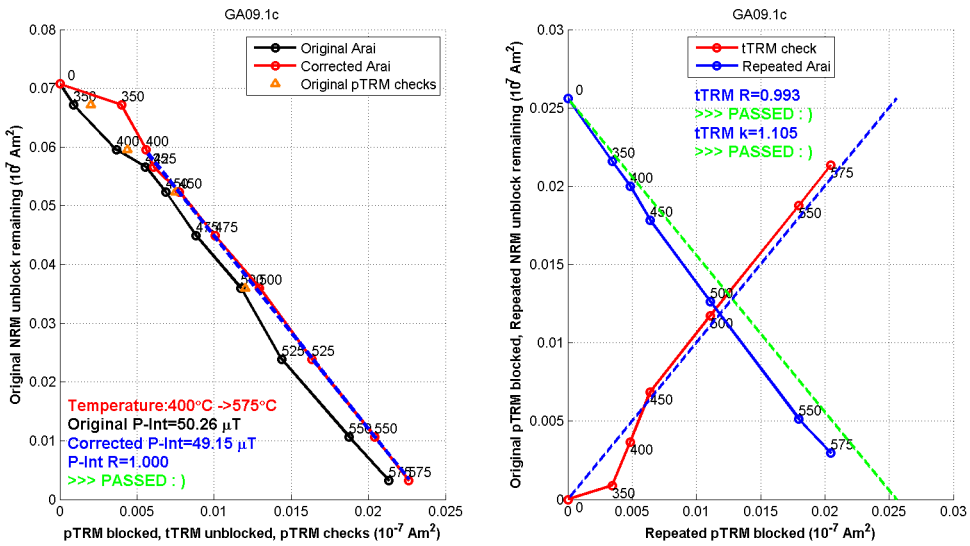

Figure 3.S2-016: Arai diagrams (left) and tTRM check (right) of specimen GA09.1c.

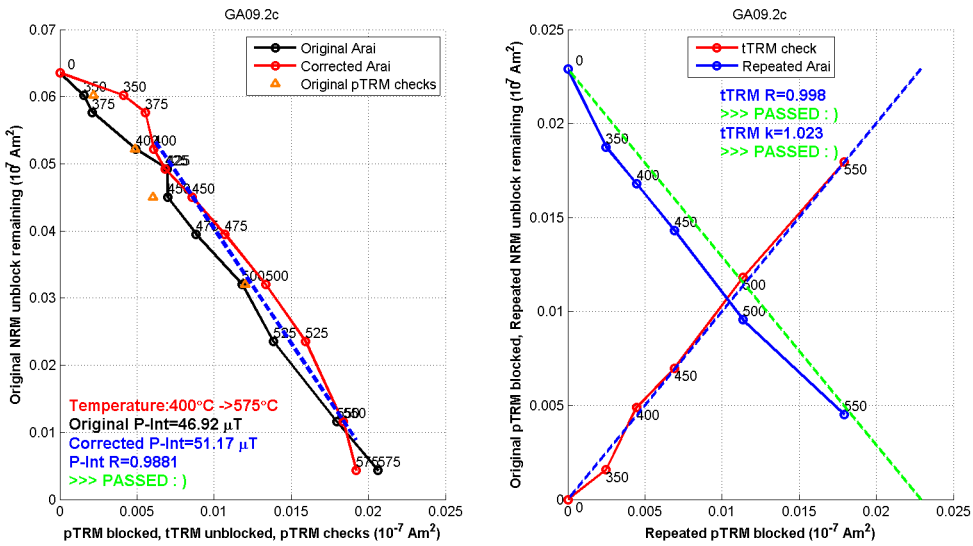

Figure 3.S2-017: Arai diagrams (left) and tTRM check (right) of specimen GA09.2c.

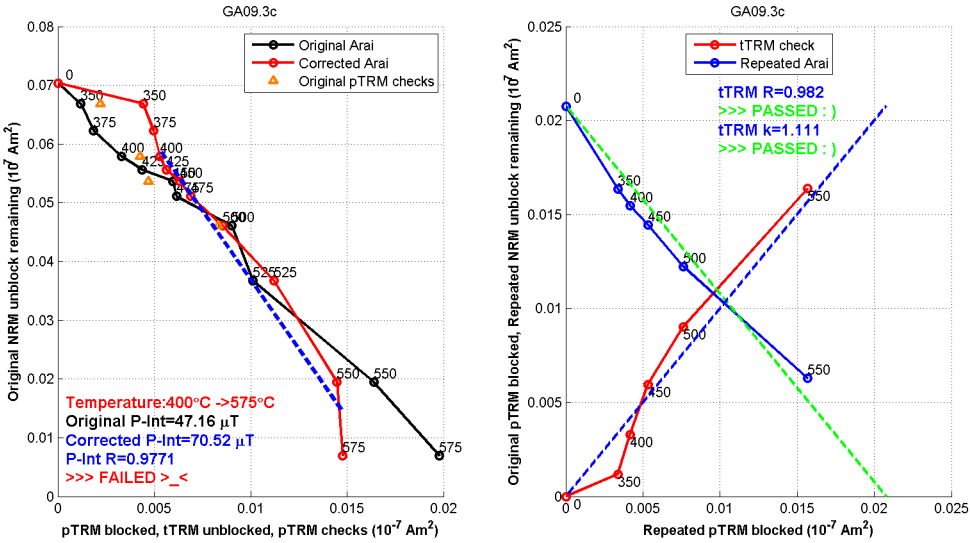

Figure 3.S2-018: Arai diagrams (left) and tTRM check (right) of specimen GA09.3c.

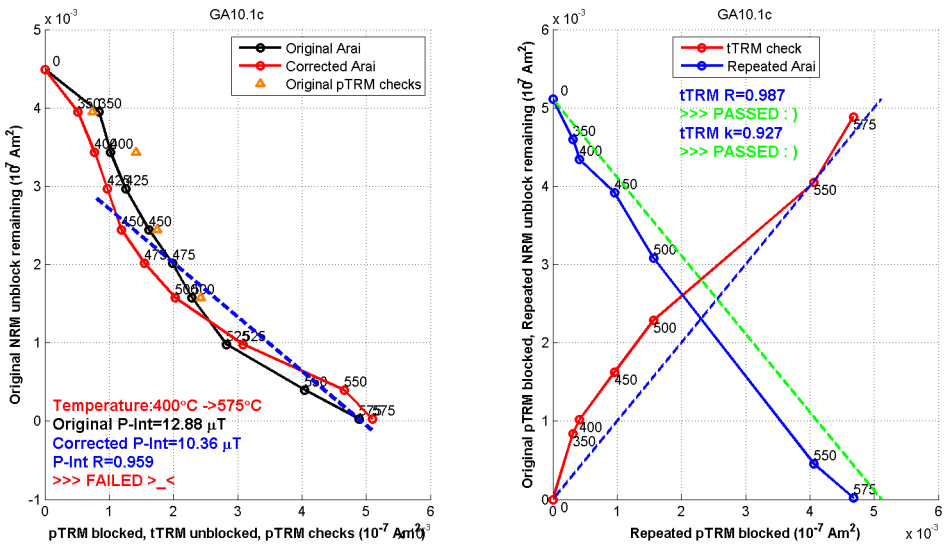

Figure 3.S2-019: Arai diagrams (left) and tTRM check (right) of specimen GA10.1c.

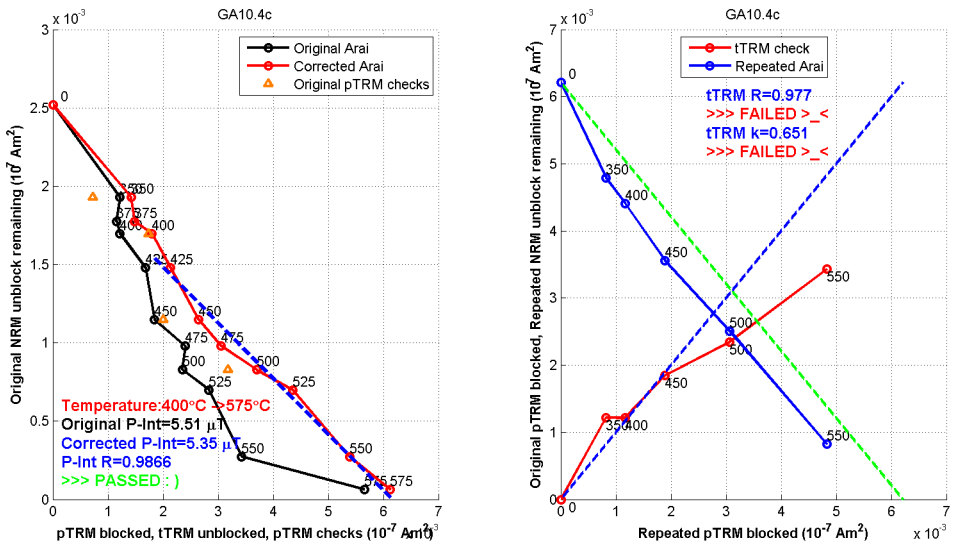

Figure 3.S2-020: Arai diagrams (left) and tTRM check (right) of specimen GA10.4c.

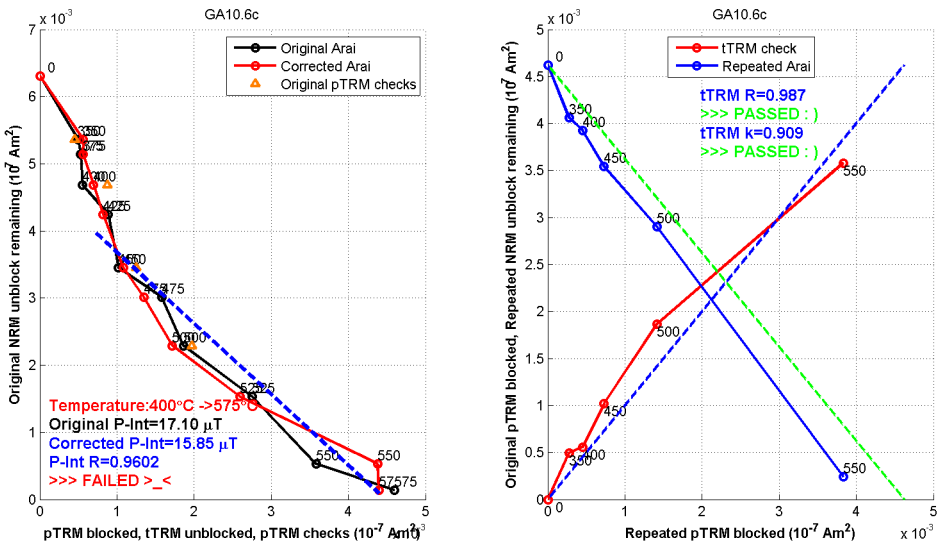

Figure 3.S2-021: Arai diagrams (left) and tTRM check (right) of specimen GA10.6c.

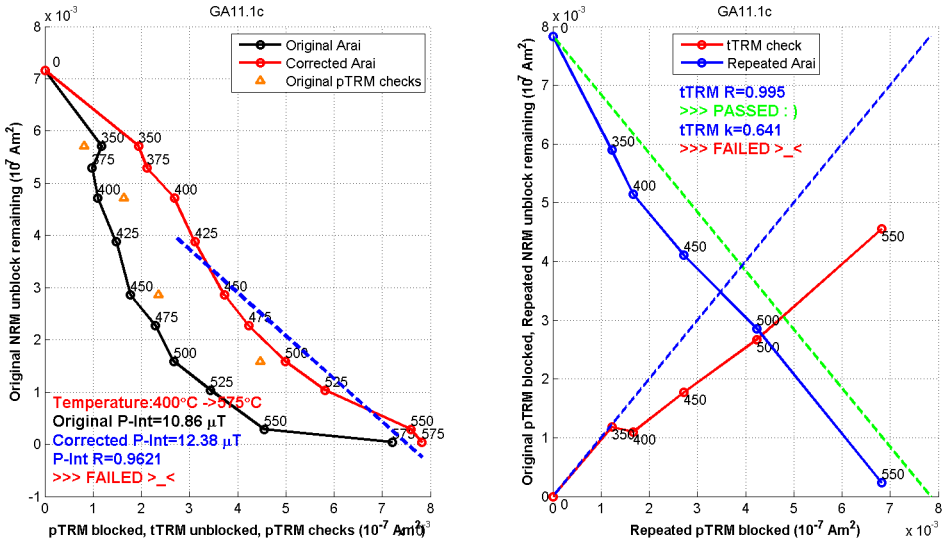

Figure 3.S2-022: Arai diagrams (left) and tTRM check (right) of specimen GA11.1c.

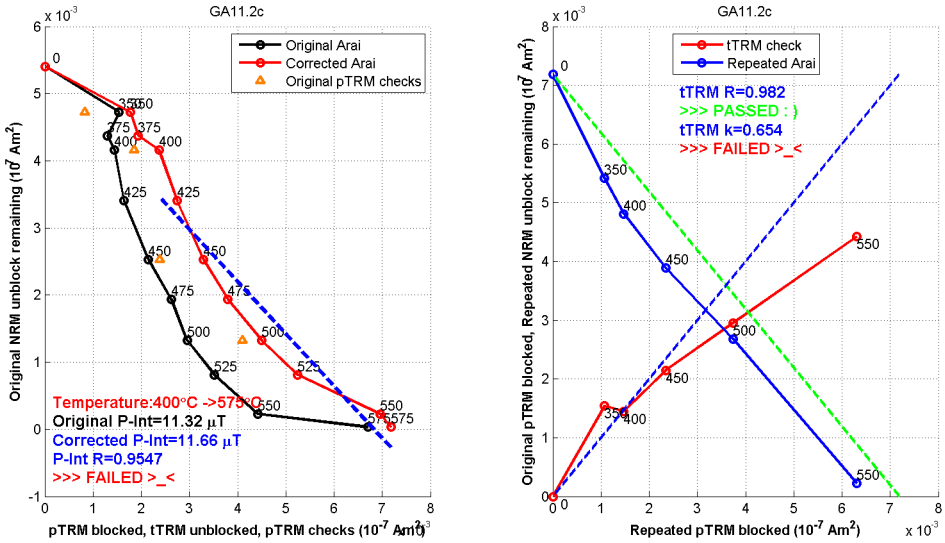

Figure 3.S2-023: Arai diagrams (left) and tTRM check (right) of specimen GA11.2c.

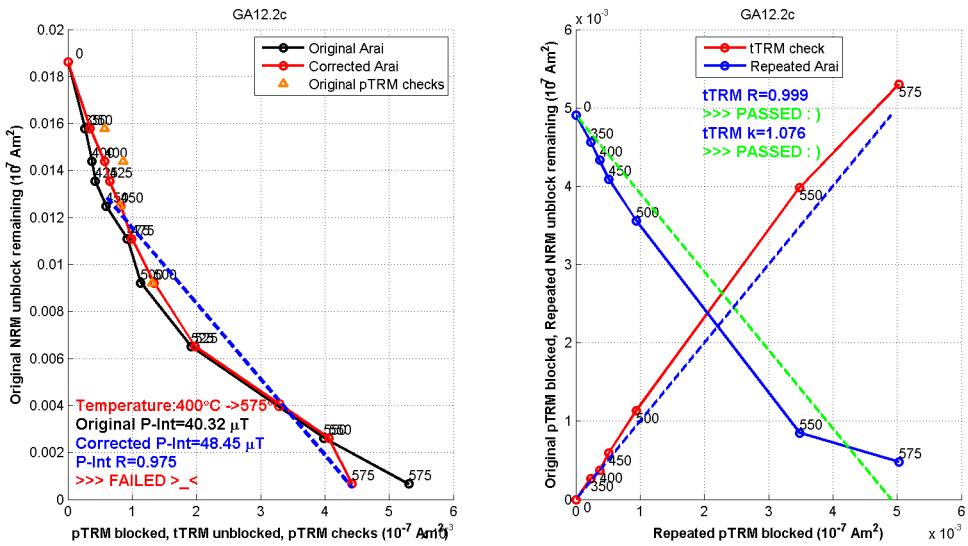

Figure 3.S2-024: Arai diagrams (left) and tTRM check (right) of specimen GA12.2c.

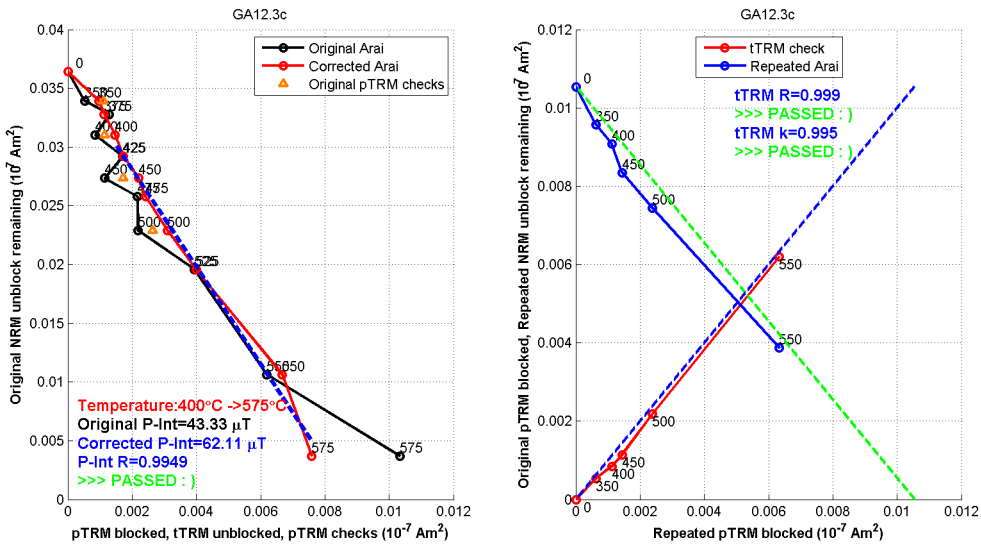

Figure 3.S2-025: Arai diagrams (left) and tTRM check (right) of specimen GA12.3c.

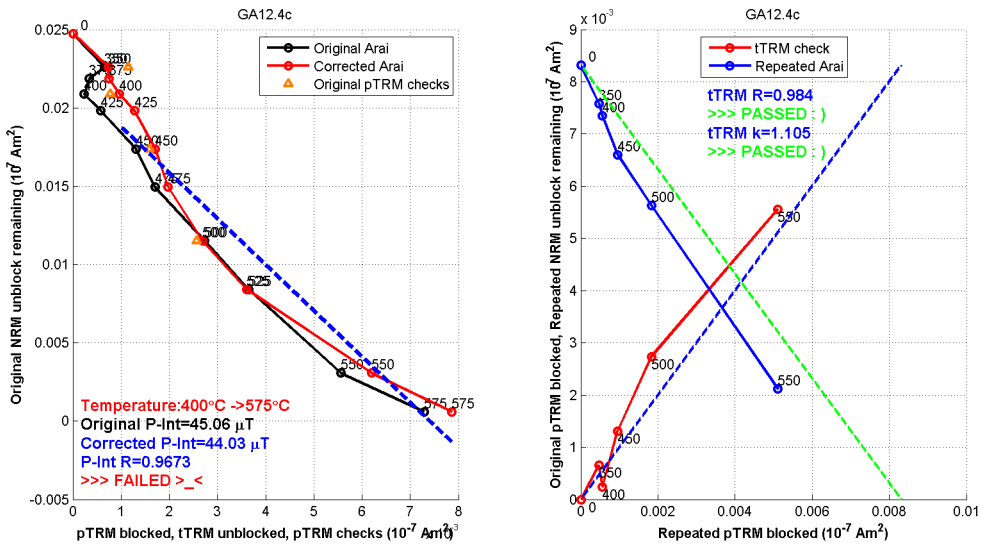

Figure 3.S2-026: Arai diagrams (left) and tTRM check (right) of specimen GA12.4c.

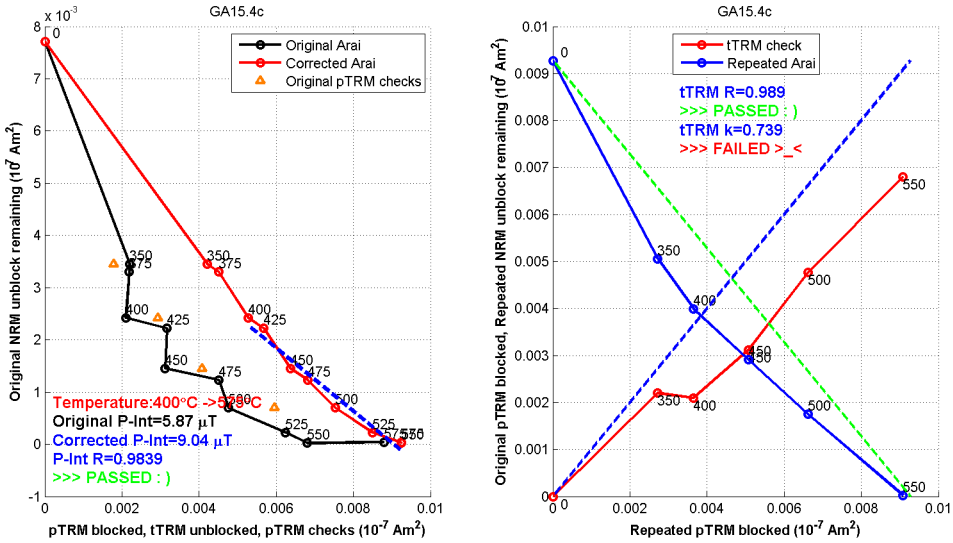

Figure 3.S2-027: Arai diagrams (left) and tTRM check (right) of specimen GA15.4c.

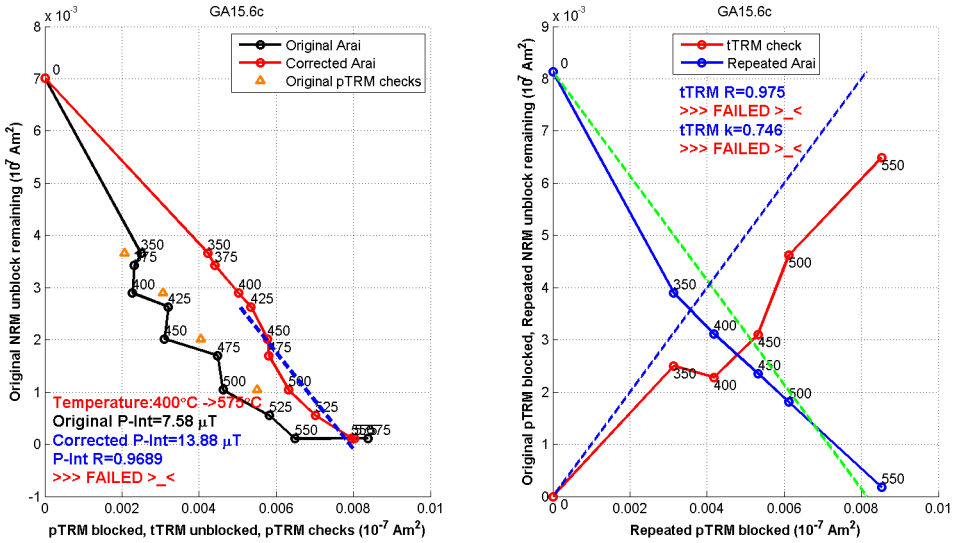

Figure 3.S2-028: Arai diagrams (left) and tTRM check (right) of specimen GA15.6c.

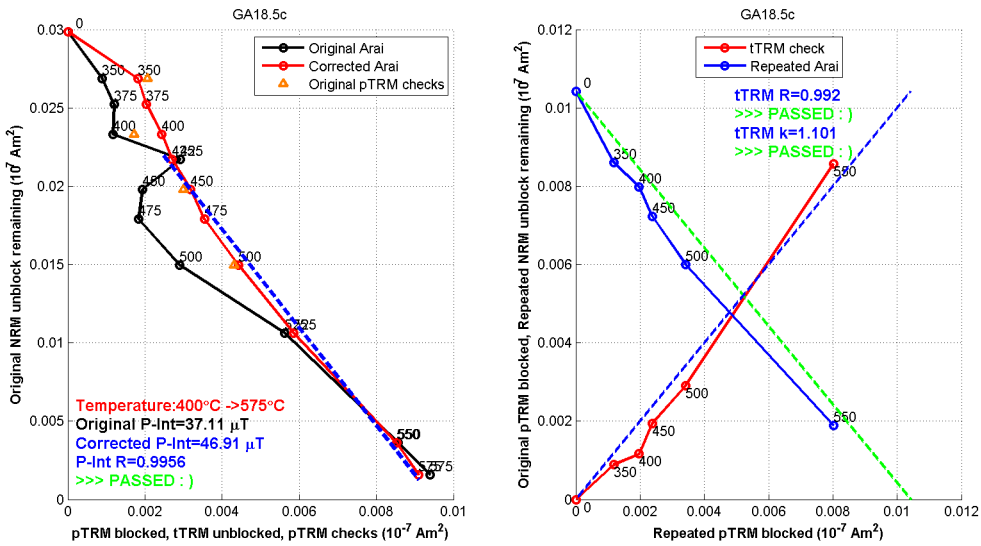

Figure 3.S2-029: Arai diagrams (left) and tTRM check (right) of specimen GA18.5c.

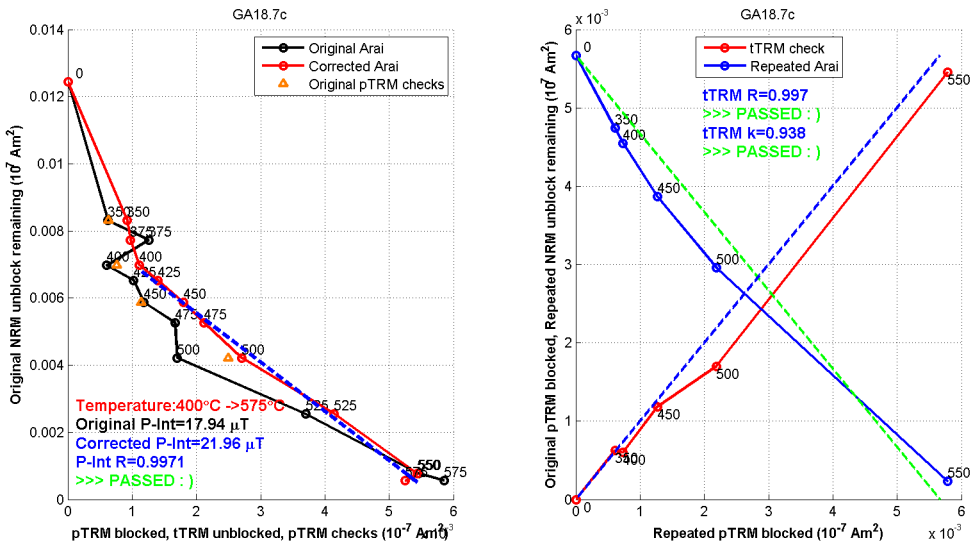

Figure 3.S2-030: Arai diagrams (left) and tTRM check (right) of specimen GA18.7c.

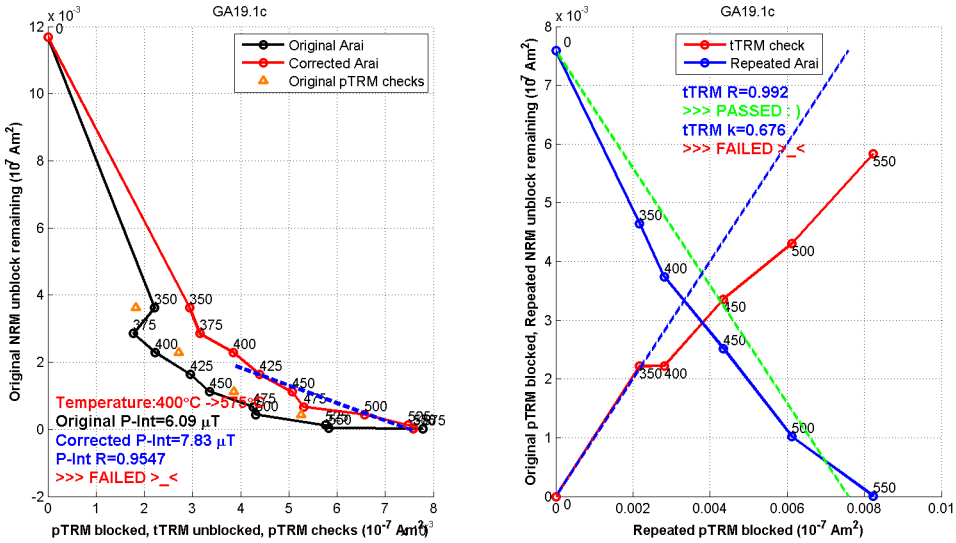

Figure 3.S2-031: Arai diagrams (left) and tTRM check (right) of specimen GA19.1c.

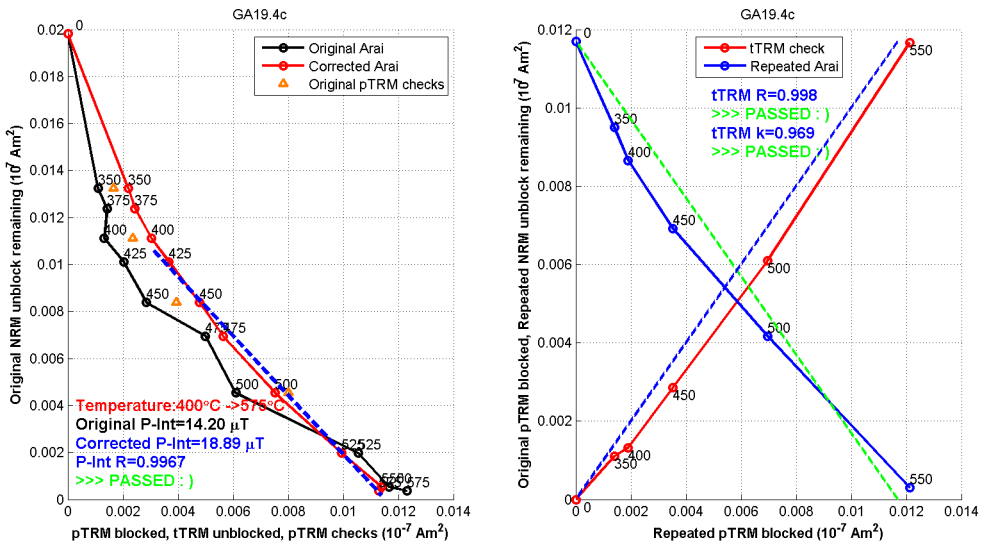

Figure 3.S2-032: Arai diagrams (left) and tTRM check (right) of specimen GA19.4c.

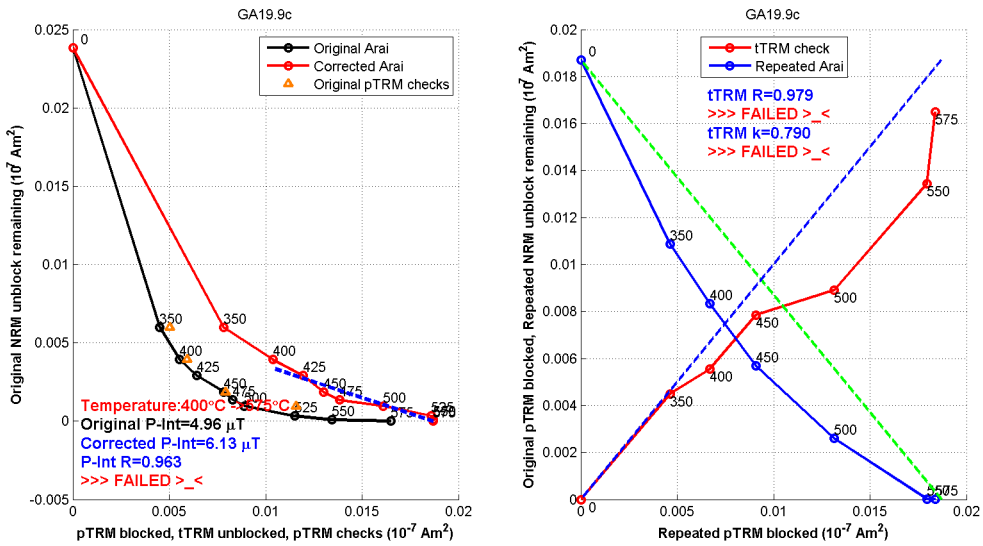

Figure 3.S2-033: Arai diagrams (left) and tTRM check (right) of specimen GA19.9c.

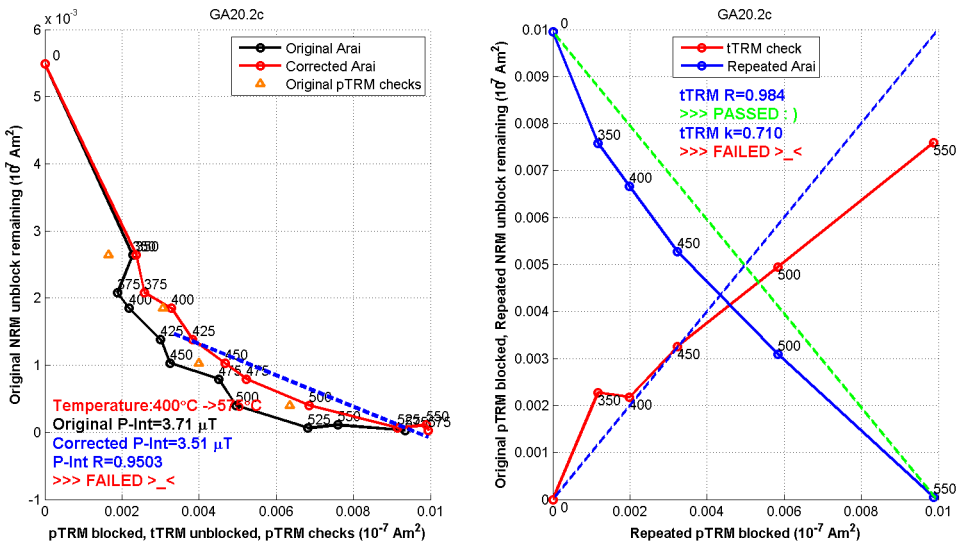

Figure 3.S2-034: Arai diagrams (left) and tTRM check (right) of specimen GA20.2c.

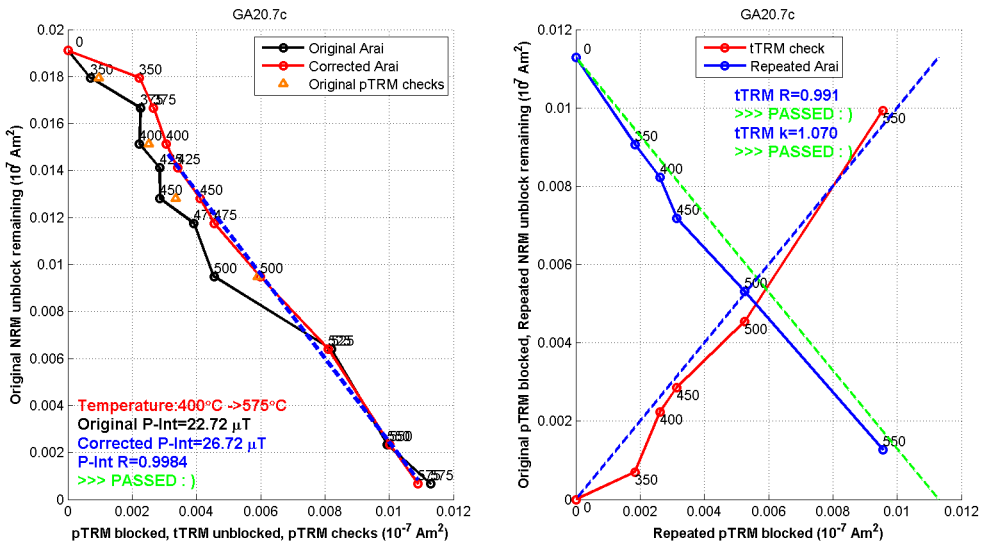

Figure 3.S2-035: Arai diagrams (left) and tTRM check (right) of specimen GA20.7c.

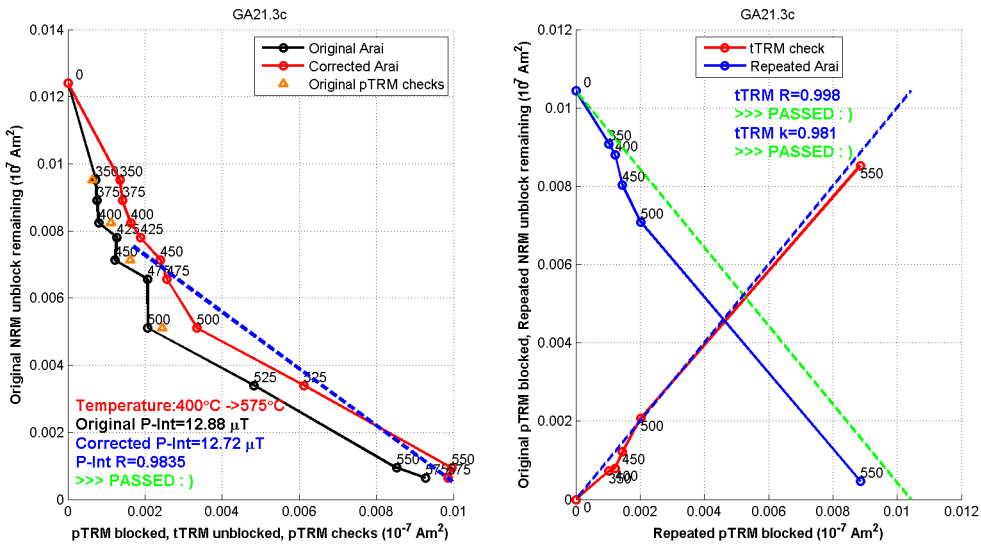

Figure 3.S2-036: Arai diagrams (left) and tTRM check (right) of specimen GA21.3c.

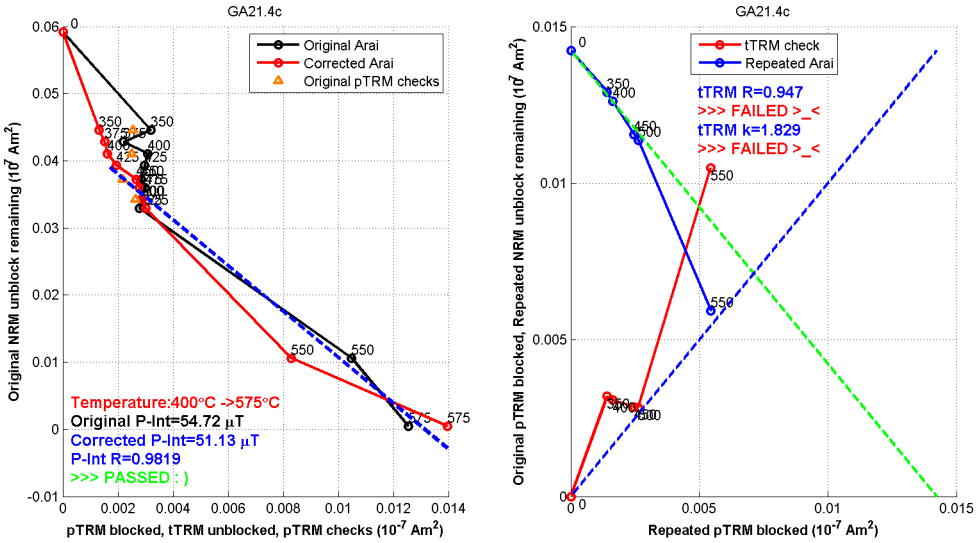

Figure 3.S2-037: Arai diagrams (left) and tTRM check (right) of specimen GA21.4c.

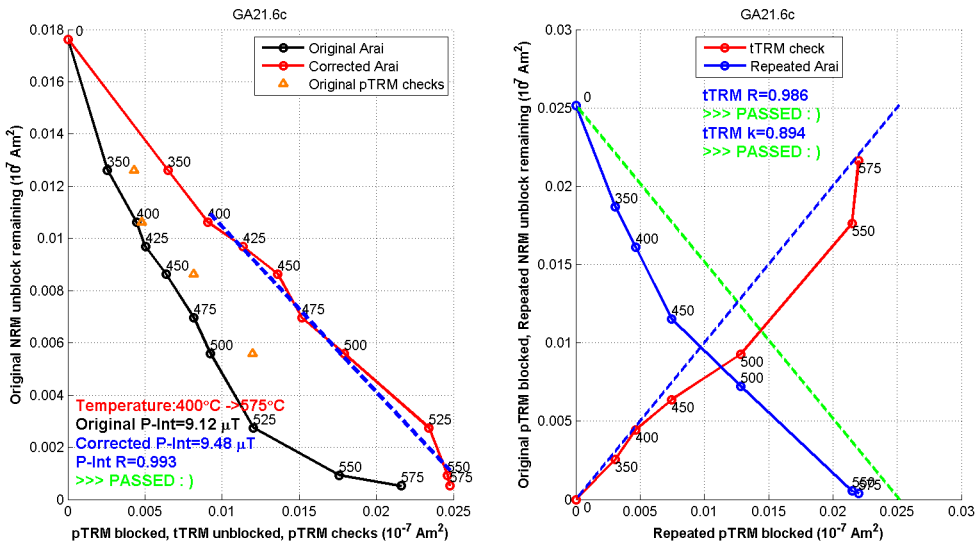

Figure 3.S2-038: Arai diagrams (left) and tTRM check (right) of specimen GA21.6c.

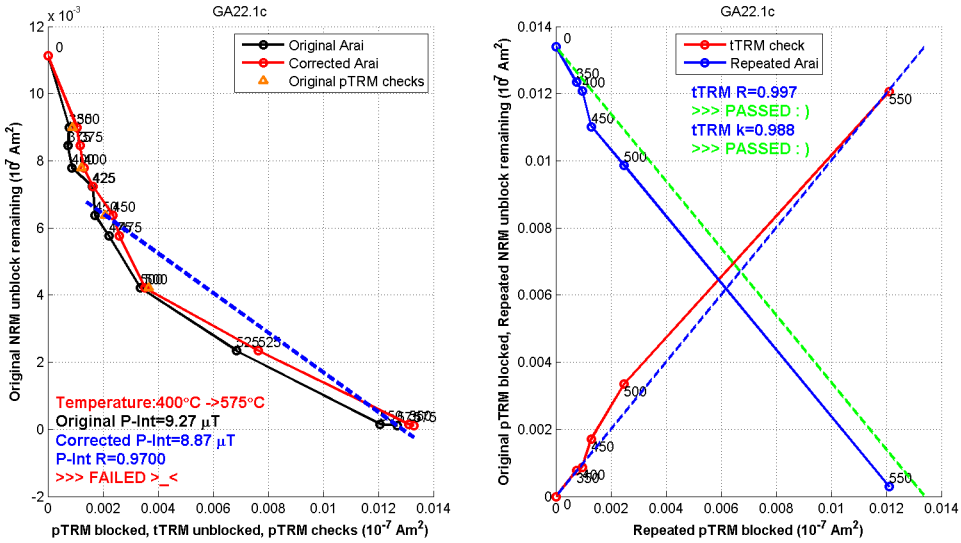

Figure 3.S2-039: Arai diagrams (left) and tTRM check (right) of specimen GA22.1c.

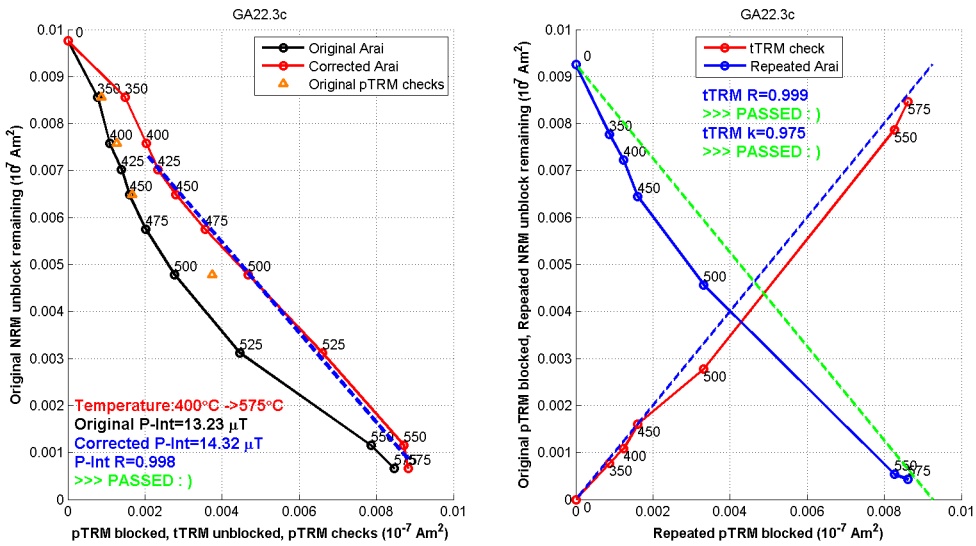

Figure 3.S2-040: Arai diagrams (left) and tTRM check (right) of specimen GA22.3c.

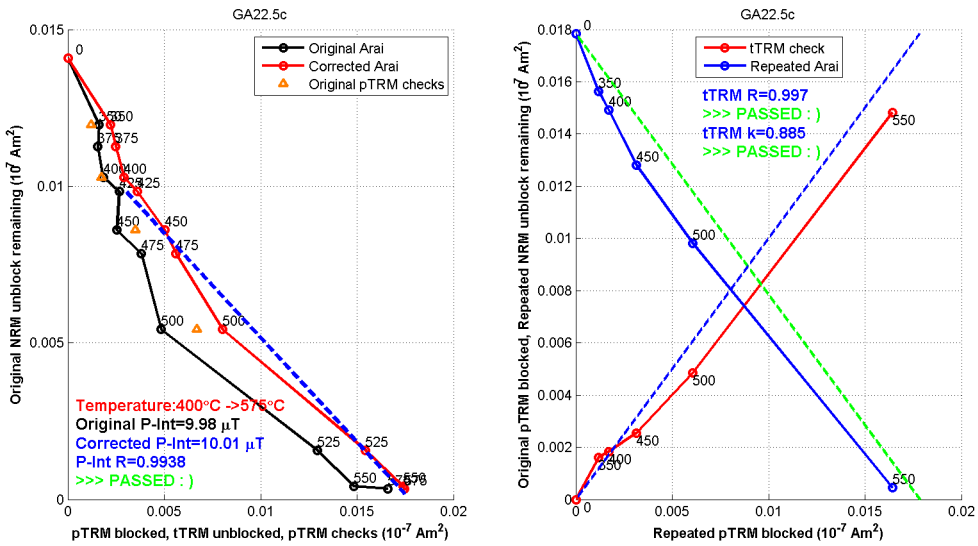

Figure 3.S2-041: Arai diagrams (left) and tTRM check (right) of specimen GA22.5c.

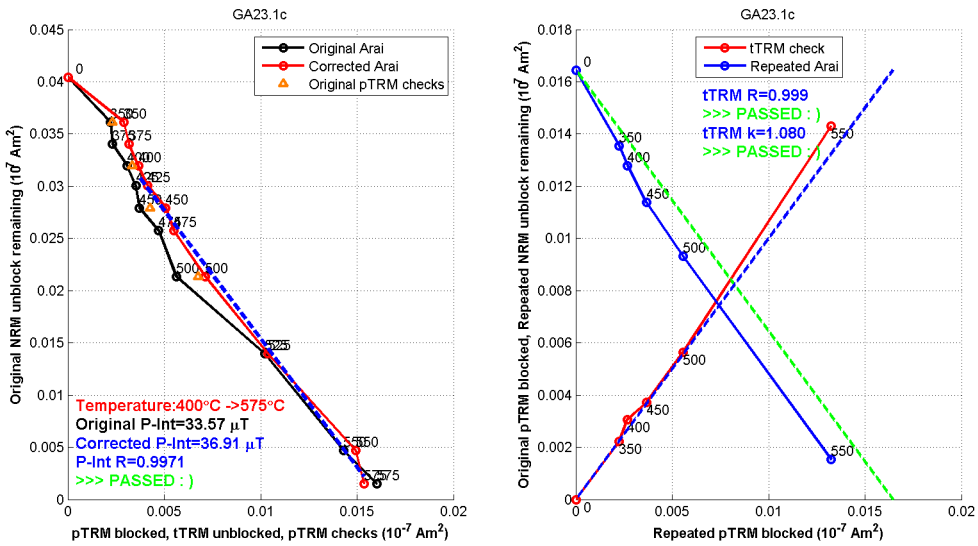

Figure 3.S2-042: Arai diagrams (left) and tTRM check (right) of specimen GA23.1c.

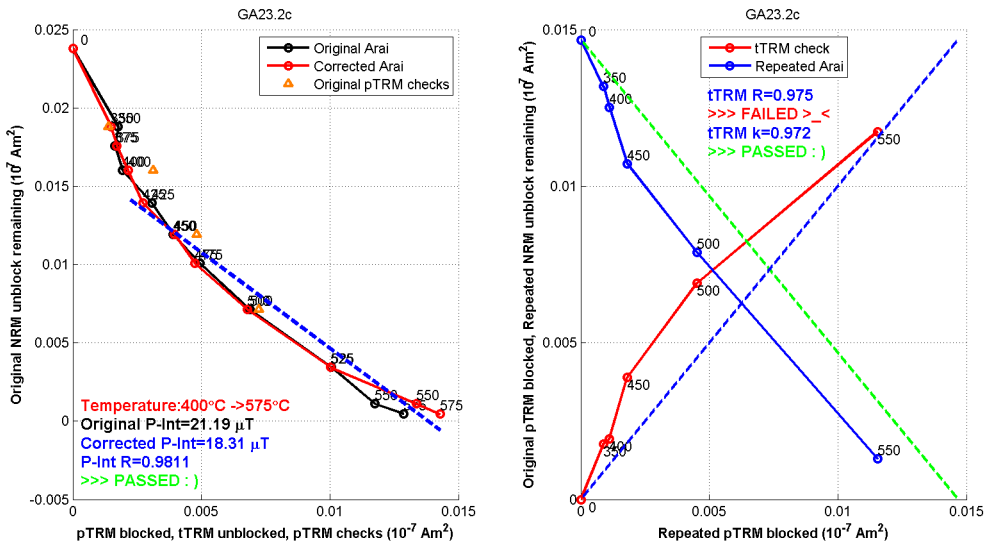

Figure 3.S2-043: Arai diagrams (left) and tTRM check (right) of specimen GA23.2c.

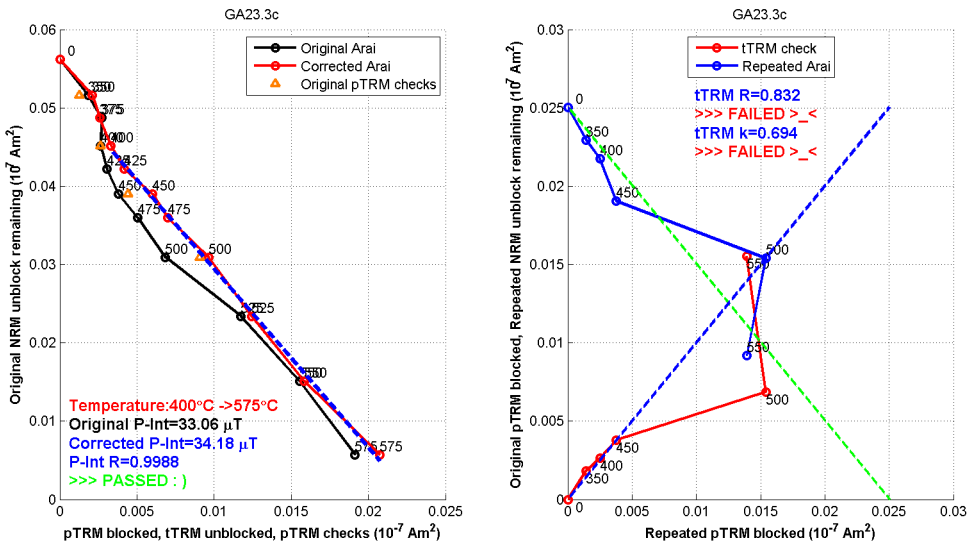

Figure 3.S2-044: Arai diagrams (left) and tTRM check (right) of specimen GA23.3c.

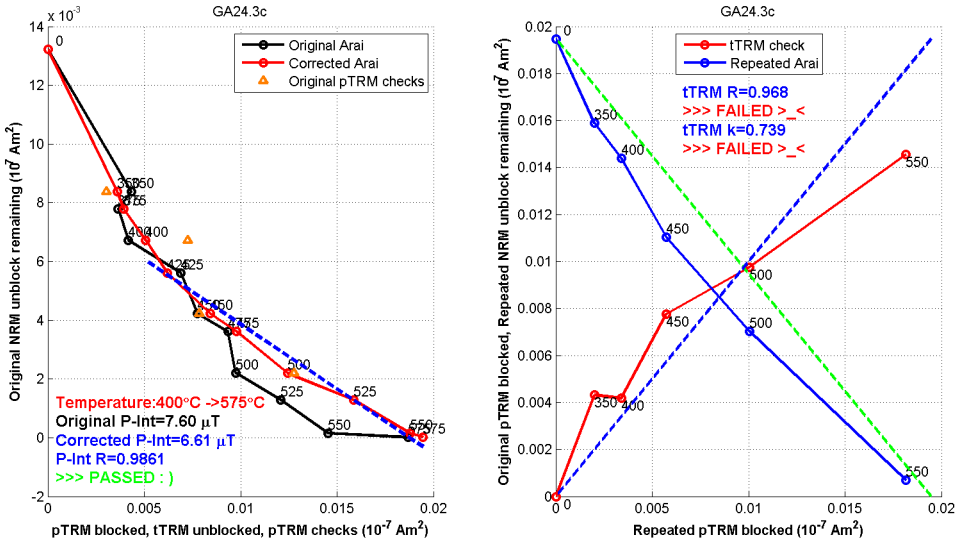

Figure 3.S2-045: Arai diagrams (left) and tTRM check (right) of specimen GA24.3c.

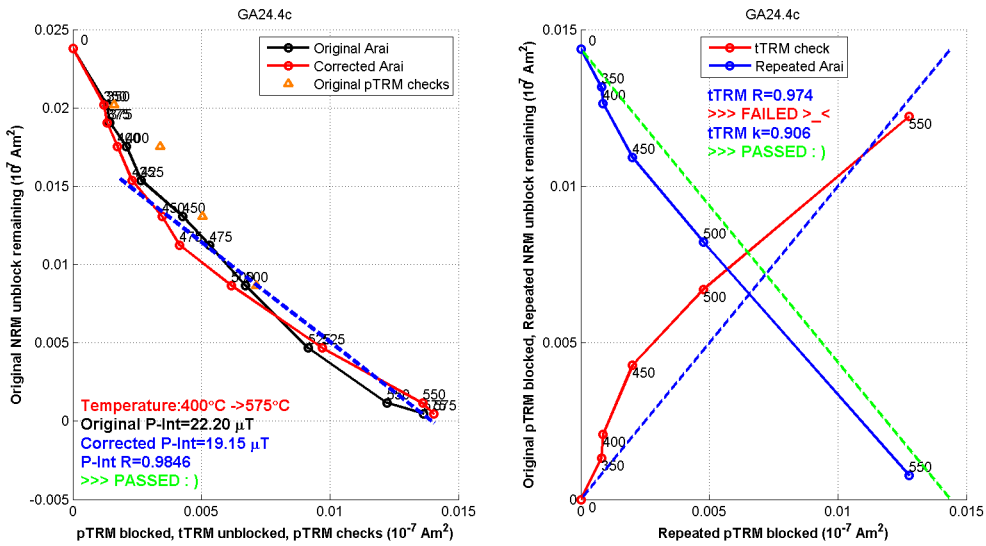

Figure 3.S2-046: Arai diagrams (left) and tTRM check (right) of specimen GA24.4c.

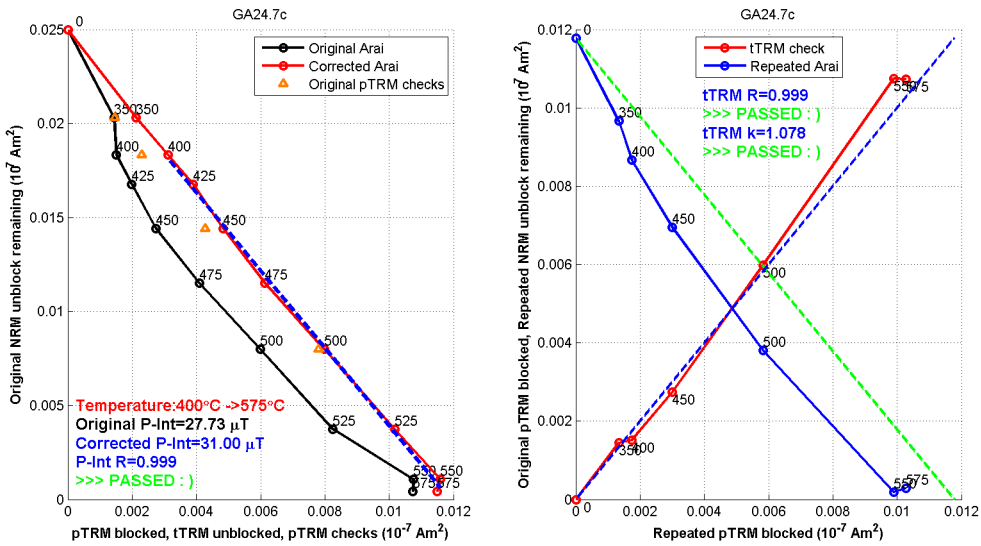

Figure 3.S2-047: Arai diagrams (left) and tTRM check (right) of specimen GA24.7c.

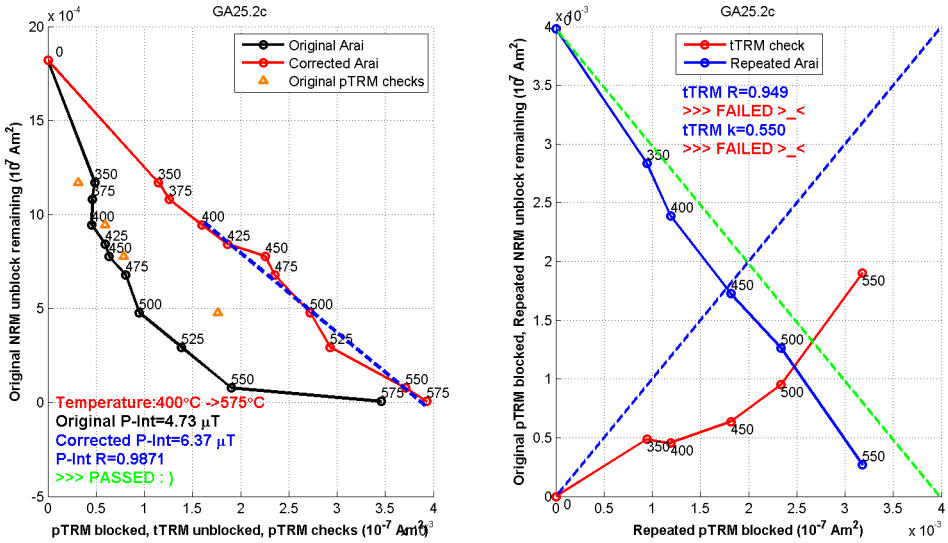

Figure 3.S2-048: Arai diagrams (left) and tTRM check (right) of specimen GA25.2c.

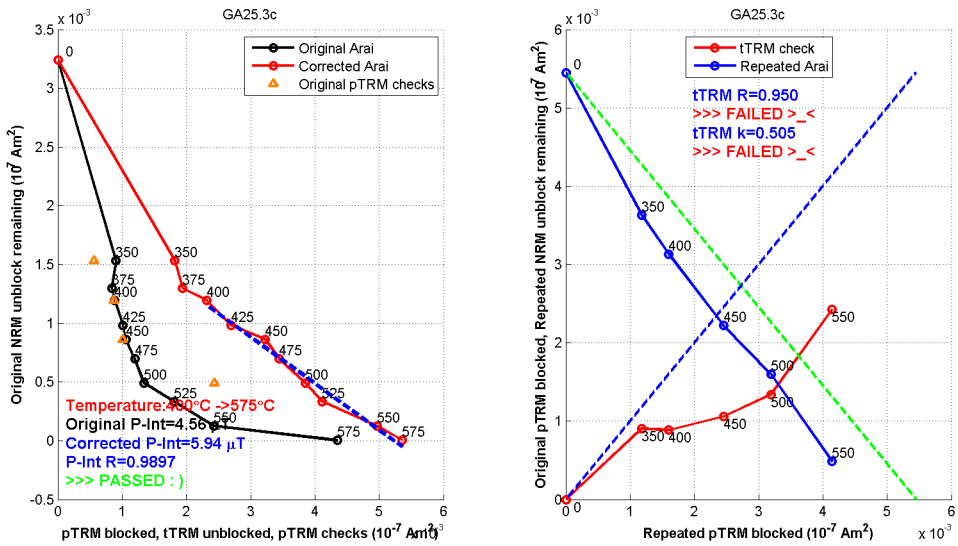

Figure 3.S2-049: Arai diagrams (left) and tTRM check (right) of specimen GA25.3c.

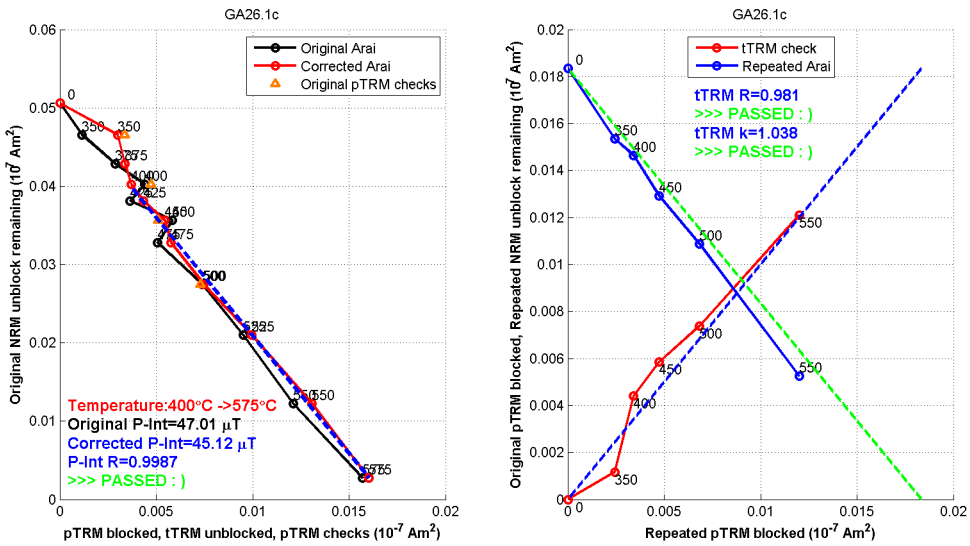

Figure 3.S2-050: Arai diagrams (left) and tTRM check (right) of specimen GA26.1c.

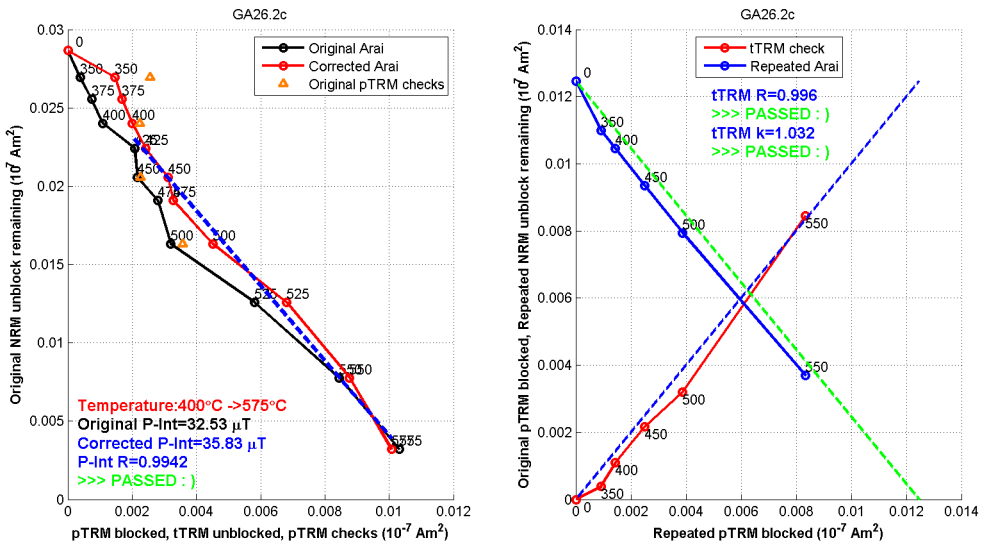

Figure 3.S2-051: Arai diagrams (left) and tTRM check (right) of specimen GA26.2c.

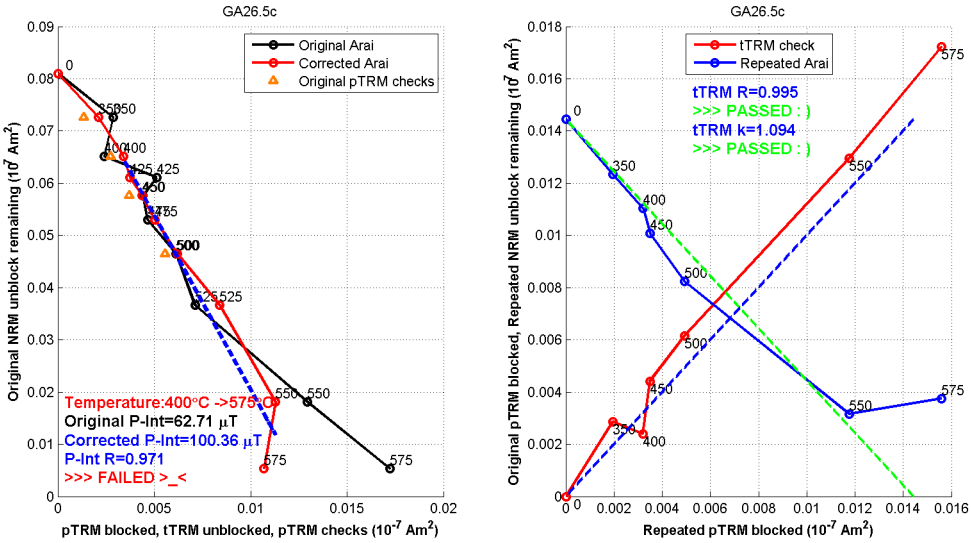

Figure 3.S2-052: Arai diagrams (left) and tTRM check (right) of specimen GA26.5c.

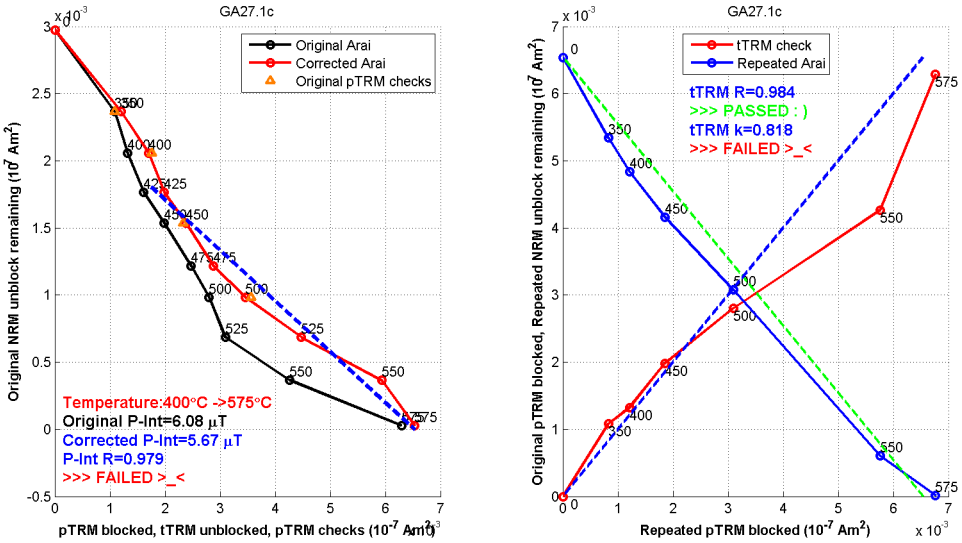

Figure 3.S2-053: Arai diagrams (left) and tTRM check (right) of specimen GA27.1c.

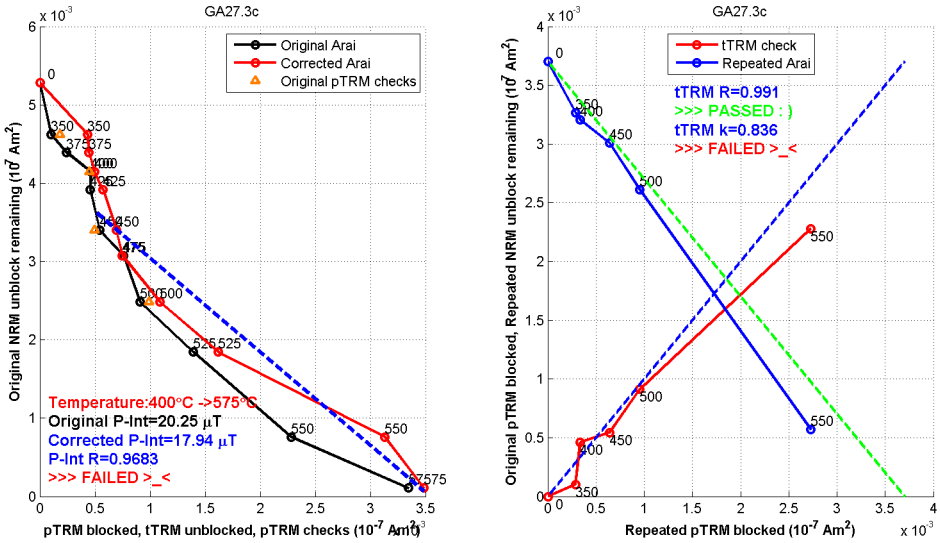

Figure 3.S2-054: Arai diagrams (left) and tTRM check (right) of specimen GA27.3c.

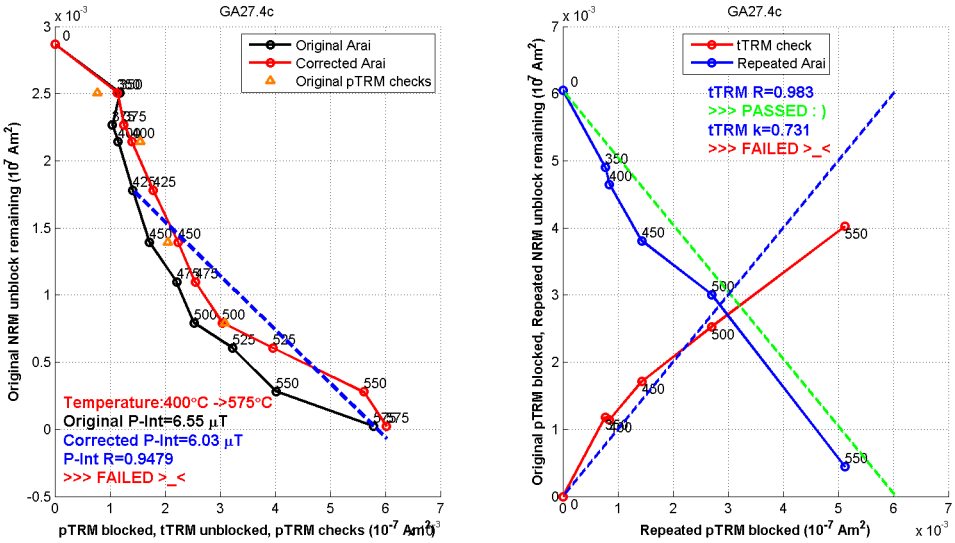

Figure 3.S2-055: Arai diagrams (left) and tTRM check (right) of specimen GA27.4c.

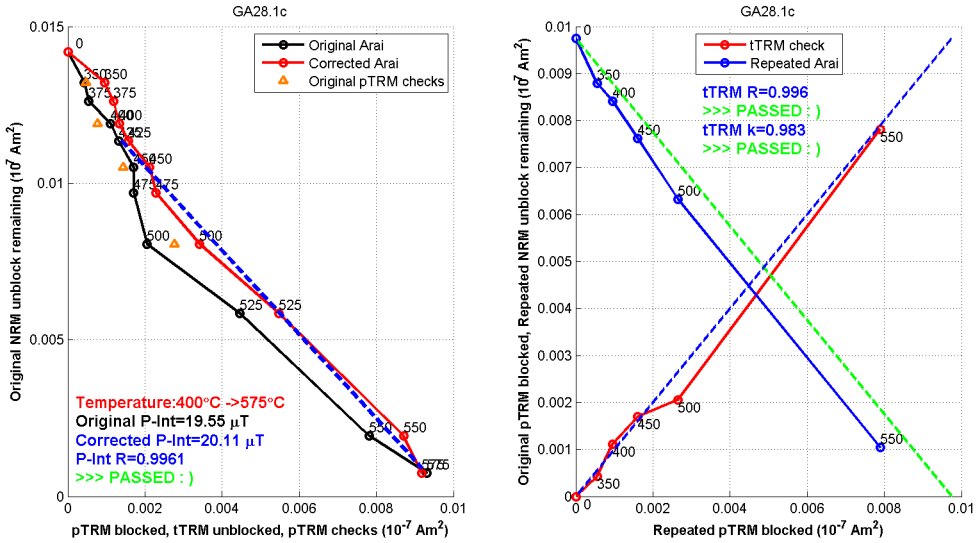

Figure 3.S2-056: Arai diagrams (left) and tTRM check (right) of specimen GA28.1c.

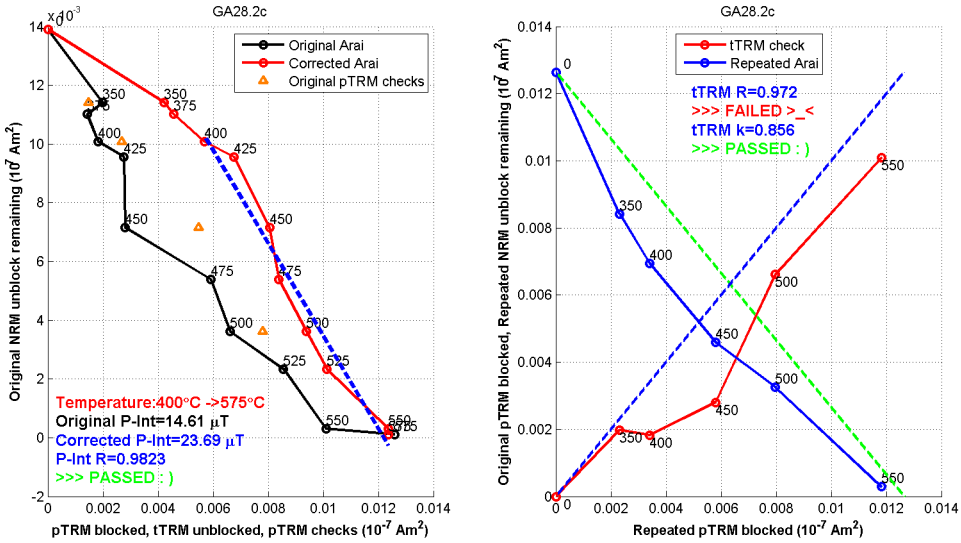

Figure 3.S2-057: Arai diagrams (left) and tTRM check (right) of specimen GA28.2c.

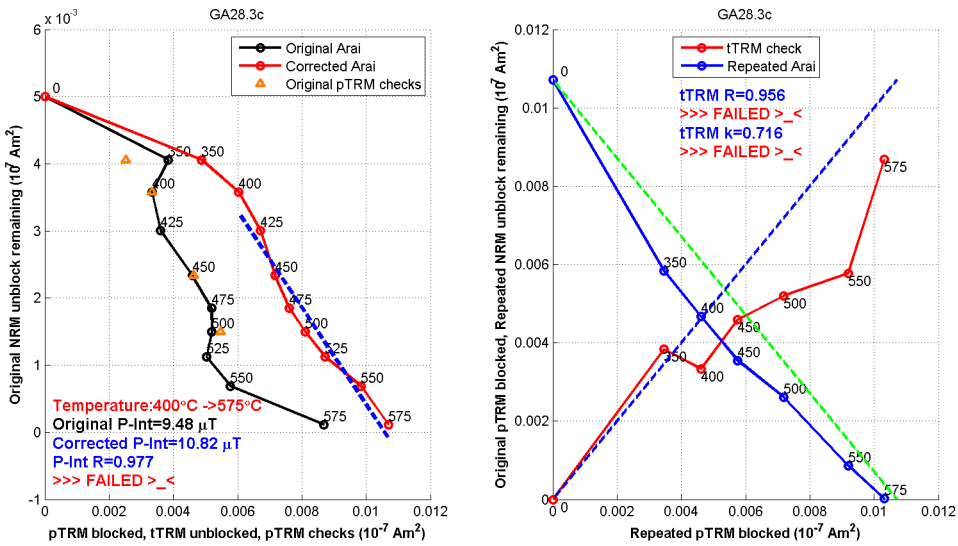

Figure 3.S2-058: Arai diagrams (left) and tTRM check (right) of specimen GA28.3c.

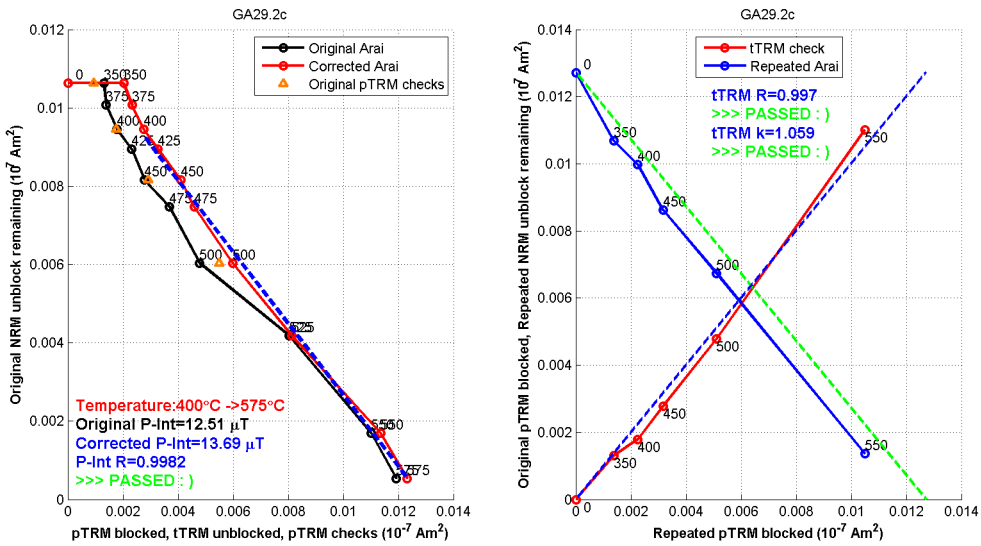

Figure 3.S2-059: Arai diagrams (left) and tTRM check (right) of specimen GA29.2c.

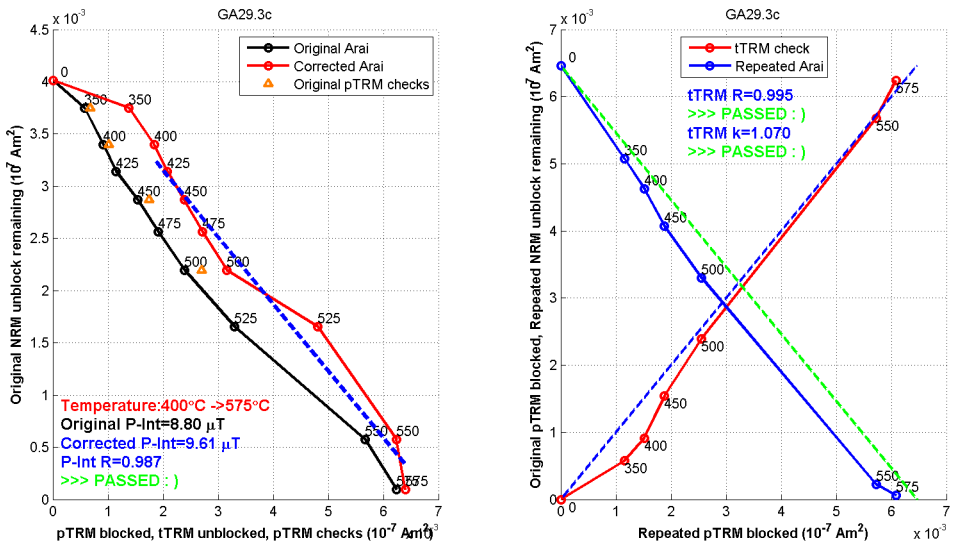

Figure 3.S2-060: Arai diagrams (left) and tTRM check (right) of specimen GA29.3c.

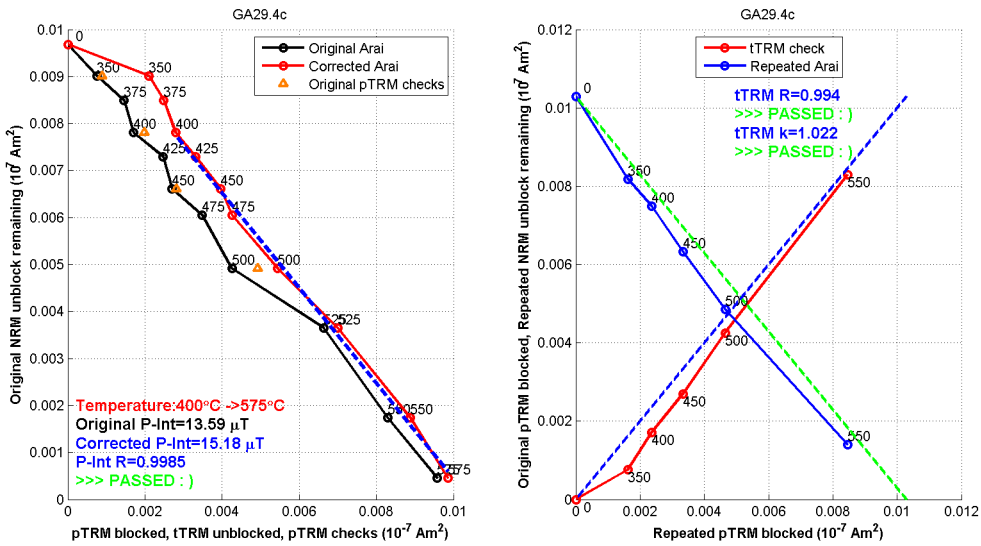

Figure 3.S2-061: Arai diagrams (left) and tTRM check (right) of specimen GA29.4c.

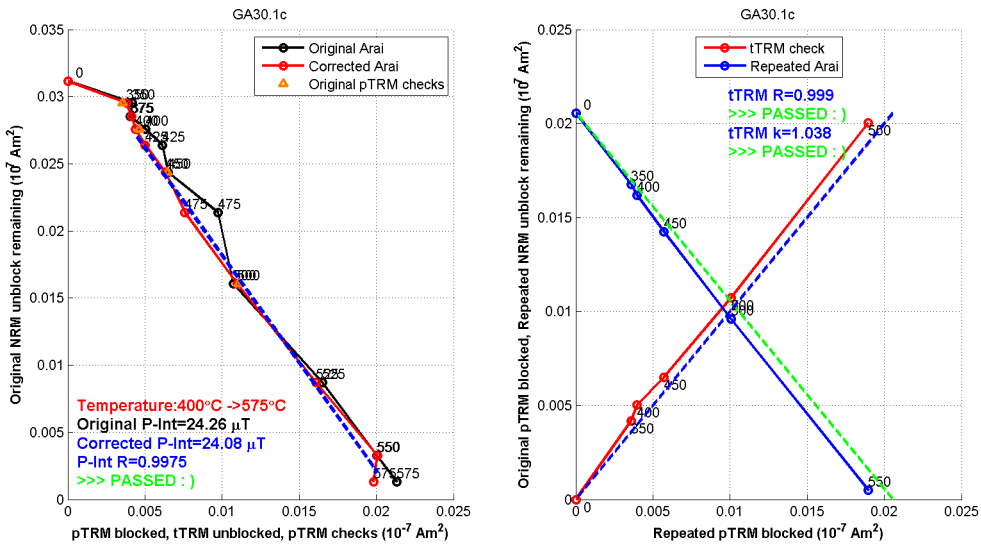

Figure 3.S2-062: Arai diagrams (left) and tTRM check (right) of specimen GA30.1c.

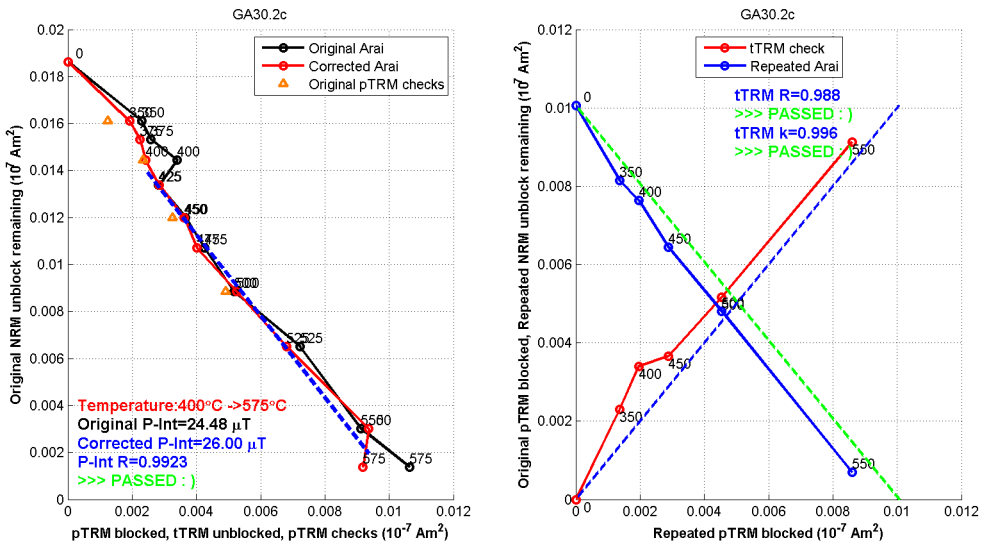

Figure 3.S2-063: Arai diagrams (left) and tTRM check (right) of specimen GA30.2c.

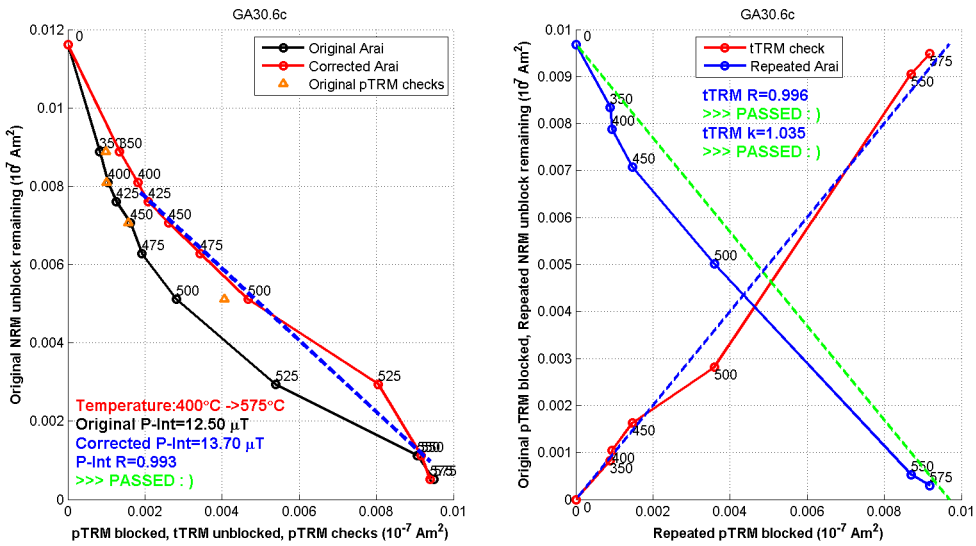

Figure 3.S2-064: Arai diagrams (left) and tTRM check (right) of specimen GA30.6c.

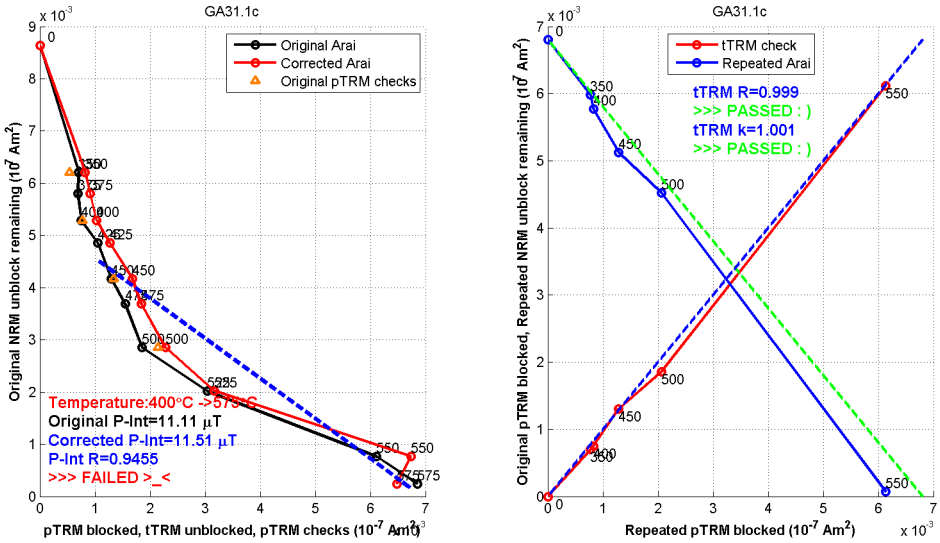

Figure 3.S2-065: Arai diagrams (left) and tTRM check (right) of specimen GA31.1c.

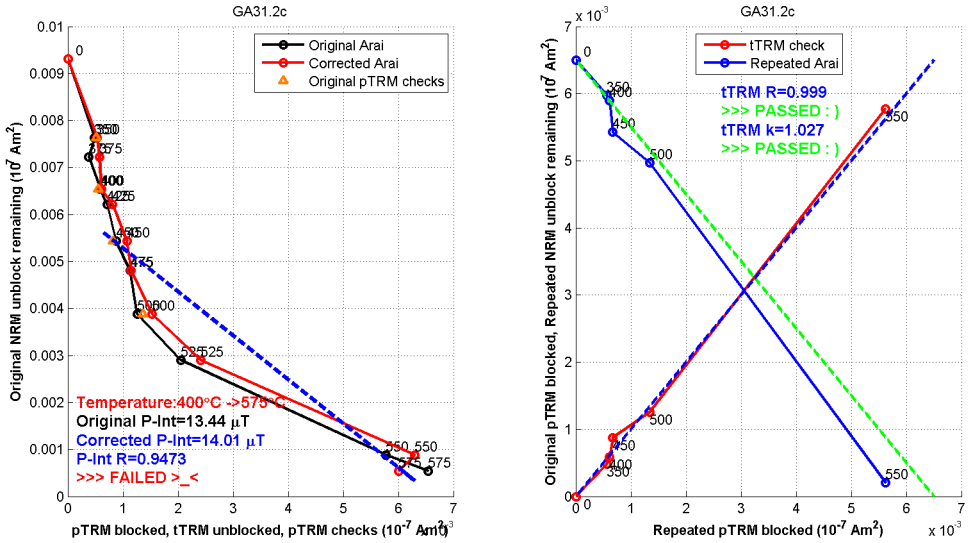

Figure 3.S2-066: Arai diagrams (left) and tTRM check (right) of specimen GA31.2c.

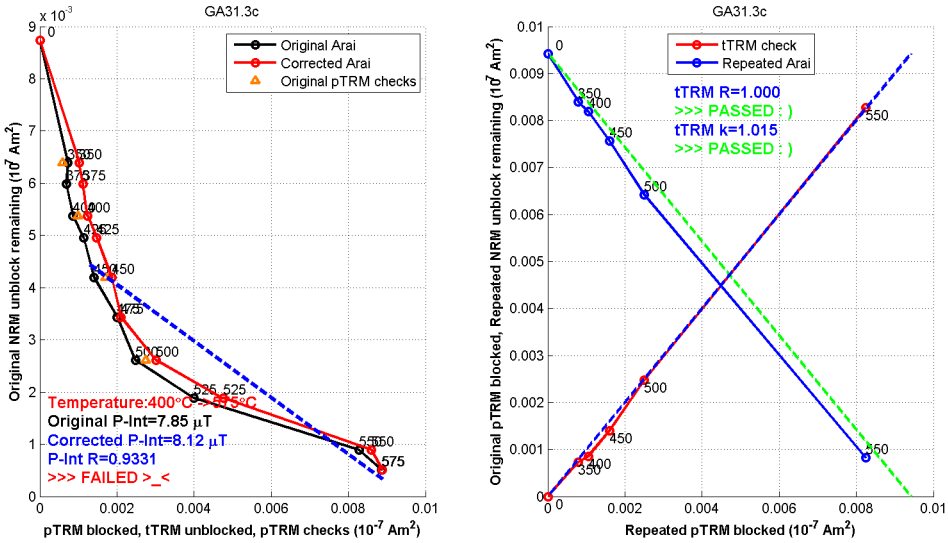

Figure 3.S2-067: Arai diagrams (left) and tTRM check (right) of specimen GA31.3c.

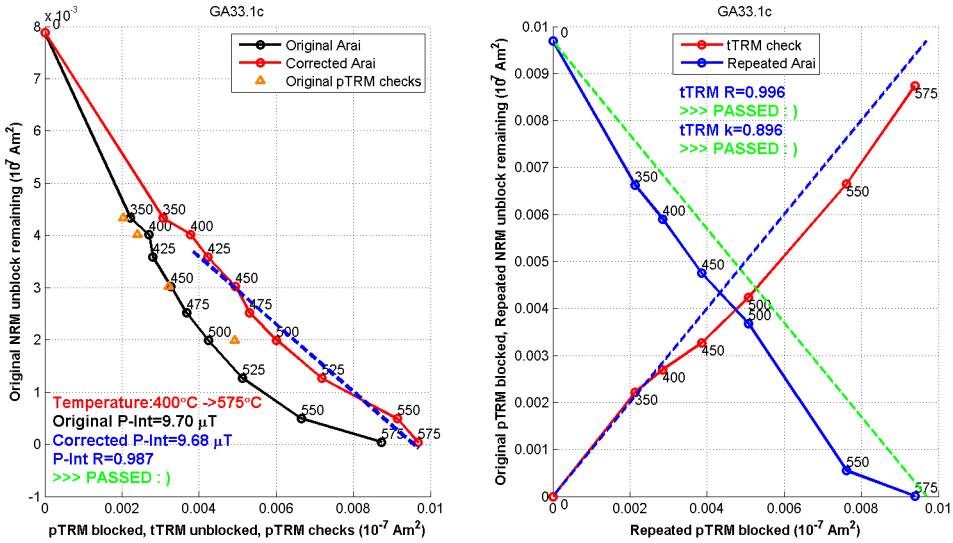

Figure 3.S2-068: Arai diagrams (left) and tTRM check (right) of specimen GA33.1c.

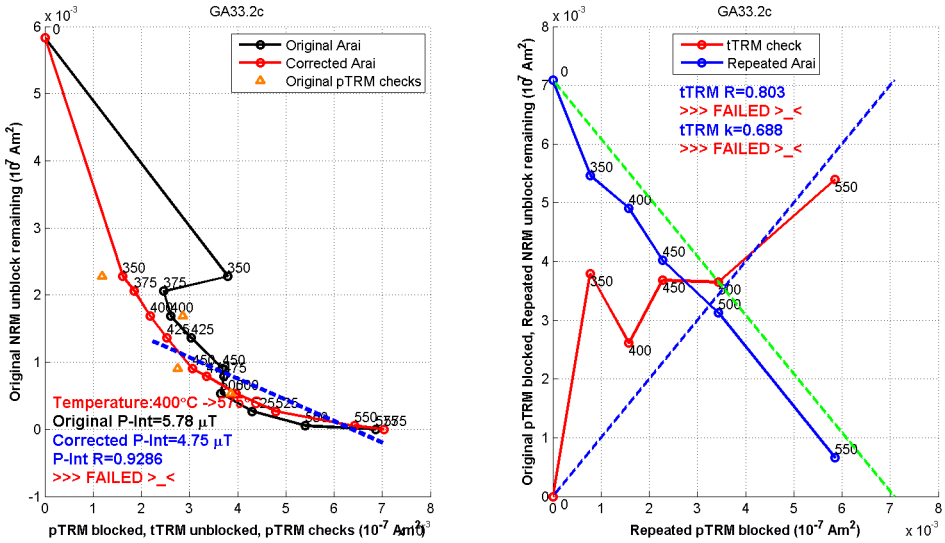

Figure 3.S2-069: Arai diagrams (left) and tTRM check (right) of specimen GA33.2c.

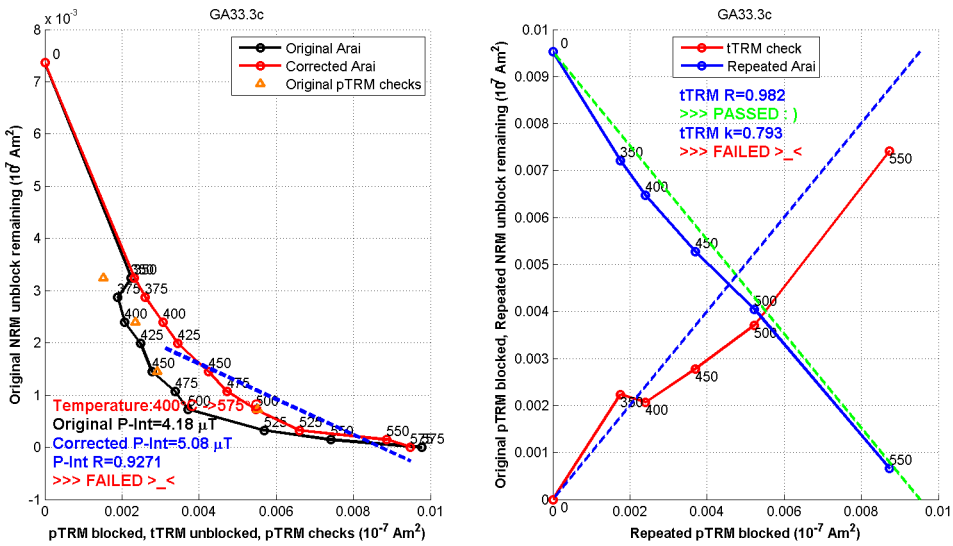

Figure 3.S2-070: Arai diagrams (left) and tTRM check (right) of specimen GA33.3c.

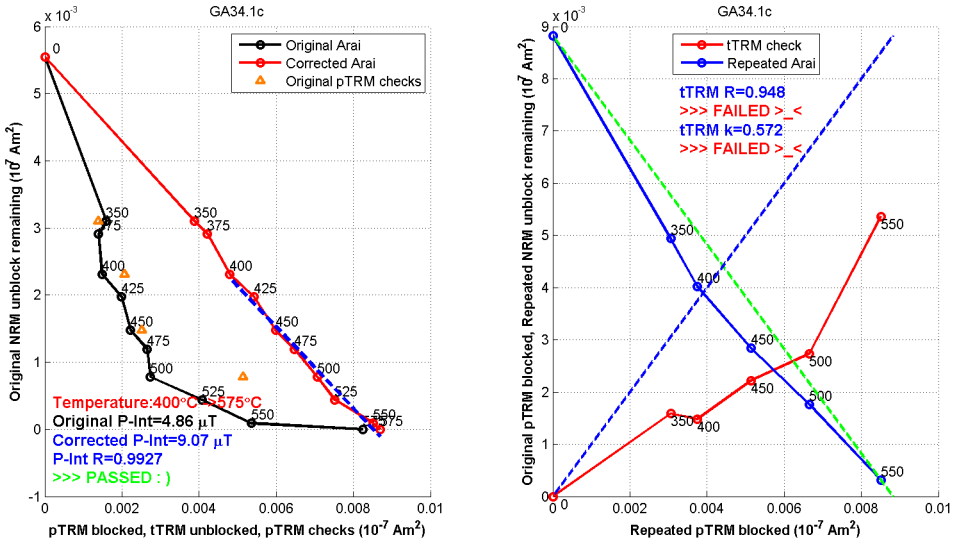

Figure 3.S2-071: Arai diagrams (left) and tTRM check (right) of specimen GA34.1c.

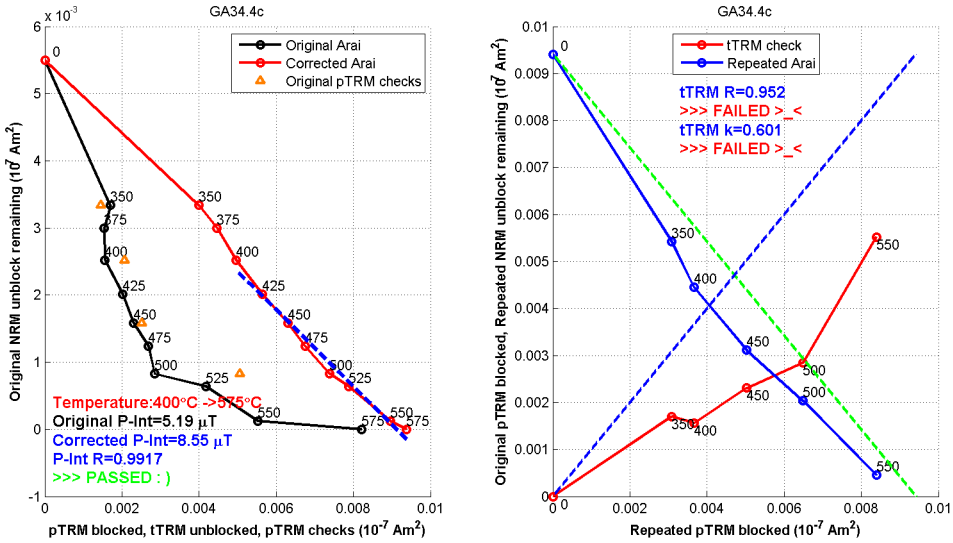

Figure 3.S2-072: Arai diagrams (left) and tTRM check (right) of specimen GA34.4c.

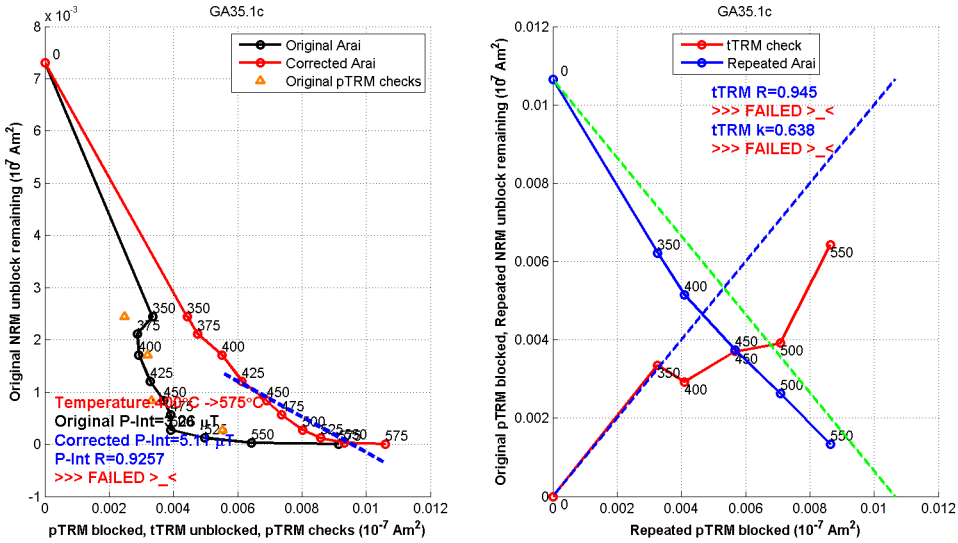

Figure 3.S2-073: Arai diagrams (left) and tTRM check (right) of specimen GA35.1c.

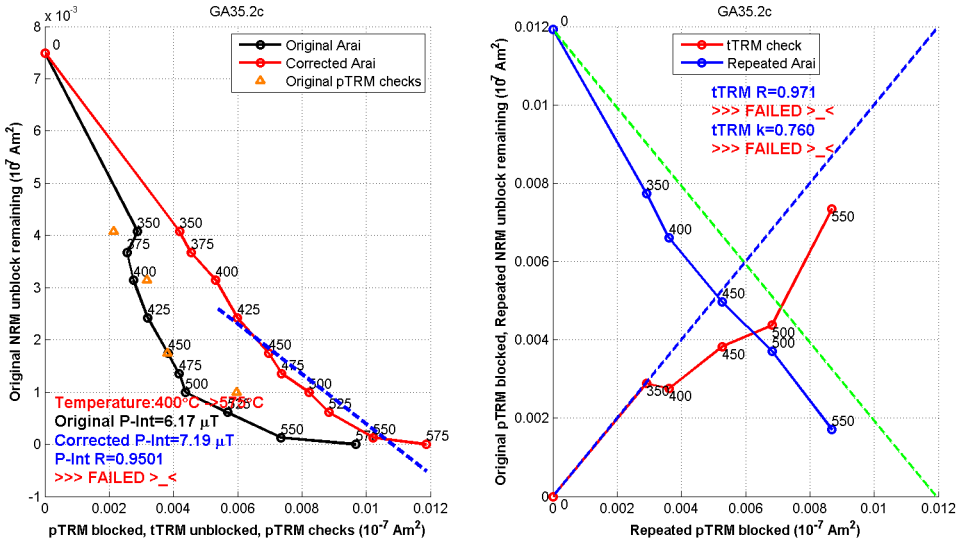

Figure 3.S2-074: Arai diagrams (left) and tTRM check (right) of specimen GA35.2c.

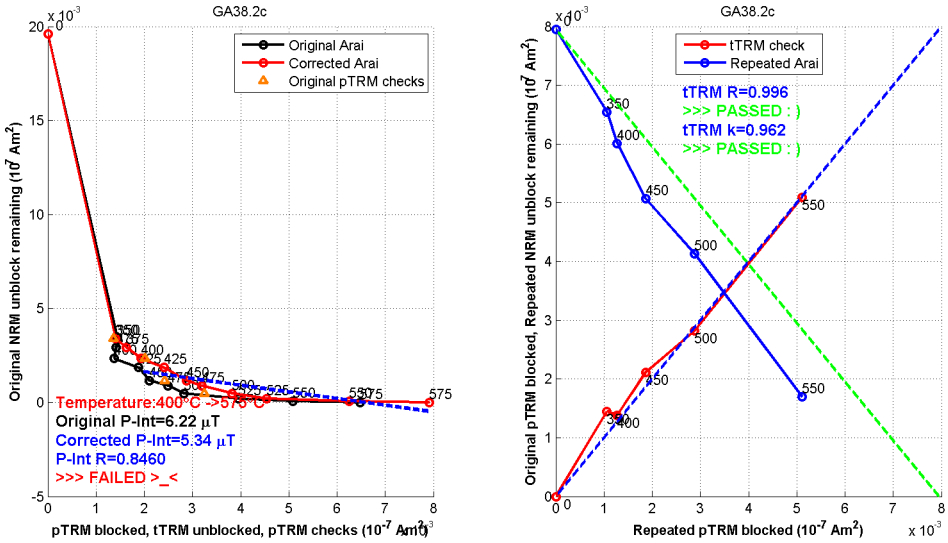

Figure 3.S2-075: Arai diagrams (left) and tTRM check (right) of specimen GA38.2c.

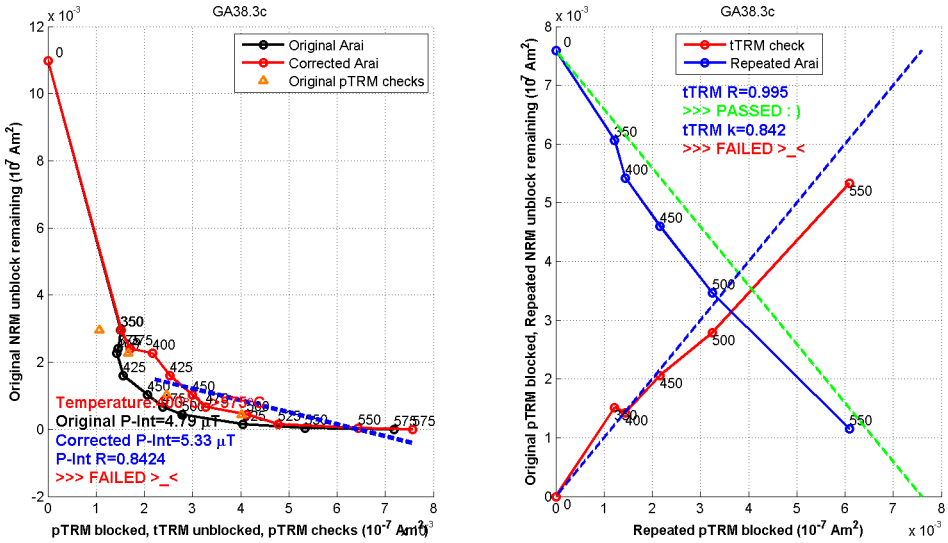

Figure 3.S2-076: Arai diagrams (left) and tTRM check (right) of specimen GA38.3c.

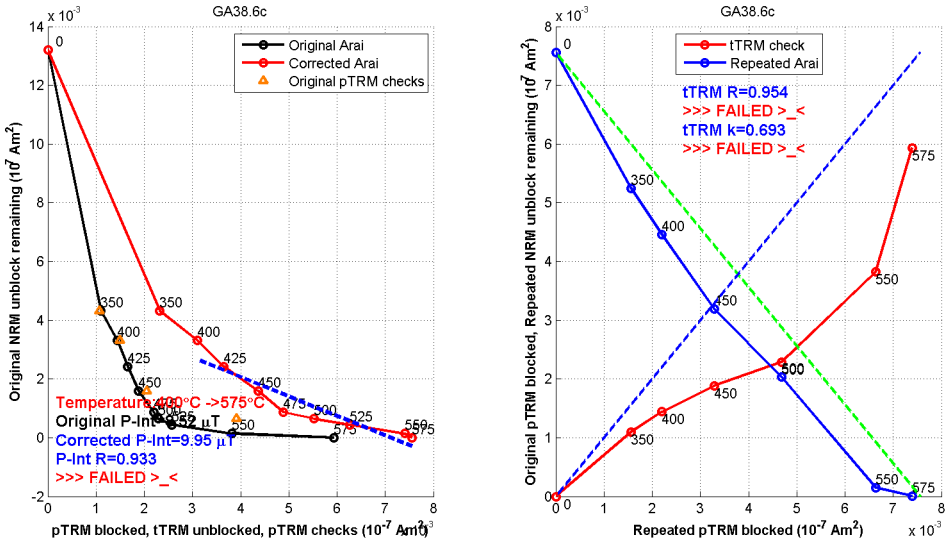

Figure 3.S2-077: Arai diagrams (left) and tTRM check (right) of specimen GA38.8c.

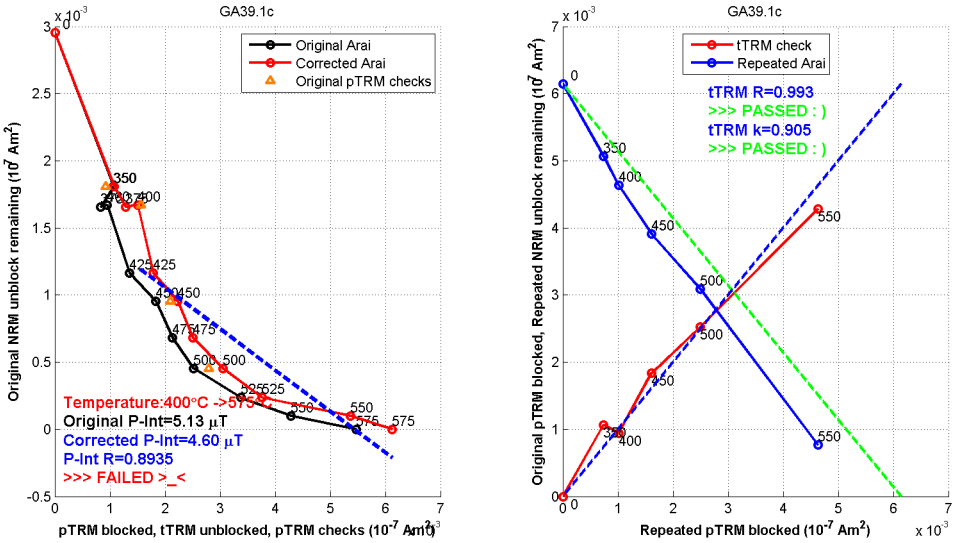

Figure 3.S2-078: Arai diagrams (left) and tTRM check (right) of specimen GA39.1c.

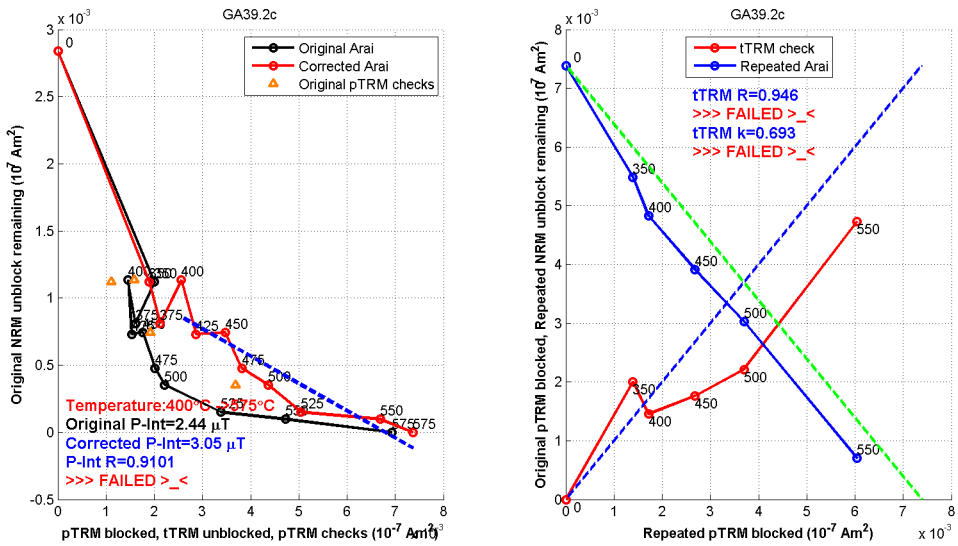

Figure 3.S2-079: Arai diagrams (left) and tTRM check (right) of specimen GA39.2c.

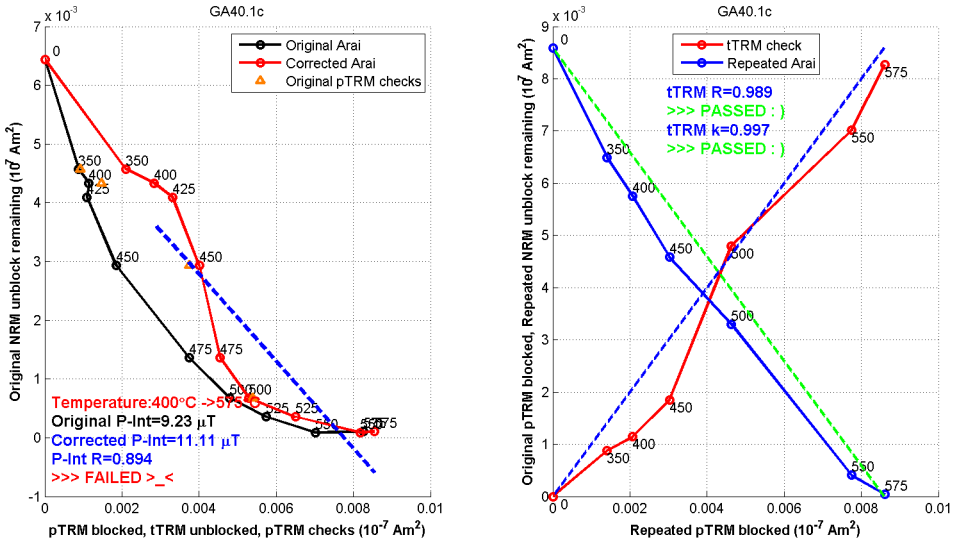

Figure 3.S2-080: Arai diagrams (left) and tTRM check (right) of specimen GA40.1c.

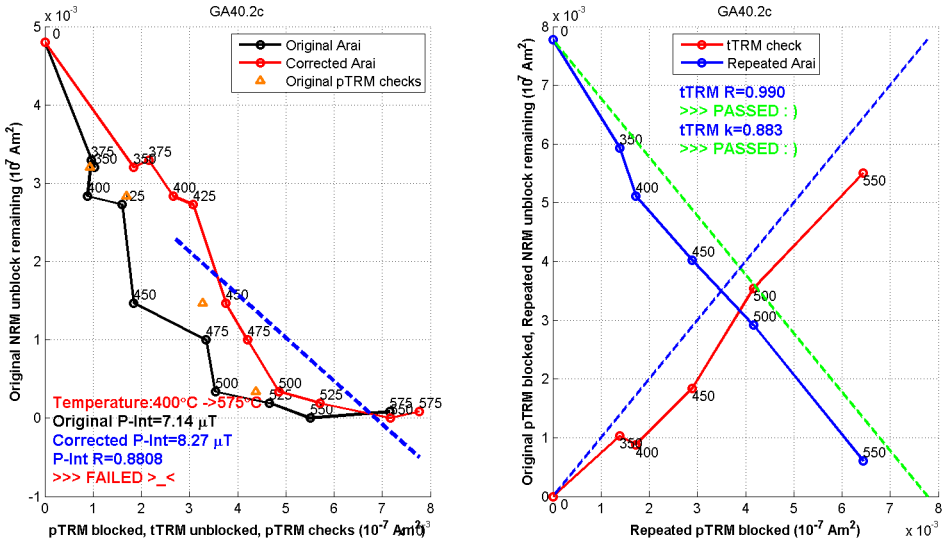

Figure 3.S2-081: Arai diagrams (left) and tTRM check (right) of specimen GA40.2c.

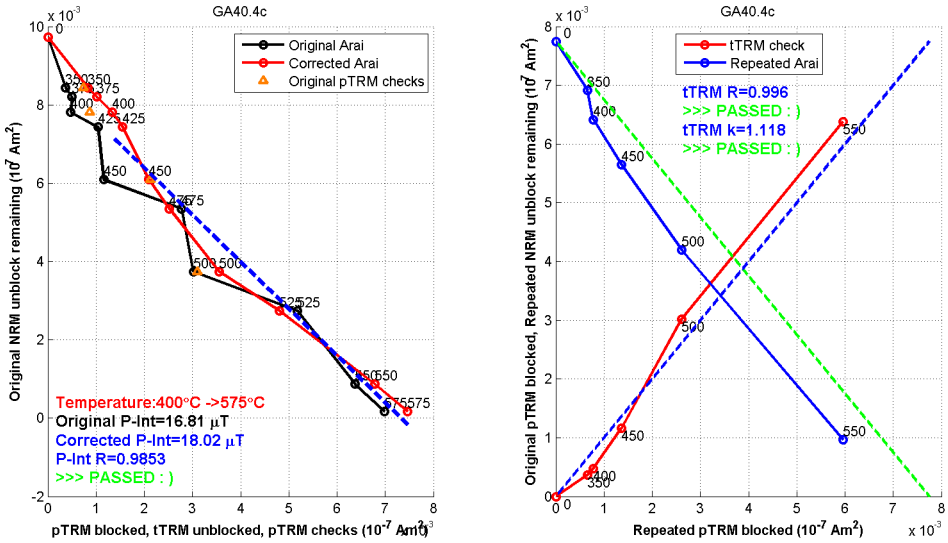

Figure 3.S2-082: Arai diagrams (left) and tTRM check (right) of specimen GA40.4c.

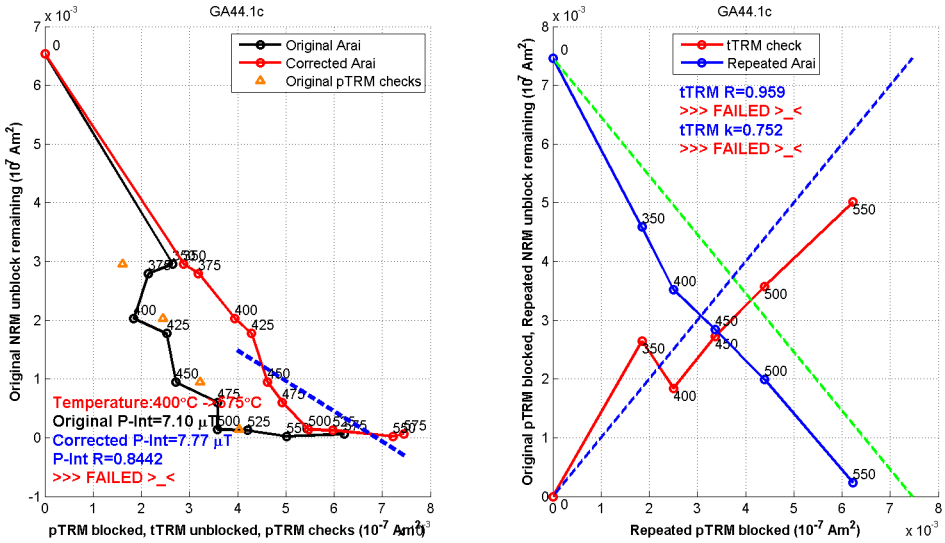

Figure 3.S2-083: Arai diagrams (left) and tTRM check (right) of specimen GA44.1c.

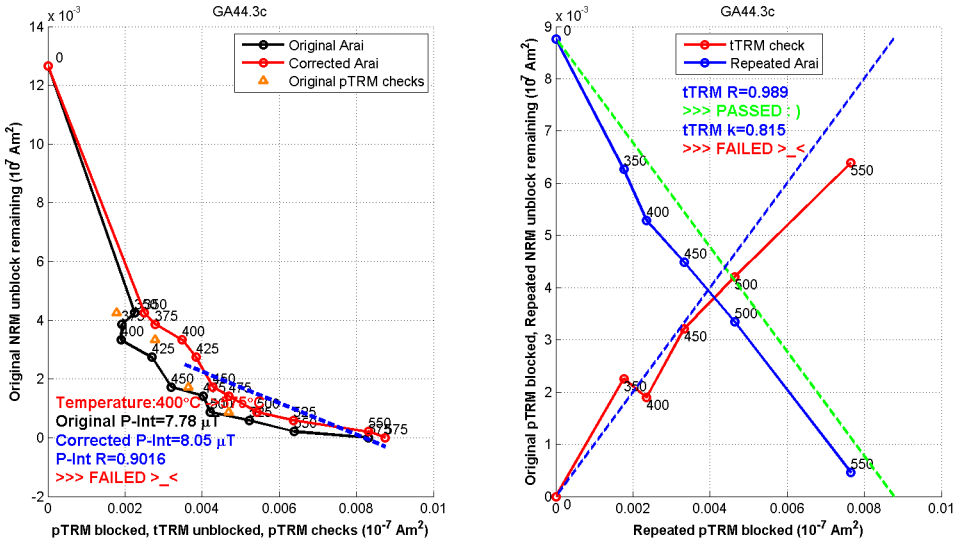

Figure 3.S2-084: Arai diagrams (left) and tTRM check (right) of specimen GA44.3c.

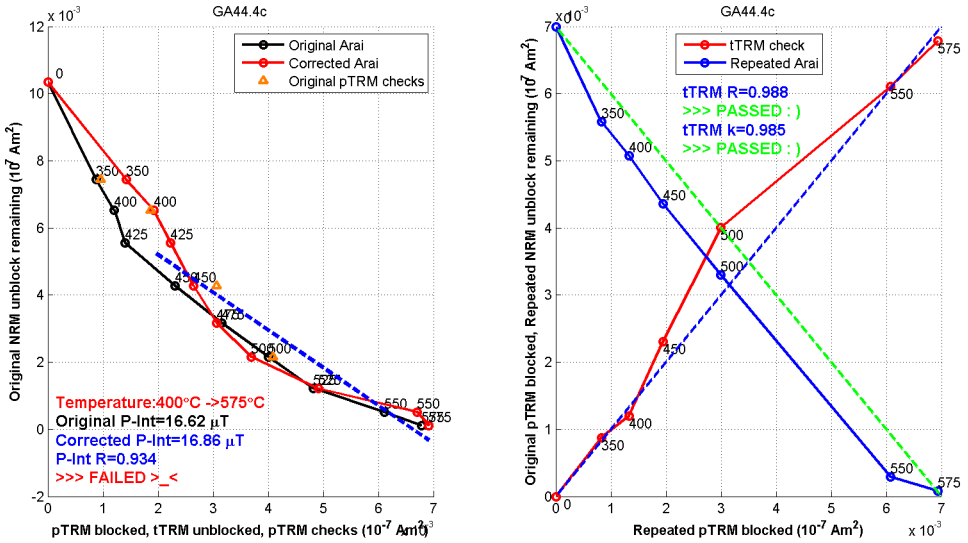

Figure 3.S2-085: Arai diagrams (left) and tTRM check (right) of specimen GA44.4c.

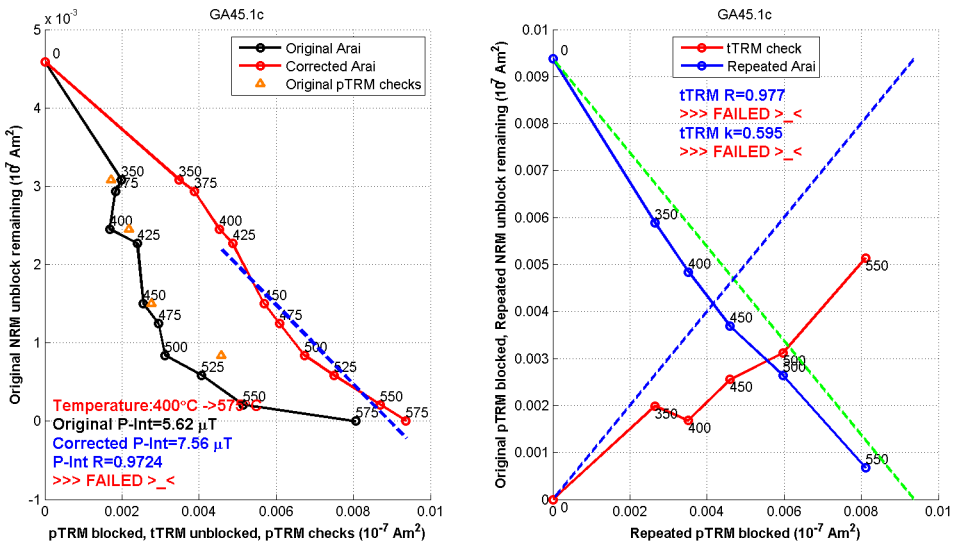

Figure 3.S2-086: Arai diagrams (left) and tTRM check (right) of specimen GA45.1c.

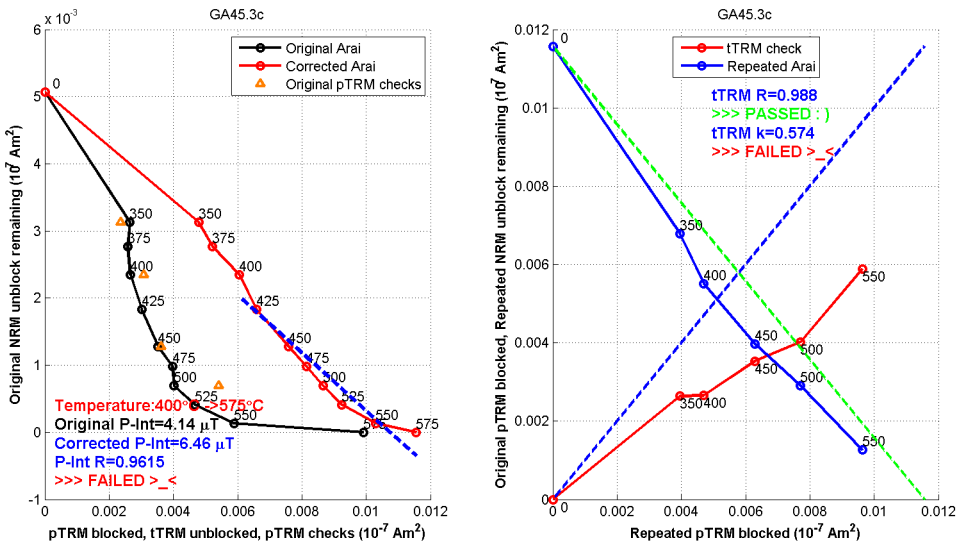

Figure 3.S2-087: Arai diagrams (left) and tTRM check (right) of specimen GA45.3c.

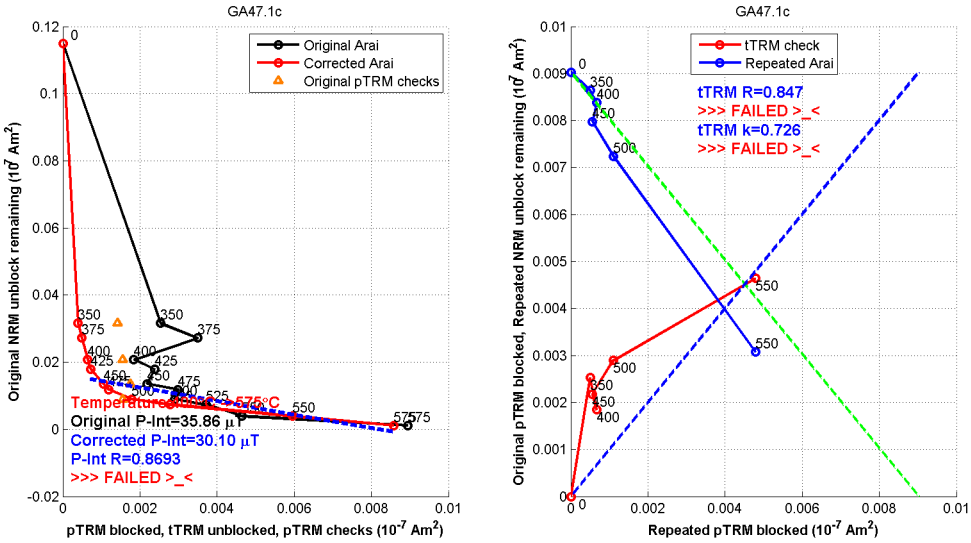

Figure 3.S2-088: Arai diagrams (left) and tTRM check (right) of specimen GA47.1c.

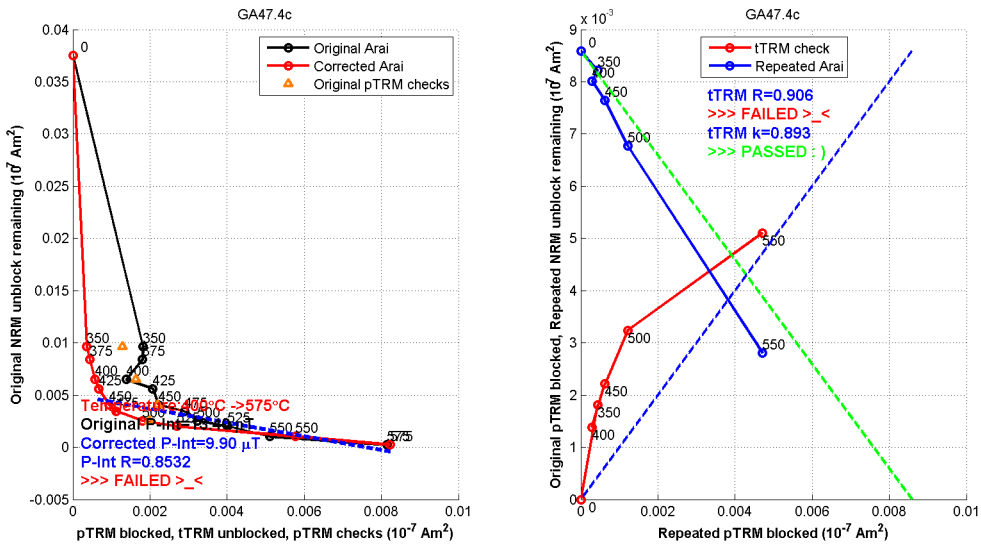

Figure 3.S2-089: Arai diagrams (left) and tTRM check (right) of specimen GA47.4c.

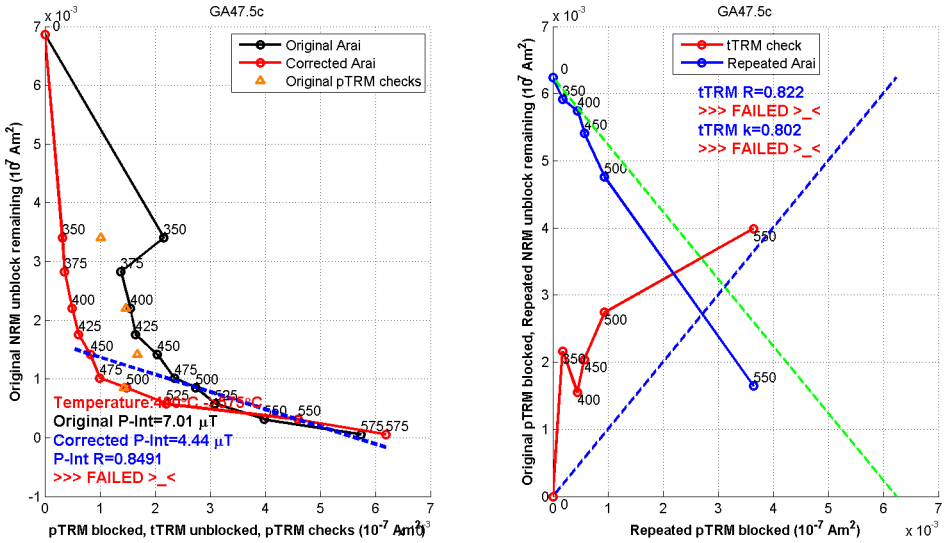

Figure 3.S2-090: Arai diagrams (left) and tTRM check (right) of specimen GA47.5c.

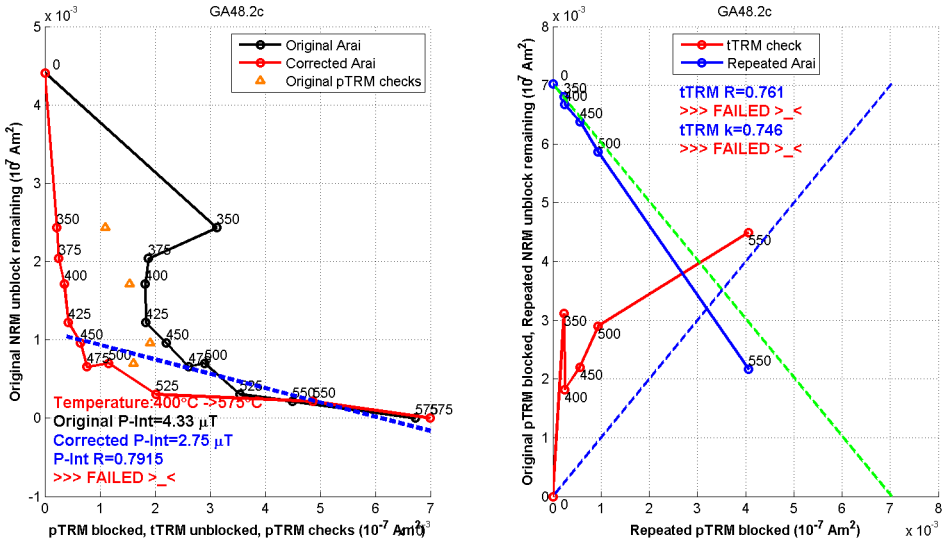

Figure 3.S2-091: Arai diagrams (left) and tTRM check (right) of specimen GA48.2c.

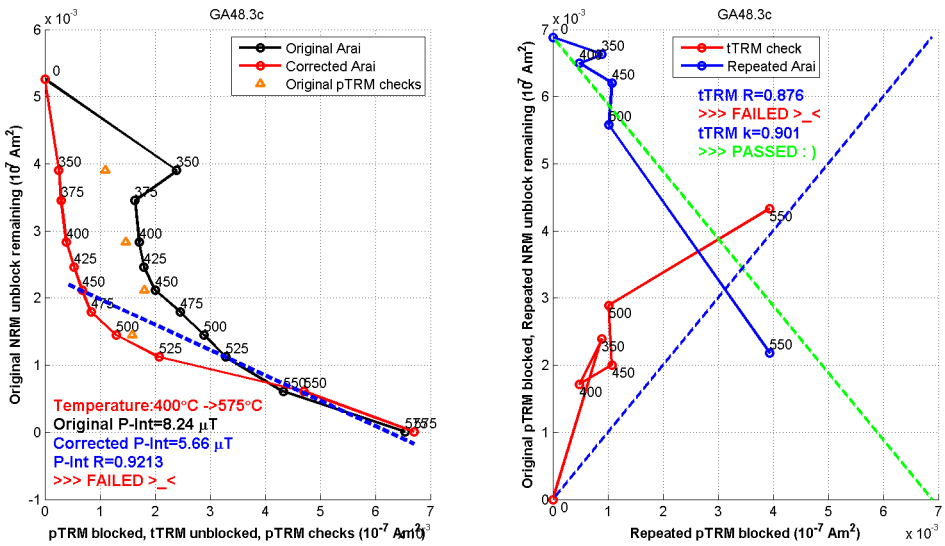

Figure 3.S2-092: Arai diagrams (left) and tTRM check (right) of specimen GA48.3c.

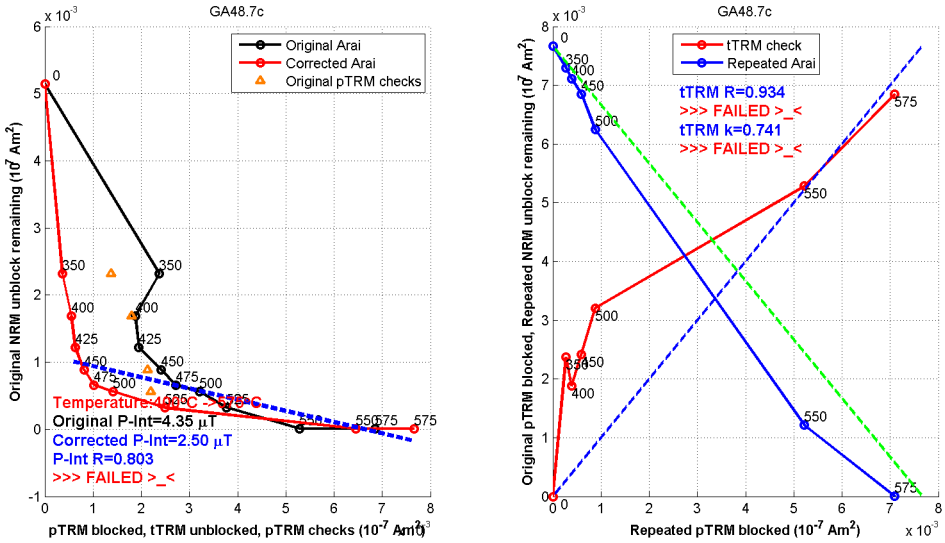

Figure 3.S2-093: Arai diagrams (left) and tTRM check (right) of specimen GA48.7c.

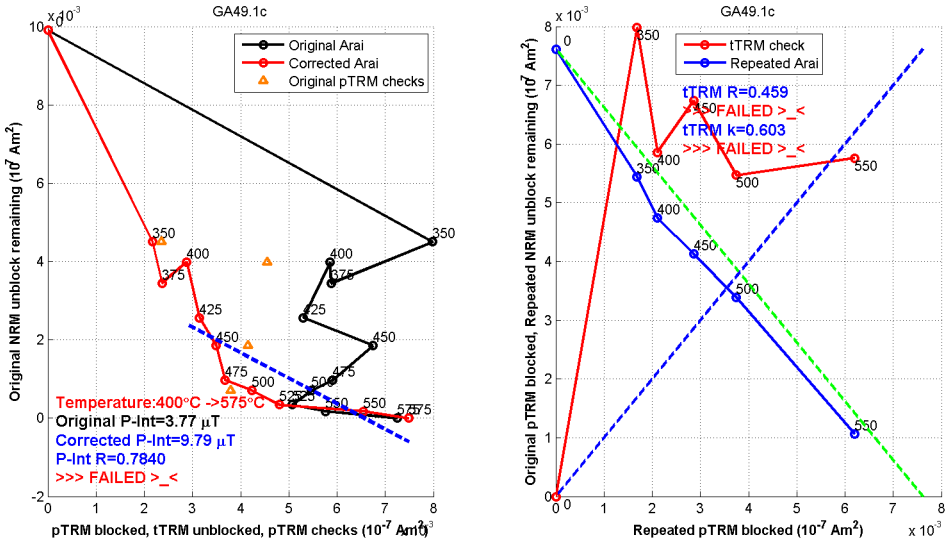

Figure 3.S2-094: Arai diagrams (left) and tTRM check (right) of specimen GA49.1c.

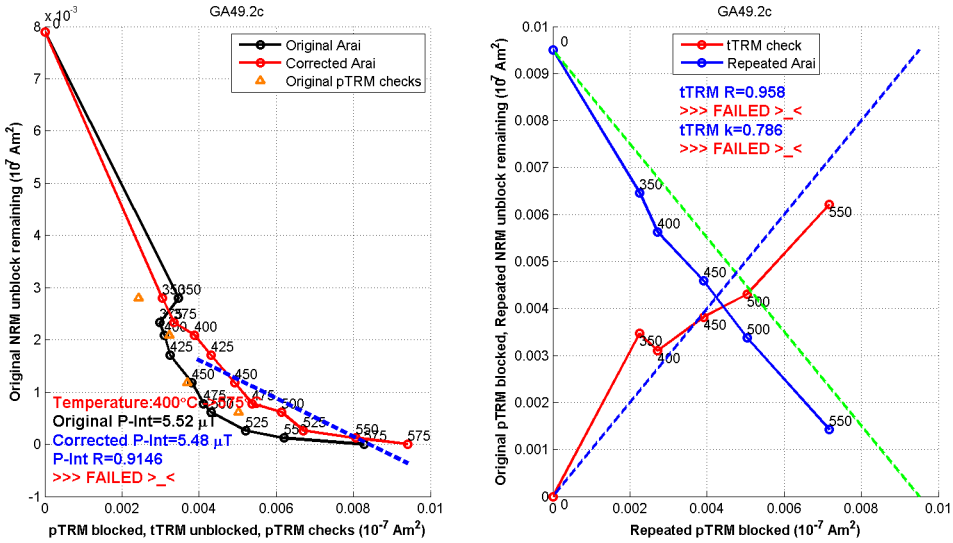

Figure 3.S2-095: Arai diagrams (left) and tTRM check (right) of specimen GA49.2c.

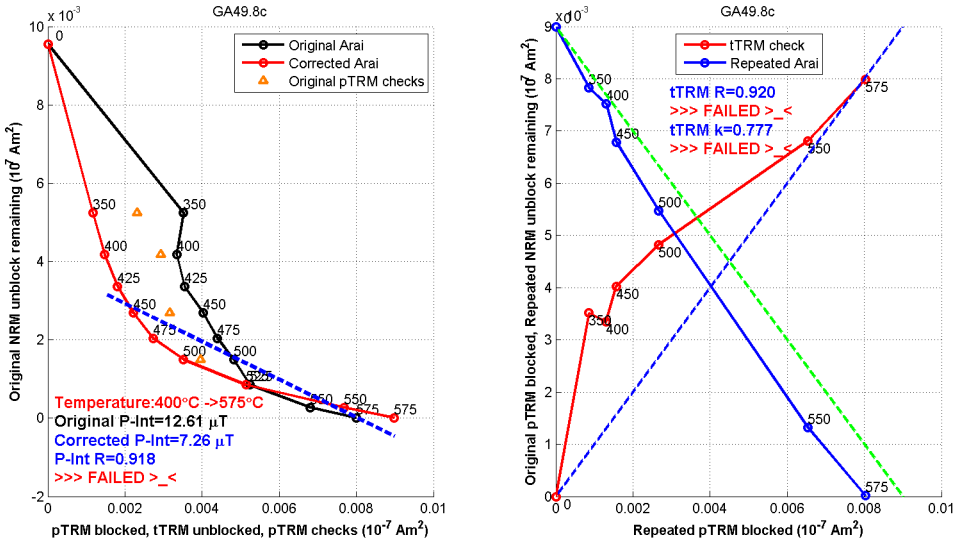

Figure 3.S2-096: Arai diagrams (left) and tTRM check (right) of specimen GA49.8c.

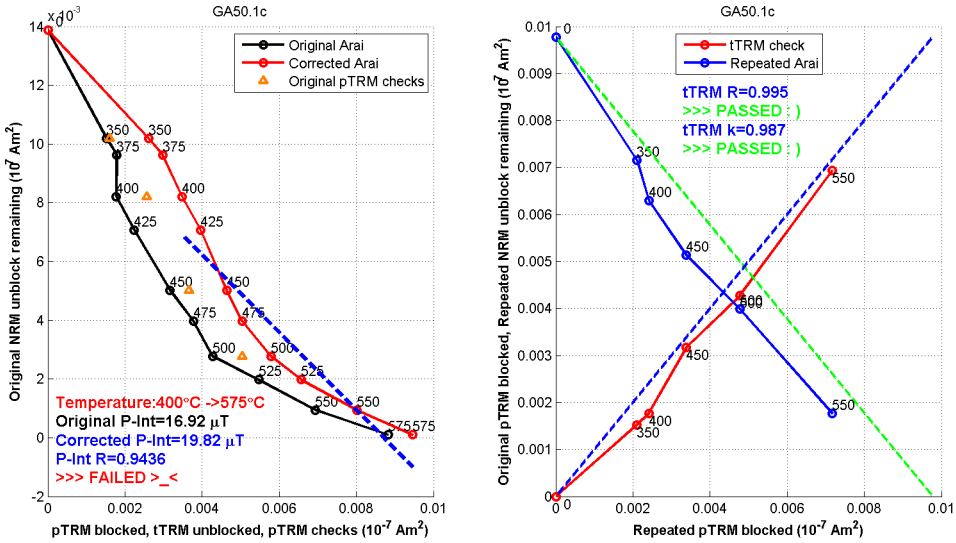

Figure 3.S2-097: Arai diagrams (left) and tTRM check (right) of specimen GA50.1c.

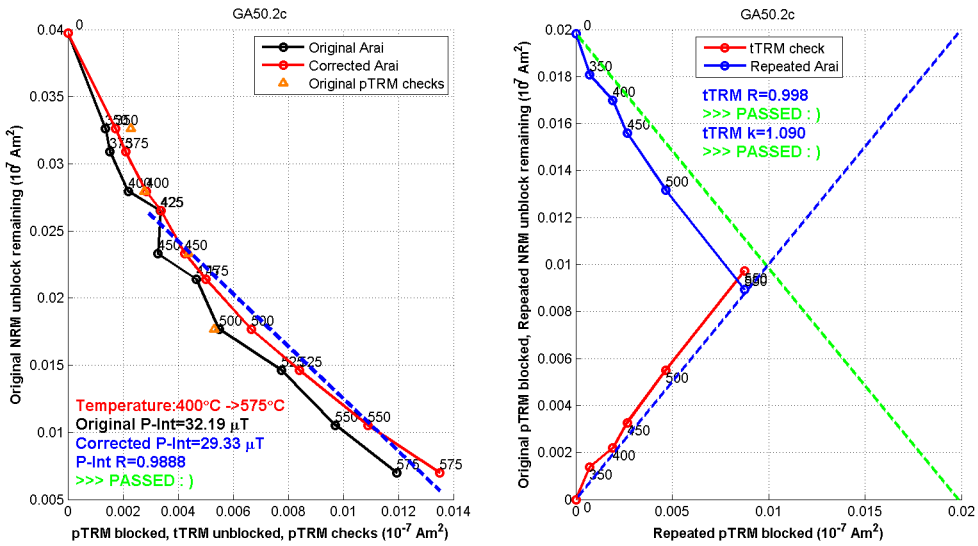

Figure 3.S2-098: Arai diagrams (left) and tTRM check (right) of specimen GA50.2c.

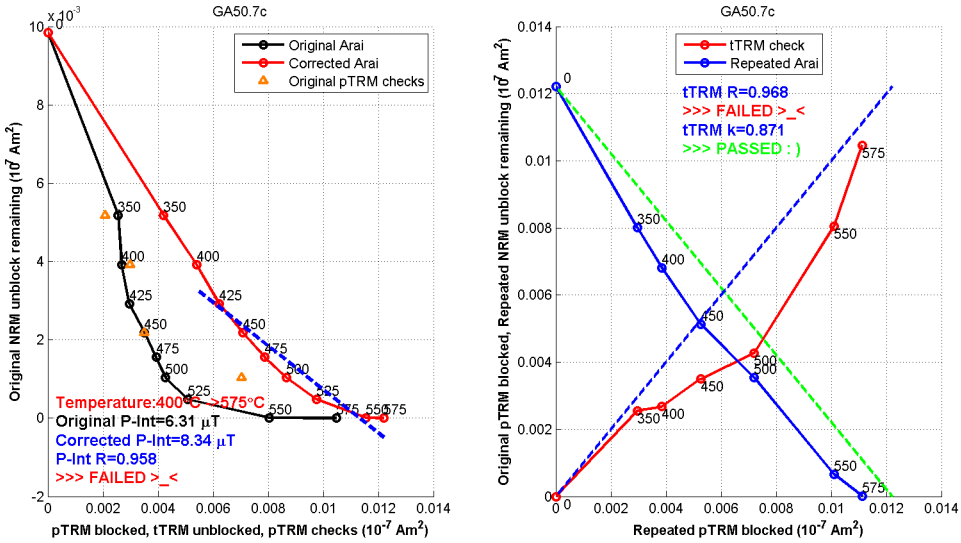

Figure 3.S2-099: Arai diagrams (left) and tTRM check (right) of specimen GA50.7c.

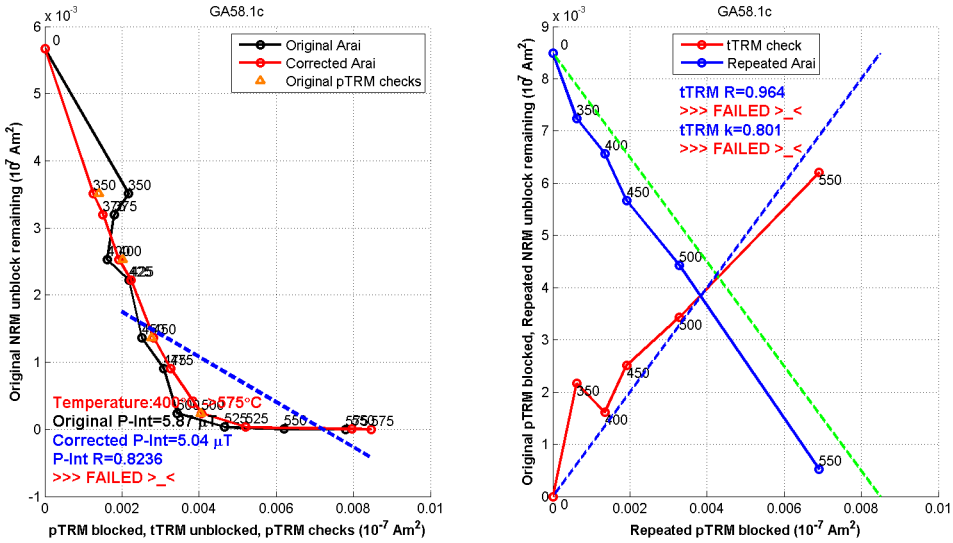

Figure 3.S2-100: Arai diagrams (left) and tTRM check (right) of specimen GA58.1c.

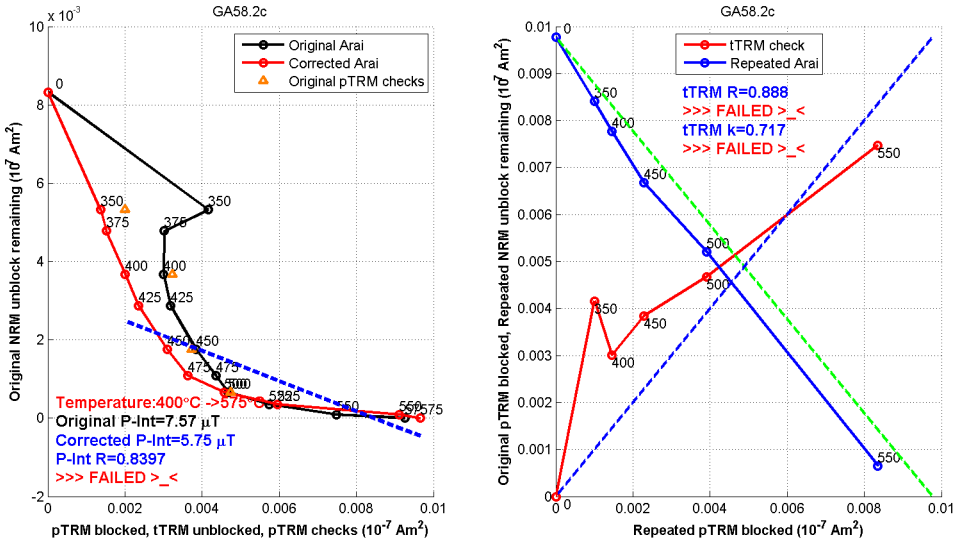

Figure 3.S2-101: Arai diagrams (left) and tTRM check (right) of specimen GA58.2c.

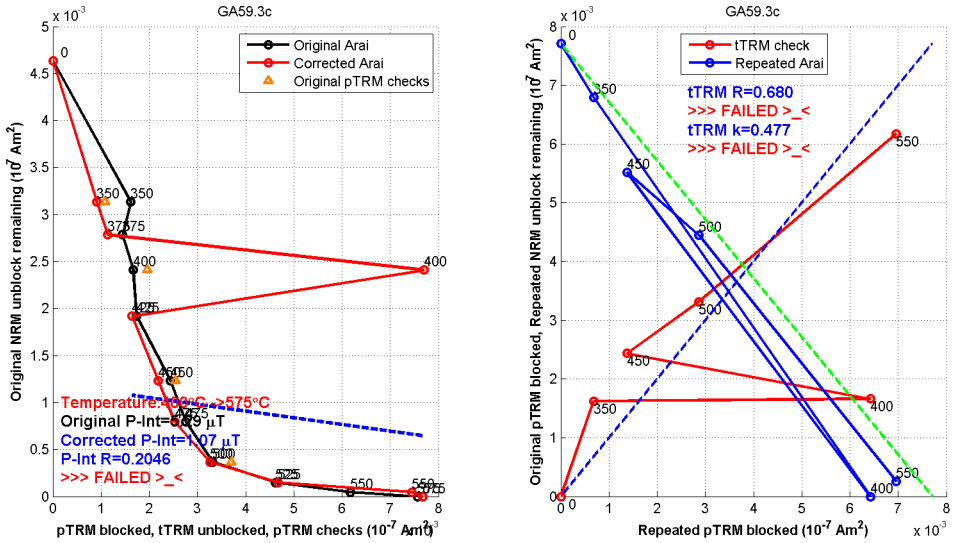

Figure 3.S2-102: Arai diagrams (left) and tTRM check (right) of specimen GA59.3c.

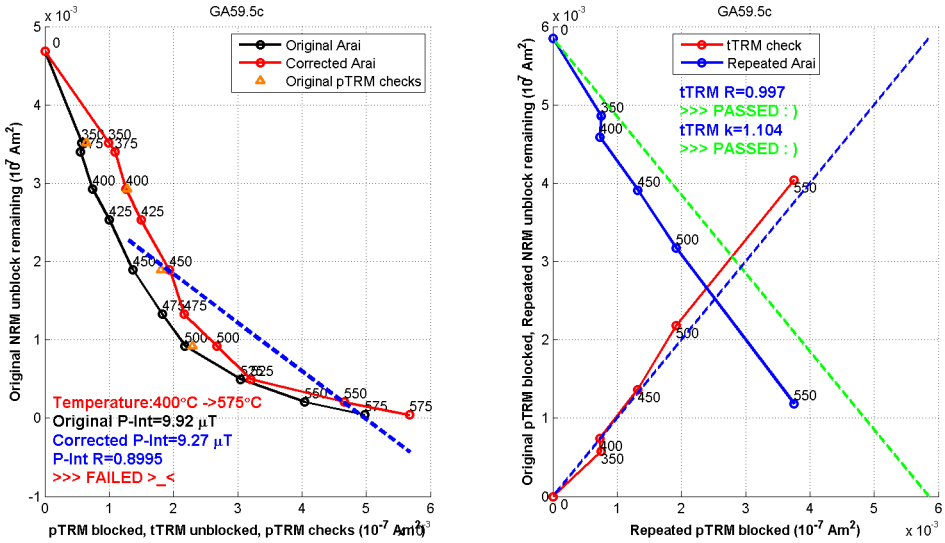

Figure 3.S2-103: Arai diagrams (left) and tTRM check (right) of specimen GA59.5c.

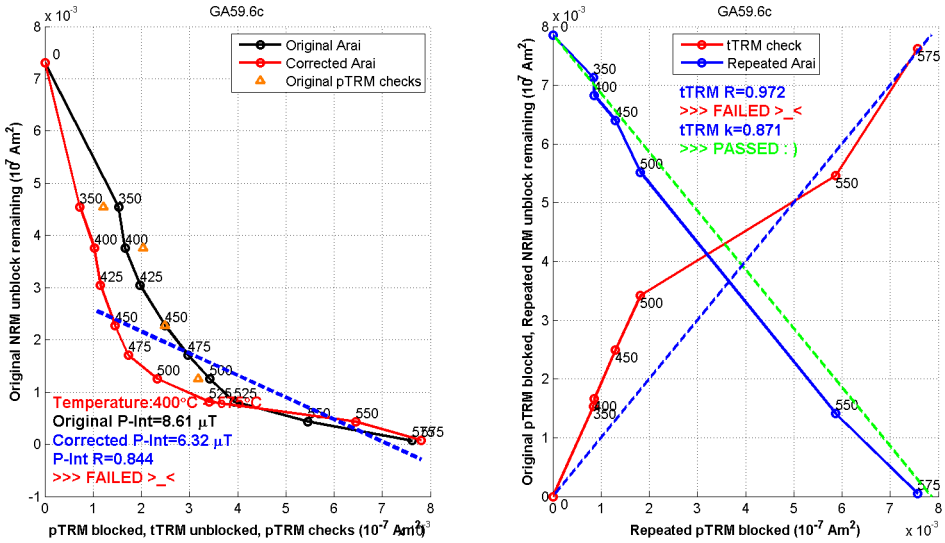

Figure 3.S2-104: Arai diagrams (left) and tTRM check (right) of specimen GA59.6c.

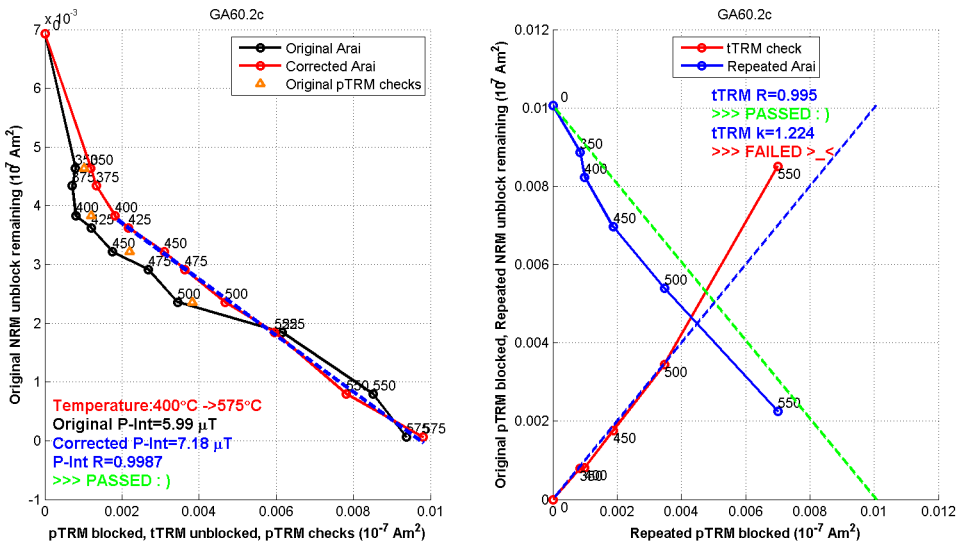

Figure 3.S2-105: Arai diagrams (left) and tTRM check (right) of specimen GA60.2c.

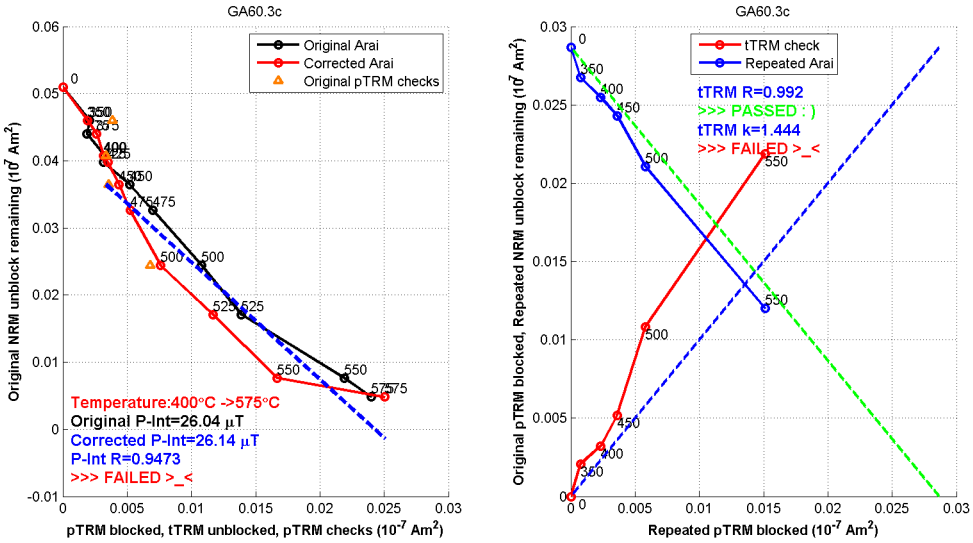

Figure 3.S2-106: Arai diagrams (left) and tTRM check (right) of specimen GA60.3c.

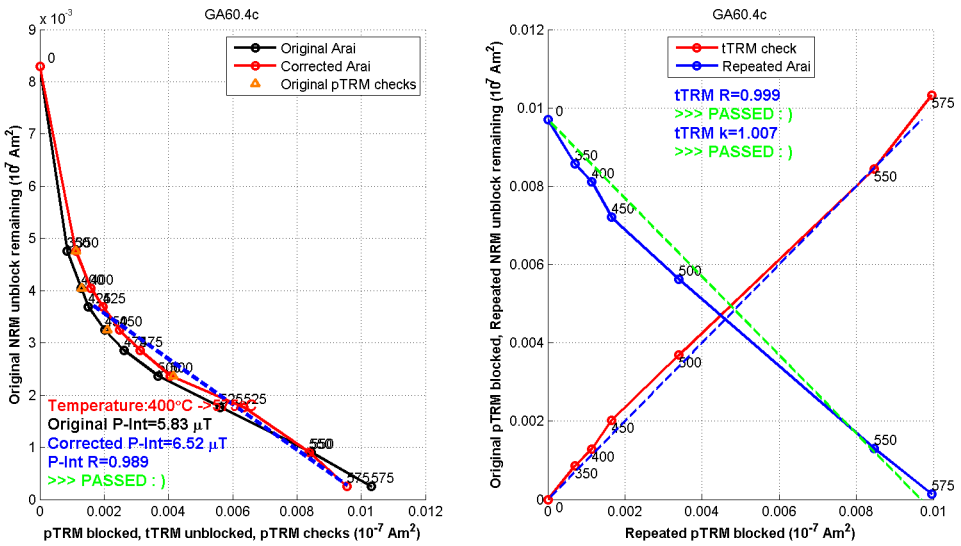

Figure 3.S2-107: Arai diagrams (left) and tTRM check (right) of specimen GA60.4c.

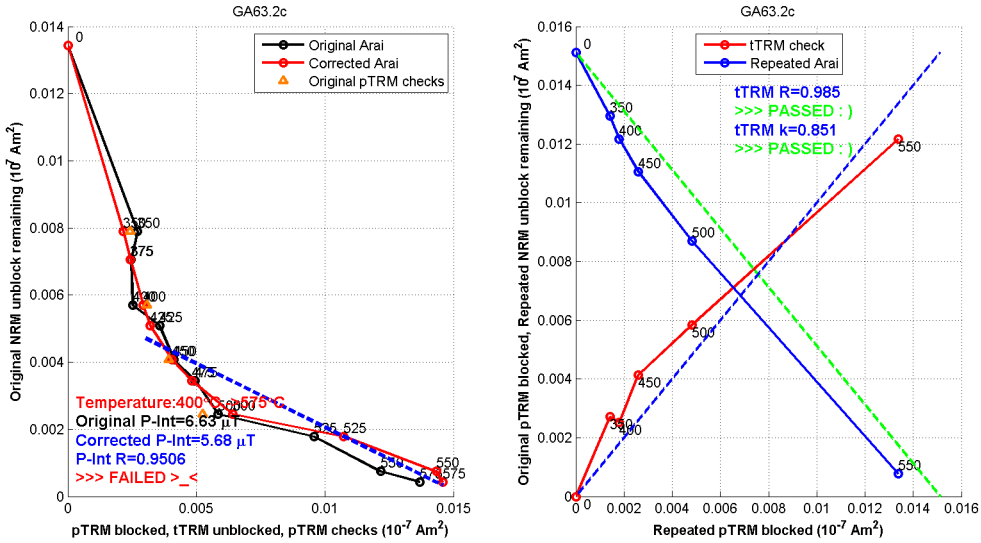

Figure 3.S2-108: Arai diagrams (left) and tTRM check (right) of specimen GA63.2c.

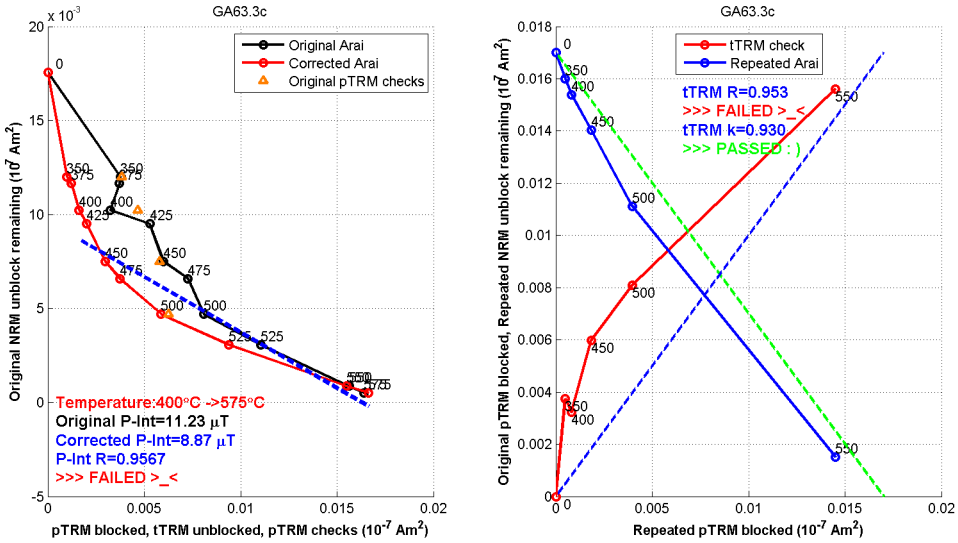

Figure 3.S2-109: Arai diagrams (left) and tTRM check (right) of specimen GA63.3c.

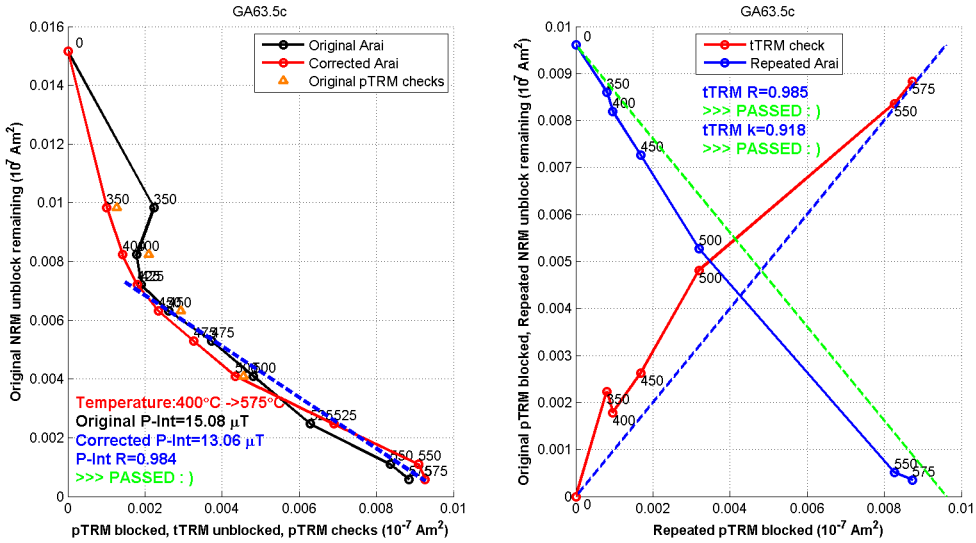

Figure 3.S2-110: Arai diagrams (left) and tTRM check (right) of specimen GA63.5c.

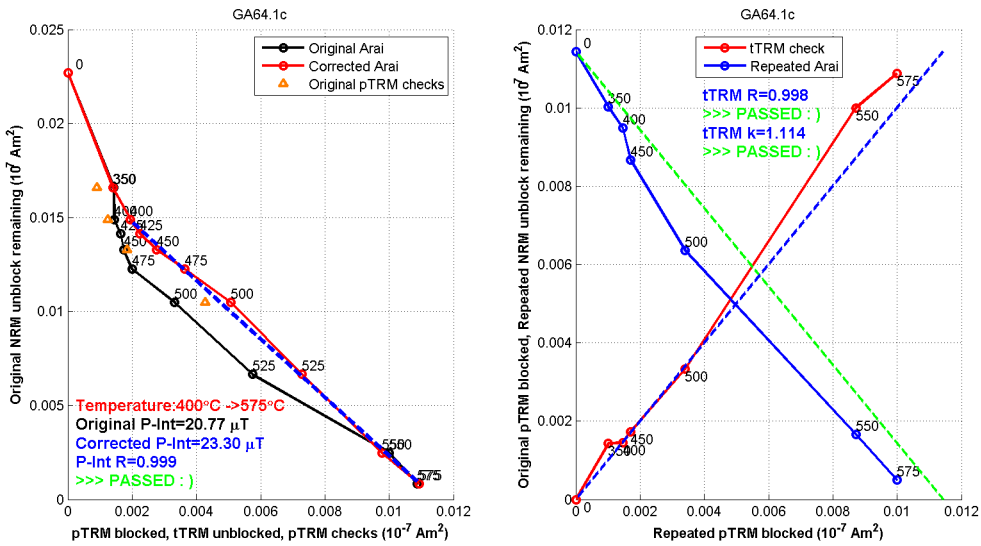

Figure 3.S2-111: Arai diagrams (left) and tTRM check (right) of specimen GA64.1c.

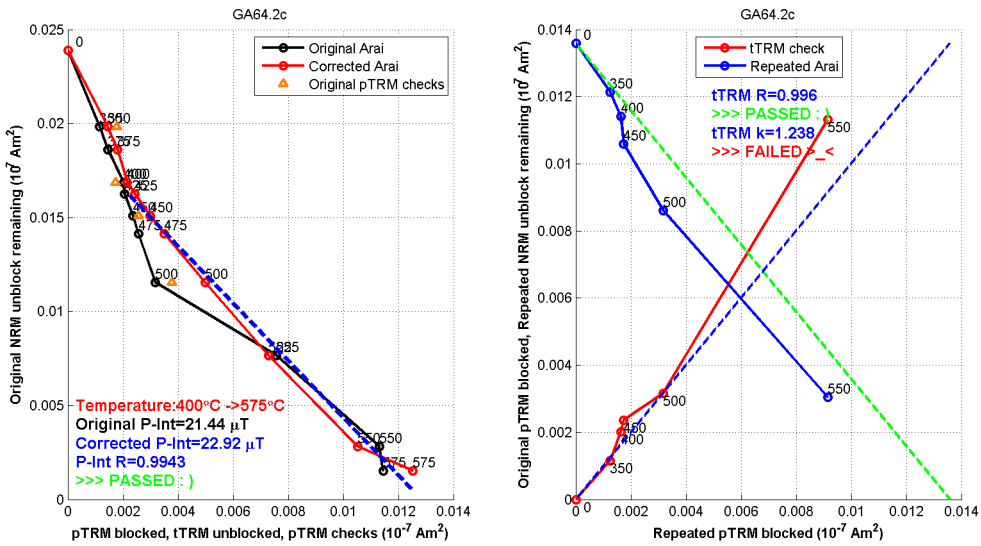

Figure 3.S2-112: Arai diagrams (left) and tTRM check (right) of specimen GA64.2c.

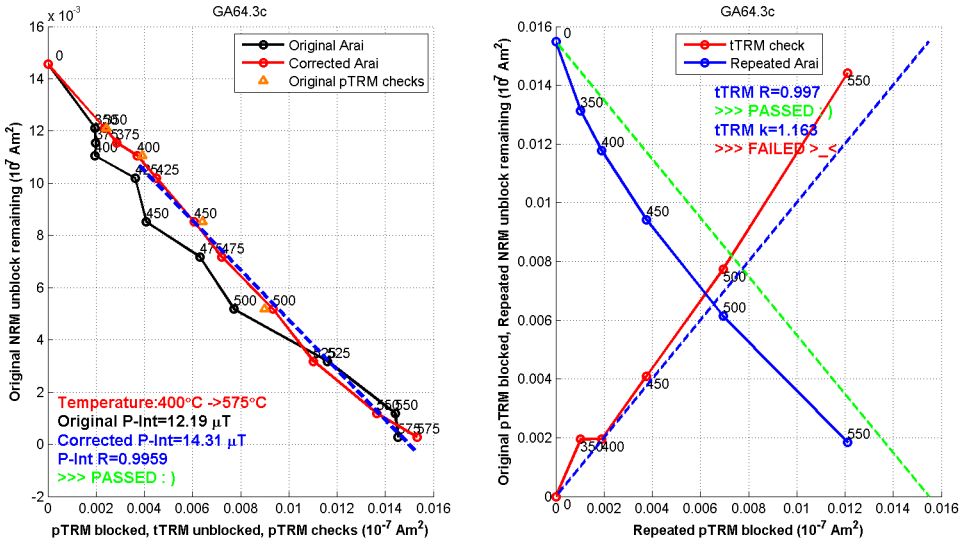

Figure 3.S2-113: Arai diagrams (left) and tTRM check (right) of specimen GA64.3c.

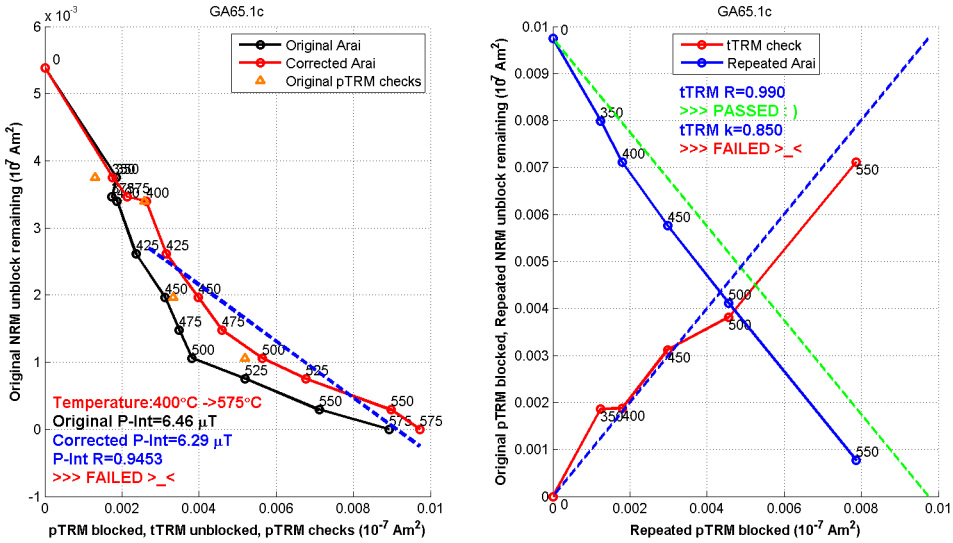

Figure 3.S2-114: Arai diagrams (left) and tTRM check (right) of specimen GA65.1c.

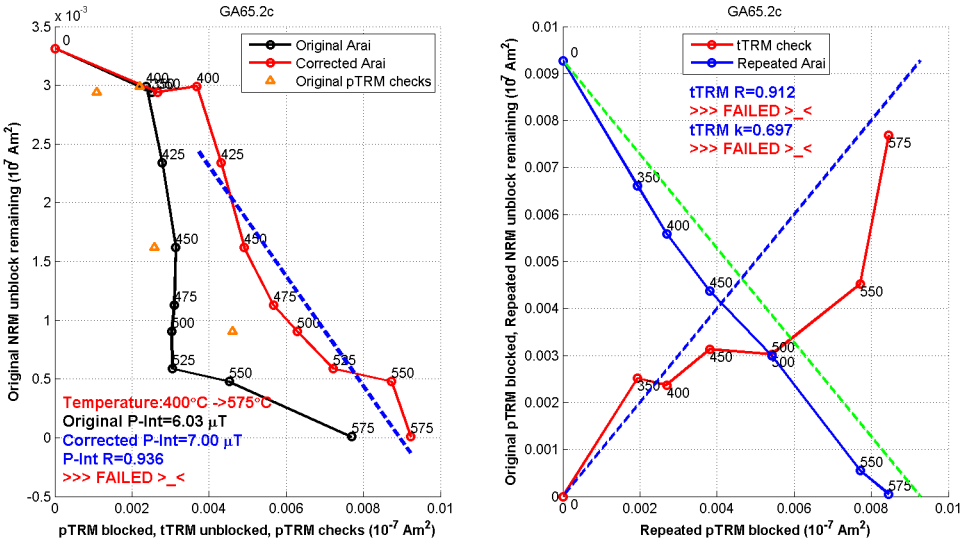

Figure 3.S2-115: Arai diagrams (left) and tTRM check (right) of specimen GA65.2c.

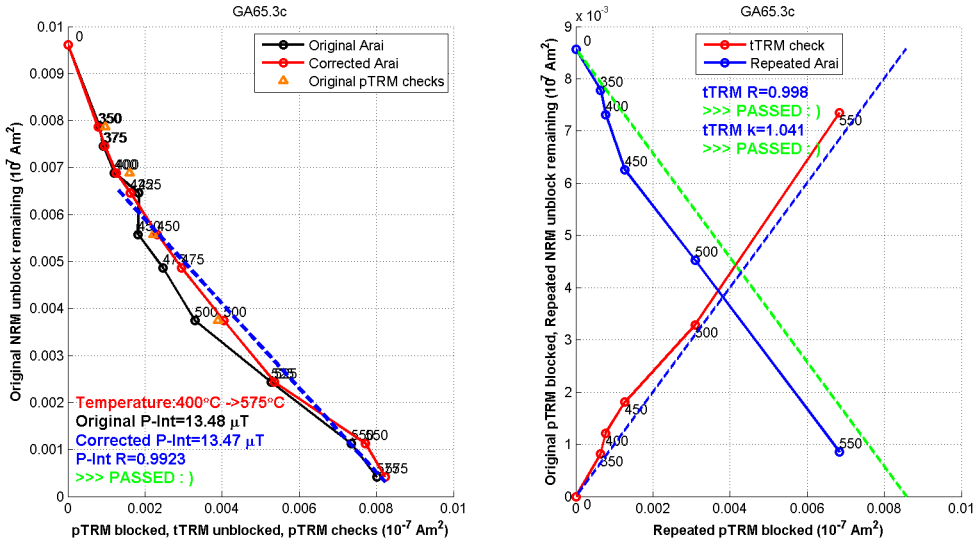

Figure 3.S2-116: Arai diagrams (left) and tTRM check (right) of specimen GA65.3c.

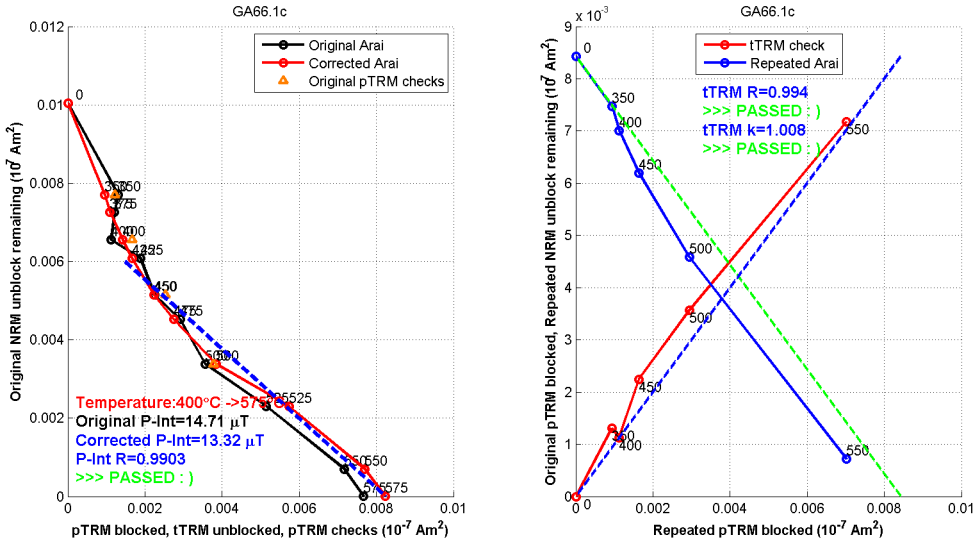

Figure 3.S2-117: Arai diagrams (left) and tTRM check (right) of specimen GA66.1c.

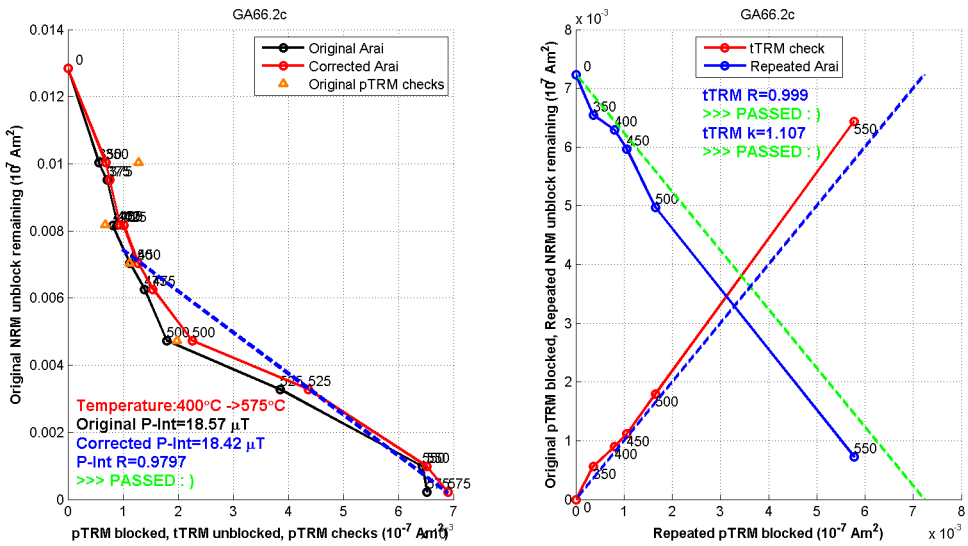

Figure 3.S2-118: Arai diagrams (left) and tTRM check (right) of specimen GA66.2c.

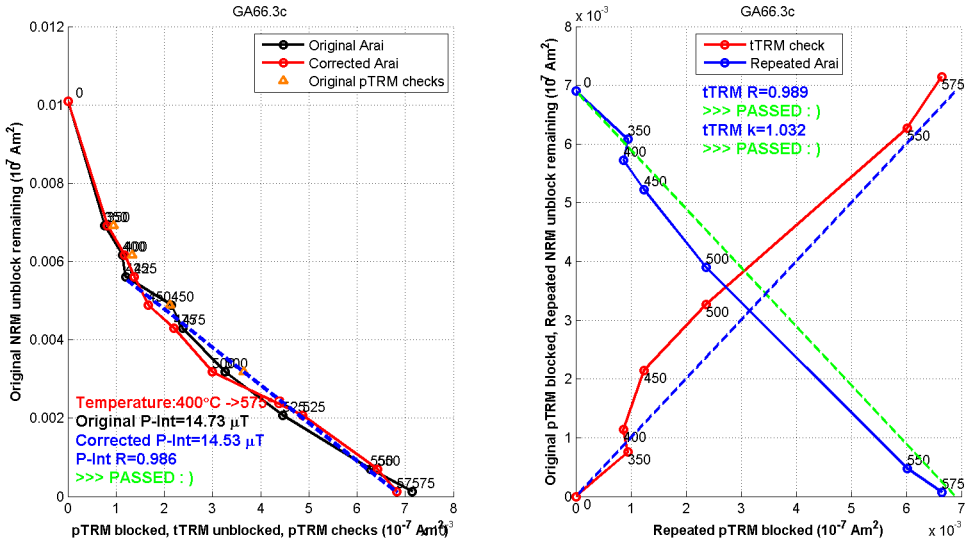

Figure 3.S2-119: Arai diagrams (left) and tTRM check (right) of specimen GA66.3c.

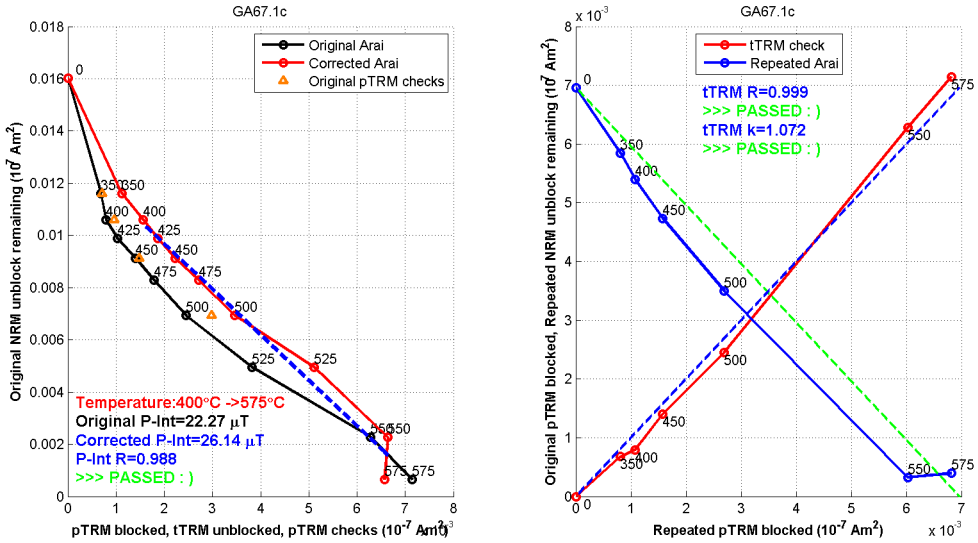

Figure 3.S2-120: Arai diagrams (left) and tTRM check (right) of specimen GA67.1c.

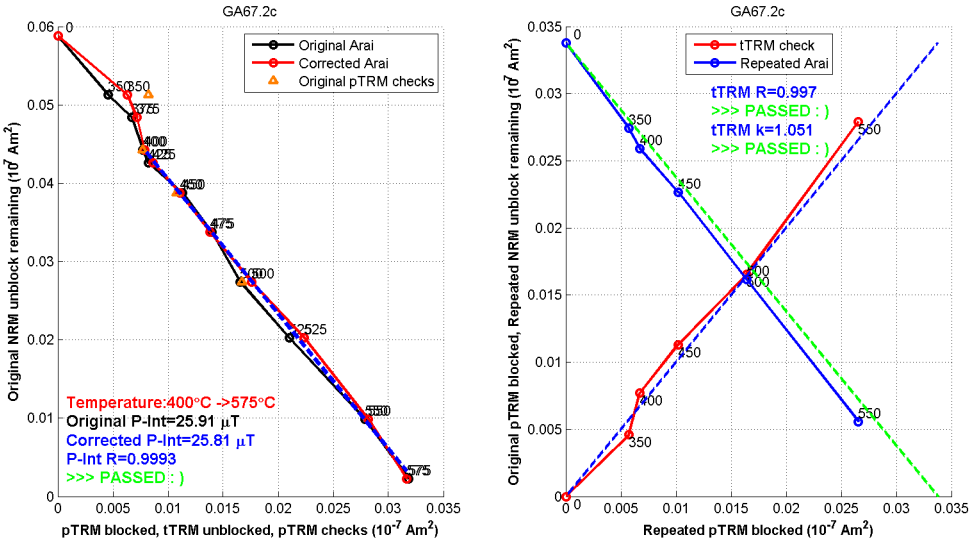

Figure 3.S2-121: Arai diagrams (left) and tTRM check (right) of specimen GA67.2c.

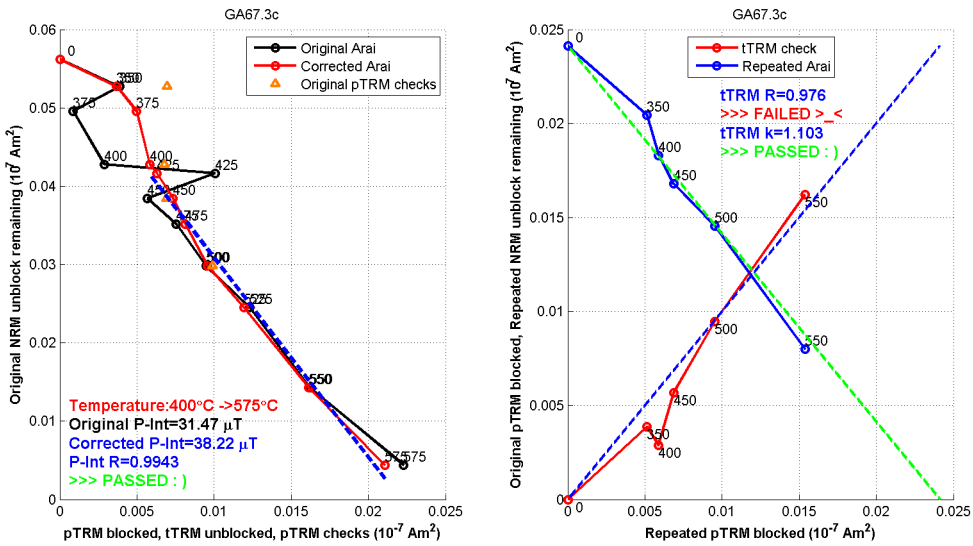

Figure 3.S2-122: Arai diagrams (left) and tTRM check (right) of specimen GA67.3c.

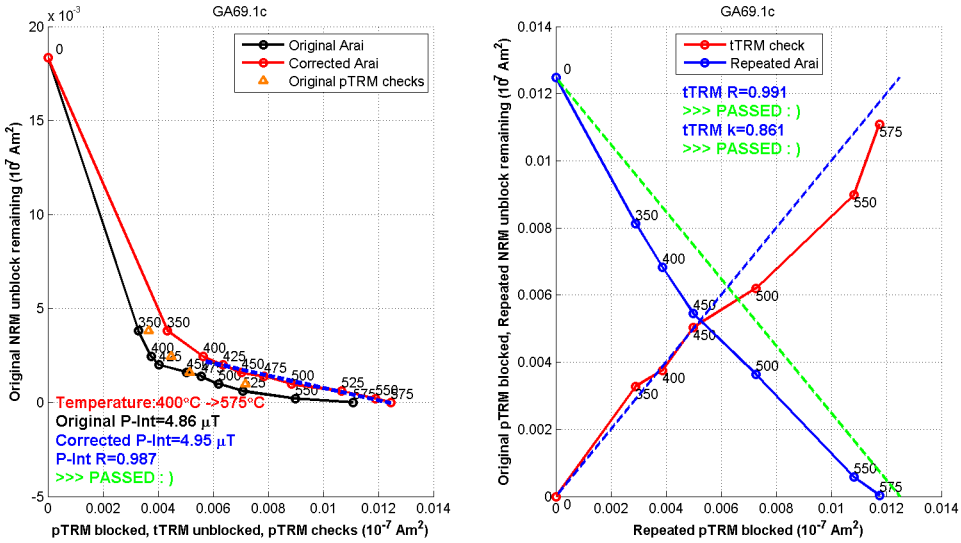

Figure 3.S2-123: Arai diagrams (left) and tTRM check (right) of specimen GA69.1c.

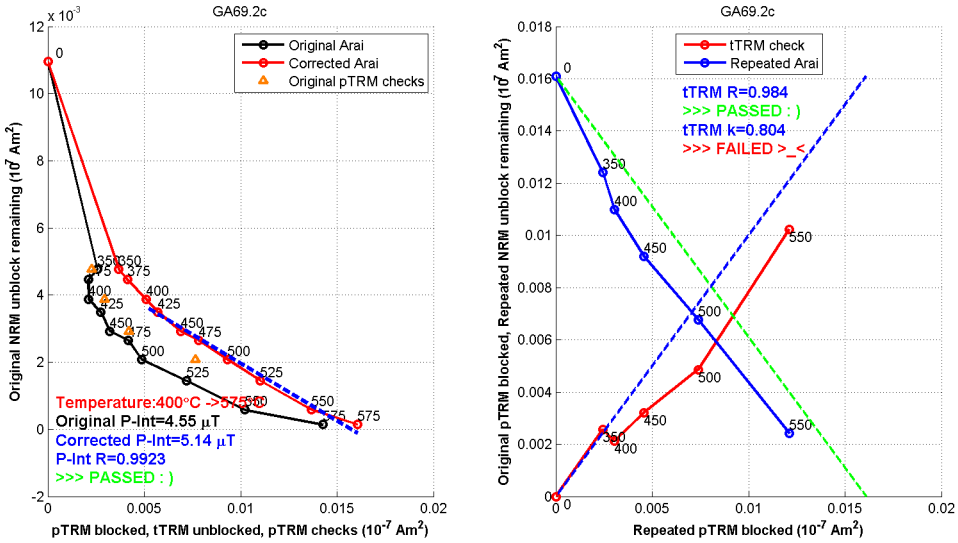

Figure 3.S2-124: Arai diagrams (left) and tTRM check (right) of specimen GA69.2c.

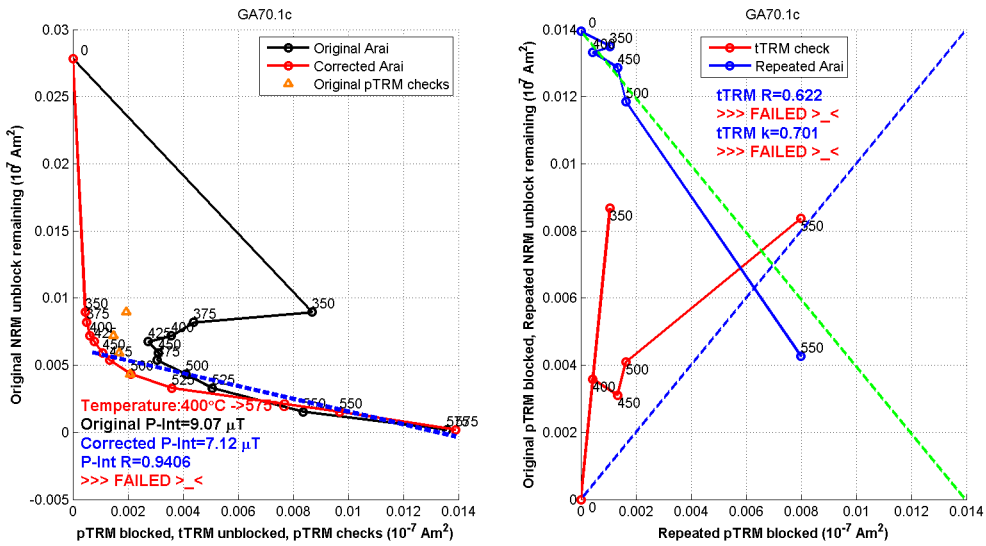

Figure 3.S2-125: Arai diagrams (left) and tTRM check (right) of specimen GA70.1c.

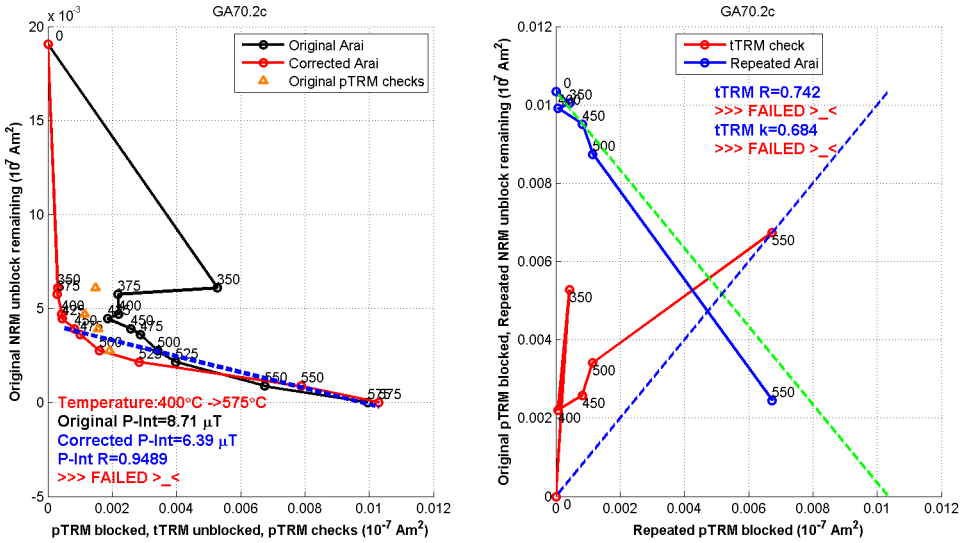

Figure 3.S2-126: Arai diagrams (left) and tTRM check (right) of specimen GA70.2c.

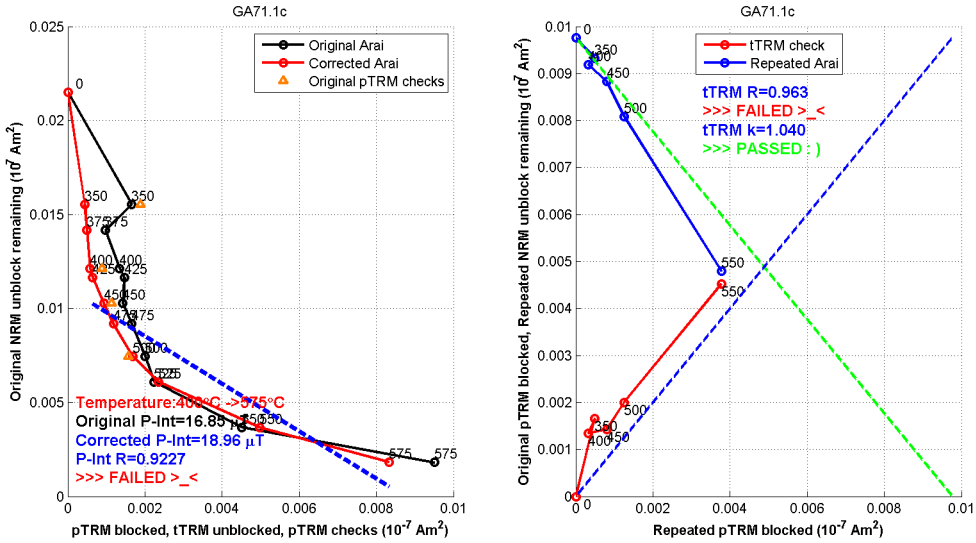

Figure 3.S2-127: Arai diagrams (left) and tTRM check (right) of specimen GA71.1c.

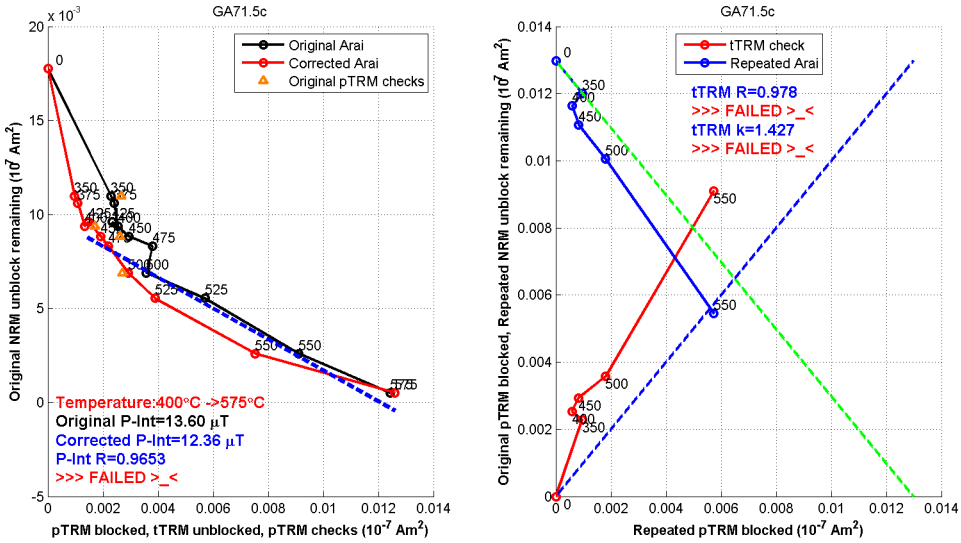

Figure 3.S2-128: Arai diagrams (left) and tTRM check (right) of specimen GA71.5c.

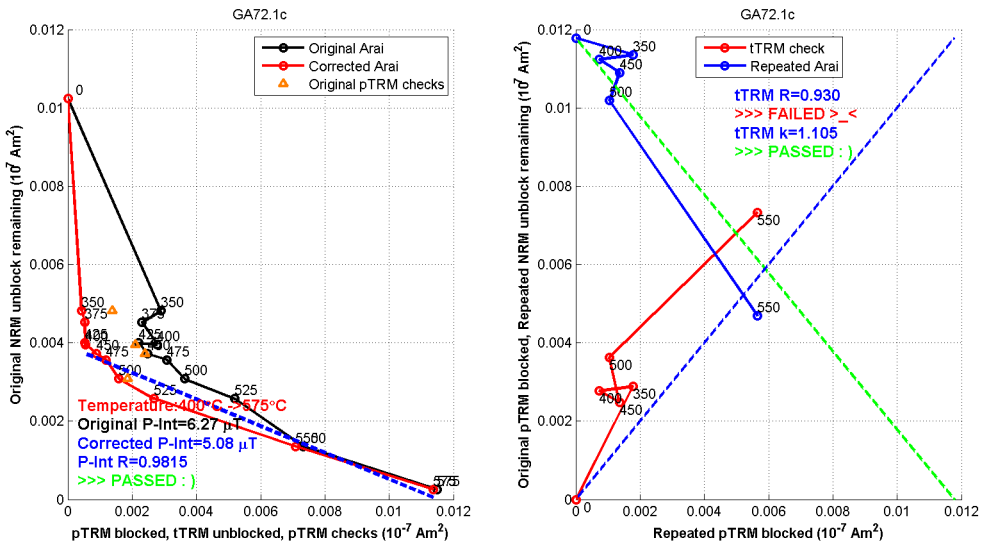

Figure 3.S2-129: Arai diagrams (left) and tTRM check (right) of specimen GA72.1c.

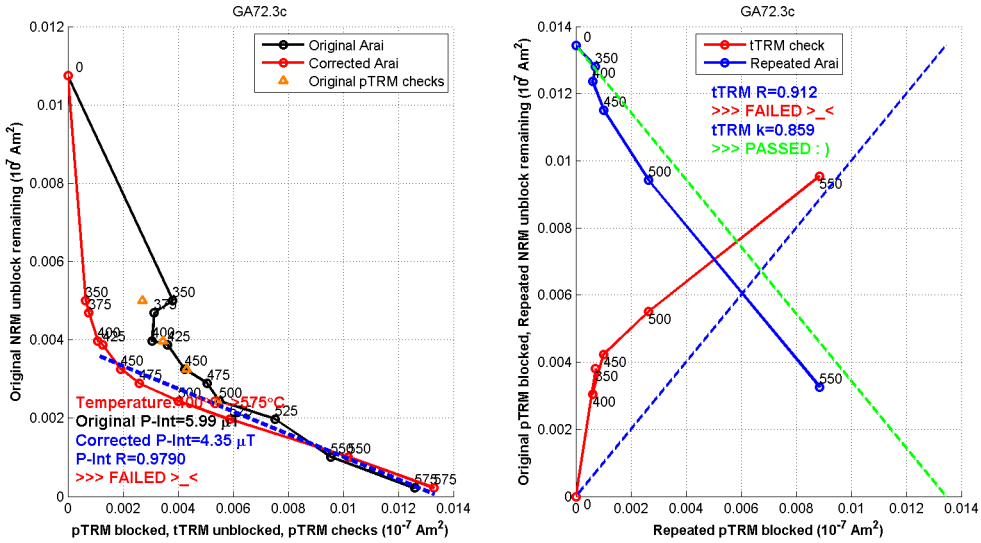

Figure 3.S2-130: Arai diagrams (left) and tTRM check (right) of specimen GA72.3c.

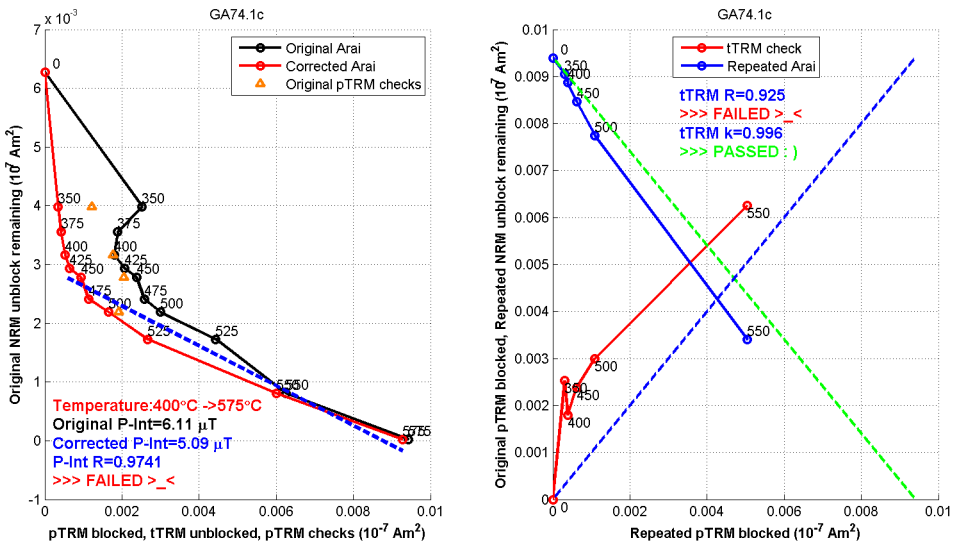

Figure 3.S2-131: Arai diagrams (left) and tTRM check (right) of specimen GA74.1c.

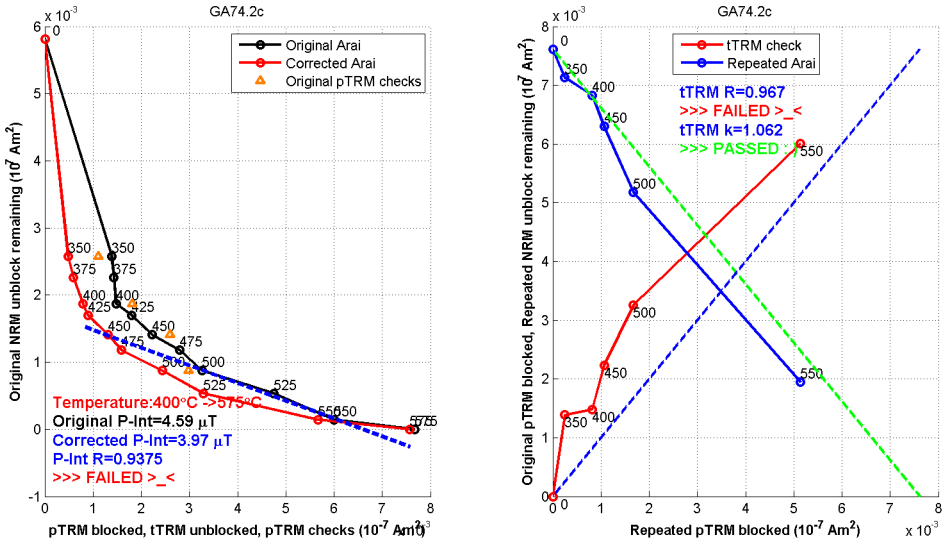

Figure 3.S2-132: Arai diagrams (left) and tTRM check (right) of specimen GA74.2c.

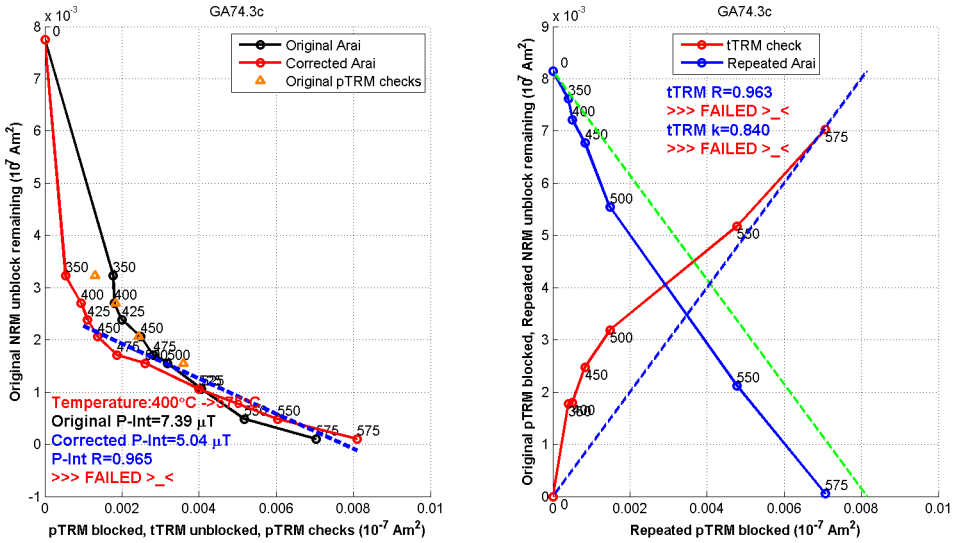

Figure 3.S2-133: Arai diagrams (left) and tTRM check (right) of specimen GA74.3c.

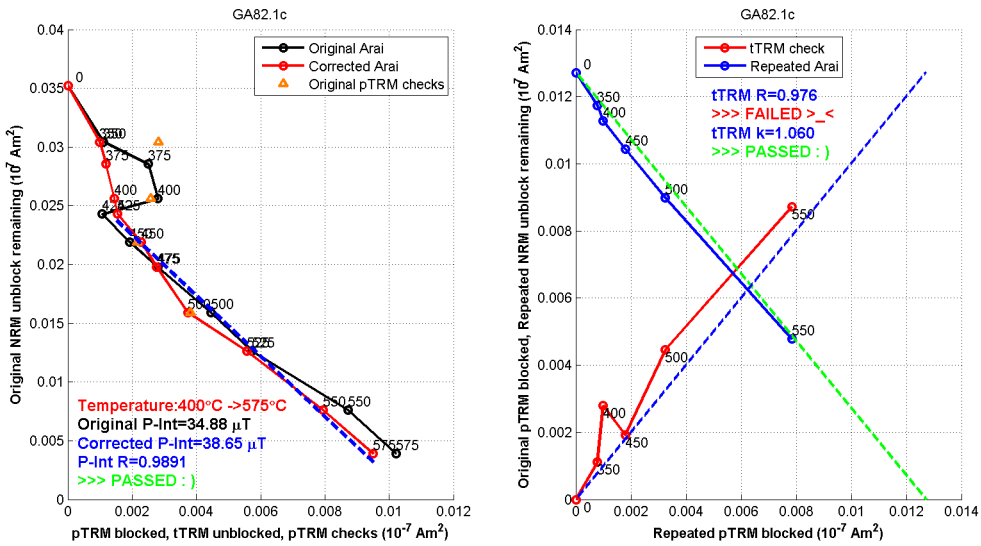

Figure 3.S2-134: Arai diagrams (left) and tTRM check (right) of specimen GA82.1c.

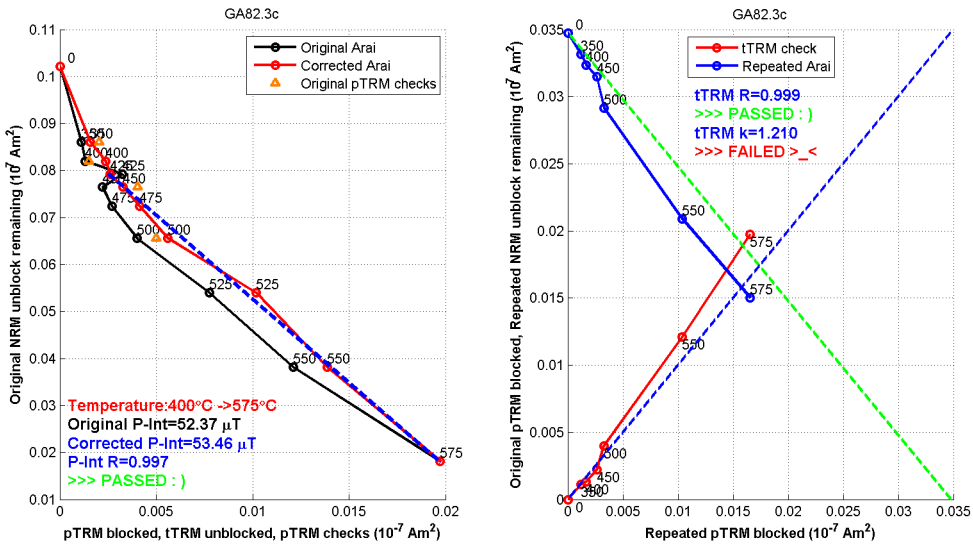

Figure 3.S2-135: Arai diagrams (left) and tTRM check (right) of specimen GA82.3c.

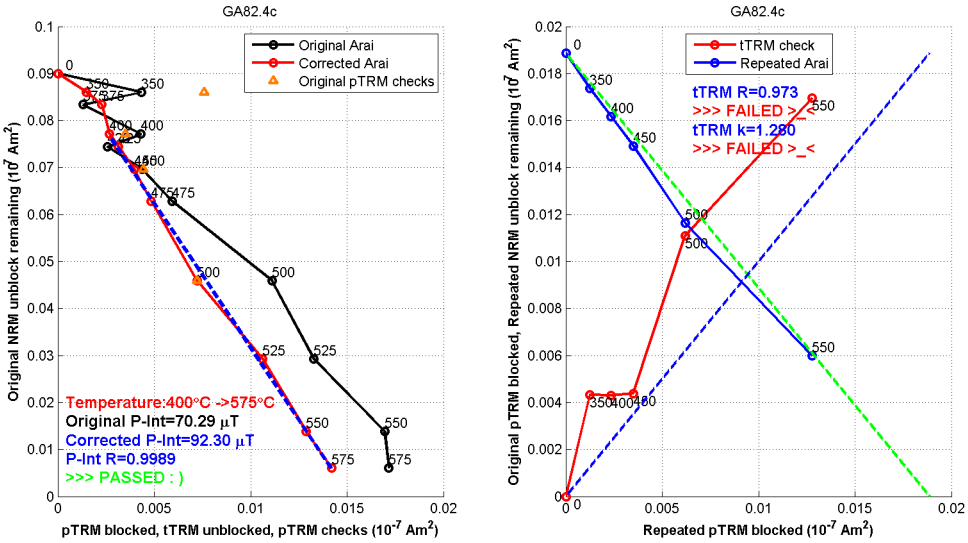

Figure 3.S2-136: Arai diagrams (left) and tTRM check (right) of specimen GA82.4c.

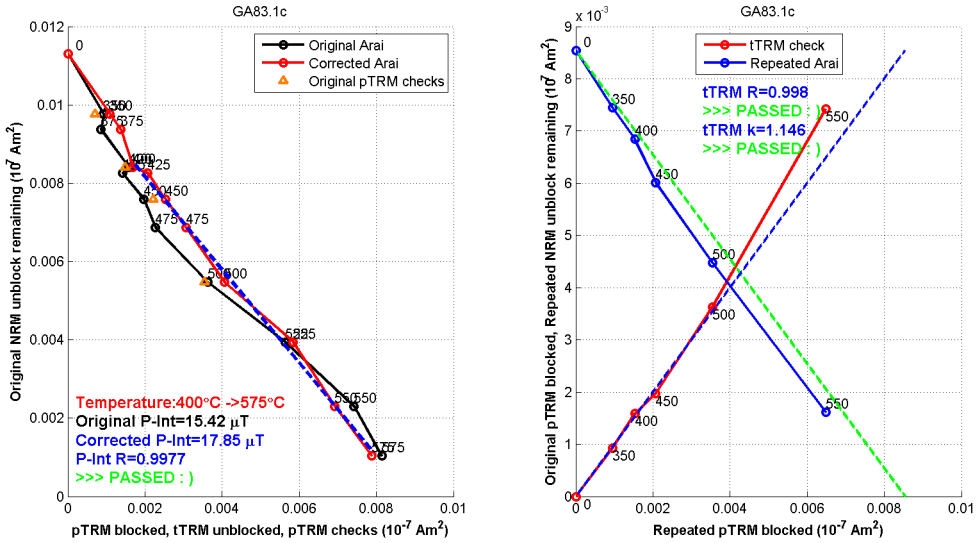

Figure 3.S2-137: Arai diagrams (left) and tTRM check (right) of specimen GA83.1c.

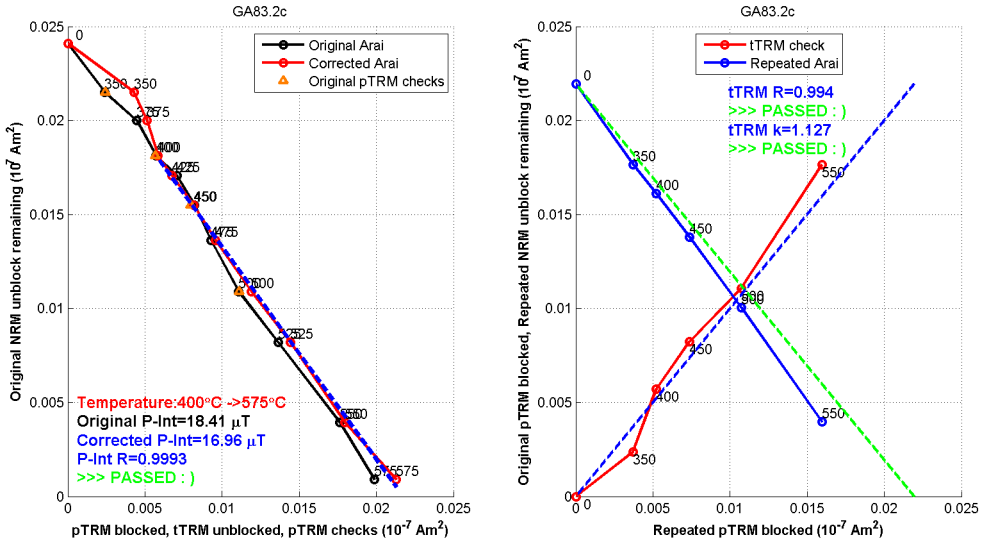

Figure 3.S2-138: Arai diagrams (left) and tTRM check (right) of specimen GA83.2c.

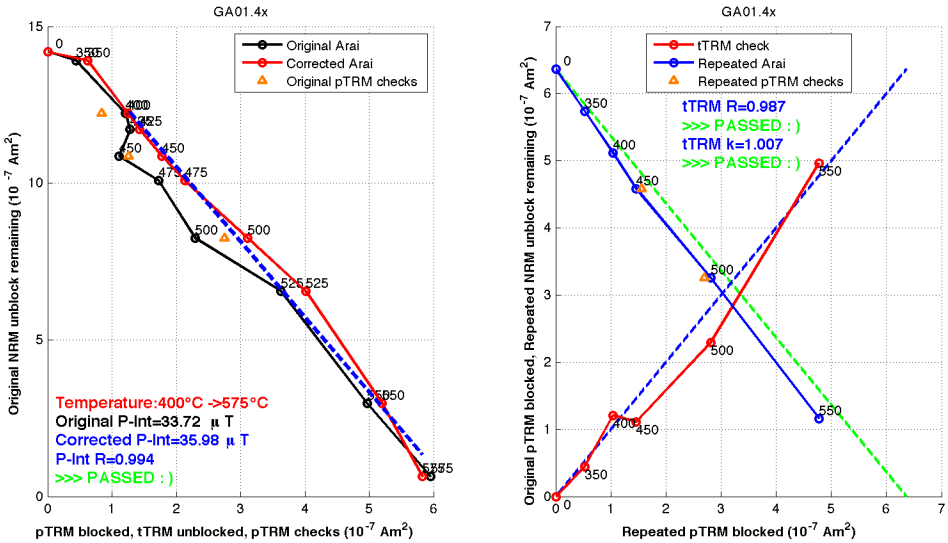

Figure 3.S2-139: Arai diagrams (left) and tTRM check (right) of specimen GA01.4x.

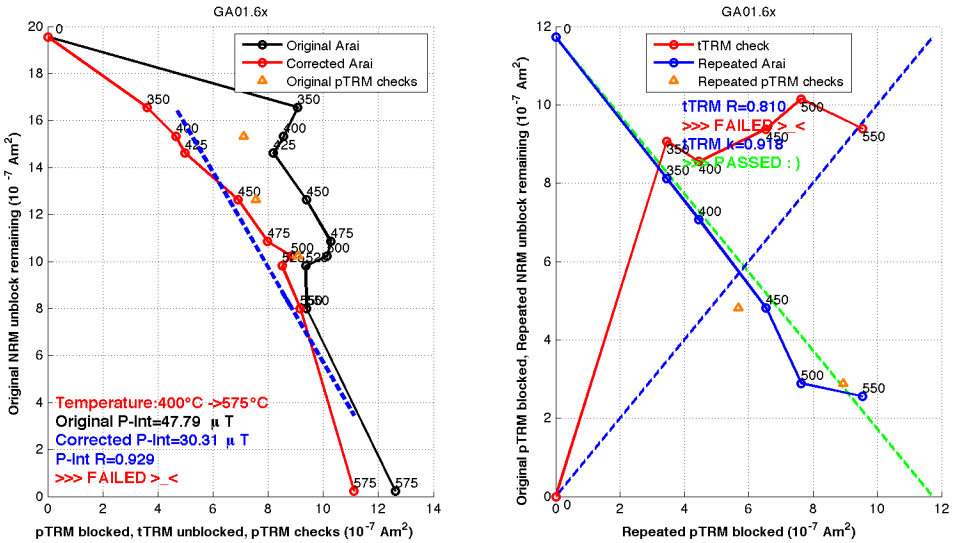

Figure 3.S2-140: Arai diagrams (left) and tTRM check (right) of specimen GA01.6x.

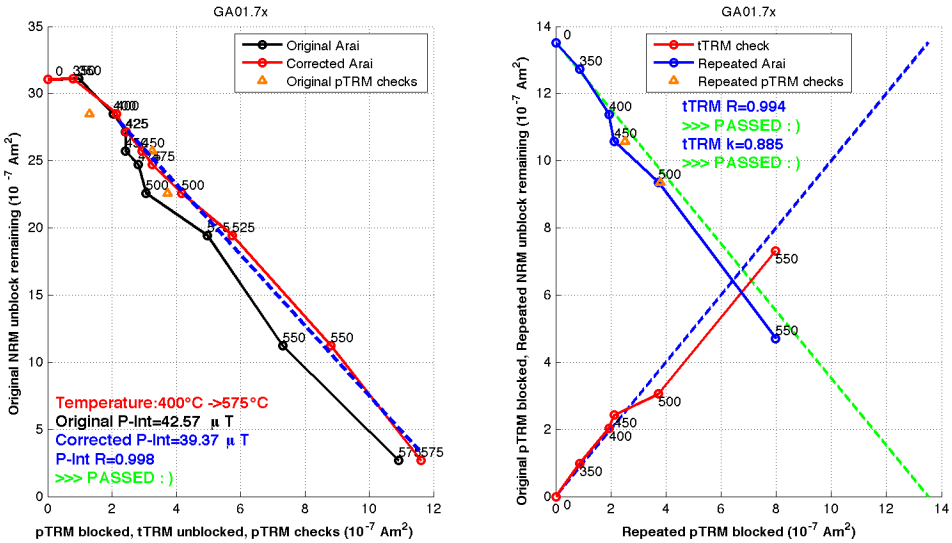

Figure 3.S2-141: Arai diagrams (left) and tTRM check (right) of specimen GA01.7x.

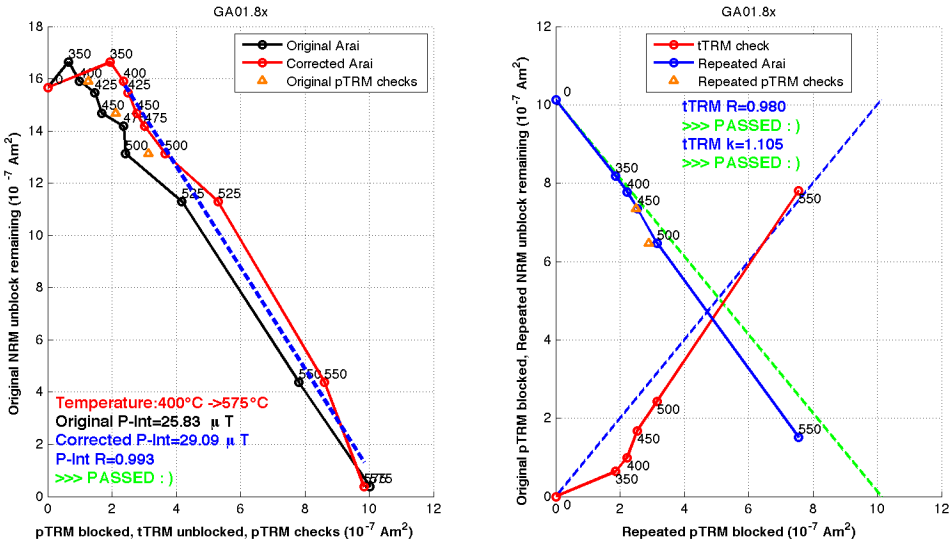

Figure 3.S2-142: Arai diagrams (left) and tTRM check (right) of specimen GA01.8x.

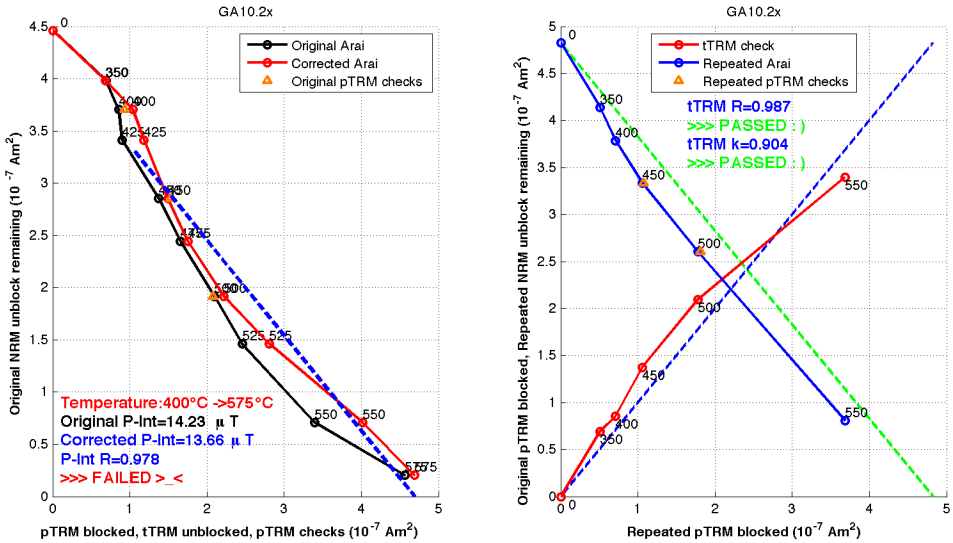

Figure 3.S2-143: Arai diagrams (left) and tTRM check (right) of specimen GA10.2x.

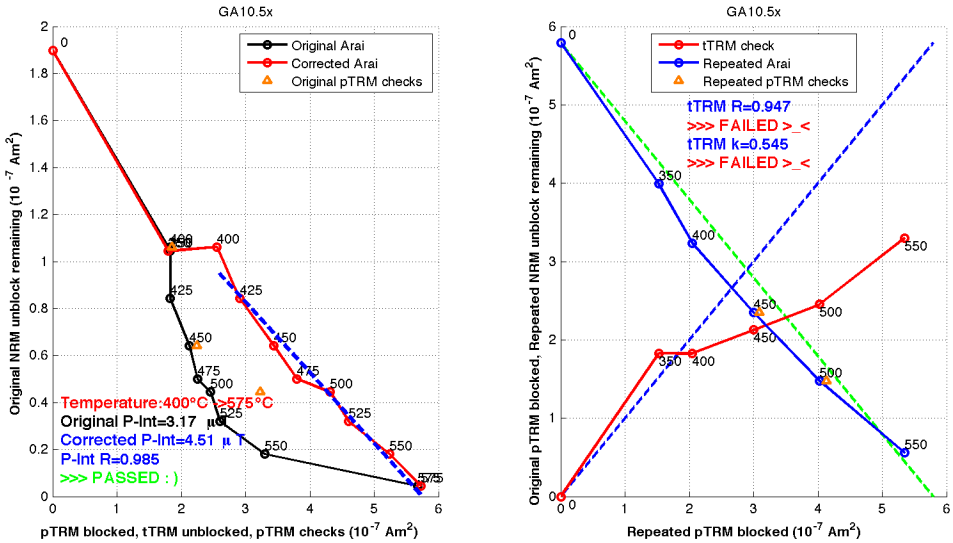

Figure 3.S2-144: Arai diagrams (left) and tTRM check (right) of specimen GA10.5x.

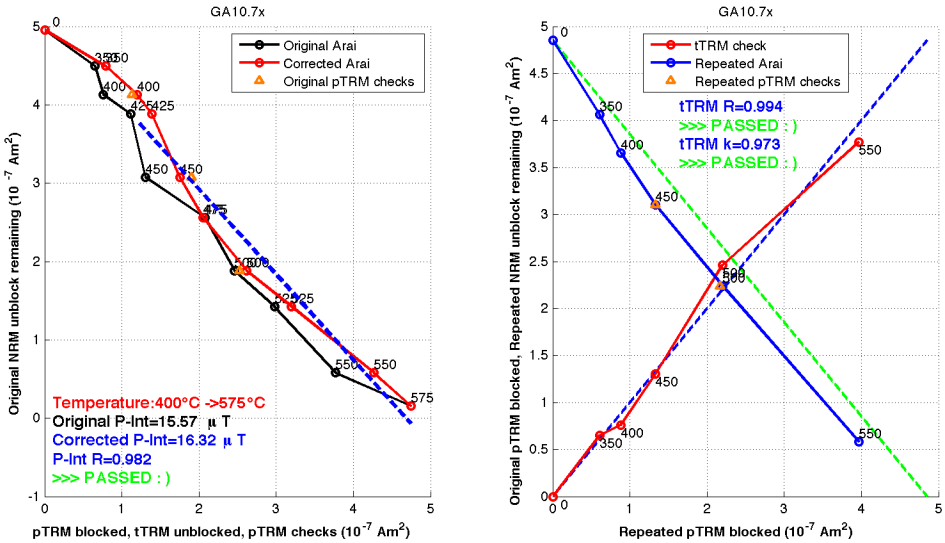

Figure 3.S2-145: Arai diagrams (left) and tTRM check (right) of specimen GA10.7x.

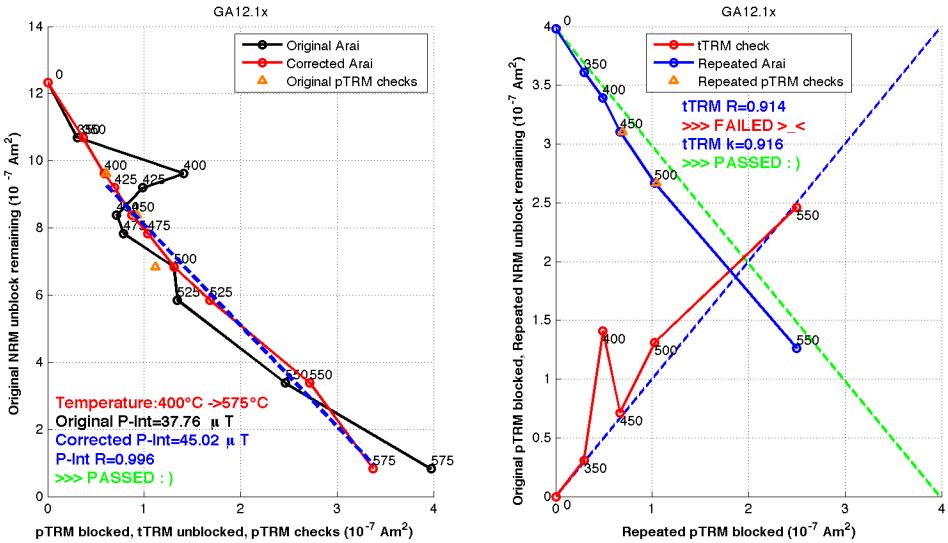

Figure 3.S2-146: Arai diagrams (left) and tTRM check (right) of specimen GA12.1x.

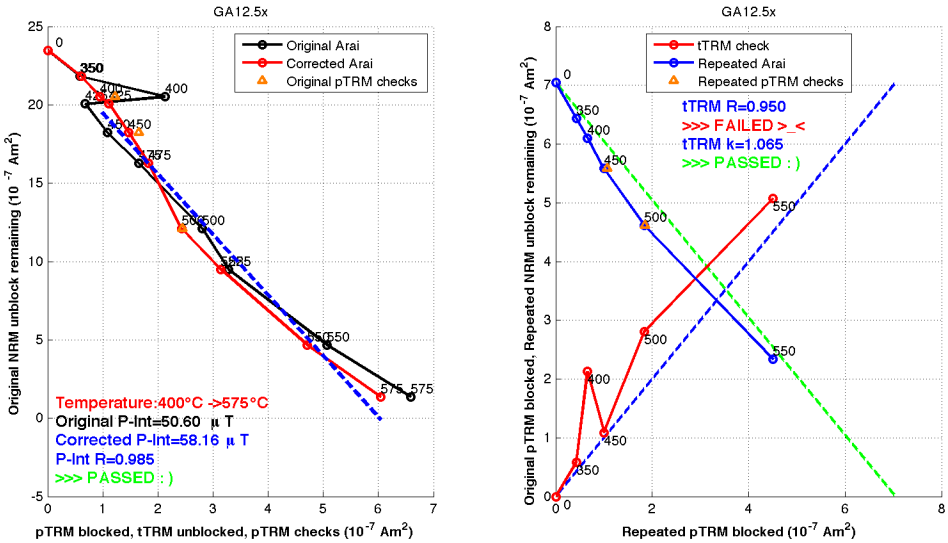

Figure 3.S2-147: Arai diagrams (left) and tTRM check (right) of specimen GA12.5x.

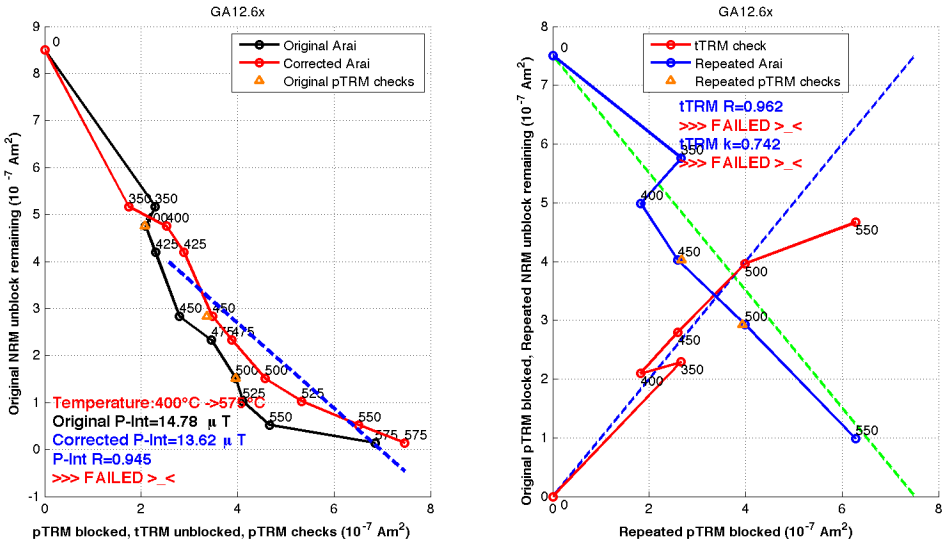

Figure 3.S2-148: Arai diagrams (left) and tTRM check (right) of specimen GA12.6x.

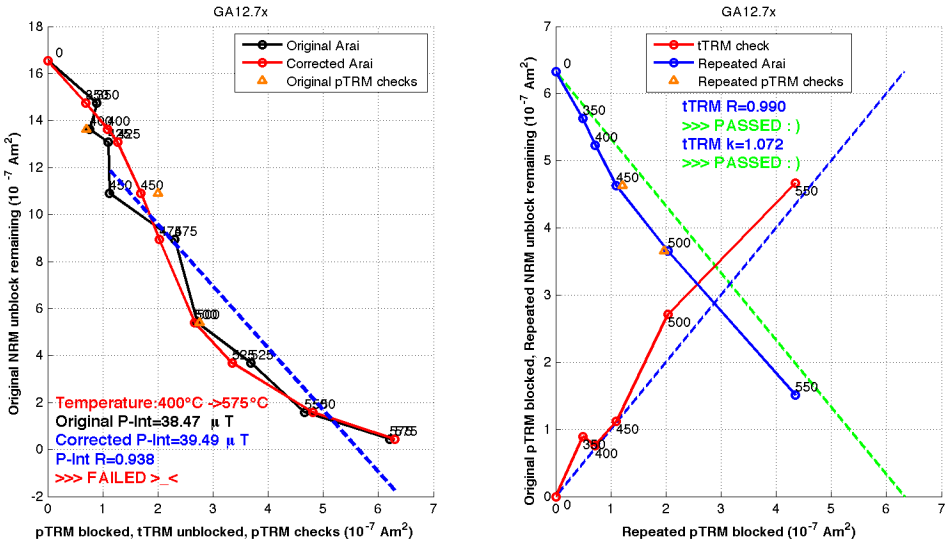

Figure 3.S2-149: Arai diagrams (left) and tTRM check (right) of specimen GA12.7x.

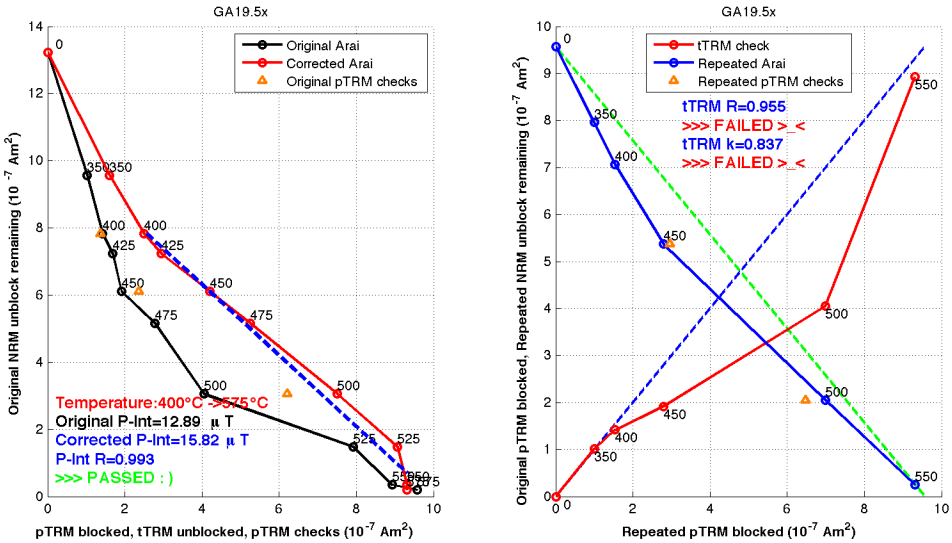

Figure 3.S2-150: Arai diagrams (left) and tTRM check (right) of specimen GA19.5x.

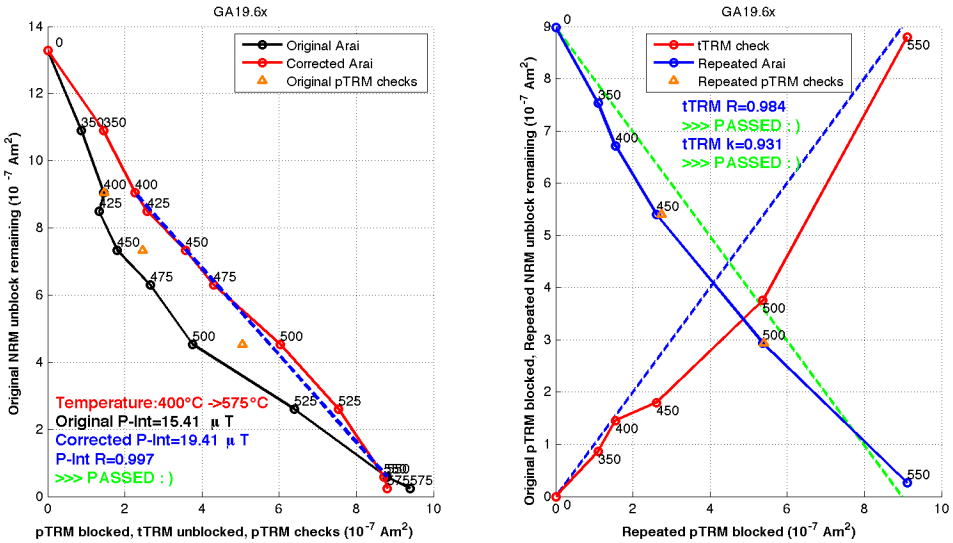

Figure 3.S2-151: Arai diagrams (left) and tTRM check (right) of specimen GA19.6x.

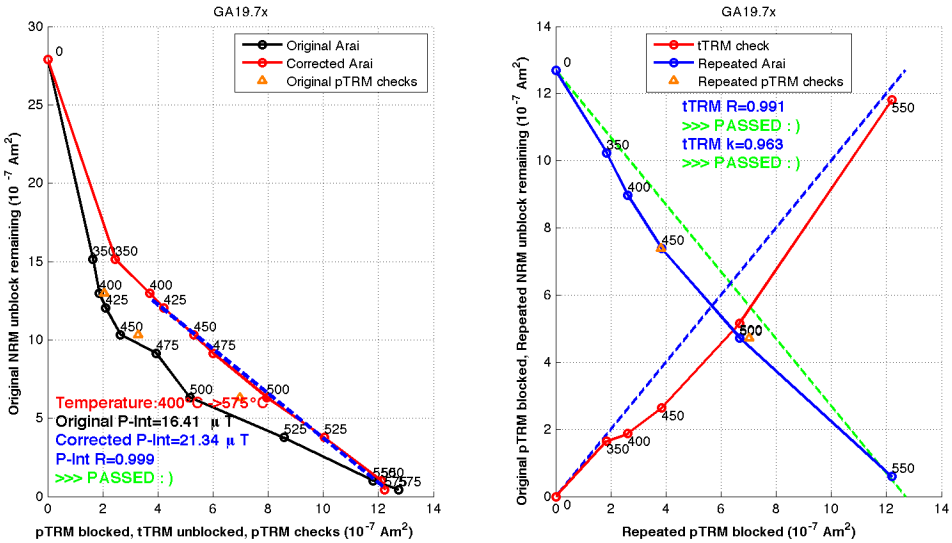

Figure 3.S2-152: Arai diagrams (left) and tTRM check (right) of specimen GA19.7x.

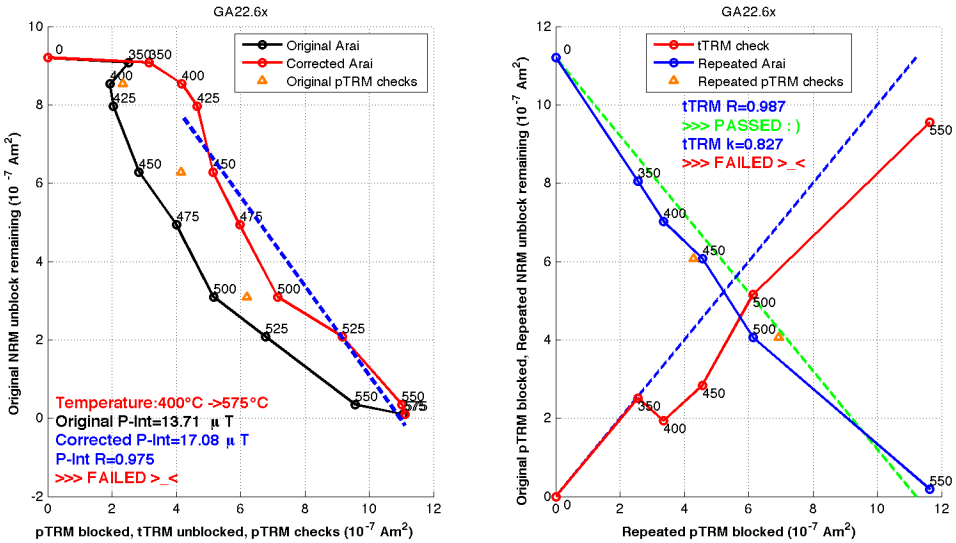

Figure 3.S2-153: Arai diagrams (left) and tTRM check (right) of specimen GA22.6x.

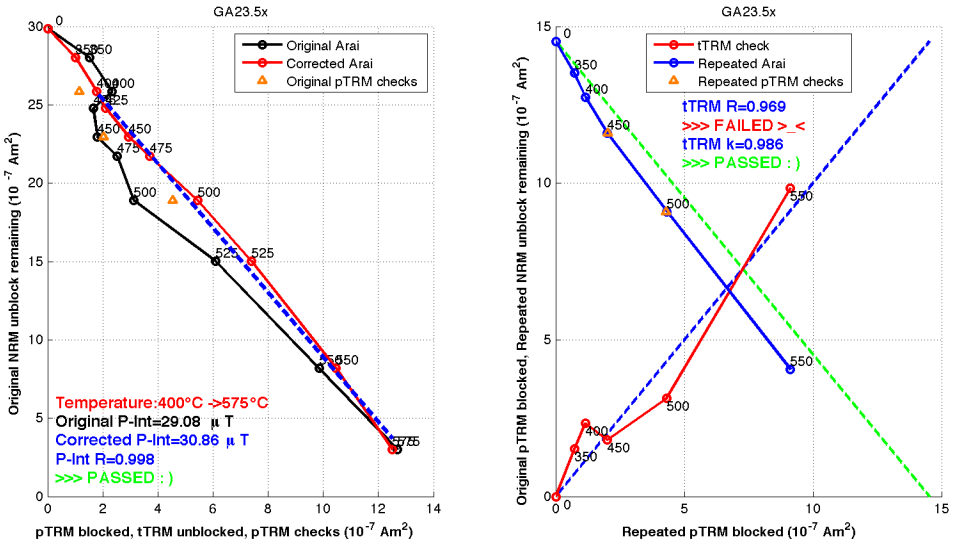

Figure 3.S2-154: Arai diagrams (left) and tTRM check (right) of specimen GA23.5x.

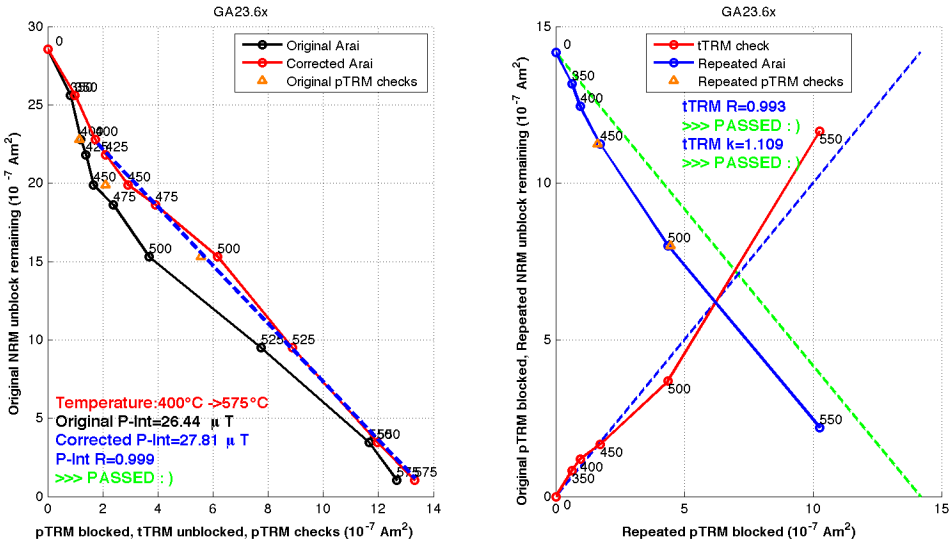

Figure 3.S2-155: Arai diagrams (left) and tTRM check (right) of specimen GA23.6x.

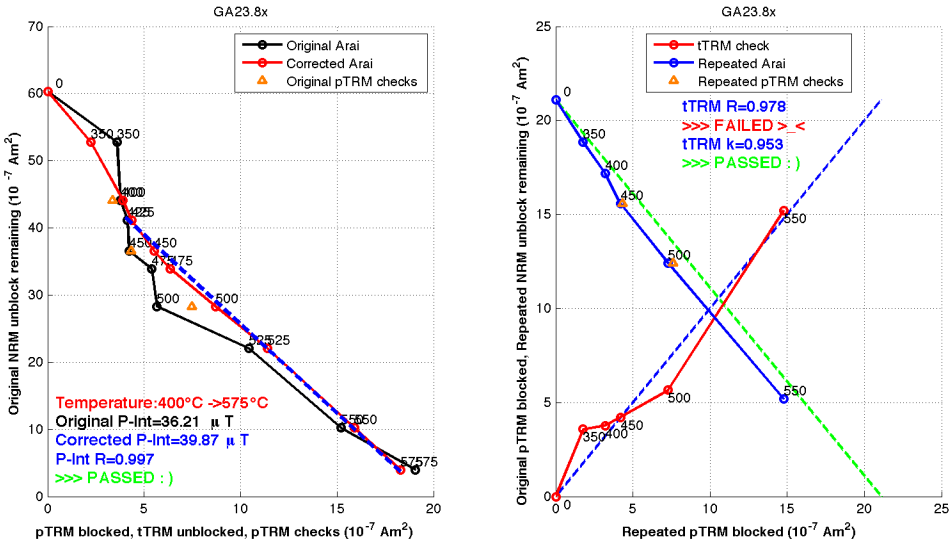

Figure 3.S2-156: Arai diagrams (left) and tTRM check (right) of specimen GA23.8x.

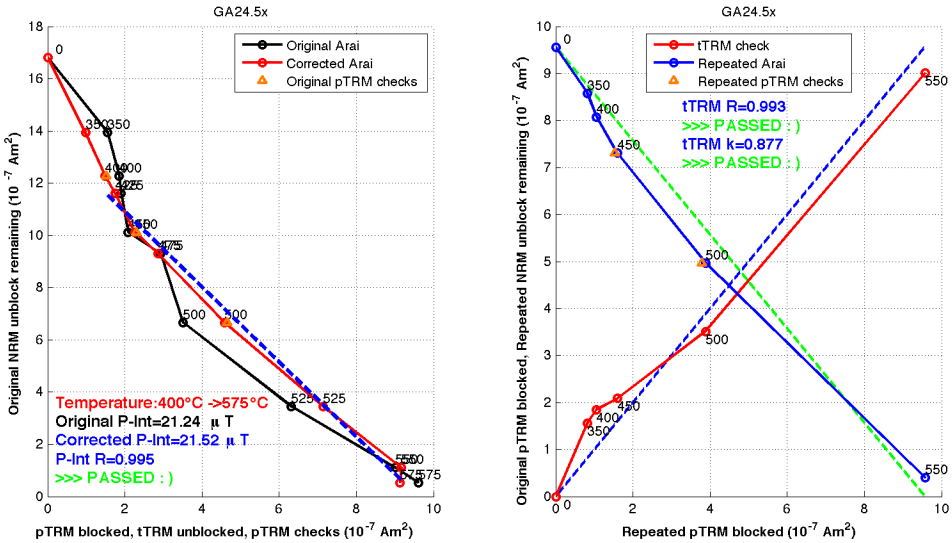

Figure 3.S2-157: Arai diagrams (left) and tTRM check (right) of specimen GA24.5x.

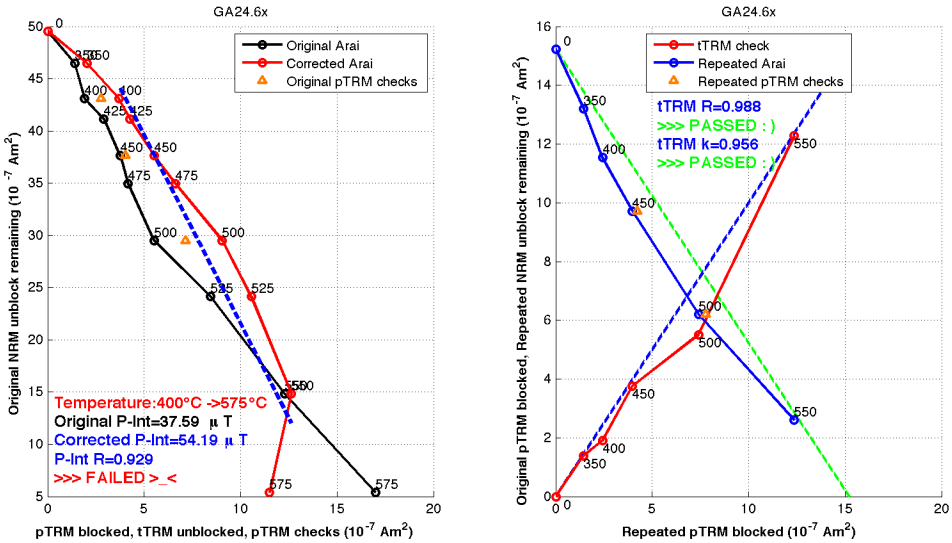

Figure 3.S2-158: Arai diagrams (left) and tTRM check (right) of specimen GA24.6x.

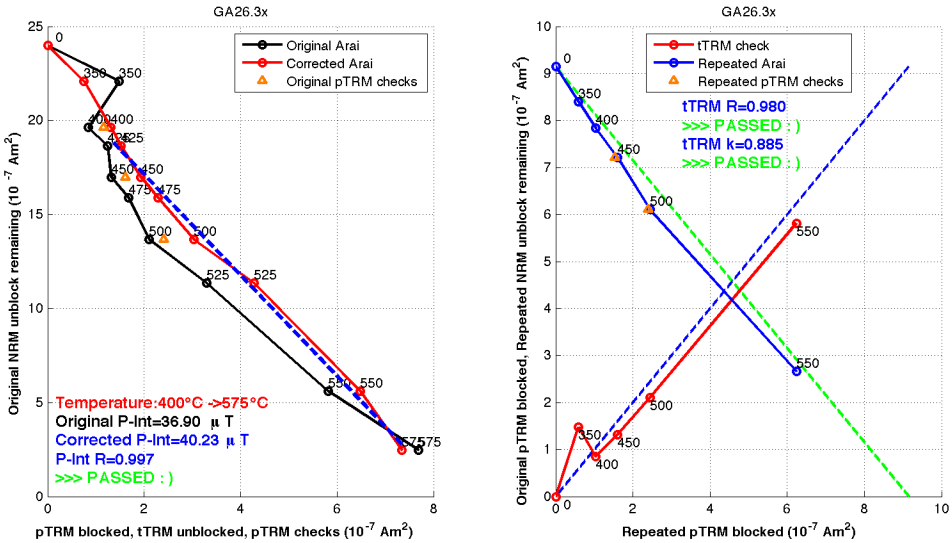

Figure 3.S2-159: Arai diagrams (left) and tTRM check (right) of specimen GA26.3x.

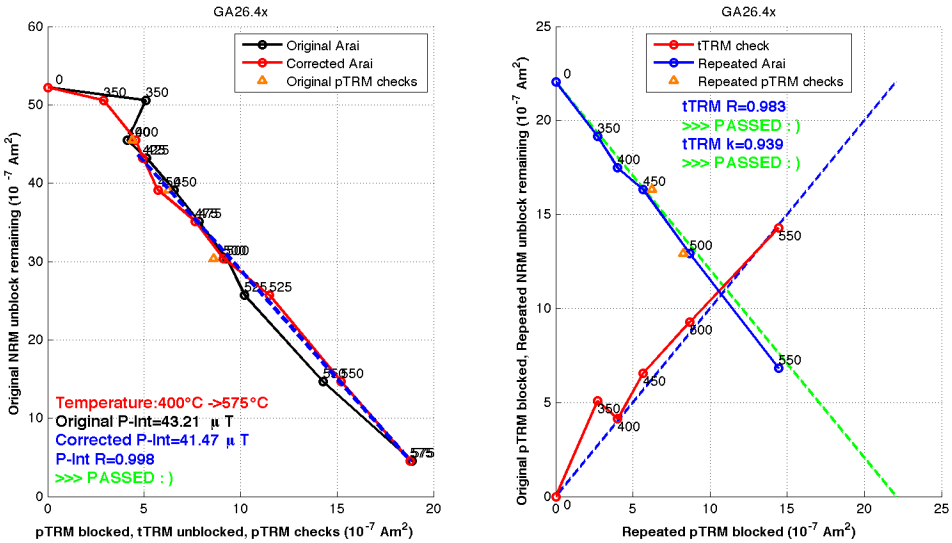

Figure 3.S2-160: Arai diagrams (left) and tTRM check (right) of specimen GA26.4x.

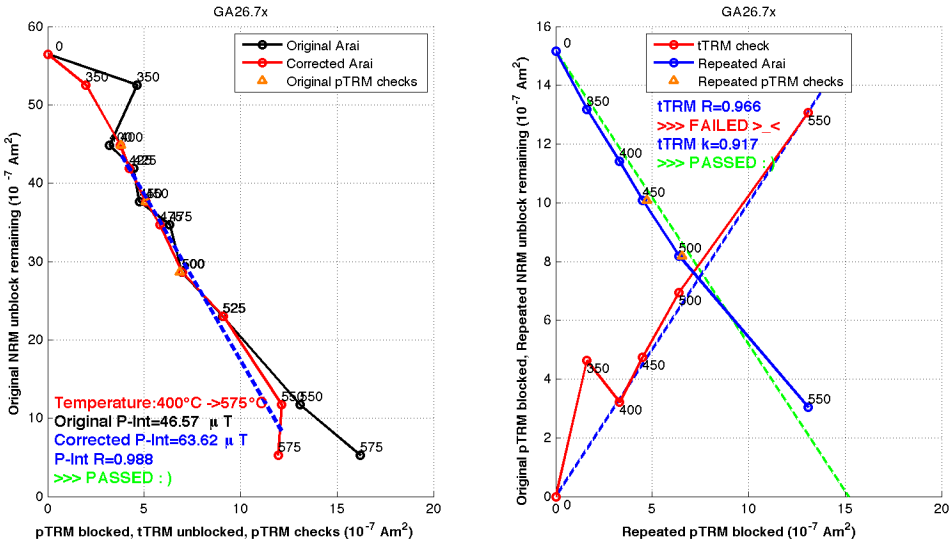

Figure 3.S2-161: Arai diagrams (left) and tTRM check (right) of specimen GA26.7x.

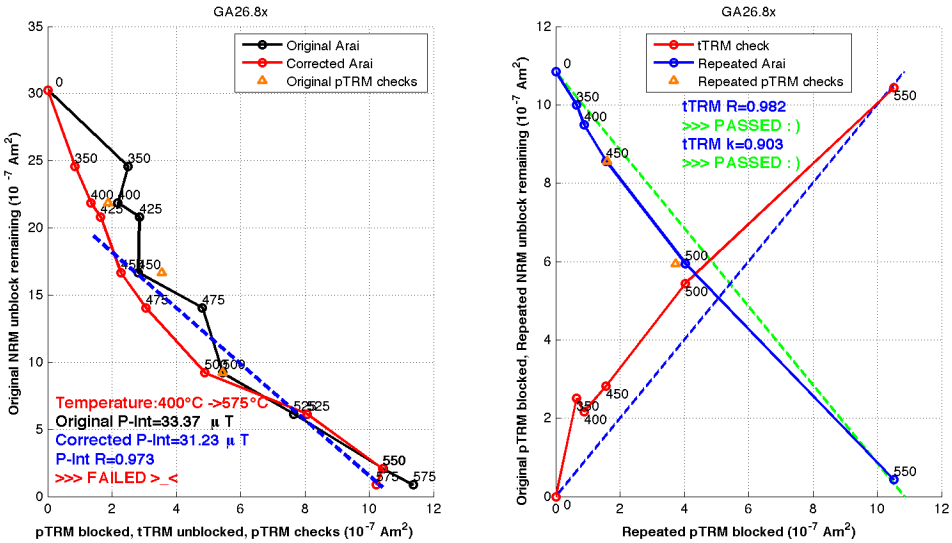

Figure 3.S2-162: Arai diagrams (left) and tTRM check (right) of specimen GA26.8x.

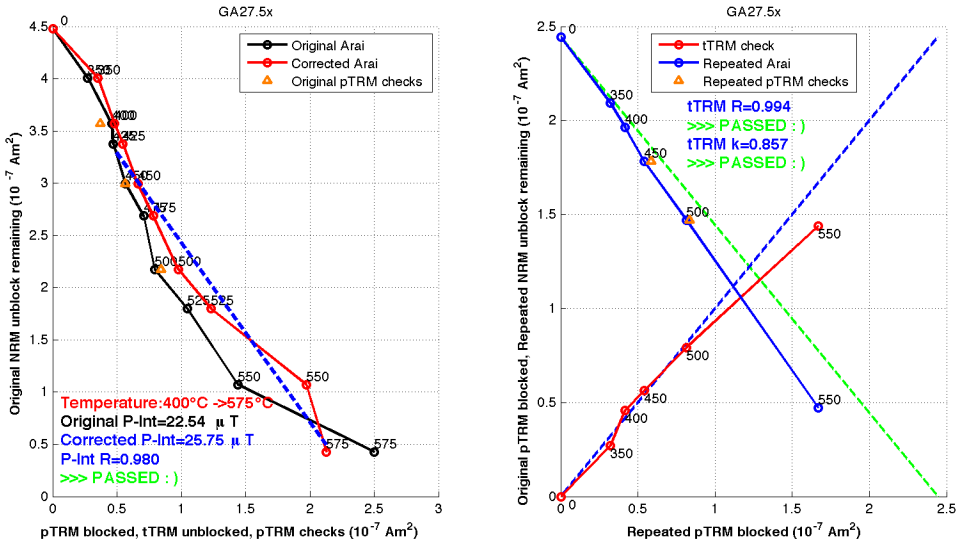

Figure 3.S2-163: Arai diagrams (left) and tTRM check (right) of specimen GA27.5x.

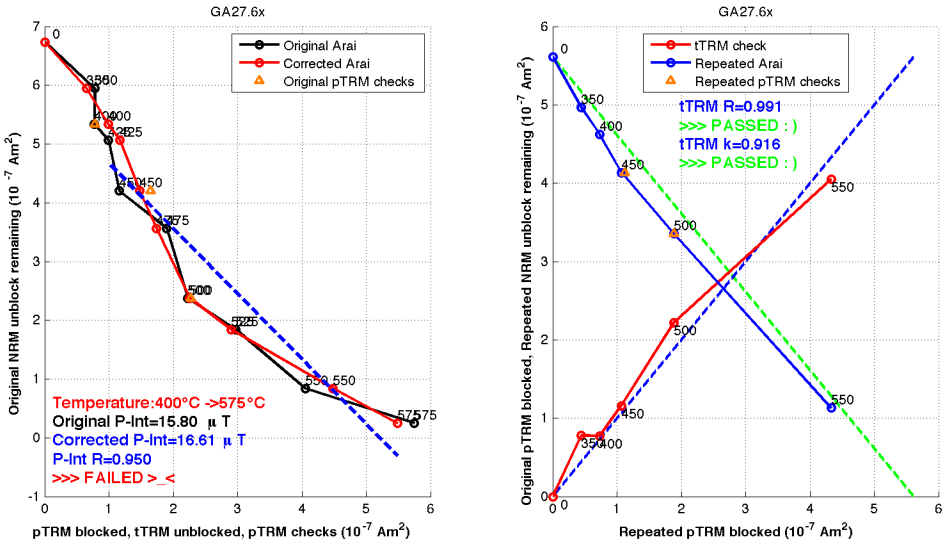

Figure 3.S2-164: Arai diagrams (left) and tTRM check (right) of specimen GA27.6x.

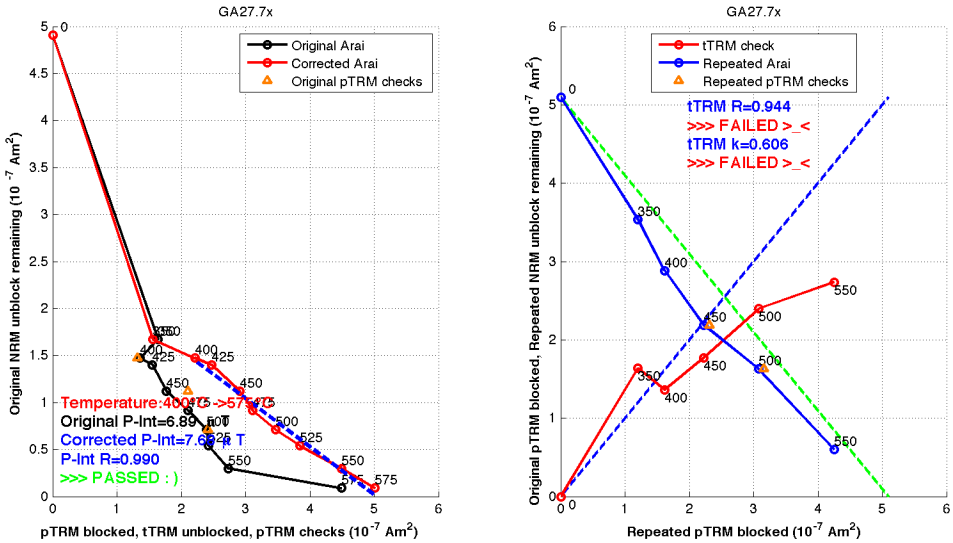

Figure 3.S2-165: Arai diagrams (left) and tTRM check (right) of specimen GA27.7x.

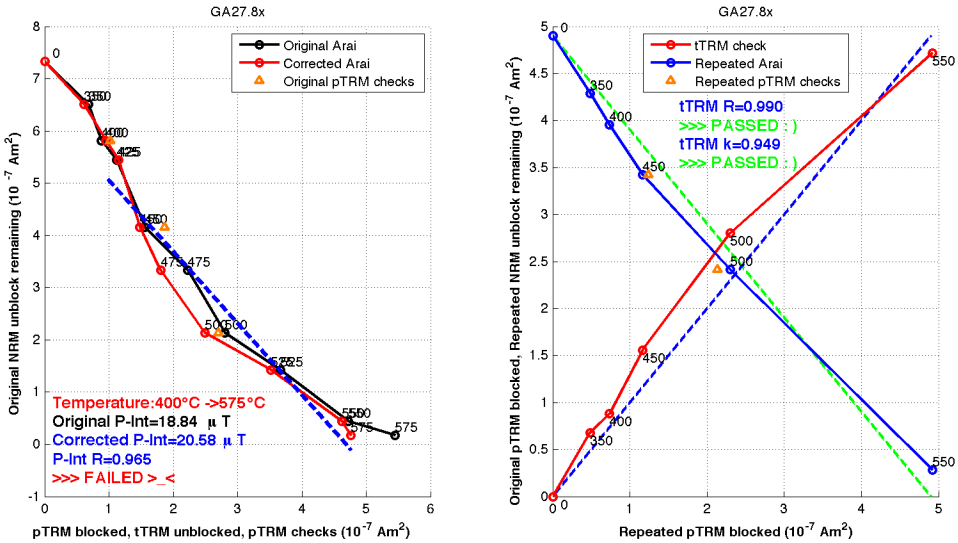

Figure 3.S2-166: Arai diagrams (left) and tTRM check (right) of specimen GA27.8x.

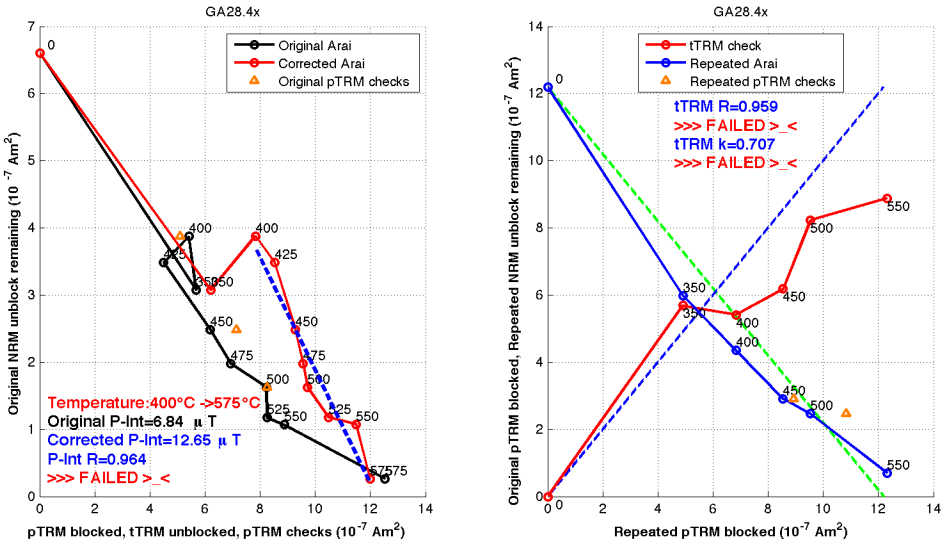

Figure 3.S2-167: Arai diagrams (left) and tTRM check (right) of specimen GA28.4x.

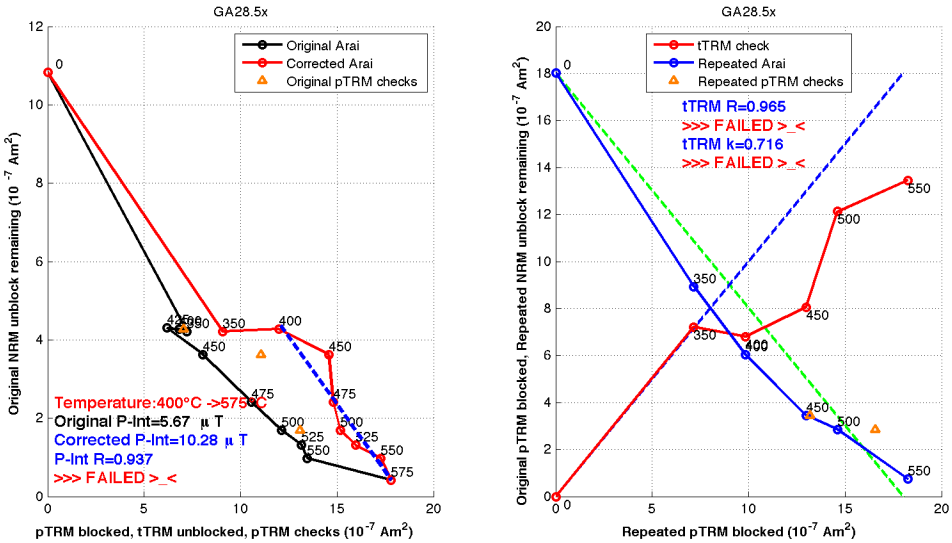

Figure 3.S2-168: Arai diagrams (left) and tTRM check (right) of specimen GA28.5x.

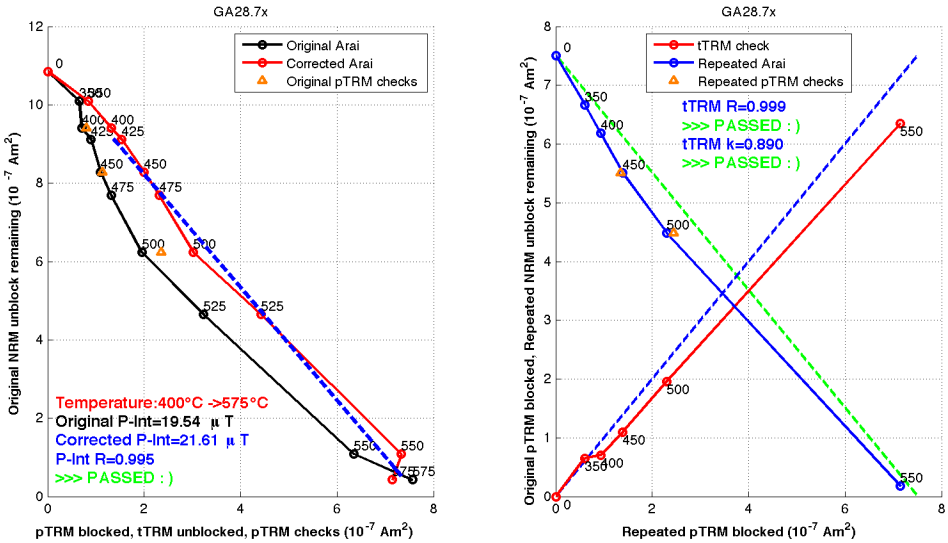

Figure 3.S2-169: Arai diagrams (left) and tTRM check (right) of specimen GA28.7x.

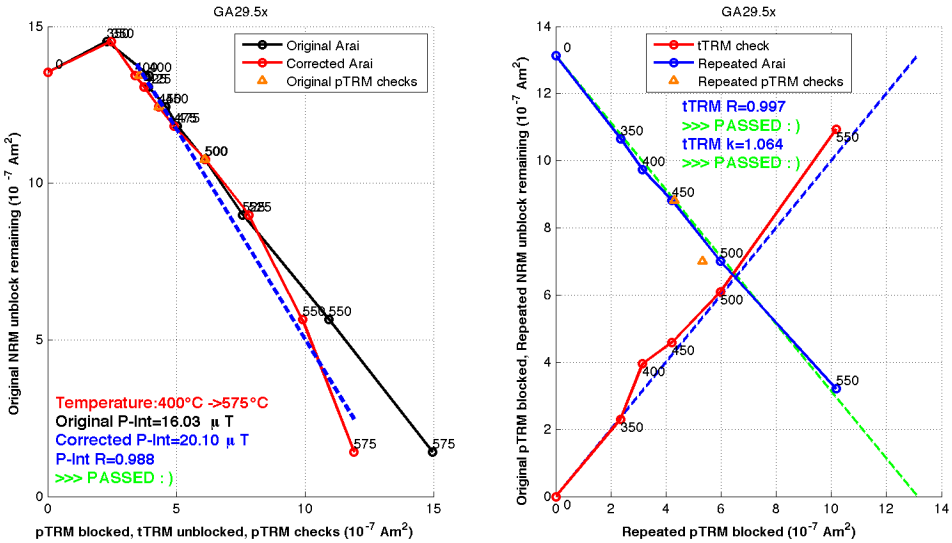

Figure 3.S2-170: Arai diagrams (left) and tTRM check (right) of specimen GA29.5x.

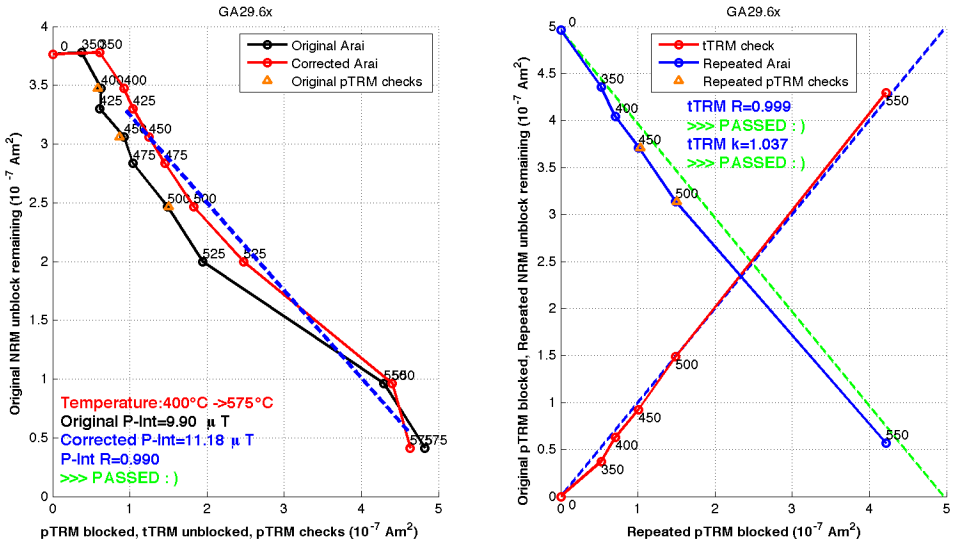

Figure 3.S2-171: Arai diagrams (left) and tTRM check (right) of specimen GA29.6x.

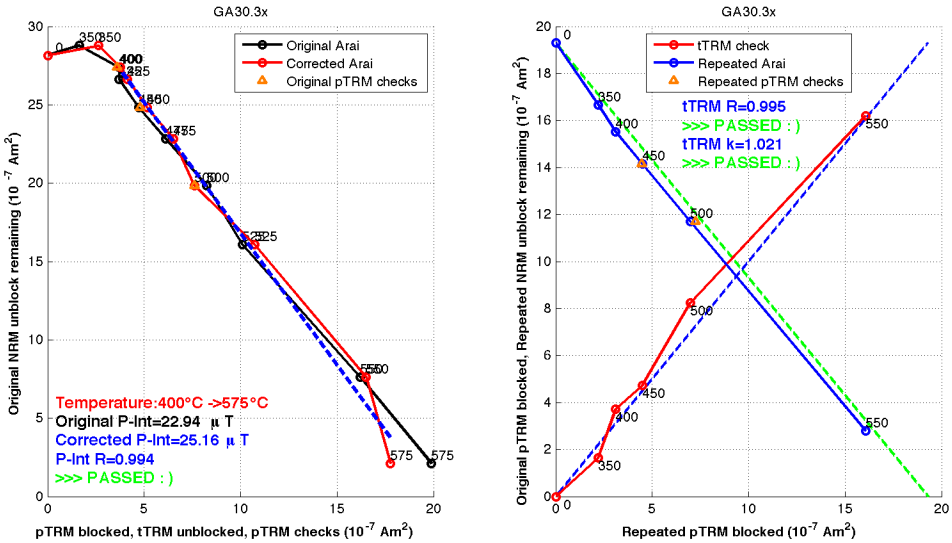

Figure 3.S2-172: Arai diagrams (left) and tTRM check (right) of specimen GA30.3x.

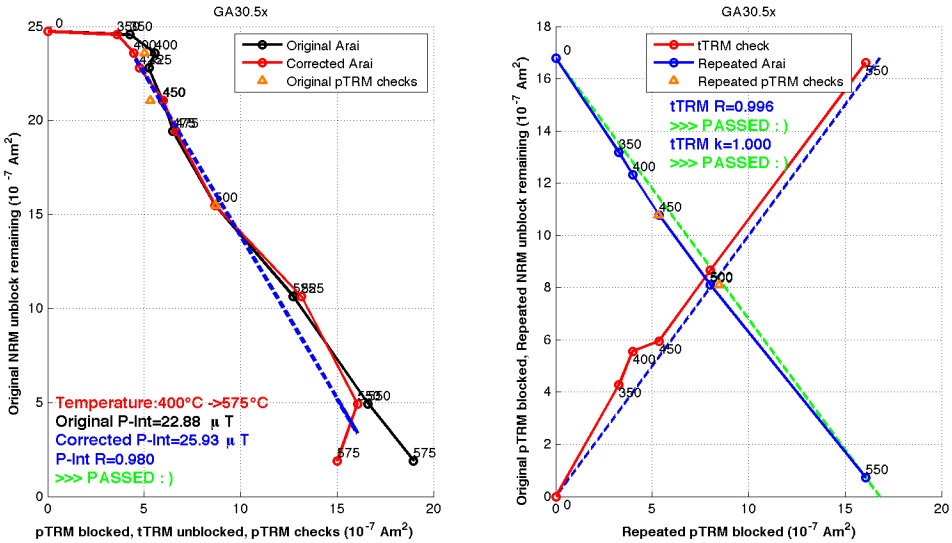

Figure 3.S2-173: Arai diagrams (left) and tTRM check (right) of specimen GA30.5x.

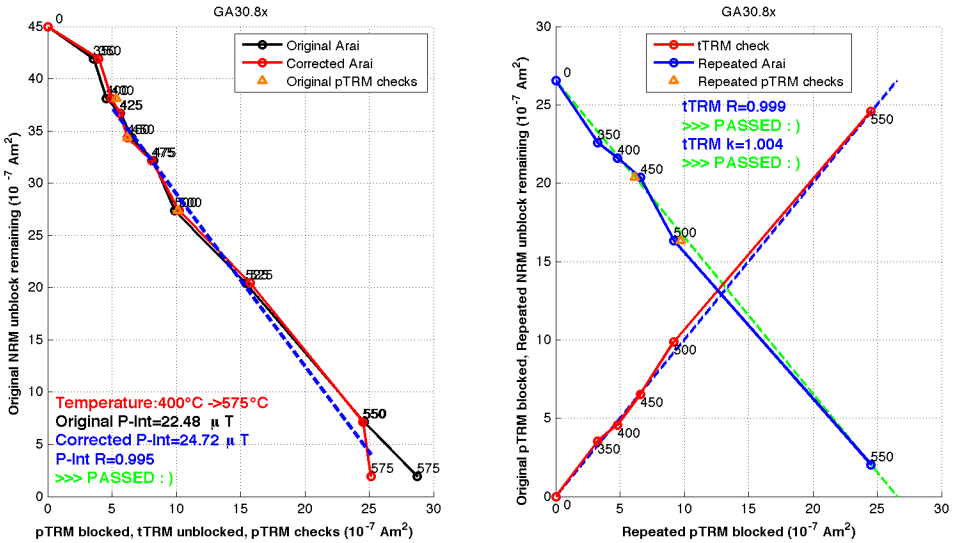

Figure 3.S2-174: Arai diagrams (left) and tTRM check (right) of specimen GA30.8x.

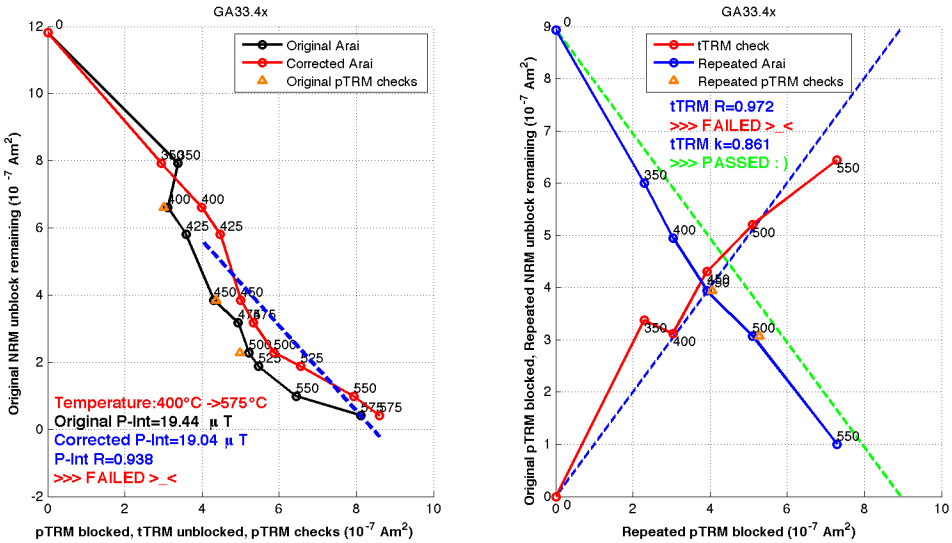

Figure 3.S2-175: Arai diagrams (left) and tTRM check (right) of specimen GA33.4x.

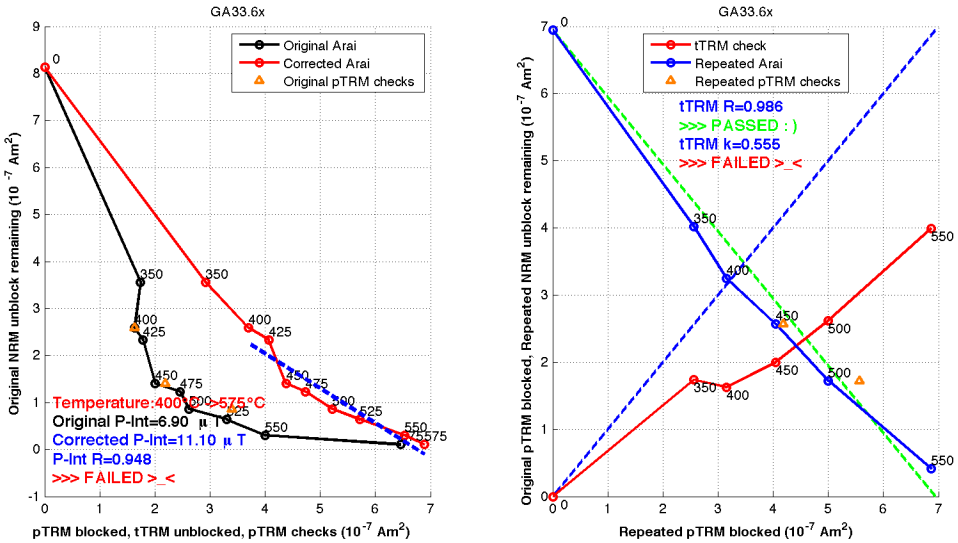

Figure 3.S2-176: Arai diagrams (left) and tTRM check (right) of specimen GA33.6x.

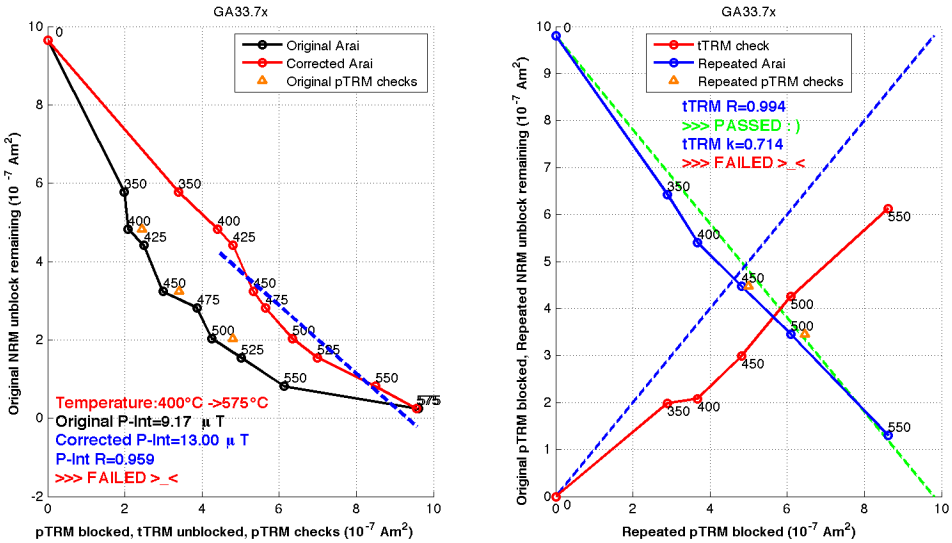

Figure 3.S2-177: Arai diagrams (left) and tTRM check (right) of specimen GA33.7x.

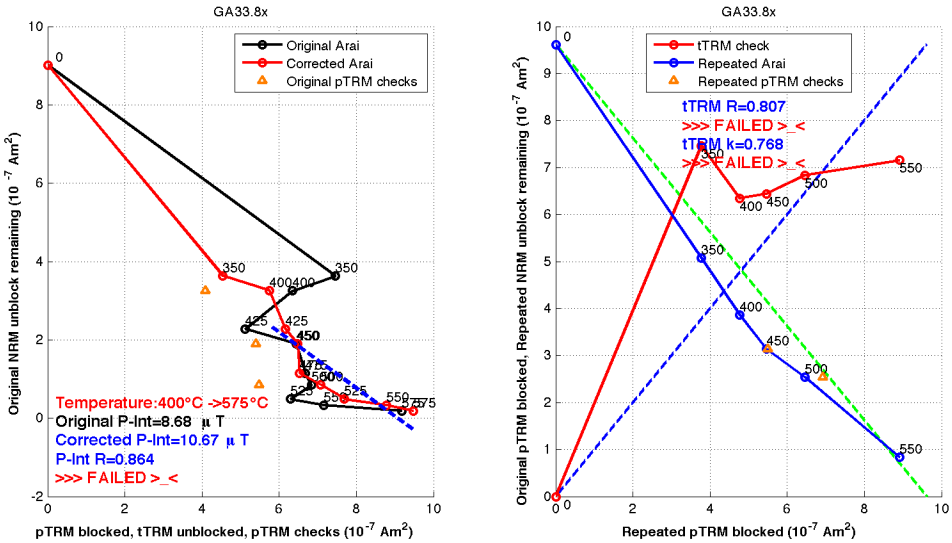

Figure 3.S2-178: Arai diagrams (left) and tTRM check (right) of specimen GA33.8x.

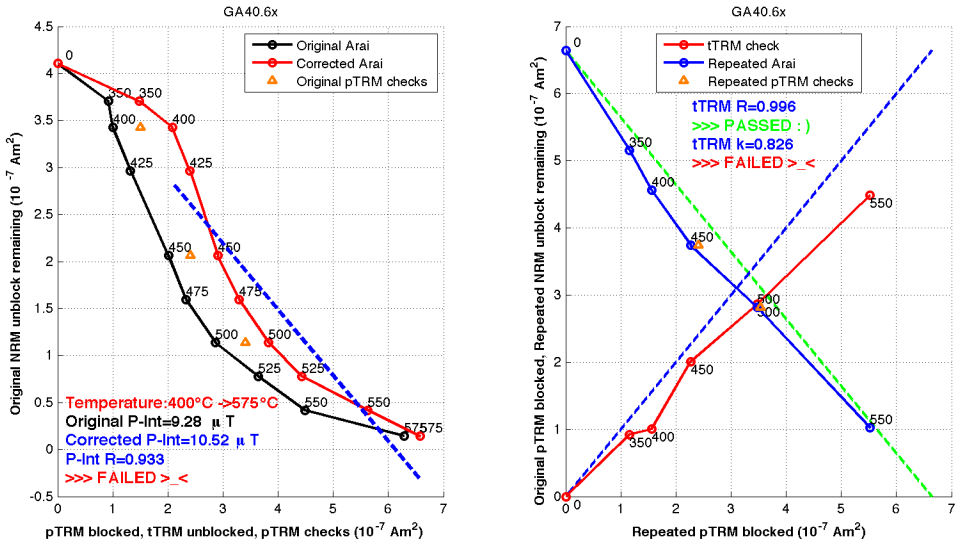

Figure 3.S2-179: Arai diagrams (left) and tTRM check (right) of specimen GA40.6x.

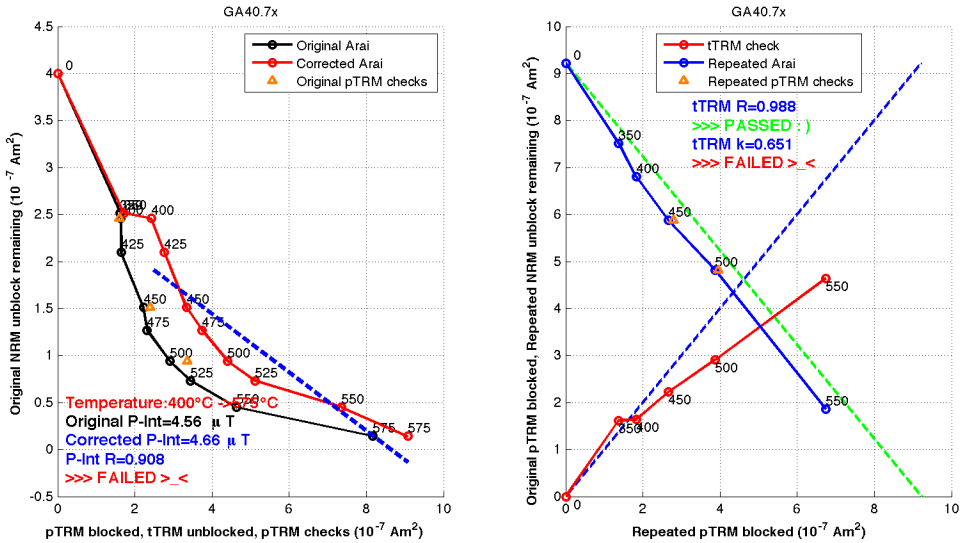

Figure 3.S2-180: Arai diagrams (left) and tTRM check (right) of specimen GA40.7x.

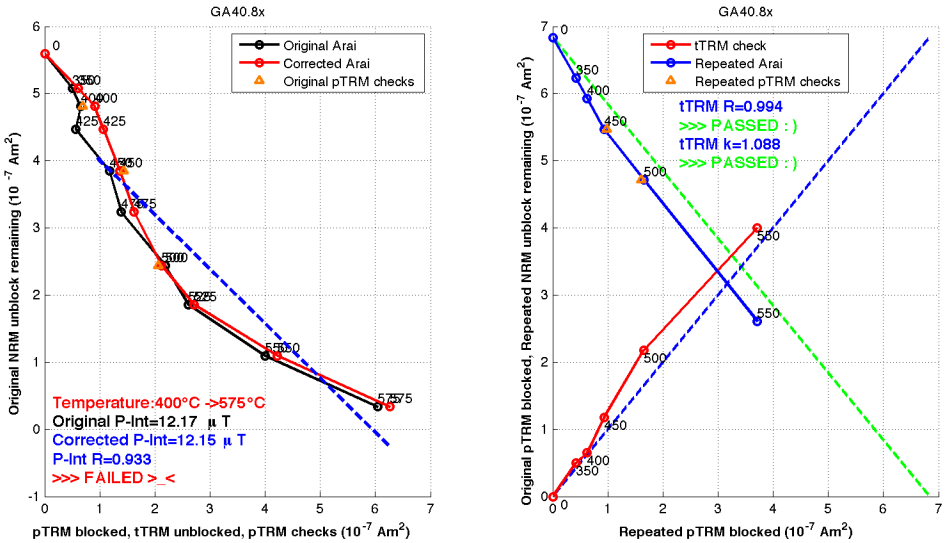

Figure 3.S2-181: Arai diagrams (left) and tTRM check (right) of specimen GA40.8x.

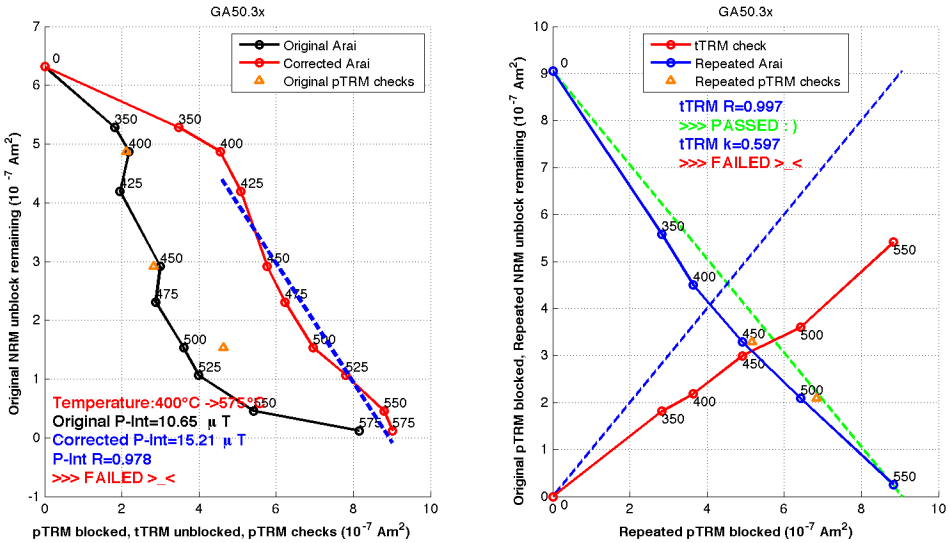

Figure 3.S2-182: Arai diagrams (left) and tTRM check (right) of specimen GA50.3x.

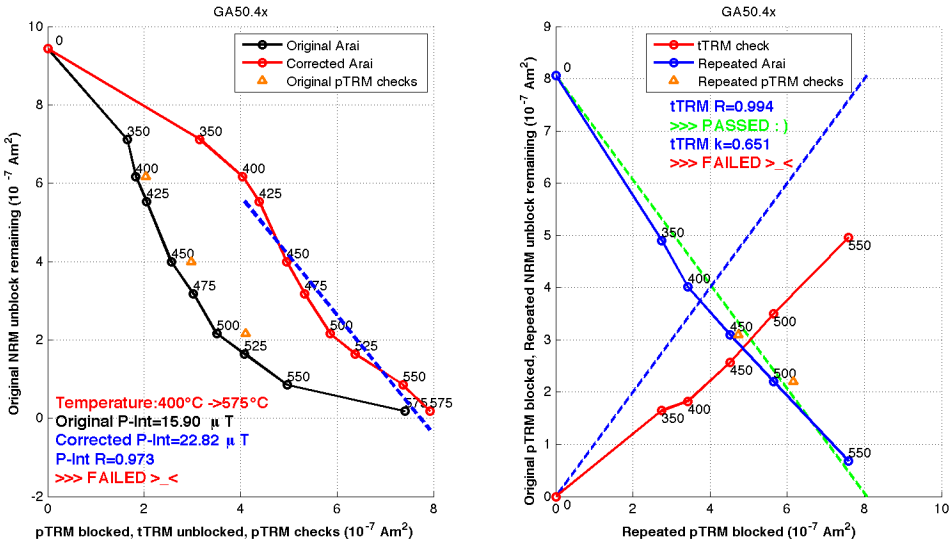

Figure 3.S2-183: Arai diagrams (left) and tTRM check (right) of specimen GA50.4x.

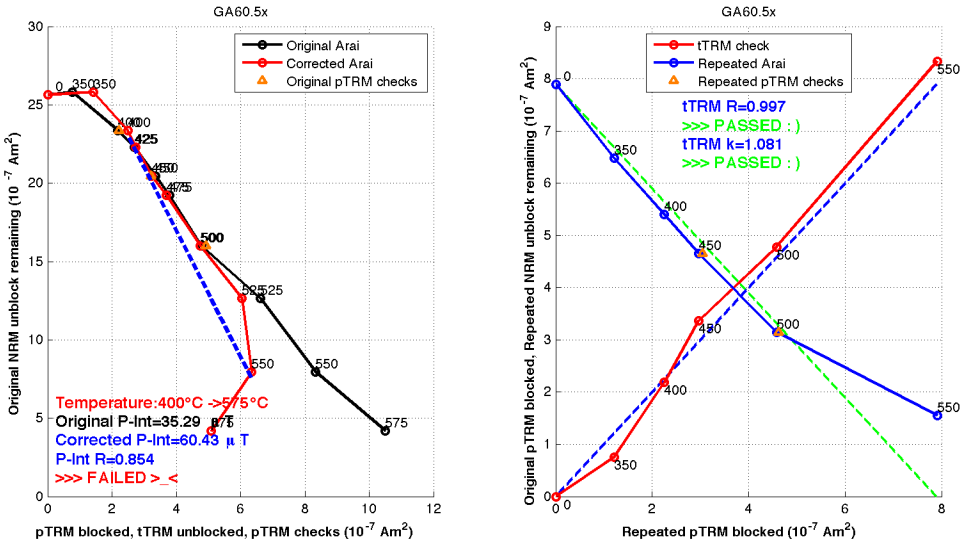

Figure 3.S2-184: Arai diagrams (left) and tTRM check (right) of specimen GA60.5x.

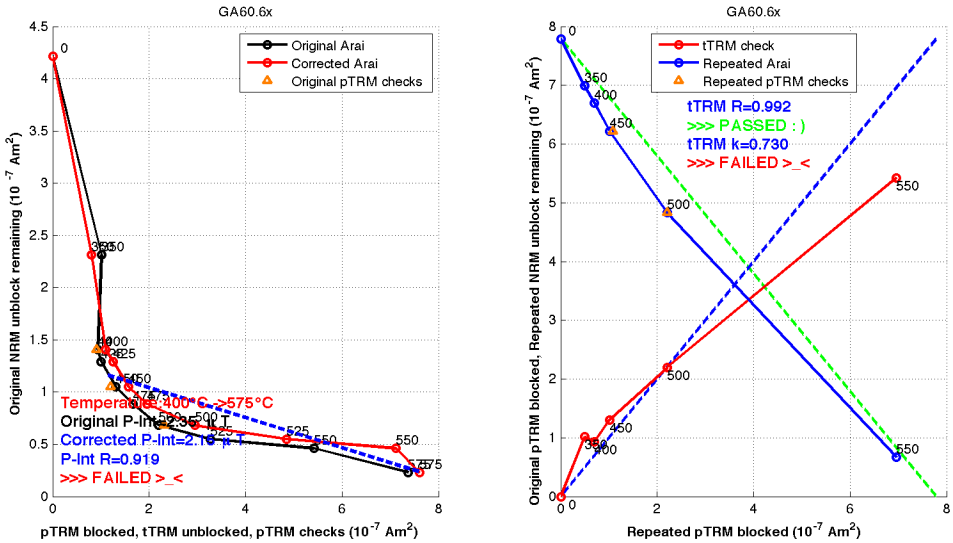

Figure 3.S2-185: Arai diagrams (left) and tTRM check (right) of specimen GA60.6x.

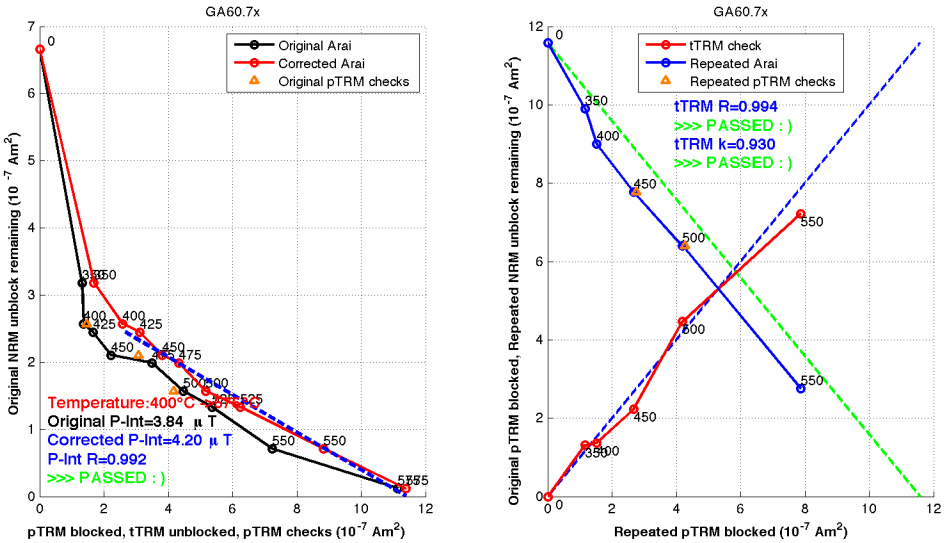

Figure 3.S2-186: Arai diagrams (left) and tTRM check (right) of specimen GA60.7x.

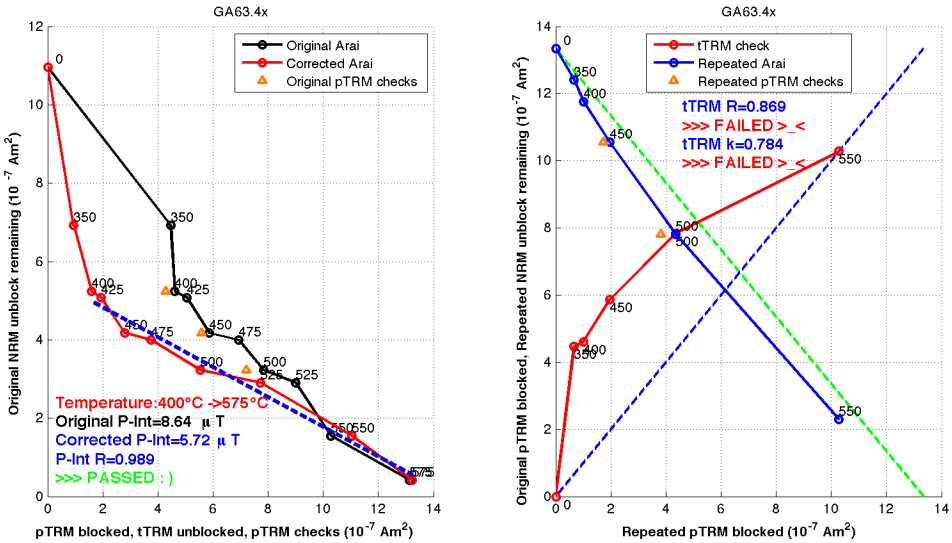

Figure 3.S2-187: Arai diagrams (left) and tTRM check (right) of specimen GA63.4x.

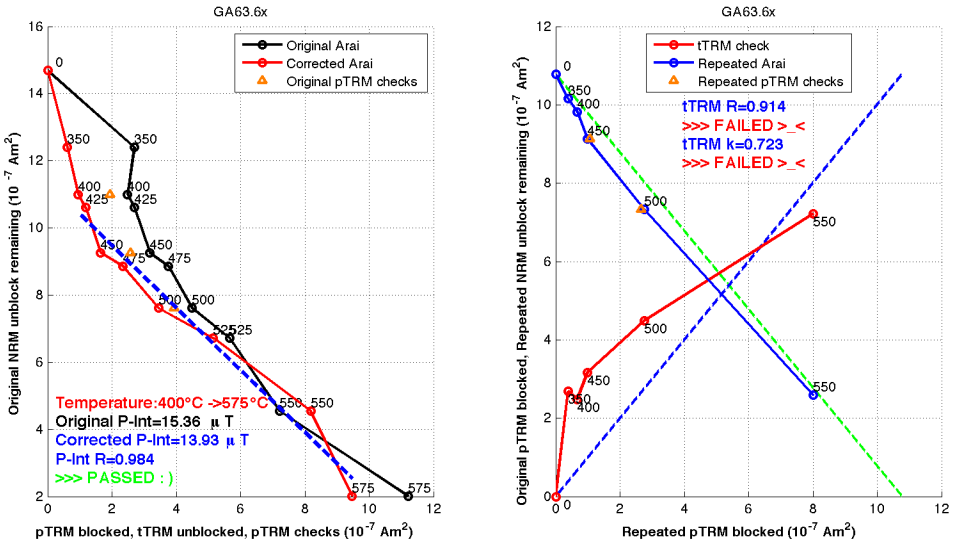

Figure 3.S2-188: Arai diagrams (left) and tTRM check (right) of specimen GA63.6x.

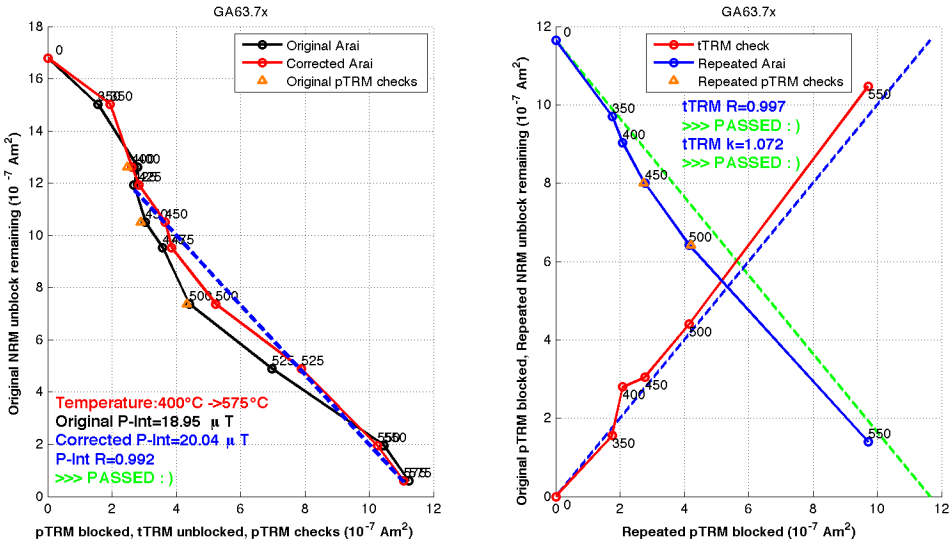

Figure 3.S2-189: Arai diagrams (left) and tTRM check (right) of specimen GA63.7x.

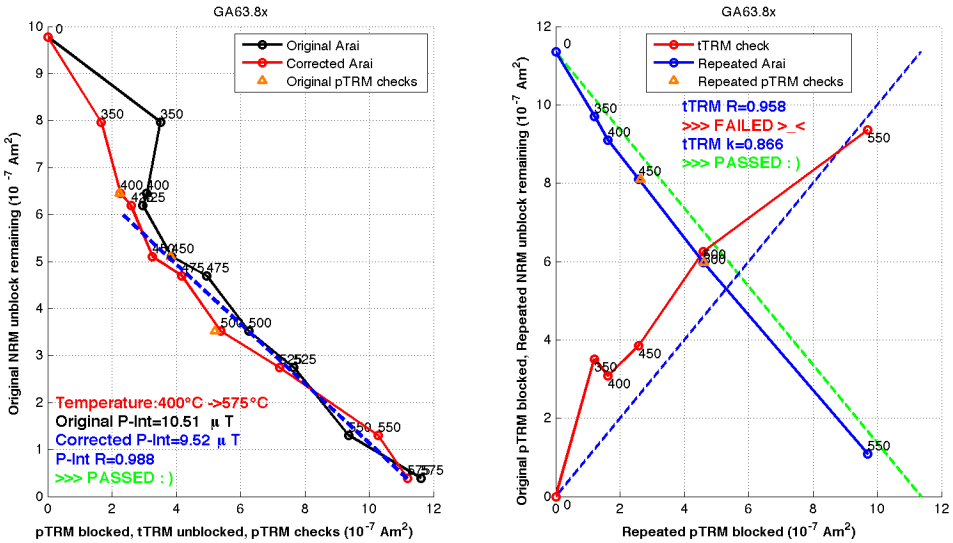

Figure 3.S2-190: Arai diagrams (left) and tTRM check (right) of specimen GA63.8x.

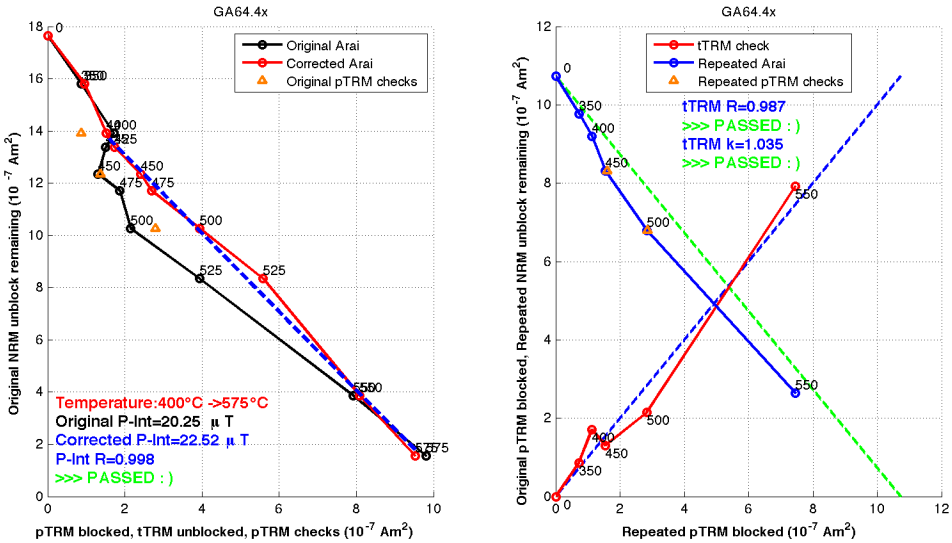

Figure 3.S2-191: Arai diagrams (left) and tTRM check (right) of specimen GA64.4x.

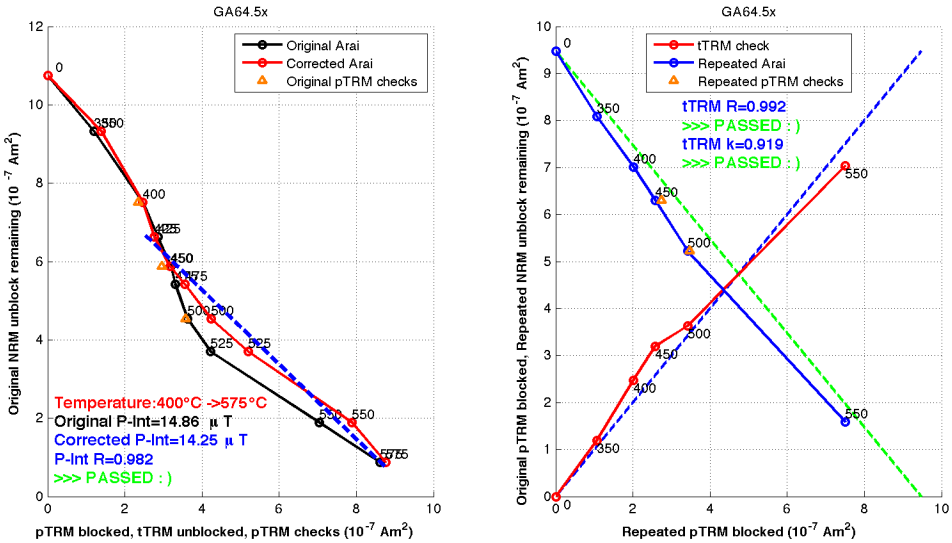

Figure 3.S2-192: Arai diagrams (left) and tTRM check (right) of specimen GA64.5x.

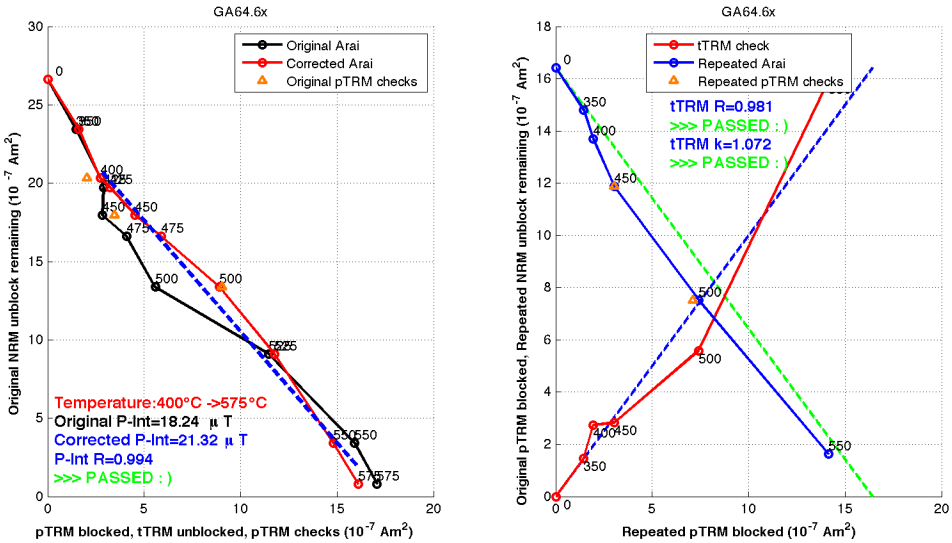

Figure 3.S2-193: Arai diagrams (left) and tTRM check (right) of specimen GA64.6x.

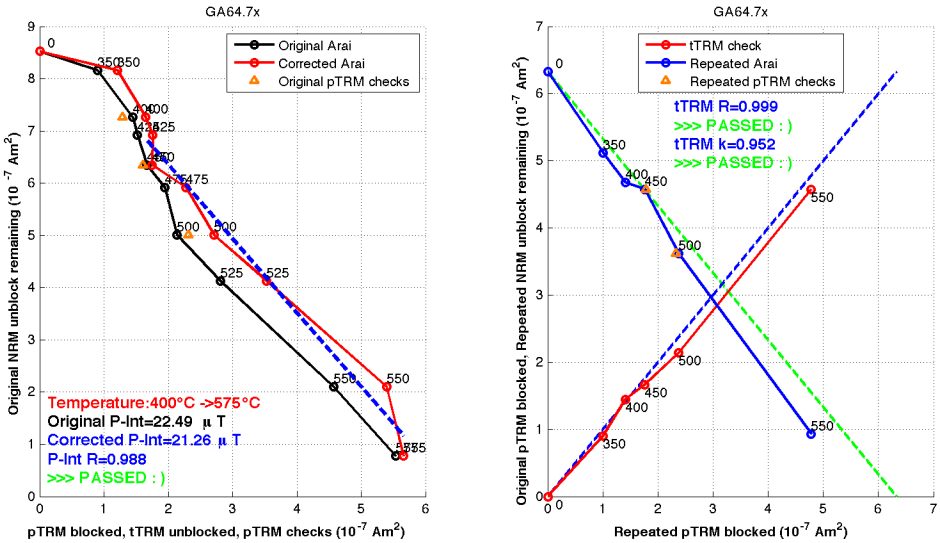

Figure 3.S2-194: Arai diagrams (left) and tTRM check (right) of specimen GA64.7x.

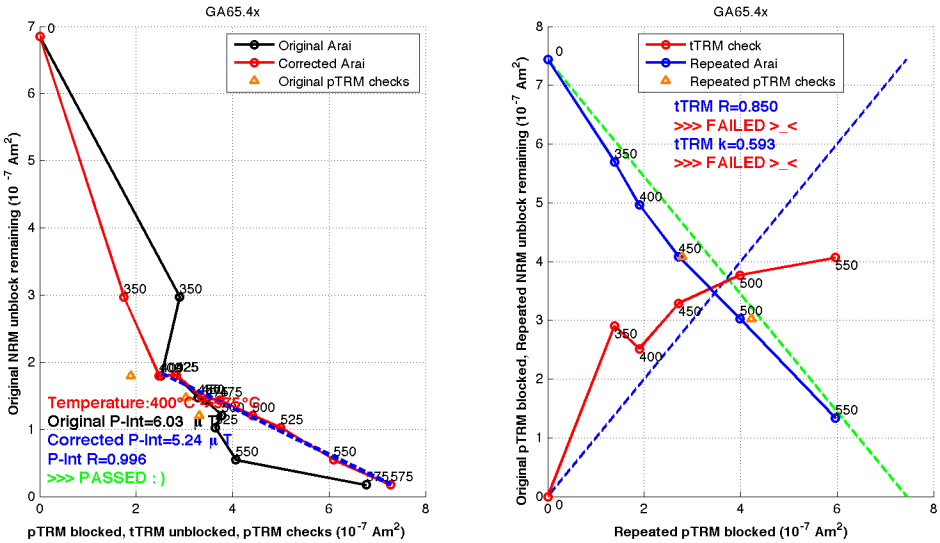

Figure 3.S2-195: Arai diagrams (left) and tTRM check (right) of specimen GA65.4x.

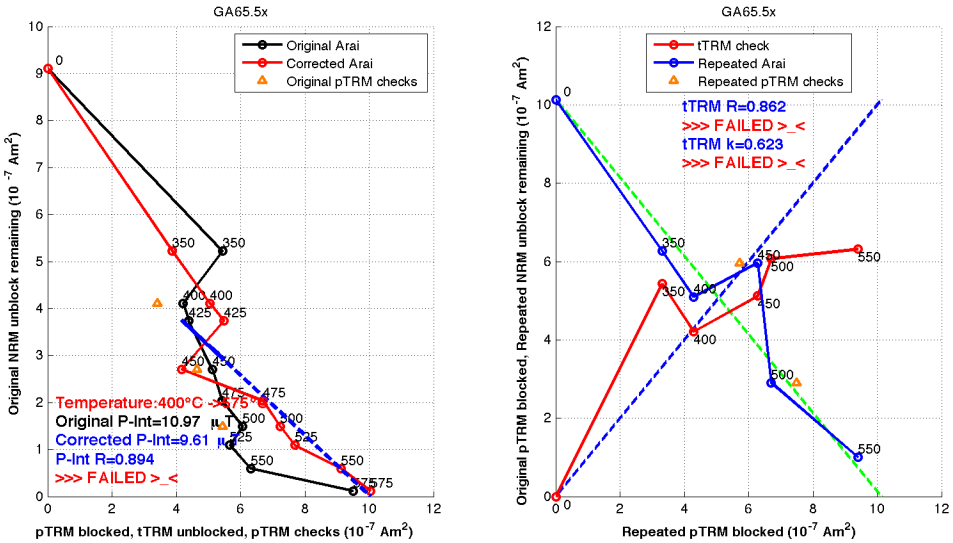

Figure 3.S2-196: Arai diagrams (left) and tTRM check (right) of specimen GA65.5x.

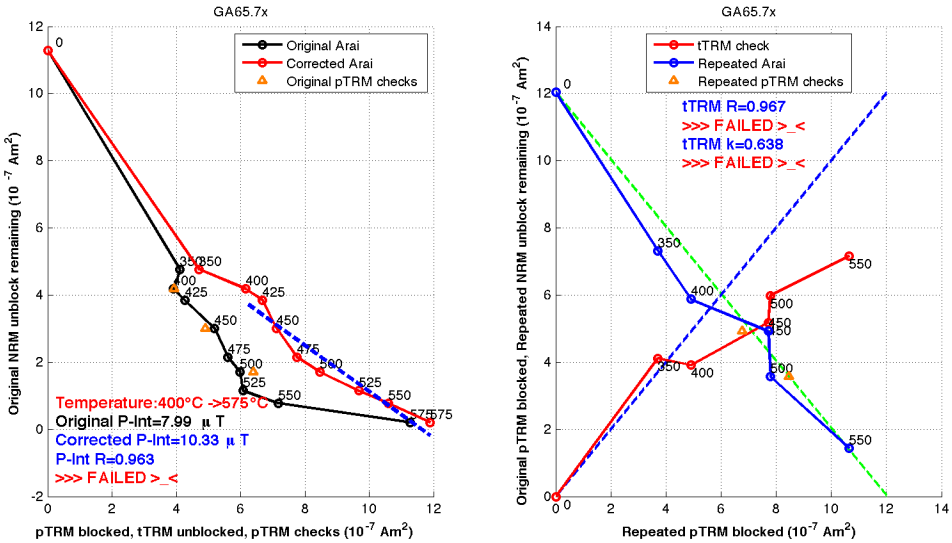

Figure 3.S2-197: Arai diagrams (left) and tTRM check (right) of specimen GA65.7x.

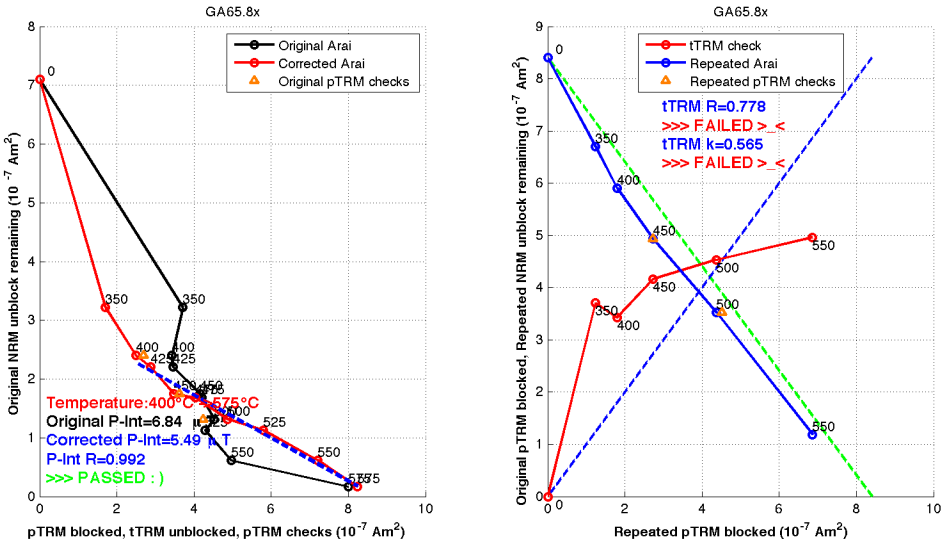

Figure 3.S2-198: Arai diagrams (left) and tTRM check (right) of specimen GA65.8x.

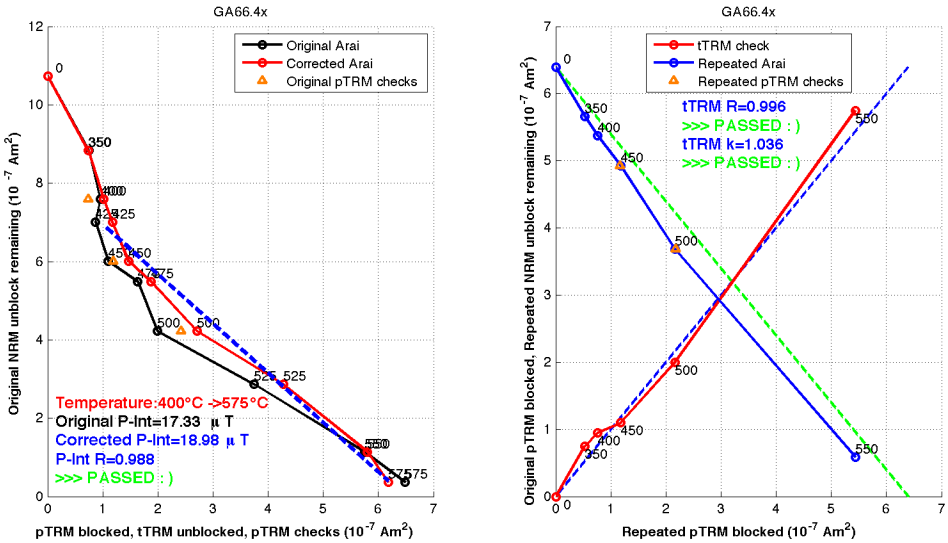

Figure 3.S2-199: Arai diagrams (left) and tTRM check (right) of specimen GA66.4x.

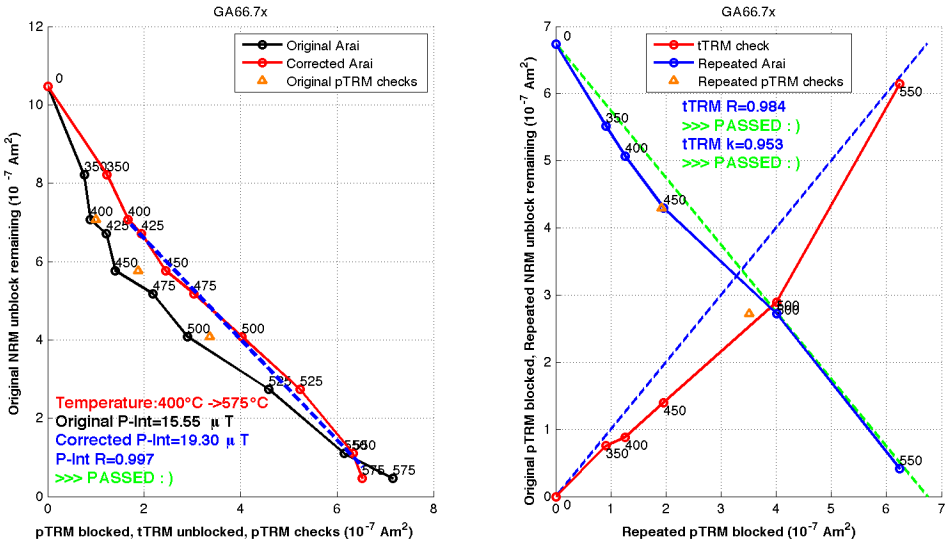

Figure 3.S2-200: Arai diagrams (left) and tTRM check (right) of specimen GA66.7x.

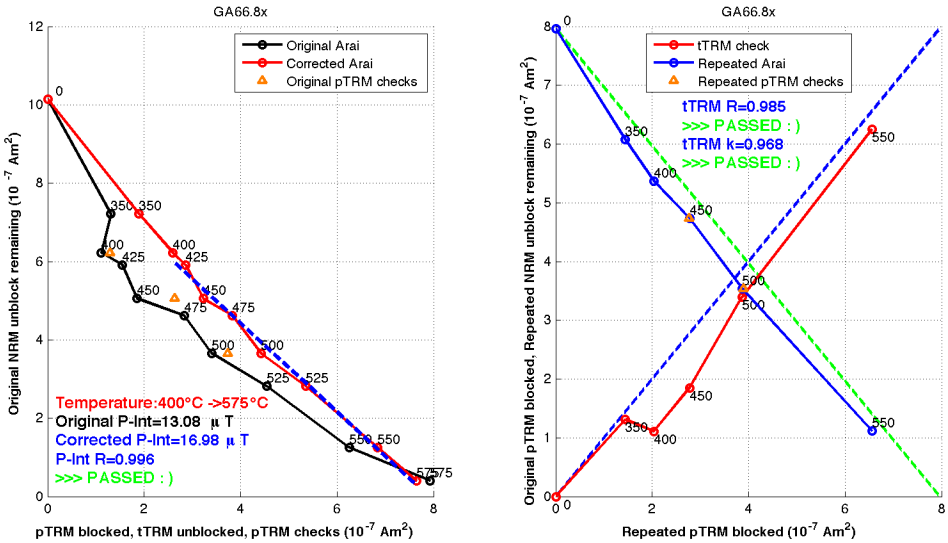

Figure 3.S2-201: Arai diagrams (left) and tTRM check (right) of specimen GA66.8x.

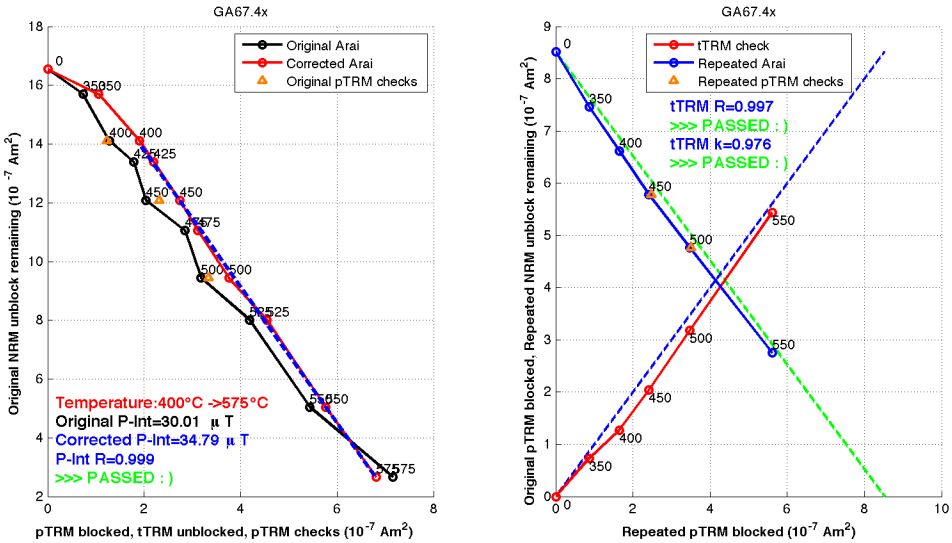

Figure 3.S2-202: Arai diagrams (left) and tTRM check (right) of specimen GA67.4x.

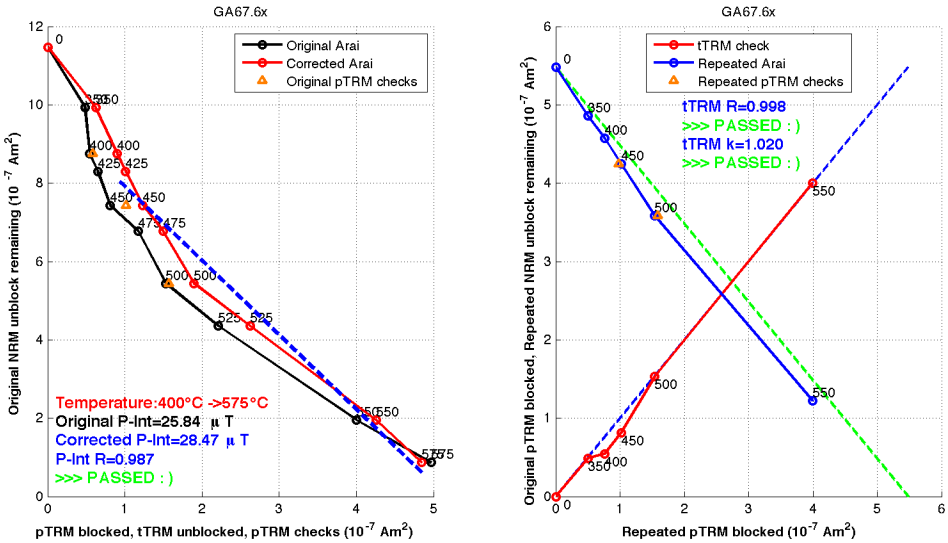

Figure 3.S2-203: Arai diagrams (left) and tTRM check (right) of specimen GA67.6x.

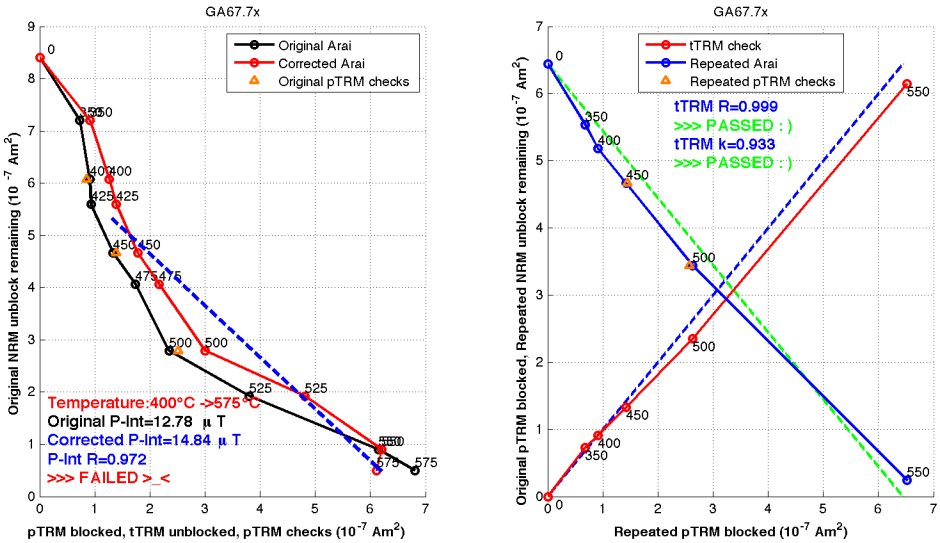

Figure 3.S2-204: Arai diagrams (left) and tTRM check (right) of specimen GA67.7x.

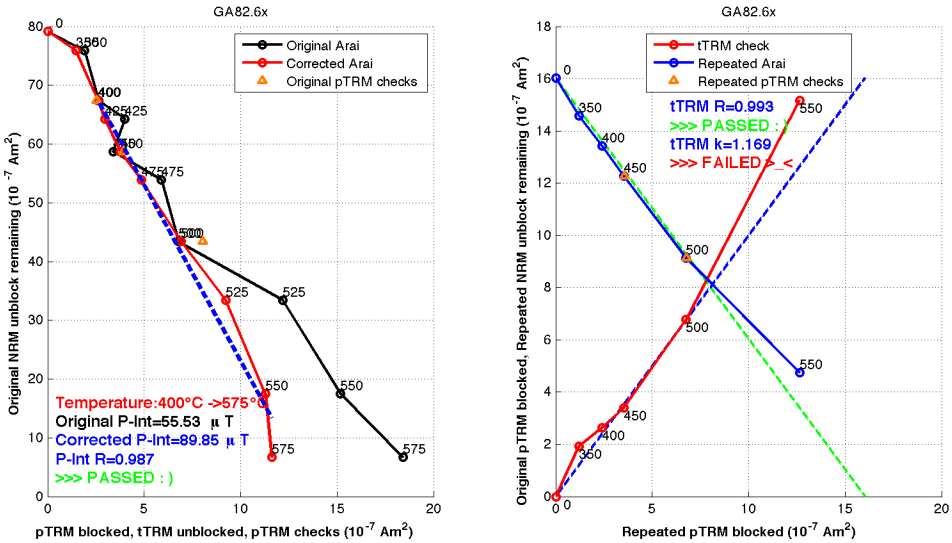

Figure 3.S2-205: Arai diagrams (left) and tTRM check (right) of specimen GA82.6x.

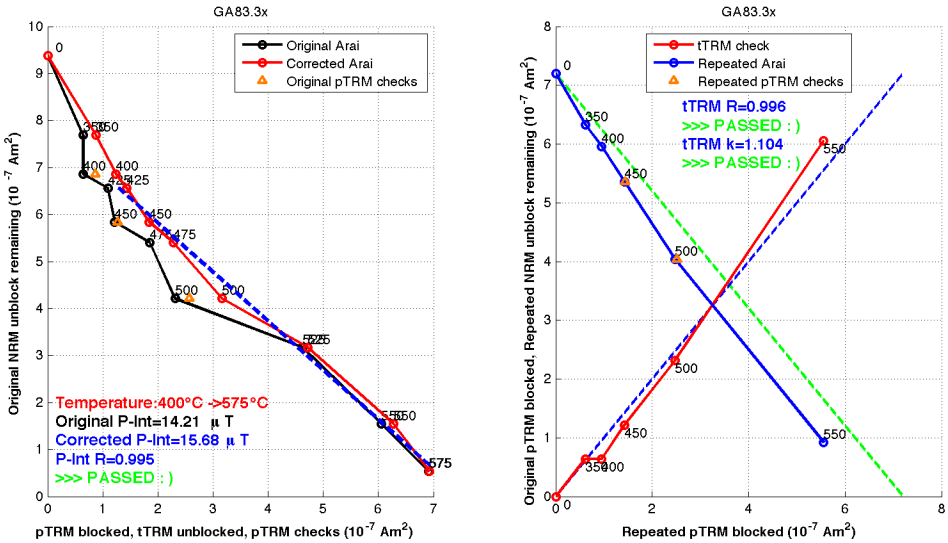

Figure 3.S2-206: Arai diagrams (left) and tTRM check (right) of specimen GA83.3x.

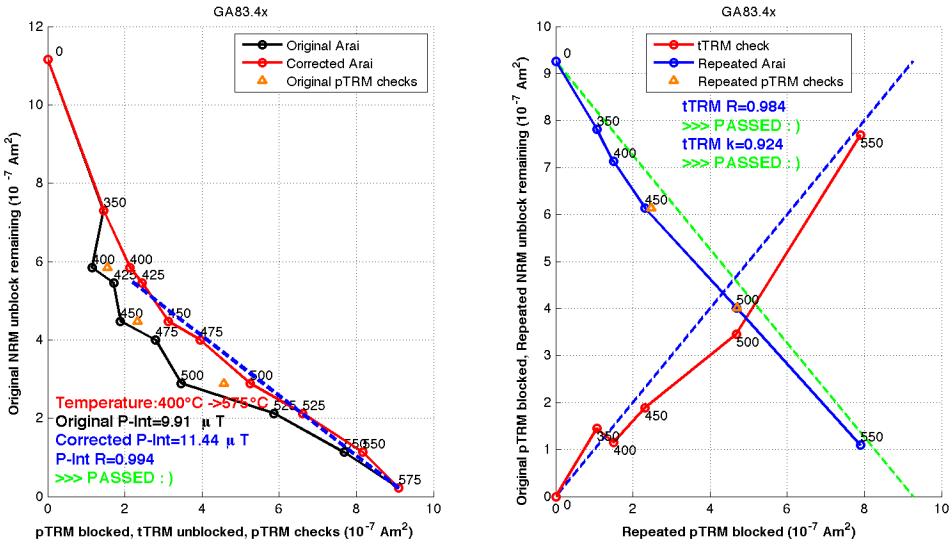

Figure 3.S2-207: Arai diagrams (left) and tTRM check (right) of specimen GA83.4x.

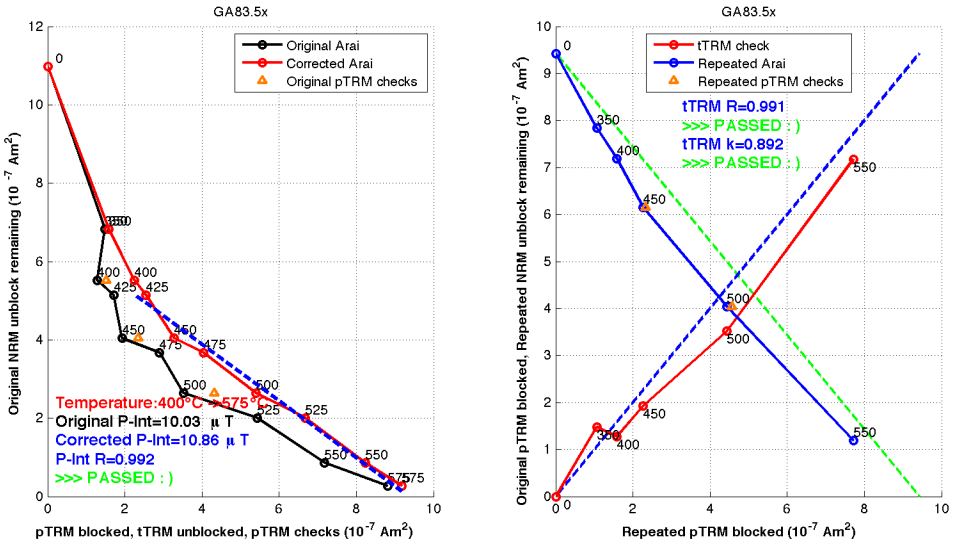

Figure 3.S2-208: Arai diagrams (left) and tTRM check (right) of specimen GA83.5x.

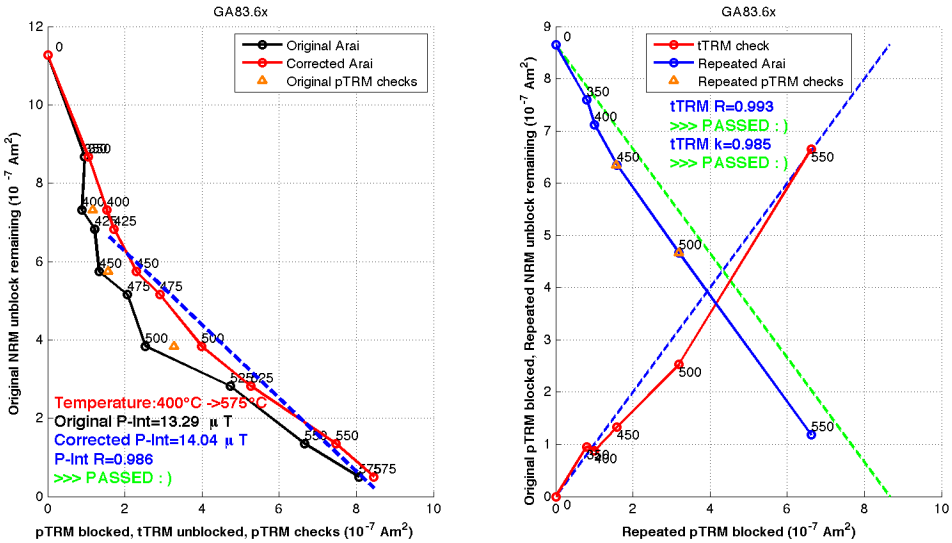

Figure 3.S2-209: Arai diagrams (left) and tTRM check (right) of specimen GA83.6x.

Chapter 4

Conclusion

In order to test the GAD model for the last few million years during the time period of Pliocene-Pleistocene, this dissertation generates paleomagnetic direction (Chapter 1; [*Kent et al.*, 2010]) and paleointensity (Chapter 3) data of lava flows from Galapagos Islands that are only 1º South from the Equator.

Paleomagnetic direction results (overall mean inclination = 1.9º) in this dissertation confirm previous paleomagnetic direction results from time average field initiative (TAFI) studies [*Opdyke et al.*, 2010], which suggest that the average directions of the geomagnetic field for the past ~5 million years coincide with the GAD model very well (Chapter 1; [*Kent et al.*, 2010]).

In order to get reliable absolute paleointensity estimations from basaltic lava flows that contain MD magnetite as major magnetization carriers, this dissertation develops a new comprehensive Back-Zero-Forth triple-heating paleointensity experiment protocol and an MD correction technique by repeating the experiment and successfully applies both on a trail lava site from Galapagos (Chapters 2; [*Wang and Kent*, 2013]; Chapters A1 and A2 [*Wang et al*, 2013]).

The average paleointensity (mean value = 21.6 μT) for the last a few million years from Galapagos Islands at the equatorial region generated in this dissertation is close to about half of that from McMurdo at the polar region (33.4 μT) [*Lawrence et al*., 2009], which fulfills the predictions of the GAD model on the geomagnetic field intensity latitudinal distribution (Chapter 3).

In order to test the MD correction technique for paleointensity experiments in reality, MD magnetization carrying samples from historical lava flows with known paleointensities should be experimented by the same procedure developed in this dissertation. In order to confirm the findings presented here in this dissertation, more high quality paleointensity results are needed, especially from both equatorial and polar regions, in future studies.

Reference

Kent, D. V., H. Wang, and P. Rochette (2010), Equatorial paleosecular variation of the geomagnetic field from 0-3 Ma lavas from the Galapagos Islands, *Physics of the Earth and Planetary Interiors*, *183*, 404-412.

Lawrence, K. P., L. Tauxe, H. Staudigel, C. Constable, A. Koppers, W. McIntosh, and C. L. Johnson (2009), Paleomagnetic field properties at high southern latitude, *Geochemistry Geophysics Geosystems*, *10*, Q01005, doi:01010.01029/02008GC002072.

Opdyke, N. D., D. V. Kent, K. Huang, D. A. Foster, and J. P. Patel (2010), Equatorial paleomagnetic time averaged field results from 0-5 Ma lavas from Kenya and the latitudinal variation of angular dispersion, *Geochemistry Geophysics Geosystems*, *11*, Q05005, doi:05010.01029/02009GC002863.

Wang, H. and D. V. Kent, (2013), A Paleointensity Technique for Multidomain Igneous Rocks, *Geochemistry Geophysics Geosystems, 14*, 4195-4213, doi: 10.1002/ggge.20248

Wang, H., D. V. Kent, and M. J. Jackson (2013), Evidence for abundant isolated magnetic nanoparticles at the Paleocene-Eocene boundary, *Proceedings of the National Academy of Sciences, USA*, *110*, 425-430.

Appendix Chapter A1

Rock Magnetic Properties and Thermal Alteration of Galapagos Lavas

In order to study rock magnetic property changes of lavas and their thermal alteration paths during the paleointensity experiments in detail. We also conducted the following measurements as supplementary materials for Chapter 2.

A1.1 First-Order Reversal Curves

To confirm if the chips had been thermophysicochemically altered, besides the hysteresis loops and Js-T curves presented in Figure 2.3, we also conducted first-order reversal curves (FORC) [*Pike et al.*, 1999, *Roberts et al., 2000*] measurements on each of the 24 chips before and after the first thermomagnetic (J_s-T) experiments, using a Princeton Measurement Corporation alternating gradient magnetometer (AGM) at Rutgers paleomagnetic laboratory. Selected hysteresis loops, Js-T curves and FORC diagrams are shown in Figures A1.1-A1.3.

A1.2 Thermal Fluctuation Tomography

In order to provide more insights on the thermophysicochemical alteration characteristics, we also conducted thermal fluctuation tomography (TFT) experiments [*Jackson et al.*, 2006, *Wand and Kent*, 2013] on about a dozen of rock magnetic chips, using Princeton Measurement Corporation vibrating sample magnetometers (VSM) equipped with high temperature furnace and low temperature cryostat at the Institute for Rock Magnetism (IRM), University of Minnesota (UM).

High temperature TFT experiments of "w" specimens were performed by measuring hysteresis loops and back-field direct current demagnetization (DCD) curves from 300K (27ºC) to 880K (607ºC) for every 20K (ºC) by using a high temperature VSM. Low temperature TFT experiments of "v" specimens were performed by measuring hysteresis loops and DCD curves from 10K to 320K for every 10K by using a low temperature VSM.

These measurements at high and low temperatures allow us to calculate many rock magnetic parameters, i.e. low-field ferromagnetic susceptibility; high-field paramagnetic susceptibility; remanent magnetization, Mr; saturation magnetization, Ms; magnetic coercivity, Bc (Hc); remanent coercivity, Bcr (Hcr); and the ratios of Bcr/Bc (Hcr/Hc) and Mr/Ms. For some "w" specimens, after the first high temperature TFT experiments, we conducted second high temperature TFT experiments to detect thermal alterations between the two heating cycles. Selected results are shown in Figures A1.4-

A1.6 for high temperature experiments and Figures A1.7-A1.9 for low temperature experiments.

In order to compare the ferromagnetic susceptibility vs temperature curve (κ_f –T) to the usual bulk susceptibility vs temperature curves (κ –T), for sample GA79.5 and GA86.4, we also sent subsamples to the Paleomagnetism and Geochronology Laboratory at Institute of Geology and Geophysics, Chinese Academy of Sciences. Dr. Huafeng Qing helped us to measure their κ –T curves (Figure A1.10) by using AGICO KLY-3 Kappabridge equipped with high temperature furnace.

Although the TFT inverse calculations from DCD curves to plot size-shape distribution diagrams are only valid for SSD and SP (superparamagnetic) ferromagnetic particles [*Jackson et al.*, 2006], the TFT diagrams of specimens from GA79.5 and GA84.6 presented in Figure A1.11 still provide us some information on the rock magnetic characteristics of Galapagos lavas. GA79.5w has a concentrated peak distribution, while GA84.6w has a more spread out peak distribution. These results can be used in the future to assist gauging thermophysicochemical alterations of samples.

A1.3 Low Temperature Magnetic Properties

In order to study the properties and to infer the size of the fine magnetite particles in Galapagos lavas, we also conducted field cooled and zero-field cooled (FC–ZFC)

remanence warming curves [Moskowitz et al., 1993] as well as low temperature demagnetization (LTD) cooling and warming curves of room temperature saturation isothermal remanence ($SIRM_{RT}$) at every 5 K from 10K to 300K for about a dozen of Galapagos lava samples, using the Quantum Designs magnetic properties measuring system (MPMS) at IRM, UM. Selected results of the Low Temperature Magnetic Property curves are shown in Figure A1.12.

A1.4 High-Resolution FORCs

In order to track the thermal alteration of Galapagos lavas step-by-step as they are being heated in the paleointensity experiments, we also measured hysteresis loops, DCD curves, and high-resolution FORCs [Egli et al., 2010; Wang et al., 2013] for "y" specimens of GA79.5 and GA84.6 after they are heated to each high temperature (200ºC, 300ºC, 350ºC, 400ºC, 450ºC, 500ºC, 550ºC and 600ºC). We used the Curie balance at Rutgers paleomagnetic laboratory for the heating cycles, and AGM for the rock magnetic measurements. Similar to the TFT measurements, we calculated many rock magnetic parameters (i.e. low-field ferromagnetic susceptibility; high-field paramagnetic susceptibility; Mr; Ms; Bc (Hc); Bcr (Hcr); and the ratios of Bcr/Bc (Hcr/Hc) and Mr/Ms, respectively) after the specimens were heated to each high temperature. Rock magnetic parameters vs temperature curves are shown in Figure A1.13. HiResFORC diagrams are shown in Figures A1.14 – A1.16.

A1.5 Rock Magnetic Conclusions

After conducting all the above sophisticated rock magnetic measurements, we found out that they were many times indicative of thermal alterations of magnetization carrying minerals in lavas. However, no direct quantities can be concluded to gauge the affects to the paleointensity results from these thermal alterations.

The before and after heating rock magnetic stability may be used as a criteria to exclude paleointensity results, but not vice versa.

References

Egli, R., A. P. Chen, M. Winklhofer, K. P. Kodama, and C.-S. Horng (2010), Detection of noninteracting single domain particles using first-order reversal curve diagrams, *Geochem. Geophys. Geosyst.*, *11*.

Jackson, M., B. Carter-Stiglitz, R. Egli, and P. Solheid (2006), Characterizing the superparamagnetic grain distribution f(vi, H-k) by thermal fluctuation tomography, *J. Geophys. Res.-Solid Earth*, *111*.

Moskowitz B. M., Frankel R. B., Bazylinski D. A. (1993) Rock magnetic criteria for the detection of biogenic magnetite. Earth Planet Sci Lett 120:283–300.

Pike, C. R., A. P. Roberts, and K. L. Verosub (1999), Characterizing interactions in fine magnetic particle systems using first order reversal curves, *Journal of Applied Physics*, *85*, 6660-6667.

Roberts, A. P., C. R. Pike, and K. L. Verosub (2000), First-order reversal curve diagrams: A new tool for characterizing the magnetic properties of natural samples, *J. Geophys. Res.-Solid Earth*, *105*, 28461-28475.

Wang, H., D. V. Kent, and M. J. Jackson (2013), Evidence for abundant isolated magnetic nanoparticles at the Paleocene-Eocene boundary, *Proceedings of the National Academy of Sciences, USA*, *110*, 425-430.

Figure Captions

Figure A1.1-A1.3. Column 1 and 2: Js-T curves for the 1st and 2nd heating cycles; Column 3 and 4: hysteresis loops before and after heating; Column 5: FORC diagrams before (upper half) and after (lower half) heating.

Figure A1.4-A1.9. Results for high-temperature (Fig. A1.4-A1.6) and low-temperature (Fig. A1.7-A1.9) TFT measurements. Column 1: low-field ferromagnetic and high-field paramagnetic susceptibility curves; Column 2: Mr and Ms curves; Column 3: Mr/Ms ratio curves; Column 4: Bcr (Hcr) and Bc (Hc) curves; Column 3: Bcr/Bc (Hcr/Hc) ratio curves. Blue curves for the 1st heating; red curves for the 2nd heating, if applicable.

Figure A1.10. Bulk susceptibility vs temperature (κ –T) curves for subsamples of GA79.5 (left) and GA84.6 (right).

Figure A1.11. High-temperature TFT size-shape distributions of specimens GA79.5w (a) and GA84.6w (c); low-temperature TFT size-shape distributions of specimens GA79.5v (b) and GA84.6v (d). Color scale represents linear increase of probability of distribution.

Figure A1.12. Low temperature magnetic property curves (FC-ZFC, $SIRM_{RT}$ cooling and warming) for selected specimens.

Figure A1.13. Results for stepwise after heating rock magnetic measurements for GA79.5y (upper row) and GA84.6y (lower row). Column 1: low-field ferromagnetic and high-field paramagnetic susceptibility curves; Column 2: Mr and Ms curves; Column 3: Mr/Ms ratio curves; Column 4: Bcr (Hcr) and Bc (Hc) curves; Column 3: Bcr/Bc (Hcr/Hc) ratio curves.

Figure A1.14-A1.16. HiResFORC diagrams for GA79.5y and GA84.6y after each heating.

Figure A1.1

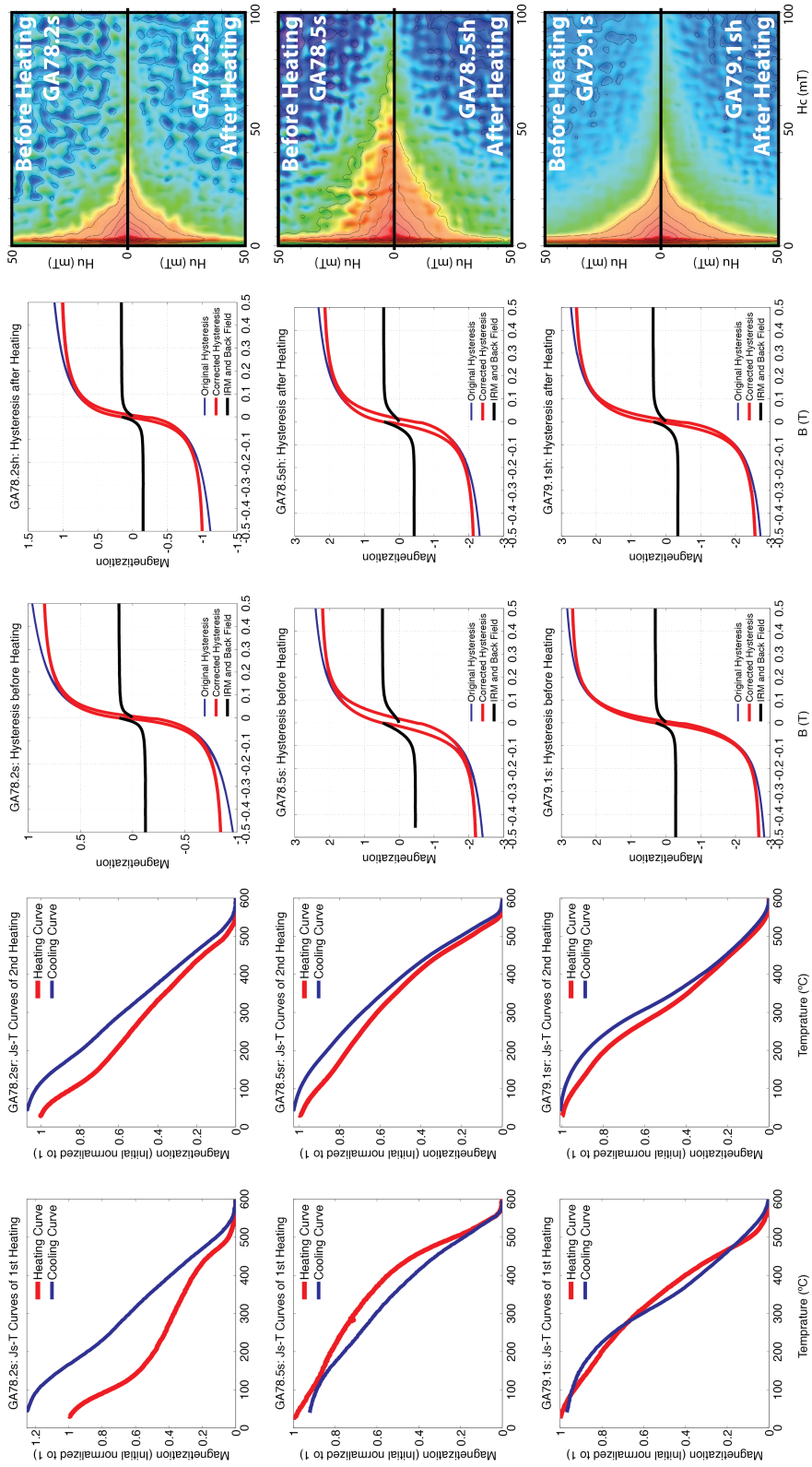
GA78.2s: Js-T Curves of 1st Heating
GA78.2sr: Js-T Curves of 2nd Heating
GA78.2s: Hysteresis before Heating
GA78.2sh: Hysteresis after Heating
GA78.5s: Js-T Curves of 1st Heating
GA78.5sr: Js-T Curves of 2nd Heating
GA78.5s: Hysteresis before Heating
GA78.5sh: Hysteresis after Heating
GA79.1s: Js-T Curves of 1st Heating
GA79.1sr: Js-T Curves of 2nd Heating
GA79.1s: Hysteresis before Heating
GA79.1sh: Hysteresis after Heating
Heating Curve
Cooling Curve
Magnetization (Initial normalized to 1)
Temprature (°C)
Magnetization
B (T)
Original Hysteresis
Corrected Hysteresis
IRM and Back Field
Hu (mT)
Hc (mT)
Before Heating
After Heating
GA78.2s
GA78.2sh
GA78.5s
GA78.5sh
GA79.1s
GA79.1sh

Figure A1.2

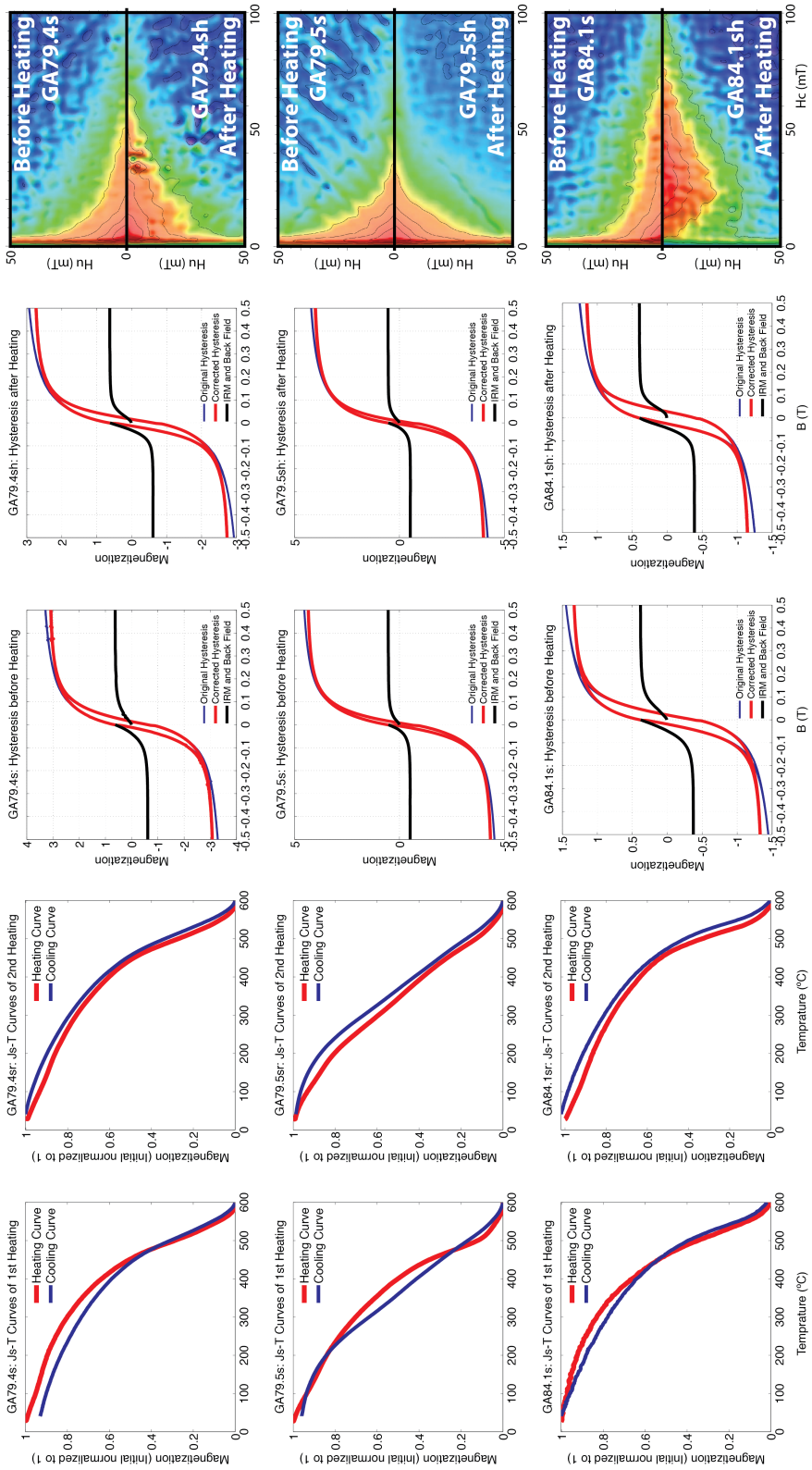
GA79.4s: Js-T Curves of 1st Heating
GA79.4sr: Js-T Curves of 2nd Heating
GA79.4s: Hysteresis before Heating
GA79.4sh: Hysteresis after Heating
Before Heating GA79.4s
After Heating GA79.4sh
GA79.5s: Js-T Curves of 1st Heating
GA79.5sr: Js-T Curves of 2nd Heating
GA79.5s: Hysteresis before Heating
GA79.5sh: Hysteresis after Heating
Before Heating GA79.5s
After Heating GA79.5sh
GA84.1s: Js-T Curves of 1st Heating
GA84.1sr: Js-T Curves of 2nd Heating
GA84.1s: Hysteresis before Heating
GA84.1sh: Hysteresis after Heating
Before Heating GA84.1s
After Heating GA84.1sh
Heating Curve
Cooling Curve
Original Hysteresis
Corrected Hysteresis
IRM and Back Field
Magnetization (Initial normalized to 1)
Temprature (°C)
Magnetization
B (T)
Hu (mT)
Hc (mT)

Figure A1.3

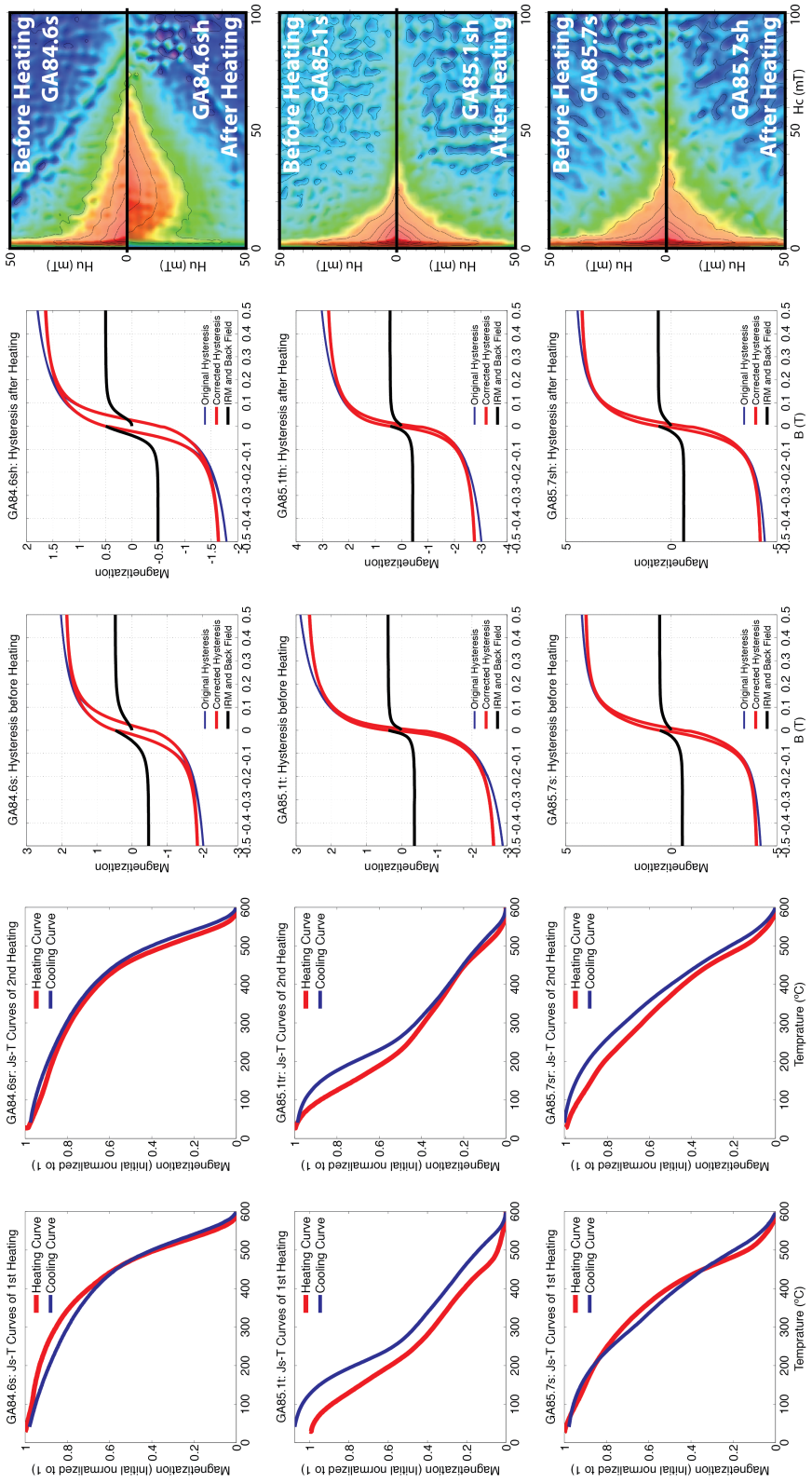
GA84.6s: Js-T Curves of 1st Heating
GA84.6sr: Js-T Curves of 2nd Heating
GA84.6s: Hysteresis before Heating
GA84.6sh: Hysteresis after Heating
GA84.6s
GA84.6sh
Before Heating
After Heating
GA85.1t: Js-T Curves of 1st Heating
GA85.1tr: Js-T Curves of 2nd Heating
GA85.1t: Hysteresis before Heating
GA85.1th: Hysteresis after Heating
GA85.1s
GA85.1sh
GA85.7s: Js-T Curves of 1st Heating
GA85.7sr: Js-T Curves of 2nd Heating
GA85.7s: Hysteresis before Heating
GA85.7sh: Hysteresis after Heating
GA85.7s
GA85.7sh
Heating Curve
Cooling Curve
Original Hysteresis
Corrected Hysteresis
IRM and Back Field
Magnetization (Initial normalized to 1)
Temprature (°C)
Magnetization
B (T)
Hu (mT)
Hc (mT)

Figure A1.4

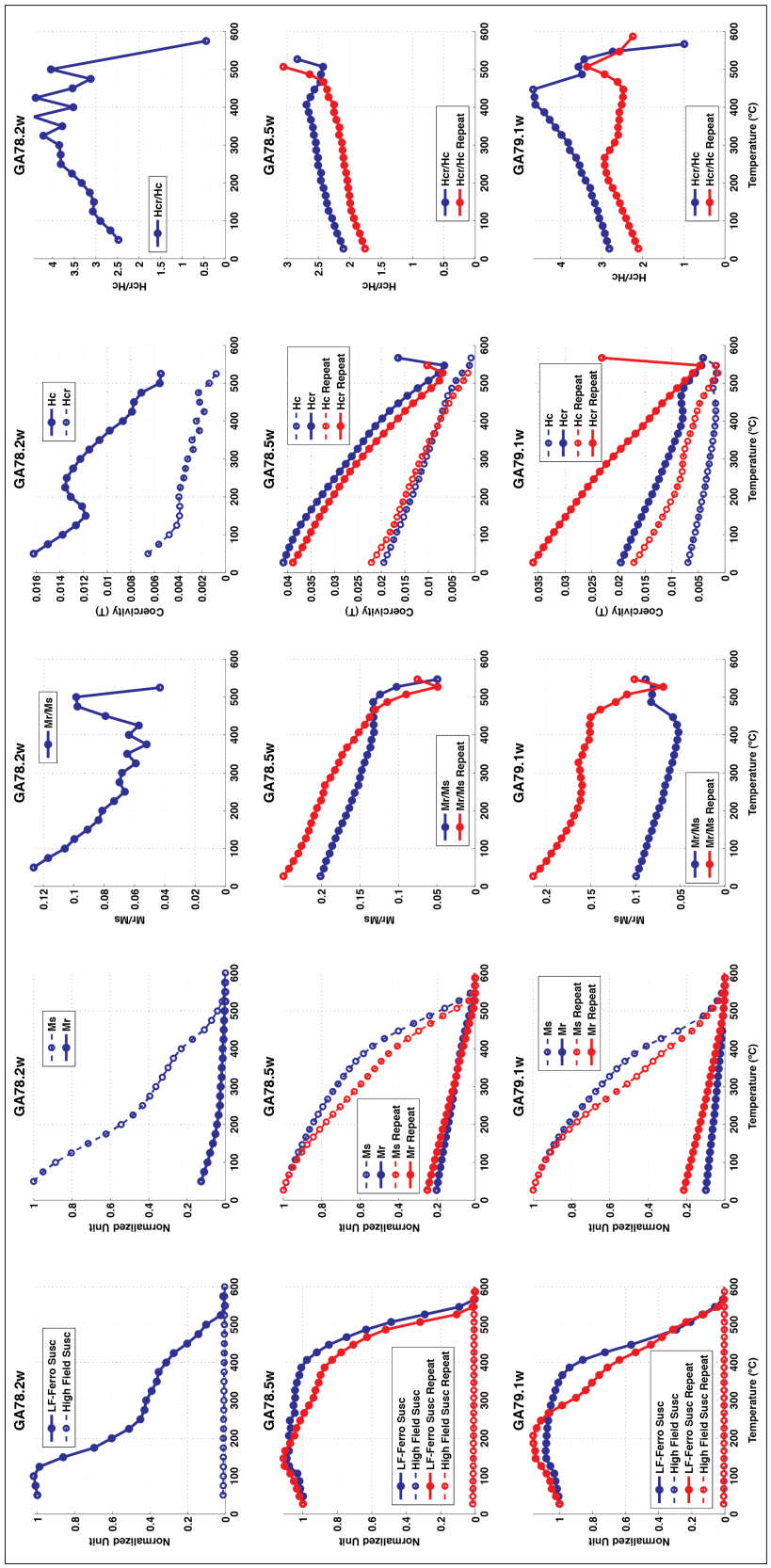
GA78.2w
GA78.5w
GA79.1w
Normalized Unit
Mr/Ms
Coercivity (T)
Hcr/Hc
Temperature (°C)
LF-Ferro Susc
High Field Susc
LF-Ferro Susc Repeat
High Field Susc Repeat
Ms
Mr
Ms Repeat
Mr Repeat
Mr/Ms
Mr/Ms Repeat
Hc
Hcr
Hc Repeat
Hcr Repeat
Hcr/Hc
Hcr/Hc Repeat

Figure A1.5

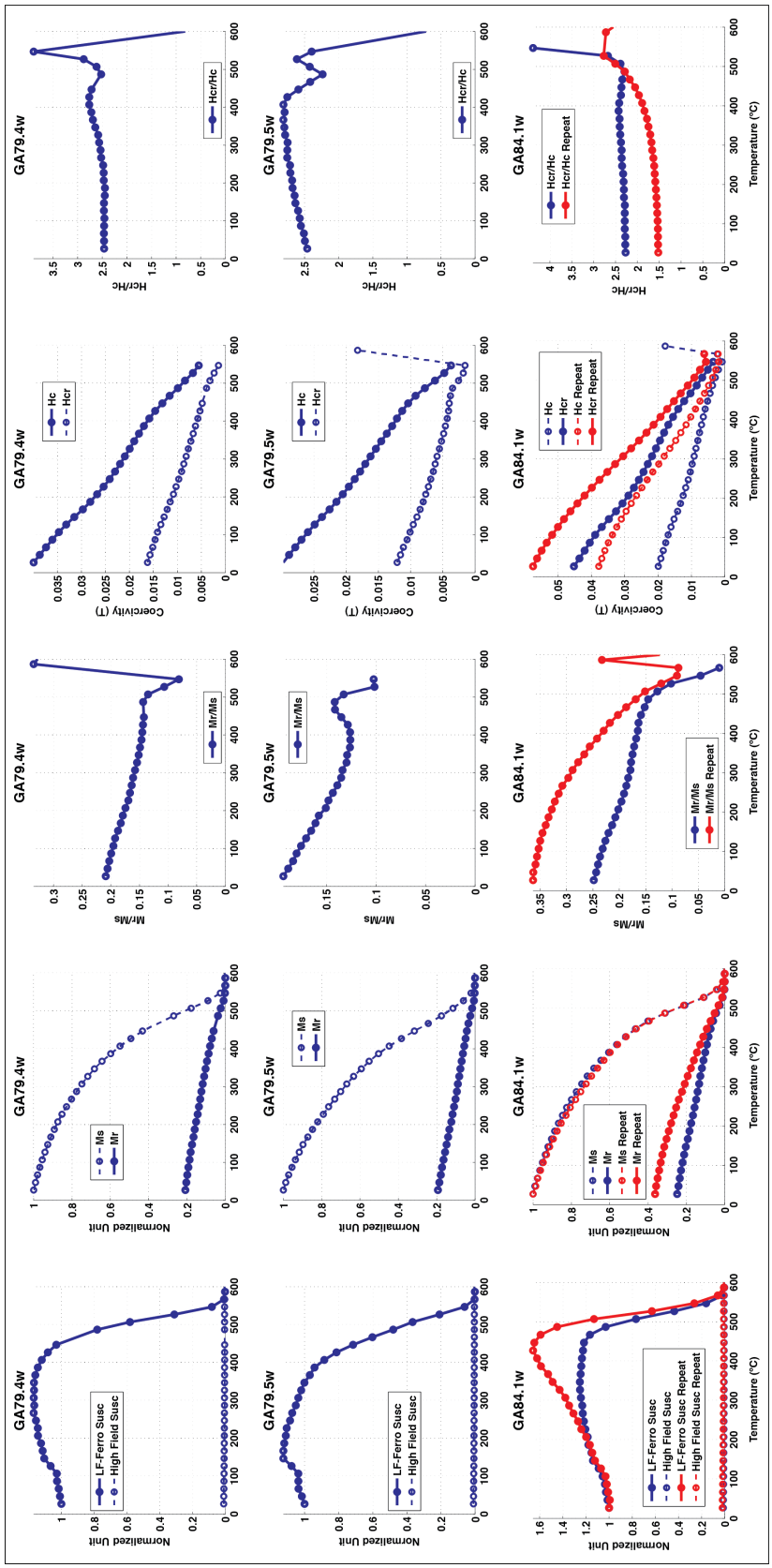
GA79.4w
GA79.5w
GA84.1w
Normalized Unit
Temperature (°C)
LF-Ferro Susc
High Field Susc
LF-Ferro Susc Repeat
High Field Susc Repeat
Ms
Mr
Ms Repeat
Mr Repeat
Mr/Ms
Mr/Ms Repeat
Hc
Hcr
Hc Repeat
Hcr Repeat
Coercivity (T)
Hcr/Hc
Hcr/Hc Repeat

Figure A1.6

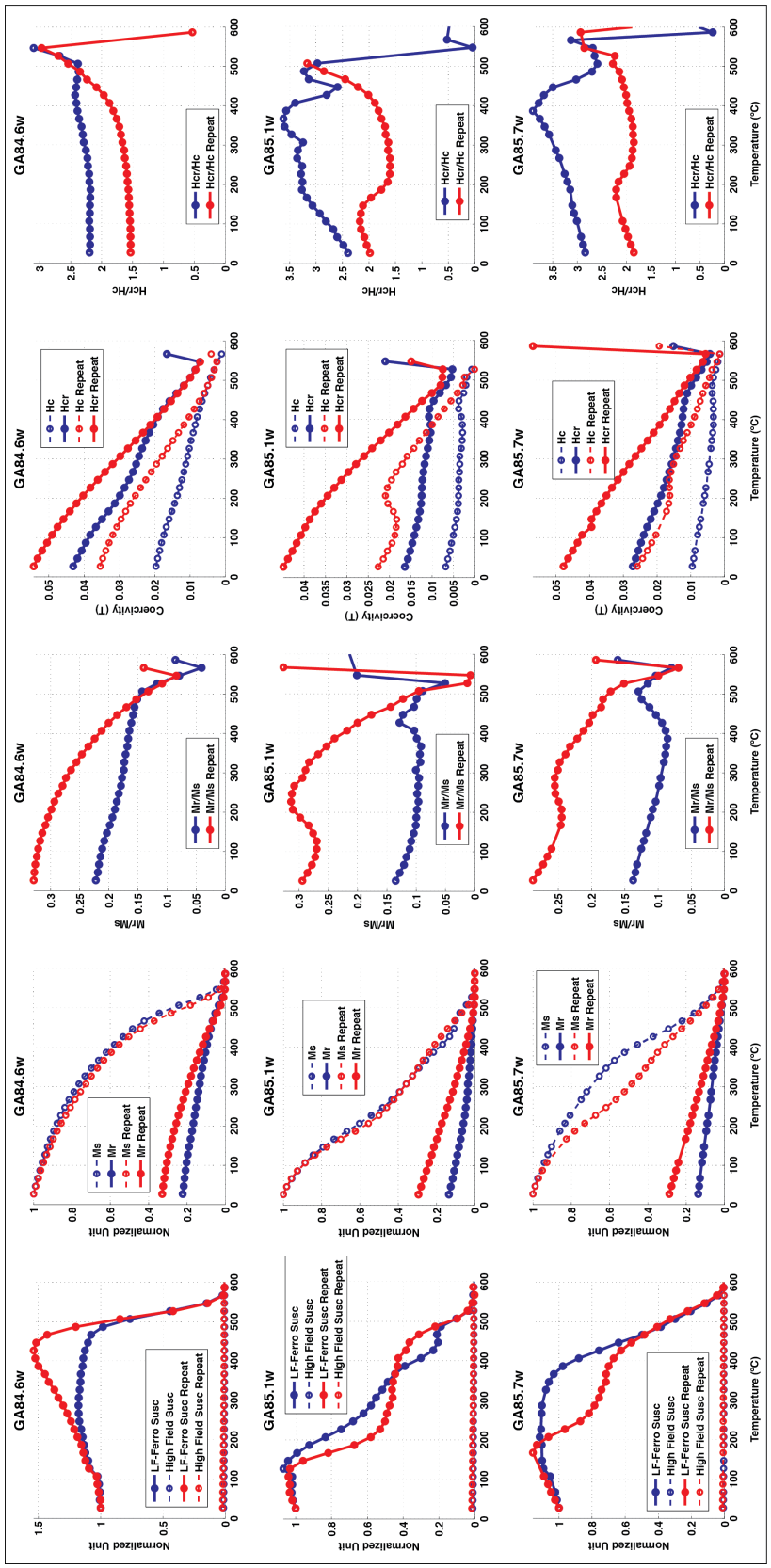
GA84.6w
GA84.6w
GA84.6w
GA84.6w
GA85.1w
GA85.1w
GA85.1w
GA85.1w
GA85.7w
GA85.7w
GA85.7w
GA85.7w
Normalized Unit
Mr/Ms
Coercivity (T)
Hcr/Hc
Temperature (°C)
LF-Ferro Susc
High Field Susc
LF-Ferro Susc Repeat
High Field Susc Repeat
Ms
Mr
Ms Repeat
Mr Repeat
Mr/Ms
Mr/Ms Repeat
Hc
Hcr
Hc Repeat
Hcr Repeat
Hcr/Hc
Hcr/Hc Repeat

Figure A1.7

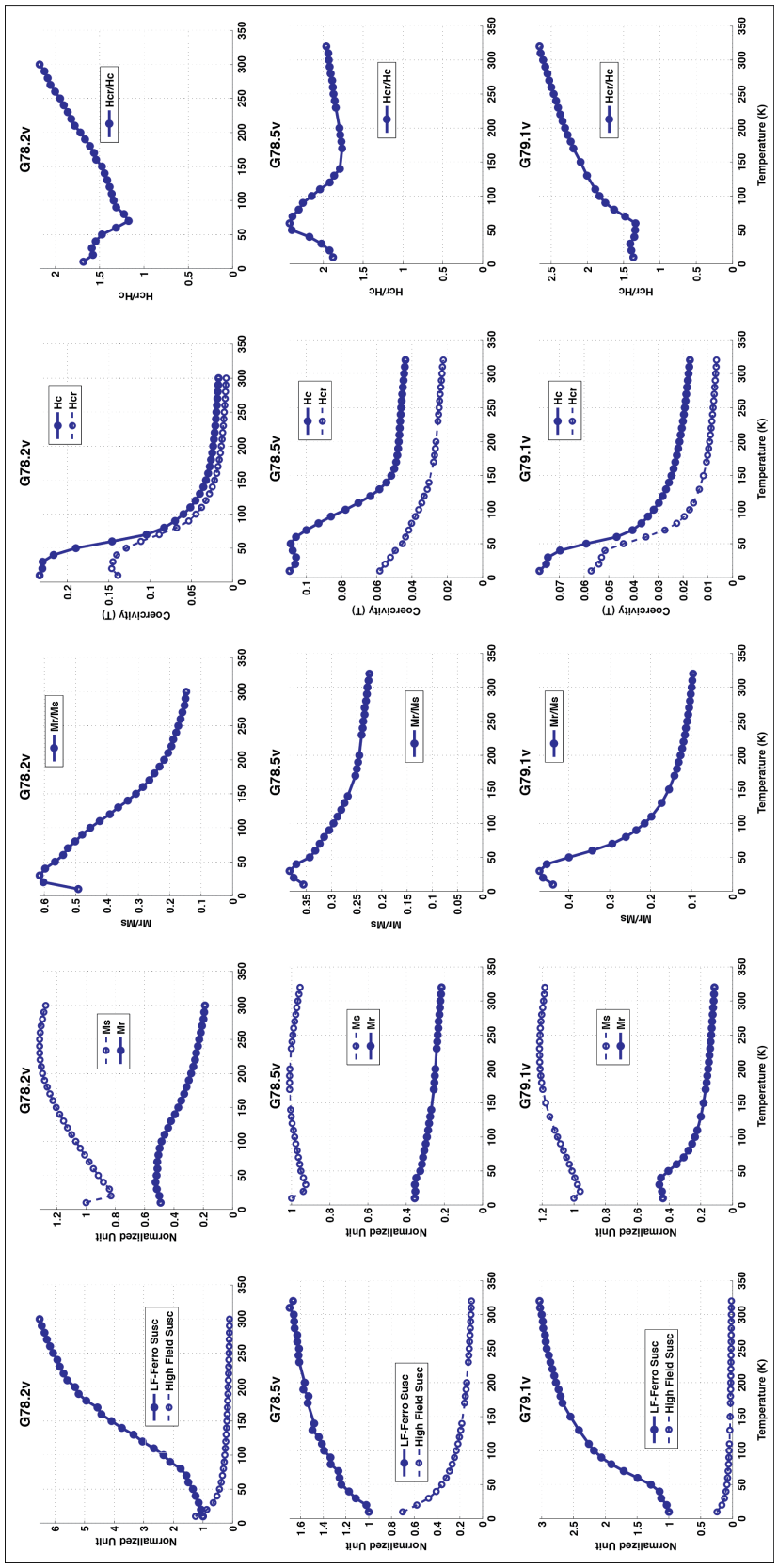
G78.2v
G78.5v
G79.1v
LF-Ferro Susc
High Field Susc
Normalized Unit
Ms
Mr
Mr/Ms
Hc
Hcr
Coercivity (T)
Hcr/Hc
Temperature (K)

Figure A1.8

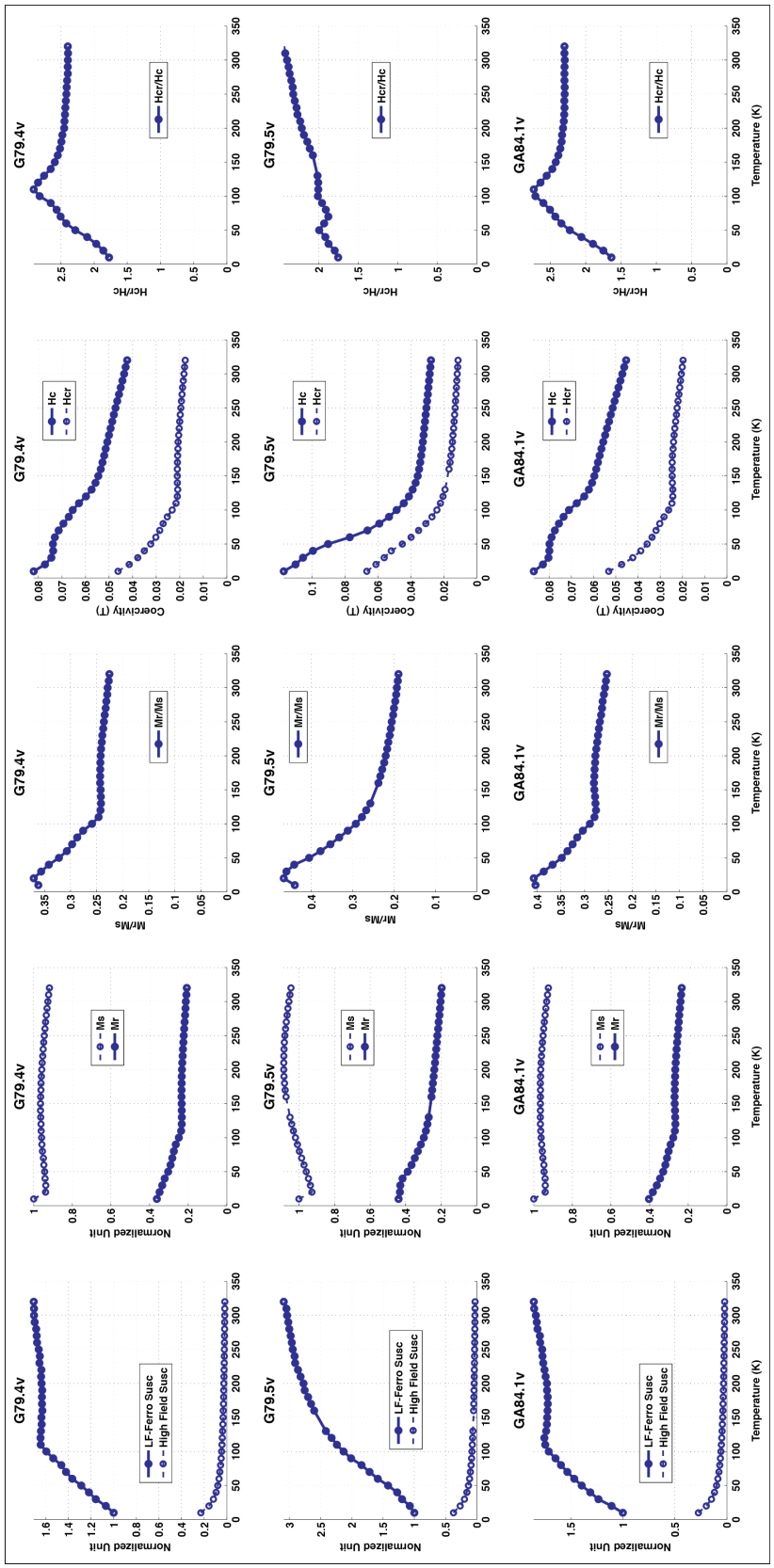
G79.4v
G79.5v
GA84.1v
Normalized Unit
Temperature (K)
LF-Ferro Susc
High Field Susc
Ms
Mr
Mr/Ms
Coercivity (T)
Hc
Hcr
Hcr/Hc

Figure A1.9

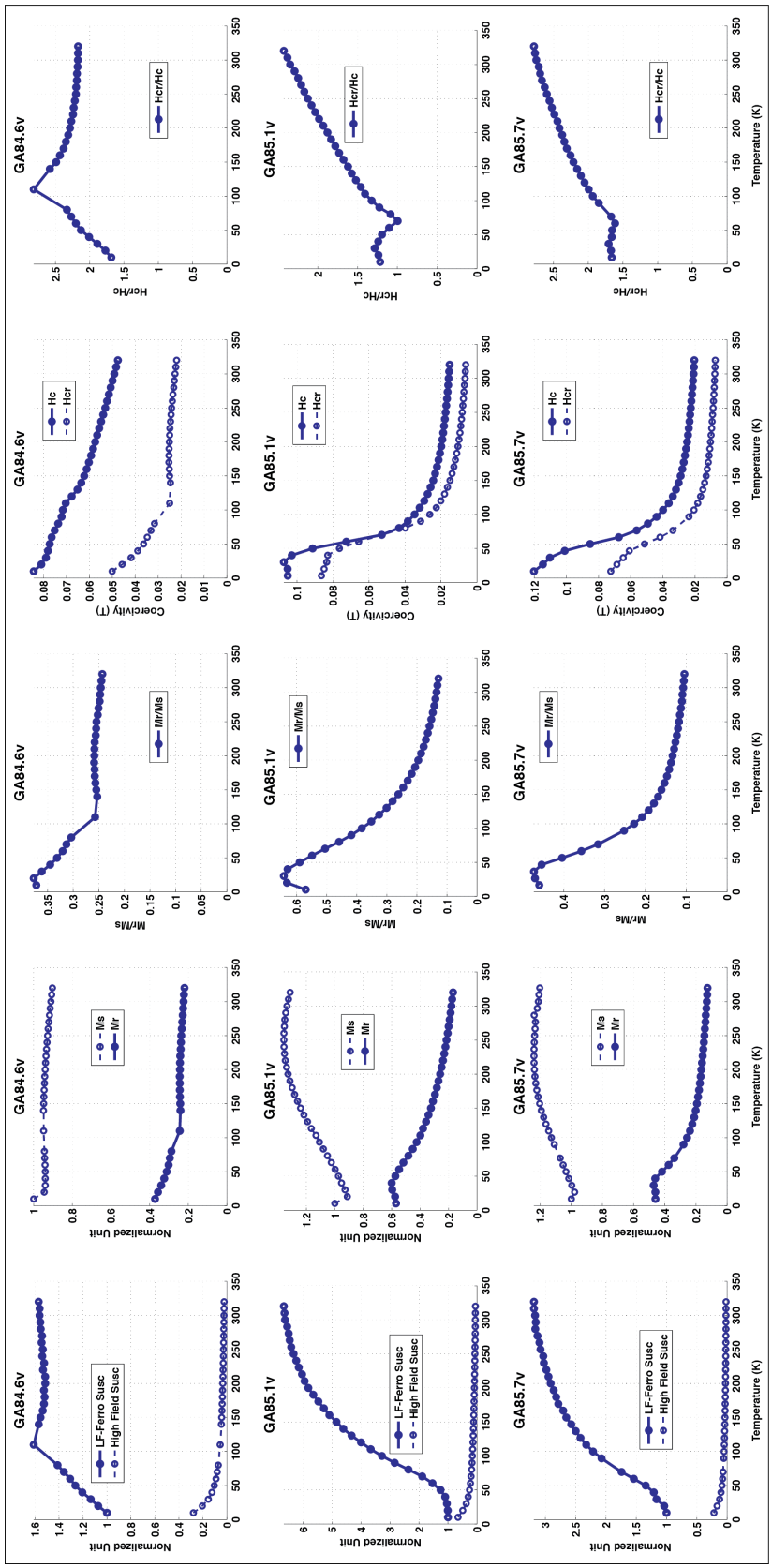
GA84.6v
GA84.6v
GA84.6v
GA84.6v
GA85.1v
GA85.1v
GA85.1v
GA85.1v
GA85.7v
GA85.7v
GA85.7v
GA85.7v
LF-Ferro Susc
High Field Susc
Ms
Mr
Mr/Ms
Hc
Hcr
Hcr/Hc
Normalized Unit
Coercivity (T)
Temperature (K)

Figure A1.10

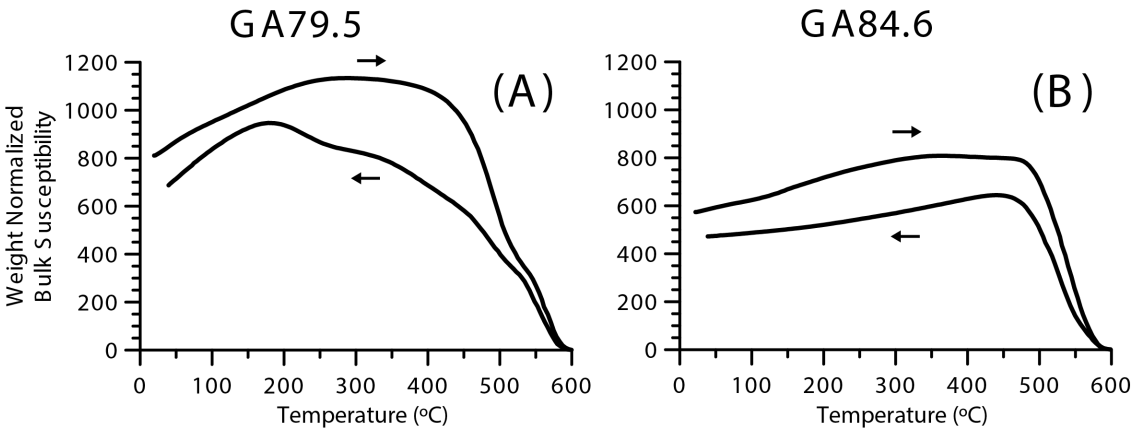
GA79.5
(A)
GA84.6
(B)
Weight Normalized
Bulk Susceptibility
1200
1000
800
600
400
200
0
0
100
200
300
400
500
600
Temperature (°C)

Figure A1.11

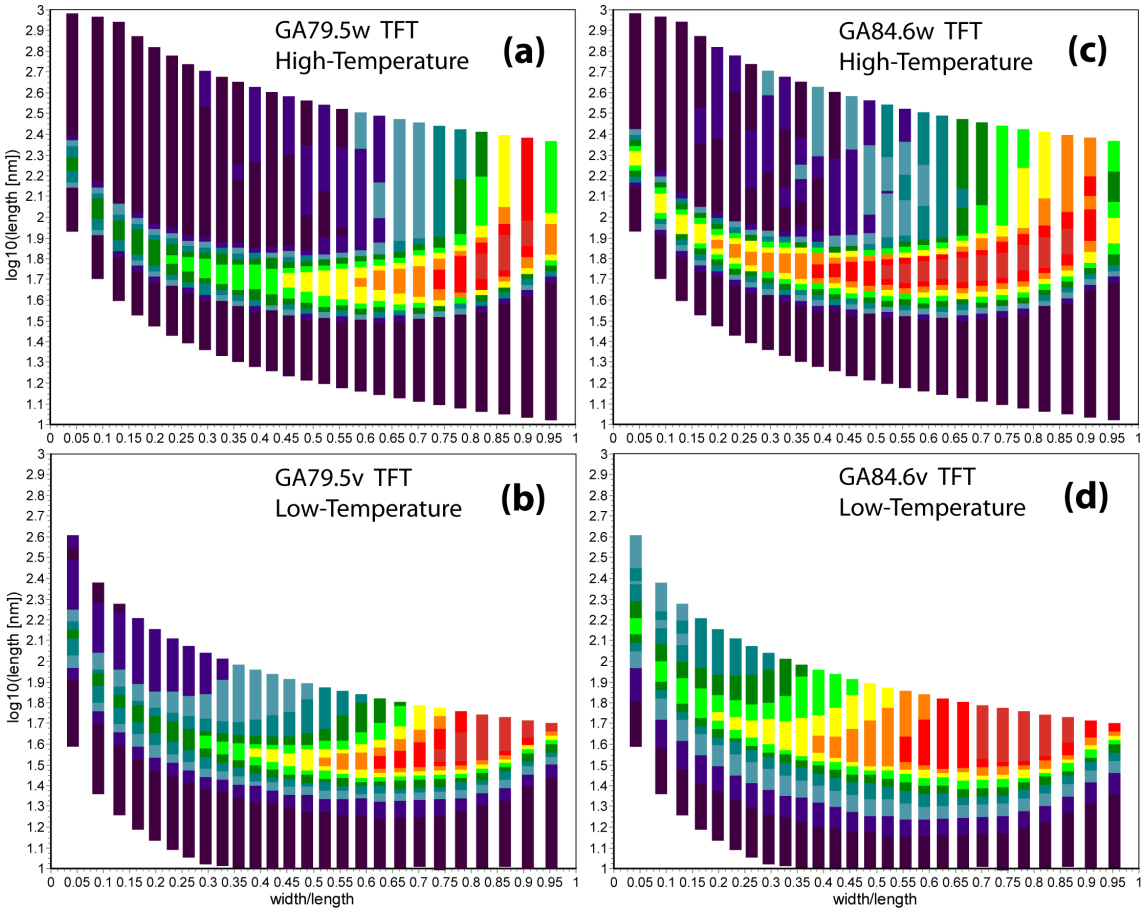
GA79.5w TFT
High-Temperature
(a)
GA84.6w TFT
High-Temperature
(c)
GA79.5v TFT
Low-Temperature
(b)
GA84.6v TFT
Low-Temperature
(d)
log10(length [nm])
width/length

Figure A1.12

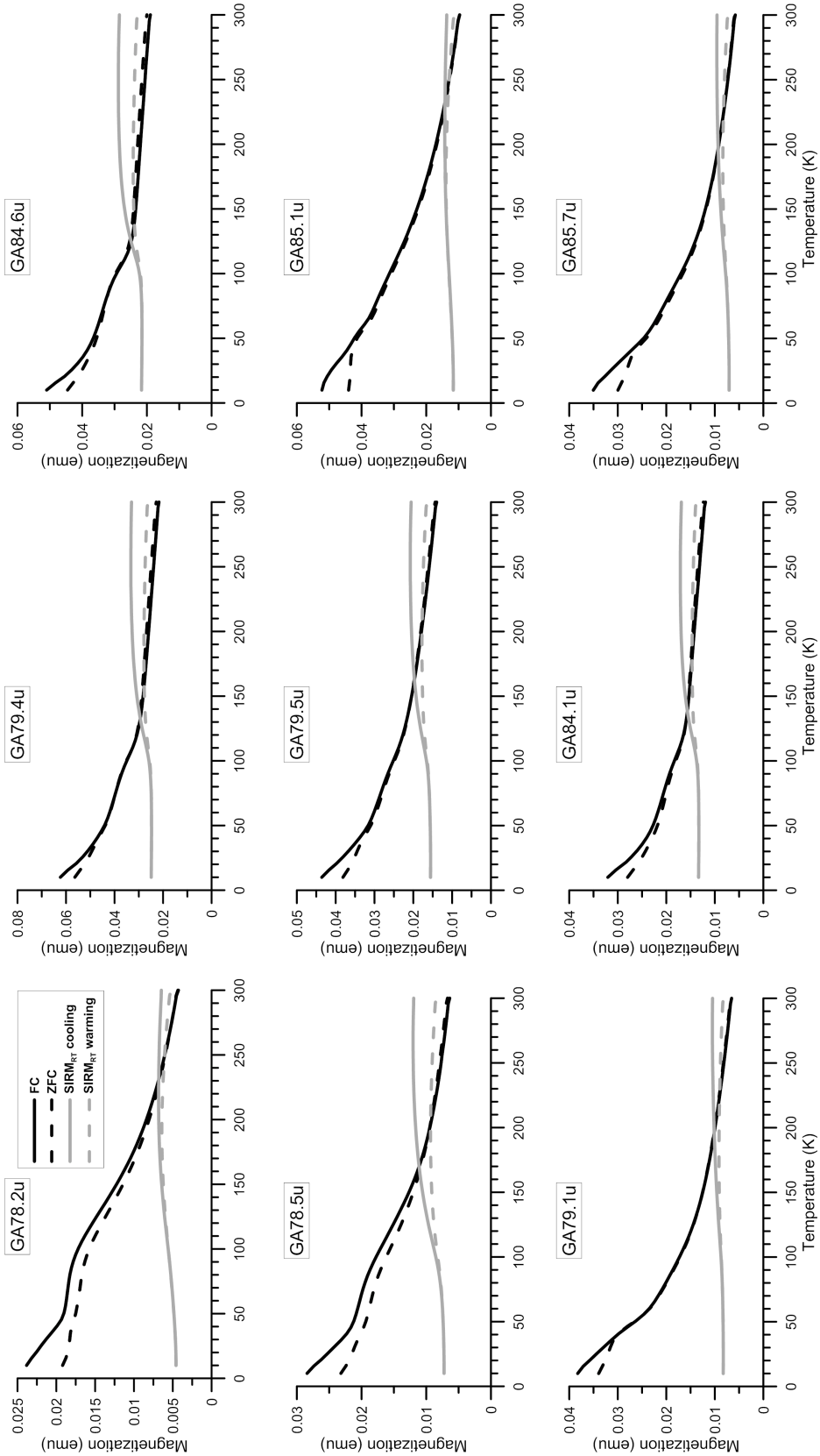
GA78.2u
GA79.4u
GA84.6u
GA78.5u
GA79.5u
GA85.1u
GA79.1u
GA84.1u
GA85.7u
FC
ZFC
SIRM$_{RT}$ cooling
SIRM$_{RT}$ warming
Magnetization (emu)
Temperature (K)

Figure A1.13

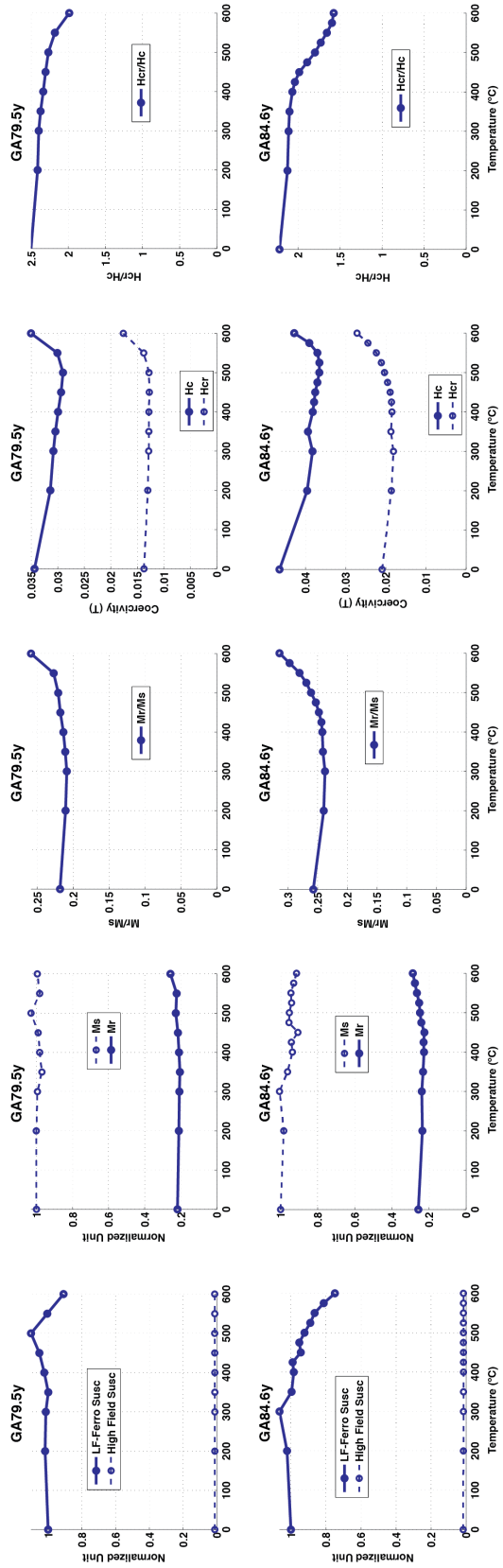
GA79.5y
GA84.6y
LF-Ferro Susc
High Field Susc
Normalized Unit
Ms
Mr
Mr/Ms
Coercivity (T)
Hc
Hcr
Hcr/Hc
Temperature (°C)

Figure A1.14

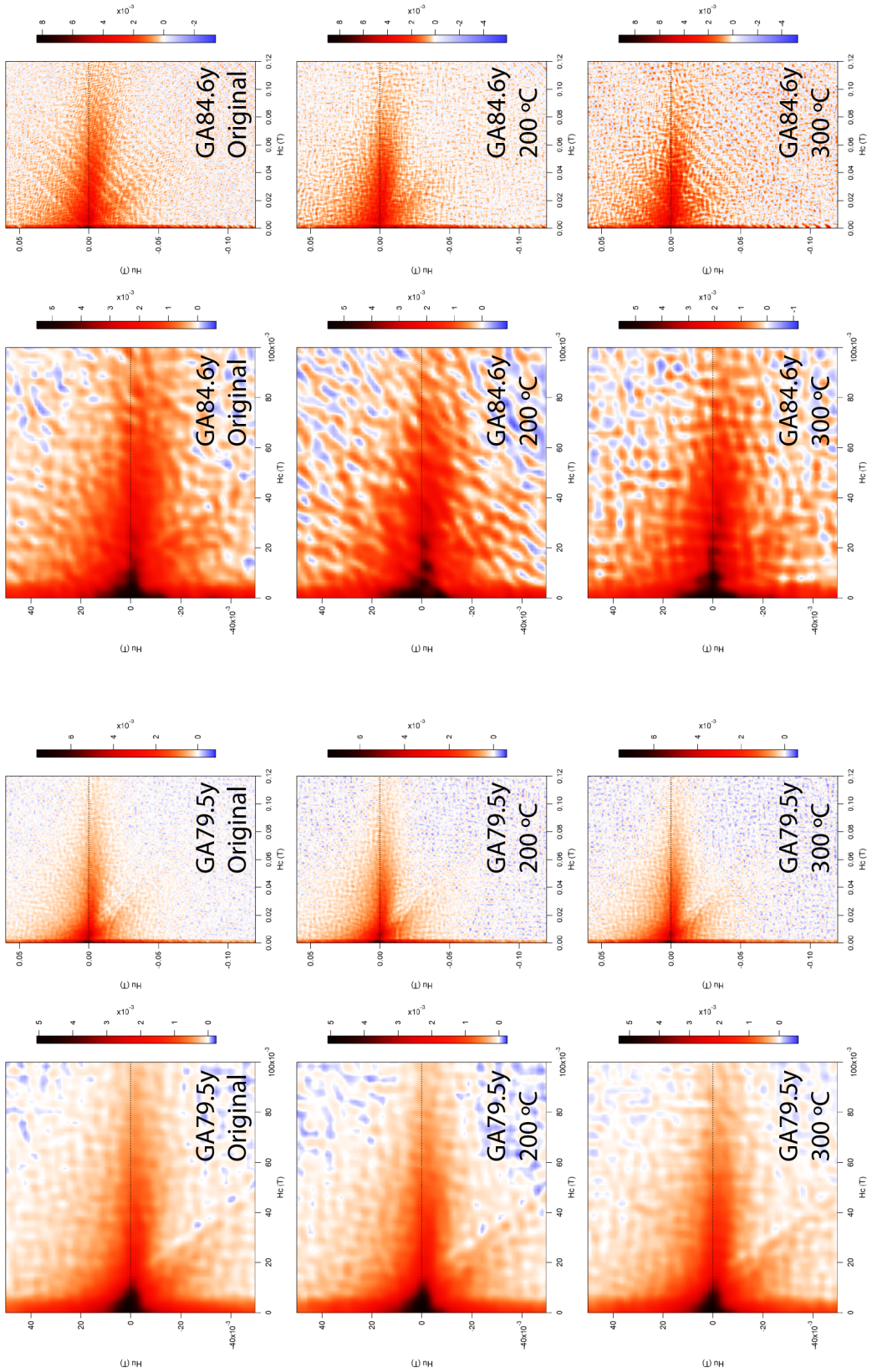
GA79.5y
Original
GA79.5y
200 °C
GA79.5y
300 °C
GA84.6y
Original
GA84.6y
200 °C
GA84.6y
300 °C
Hc (T)
Hu (T)

Figure A1.15

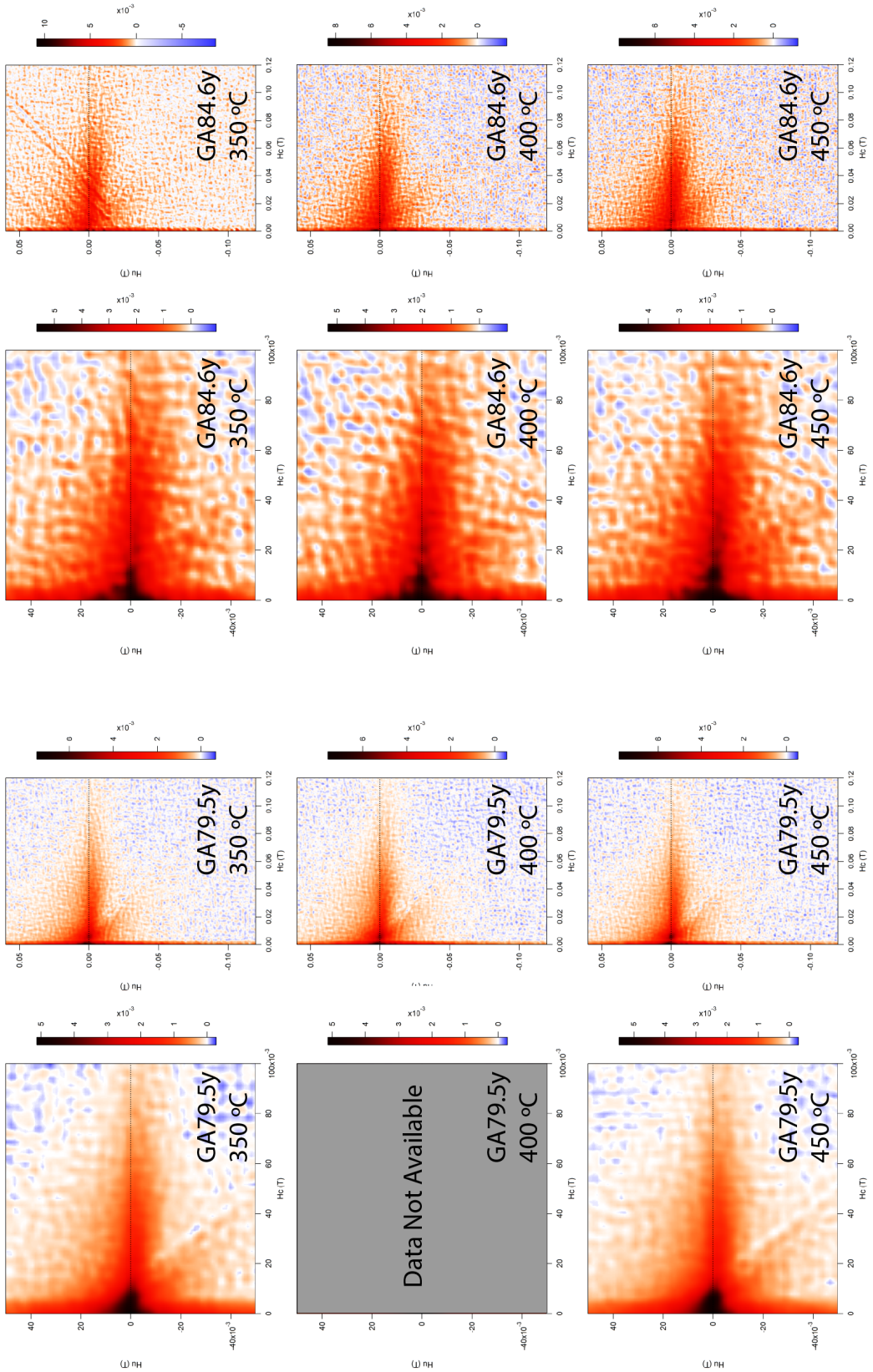
GA79.5y
350 oC
GA79.5y
400 oC
Data Not Available
GA79.5y
450 oC
GA84.6y
350 oC
GA84.6y
400 oC
GA84.6y
450 oC
Hc (T)
Hu (T)

Figure A1.16

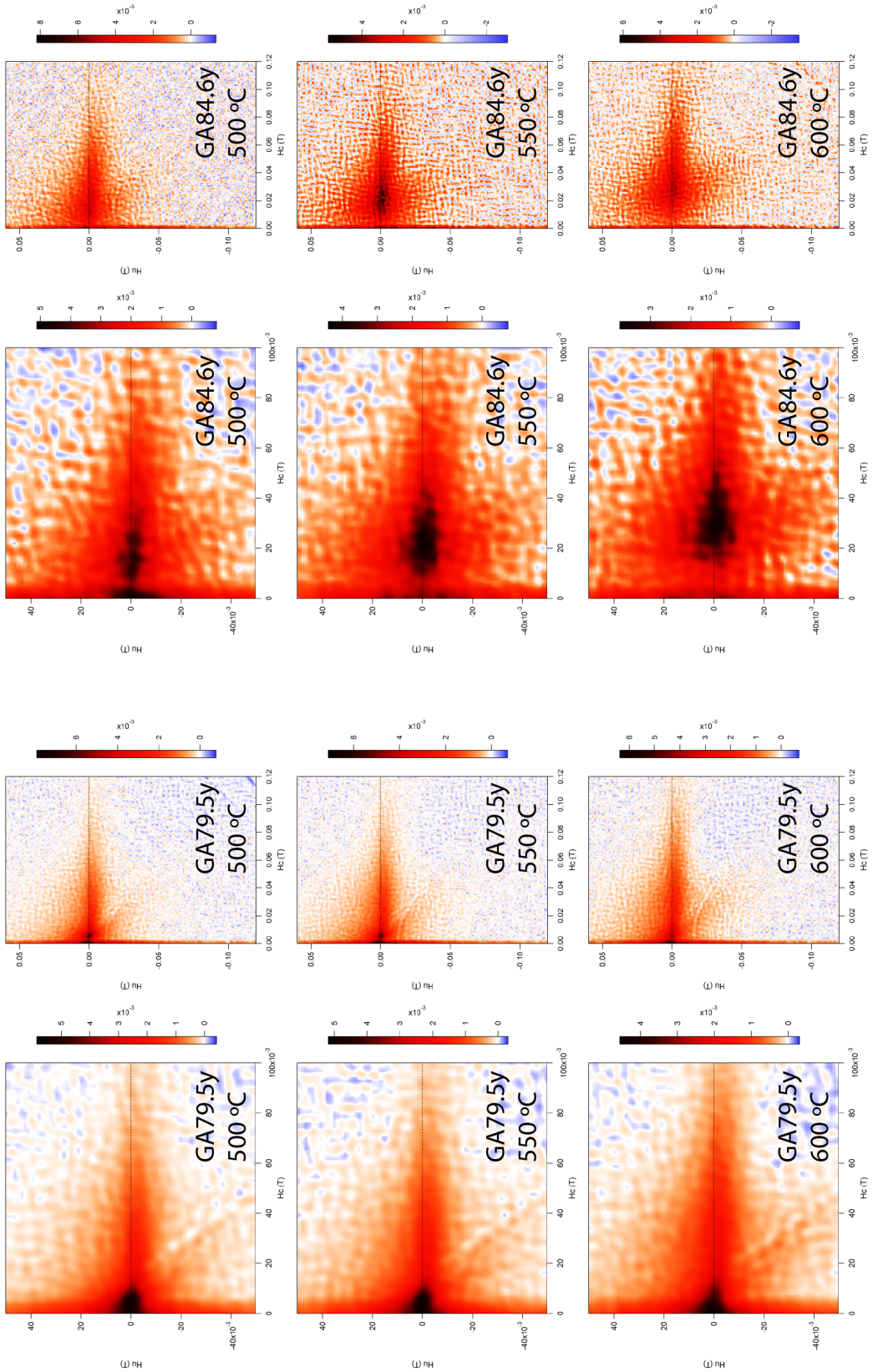
GA79.5y
500 ºC
GA79.5y
550 ºC
GA79.5y
600 ºC
GA84.6y
500 ºC
GA84.6y
550 ºC
GA84.6y
600 ºC
Hc (T)
Hu (T)

Appendix Chapter A2

Applications of thermal fluctuation tomography and high-resolution first-order reversal curves: Evidence for abundant isolated magnetic nanoparticles at the Paleocene–Eocene boundary

A2.1 Abstract

New rock magnetic results (thermal fluctuation tomography, high-resolution first-order reversal curves and low temperature measurements) for samples from the Paleocene–Eocene thermal maximum and carbon isotope excursion in cored sections at Ancora and Wilson Lake on the Atlantic Coastal Plain of New Jersey indicate the presence of predominantly isolated, near-equidimensional single-domain magnetic particles rather than the chain patterns observed in a cultured magnetotactic bacteria sample or magnetofossils in extracts. The various published results can be reconciled with the recognition that chain magnetosomes tend to be preferentially extracted in the magnetic separation process but, as we show, may represent only a small fraction of the overall magnetic assemblage that accounts for the greatly enhanced magnetization of the carbon isotope excursion sediment but whose origin is thus unclear.

A2.2 Introduction

The Paleocene–Eocene boundary (~55.8 Ma) is marked by an abrupt negative carbon isotope excursion (CIE) (1, 2) that coincides with an oxygen isotope decrease interpreted as the Paleocene–Eocene thermal maximum (PETM) (3). In a cored section at Ancora (AN) (Ocean Drilling Program Leg 174AX) on the Atlantic Coastal Plain of New Jersey (Fig. A2.1), a zone of anomalously high magnetic susceptibility was discovered coincident with the CIE at the base of the Manasquan Formation (now known as the Marlboro Clay) (4). Bulk sediment magnetic hysteresis measurements indicated that the high magnetization corresponds to an increased abundance of very fine-grained magnetite with single domain (SD)-like magnetic properties. A similar association of high concentration of SD magnetite in a kaolinite-rich interval with minimum carbon isotope values was subsequently found in two other drill cores (Clayton and Bass River), which with the Ancora site, formed a transect across the New Jersey Atlantic Coastal Plain (5). The average distance between the magnetic particles is estimated to be 20 times larger than their lengths, given a concentration of 100 parts per million (ppm) estimated from the bulk saturation magnetization. Attempts to image the magnetic grains by transmission electron microscopy (TEM) in a bulk sample from the CIE interval in the Clayton site resulted in finding only a handful of isolated grains, which nevertheless had the requisite nanoscale dimensions (~50–70 nm) expected from the bulk hysteresis properties (5). Iron-rich nanophase material had been previously detected (with Mössbauer techniques) at several Cretaceous–Paleogene boundary sites and was ascribed to condensates from an impact ejecta plume (6, 7). Accordingly, the nanoparticle-rich interval associated with the CIE on the New Jersey Atlantic Coastal Plain was suggested to have a similar origin,

providing circumstantial evidence for a major extraterrestrial (in this case cometary) impact at the onset of the CIE (5, 8).

Anomalously high concentrations of SD-like material have been confirmed by subsequent studies of the CIE from the Atlantic Coastal Plain, making these CIE sections perhaps the thickest dominated by SD magnetite recognized thus far in the stratigraphic record (9–13). In these studies, TEM observations on magnetic extracts were used to support the rock magnetic results and revealed the presence of chains of magnetic crystals that strongly resembled magnetofossils, with the implicit supposition that the separated fractions were representative of the entire magnetic assemblage. Unfortunately, most bulk magnetic properties such as hysteresis and first-order reversal curve (FORC) analyses are not able to establish if a SD-like grain assemblage is aligned in chains, the most distinctive crystallographic property for a biogenic origin (14). Some examples of naturally occurring SD-like assemblages in nature that are non-biogenic include some pyroclastic tuffs (15), submarine basaltic glass (16), meteoritic smoke in polar ice cores (17), and even the magnetite nanoparticles of enigmatic origin in Martian meteorite ALH84001 (ref. 14; but see ref. 18).

In this paper, we present rock magnetic results from a relatively new technique, thermal fluctuation tomography (TFT) (19), as well as low temperature magnetic properties and high-resolution (HiRes) FORCs (20), in an effort to distinguish between isolated particles and chain structures. We selected for study the well-characterized Ancora (AN) core, making a comparison between sample AN560.1 from the CIE clay

and sample AN567.7 from just before the CIE (Fig. A2.1); we also obtained supporting data from a CIE sediment sample from a shallower-water section cored at Wilson Lake (WL). Importantly, we compare magnetic results from a magnetic extract obtained from CIE bulk sample AN560.1 with those from a freeze-dried sample from an untreated culture of magnetotactic bacteria (MTB) MV-1 (21). These comparisons provide critical insights into the interpretation of the magnetic grain size and shape distribution in the CIE on which the origin of the magnetic particles is largely based and suggest a reevaluation of results from the more widely applied ferromagnetic resonance (FMR) technique (9, 12, 13).

A2.3 Results

The magnetic particle size and shape distribution from TFT for Ancora CIE bulk sample AN560.1 (Fig. A2.2A) has a mode at length (L) = 56 nm and width-to-length aspect ratio (W/L) = 0.84. These TFT size and shape values are consistent with isolated near-equidimensional SD grains and TEM results on a bulk sample from the CIE (5). The TFT calculations for a sample from an untreated culture of MTB MV-1 (21) (Fig. A2.2B) show that the distribution of effective ferromagnetic particle sizes and shapes has multiple peaks that we interpret as corresponding to magnetosome chains (40 nm < L < 50 nm, 0.35 < W/L < 0.55) and individual particles (mode at L = 57 nm, W/L = 0.67), with a slightly larger major peak. These values are consistent with TEM images (12, 23, 24) but very different from the TFT results from the CIE bulk sample shown in Fig.

A2.2A. This firstly reported TFT result for MV-1 shows the potential for detecting MTB magnetosome chains by the TFT technique.

The size and shape distribution for AN560.1 CIE magnetic extract residue (Fig. A2.2C) has a mode at L = 109 nm, W/L = 0.88, showing a much smaller tail toward the low W/L direction than the CIE bulk sample (Fig. A2.2A), indicating less elongated magnetic particles or fewer magnetosome chains. The TFT result for the AN560.1 CIE extract in its in situ state, derived by subtracting extract residue from bulk sediment data, shows two major peaks (Fig. A2.2D). One is around L = 100 nm, W/L = 0.9, very similar to the values for the extract residue (Fig. A2.2C); the other is around $40 < L < 50$, $0.6 < W/L < 0.7$, indicating more elongated particles or magnetosome chains.

The TFT size and shape distribution inferred for the CIE bulk sample more clearly impinges on the superparamagnetic (SP)–SD boundary than the MV-1 distribution, which is more tightly constrained within the SD field (Fig. A2.2 A and B). This might reflect a somewhat wider grain size distribution for the CIE clay than for the MV-1 magnetotactic bacteria sample, although the high Mr/Ms ratios preclude a large SP population in either case. The SP population can be imaged with low temperature TFT but requires cross-calibration to a different instrument than used for the high temperature TFT. A low temperature experiment was performed on a split of bulk sample AN560.1 but unfortunately the 300 K data in common did not match well (Fig. A2.3 A and B), indicating specimen differences or instrument offsets. However, 300 K data in common

matched well (Fig. A2.3 C and D) for paired specimens of a bulk sample (WLb357.3) from an expanded section of the CIE from the B core at Wilson Lake, essentially the same as the cored section investigated by others (9, 11, 25). The high temperature TFT results for WLb357.3 (Fig. A2.4A) are virtually identical to those of AN560.1 (Fig. A2.2A) with the TFT size and shape distribution patterns for CIE bulk sample WLb357.3 mainly showing a small shift in the SP direction along the trend of the SP–SD boundary line between the 300 K to 640 K range (mode at L = 65 nm, W/L = 0.84) and the 120 K to 640 K range (mode at L = 45 nm, W/L = 0.74) (Fig. A2.4 A and B).

Based on the field cooled and zero-field cooled (FC–ZFC) remanence warming curves (26) as well as low temperature demagnetization (LTD) cooling and warming curves of room temperature saturation isothermal remanence (SIRMRT) from 5 K to 300 K), Verwey transitions (27) are observed at about 100–110 K for the CIE extract and at about 90–100 K for MV-1, with FC yielding higher remanence than ZFC, a typical signature for biogenic magnetosomes of SD magnetite (26) (Fig. A2.5 A and B). Although magnetic interactions may change the shape of FC– ZFC curves (28), a Verwey transition signal should still be present (29). The Verwey temperatures indicate that the magnetite particles in the CIE extract as well as the magnetosomes in the MV-1 culture are only partially oxidized. In contrast, the Verwey transition is not apparent for the CIE bulk samples (Fig. A2.5 C and D) and CIE magnetic extract residue (Fig. A2.5E), which we attribute to the dominant ferromagnetic mineral being SD maghemite (30) that formed either by crystallization in an oxidizing environment or by later oxidization of magnetite (31, 32). The presence of biogenic SD magnetite in the CIE extracts based on TEM

observations (9–11) and our Verwey transition data for the CIE magnetic extract (Fig. A2.5A) suggest that the coexisting dominant SD maghemite particles and subordinate SD magnetite particles could be original independent components of the CIE sediments. A weak Verwey transition signal previously reported from a sample at the onset of the CIE from Wilson Lake (109.118 m depth) (11) may indicate a slightly higher biogenic SD magnetite portion. For the Ancora CIE bulk sample (Fig. A2.5 C and D), we also observe an inflection at around 37 K, which corresponds to the Neel temperature of siderite (33, 34). We estimate the mass concentration of siderite of about 1–2‰. In contrast, no clear trace of Verwey transition or siderite signal can be identified for the late Paleocene sample (AN567.7) just before the CIE (Fig. A2.5F).

A FORC diagram of AN560.1 CIE bulk (Fig. A2.6A) shows a narrow central ridge and faint reversible contributions appearing as a 45° asymmetric ridge, typical signatures for an assemblage of SD magnetic particles (20, 35). HiResFORC diagrams bring some characteristics into sharper focus and enable us to differentiate between the CIE bulk (Fig. A2.6B), CIE extract residue (Fig. A2.6C), CIE extract (Fig. A2.6D), and the extract in its in situ state derived by subtraction (Fig. A2.6E). From their coercivity profiles, it appears that there is a greater abundance of higher coercivity particles in the extract in its in situ state (Hc peaking at around 30–40 mT) than in the residue (Hc peaking at around 20–30 mT), indicating higher coercivity magnetosome chains are preferably extracted. A direct HiResFORC experiment on the AN560.1 CIE extract (Fig. A2.6D) shows a larger magnetic interaction signal, indicating that the extracted magnetic particles were probably crowded together around the magnet finger during extraction. A

HiResFORC diagram for MTB MV-1 (Fig. A2.6F) also shows a narrow central ridge and clear reversible contribution. However, its coercivity profile is much more concentrated around 40 mT compared with the much broader coercivity profiles for the CIE bulk sample (Fig. A2.6B).

In light of the TFT data, we reanalyzed the reported FMR results for the laboratory cultured MTBs (12) and the CIE bulk samples (9) in a ΔB_{FWHM}-A plot (13) (Fig. A2.7). We find that the CIE bulk samples plot very close to sodium dodecyl sulfate (SDS)-treated and ultrasonicated Magnetospirillum magneticum strain AMB-1 mutant mnm18, which contains freed isolated approximately equidimensional magnetosome crystals. The reported FMR results of the CIE data compared with untreated and treated MTB data suggest a redefinition of the zones for lithogenic large grains, independent SD grains, and biogenic magnetosome chains in ΔB_{FWHM}-A parameter space (shaded ellipses in Fig. A2.7). In this perspective, the FMR data cannot exclude the interpretation that the ferromagnetic particles in the CIE clay are predominantly isolated near-equidimensional SD grains.

A2.4 Discussion

We find that a broad array of rock magnetic results (TFT, FC–ZFC, LTD SIRMRT, HiResFORC, and FMR) for CIE bulk samples from Ancora (and Wilson Lake) is consistent with the predominant presence of near-equidimensional non-interacting SD

particles. These results allow alternative possibilities for the nature and origin of the dominantly SD magnetic particles that occur in greatly increased abundance in the CIE sediments. Populations of many different species of MTB, with differing magnetosome/chain geometries and admixed in suitable proportions, might conceivably produce similar TFT and FORC distributions. Such a hypothetical assemblage would indeed provide a natural explanation for the sharp confinement of the size/shape distribution to the stable SD field, and for the relatively pure magnetite/maghemite composition, both resulting from biological control of magnetic particle formation. In contrast, the particle size distribution and mineralogical composition of impact plume condensates depend on many factors, and model calculations (36, 37) generally predict neither a narrow particle size distribution nor a preponderance of submicron sizes nor end member iron spinel compositions, and so these characteristics of the CIE sediments are rather fortuitous under the impact-plume scenario.

However, the TFT results show little indication of alignment in chains, a key signature of biogenic origin that also produces a distinct size and shape distribution in TFT results from cultured magnetotactic bacteria sample MV-1. The apparent discrepancy can be reconciled with the recognition that chain magnetosomes are preferentially extracted in the magnetic separation process (and subsequently imaged in TEM studies) but may be an unrepresentative small fraction of the overall magnetic assemblage in the CIE sediment. Fossil magnetosomes may very well become more prevalent during the CIE but the evidence is unclear whether they are solely or even mainly responsible for the greatly enhanced and geographically widespread SD-like

magnetic properties of CIE bulk sediments. We would also point to the close resemblance of FMR parameters (Fig. A2.7) of CIE sediment and those reported for magnetic nanoparticles in Martian meteorite ALH84001, where it was concluded that no more than 10% of the magnetic particles were likely to be arranged in chains and thus difficult to prove to be of magnetosome origin (14). We believe our results are starting to build a similar case for the unusual SD-like characteristics of CIE sediment on the Atlantic Coastal Plain.

A2.5 Materials and Methods

We performed a magnetic finger extraction procedure (9, 38) with a peristaltic pump circulation system at the Institute for Rock Magnetism (IRM) on CIE bulk sample AN560.1. The procedure was done using a very slow flow rate for over 24 h. Despite the deliberate care, we were able to extract only a small fraction of the total ferromagnetic particles as estimated by saturation remanent magnetization determined from hysteresis loops on the extract (5% of initial bulk value) and on the residue (94% of initial value), together indicating minimal (~1%) overall loss of the ferromagnetic minerals during the extraction procedure. TEM images on magnetic separates from Ancora CIE sediment reveal features like chain alignments that resemble bacterial magnetite (9), but at issue is how representative these observations are of the bulk of the CIE magnetic assemblage, which could just as well be largely composed of isolated equidimensional grains (5).

We conducted high temperature TFT (19) using a Princeton Measurements Corporation (PMC) vibrating sample magnetometer (VSM) equipped with a high temperature furnace (HT-VSM) at the IRM at the University of Minnesota on bulk samples from the CIE in the Ancora core to characterize the dominant W/L aspect ratio of the SD magnetic grains, which should approach 1 for isolated equidimensional grains and be much less than 1, depending on the effective elongations, for particles in chains. For bulk sample AN560.1 (170.72 m in the Ancora core, within the CIE; Fig. A2.1) and its magnetic extract residue, we measured back-field demagnetization (BFD) curves at logarithmic increments from 2 mT to 450 mT for 39 points from 300 K to 640 K (before any trace of severe chemical alteration sets in) at 10-K intervals. To avoid the undesirable effects of magnetostatic interactions introduced by the extraction process, we derived an unbiased estimate of the in situ BFD for the AN560.1 magnetic extract by subtracting each of the BFD curves of the extract residue from the BFD curves of the bulk sediment. We also conducted a TFT experiment on a sample from an untreated culture of MTB MV-1 (21), which was freeze dried and kept frozen for over 10 y (and thus likely to be partially oxidized), using back-field demagnetization curves from 300 K to 470 K at every 10 K for comparison (Fig. A2.2B).

We also conducted low temperature TFT (19) using another PMC VSM equipped with a low temperature cryostat (LT-VSM) at the IRM. We measured BFD curves at logarithmic increments from 2 mT to 1,500 mT for 45 points from 120 K (above the Verwey transition temperature) to 300 K at 10-K intervals. The BFD curves at 300 K on both instruments were almost identical after linear normalization for the specimens from

the CIE bulk sample from Wilson Lake (WLb357.3; Fig. A2.3 C and D), allowing us to calculate the size–shape distribution using only high temperature data (Fig. A2.4A) and as well as by combining the high and low temperature data (Fig. A2.4B). Unfortunately, the 300-K BFD curves did not match the specimens from the CIE bulk sample from Ancora (AN560.1; Fig. A2.3 A and B), indicating specimen differences or instrumental offsets.

In the TFT calculations these temperature-dependent switching-field distributions are inverted to obtain the distribution of particle volumes and microcoercivities, f(V, Hk). For strongly magnetic cubic minerals such as magnetite and maghemite (we used Ms = 480 kA/m, which is appropriate for magnetite although a somewhat lower value may apply for maghemite depending on exact composition), shape anisotropy dominates the magnetic behavior, and Hk is directly related to aspect ratio (22). The cells of the original rectangular (V, Hk) grid can thus be mapped into corresponding points in the (L, W/L) parameter space to represent the distribution of ferromagnetic particle lengths and aspect ratios, f(L, W/L) (Fig. A2.2A). The TFT inversion assumes that particles are non-interacting and that their moments reverse by coherent rotation. In intact chains of magnetosomes these assumptions are not satisfied, but we can anticipate the effects of this on the results. The critical field for incoherent reversal of magnetic moments in a chain of particles is somewhat larger than that for individual magnetosomes because inter-particle interactions add to the anisotropy energy due to particle shape. Similarly the effective thermally activated volume is slightly larger than that of an individual magnetosome, due to the stabilizing effect of interactions along the chain. Thus, the

expected behavior of intact chains in the TFT experiment is effectively that of isolated particles that are more elongate and slightly larger than individual magnetosomes, but much less elongate and smaller than the complete chains.

Low temperature magnetic properties were measured every 5 K for the CIE bulk samples (AN560.1 andWLb357.3), a late Paleocene (pre-CIE) bulk sample (AN567.7, 173.03 m in the Ancora core, Fig. A2.1), the CIE magnetic extract (AN560.1), the CIE extract residue, and the MV-1 culture, using the Quantum Designs magnetic properties measuring system (MPMS) at IRM (Fig. A2.5).

We performed regular FORC [field increment (δH) = 2 mT, smoothing factor (SF) = 3] and HiResFORC (δH = 0.6 mT, SF = 6) measurements (20) on the CIE bulk sample (AN560.1), the CIE extract, the CIE extraction residue, and MV-1, using a PMC alternating gradient force magnetometer (AGFM) at Rutgers University and analyzed the FORC data using FORCinel (39). For the CIE bulk sample and CIE extraction residue, we stacked nine HiResFORC measurements each by normalizing and averaging individual FORC measurements to improve the signal-to-noise ratio. We also performed subtraction of FORC results from CIE bulk and extraction residue to derive an unbiased FORC representation of the CIE extract in its in situ state.

A2.6 Acknowledgments

We thank Morgan F. Schaller and James D. Wright (Rutgers University) for discussions on the PETM/CIE that inspired this study, Bruce M. Moskowitz (Institute for Rock Magnetism, IRM) for the MV-1 sample, Robert E. Kopp (Rutgers University) for discussions on ferromagnetic resonance and magnetotactic bacteria, and two anonymous reviewers for constructive comments and suggestions. H.W. is grateful to the IRM for support of a Rock Magnetism Summer School and two Student Visiting Fellowships that allowed many of these measurements to be made and for support from a Schlanger Fellowship awarded by the National Science Foundation-sponsored US Science Support Program for the Integrated Ocean Drilling Program, which is administered by the Consortium for Ocean Leadership. This is contribution 7639 of Lamont-Doherty Earth Observatory.

Reference

1. Kennett JP, Stott LD (1991) Abrupt deep-sea warming, palaeoceanographic changes and benthic extinctions at the end of the Palaeocene. Nature 353:225–229.

2. Koch PL, Zachos JC, Gingerich PD (1992) Correlation between isotope records in marine and continental carbon reservoirs near the Paleocene Eocene boundary. Nature 358:319–322.

3. Zachos JC, Lohmann KC, Walker JCG, Wise SW (1993) Abrupt climate change and transient climates during the Paleogene: A marine perspective. J Geol 101:191–213.

4. Lanci L, Kent DV, Miller KG (2002) Detection of Late Cretaceous and Cenozoic sequence boundaries on the Atlantic coastal plain using core log integration of magnetic susceptibility and natural gamma ray measurements at Ancora, New Jersey. J Geophys Res 107:2216, 10.1029/2000JB000026.

5. Kent DV, et al. (2003) A case for a comet impact trigger for the Paleocene/Eocene thermal maximum and carbon isotope excursion. Earth Planet Sci Lett 211:13–26.

6. Verma HC, et al. (2001) Nano-sized iron phases at the K/T and P/T boundaries revealed by Mössbauer spectroscopy. Lunar and Planetary Science XXXII 1:1270.

7. Wdowiak TJ, et al. (2001) Presence of an iron-rich nanophase material in the upper layer of the Cretaceous-Tertiary boundary clay. Meteorit Planet Sci 36:123–133.

8. Cramer BS, Kent DV (2005) Bolide summer: The Paleocene/Eocene thermal maximum as a response to an extraterrestrial trigger. Palaeogeogr Palaeoclimatol Palaeoecol 224:144–166.

9. Kopp RE, et al. (2007) Magnetofossil spike during the Paleocene-Eocene thermal maximum: Ferromagnetic resonance, rock magnetic, and electron microscopy evidence from Ancora, New Jersey, United States. Paleoceanography 22:PA4103, 10.1029/2007PA001473.

10. Kopp RE, et al. (2009) An Appalachian Amazon? Magnetofossil evidence for the development of a tropical river-like system in the mid-Atlantic United States during the Paleocene-Eocene thermal maximum. Paleoceanography 24:PA4211, 10.1029/ 2009PA001783.

11. Lippert PC, Zachos JC (2007) A biogenic origin for anomalous fine-grained magnetic material at the Paleocene-Eocene boundary at Wilson Lake, New Jersey. Paleoceanography 22:PA4104, 10.1029/2007PA001471.

12. Kopp RE, et al. (2006) Ferromagnetic resonance spectroscopy for assessment of

magnetic anisotropy and magnetostatic interactions: A case study of mutant magnetotactic bacteria. J Geophys Res 111:B12S25, 10.1029/2006JB004529.

13. Kopp RE, et al. (2006) Chains, clumps, and strings: Magnetofossil taphonomy with ferromagnetic resonance spectroscopy. Earth Planet Sci Lett 247:10–25.

14. Weiss BP, et al. (2004) Magnetic tests for magnetosome chains in Martian meteorite ALH84001. Proc Natl Acad Sci USA 101:8281–8284.

15. Schlinger CM, Veblen DR, Rosenbaum JG (1991) Magnetism and magnetic mineralogy of ash flow tuffs from Yucca Mountain, Nevada. J Geophys Res 96:6035–6052.

16. Pick T, Tauxe L (1993) Holocene paleointensities: Thellier experiments on submarine basaltic glass from the East Pacific Rise. J Geophys Res 98:17,949–17,964.

17. Lanci L, et al. (2012) Magnetization of polar ice: A measurement of terrestrial dust and extraterrestrial fallout. Quat Sci Rev 33:20–31.

18. Thomas-Keprta KL, Clemett SJ, Mckay DS, Gibson EK, Wentworth SJ (2009) Origins of magnetite nanocrystals in Martian meteorite ALH84001. Geochim Cosmochim Acta 73:6631–6677.

19. Jackson M, Carter-Stiglitz B, Egli R, Solheid P (2006) Characterizing the superparamagnetic grain distribution f(vi, H-k) by thermal fluctuation tomography. J Geophys Res 111:B12S07, 10.1029/2006JB004514.

20. Egli R, Chen AP, Winklhofer M, Kodama KP, Horng C-S (2010) Detection of noninteracting single domain particles using first-order reversal curve diagrams. Geochem Geophys Geosyst 11:Q01Z11, 10.1029/2009GC002916.

21. Dean AJ, Bazylinski DA (1999) Genome analysis of several marine, magnetotactic bacterial strains by pulsed-field gel electrophoresis. Curr Microbiol 39:219–225.

22. Butler RF, Banerjee SK (1975) Theoretical single-domain grain size range in magnetite and titanomagnetite. J Geophys Res 80:4049–4058.

23. Devouard B, et al. (1998) Magnetite from magnetotactic bacteria: Size distributions and twinning. Am Mineral 83:1387–1398.

24. Dunin-Borkowski RE, et al. (2001) Off-axis electron holography of magnetotactic bacteria: Magnetic microstructure of strains MV-1 and MS-1. Eur J Mineral 13: 671–684.

25. Zachos JC, et al. (2006) Extreme warming of mid-latitude coastal ocean during the Paleocene-Eocene Thermal Maximum: Inferences from TEX86 and isotope data. Geology 34:737–740.

26. Moskowitz BM, Frankel RB, Bazylinski DA (1993) Rock magnetic criteria for the detection of biogenic magnetite. Earth Planet Sci Lett 120:283–300.

27. Stacey FD, Banerjee SK (1974) The Physical Principles of Rock Magnetism (Elsevier, Amsterdam), 195 pp.

28. Carter-Stiglitz B, Jackson M, Moskowitz B (2002) Low-temperature remanence in stable single domain magnetite. Geophys Res Lett 29, 10.1029/2001gl014197.

29. Carter-Stiglitz B, Jackson M, Moskowitz B (2003) Correction to "low-temperature remanence in stable single domain magnetite" Geophys Res Lett 30, 10.1029/ 2003GL018727.

30. Ozdemir O, Dunlop DJ, Moskowitz BM (1993) The effect of oxidation on the Verwey transition in magnetite. Geophys Res Lett 20:1671–1674.

31. Colombo U, Fagherazzi G, Gazzarrini F, Lanzavecchia G, Sironi G (1968) Mechanism of low temperature oxidation of magnetites. Nature 219:1036–1037.

32. Gallagher KJ, Feitknecht W, Mannweiler U (1968) Mechanism of oxidation of magnetite to gamma-Fe2O3. Nature 217:1118–1121.

33. Frederichs T, von Dobeneck T, Bleil U, DekkersMJ (2003) Towards the identification of siderite, rhodochrosite, and vivianite in sediments by their low-temperature magnetic properties. Phys Chem Earth 28:669–679.

34. Jacobs IS (1963) Metamagnetism of siderite (FeCO3). J Appl Phys 34:1106–1107.

35. Newell AJ (2005) A high-precision model of first-order reversal curve (FORC) functions for single-domain ferromagnets with uniaxial anisotropy. Geochem Geophys Geosyst 6:Q05010, 10.1029/2004GC000877.

36. Ebel DS, Grossman L (2005) Spinel-bearing spherules condensed from the Chicxulub impact-vapor plume. Geology 33:293–296.

37. Johnson B,Melosh H (2012) Formation of spherules in impact produced vapor plumes. Icarus 217:416–430.

38. Petersen N, Vondobeneck T, Vali H (1986) Fossil bacterial magnetite in deep-sea sediments from the South Atlantic Ocean. Nature 320:611–615.

39. Harrison RJ, Feinberg JM (2008) FORCinel: An improved algorithm for calculating first-order reversal curve distributions using locally weighted regression smoothing. Geochem Geophys Geosyst 9:Q05016, 10.1029/2008GC001987.

Figure Captions

Figure A2.1. (A) Location map for Ancora, Clayton,Wilson Lake, and Bass River drill sites on the Atlantic Coastal Plain of New Jersey. (B) Stratigraphic plots of sand percentage, bulk carbonate δ13C, saturation magnetization (Ms), and ratio of saturation remanence to saturation magnetization (Mr/Ms) for the interval in the Ancora cored section with the CIE (interval from ~171.5 m to ~165.5 m) with low δ13C values (5). Positions are indicated of the CIE sample AN560.1 and the pre-CIE (Late Paleocene) sample AN567.7 from the Ancora core.

Figure A2.2. TFT size and shape distributions calculated by back-field demagnetization (BFD) curves for (A) AN560.1 CIE bulk sediment, where a star marks the distribution mode. (B) Sample of laboratory cultured magnetotactic bacteria (MTB) MV-1 with TEM image of untreated freeze-dried MV-1 (12); a star marks the distribution mode that corresponds to individual magnetosome particles. (C) AN560.1 CIE magnetic extract residue, where a star marks the distribution mode. (D) AN560.1 CIE magnetic extract in its in situ state, derived by subtraction. Light blue lines delineate SP (superparamagnetic), SD (stable single domain), and MD (multidomain) regions in this parameter space (22). Color scale represents linear increments of probability density.

Figure A2.3. Comparison of back-field demagnetization (BFD) curves at 300 K on high temperature (HT)-VSM (red) and low temperature (LT)-VSM (blue) for CIE bulk sediment samples AN560.1 (A and B) andWLb357.3 (C and D). BFD curve extrapolations (black dashed lines; A and C) were performed by the inverse of the 1.5-T saturation remanences. Comparisons of BFD remanences at 300 K measured with HT VSM vs. LT-VSM for the same demagnetization steps are shown in B for AN560.1, which has poor agreement, and in D for WLb357.3, which has good agreement.

Figure A2.4. Thermal fluctuation tomography (TFT) size and shape distributions for carbon isotope excursion (CIE) bulk sediment WLb357.3 calculated by back-field demagnetization (BFD) curves from (A) 300 K to 640 K and (B) 120 K to 640 K. Star, superparamagnetic (SP), single domain (SD), and multidomain (MD) as in Fig. A2.2.

Figure A2.5. Linearly normalized (to SIRMRT) FC–ZFC and SIRMRT LTD curves for (A) AN560.1 CIE magnetic extract; (B) untreated freeze-dried cultured MTB sample of MV-1; (C) AN560.1 CIE bulk sediment; (D) WLb357.3 CIE bulk sediment; (E) AN560.1 CIE magnetic extract residue; and (F) AN567.7 late Paleocene (pre-CIE) bulk sediment.

Figure A2.6. FORC diagrams with inserts showing their coercivity (horizontal, Hu = 0) profiles, with peak coercivities marked by red bars. (A) AN560.1 CIE bulk sediment; (B) stacked (n = 9) HiResFORC for AN560.1 CIE bulk sediment; (C) stacked (n = 9) HiResFORC for magnetic extract residue; (D) single HiResFORC for AN560.1 CIE

magnetic extract; (E) AN560.1 magnetic extract in its in situ state, derived by subtraction of (C) from (B); and (F) untreated freeze-dried cultured MTB sample of MV-1. All of the FORC diagrams share the same linear color scale on the right with 0 near the transition from white to light blue.

Figure A2.7. FMR results of MTB data (12), CIE data (9), and Martian meteorite ALH84001 data (14) plotted in δB_{FWHM}-A parameter space (13). TEM images show the ferromagnetic particles of CIE clay (5) and untreated freeze-dried mnm18 (12) that consists of two particle strings and isolated free particles (expected for SDS-treated and ultrasonicated sample). Zones of different magnetic origin are revised based on our assessment of all the plotted data.

Figure A2.1

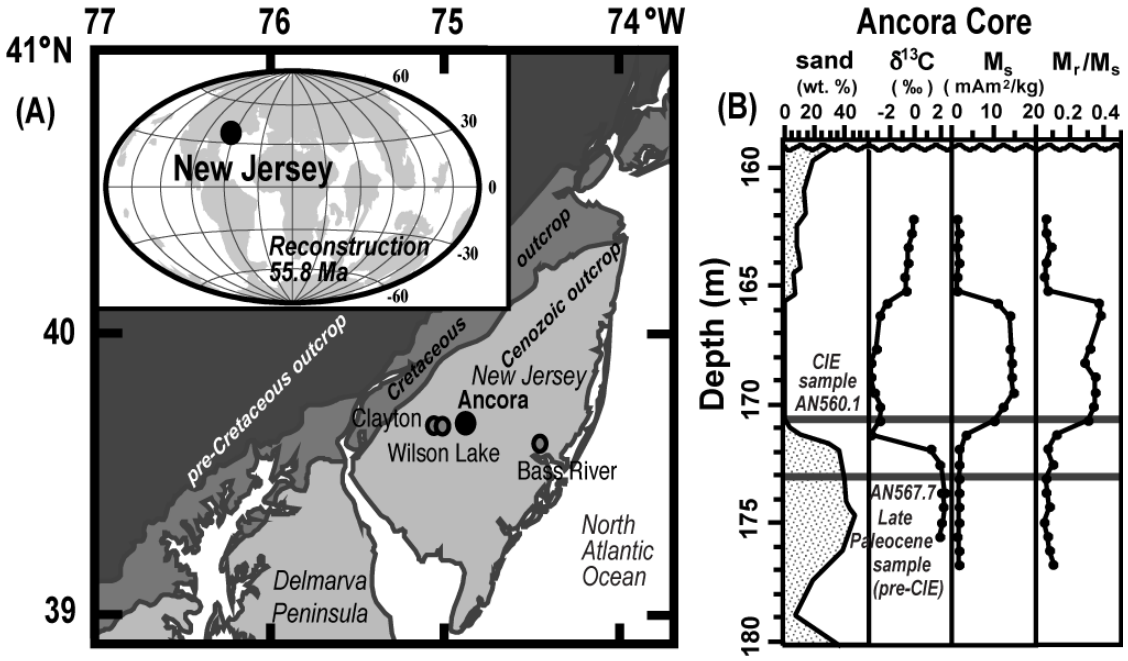
77
76
75
74°W
41°N
(A)
40
39
New Jersey
Reconstruction
55.8 Ma
60
30
0
-30
-60
pre-Cretaceous outcrop
Cretaceous outcrop
Cenozoic outcrop
New Jersey
Ancora
Clayton
Wilson Lake
Bass River
North Atlantic Ocean
Delmarva Peninsula
Ancora Core
(B)
sand (wt. %)
δ13C (‰)
Ms (mAm2/kg)
Mr/Ms
Depth (m)
CIE sample AN560.1
AN567.7 Late Paleocene sample (pre-CIE)

Figure A2.2

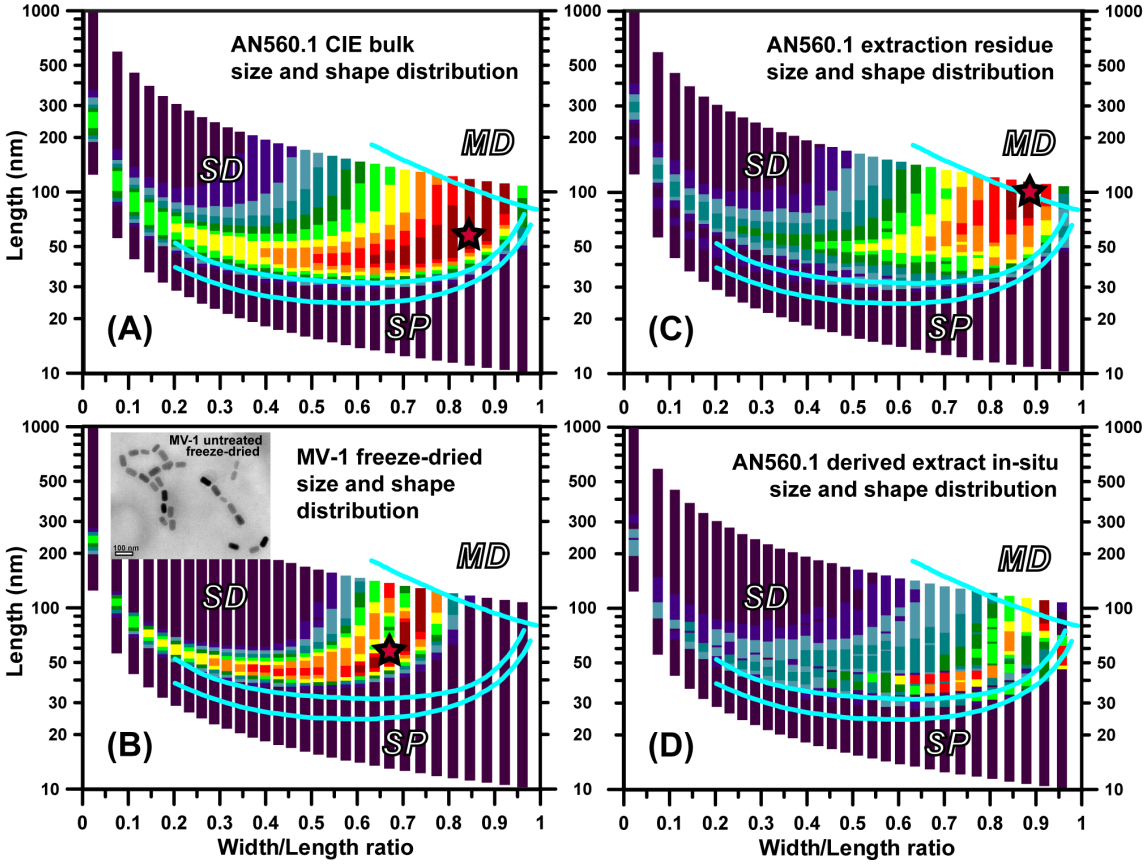
AN560.1 CIE bulk
size and shape distribution
(A)
AN560.1 extraction residue
size and shape distribution
(C)
MV-1 untreated
freeze-dried
MV-1 freeze-dried
size and shape
distribution
(B)
AN560.1 derived extract in-situ
size and shape distribution
(D)
SD
MD
SP
Length (nm)
Width/Length ratio

Figure A2.3

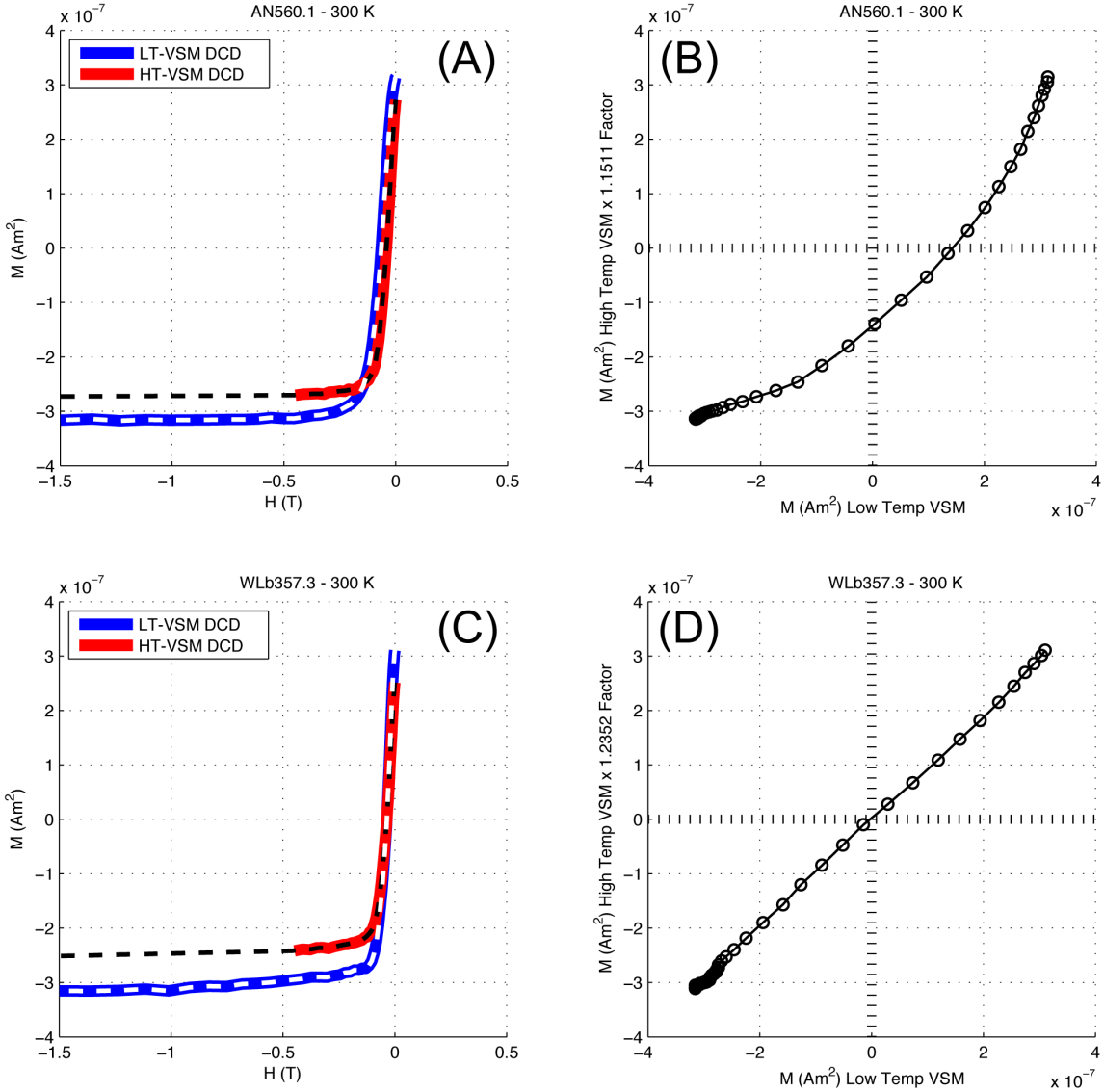
AN560.1 - 300 K
(A)
LT-VSM DCD
HT-VSM DCD
M (Am^2)
H (T)
x 10^{-7}
(B)
M (Am^2) High Temp VSM x 1.1511 Factor
M (Am^2) Low Temp VSM
WLb357.3 - 300 K
(C)
(D)
M (Am^2) High Temp VSM x 1.2352 Factor

Figure A2.4

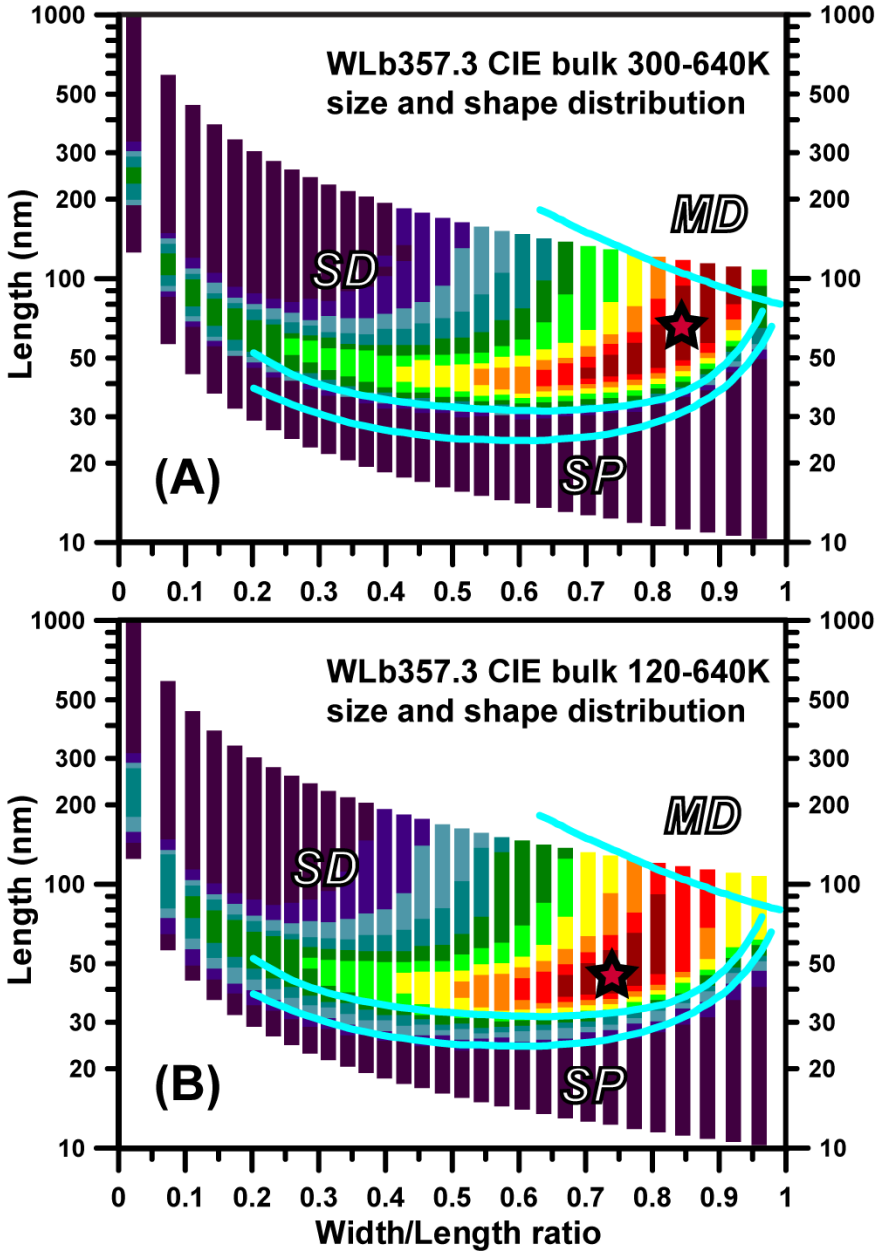
WLb357.3 CIE bulk 300-640K
size and shape distribution
MD
SD
SP
(A)
WLb357.3 CIE bulk 120-640K
size and shape distribution
MD
SD
SP
(B)
Length (nm)
Width/Length ratio
1000
500
300
200
100
50
30
20
10
0
0.1
0.2
0.3
0.4
0.5
0.6
0.7
0.8
0.9
1

Figure A2.5

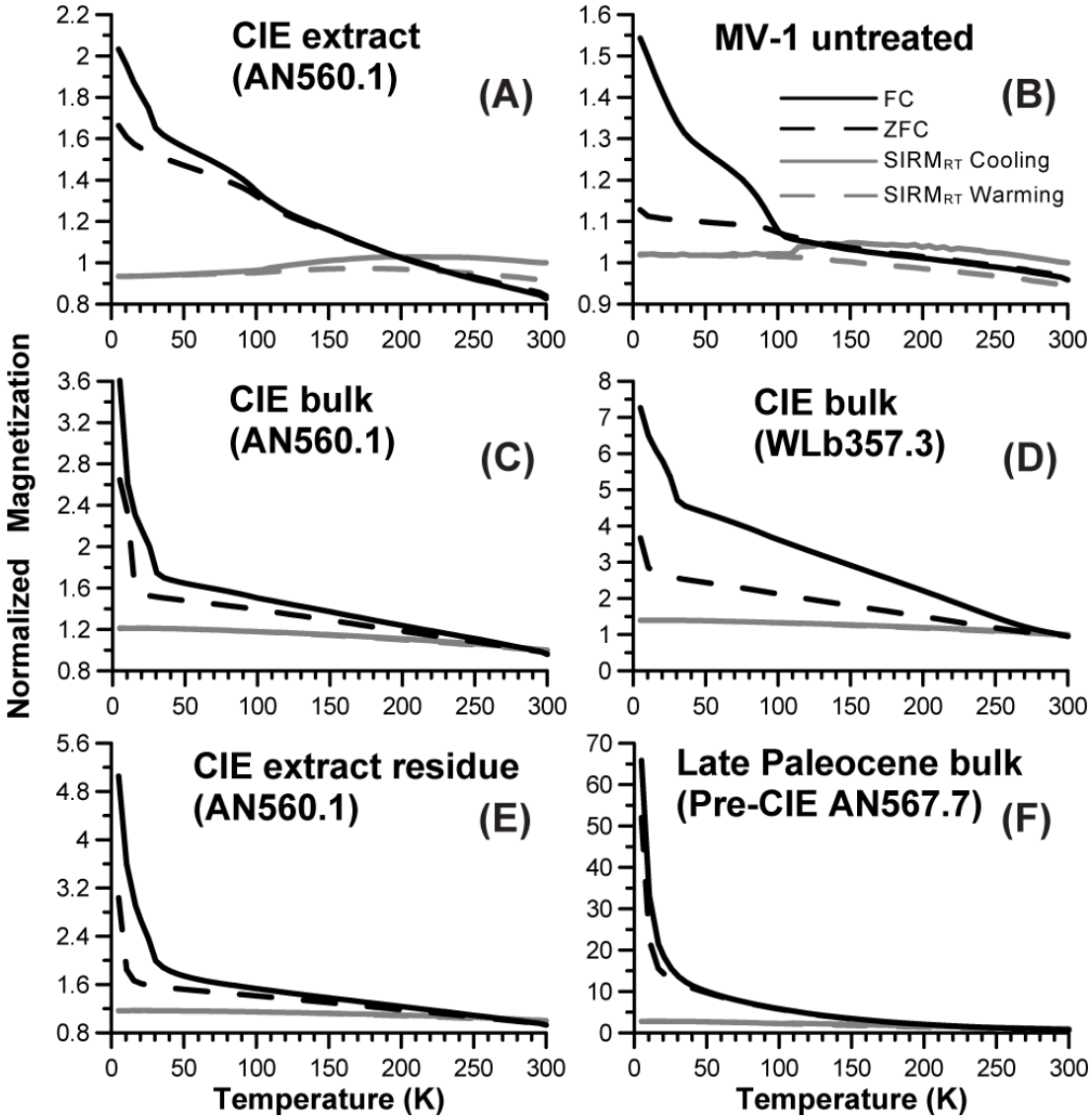
CIE extract
(AN560.1)
(A)
MV-1 untreated
(B)
FC
ZFC
SIRM$_{RT}$ Cooling
SIRM$_{RT}$ Warming
CIE bulk
(AN560.1)
(C)
CIE bulk
(WLb357.3)
(D)
CIE extract residue
(AN560.1)
(E)
Late Paleocene bulk
(Pre-CIE AN567.7)
(F)
Normalized Magnetization
Temperature (K)
Temperature (K)

Figure A2.6

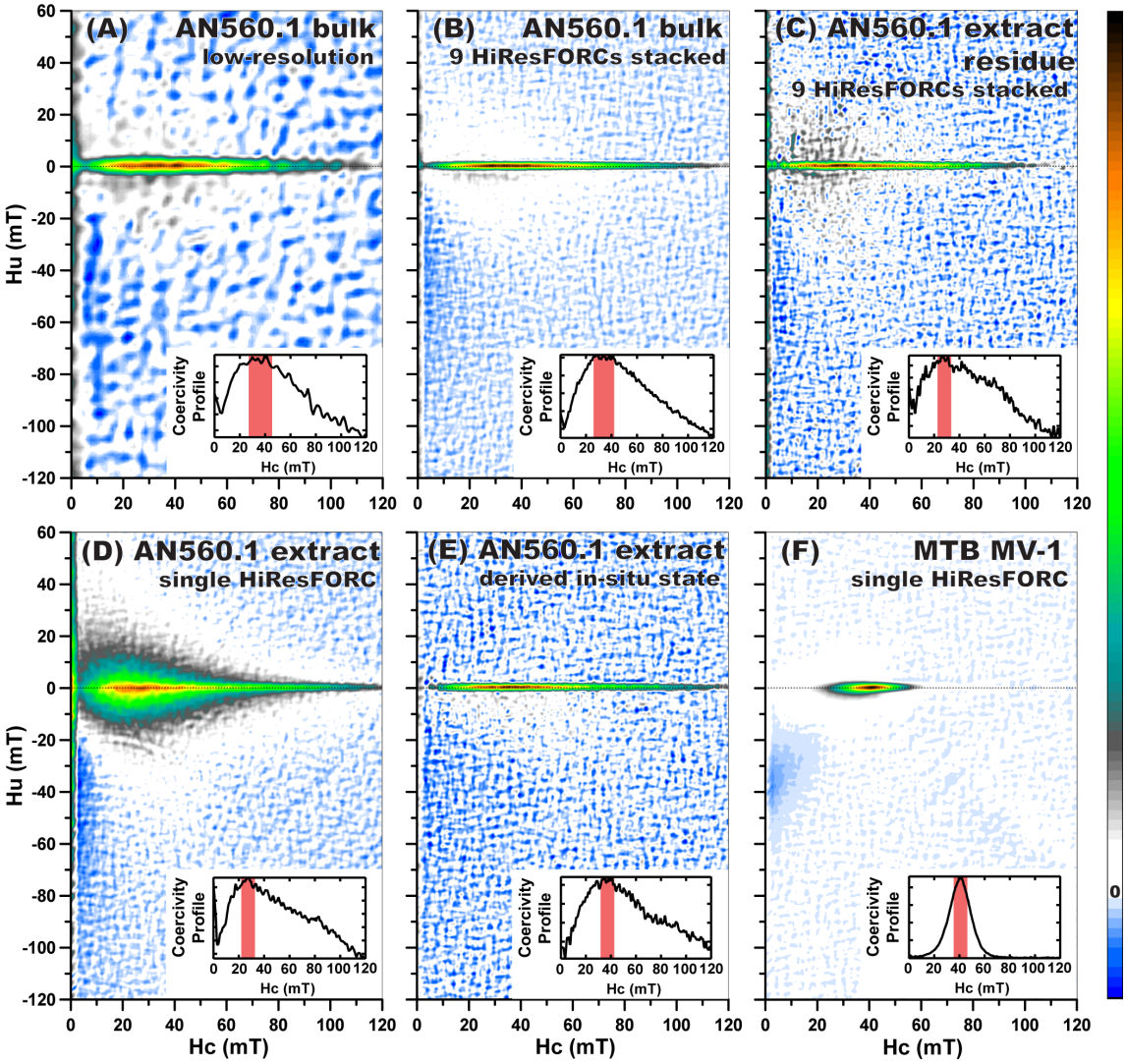
(A) AN560.1 bulk
low-resolution
(B) AN560.1 bulk
9 HiResFORCs stacked
(C) AN560.1 extract
residue
9 HiResFORCs stacked
(D) AN560.1 extract
single HiResFORC
(E) AN560.1 extract
derived in-situ state
(F) MTB MV-1
single HiResFORC
Coercivity Profile
Hc (mT)
Hu (mT)
0

Figure A2.7

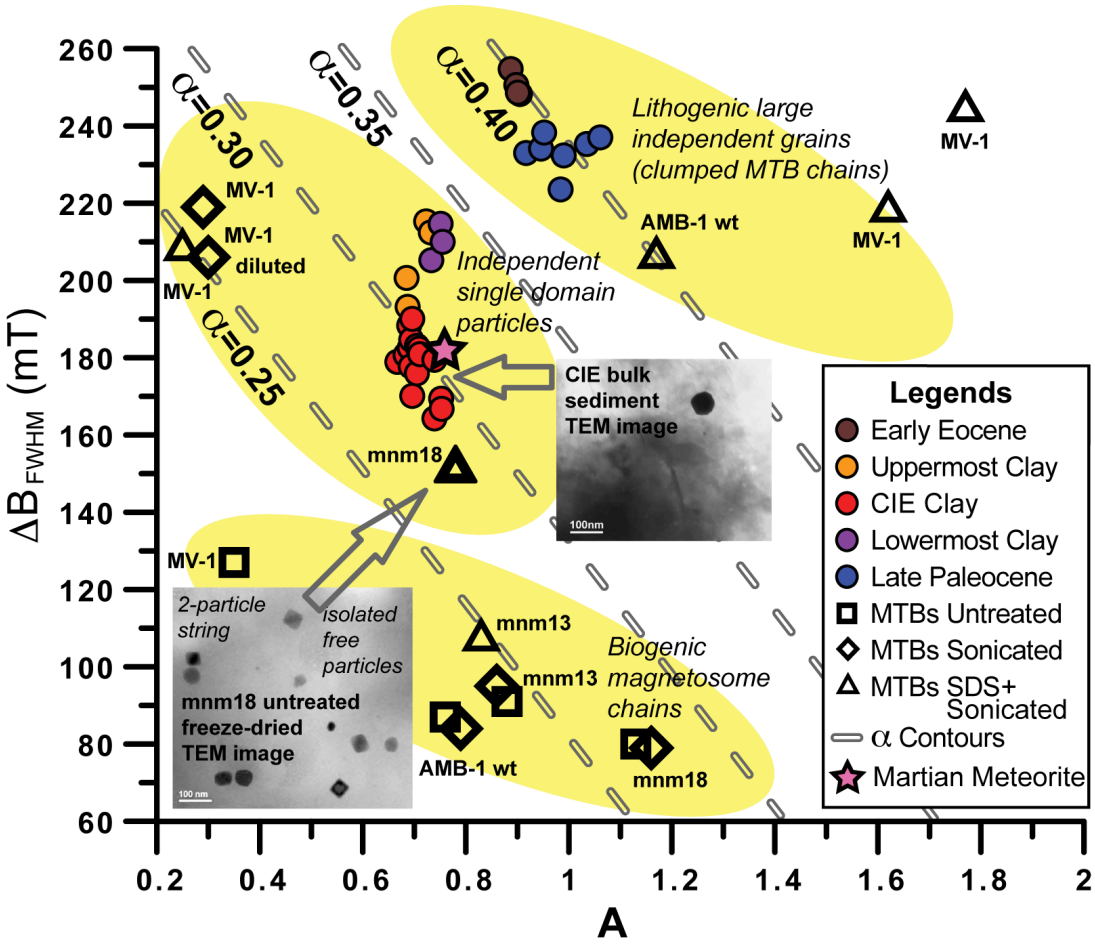
ΔB FWHM (mT)
A
α=0.30
α=0.35
α=0.40
α=0.25
Lithogenic large independent grains (clumped MTB chains)
Independent single domain particles
Biogenic magnetosome chains
MV-1
MV-1 diluted
AMB-1 wt
mnm18
mnm13
CIE bulk sediment TEM image
2-particle string
isolated free particles
mnm18 untreated freeze-dried TEM image
Legends
Early Eocene
Uppermost Clay
CIE Clay
Lowermost Clay
Late Paleocene
MTBs Untreated
MTBs Sonicated
MTBs SDS+ Sonicated
α Contours
Martian Meteorite

Acknowledgment of Previous Publications

Chapter 1 of this dissertation was previously published as:

Kent, D. V., H. Wang, and P. Rochette (2010), Equatorial paleosecular variation of the geomagnetic field from 0-3 Ma lavas from the Galapagos Islands, *Physics of the Earth and Planetary Interiors*, *183*, 404-412.

Chapter 2 of this dissertation was previously published as:

Wang, H. and D. V. Kent, (2013), A Paleointensity Technique for Multidomain Igneous Rocks, *Geochemistry Geophysics Geosystems, 14*, 4195-4213, doi: 10.1002/ggge.20248

Chapter A2 of this dissertation was previously published as:

Wang, H., D. V. Kent, and M. J. Jackson (2013), Evidence for abundant isolated magnetic nanoparticles at the Paleocene-Eocene boundary, *Proceedings of the National Academy of Sciences, USA*, *110*, 425-430.